18th Numerical Towing Tank Symposium

28-30 September 2015

Cortona/Italy

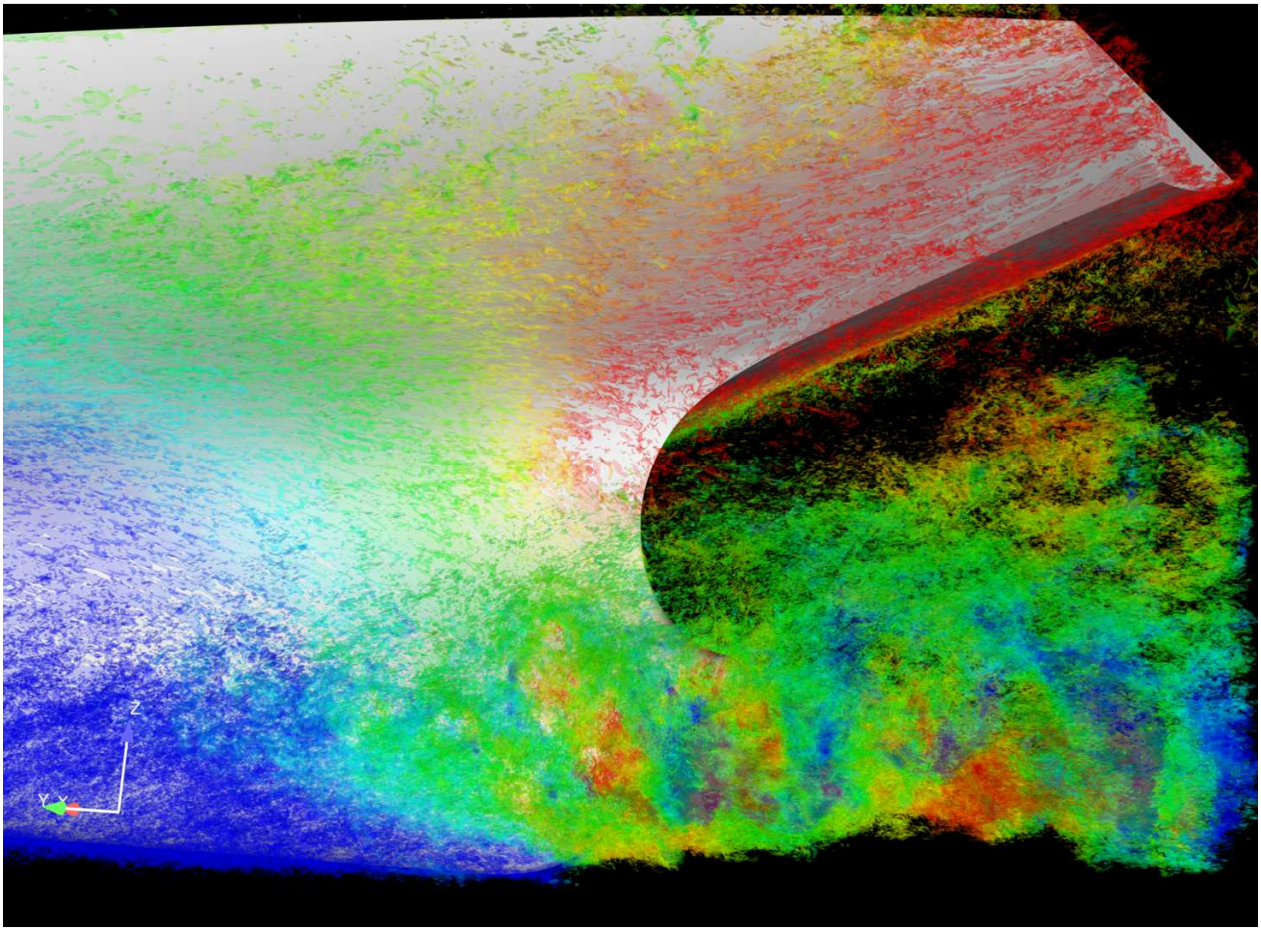

Volker Bertram, Emilio F. Campana (Eds.)

TuTech
TUHH Technologie GmbH

Sponsored by

CD-Adapco
www.cd-adapco.com

CNR INSEAN
www.insean.cnr.it

DNV GL
www.dnvgl.com

Cover image source: Tatsuo Nishikawa (SRIJ)

Index of Papers

Jarle Andre Kramer, Sverre Steen
Importance of the Free Surface for the Drift-Induced Forces on a Ship-Like Foil

Christian Krüger, Nikolai Kornev
Implementation of the Ffowcs Williams-Hawkings Equations into OpenFOAM for Hydro-Acoustic Ship Evaluation

Alex Kruijswijk
CFD Prediction of Shallow Water Performance of a Trailing Suction Hopper Dredger Validated with Full-Scale Measurements

Da-Qing Li, Jan Hallander, Roger Karlsson
Progress in Prediction of Pressure Pulses and Underwater Radiated Noise Induced by Propeller with Pressure-Side Cavitation

Thomas Lloyd, Artur Lidtke, Douwe Rijpkema, Erik van Wijngaarden, Stephen Turnock, Victor Humphrey
Using the FW-H equation for hydroacoustics of propellers

Benoit Mallol, Barbara D'Aure
Adaptive Mesh Technology in Marine CFD Simulations

Laura Marimon-Giovannetti, Joseph Banks, Stephen Turnock, Stephen Boyd
Developing Tools for Assessing Bend-Twist Coupled Foils

Sankar Menon CP, Rickard Bensow, Claes Eskilsson
Interface Capturing Methods on DTC Post-Panamax Hull

Masafumi Okazaki, Yoshihisa Okada, Kenta Katayama, Taro Kajihama
Propeller Particulars and Scale Effect Analysis of ECO-Cap by CFD

Riccardo Pellegrini, Cecilia Leotardi, Umberto Iemma, Emilio Campana, Matteo Diez
Structural and Hydrodynamic Characterization of a NACA 0009 Hydrofoil by Finite Elements

Alessio Pistidda, Harald Ottens
Numerical Investigation on the Use of the Euler Overlay Method for a Floating Structure

Dmitriy Ponkratov
CFD Cavitation Model Parameters and Their Influence on Simulation Case

Yoann Robert, Alban Leroyer, Jeroen Wackers, Michel Visonneau, Patrick Queutey
Time-Splitting Procedure for the Resolution of the Volume Fraction for Unsteady Flows

Nobuaki Sakamoto, Hikaru Kamiirisa
CFD Prediction of Unsteady Cavitation Extent on Marine Propellers and its Application to Ship Radiated Noise

Lars-Uve Schrader
Drag Reduction for Ships Inspired by Dolphins

Keun Woo Shin, Poul Andersen
CFD Analysis of Cascade Effects in Marine Propellers with Trailing Edge Modification

Håkon Strandenes, Audun Yrke, Lennard Bösch, Christian Kosacki, Bjørnar Pettersen, Helge Andersson
Recent DNS, LES and Experiments on a Cylinder with Fairings

Vuko Vukcevic, Hrvoje Jasak, Sime Malenica
Assessment of Higher-Order Forces on a Vertical Cylinder with Decomposition Model based on SWENSE Approach

Jeroen Wackers, Ganbo Deng, Emmanuel Guilmineau, Alban Leroyer, Patrick Queutey, Michel Visonneau
What is happening around the KVLCC2?

Michał Wawrzusiszyn, Tomasz Bugalski, Paweł Hoffmann
Numerical Simulations of Ship Hull-Propeller Interaction Phenomena

Gabriel Weymouth
Lily Pad: Towards Real-time Interactive Computational Fluid Dynamics

Stefano Zaghi, Cecilia Leotardi, Roberto Muscari, Giulio Dubbioso, Riccardo Broglia
RANS Hydrodynamic Characterization of a USV SWATH Configuration Including Design Optimization

Oleksandr Zverkhovskyi, Maarten Kerkvliet, Arjan Lampe, Guilherme Vaz, Tom van Terwisga
Numerical Study on Air Cavity Flows

CFD Simulations of the Japan Bulk Carrier Test Case

Jennie Andersson[1], Marko Hyensjö[2], Arash Eslamdoost & Rickard Bensow

Department of Shipping and Marine Technology, Chalmers University of Technology, Gothenburg, Sweden
[2]Rolls-Royce Hydrodymanic Research Centre, Kristinehamn, Sweden
[1]jennie.andersson@chalmers.se

This computational fluid dynamics (CFD) validation study is performed as a foundation for further studies with focus on the interaction effects between propulsor and hull. To be able to study the interaction effects, an appropriate CFD methodology need to be established and validated for a bare hull, for the propulsion unit and for the combined system, a self-propelled hull.

The work to validate a CFD model is initiated through the use of the JBC, Japan Bulk Carrier, open test case. The JBC test case is developed for the 2015 workshop on CFD in Ship Hydrodynamics. The tested JBC only exists in model scale with scale factor 1:40 (L_{PP} = 7 m). Model ship speed is 1.179 m/s, corresponding to Fn = 0.142 and 14.5 kn, only calm water conditions are tested. There are two variants of the hull, with and without an energy saving device, within this study the one without is used. Test data used for validation of the CFD results are from towing tank experiments at NMRI. The aim of further studies is to study propulsor hull interaction in full scale, but since detailed test data in full scale is limited, all computations will be performed in model scale.

The commercial CFD package STAR-CCM+, a finite volume method solver, is employed for all studies. STAR-CCM+ is a general purpose CFD code used for a wide variety of applications. It solves the conservation equations for momentum and mass, turbulence quantities and volume fraction of water using a segregated solver based on the SIMPLE-algorithm. A 2nd order upwind discretization scheme in space is used. It is of interest to study how a general purpose code can perform for detailed ship hydrodynamic analyses and which limitations that could be identified.

1. Bare hull simulation

For this case, simulations are performed with free surface and the hull free to heave and pitch, but only with a half hull since symmetrical conditions are assumed. Focus has been on construction of a computational grid and selection of turbulence model, suitable for the purpose of wave pattern prediction, detailed studies of the flow field at the stern and overall resistance prediction.

The free surface is modelled using the Volume-of-fluid (VOF) method, implying that the domain is consisting of one fluid whose properties varies according to the volume fraction of water/air. The convective term is discretized using the High resolution interface capturing (HRIC) scheme [1]. The heave and pitch motion is modelled with the *DFBI Equilibrium* model, implemented in STAR-CCM+ v10.4; the model moves the body stepwise to obtain balanced forces and moments. Initially, effort was put into obtaining results using a model where the motion of the hull is physically correct modelled (*DFBI Free motion*). However, satisfying results could not be obtained using this model due to large oscillations in the results, similar problems have earlier been noticed [2]. Since a steady state solution is sought and time accuracy is not of importance, a 1st order implicit scheme is used for time integration, the time step is 0.04s.

The domain size in [X,Y,Z] is given by [-3.5L_{PP} : 2.5L_{PP}, 0:2L_{PP}, -1.5L_{PP}:1L_{PP}] and where L_{PP} is the length between perpendiculars for the model ship, [0,0,0] at mid-ship. An inlet velocity boundary condition is specified at the inlet, upper, lower and outer sides of the domain. At the outlet a static pressure is specified. The water surface level is initialized as the declared draft of the hull (0.4125 m above the keel). A symmetry plane is specified at mid-ship.

The computational grids are generated using STAR-CCM+. A trimmed hexahedral grid (polyhedral cells) with prism layers along the walls is used. A mesh sensitivity study consisting of three grids is performed and the same mesh topology is applied for all grids and the level of refinement is modified through a characteristic cell size. Volumetric controls and anisotropic refinements are used to refine the

region close to the hull, the wake and the water surface in general, see Figure 1 for the resulting mesh structure.

Within this study, a comparison is made between resolved boundary layers down to $y+ < 1$ and application of wall functions. For the resolved boundary layers (denoted $y+ < 1$) 31 prism layers with a near wall cell height of 0.02 mm is applied. When applying a wall function model 8 prism layers are used, with a near wall cell height of 4.4 mm, corresponding to $y+ > 30$ over the hull surface. The prism layers are kept constant in height for the different mesh refinements. The coarse, medium and fine grids had $3.3 \cdot 10^6$, $4.8 \cdot 10^6$ and $6.8 \cdot 10^6$ cells respectively for $y+ > 30$, and $7.1 \cdot 10^6$, $9.9 \cdot 10^6$ and $13.9 \cdot 10^6$ for $y+ < 1$, implying a ~100 % increase in mesh count when resolving the boundary layers.

Suitable turbulence models, for the investigation of ship hydrodynamics are thoroughly discussed in [3]. The main conclusion is that linear eddy viscosity models, without ad-hoc rotation correction, in general under estimate the intensity of the bilge vortex. Best performance is seen for various anisotropic turbulence models, such as explicit algebraic stress models (EASM) [4], not yet available in STAR-CCM+, and Reynolds stress models (RSM). The Elliptic-Blending RSM [4] and the k-ω SST model [6] with curvature correction (k-ω SST-CC) [7] are applied within this study.

First, the overall wave pattern, for CFD results with k-ω SST-CC, is compared to test. For all grid refinements, and for both $y+ > 30$ and $y+ < 1$, the results are similar and in good accordance with test data; see Figure 2 for the fine grid, $y+ < 1$, wave profile along the hull and a wave cut at $y/L_{PP} = -0.1043$. The wave elevations are very small, but the grid surface resolution and HRIC scheme capture the wave profile, except a slightly underpredicted wave elevation close to stern. Applying RSM, a converged solution has not yet been obtained, large disturbances of the water surface are observed already upstream the hull. Instead, to be able to compare the different turbulence models, a model with the free water surface replaced by a symmetry plane (denoted double model) and the motion of the hull neglected (the sinkage and trim motions of the hull are very low) is constructed.

Comparing the full model including free surface and the double model, for both cases applying the finest grid and $y+ < 1$, the flow field at the stern are very similar. The total resistance is 0.47 N higher for the free surface model, which could be seen as the wave resistance and added resistance due to different sinkage and trim; this resistance discrepancy is only 1.4 % of the total resistance for the free surface model. This confirms the possibility of studying the relative differences between the turbulence models by applying a double model assumption for the JBC test case.

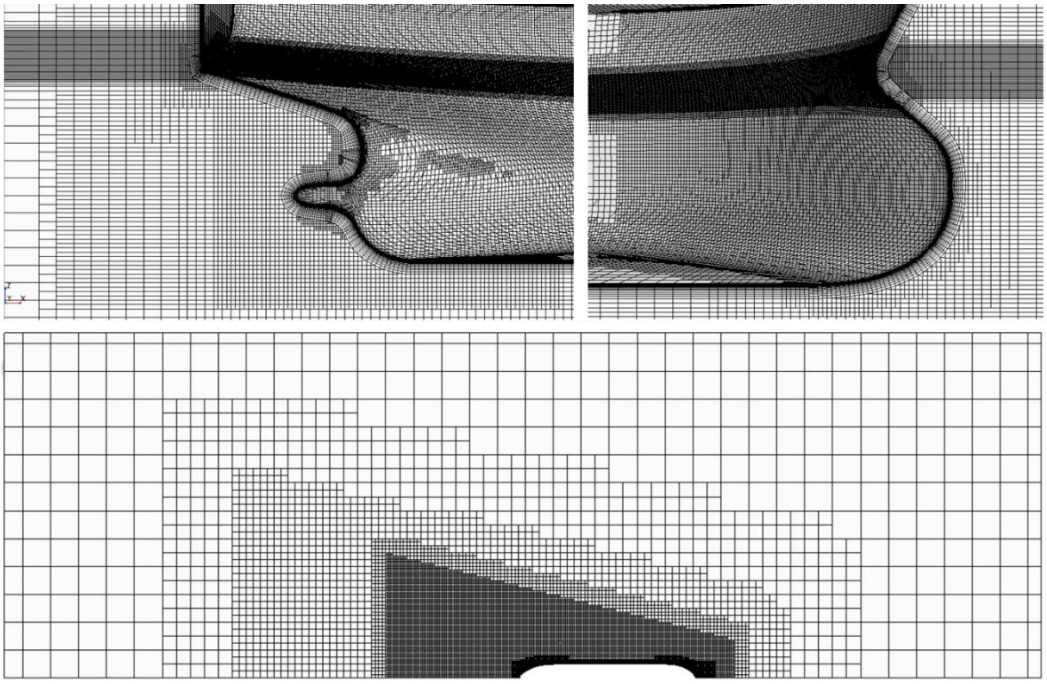

Figure 1: The structure of the coarse mesh with resolved boundary layers around the JBC hull, showing refinements near the hull, for the water surface and for the wake

The axial velocity field prediction at the stern, for the free surface model using k-ω SST-CC and the fine grid, with y+ < 1 and y+ > 30 respectively, is compared to test data for a plane located at $x/L_{pp} = 0.9625$ in Figure 3. It is clear that the wall function model fails to accurately predict the hook shape of the bilge vortex. Different prism layer configurations, fulfilling y+ > 30, have been investigated but without success. The simulations on the y+ < 1 grid predict the hook shape of the bilge vortex more accurately and is also in better accordance with other test data available further downstream.

The axial velocity, on the same plane as shown in Figure 3, is shown for k-ω SST-CC, RSM and k-ω SST, from the double model results in Figure 4. The flow field is relatively similar for k-ω SST-CC and the RSM model while the standard k-ω SST model predict a less intense bilge vortex, in a similar manner as seen for several contributions applying a linear eddy viscosity model in the 2010 workshop on ship hydrodynamics [3].

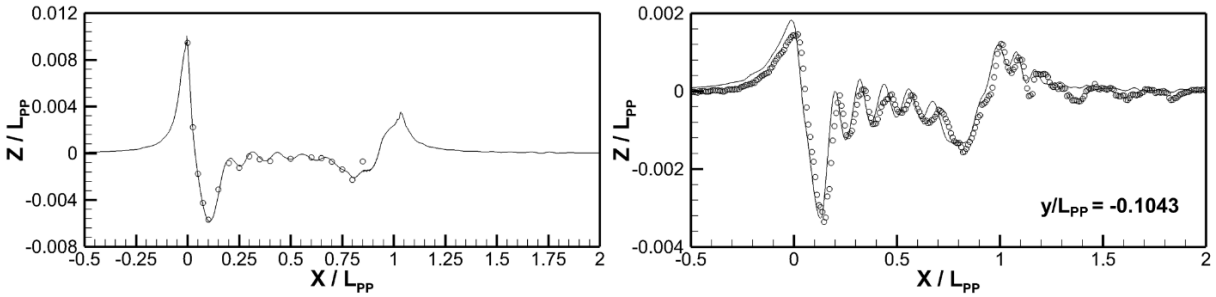

Figure 2: Wave profile along hull (left) and wave cut at $y/L_{PP} = -0.1043$ (right) for the fine grid, y+ < 1. CFD results (line) compared to test data (circles).

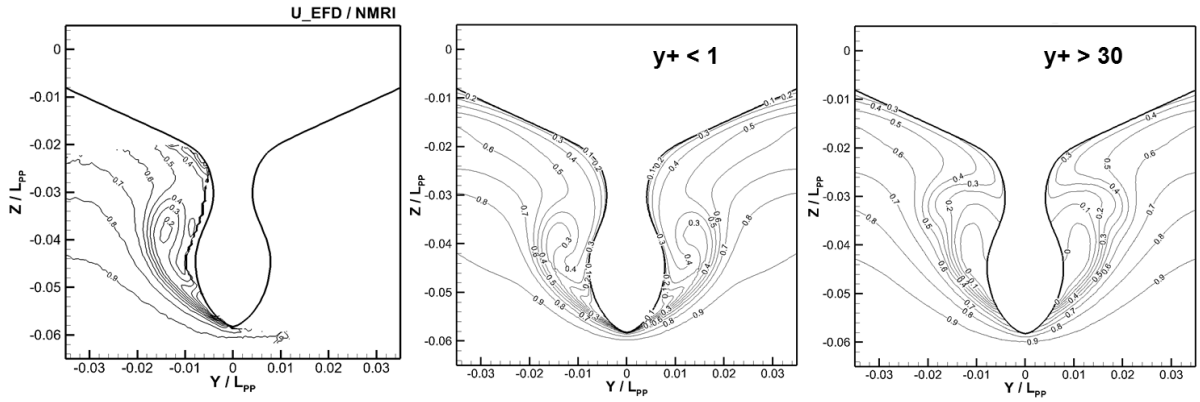

Figure 3: Mean axial velocity at $x/L_{pp} = 0.9625$. CFD results (k-ω SST-CC, fine grid, y+ < 1) compared to test.

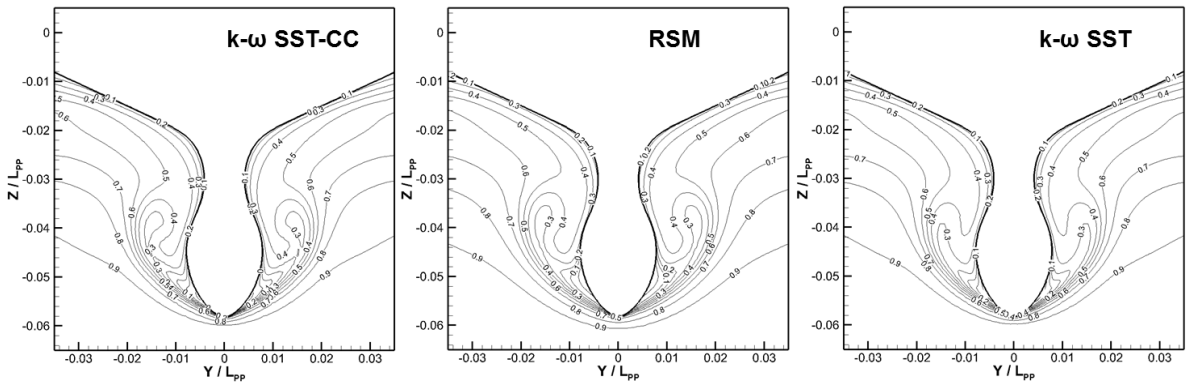

Figure 4: Mean axial velocity at $x/L_{pp} = 0.9625$. Double model CFD results (fine grid, y+ < 1) for different turbulence models.

At last, the hull resistance, sinkage and trim predictions for the free surface models, are compared to test in Table 1. The total resistance is clearly underpredicted by all models using k-ω SST-CC, while RSM predict the resistance more accurately. Note however that the RSM resistance prediction is based on a double model and that ~1.4 % is assumed to be added due to wave resistance and motion. The difference in resistance between the turbulence models can mainly be deduced from an increased wall shear stress, evenly distributed over the hull surface. Interesting to note is that the resistance prediction is in better accordance with test data for the wall function grids, with an average deviation of ~2-3 %. It has further been observed that the use of curvature correction has a minor influence on the resistance. Different sensitivity studies are conducted for the boundary layer mesh; it could be observed that a reduction of the height of the near wall cell so that $y+_{max} < 0.2$ implies a ~3 % increased resistance.

For the free surface model resistance prediction, no clear mesh convergence can be observed, but a slightly larger difference is seen between the coarse and medium grids than between the medium and fine grids. Neither for sinkage and trim can a clear mesh convergence be observed as the grids are refined. The average difference to test data is 4.2% and 4.0% for sinkage and trim respectively, compared to the mean deviation for the KVLCC2 test case from the 2010 workshop [3] of -33.3% and 7.4% respectively, these figures are in a clearly better agreement with measurements.

Table 1: Resistance coefficients, sinkage and trim compared to test. Relative differences included.

	Test	***Coarse, y+<1 VOF***	***Medium, y+<1 VOF***	***Fine, y+<1 VOF***	***Fine, y+<1 Sym.***	***Fine, y+<1 Sym. RSM***
$C_T \cdot 10^3$	4.289	3.987/*-7.0%*	3.967/*-7.5%*	3.963/*-7.6%*	3.908/*-8.9%*	4.289/*0.0%*
$C_F \cdot 10^3$	N/A	2.910	2.848	2.901	2.910	3.244
$C_P \cdot 10^3$	N/A	1.077	1.119	1.062	0.998	1.045
Sinkage [$\%L_{PP}$], upward positive	-0.086	-0.090/*4.3%*	-0.088/*1.8%*	-0.092/*6.6%*	N/A	N/A
Trim [$\%L_{PP}$], bow up positive	-0.180	-0.186/*3.6%*	-0.188/*4.6%*	-0.187/*3.7%*	N/A	N/A

These last results imply that currently there is no established method that both provides an accurate prediction of the stern wake as well as the resistance except from the Reynolds stress model in STAR-CCM+. Applying RSM is time consuming, an estimation based on the current case is ~2.5 times the k-ω SST simulation time, it requires a very high quality mesh and, as described above, is not straight-forward to use together with VOF.

2. Propeller open water simulation

In the open water test the inflow to the propeller is symmetrical which implies that it is possible to perform steady state simulations with only one propeller blade and utilize periodic interfaces. The grid created for one blade can then be multiplied to form a full propeller. The propeller domain is embedded in a larger stationary domain in the open water simulations, similarly to the setup for self-propulsion simulations. Mixing plane interfaces are applied between the regions.

The provided open water characteristics covers J =0.1-0.8 (Δ=0.05) and these operating conditions are simulated. The propeller rotation rate is set to 17 rps, while the advance velocity is varied to meet requested advance ratio, implying that the Reynolds number during test ($4 \cdot 10^5$) is met with -2.5% to +3.6%. The advance velocity is specified on the inlet boundary ($5D_P$ upstream propeller) and a static pressure is set on the outlet boundary ($6D_P$ downstream propeller). The far field outer boundary ($7D_P$ in diameter) is modelled as a symmetry plane. The inlet turbulence intensity is set to 1 % and $\mu_T/\mu = 10$, but sensitivity studies showed minor influence on the results of these boundary conditions.

The computational grid for the propeller domain consists of polyhedral cells with prism layers along wall surfaces. Polyhedral cells are used instead of the trimmed cells due to the complex geometry with high curvature. The resulting mesh structure is shown in Figure 5, a close up of the trailing edge is also shown. A sensitivity study to the leading and trailing edge resolution was conducted, but reducing the cell surface size to 50 % and 25 % respectively, did not significantly modify the overall results (the

efficiency increased with 0.1 %-points at J=0.6). The general mesh resolution was also studied and considered sufficient (a reduction of the average cell size with 50 %, implied a difference in efficiency of <0.01 %-points). The stationary domain consists of trimmed polyhedral cells. Both wall function grids (y+ > 30) and grids resolving the boundary layers (y+ < 1) have been investigated, for these 6 respectively 15 prism layers with a near wall cell height of 0.4 mm resp. 0.01 mm are applied. The wall function grid has $1.3 \cdot 10^6$ cells per propeller blade whereas the y+ < 1 grid has $2.1 \cdot 10^6$ cells.

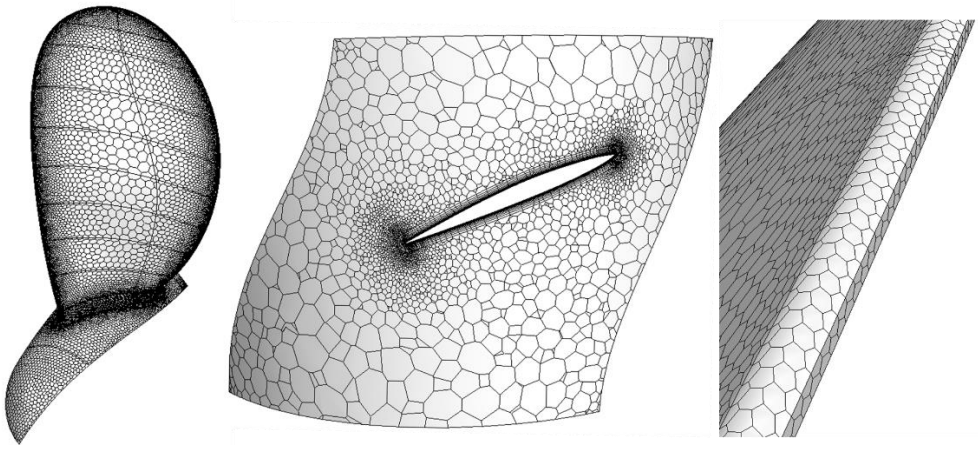

Figure 5: Structure of the y+ < 1 mesh. Surface grid, a section at 0.7R a close up of the trailing edge shown.

The CFD results, for the y+ > 30 and y+ < 1 grids, applying the k-ω SST turbulence model are compared to open water test data in Figure 6. Here the k-ω SST-CC model results are not presented, as it did not influence the overall results significantly (for instance, the efficiency increased with 0.2 %-points at J=0.6). Both CFD models are underpredicting the measured efficiency. For the y+<1 grid, which is most close to test data, this is a result of an underpredicted thrust and a less underpredicted torque. At J=0.6 the calculated thrust, torque and efficiency differs with -5.2 %, -0.7 % and -4.4 % compared to measured values, respectively.

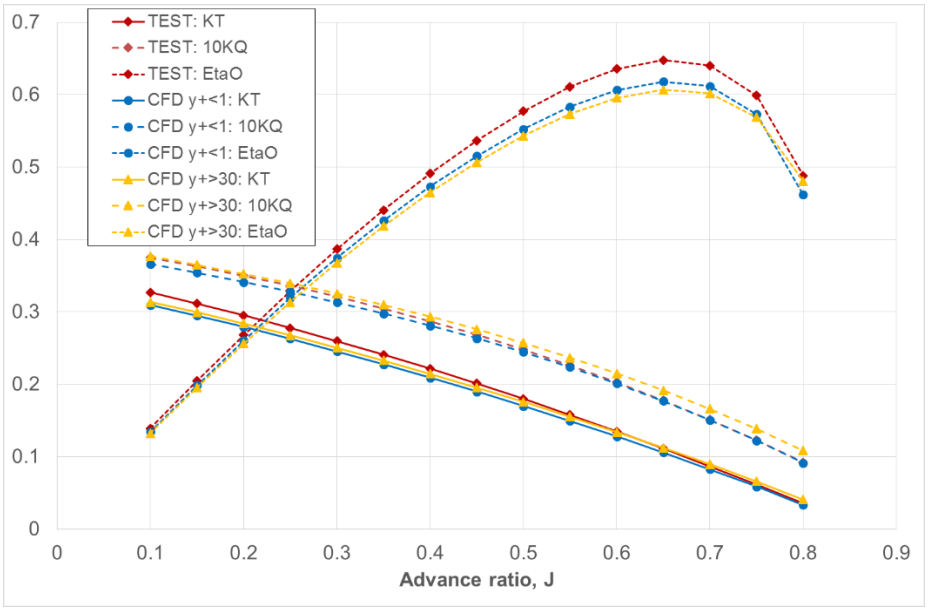

Figure 6: K_T, K_Q and η_O from open water test and CFD results.

Summing up, the differences between the simulation results and open water test data are considered to be slightly higher than expected. Since detailed knowledge about the test setup is not available, it has not been considered meaningful to further investigate the reason behind the differences. However, one possible reason is that the CFD model wrongly assumes that the boundary layer is fully turbulent (which then not was the case during the open water tests), but this is not fully clarified.

3. Self-propulsion simulation

The CFD method for the self-propulsion simulations, with a full hull and actual propeller, including a free water surface and heave and pitch motion of the hull, is tested applying the coarse grids with wall functions. The rotating motion of the propeller is simulated through the use of sliding interfaces. The time step is chosen to correspond to ~1° of propeller rotation (to speed up convergence the simulation is started with a stationary propeller using a moving reference frame and a larger time step).

The simulation, despite its complexity, is converging fine, but there are still some main issues to be addressed. Firstly, as concluded above, $y+ < 1$ are necessary to resolve the flow properly at the stern, this implies a grid size of $\sim 25 \cdot 10^6$ cells, which considering the physics solved for, is not very suitable as an engineering work tool. Simplifications, as for instance application of a symmetry plane as water surface could be considered for this case, but is not a general solution. Secondly, the method to automatically adjust the rotational speed of the propeller to match the applied rope force from test need to be developed. This is important for a proper modelling of the interaction effects.

4. Concluding remarks

For our further studies with focus on the interaction effects between propulsor and hull, there are still issues concerning the CFD methodology to be sorted out. The k-ω SST turbulence model incl. curvature correction shows promising results, but clearly underestimate the hull resistance, this could for instance be studied further applying another test case. Another strategy is to apply RSM, which showed very good accordance with measurements, it however requires more effort to get converged results for a free surface model. Applying the knowledge gained from the bare hull and open water simulations for the self-propelled hull implies a large total grid size, to facilitate further analyses possible simplifications need to be further investigated.

5. Acknowledgements

This research is supported by Rolls-Royce Marine through the University Technology Centre in Computational Hydrodynamics hosted by the Department of Shipping and Marine Technology at Chalmers. The simulations were performed on resources at Chalmers Centre for Computational Science and Engineering (C3SE) provided by the Swedish National Infrastructure for Computing (SNIC).

6. References

[1] Muzaferija, S. and Peric, M. (1999) Computation of free surface flows using interface-tracking and interface-capturing methods. In *Nonlinear Water Wave Interaction*, Marenholtz, O. and Markiewicz, M. (eds.). Southampton: WIT Press

[2] Krasilnikov, V. (2014) *Numerical Modelling of Ship-Propeller Interaction under Self-Propulsion Condition* STAR Global Conference 17-19 March 2014, Vienna

[3] Larsson, L., Stern, F. and Visonneau, M. (2014) *Numerical Ship Hydrodynamics – An assessment of the Gothenburg 2010 Workshop*. Dordrecht: Springer

[4] Deng, G., Queutey, P. and Visonneau, M. (2005) Three-dimensional flow computation with Reynolds stress and algebraic stress models. In *Engineering turbulence modelling and experiments*, Rodi, W and Mulas, M. (eds.) Vol 6, pp 389-398

[5] Manceau, R. and Hanjalic, K. (2002) *Elliptic blending model: A new near-wall Reynolds stress turbulence closure* Physics of Fluids Vol 14, pp 744

[6] Menter, F.R. (1994) *Two-equation eddy-viscosity turbulence modeling for engineering applications* AIAA Journal 32(8), pp 1598-1605

[7] Arolla, S and Durbin, P (2012) *Modeling rotation and curvature effects within scalar eddy viscosity model framework* International Journal of Heat and Fluid Flow Vol 39, pp 78-89

Numerical Simulation of Cavitating Flows Using OpenFOAM

Abolfazl Asnaghi, Andreas Feymark, Rickard E Bensow, Chalmers University of Technology, Gothenburg/Sweden, {abolfazl.asnaghi,andreas.feymark,rickard.bensow}@chalmers.se

Cavitation is the formation of vapour in a liquid when local static pressure of liquid falls below a critical pressure threshold. As pressure of a larger region gets below the threshold pressure, more liquid will change phase into vapour. Without considering the effects of shear forces in flowing fluids, the pressure threshold is equal to the thermodynamic saturation pressure. This definition, however, has some drawbacks. The thermodynamic saturation pressure is calculated in the conditions where the fluid is steady and in the equilibrium state. Therefore, the rupture of the liquid pocket is just due to the pressure tensile, and effects of shear stress caused by shear velocity are not included. In the previous study by the authors [1], concepts and derivation of cavitation inception by considering the viscous shear stresses were presented, and modification of pressure threshold was addressed. Another modification proposed previously by the authors was to improve the mass transfer rate by considering the velocity strain rate time scale. This modification increases the coupling between the mass transfer rate and the flow local properties, [2].

In the current study, interPhaseChangeFoam solver of OpenFOAM is used to simulate cavitating flows where previously proposed modifications are implemented and analysed in further details. Cavitating flows around NACA0009 and NACA66MOD hydrofoils are simulated to firstly validate the capability of the solver in prediction of cavitation in different operating conditions and secondly to highlight the positive impacts of the proposed modifications on the cavitating flow prediction.

OpenFOAM package, used in this study for numerical simulation, is an open source code written in C++ to model and simulate fluid dynamics and continuum mechanics. It is possible to adopt the code and build new functionalities, libraries, solvers, and utilities. The software is community driven where various communities are working on different fields of applications. This has expedited the progress and development of the software. In OpenFOAM, the spatial discretization is performed using a cell centred collocated finite volume (FV) method for unstructured meshes with arbitrary cell shapes, and a multi-step scheme is used for the time derivatives. To complete the FV-discretization the face fluxes need to be reconstructed from grid variables at adjacent cells, requiring interpolation of the convective fluxes and difference approximations for the inner derivatives of the diffusive fluxes; see [3-5] for more details on the discretization and the numerical schemes used in OpenFOAM.

InterPhaseChangeFoam solver uses Transport Equation Model (TEM) of volume fraction to predict phases' distributions. In this solver, both of the phases are treated as incompressible, isothermal, and immiscible. In order to model the mass transfer between phases, different phase-change models are provided in the solver to simulate cavitation but other mechanisms of phase-change are also supported within this solver framework.

In incompressible TEM approach, the governing equations consist of conservation of mass, and momentum of the effective fluid, and TEM of volume fraction. The filtered equations of mass and momentum can be written as follow,

$$\frac{\partial \rho_m}{\partial t} + \frac{\partial (\rho_m \overline{u_i})}{\partial t} = 0, \tag{1}$$

$$\frac{\partial (\rho_m \overline{u_i})}{\partial t} + \frac{\partial \left(\rho_m \overline{u_i u_j}\right)}{\partial x_j} = -\frac{\partial \bar{p}}{\partial x_i} + \frac{\partial}{\partial x_j}\left(\overline{S_{ij}} - B_{ij}\right) + \rho_m g_i. \tag{2}$$

In this equation, $B = \rho_m\left(\overline{u_i u_j} - \overline{u_i}\,\overline{u_j}\right)$ is the subgrid stress tensor and $S_{ij} = \mu\left(\partial u_i/\partial x_j - \partial u_j/\partial x_i\right)$ is the shear stress. In Implicit LES (ILES) model used in this study, no explicit function is applied for B; instead the numerical dissipation is considered enough to mimic the action of *B* [6, 7].

The transport equation of liquid volume fraction can be written as follow,

$$\frac{\partial \alpha_l}{\partial t} + \frac{\partial (\alpha_l \overline{u_i})}{\partial x_i} = \frac{\dot{m}}{\rho_l}, \tag{3}$$

α_l is the liquid volume fraction and $\dot{m}$ is the phase change rate between vapour and liquid phases.

Different models have been proposed to represent the phase change rate based on the fluid properties as well as the local flow properties. In the current study, the mass transfer model proposed by Schnerr-Sauer [8] is used and modified according to the proposed modifications.

The Schnerr-Sauer model assumes that there are several vapour bubbles, also called nuclei, inside the liquid which act as the initial sources of the phase change, and cavitation inception starts from their locations and due to their presence. The number, size and distribution of these bubbles can be determined in water quality experiment tests. To simplify the numerical modelling, it is assumed that the initial nuclei have been distributed evenly throughout the liquid, and they have equal size which is the smallest size that vapour bubbles can have. The mass transfer rate between liquid and vapour phases can be defined as follow,

$$\dot{m}_{\alpha c} = C_c \alpha_l \frac{3\rho_v \rho_l}{\rho_m R_B} \sqrt{\frac{2}{3\rho_l}} \sqrt{\frac{1}{|p - p_{threshold}|}} . max(p - p_{threshold}, 0), \tag{4}$$

$$\dot{m}_{\alpha v} = C_v (1 + \alpha_{Nuc} - \alpha_l) \frac{3\rho_v \rho_l}{\rho_m R_B} \sqrt{\frac{2}{3\rho_l}} \sqrt{\frac{1}{|p - p_{threshold}|}} . min(p - p_{threshold}, 0), \tag{5}$$

$$\dot{m} = \alpha_l \dot{m}_{\alpha v} + (1 - \alpha_l) \dot{m}_{\alpha c} . \tag{6}$$

One of the main issues in the simulation of cavitating flows using TEM is choosing the phase change model coefficients, C_v and C_c, [2]. These coefficients represent the relaxation time that vapour or liquid phase needs to be transferred into the other phase. For instance in the phase change models which are developed based on the bubble dynamics [8, 9], the first derivative of the bubble radius over time represents the relaxation time. However, when the region covered with vapour is larger than one bubble, using this term as the relaxation time may no longer correctly represent the accurate time scale of the phase change making it necessary to modify the coefficients. The chosen values for these coefficients therefore will have direct effects on final results. Another issue which should be taken into account is the dependency of the cavitation characteristics to the local flow properties. Using constant coefficients for mass transfer modelling, or in another word phase change relaxation time, without considering the local properties may impose unrealistic constrains. So, since the cavitation and phase change rate interact locally with the flow properties, one can expect a correlation between flow local time scales and the phase change relaxation time. In previous study [1], we proposed to use the symmetric part of the velocity strain rate for correction of the local phase change relaxation time scale, or in another word modification of the mass transfer coefficients.

Since the modified coefficient is usually bigger than one, using this modification will increase the rate of condensation and evapouration. It has been observed that in cavitating flows, the vapour production coefficient should be large, as high as possible according to [10], to satisfy near instantaneous evapouration. The destruction term, however, allows for some retardation in the condensation [10]. Therefore, the coefficient modification is limited to the evapouration coefficient, Cv where the main flow time scale, $t_\infty = \frac{L_\infty}{U_\infty}$, is employed to normalize the velocity strain rate,

$$C_{v-mod} = C_v \left(1 + t_\infty \left| \frac{1}{2} \left(\frac{\partial u_i}{\partial x_j} + \frac{\partial u_j}{\partial x_i} \right) \right| \right). \tag{7}$$

In [1, 2], the concept of shear stress effects on liquid rupturing and cavitation inception modification were presented and formulated. As it is stated the pressure threshold that determines the onset of cavitation in the flowing fluid can be expressed as,

$$p_{threshold} = \mu\dot{\gamma} + p_{saturation}, \tag{8}$$

where $\dot{\gamma}$ is shear strain rate. It should be noted that the current study is performed using the Schnerr-Sauer model modified according to these two modifications.

Depending on the local properties of the flow, in the matrix of the discretized volume fraction transport equation, the source term of TEM can become very large compared to the diagonal part due to the very high phase change rate. This may make solving the matrix of discretised equations problematic. In order to improve the solution stability, the source term needs to be rewritten, so the diagonal part can take into account some parts of the source term as an implicit term. The TEM equation can be rewritten by introducing $\dot{V}$ as follow,

$$\dot{V} = \left(\frac{1}{\rho_l} - \alpha_l\left(\frac{1}{\rho_l} - \frac{1}{\rho_v}\right)\right)\dot{m} \tag{9}$$

$$\frac{\partial \alpha_l}{\partial t} + \frac{\partial(\alpha_l \bar{u}_i)}{\partial x_i} = \left(\frac{\partial \bar{u}_i}{\partial x_i} + \dot{V}_v - \dot{V}_c\right)\alpha_l + \dot{V}_c \quad . \tag{10}$$

Here, the source term has been decomposed in two terms. The first term can be treated as an implicit term to increase the stability of solution.

The Schnerr-Sauer phase change model requires that the initial number of nuclei and initial nuclei diameter are predefined to adjust the phase change rate. In order to investigate effects of the phase change model parameters on cavitation behaviour, the cavitating flow around NACA0009 is investigated. The main interest here is to test effects of the number of nuclei and diameter on the cavitation development in a semi-steady flow over a simple geometry. Since the experimental data dose not report time dependency, time averaged numerical results are used for comparison and verification. The details of the experiment can be found in [2]. For numerical simulation, the inlet velocity is set fixed equal to 15m/s, outlet cavitation number is set equal to 0.75, and the foil angle of attack is set equal to 4 degree.

Pressure coefficient distribution over the foil which also presents the cavity size is employed to compare the numerical results with the experiment. In Figure 1, the numerical results using different number of nuclei, 10^6; 10^8; 10^{10} and 10^{12} are presented where the nuclei diameter is kept constant equal to 10^{-5} m. As it can be seen from this figure, using very small value for number of nuclei will lead to under prediction of the cavity. Moreover, at this condition the pressure at the leading edge becomes negative which cannot be correct for the foil with roughness applied on the leading edge. By increasing the number of nuclei, the accuracy of cavity size prediction and pressure distribution increases. For the current condition, it was noticed that increasing the number of nuclei to values higher than 10^{12} does not change the results any further.

Effects of nuclei diameter variation are presented in Figure 2. For these simulations the number of nuclei is kept constant equal to 10^8. This relatively small value for number of nuclei has been selected in order to make the mass transfer rate more sensitive to the variation of nuclei diameter. Increasing the diameter of the nuclei will lead to larger cavity size, and better prediction of the pressure distribution. However, even for very big nuclei diameter, e.g. 10^{-3} m, still the accuracy of the results is very poor. The results also indicate that the Schnerr-Sauer mass transfer rate is more dependent on the number of nuclei than the nuclei diameter.
The quality of water can be measured during the tests, and then the average number of nuclei and diameter can be used as phase change model parameters for simulation. For the cases that the quality

of the water is unknown, however, it can be very laborious to find the appropriate values to obtain reasonable results.

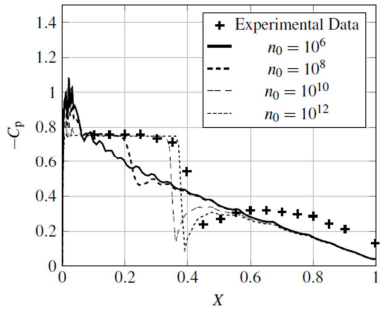

Figure 1. Pressure coefficient distribution of NACA0009 for different number of nuclei

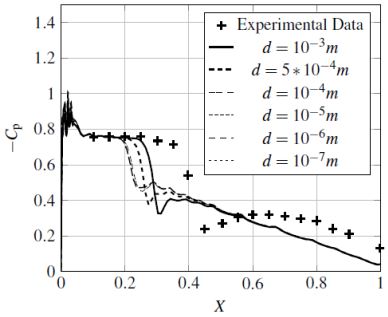

Figure 2. Pressure coefficient distribution of NACA0009 for different nuclei diameter

Since number and diameter of nuclei have direct effects on the mass transfer rate [2], one way to prevent or minimize the negative effects of inappropriate selection of nuclei values is to modify the mass transfer rate coefficients. As it is presented in Figure 3, applying the strain rate modification clearly improves the accuracy of the results. For the results related to the modified coefficient, the pressure at the leading edge is positive which matches with the experiment, and suggests that the mass transfer model is able to predict the vapour generation at the leading edge correctly. Moreover, the simulation is able to predict the sharp pressure variation at the stagnation point next to the cavity closure area, here at the location X=0.4.

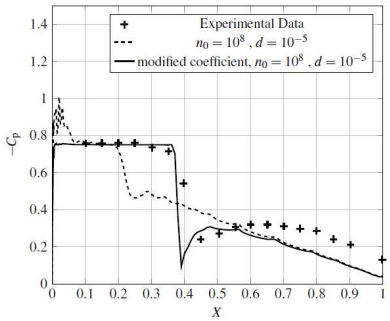

Figure 3. Pressure coefficient comparison between modified and original coefficients of Schnerr-Sauer mass transfer model

The leading edge and mid-chord cavitation on NACA 66 (MOD) hydrofoil is of particular interest for propeller cavitation studies, as it represents the two-dimensional characteristics of propeller blade cavitation. The study here is focus on the mesh resolution effects on the cavitation simulation and force distribution under three different operating conditions. The tested foil has camber ratio of 0.02, thickness ratio of 0.09 and mean line of 0.8 m.

A 2D computational domain is employed for numerical simulation of cavitation around NACA66MOD foil. In the used configuration, the inlet is located 2C upstream of the foil, outlet is located 8C downstream of the foil, and the tunnel width is set equal to 5C, where C is the chord length of the foil. Numerical simulations are carried out for three different cavitation numbers where the angle of attack, 4 degree, and the flow Reynolds number, $2*10^6$, are kept constant. The Reynolds number is calculated based on the chord length and inlet velocity. Three different cavitation numbers have been tested, 0.84, 0.91 and 1.0. The outlet pressure is adjusted to meet these cavitation numbers while the inlet velocity has been kept constant in the simulations.

The computational domain consists of 21000 hexahedral cells which are clustered towards the leading edge, where the pressure gradients are stronger and therefore finer resolution is necessary to capture the flow physics. The cells are also clustered near the foil to provide averaged normal to surface resolution (y^+) equal to 5. More details about the boundary setup and mesh specifications can be found in [2].

In Figure 4 and Figure 5, the pressure coefficient distributions and averaged liquid volume fraction for different cavitation numbers are presented over the foil in the streamwise direction which is normalized by the chord length. Comparing the numerical results with experimental data at the leading edge region indicates that the cavitation has been predicted reasonably well. The main

difference between the numerical results and experimental data is at the end of cavity. There, due to the higher pressure values, condensation is stronger and cavitation simulation will be affected mainly by the accuracy of condensation prediction. At the cavitation number 1.0, the pressure coefficient curve is sharp at the end of the cavity showing clear stagnation point while in the lower cavitation number, e.g. 0.84, the variation of the pressure is smoother. At σ =1.0, the numerical simulation is able to predict the cavitation size and stagnation point very well. At σ = 0.84, the numerical simulation is able to predict the trend well but the discrepancy between the numerical results and experimental data at the end of the cavity is noticeable.

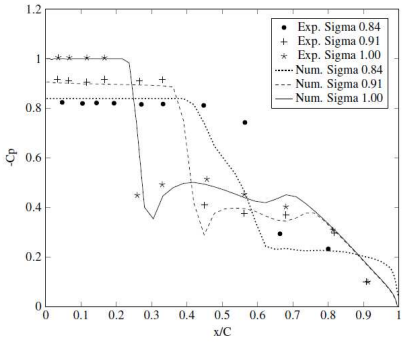

Figure 4. Pressure coefficient of NACA66MOD for different cavitation numbers

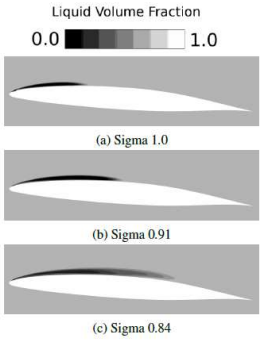

Figure 5. Averaged cavity distribution around NACA66MOD for different cavitation numbers

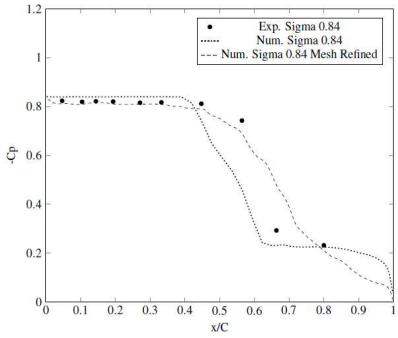

Figure 6. Effects of the mesh resolution at the closure region of the cavity on the pressure distribution, NACA66MOD

As it can be observed from Figure 4, the discrepancy between numerical results and experimental data at the closure region ($0.4 < x/C < 0.8$) is higher for σ = 0.84. Assuming that the transportation of vapour from the leading edge to the closure region is done reasonably acceptable, the pressure distribution at this region is highly dependent on the accuracy of vapour to liquid phase change simulation. Condensation phase change model, compressibility effects, and also numerical settings such as mesh resolution and alpha transportation scheme are some of the parameters that can affect the accuracy of condensation prediction. One possible candidate for the discrepancy between the numerical results and the experimental data is the spatial mesh resolution. As stated previously, the mesh has been clustered towards the leading edge and also trailing edge in order to capture the high flow gradients at those regions. Therefore, the spatial resolution is coarser at the middle region of the foil. By decreasing the cavitation number, the cavity size will increase and gets closer to the middle of the foil which as described has coarser mesh resolution, for instance in σ = 0.84 the closure region is in $0.4 < x/C < 0.6$. In order to investigate the effects of the mesh resolution, the mesh has been refined in the streamwise direction in two steps. At first step the cells inside $0.25 < x/C < 0.9$, and then at the second step the cells inside $0.375 < x/C < 0.8$ are refined. So the cells inside the second box would be four times smaller than the initial cells at that location. In Figure 6, the numerical results of different spatial resolutions are compared with the experimental data for σ = 0.84. As it can be seen from the results, the refinement of the spatial resolution at the closure region has increased the accuracy of prediction of pressure distribution especially at $0.5 < x/C < 0.6$ region. For sheet or semi-steady cavities, it is possible to refine the spatial resolution based on the primary results to get more accurate results later without increasing the computational cost considerably. However, for shedding cavity or vortex cavitation where usually the flow is also three dimensional, providing appropriate spatial resolutions to reasonably model the condensation is not straight forward.

In this paper, numerical simulations of the cavitating flows around the NACA0009 and NACA66MOD foils are computed and compared with experimental data. Schnerr-Sauer mass transfer model and its implementation in OpenFOAM are presented, and effects of the numerical setup (nuclei diameter and number of nuclei) on the final results are investigated. Current results show that considering the velocity strain rate to modify the mass transfer rate will improve the accuracy of the

cavitation prediction. Obtained results also indicate that the cavitation simulation depends on the spatial mesh resolution where lack of appropriate resolution can lead to higher deviation between numerical results and experiment.

Acknowledgements

Financial support of this work has been provided by Rolls-Royce Marine through the University Technology Centre in Computational Hydrodynamics hosted at the Dept. of Shipping and Marine Technology, Chalmers. Computational resources have been provided by Chalmers Centre for Computational Science and Engineering, C3SE.

References

[1] Abolfazl Asnaghi, Andreas Feymark, Rickard Bensow, 'Shear Stress Effects in Cavitating Flows', 17th Numerical Towing Tank Symposium (NuTTS'14)

[2] Abolfazl Asnaghi, 'Developing Computational Methods for Detailed Assessment of Cavitation on Marine Propellers', Licentiate Thesis, Department of Shipping and Marine Technology, Chalmers University of Technology

[3] H. Jasak H.G. Weller, G. Tabor and C. Fureby, 'A tensorial approach to CFD using object oriented techniques'. Computational physics, 12, 1997.

[4] Hrvoje Jasak. 'Error Analysis and Estimation for the Finite Volume Method with Applications to Fluid Flows' PhD thesis, Department of Mechanical Engineering, Imperial College of Science, Technology and Medicine, 1996.

[5] Rusche Henrik. 'Computational Fluid Dynamics of Dispersed Two-Phase Flows at High Phase Fractions', PhD thesis, Department of Mechanical Engineering, University of London, Technology and Medicine, 2002.

[6] Bensow R.E. (2011). 'Capturing Secondary Cavitation - A Step Towards Numerical Assessment of Cavitation Nuisance'. Ship Technology Research 58(2).

[7] Bensow, R.E. & Bark, G. (2010). 'Implicit LES predictions of the cavitating flow on a propeller'. J. Fluids Engng. 132.

[8] J. Sauer and G.H. Schnerr. Unsteady cavitating flow - a new cavitation model based on a modified front capturing method and bubble dynamics. In Fluids Engineering Summer Conf. (FEDSM), 2000.

[9] Sauer, J. (2000). 'Instationäre kaviterende Strömung – Ein neues Modell, basierend auf Front Capturing (VoF) and Blasendynamik'. PhD Thesis, Univ. Karlsruhe.

[10] N Wikstrom, G Bark, and C Fureby. Large eddy simulation of cavitation submerged objects. In 8th Int. conference on numerical ship hydrodynamics, Busan, Korea, 2003.

Assessment of Erosion Aggressiveness for the Cavitating Model Propeller *VP1304* by Fully Compressible Numerical Simulation

Bernd Budich, Franziska Borrmann, Steffen J. Schmidt, Nikolaus A. Adams
Institute of Aerodynamics and Fluid Mechanics, Technische Universität München
e-mail: bernd.budich@tum.de

1 Introduction

Marine propulsion systems, even at moderate loading conditions, are often affected by cavitation, causing highly undesirable consequences [1]. Propeller performance is limited by cavitation-induced thrust break-down and degradation of propeller efficiency. Pressure fluctuations generated by transient cavity dynamics and collapse of vapor structures are a major source for both radiated noise and structural vibrations. Moreover, material erosion, caused by high-intensity pressure peaks in the vicinity of solid surfaces, reduces the lifespan of the propeller or a rudder located in the propeller slip-stream.

These phenomena are caused by the inherently unstable and thus transient behavior of cavitating flow. Therefore, in addition to controlling the extent of vapor regions, also cavitation dynamics need to be taken into account during propeller design. An in-depth understanding of the unsteadiness of cavitating flow, a prediction of flow aggressiveness due to cavitation, and an estimate of expected material erosion is of primary interest.

Numerical simulation enables a detailed study of a flow at a spatial and temporal resolution that is difficult to achieve with experiments. Current numerical approaches predict mean cavitation patterns as well as flow dynamics, including an estimate of the thrust break-down. Many methods for the analysis of cavitating propeller flow utilize the assumption of (pseudo-)incompressibility. From studies of single and multi-bubble arrangements, however, it is well known that collapsing vapor structures lead to the formation of strong pressure waves [2], which possess the potential for material erosion [3]. Moreover, wave dynamics plays an important role for the transient nature of the two-phase flow. While shock waves can initiate further collapse events, expansion waves may lead to the generation of new vapor structures.

In order to accurately capture the intrinsic coupling between cavity- and wave-dynamics, as well as the mechanisms leading to erosive pressure pulses, two-phase compressibility has to be included in the model. We thus apply a fully compressible numerical method to simulate the cavitating flow around a model propeller geometry, with the aim to identify erosion-endangered areas on the blade and hub surfaces.

2 Physical Model and Numerical Method

The cavitation model for the present study is based on the assumption of local thermodynamic equilibrium, which allows to apply a homogeneous mixture approach. We assume barotropic flow and two-phase regions are treated as a saturated mixture. Both free and solved gas content are neglected for this study. Previous investigations show that the large disparity in momentum between liquid and vapor dominates the dynamics of the multiphase flow [4]. Thus, we focus on inertia-dominated flow mechanisms and assume the flow as inviscid. The method has been successfully applied for an assessment of erosion aggressiveness [5].

The governing equations for the numerical method are the unsteady compressible Euler equations, discretized on body-fitted, structured grids. The density-based finite volume method employs a low-Mach-number consistent flux function. Interface velocities are reconstructed using a high resolution TVD limiter, the interface pressure is approximated with 2^{nd} order accuracy, and an upwind reconstruction of the density is utilized [6]. An explicit, low-storage 4-stage Runge-Kutta method is employed for time integration. Rotation is handled via an Arbitrary Lagrangian-Eulerian (ALE) approach, applied to the complete domain.

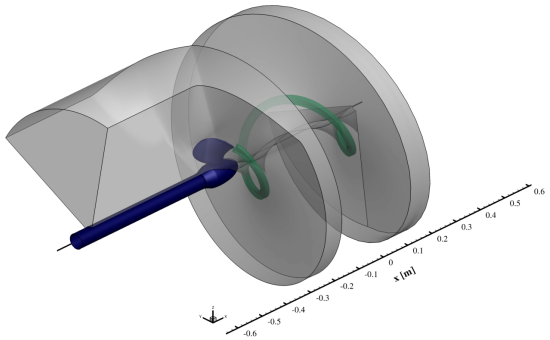

Figure 1: Numerical domain (refined tip vortex region highlighted in green).

grid level	number of cells	minimum cell size	average timestep
coarse	$1.2{\cdot}10^5$	0.5 mm	$4.6 \cdot 10^{-8}$ s
medium	$6.6{\cdot}10^5$	0.2 mm	$2.2 \cdot 10^{-8}$ s
fine	$5.2{\cdot}10^6$	0.1 mm	$6.4 \cdot 10^{-9}$ s

Table 1: Employed grid levels.

3 Test Case

The five-bladed model propeller *VP1304* with a diameter $D = 0.25\,\mathrm{m}$ at homogeneous inflow conditions is considered. Also known as the Potsdam Propeller Test Case 2011 (PPTC'11) [7], this device has been extensively investigated both experimentally and numerically.

We simulate a single blade passage, depicted in Fig. 1, with periodicity on the lateral boundaries. The domain downstream of the propeller is twisted around the propeller axis x, in order to increase spatial resolution of the trailing tip vortex structure. Three grid levels are investigated, see Tab. 1 for details. In order to control the advance coefficient $J = V_a/nD$, the inflow velocity V_a is prescribed at the inlet, while the rotational velocity n is kept constant. The PPTC'11 specification requires thrust identity under wetted conditions. Therefore, the advance coefficient is iteratively adjusted via the inflow velocity until the experimental thrust coefficient K_T is matched. The cavitation number $\sigma_\mathrm{n} = (p_0 - p_v)/(0.5\rho_\mathrm{ref}\, n^2 D^2)$ is adjusted by an asymptotic boundary condition for the static pressure p_0 at the outlet. To shorten initial transients, time-operator preconditioning is utilized during simulation startup, in conjunction with a grid sequencing procedure.

For the operating points investigated in this study, we adopt the same nomenclature as the PPTC'11 problem statement [8]. In a previous analysis, see Budich et al. [9], we validated the approach with experimental and numerical studies for PPTC operating conditions *2.2* and *2.3.1*. It was shown that the chosen method shows good agreement for the computed propeller efficiency, blade pressure distribution, and observed cavitation patterns. The wake structure is accurately predicted and simulations yield a cavitating tip vortex. In a follow-up, Budich et al. [10], we focused on the numerical quantification of flow aggressiveness for case *2.3.1*, by evaluating maximum surface pressures as well as global and local impact load spectra.

For the present contribution, the analysis is extended to PPTC conditions *2.3.2*, the nominal design point, and *2.3.3*, an off-design point at higher J. Relevant parameters for all considered operating conditions are summarized in Tab. 2. In the following, only results of the *fine* grid levels are discussed. The sampling period for the collection of flow statistics on this grid level is 9.9 rev, 4.3 rev and 4.5 rev, for cases *2.3.1*, *2.3.2*, and *2.3.3*, respectively.

		2.3.1	*2.3.2*	*2.3.3*
J	[−]	1.019	1.269	1.408
K_T	[−]	0.387	0.245	0.167
σ_n	[−]	2.024	1.424	2.000
n	[rev/s]	24.987	24.896	25.014
t_sim	[rev]	9.9	4.3	4.5

Table 2: Specification of the investigated operating conditions [8] and sampling time span on the fine mesh.

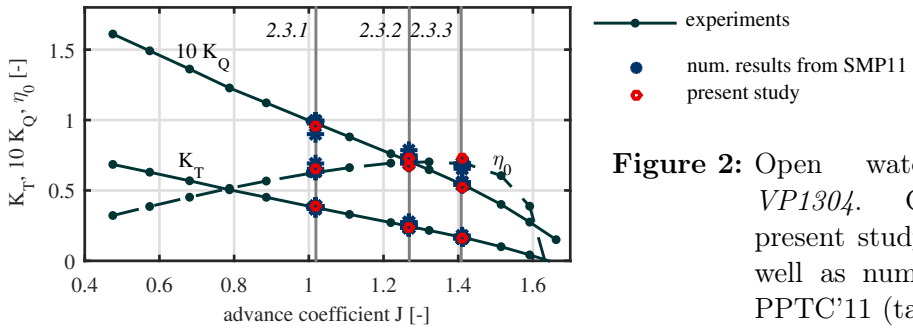

Figure 2: Open water performance of *VP1304*. Comparison between present study and experimental as well as numerical references from PPTC'11 (taken from [7]).

4 Results

The open water performance of the propeller can be found in Fig. 2. For all three operating conditions, the plot shows the thrust coefficient K_T, torque coefficient K_Q as well as the propeller efficiency η_0 for all conducted simulations under wetted conditions. Results from PPTC'11 participants and the experimentally determined open water performance are included as well. As expected, the inviscid approach systematically overestimates the propeller efficiency η_0 by $\approx 4\%$. In the context of the PPTC, the agreement with the references is satisfactory.

The extent of cavitating regions for the three operating points is displayed in Fig. 3. Sketches obtained from the experiments [8] are shown in Figs. 3 (a-c). Note that for cases *2.3.1* and *2.3.2* only the suction side is documented, whereas the sketch for *2.3.3* is only provided for the pressure side. The corresponding time-averaged numerical results are given in Figs. 3 (d-f). The visualizations show iso-surfaces of the 20%, 50% and 80% void fraction $\langle\alpha\rangle$. The simulations capture the location of cavitating regions correctly. The cavitating core of the tip vortex for *2.3.1*, suction side root cavitation for *2.3.1* and *2.3.2*, as well as pressure side cavitation along the leading edge for *2.3.3* is predicted by the simulations. For the present study, a void fraction of 50% agrees best with the extent of cavitating regions observed experimentally.

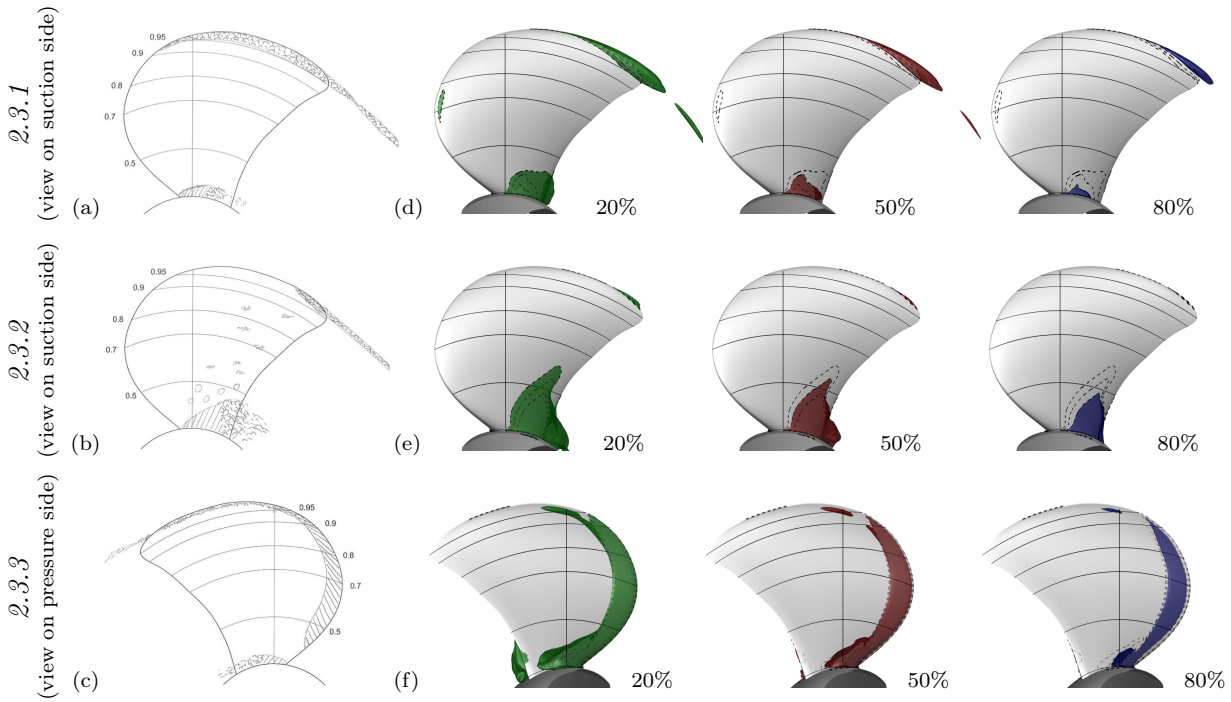

Figure 3: Cavitation extent for operating conditions *2.3.1*, *2.3.2* and *2.3.3*. Comparison between experimental cavitation sketches (a-c) and numerical results (d-f), by means of iso-surfaces of the time-averaged void fraction $\langle\alpha\rangle$ (20%, 50% and 80%).

Some discrepancies between the numerical results and experimental observation are found. The extent of the suction side root cavity for case *2.3.2* is overestimated. This can be accredited to the cavitation susceptibility within this region, suggested by the experimentally observed bubble cavitation. This type of cavitation is difficult to predict with homogeneous mixture models. The cavitating tip vortex, observed for all three experimental operation points, is present in the simulations only for case *2.3.1*. However, capturing this flow feature is demanding as it imposes high requirements on spatial accuracy and resolution. Only 3 out of 14 (*2.3.1*) and 2 out of 15 (*2.3.2*) PPTC'11 contributions predict a cavitating tip vortex. For *2.3.3*, the experiments exhibit bubbly flow in the vortex core, which seems especially challenging. None of the submitted numerical results show this phenomenon. Another disagreement with the experiments for *2.3.3* is the transition between leading edge cavitation and root cavitation on the pressure side. Again, a majority of PPTC'11 submissions (10 out 15) also show this behavior, which is not observed experimentally. It is concluded that the mentioned aspects represent challenges for the prediction of cavitating propeller flow, that still need to be solved. The present approach is in alignment with other numerical investigations of the *VP1304* propeller.

A qualitative comparison of flow aggressiveness between the investigated operating conditions is enabled by the maximum pressure criterion. For this purpose, pressure maxima are monitored during the analysis period for each grid cell. Recorded maxima on the blade and hub surfaces are 17.7 MPa (*2.3.1*), 12.7 MPa (*2.3.2*) and 23.5 MPa (*2.3.3*). Thus, both off-design points lead to noticeably higher pressure levels, compared to the design point *2.3.2*. A visualization of the recorded surface pressure maxima is shown in Fig. 4. Highest pressure loads can be found for *2.3.1* and *2.3.3* within the rear part of the suction side root area, where vapor structures of the highly unsteady root cavity collapse. Although the suction side cavitation has a larger extent for *2.3.2*, the impact on the material is attenuated, as detaching vapor clouds are convected away from the blade and hub surfaces. The cavitating blade tip and tip vortex for *2.3.1* do not cause an increase in maximum pressure, as these structures are stable. The same conclusion can be drawn for the stable, attached sheet along the leading edge of the pressure side for *2.3.3*.

The percentage of surface area, covered by pressure maxima exceeding a certain threshold, is given in Fig. 5. For the design point *2.3.2*, less than 3% of the total surface area is subjected to surface pressure maxima of $p_{\max} \geq 0.5$ MPa. At both off-design points, more than twice the area is affected by collapsing vapor structures. Simultaneously, recorded pressure maxima are noticeably higher for *2.3.1* and *2.3.3*.

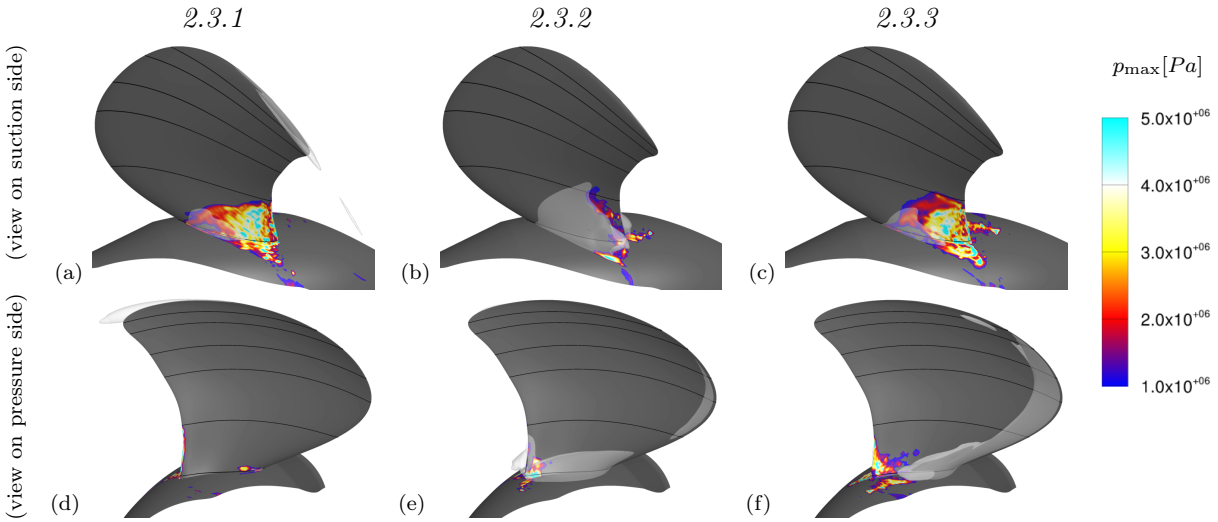

Figure 4: Pressure maxima $p_{\max}$ recorded on the blade and hub surfaces for the operating conditions *2.3.1*, *2.3.2* and *2.3.3*, pressure levels $p_{\max} \leq 1$ MPa blanked. Visualization includes iso-surfaces of the time-averaged void fraction $\langle \alpha \rangle = 0.5$.

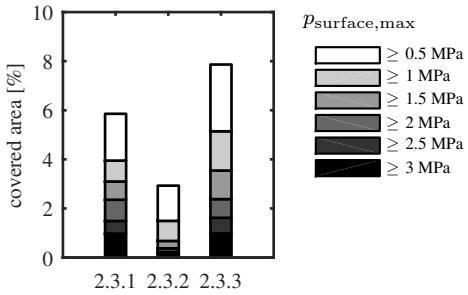

Figure 5: Percentage of propeller surface area covered by pressure maxima exceeding the specified thresholds. Comparison of operating conditions *2.3.1*, *2.3.2* and *2.3.3*.

The flow aggressiveness can be further analyzed utilizing a collapse detection algorithm [5]. By detecting collapse events of isolated cavities within the flow, this enables a statistical analysis of collapse locations, rates and intensity. The visualization in Fig. 6 shows collapses events, recorded during an analysis interval of identical length (4.3 rev) for each operating point. Each event is represented by a circle, where the size and color corresponds to the magnitude of the associated collapse pressure. Highest-intensity collapses concentrate within the vicinity of the blade trailing edge for both off-design points. The design-point, in contrast, exhibits strongest collapses further downstream. With a stand-off distance of ≈ 4 cm, these collapses are not close enough to the surface, in order to be detected by the maximum pressure criterion.

Collapse spectra, as shown in Fig. 7, are cumulative histograms of collapse rates versus collapse intensity and provide a more detailed analysis of the global and local flow aggressiveness. Involving events that occur within the complete domain, Fig. 7 (a) shows the global collapse spectra for the fine mesh level of all three investigated operating conditions. In contrast, for the collapse spectra in Fig. 7 (b), only events occurring within a distance of ≤ 4 mm to a solid surface are considered. Events occurring less than 5 times have been excluded from this analysis.

Both the global and local flow aggressiveness is maximal for condition *2.3.3*, as stronger collapses and higher collapse rates are registered. On the other hand, the global collapse spectra of *2.3.1* and *2.3.2* are comparable, as suggested by Fig. 7 (a). However, when accounting only for events within the vicinity of the propeller surface, Fig. 7 (b), the design points exhibits a much less intense collapse spectrum.

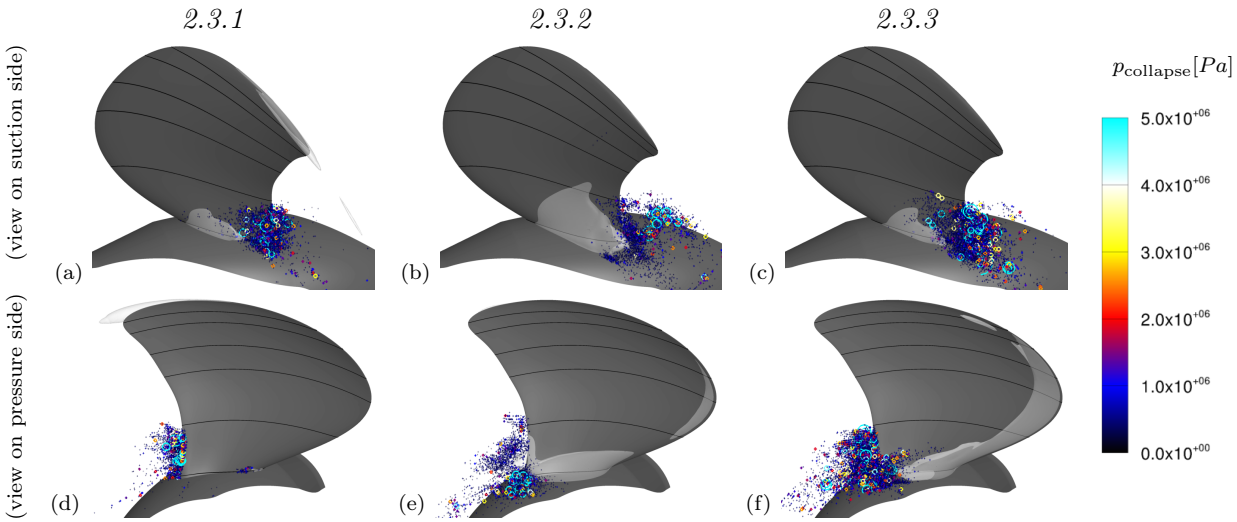

Figure 6: Scatter plot of collapse events detected within the vicinity of the propeller. The size and color of the symbols correspond to the magnitude of the pressure pulse upon cavity collapse p_{collapse}. Comparison of the operating conditions *2.3.1*, *2.3.2* and *2.3.3*, for equal analysis intervals of $\Delta t = 4.3$ rev. Blanked for $p_{\text{collapse}} \leq 0.2$ MPa.

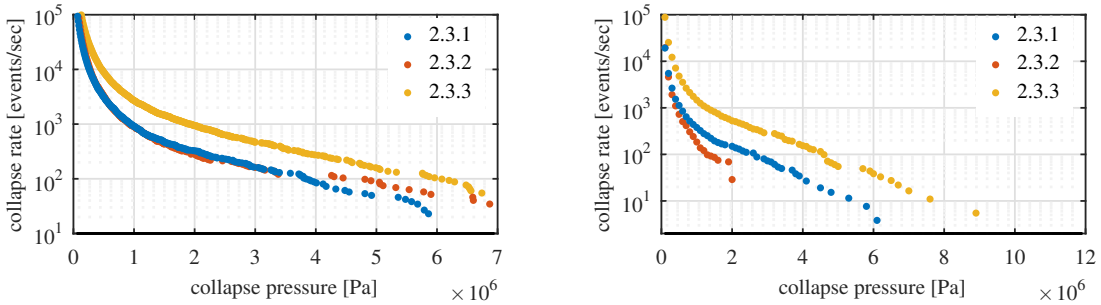

(a) Collapse events detected within the complete domain (global spectra)

(b) Collapse events detected within a distance of ≤ 4 mm to the propeller surface (local spectra)

Figure 7: Cumulative collapse spectra for the operating conditions *2.3.1*, *2.3.2* and *2.3.3* (fine mesh, events occurring ≤ 5 times excluded)

5 Conclusion

In this paper, the model propeller *VP1304* is investigated numerically, reproducing the Potsdam Propeller Test Case 2011. A homogeneous mixture model, in conjunction with the assumption of inviscid flow and barotropic thermodynamics, is employed. Two-phase compressibility is taken into account and, thus, collapse-induced shock waves as well as pressure fluctuations due to the dynamics of the cavitating flow are resolved. Flow aggressiveness therefore is analyzed with the maximum pressure criterion, and by detecting individual collapse events. The location and extent of cavitating regions is in agreement with the experiments and previous numerical studies of the propeller. Comparison of flow aggressiveness for the three operation points shows that the cavitating flow is least aggressive at the design point of the propeller.

Acknowledgments

Support for this research was provided by the U.S. Office of Naval Research (ONR) and ONR Global through the NICOP entitled "Numerical Investigation of Ship-Propeller Cavitation with Full Description of Shock-Wave Dynamics" (Contract No. N62909-12-1-7034). The authors further acknowledge the Gauss Centre for Supercomputing e.V. (www.gauss-centre.eu) for providing computing time on the GCS Supercomputer *SuperMUC* at the Leibniz Supercomputing Centre (LRZ, www.lrz.de).

References

[1] J. S. Carlton. *Marine Propellers and Propulsion*. Third Edition. 2012, Elsevier.

[2] W. Lauterborn and W Hentschel. "Cavitation bubble dynamics studied by high speed photography and holography: part two". *Ultrasonics*, Vol. 24(2), 1986, pp. 59–65.

[3] A. Philipp and W. Lauterborn. "Cavitation erosion by single laser-produced bubbles". *Journal of Fluid Mechanics*, Vol. 361, 1998, pp. 75–116.

[4] S. J. Schmidt, M. Thalhamer, and G. H. Schnerr. "Inertia controlled instability and small scale structures of sheet and cloud cavitation". In: *Proc. of the 7th International Symposium on Cavitation, CAV 2009*. Ann Arbor, Michigan, USA, Aug. 2009.

[5] M. S. Mihatsch, S. J. Schmidt, and N. A. Adams. "Cavitation Erosion Prediction based on Analysis of Flow Dynamics and Impact Load Spectra". *Physics of Fluids*, 2015 (in press).

[6] S. J. Schmidt, I. H. Sezal, G. H. Schnerr, and M. Thalhamer. "Riemann techniques for the simulation of compressible liquid flows with phase-transition at all Mach numbers – shock and wave dynamics in cavitating 3-D micro and macro systems". In: *Proc. of the 46th AIAA Aerospace Sciences Meeting and Exhibit, ASME 2008*. 2008.

[7] M. Hoekstra, T. J. C. van Terwisga, H.-J. Heinke, L. Lübke, M. Abdel-Maksoud, and M. Druckenbrod, eds. *Proceedings of SMP'11 Workshop on Cavitation and Propeller Performance: the Second International Symposium on Marine Propulsors*. 17 – 18 June, 2011, Hamburg, Germany.

[8] SVA Potsdam GmbH. *Potsdam Propeller Test Case (PPTC) - Cavitation Tests with the Model Propeller VP1304,* Report 3753. Technical Report. Apr. 2011.

[9] B. Budich, S. J. Schmidt, and N. A. Adams. "Numerical Investigation of a Cavitating Model Propeller Including Compressible Shock Wave Dynamics". In: *Proc. of the 4th International Symposium on Marine Propulsors, SMP 2015*. Austin, Texas, USA, June 2015.

[10] B. Budich, S. J. Schmidt, and N. A. Adams. "Numerical Simulation of Cavitating Ship Propeller Flow and Assessment of Erosion Aggressiveness". In: *Proc. of the 6th International Conference on Computational Methods in Marine Engineering, MARINE 2015*. Rome, Italy, July 2015.

A Review of the Implicit Motion Solver Algorithm in OpenFOAM® to Simulate a Heaving Buoy

Brecht Devolder[1,*], Pál Schmitt[2], Pieter Rauwoens[3], Björn Elsaesser[2], Peter Troch[1]

* Corresponding author. Tel.: +32 9 264 54 92; Fax: +32 9 264 58 37; Mail: Brecht.Devolder@UGent.be

[1] Ghent University, Department of Civil Engineering, Technologiepark 904, 9052 Ghent, Belgium (Brecht.Devolder@UGent.be, Peter.Troch@UGent.be)

[2] Queen's University Belfast, Marine Research Group, BT9 5AG Belfast, Northern Ireland, United Kingdom (p.schmitt@qub.ac.uk, b.elsaesser@qub.ac.uk)

[3] KU Leuven, Department of Civil Engineering, Zeedijk 101, 8400 Ostend, Belgium, (Pieter.Rauwoens@kuleuven.be)

1 Introduction

Heaving buoys are currently very interesting with regard to renewable energy. More specific, heaving buoys, in general also called Wave Energy Converters (WECs), can be used to extract wave energy from ocean waves. In order to extract a considerable amount of wave power, large numbers of WECs are arranged in farms.

Prior to the analysis of farm effects, the fluid characteristics around a single WEC have to be understood in detail. Computational Fluid Dynamics (CFD) is able to solve the viscous flow field in three dimensions around a floating object. OpenFOAM® (2014) is selected as a suitable CFD package to investigate the flow field around and the response of a heaving buoy in an incident wave field. OpenFOAM is a robust and advanced open source CFD package. The two phase flow solver with dynamic mesh handling, interDyMFoam, is available in OpenFOAM. Wave generation and absorption are implemented in the IHFOAM toolbox (Higuera, 2013a, 2013b). Being open source, it enables the user to develop a coupling strategy with another far field solver to reduce the computational cost of a simulation of an entire farm.

There are several issues regarding the simulation of floating bodies in a dense fluid with CFD which form the subject of the present contribution. Key issues are related to the convergence of the motion solver and the coupling between the motion and fluid solver.

2 Numerical framework

In the current paragraph, a concise description of the numerical setup is given, focussing on the solvers and toolboxes used for the case studies selected.

2.1 Fluid solver

The two phase interDyMFoam solver, developed for dynamic mesh handling, is based on the interFoam solver for static meshes. The flow field is calculated using the incompressible Navier-Stokes equations. The solver makes use of the Volume over Fluid (VoF) method to track the interface between the two fluids. The VoF method is an excellent tool in the field of coastal engineering to simulate complex free surfaces deformations, including wave breaking. interDyMFoam combines the VoF method and a mesh deformation solver. The mesh is deformed according to the motion of a rigid body. The motion of the body is determined by a motion solver, introduced in the next section.

The motion of a floating body will generate radiated waves. The wave height dampens out when the wave travels further away from the body. When these radiated waves hit the boundaries of the computational domain, reflection should be avoided. Therefore the IHFOAM toolbox (Higuera, 2013a, 2013b) is used to absorb the waves at the boundaries by a specific boundary condition. The absorption methodology is based on shallow water theory. The validity of the underlying assumption, shallow water, will be evaluated during the numerical simulations. As mentioned in Higuera (2013a), the absorption condition works relatively well for waves outside the shallow water range. However, a careful assessment of the suitability of the method is still desirable.

2.2 Motion solver

For the cases studied here, the buoys are restricted to move solely in the upward and downward direction. Only one degree of freedom is considered, the heave motion, instead of the general six degrees of freedom.

The standard motion solver in OpenFOAM uses a second order accurate leapfrog scheme to calculate the velocity and the position of the object based on the acceleration (Dullweber, 1997). The acceleration is derived from Newton's second law.

2.3 Coupling strategy

The fluid solver and motion solver are coupled to simulate rigid body motions. The coupling is explained by following the methodology inside the interDyMFoam solver of OpenFOAM-2.3.1, which is visualised in the flow chart provided in Figure 1. At the start of a certain time step, the motion solver is called first, represented by the dashed box in Figure 1. Different functions are evaluated inside that motion solver. Details about "Update position" and "Update acceleration", which are based on a leapfrog scheme, are given in paragraph 4.2. In between the "Update position" and "Update acceleration", the total force (i.e. pressure, viscous, weight and acceleration forces) on the body is calculated. After the new position of the rigid body is determined, the object is moved to its new position ("Move object"). Next, the mesh is deformed and moved ("Move mesh") where the new position of the rigid body serves as a boundary condition. When the mesh is moved to the new position, the reference mesh is always the one obtained from the previous time step. After the new mesh is obtained, the fluid solver is started. First the field flux is corrected, followed by the VoF method to track the free surface. Thereafter, the PIMPLE algorithm solves respectively the momentum and pressure equations to calculate the velocity field and the pressure field. If the maximum number of PIMPLE iterations is not reached, a new iteration is started within the same time step. Otherwise, a new time step is triggered. The motion state of the rigid body (i.e. acceleration, velocity, centre of mass) from the old time step is stored when the function "New time" is called to access it during the new time step.

The coupling between the fluid and motion solver is regulated by multiple PIMPLE iterations in every time step. This is because the motion state and the flow field are calculated one after the other. The purpose of these iterations is to obtain a solution where the motion of the object is in equilibrium with the flow field at a certain time step. The implicit iterations between the fluid and motion solver are only implemented since OpenFOAM-2.3.x. The number of iterations is key to faster simulation times. The stronger the coupling, the lower the number of iterations, the faster the simulation speed. Therefore a strong coupling between fluid and motion solver must be achieved.

3 Test cases

Two different case studies are presented to explain some principle ideas regarding the motion and the force on a floating body. The first geometry is a 3D floating buoy which solely operates in heaving mode. Figure 2 visualises a slice of the hexahedral grid structure around the heaving buoy.

Due to the complex mesh structure around a heaving buoy, a simplistic 2D floating body is used as a second test case: a floating block in a two dimensional situation which again only moves in the

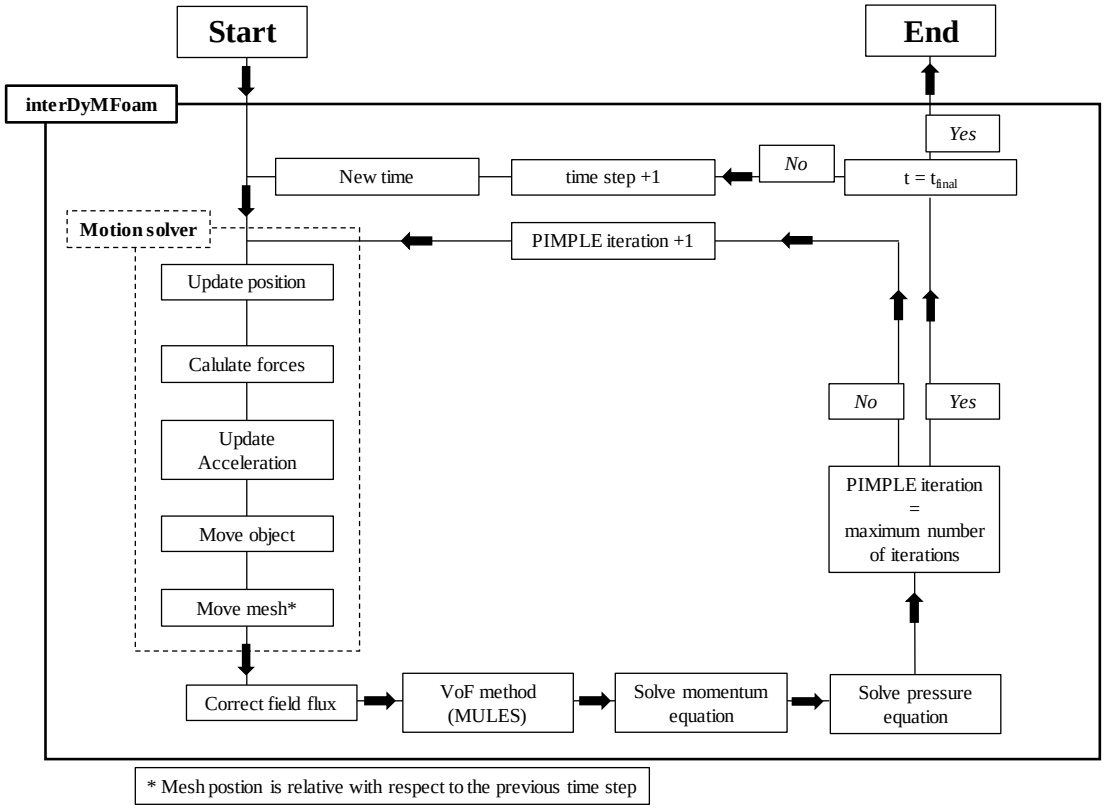

Figure 1: Flow chart of the interDyMFoam solver in which a detail of the motion solver is provided.

heave direction. A definition sketch of the second test case is provided in Figure 3. The mesh structure consists of a dense hexahedral Cartesian grid. Compared to the buoy shown in Figure 2, the width of the object in Figure 3 is deliberately chosen larger than the height in order to reveal the deficiencies of the present numerical implementation (see further).

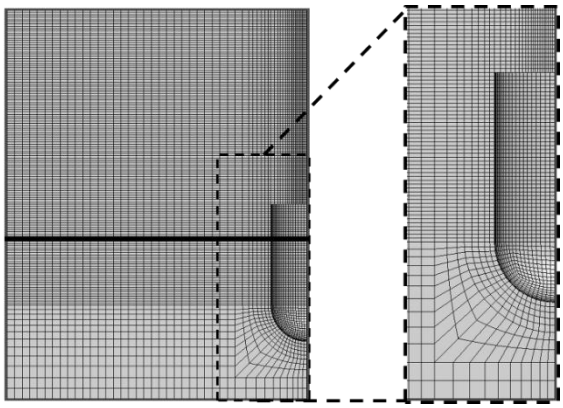

Figure 2: The hexahedral mesh structure around a heaving buoy (3D). The thick horizontal solid black line at the left figure indicates the initial free surface.

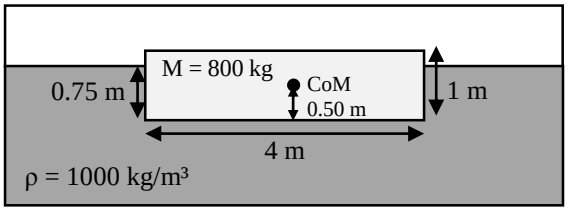

Figure 3: A definition sketch showing the geometry of a 2D floating block (ρ_{block} = 200 kg/m³). The initial draft is 0.75 m and the position of the centre of mass (CoM) is located in the middle of the block.

4 Results and solver optimization

4.1 Force on a floating body

The force on a floating object is determined for a free decay test. In that particular test, the floating object is placed out of equilibrium leading to a damped oscillatory motion until all the forces acting on the object are in equilibrium. Numerical results for the free decay test of a heaving buoy (Figure 2) show spikes in the total force acting on the floating object, as indicated in Figure 4. These spikes are not expected because the total force on the object during a free decay test is theoretically described by a sinusoidal function multiplied by an exponential decay which is per definition a smooth function. The spikes disappear in the graph expressing the position of the centre of mass of the heaving buoy in function of the time, as shown in Figure 5. However, the position is the second derivative of the acceleration which is in itself a linear function of the total force on the floating object.

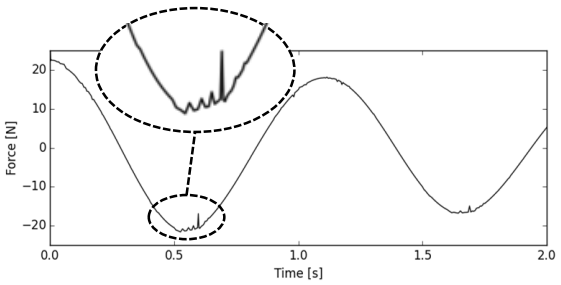

Figure 4: Total vertical force on a heaving buoy (Figure 2) in function of the time. The dashed circle shows a detail of the spikes in the total force.

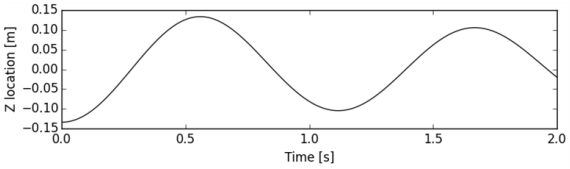

Figure 5: Centre of mass in the Z-direction of a heaving buoy (Figure 2) in function of the time (reference Z = 0 m is equal to the initial Still Water Level).

These observations have led to a more profound analysis of the motion solver implemented in OpenFOAM. In the remaining part of the paper, the geometry is changed and simplified from a heaving buoy, Figure 2, to a 2D floating block operating in heave, Figure 3.

4.2 Leapfrog scheme instability

The leapfrog scheme originally programmed in the motion solver consists of three subsequent steps to update the motion state (for the heave motion only):

- Update position:

$$v_{i+1}^{n+1/2} = v^n + 0.5 \cdot \Delta T^n \cdot a_i^{n+1} \quad (4\text{-}1)$$

$$CoM_{i+1}^{n+1} = CoM^n + \Delta T^{n+1} \cdot v_{i+1}^{n+1/2} \quad (4\text{-}2)$$

- Calculate the total force acting on the body:

$$f_{Global}{}_{i+1}^{n+1} = \sum_j^{body} p_j A_j + \sum_j^{body} \tau_j A_j - m \cdot g \quad (4\text{-}3)$$

- Update acceleration:

$$a_{i+1}^{n+1} = \frac{f_{Global}{}_{i+1}^{n+1}}{m} \quad (4\text{-}4)$$

$$v_{i+1}^{n+1} = v_{i+1}^{n+1/2} + 0.5 \cdot \Delta T^{n+1} \cdot a_{i+1}^{n+1} \quad (4\text{-}5)$$

in which *n+1* is the current time step, *i+1* is the current PIMPLE iteration, *v* is the velocity of the body, *CoM* is the centre of mass of the body, ΔT is the time step, f_{Global} is the total force acting on the body, p_j is the pressure acting on each boundary face

around the body, τ_j is the shear stress acting on each boundary face around the body, A_j is the area of a boundary face, m is the dry mass of the body and g is the gravitational acceleration.

According to Birdsall & Langdon (2004), the leapfrog scheme is stable for a fixed time interval. In order to rule out any problems related to a variable time step, all simulations hereafter are performed using a fixed time step for the entire simulation time.

First, the originally implemented leapfrog scheme is analysed by a free decay test of the case study given in Figure 3, a 2D floating block. The number of PIMPLE iterations is set to 25 and a fixed time step of 0.005 s is used. Due to instability problems, relaxation of acceleration is set to 0.1. A more detailed description regarding acceleration relaxation is given in the section 4.3. Figure 6 and Figure 7 show the total vertical force on the 2D block, respectively as a function of the iterations and as a function of the time. In general, the forces are converging in a certain time step (Figure 6). It means that the body and fluid motion are in equilibrium after 25 PIMPLE iterations. However, the main problem is related to the converged value of the total force in every time step. As shown in Figure 7, large oscillations in the total force on the floating block between the different time steps are observed. Again, these spikes are not expected in the beginning of the simulation because the total force during a free decay test should be smooth and follow a damped cosine function.

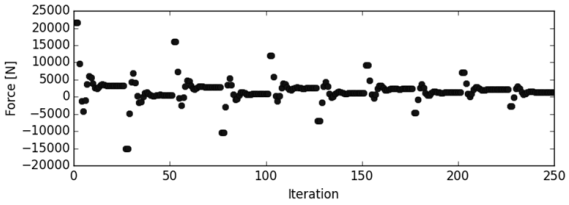

Figure 6: Total vertical force on the 2D block in function of the iterations for a fixed time step of 0.005 s.

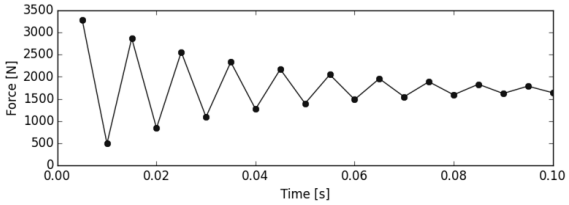

Figure 7: Total vertical force on the 2D block in function of the time for a fixed time step of 0.005 s.

The results presented in this section show that a fundamental problem exists in the implementation of the motion solver. Theoretically, the leapfrog scheme is an explicit scheme. However, equation (4-1), which is originally implemented in OpenFOAM, has an implicit character. This is because the acceleration from the previous iteration of the same time step, a_i^{n+1}, is used to update the *CoM* at the current iteration of the same time step, CoM_{i+1}^{n+1}. This is opposite to the theoretical formulation of the leapfrog scheme, which uses the acceleration from the previous time step, a^n (Dullweber, 1997). Therefore equation (4-1) is rewritten to:

$$v_{i+1}^{n+1/2} = v^n + 0.5 \cdot \Delta T^n \cdot a^n \qquad (4\text{-}6)$$

It means that the leapfrog scheme is made explicit because the acceleration from the previous time step, a^n, is used to calculate the position at the current time step, CoM_{i+1}^{n+1}. This also means that the time consuming fluid solver is only needed once in every time step because the position of the object remains constant in a certain time step.

The implementation of equation (4-6) is checked by using a mock-up fluid solver where in the first instance the force on the object is analytically determined by the upward hydrostatic force and the downward weight of the body:

$$\begin{aligned} f_{Global} &= \rho_w \cdot V_{wet} \cdot g - m \cdot g \\ &= -\rho_w \cdot A_{wet} \cdot g \cdot \Delta z \end{aligned} \qquad (4\text{-}7)$$

in which ρ_w is the density of water, V_{wet} is the underwater volume of the floating object, A_{wet} is the horizontal water plane area and Δz is the distance between the *CoM* at time step *n+1* and the *CoM* in equilibrium. The first line in equation (4-7) can be rewritten to the second line by some basic geometrical considerations. Newton's second law is used to derive the acceleration of the object:

$$\begin{aligned} a^{n+1} &= \frac{f_{Global}}{m} = \frac{-\rho_w \cdot A_{wet} \cdot g \cdot \Delta z}{m} \\ &= -\Delta z \cdot \frac{\rho_w \cdot g}{\rho_b \cdot h_b} = -\Delta z \cdot k \end{aligned} \qquad (4\text{-}8)$$

in which ρ_b is the density of the floating block, h_b is the total height of the block and k can be seen as constant value.

Numerical results for the acceleration (eq. (4-8)) of the 2D block are provided in Figure 8. One iteration in every time step is performed. The figure shows the acceleration in function of the time. The progress of the acceleration matches the expectations, starting at a maximum value and going downward without any spikes. It proves that the leapfrog scheme based on equation (4-6) is working correctly without any issues regarding stability or convergence.

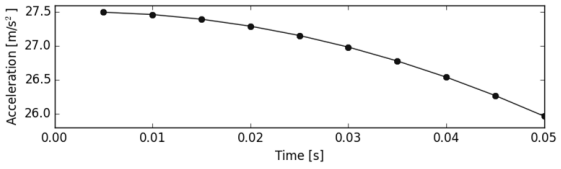

Figure 8: Vertical acceleration of the 2D block in function of the time for a fixed time step of 0.005 s.

4.3 Added mass instability

As mentioned in paragraph 4.1, the simulation of a 2D floating block failed when the width of the object increases with respect to the height. The reason for that phenomenon is probably due to an added mass instability. A possible solution was to use relaxation of acceleration.

In the present implementation, an explicit leapfrog scheme is used inside the motion solver (eq. (4-6)). Starting from the following equation:

$$m \cdot a + m_a \cdot a = -\Delta z \cdot k \cdot m \qquad (4\text{-}9)$$

in which m_a is the added mass and the right hand side is the force (hydrostatic part and weight of the block) derived from equation (4-8). Compared to equation (4-8), the term $m_a \cdot a$ is added to account for the acceleration force of the fluid on the object. This is a better approximation to the reality than equation (4-8) because all the fluid dynamics are incorporated in equation (4-9), except for the viscous forces (damping forces). Equation (4-9) can be rewritten to:

$$a^{n+1} = -\Delta z \cdot k - \frac{m_a}{m} \cdot a^n \qquad (4\text{-}10)$$

in which a^{n+1} is the acceleration at time step *n+1* and a^n is the acceleration from the previous time step. Three different numerical simulations are performed to check the influence of the added mass m_a. Again, only one iteration for every time step is simulated. Figure 9 shows the numerical results for the acceleration (eq. (4-10)) of the 2D block in function of time for respectively $m_a/m = 0.5$, *1.0* and *1.5*. In case $m_a < m$, the oscillation in acceleration damps out. For $m_a = m$, the oscillation remains constant. For $m_a > m$, the oscillation increases and the simulation fails.

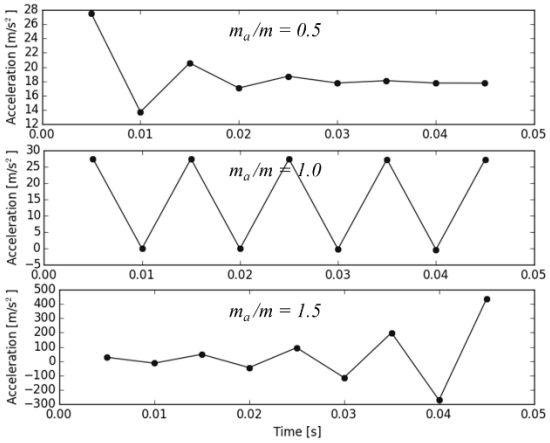

Figure 9: Vertical acceleration of the 2D block in function of the time where $m_a/m = 0.5$ (a), *1.0* (b) and *1.5* (c).

A possible solution to obtain a stable result is to rewrite equation (4-9) to an implicit formulation:

$$a_{i+1}^{n+1} = -\Delta z \cdot k - \frac{m_a}{m} \cdot a_i^{n+1} \qquad (4\text{-}11)$$

in which a_{i+1}^{n+1} is the acceleration at the current iteration of time step *n+1* and a_i^{n+1} is the acceleration from the previous iteration in the same time step. Also relaxation of acceleration is needed to reach a converged solution via a stable way in every time step, independent of the value of the relaxation factor. A smart way of applying relaxation exist in literature, related to the added mass effect (Söding, 2001):

$$a_{relax}{}_{i+1}^{n+1} = \frac{m \cdot a_{i+1}^{n+1} + m_a \cdot a_i^{n+1}}{m + m_a} = \alpha \cdot a_{i+1}^{n+1} + (1-\alpha) \cdot a_i^{n+1} \qquad (4\text{-}12)$$

in which m is the dry mass of the body, m_a is the added mass and α is the relaxation factor. The value of the relaxation factor is strongly coupled to the value of the added mass ($\alpha = m_a/(m+m_a)$) and will determine the way how to reach a converged time step. This is explained with Figure 10, Figure 11 and Figure 12 where the acceleration (eq. (4-12)) of the 2D block is given in function of the time or number of iterations. The added mass is set equal to the dry mass of the object ($m_a = m$), a fixed time step of 0.005 s is used and 20 iterations per time step are performed. In Figure 10, the value of the relaxation factor is equal to 0.5, which is exact $m_a/(m+m_a)$. Only one iteration is needed to reach convergence in the acceleration. In case the relaxation factor is 0.75 (Figure 11), convergence of the acceleration is reached with oscillations. This is opposite when a relaxation factor of 0.25 is used (Figure 12). Then, convergence of the acceleration is reached homogeneously without oscillations. The converged value of acceleration in every time step is the same for the three different relaxation factors presented. However, the way to reach convergence over the iterations for a certain time step is different. The same observations are obtained when the added mass increases (e.g. $m_a = 9m$). However, the stability region is narrower which means that the relaxation factor should not deviate too much from $m/(m+m_a)$. It proves that for the method presented, the value of the added mass should be known sufficiently accurate in case of significant added mass effects. Söding (2001) proposes a strategy to calculate the added mass based on a non-linear least squares method to obtain a converged time step after three implicit iterations. The trick is to understand that the total force on the object is dependent on the acceleration, linked by the added mass.

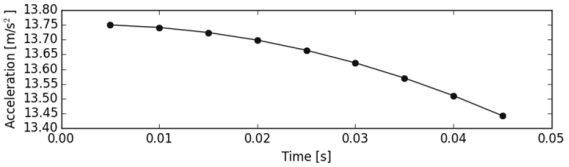

Figure 10: Vertical acceleration of the 2D block in function of the time ($m_a/m = 1.0$, relaxation factor = 0.5).

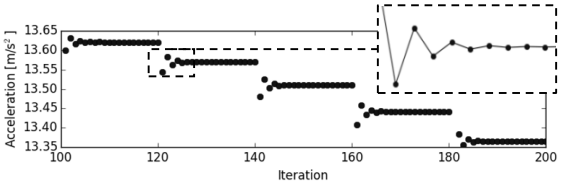

Figure 11: Vertical acceleration of the 2D block in function of the number of iterations ($m_a/m = 1.0$, relaxation factor = 0.75).

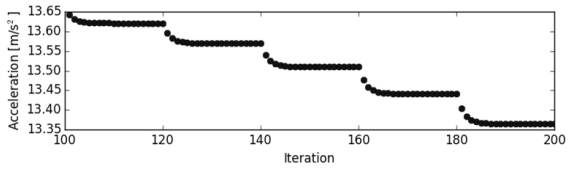

Figure 12: Vertical acceleration of the 2D block in function of the number of iterations ($m_a/m = 1.0$, relaxation factor = 0.25).

5 Research topics under investigation

The coupling between the fluid and motion solver has to be analysed to the finest details. The the acceleration must be calculated based on the force obtained with a real fluid solver (eq. (4-3)). The value of added mass should be determined accurate to obtain a stable simulation leading to a converged solution. Söding (2001) could serve as a guideline to calculate the added mass. However, the added mass instability is only significant for a wide object (e.g. Figure 3) but maybe it can be important for a 3D heaving buoy. What will happen if (extreme) waves are added to the numerical model? The motion solver may become unstable for a single heaving buoy. Therefore the presented research aims to develop a general motion solver which operates in all conditions for an arbitrary geometry. With only a relatively small effort, a complete six degrees of freedom motion solver can be developed.

The theoretical leapfrog scheme needs a fixed time step to be stable. However, a time step varying according the Courant number could lead to significant faster simulation times.

For coastal engineering purposes, the radiated wave field at a considerable distance from the buoy is important. However, there are some indications that propagation of radiated waves is a difficult problem in numerical studies using VoF methods. The start point of the propagation is the quality of the generated radiated waves. The quality is directly linked to the performance of the motion solver and the coupling between the motion and fluid solver. When waves are going to be generated at the inlet of the computational domain, two different wave fields are combined. The incident and radiated waves have both a different time and length scale which can be a challenge for a numerical study.

6 Conclusions

The aim of the paper was to present a thorough review of the interDyMFoam solver, especially the motion solver. Some pitfalls in the implemented methodology came up and were described. A new implementation has been presented and used to describe an academic case study of a 2D floating block.

The paper presented is a trigger to develop a stable motion solver for an arbitrary object. The added mass effect should be included. An introduction to the added mass instability was presented. A fast converging methodology is found in Söding (2001) which seems to be worth to investigate within OpenFOAM. A successful implementation would lead to a low number of implicit iterations, minimal three, together with larger time steps.

Acknowledgements

The Research Foundation – Flanders, Belgium (FWO) is gratefully acknowledged for the funding grant.

References

Birdsall, C. K., & Langdon, A. B. (2004). *Plasma Physics via Computer Simulation*. Taylor & Francis.

Dullweber, A., Leimkuhler, B., & McLachlan, R. (1997). Symplectic splitting methods for rigid body molecular dynamics. *The Journal of Chemical Physics*, *107*(15), 5840–5851.

Higuera, P., Lara, J. L., & Losada, I. J. (2013a). Realistic wave generation and active wave absorption for Navier-Stokes models. Application to OpenFOAM. *Coastal Engineering*, *71*, 102–118.

Higuera, P., Lara, J. L., & Losada, I. J. (2013b). Simulating coastal engineering processes with OpenFOAM. *Coastal Engineering*, *71*, 119–134.

OpenFOAM®. (2014). http://www.openfoam.org/

Söding, H. (2001). How to Integrate Free Motions of Solids in Fluids. In *4th Numerical Towing Tank Symposium*. Hamburg, Germany.

Analysis of the Manoeuvring Prediction of a Submarine by CFD Effects of Stern Appendage Configuration

Giulio Dubbioso. Stefano Zaghi and Riccardo Broglia

CNR-INSEAN, Rome/Italy, riccardo.broglia@cnr.it

Introduction

The prediction of the manoeuvring behaviour of a submarine vehicle is usually achieved by means of simplified manoeuvring mathematical models. Broadly accepted mathematical models describing a submarine manoeuvring performance are based on the traditional approach of Gertler and Hagen [1], later on modified by Feldman [2] in order to account for the typical phenomenon characterising the submarine dynamic response, namely the cross coupling effect between yaw and heave-pitch motions. These tools are extremely efficient and fast from the computational point of view because the forcing terms of the Euler rigid body equations, or alternatively, forces and moments acting on the body, are prescribed by means of hydrodynamic derivatives; in other words, hydrodynamic derivatives synthetize hydrodynamic loads acting on a body during a general motion. The success of these tools is strictly dependent on the reliability of the procedure followed for the evaluation of hydrodynamic coefficients. In case of a submarine, derivatives are evaluated ad-hoc case by case, due to critical operational task required for these vehicles.

It has to be emphasized that typical operational requirements of these vehicles are littoral surveillance and, of course, they're necessitate to sail near the free surface at "periscope depth" [3]. In these circumstances, the presence of the boundaries (free surface or bottom) can affect noticeably the vehicle manoeuvring response and, if not properly controlled, compromise its operational tasks. Moreover, new asymmetric threats require modern submarines to be able not only to ASW and ASuW roles in open water, but also to ISR, SPECOPs and complete integration with other assets in littoral scenarios, exactly where they're necessitate to sail near the free surface at "periscope depth" [3].

In this operational background, the Italian General Secretariat of Defence has been supporting and co-funding research projects on submarines maneuverability since 2003 (see for example [4]), previously with EUCLID (European Cooperation for Long Term in Defence) SUBMOTION and now with EDA (European Defence Agency) SUBMOTION 2, in pursuit of improvement in:

- **tactic:** looking for maneuver training simulators motions laws even more realistic;
- **technique:** accurate and reliable CFD predictions in the early stages of design process can reduce the need for physical prototypes to optimize maneuverability (choosing X or cross rudders, for example), in turn greatly accelerating development process and cutting costs of future submarines;
- **procedures:** enhancing the maneuvering prediction methods in confined waters to provide guidance to operators of existing submarines.

The principal aim of present research is to develop a reliable and practical procedure for the analysis of submarine maneuvering qualities while operating in different operative scenarios (open water, confined motions, escape or emergency maneuvers). In the present paper results of the free running, turning circle simulations are presented and discussed. Cross rudder and X-rudder configurations, sailing in open water are investigated. Simulations have been carried out using the CNR-INSEAN in-house finite volume solver, χnavis. The effect of the propeller is modeled by an actuator disk.

Numerical Setup

The CFD code solves the Navier-Stokes Equations for unsteady high Reynolds number (turbulent) free surface flows around complex geometries. The numerical solution of the governing equations is computed by means of the solver χnavis, which is a general purpose simulation code developed at CNR-INSEAN; the code yields the numerical solution of the unsteady Reynolds averaged Navier Stokes equations for unsteady high Reynolds number (turbulent) free surface flows around complex geometries (the interested reader is referred to [5]-[10] for details). The solver is based on a finite volume formulation with conservative variables co-located at cell centre. The spatial discretization of the convective terms is done with a third order upwind based scheme, whereas the diffusive terms are discretized with second order centred scheme and the time integration is done by second order implicit scheme (three points backward). The solution at each time step is computed iteratively by a pseudo-time integration that exploits an Euler implicit scheme with approximate factorization, local pseudo time step and multi-grid acceleration [11]. Although several turbulence models have been implemented in the code, in

all the simulations reported the turbulent viscosity has been calculated by means of the one-equation model of Spalart and Allmaras [12]. Free surface effects are taken into account by a single phase level-set algorithm [6]. Complex geometries and multiple bodies in relative motion are handled by a dynamical overlapping grid approach [8]. High performance computing is achieved by an efficient shared and distributed memory parallelization [9] and [10].

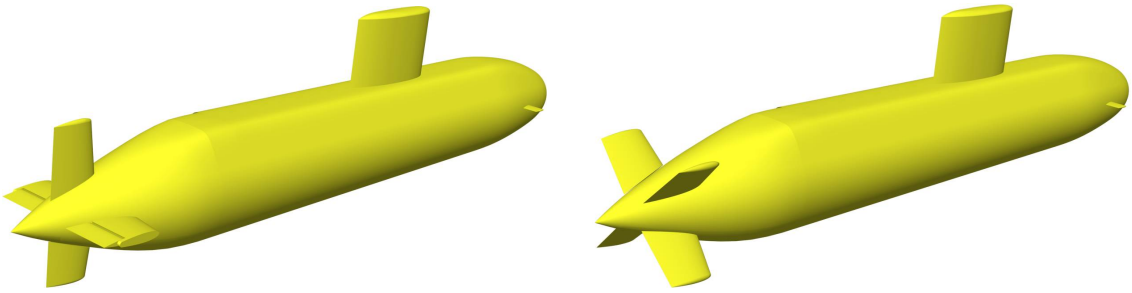

Figure 1: Submarine CNR-INSEAN 2475 model. Left, cruciform rudder; right, X rudder.

Geometry and Test Parameters

Numerical simulations have been carried out for the submarine chosen within the project (CNR-INSEAN 2475 model), see Figure 1. The model is fully appended with forward planes, the sail, and the stern appendages (rudders). The model is propelled by a seven blades propeller; in the numerical simulations the effect of the propeller is taken into account by means of the modified Hough and Ordway model, supplemented with an estimation of the lateral forces.

In the following, all the quantities are made non dimensional using the length of the main body and the advancement speed at model scale. The corresponding Reynolds and Froude numbers are Re=6.65 10^6 and Fr=0.21, respectively. Two different configurations have been tested, the original cruciform layout and a new X configuration; the rudder geometry was designed maintaining the same total rudder area of the C–rudder configuration in order to first assess a comparison about the course keeping qualities (i.e. directional stability).

Computational Mesh

The computational grid used consists of structured patched and overlapped blocks. The total number of volumes is about 11.8 and 10.5 million for the cross and the X rudder configuration, respectively. Grid distribution is such that the thickness of the first cell on the wall is always below 1 in terms of wall units, i.e. no wall functions have been used. The inclusion of the appendages is achieved by means of a Chimera approach; the relative motion of the different topologies is achieved by means of a dynamical overlapping grid algorithm. A multigrid technique is exploited in order to achieve a faster convergence to the solution in the pseudo-time; four levels of computational mesh are used. Every level is obtained from the finer one, by removing every other point along each spatial direction.

Numerical Results

In this paragraph the predictions of the numerical solver are presented for the C and X rudder configuration sailing in infinite depth (open water, OW). The analysis aims to systematically investigate the effect of the control surface configuration. In order to provide a grid study, free running maneuvers were carried out both on the reference (F) and a coarser (C) grid obtained by removing every other point along each coordinate.

It has to be pointed out that in case of the X-rudder configuration experimental free running maneuvering tests are not available, this configuration being exploratory in the present Research Project; in order to grasp an equivalent turning performance to the C rudder, two different rudder angles were considered in order to identify an equivalent control surface angle to perform a direct comparison between the two control surface arrangements. The maneuvering performance is evaluated in terms of typical macroscopic maneuvering parameters traditionally adopted in ship maneuvering, as well as kinematic parameter experienced during the steady phase of the turn; namely: advance (ADV), transfer (TRA), tactical diameter (TAD), turning radius (TCD), yaw rate, speed drop (during the steady phase) and drift angle. In order to investigate the reliability of the CFD predictions, a comparison in term of final diameter is made with available results from manoeuvring a mathematical model Cetena [16] and experimental results from QinetiQ [15].

Table 1: Trajectory and kinematic parameters, including grid refinement study.

Conf.	Man.	Grid	ADV	TRA	DTAC	DFIN	u/u0	r [deg/s]	Drift [deg]
C	*δ=15°*	C	2.83	1.35	2.97	3.01	0.66	7.04	10.01
		F	2.72	1.35	3.00	3.02	0.70	7.49	9.70
		Extr.	2.68	1.35	3.01	3.02	0.72	7.64	9.60
		U_{SN}%	1.40%	0.00%	0.33%	0.11%	1.92%	1.89%	1.10%
X	*δ=5°*	C	4.06	2.09	4.15	3.86	0.74	6.17	7.94
		F	3.91	2.00	4.09	3.83	0.79	6.67	7.80
		Extr.	3.86	1.97	4.07	3.82	0.82	6.84	7.75
		U_{SN}%	1.36%	1.57%	0.50%	0.26%	1.98%	2.32%	0.61%
	δ=10°	C	2.77	1.28	2.72	2.64	0.62	7.53	11.12
		F	2.62	1.12	2.63	2.61	0.65	8.01	11.01
		Extr.	2.57	1.07	2.60	2.60	0.66	8.17	10.97
		U_{SN}%	2.02%	5.56%	1.18%	0.39%	1.47%	1.88%	0.34%

Maneuvering Analysis

In Table 1 the results of the turning circle maneuvers are summarized for the C- and X-rudder configurations in terms of trajectory and kinematics parameters. Values refer to the coarse and fine grids adopted; the extrapolate value is obtained by the classical Richardson extrapolation, whereas, the numerical uncertainty U_{SN} (expressed as percentage of the extrapolated value) is evaluated following the procedure of Roache [16] for two grids.

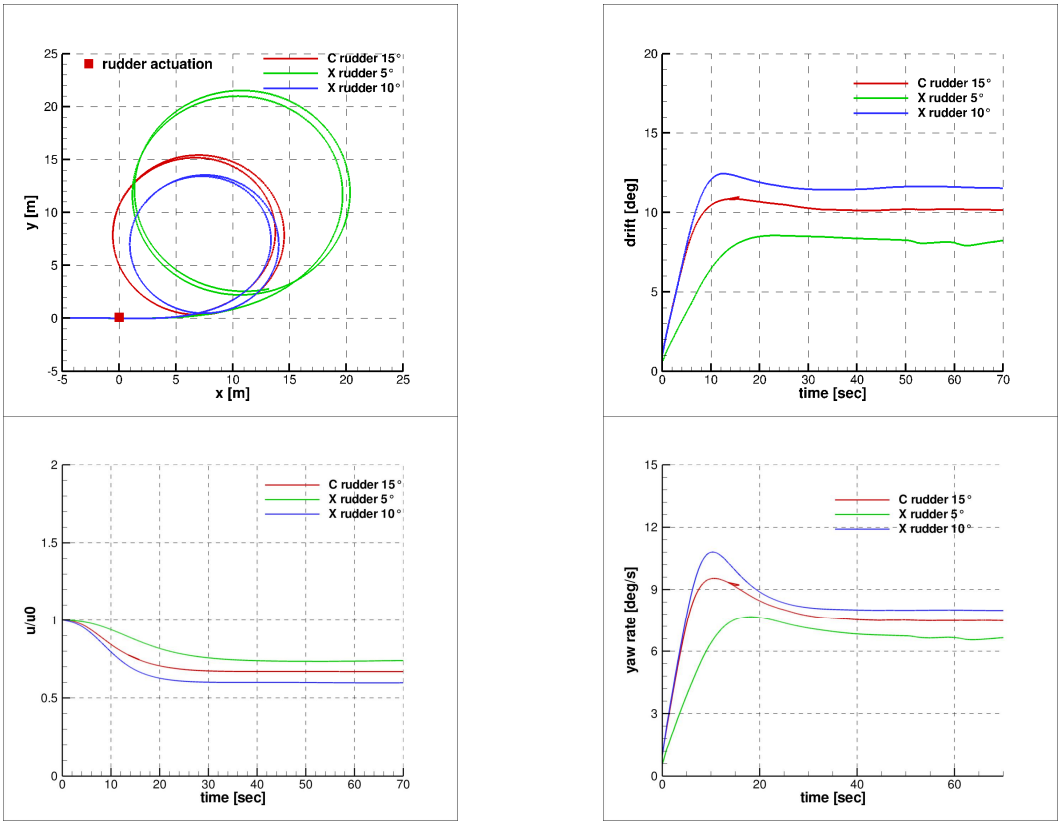

Figure 2: Trajectory and kinematics. Comparison between C- and X-rudder configurations.

In general, the X-rudder configuration is characterized by better turning qualities with respect to the C-rudder configuration. This is evidenced by the fact that a similar response to the C-rudder configuration is achieved with a 25% reduction of the rudder angle (i.e. δ=10°). This behavior is consequent to the criteria adopted to design the novel configuration: the rudder geometry was designed maintaining the same total rudder area of the C--rudder configuration in order to first assess a comparison about the course keeping qualities (i.e. directional stability). In

case of the X-rudder configuration, the effective (movable) area is greater with respect to the C configuration (all 4 rudders are deflected) and, consequently, a larger maneuvering (destabilizing) lateral force is exerted to the submarine. In order to stress the comparison between the two configurations, in Figure 2 both trajectories and time-histories of the kinematic parameters (axial velocity, drift angle and yaw speeds) are shown; the data considered refer to the results obtained on the finest mesh. The matching between the trajectories at $\delta=15°$ (C-rudder) and $\delta=10°$ (X-rudder) as well as the kinematic response confirms the synthesized results in Table 1.

Good grid convergences are inferred from the general very low numerical uncertainty. The effect of grid refinement is more evident for the trajectory parameters in the transient phase of the maneuver; in general, the numerical uncertainty of the ADV and the TRA is not higher than 2% and 5%, respectively (maximum values are observed for the tighter maneuver, i.e. $\delta=10°$, with the X-rudder configuration). On the contrary, both trajectory and kinematic parameters relative to the stabilized phase show a negligible numerical uncertainty lower than 1% and 2%, respectively. Refining the grid the ADV and the TRA parameters are noticeably reduced for both configurations (i.e., a more reactive response to the rudder control force is predicted when refining the grid). Moreover, the faster reduction of the speed drop (i.e. u/u0) and, on the other hand, the increase of drift angle and yaw rate immediately after the actuation of the rudder, further highlight as a less stable vehicle is predicted when increasing the grid refinement.

Table 2: Final diameter comparison (in meter at model scale (L_{PP}=4.95m)).

	EXP	**CFD**	**CET**
DFIN [m]	17.06	14.95	18.01
Δ%	-	-12.43%	5.57%

In Table 2 numerical results (i.e. the extrapolated value) of the C-rudder configuration are compared with the available experimental data and those gathered with two simplified maneuvering mathematical model performed by Cetena (CET) in terms of final diameter. The final diameter predicted by the CFD simulation is in good agreement with both experiments and CET simulation (differences are about 12% and 15%, respectively).

Flow Field Analysis

A global overview of distribution of the pressure field during the steady phase of the turn is shown in Figure 3 for the C- ($\delta=15°$) and X-rudder ($\delta=10°$) configuration. The results correspond to the finest grid level. For the sake of comprehension, the submarine is turning port-to-starboard side and the incoming flow (relative to the body) is directed from right to left, accordingly. A relatively large stagnation region is observed around the nose; immediately downstream, the pressure drops. In the forward portion of the body (approximately $0.15L_{PP}$ from the nose) the pressure levels on the wind side (i.e. right side viewing the submarine from the bow to the stern) seem higher than the lee side. This is consistent to the fact that the resultant force acts in the forward part of the body and is directed toward to the center of the turn. The flow impinges the sail with an incidence angle; as a consequence, the sail behaves like a small aspect ratio wing and develops lift directed from the wind to the lee side. A similar distribution can be glimpsed over the rudders in case of both configurations; it is seen that a stabilizing effect is provided by the control surfaces. A zoomed views of the pressure field around the rudders is reported in Figure 4 for the C and X configuration, respectively; in case of the X-rudder configuration, the performance of the rudders can be affected by interference with sail and the wake of the hull, as it can be clearly observed by the different extent of the stagnation region for the windward and leeward rudder positioned over the upper half of the submarine.

Finally, a further consideration has to be pointed out on the contribution of the stern rudder during the maneuver: after their actuation, the rudders provide a destabilizing effect, i.e. the force is directed from the lee to the wind side; the hull progressively attains an incidence with respect to the flow and the pressure distribution that develops over the body is such to sustain the turn of the submarine. The lateral and rotational velocity progressively increase while the effective incidence angle of the rudders diminishes and then changes sign (this is inevitable because up to this moment there is not any contribution that opposes to the turning motion); in this new hydrodynamic condition, the rudders exert a stabilizing effect that counteracts the (opposite) hydrodynamic moment developed by the hull. When the two contributions are close to each other, the equilibrium is achieved and the steady turn establishes.

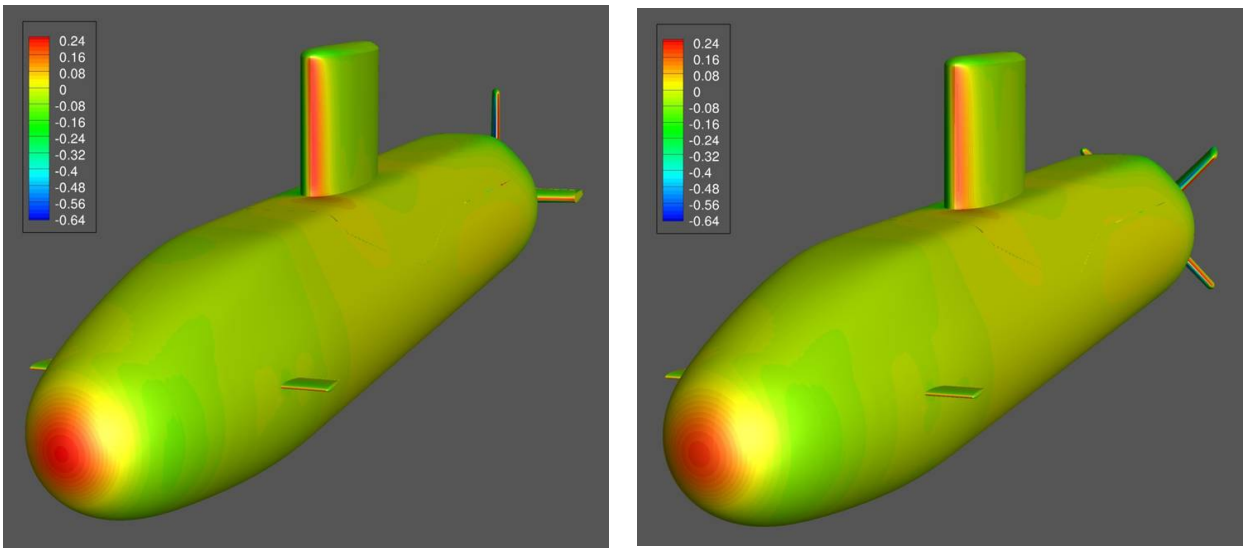

C-rudder $\delta=15°$ X-rudder $\delta=10°$

Figure 3: Pressure field on hull and control surfaces.

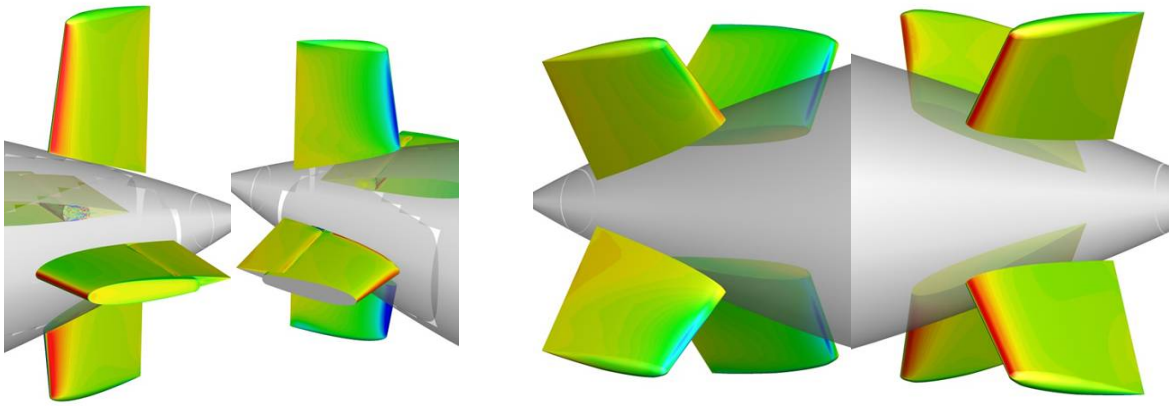

C-rudder configuration $\delta=15°$ X-rudder configuration $\delta=10°$

Figure 4: Pressure field on rudders.

Conclusions

The turning qualities of the submarine model equipped with the two different rudder configurations (cross and X) were investigated by means of numerical simulations. In particular, free running model tests were carried out by the CNR-INSEAN in-house general purpose χnavis solver. The analysis allowed examining many aspects related to the maneuvering prediction of a submarine vehicle. In particular:

- Capabilities of CFD solver based on the discretization of the unsteady Reynolds-Averaged Navier-Stokes equations in accurately reproduce the turning circle maneuver of a fully appended submarine have been demonstrated. The tool is also able to distinguish between two different stern appendages configurations without making use of any empiricism. The quality of the provided results has been proved by the good convergence properties and the very low numerical uncertainty. The comparison in terms of the final diameter was very satisfactory, the error being of the order of 10% both in the deep water and close to free surface condition.
- The turning qualities of the X-rudder configuration is superior with respect to the original one, principally because the movable area is larger; further studies are necessary to compare the realistic performance of the new configuration with during a realistic 6DoF simulation to better understand complex interaction phenomena due to hydrodynamic interference with the wake of the hull and the sail, as evidenced by the

different pressure field distributions.

- For the condition investigated, the rudder acts as a fixed appendage during the steady turning phase; this phenomenological behavior might be different from that characterizing the maneuvering response of surface vessel. Moreover, in this regard, a direct comparison between the hydrodynamic loads derived by CFD and System Based approaches can provide useful suggestion and guidelines for the improvement of simplified maneuvering modeling codes extensively applied in the preliminary design of a submarine.

Aknowledgements

This work has been supported by the Research Project "Submarine Coupled 6DoF Motions Including Boundary Effects", SUBMOTION II, financially supported by the Italian and the Norwegian MoDs.

References

[1] Gertler, M., Hagen, G.R., "Standard equations of motion for Submarine Simulation", 1967, NSRDC 2510
[2] Feldman J., "Revised Standard Submarine Equations of Motion", 1979, DTNSRDC/SPD-0393-39
[3] Burcher, R., Rydill, L., "Concept in Submarine Design"[M], 1994, Cambridge Ocean Technology Series 2.
[4] Broglia, R., Di Mascio A., Muscari, R., "Numerical Study of Confined Water Effects on Self Propelled Sibmarine in Steady Manoeuvres" [J], IJOPE, Vol.17, No 48, 89-96.
[5] Di Mascio A., Broglia R. Favini, B., 2001, "A second order Godunov-type scheme for naval hydrodynamics, in: Godunov Methods: Theory and Applications", Kluwer Academic/Plenum Publishers.
[6] Di Mascio A., Broglia R. and Muscari R., 2007, "On the application of the single-phase level set method to naval hydrodynamic flows", Computers & Fluids 36, 868–886.
[7] Di Mascio, A., Broglia, R., and Muscari, R. (2009). "Prediction of hydrodynamic coefficients of ship hulls by high-order Godunov-type methods". J. Marine Sci. Tech., Vol. 14, pag. 19-29.
[8] Di Mascio, A., Muscari, R., and Broglia, R. (2006). "An Overlapping Grids Approach for Moving Bodies Problems". 16th ISOPE, San Francisco, California (USA).
[9] Broglia R., Di Mascio A., Amati, G., 2007. "A Parallel Unsteady RANS Code for the Numerical Simulations of Free Surface Flows", Proc. of 2nd International Conference on Marine Research and Transportation, Ischia, Naples, Italy.
[10] Broglia, R., Zaghi, S., Muscari, R., and Salvadore, F. (July 2014). Enabling hydrodynamics solver for efficient parallel simulations. In Proc. International Conference on High Performance Computing & Simulation (HPCS), pages 803–810, Bologna, Italy.
[11] Favini, B., Broglia, R., and Di Mascio, A. (1996). "Multigrid Acceleration of Second Order ENO Schemes from Low Subsonic to High Supersonic Flows". Int. J. Num. Meth. Fluids, vol. 23, pag. 589-606.
[12] Spalart P.R. and Allmaras S.R., "A One-Equation Turbulence Model for Aerodynamic Flows", La Recherche Aerospatiale 1 (1994) 5-21.
[13] Broglia, R., Dubbioso, G., La Gala, F., Santic, F. and Sellini, M., (2013). CNR-INSEAN TR: WP-1.1: Studies on a submarine with fixed and moving appendages: measurement of global and appendage loads.
[14] Watt, G.D., "Estimates for the added mass of a multi component, deeply submerged vehicle", 1988, DREA Technical Memorandum 88/213.
[15] Kimber, N.I. Submarine motions in confined waters - EUCLID RTP 10.17 Free-maneuvering model experiments (Work Element 1.3), 2006. QinetiQ/06/01419.
[16] C. Notaro and J. Labanti. Submotion II –WP3 - Simulation tools. Improvement of simulator models using data from WP1., 2015. CETENA TR 12131.
[17] Roache, P. J. (1997). Quantification of Uncertainty in Computational Fluid Dynamics. Ann. Rev. Fluid Mech., 29:123–160.

Performance Prediction of a Semi-Displacement Luxury Yacht

Danilo Durante, Riccardo Broglia

CNR-INSEAN, Rome/Italy, danilo.durante@cnr.it

Introduction

The study of semi-displacement and planing vessels is an actual topic since the wide applications range, spanning from sport competitions to patrol boats. From a physical point of view, the high speed reached by these vessels implies a complex interaction between the structure and the free surface of the fluid with a complicate wave pattern developed downstream. The impact of the vessel on the water surface during its motion gives rise to a jet formation with a significant air entrapment and bubbles production. Actually the side jet is substantially definable in terms of a spray sheet, the dynamics of which is highly difficult to study both in experimental and numerical approaches. A lateral chine is intended to throw spray to the sides of the hull, to prevent water from rising up the hull sides and to create a smooth ride in seaway; moreover chines with a wide flat area (called chine flats) contribute significantly to create lift in the moving boat.

In the framework of a numerical approach, an important contribution has been recently addressed by Akkerman *et. al.* (2012) where an investigation at different Froude numbers was carried out on a Fridsma planing hull through a ALE-VMS approach. A comparison with the experimental data showed a good agreement for low Froude numbers, while discrepancies of $10 - 12\%$ are found on high speed cases.

The free surface bow flow around a fast and fine ship in calm water was studied in Landrini *et. al.* (2012) with an emphasis on generation and evolution of the breaking and splashing bow wave using the $2D + t$ theory. A validation was performed through comparison with experimental data and other numerical solutions available in the literature. The DDG51 vessel was used to carry on a parameter investigation in terms of the ship speed (Froude number) and surface tension. The influence of the Froude number on the patterned morphology and the importance of surface tension for small-scale ships in inhibiting the jet formation and evolution were verified.

The impact on the free surface during the hull motion (especially in waves) inspired a long number of works: from a numerical point of view Iafrati & Broglia (2008) and Broglia & Iafrati (2010) studied the effect of the impact of a symmetric and an asymmetric wedge on the free surface through a Finite Volume approach evaluating the wave pattern generated and the jet dynamics; Fu *et. al.* (2012) exploited an immersed boundary approach together with a VOF method (the Numerical Flow Analysis (NFA) code) for the study of the forces and moments on a deep-V planing craft. The impact of a wedge on the free surface was numerically simulated and experimentally validated as test case. In Fu *et. al.* (2014) results from a collaborative research effort involving the Computational Fluid Dynamics (CFD) codes CFDShip-Iowa and NFA were presented and discussed to examine the hydrodynamic forces, moments, hull pressures, accelerations, motions, and the multiphase free surface flow field generated by a planing craft at high-speed (Froude number $Fr = 1.8 - 2.1$) in calm water and waves. The steady forward speed test were performed for two kind of hulls: a prismatic and a double-stepped planing hulls. The sinkage and resistance were in good agreement for the two codes for the last configuration. The irregular wave simulations were carried out with CFDShip-Iowa and compared with experiments, showing a well modelled overall behaviour. Moreover, in Brizzolara & Serra (2007) an extensive study using an up to date RANSE VOF solver with free surface tracking capability was performed, testing the method on a wedge shaped prismatic planing hull, having a constant

deadrise angle of 20 degrees, systematically varying the running trim angle and wetted length. Results obtained, in terms of drag lift forces and longitudinal trimming moment, were compared with available experimental and semi-empirical theories.

In the present paper, the towing simulations of a semi-displacement vessel are carried out for Fr spanning from 0.6 to 1.2; sinkage and trim, and resistance curves are evaluated. The numerical computations have been pursued by using the unsteady RANS solver χnavis, which is a general purpose simulation code developed at CNR-INSEAN.

Figure 1: Azimut Grande 95RPH

Problem Assessment

In the present paper, the towing of the semi-displacement sailing yacht *Azimut Grande 95RPH* (figure (1)) is simulated. The vessel is characterized by a length between the perpendiculars of $L_{pp} = 22.54m$ and a displacement of $\Delta = 104t$. The global towing force is reduced to the center of gravity, the vertical and horizontal components of which are $-D\tan(\varepsilon+\varphi)$ and $-D$ respectively where D is the drag force and φ is the trim angle. Moreover, the vessel is towed along the propellers axis line, being f the distance respect to the center of gravity G, so a torque $-fD/\cos(\varepsilon+\varphi)$ is applied also. The sketch of the towing setup is reported in figure (2). The sinkage and trim are assumed free and nine simulations spanning from 18 to 34 knots are

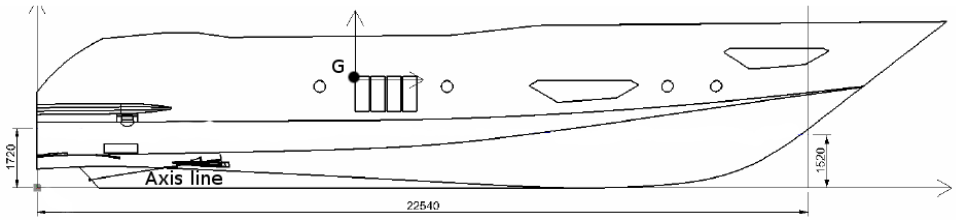

Figure 2: Hull longitudinal profile

carried out, the corresponding Froude and Reynolds numbers varying in the range $[0.623; 1.176]$ and $[2.09\,10^8; 3.94\,10^8]$, respectively.

In order to obtain a high and accurate refinements close to the hull and skeg, the domain has been discretized by 86 body–fitted patched and overlapped blocks, for a total of 4,670,464 cells. A multigrid technique is exploited in order to achieve a faster convergence to the solution in the pseudo-time; four levels of computational mesh are used. Every level is obtained from the finer one, by removing every other point along each spatial direction.

Grid distribution is such that the thickness of the first cell on the wall is always below 1 in terms of wall units, and at least 20 cells are within the boundary layer thickness ($y^+ = O(1)$,

i.e. and $\Delta/L_{pp} = O(20/Re)$, Δ being the thickness of the cell).

Numerical Approach

The study is pursued by means of numerical simulations; solution of the unsteady Navier-Stokes equations are achieved by the simulation code developed at CNR-INSEAN. The code yields the numerical solution of the Unsteady Reynolds averaged Navier Stokes equations with proper boundary and initial conditions. The algorithm is formulated as a finite volume scheme, with variable co-located at cell centers. Turbulent stresses are taken into account by the Boussinesq hypothesis, with several turbulence models (both algebraic and differential) implemented. Free surface effects are taken into account by a single phase level-set algorithm. Complex geometries and multiple bodies in relative motion are handled by a dynamical overlapping grid approach. High performance computing is achieved by an efficient shared and distributed memory parallelization (Broglia *et. al.* (2014)). For more details on the numerical code used the interested reader is referred to Di Mascio *et. al.* (2001, 2007, 2009) and Muscari *et. al.* (2006).

Results

The simulations performed in the velocity range $[18 - 34]$ Knots are carried out on four grid levels: the converged solutions on the three finest grids are sketched in figure (3) in terms of sinkage (left plot) and trim (right plot) and in figure (4) in terms of resistance. A satisfactory convergence of the sinkage is observed for the Froude numbers spanning from 0.7 to 1.1 while some problems are evident for the lowest (≈ 0.6) and the highest (≈ 1.2) Froude where the longer and shorter gravity waves occur, respectively: it is supposed that the coarsest grids are unable to solve in a reliable way the wave pattern produced by the vessel with the consequent over-estimation or under-estimation of the sinkage.

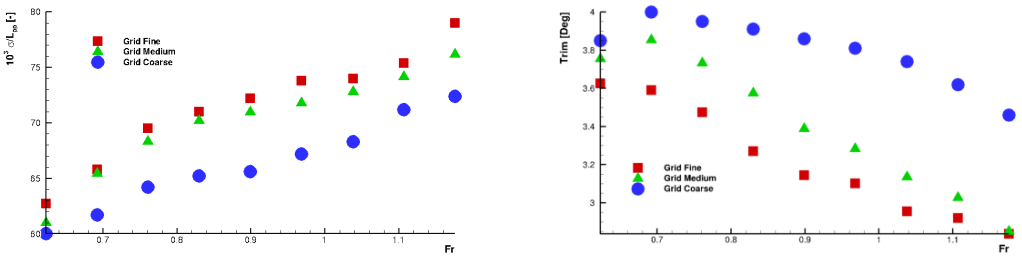

Figure 3: Sinkage (left) and Trim (right) versus Froude number.

The difficulties of the numerical simulations in the correct prevision of the trim angle is a well-known topic and for fast ships may be tricky to overcome, as evident in Akkerman *et. al.* (2012) where a mean error of one degree is appreciable in the simulations performed.

Good convergence properties are also seen for the drag coefficient $C_T = D/(1/2\rho U_\infty^2 L_{pp}^2)$ estimation, reported in figure (4); the worst trends are visible for the lowest and the highest Froude numbers caused by the reasons discussed above regard to the sinkage. It is worth to stress that in the present simulations the towing force, reduced to the center of gravity, possesses a vertical component proportional to the drag force. Therefore, large errors on the drag induce proportional errors on the sinkage, worsening the convergence of the solution for both quantities. For the sake of clearness and to stress the increasing of the total resistance with the Froude number, the dimensional resistance (in KN) is shown in the right plot of figure (4)

Results are summarized in table (1). In the table, extrapolated values (following Roache (1997)) for sinkage, trim and resistance coefficient are reported. Verification assessment is re-

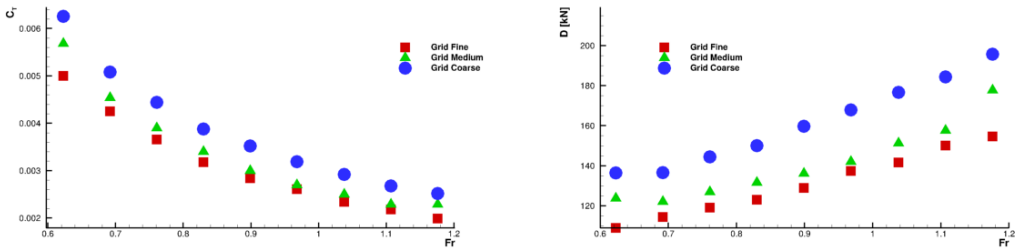

Figure 4: Resistance convergence respect to the Froude number in terms of C_T (left) and dimensional drag (right).

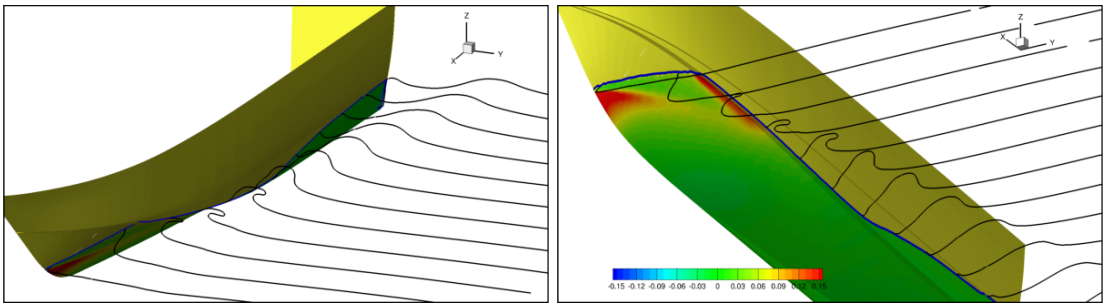

Figure 5: Wave cuts for $Fr \approx 1$ along the hull.

		Extrapolated values			Order of convergence			Uncertainty $U_{SN}(\%S_{RE})$			
Fr	Re	$\sigma/L_{pp}[-]$	$\tau[deg]$	$C_T[-]$	p_σ	p_τ	p_{C_T}	$U_{SN}(\sigma)$	$U_{SN}(\tau)$	$U_{SN}(C_T)$	**Aver.**
0.623	$2.09\,10^8$	$6.327\,10^{-2}$	3.58	$4.773\,10^{-3}$	−0.79	−0.45	−0.23	0.90%	1.21%	4.75%	2.29%
0.692	$2.32\,10^8$	$6.593\,10^{-2}$	3.50	$4.153\,10^{-3}$	3.21	−0.85	0.90	0.20%	2.51%	2.33%	1.68%
0.761	$2.55\,10^8$	$6.991\,10^{-2}$	3.39	$3.580\,10^{-3}$	1.74	−0.24	1.17	0.58%	2.53%	2.23%	1.78%
0.830	$2.78\,10^8$	$7.128\,10^{-2}$	3.17	$3.107\,10^{-3}$	2.56	0.14	1.13	0.39%	3.21%	2.36%	1.99%
0.899	$3.01\,10^8$	$7.262\,10^{-2}$	3.06	$2.787\,10^{-3}$	2.10	0.96	1.70	0.57%	2.64%	1.91%	1.71%
0.969	$3.25\,10^8$	$7.447\,10^{-2}$	3.04	$2.580\,10^{-3}$	1.19	1.54	2.44	0.90%	1.98%	1.16%	1.35%
1.038	$3.48\,10^8$	$7.441\,10^{-2}$	2.90	$2.287\,10^{-3}$	1.88	1.75	1.39	0.55%	2.07%	2.33%	1.65%
1.107	$3.71\,10^8$	$7.582\,10^{-2}$	2.88	$2.143\,10^{-3}$	1.21	2.47	1.83	0.56%	1.24%	1.71%	1.17%
1.176	$3.94\,10^8$	$7.995\,10^{-2}$	2.83	$1.891\,10^{-3}$	0.40	5.67	−0.36	1.19%	0.14%	5.25%	2.19%
							Overall	0.65%	1.95%	2.67%	1.76%

Table 1: Verification study.

ported as well; the estimation of the order of convergence and the numerical uncertainty (in percentage of the extrapolated value) are reported for all the computed variables. As observed above, good convergence properties are observed for medium speed tests only, and, primary, for sinkage and resistance computations. Numerical uncertainty is always very low, indicating that a grid converged results are practically achieved (i.e. similar results are obtained on the medium and fine grids). Numerical uncertainty for sinkage prediction is kept below 1% almost for the entire Froude range; larger uncertainty is seen for the trim estimation, with maximum value around 3% and an average (on the speed range) of about 2%. Numerical uncertainty for the resistance prediction shows larger values at the smaller and larger speeds (up to $\sim 5\%$); averaged numerical uncertainty is less than 3%. The overall numerical uncertainty (i.e. averaged over the speed range and the computed variables) is less than 2%.

An analysis of the free surface near the vessel reveals very interesting details. The case $U_\infty = 28Kn$ (i.e. $Fr \approx 1$) is discussed below as an example: same considerations can be drawn for the whole velocity range considered. The figure (5) is obtained through a collection of 12 wave cuts spanning from transom to the bow: the pressure field over the vessel is over-imposed for highlight the areas most stressed on the wetted surface of the hull. As stressed in the introduction, an important feature of the fast ship vessels is the presence of an intense bow jet

that is deflected by the hard chines on the boat sides.

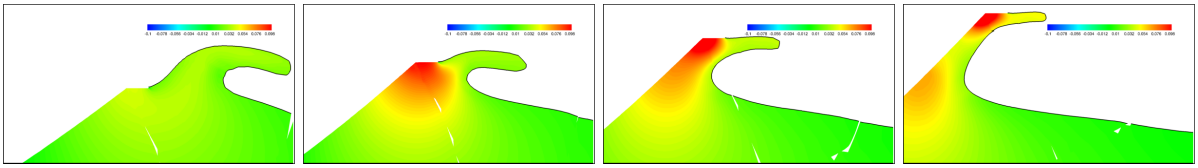

Figure 6: Wave cuts for $Fr \approx 1$ along the hull: magnification of spray for (from left to right) $x/L_{pp} = 0.65$, 0.7, 0.75 and 0.8.

From the figure (5) is clearly visible this mechanism that induces an intensive spilling with a consequent bubbles entrapment and the side foam formation. The spilling jet interests about an half of the hull length and some sections (0.65,0.7,0.75,0.8 L_{pp}) are magnified in figure (6): the jet presents a root with an high pressure which justifies the intense area on the side of the hull, visible in the right plot of figure (5) just beneath the chine. A similar behaviour in a simpler case is described in Durante *et. al.* (2014) where the jet root formed by a planing flat plate is discussed. In the bottom row plots of figure (6), the developing of the jet along the hull when approaching to the bow is depicted. The jet root becomes more intense and finally splits in two structures: a weak jet due to the hull advancing and a second and stronger one due to the impact of the latter with the hard chine (see the right plot in the bottom row of figure (6)).

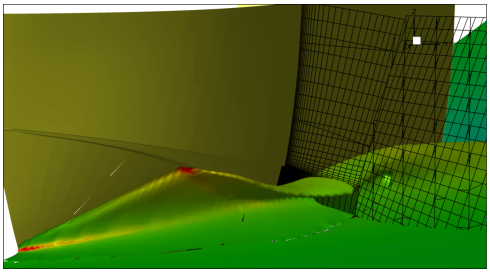

Figure 7: Pressure distribution over the free surface for $Fr \approx 1$ and grid stretching.

A remark on the grid stretching is the purpose of the figure (7), where a slice of the computational mesh near the side wave crest indicates an important change in the cell dimensions from the body-fitted grid to the near wake one. The overlapping grids approach allows an high time machine saving even if the complexity of the breaking of the side jet is lost and will be the matter of the future works. It may be useful to stress how the pressure field over-imposed on the free surface shows again the high pressure areas visible on the hull in figure (5).

Conclusions

In the present paper a study of the trim and sinkage of a semi-displacement vessel is addressed. A chimera overlapping grid approach is exploited in order to describe in a suitable way the flow field generated by the hull with a particular attention placed on the side jet of the hull. Even if the breaking of the jet is not resolved, some important features are well captured such as the hard chine interaction with the primary jet due to the straight motion of the vessel that produces a secondary and more intense jet. The convergence trend of the trim and sinkage is quite satisfactory in the Froude range explored and a particular accuracy is achieved for the mean Froude numbers. Validation assessment of the straight ahead results, including the comparison with experimental data, and an accurate analysis of the wave pattern in straight motion and in drift, together with a validation of numerical results with the experiments, will be the matter of future activities.

References

Akkerman, I. Dunaway, J. Kvandal, J. Spinks, J. Bazilevs, Y. Toward free-surface modeling of planing vessels: simulation of the Fridsma hull using ALE-VMS. *Computational Mechanics*, **50**: 719–727, 2012.

Brizzolara, S. and Serra, F. Accuracy of CFD codes in the prediction of planing surfaces hydrodynamic characteristics. 2^{nd} *International Conference on Marine Research and Transportation*, Ischia, Naples, 2007.

Broglia, R. Zaghi, S. Muscari, R. and Salvadore, F. Enabling hydrodynamics solver for efficient parallel simulations. *Proc. International Conference on High Performance Computing & Simulation (HPCS)*, July 2014. Bologna, Italy.

Iafrati, A. and Broglia, R. Hydrodynamics of Planing Hulls: a Comparison Between RANS and 2D+t Potential Flow Models. *Proc. of the 2727*$^{\text{th}}$ *Symposium on Naval Hydrodynamics*, Seoul, Korea, 2008.

Broglia, R. and Iafrati, A. Hydrodynamics of Planing Hulls in Asymmetric Conditions. *Proc. of the 28th Symposium on Naval Hydrodynamics*, Pasadena, CA, September 12-17, 2010.

Di Mascio, A. and Broglia, R. A second order Godunov-type scheme for naval hydrodynamics. Godunov Methods: Theory and Applications, **26**: 253–261, 2001.

Di Mascio, A. and Broglia, R. and Muscari, R. On the application of the single-phase level set method to naval hydrodynamic flows. *Computers and Fluids*, **36**: 868–886, 2007.

Di Mascio, A. and Broglia, R. and Muscari, R. Prediction of hydrodynamic coefficients of ship hulls by high-order Godunov-type methods. *Journal of Marine Science and Technology*, **14**: 19–29, 2009.

Durante, D. Broglia, R. Maki, K. J. Di Mascio, A. A study on the effect of the cushion pressure on a planing surface. *Ocean Engineering*, **91**: 122–132, 2014.

Fu, T.C. O'Shea, T.T. Judge, C.Q. Dommermuth, D. Brucker, K.A. and Wyatt, D.C. A Detailed Assessment of Numerical Flow Analysis (NFA) to Predict the Hydrodynamics of a Deep-V Planing Hull. *Proc. of the* 29^{th} *Symposium on Naval Hydrodynamics*, Gothenburg, Sweden, August 26-31, 2012.

Fu, T.C. Brucker, K.A. Mousaviraad, S.M. Ikeda, C.M. Lee, E.J. O'Shea, T.T. Wang, Z. Stern, F. and Judge, C.Q. An Assessment of Computational Fluid Dynamics Predictions of the Hydrodynamics of High-Speed Planing Craft in Calm Water and Waves. *Proc. of the* 30^{th} *Symposium on Naval Hydrodynamics*, Hobart, Tasmania, November 2-7, 2014.

Landrini, M. Colagrossi, A. Greco, M. Tulin, M.P. The fluid mechanics of splashing bow waves on ships: A hybrid BEM-SPH analysis. *Ocean Engineering*, **53**: 111–127, 2012.

Muscari, R. and Broglia, R. and Di Mascio, A. An overlapping grids approach for moving bodies problems. 16^{th} *International Offshore and Offshore and Polar Engineering Conference Proceedings*, isbn: 1880653664, 2006.

Spalart, P.R. and Allmaras, S.R. A one-equation turbulence model for aerodynamic flows. La Recherce Aerospatiale, **1**: 5–21, 1994.

Roache, P.J. Quantification of Uncertainty in Computational Fluid Dynamics. Ann. Rev. Fluid Mech., **29**: 123–160, 1997.

Conservation of the Characteristics of a Propeller Tip Vortex

Dag-Frederik Feder, Robinson Perić, Moustafa Abdel-Maksoud
Institute of Fluid Dynamics and Ship Theory
Hamburg University of Technology (TUHH), Hamburg, Germany
Email: {dag.feder, robinson.peric, m.abdel-maksoud}@tuhh.de

1 Introduction

The simulation of trailing vortices is a challenge for common computational fluid dynamics (CFD) techniques. In nature, trailing vortices extend far downstream; however, in flow simulations based on the Navier-Stokes equations, discretisation errors lead to an unphysically strong decay of coherent vortices on coarse grids. A numerical approach to overcome this problem is vorticity confinement (VC). It describes a group of methods which aim to counteract the unphysically strong vortex decay by introducing momentum source terms into the Navier-Stokes equations. The VC method was originally developed by Steinhoff in 1994 [8]. Several modifications have been presented by different authors, some of these are compared in Sec. 3; an overview can be found in [2].

In this work, a new class of approaches for the conservation of coherent vortices is suggested named vortex conservation methods. It is based on conserving fundamental characteristics of the coherent vortex. Therefore, three methods are formulated in Sec. 4. In section 6 the results of the simulation of a propeller tip vortex for a widely-used VC method and the new approaches are compared.

2 Vortex Flow

The tip vortex of a propeller is a trailing vortex generated downstream of the blade tip within a roll-up process. In this work, the Lamb-Oseen model [5] is used as analytical vortex description, where the axial and radial velocity components are zero and the tangential velocity is the same as for a Burgers vortex [1]. The tangential velocity as a function of distance r from the vortex core is

$$v_\theta(r) = v_{\theta,a}\,\frac{a}{r}\,\frac{1-e^{-\alpha\left(\frac{r}{a}\right)^2}}{1-e^{-\alpha}}, \qquad (1)$$

with core radius a, peak tangential velocity $v_{\theta,a}$ and α so that the maximum occurs at $r=a$; a sufficiently accurate value is $\alpha = 1.256$.

3 Classification of Existing Vorticity Confinement Approaches

When using VC, a source term $\vec{S}$ is introduced into the momentum conservation equations, e. g. for incompressible flow

$$\frac{\partial \vec{v}}{\partial t} + (\vec{v}\cdot\vec{\nabla})\vec{v} = -\frac{1}{\rho}\vec{\nabla}p + \nu\vec{\nabla}^2\vec{v} + \vec{S}, \qquad (2)$$

with velocity $\vec{v}$, density ρ, pressure p and kinematic viscosity ν. For different VC methods, $\vec{S}$ can be generalized to

$$\vec{S} = \varepsilon\, f(h)\, C_i\, \vec{s}. \qquad (3)$$

Direction vector $\vec{s}$ is defined by

$$\vec{s} = \frac{\vec{\nabla}|\vec{\omega}|}{|\vec{\nabla}|\vec{\omega}||} \times \frac{\vec{\omega}}{|\vec{\omega}|}, \qquad (4)$$

thus $\vec{s}$ points along vorticity magnitude contour lines. The magnitude term $\varepsilon\, f(h) C_i$ provides the distribution of the source in the flow field. The user-defined proportionality coefficient ε is case-dependent. $f(h)$ is a function of the local cell size h, that should ensure consistency of the momentum source with the mesh size. The components for some existing models are given in Tab. 1. The factor C_i describes the distribution of $\vec{S}$ in the domain. Figure 1 shows that most presented approaches introduce momentum disproportionally to the momentum within the vortex. In all methods except method H, the momentum source is strongest at the vortex centre, where in reality the momentum would approach zero. This result was obtained from flow simulation results, recorded in a tube-like domain with a Lamb-Oseen velocity profile at the inlet superimposed by a constant axial flow.

Table 1: Comparison of different VC methods: method abbreviation, reference, distribution C_i and dependence on the grid size $f(h)$

	Reference	C_i	$f(h)$
A	[8]	$\lvert\vec{\omega}\rvert$	-
B	[3]	$\lvert\vec{\omega}\rvert$	linear
C	[7]	$\lvert\vec{u}\cdot\vec{\omega}\rvert$	-
D	[2]	$\lvert\vec{u}\cdot\vec{\omega}\rvert$	logarithmic
E		$\lvert\vec{u}\rvert\,\lvert\vec{\omega}\rvert$	
F	[6]	$\lvert\vec{u}\rvert\,\lvert\vec{\omega}\rvert$	-
G		$\lvert\vec{\omega}\rvert^2$	linear
H		$\lvert\vec{\nabla}\lvert\vec{\omega}\rvert\rvert\,\lvert\vec{\omega}\rvert$	quadratic

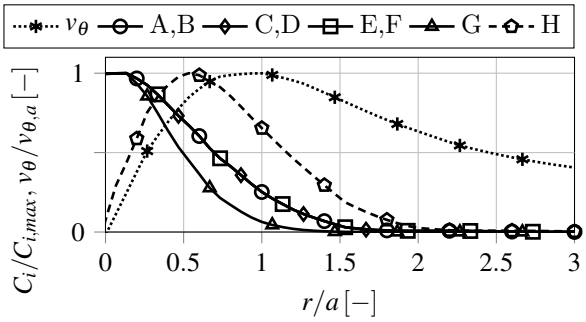

Figure 1: Distribution of the source terms C_i and the tangential velocity v_θ scaled to their maximum values over distance r to the vortex centre per vortex core radius a, given for a simulated coherent vortex

The VC source term can lead to numerical instabilities within the boundary layer as mentioned in [6]. Therefore, method H contains a formulation to turn off the source term in the vicinity of boundaries. Method H is implemented in the flow solver STAR-CCM+ and will be used for the comparison with the new approaches.

4 Vortex Conservation

This section presents a new approach for an improved prediction of coherent vortices. It is based on the forcing of vortex properties, such as a reference vorticity or a reference tangential velocity profile, with the target to conserve a coherent vortex. On this basis three methods are presented in the following. These methods introduce a momentum source term $\vec{S}$ in Eq. (2) as

$$\vec{S} = q_i \vec{t}, \tag{5}$$

where q_i represents the magnitude of the source for method i. The vector $\vec{t}$ points in the direction of the rotating flow around the vortex axis. One possible approach to determine the axis is the use of the vorticity vector at the nearest point L on the vortex core line $\vec{\omega}_L$. Hence, $\vec{t}$ is for any cell

$$\vec{t} = \frac{\vec{r}_{CL} \times \vec{\omega}_L}{\lvert\vec{r}_{CL} \times \vec{\omega}_L\rvert}, \tag{6}$$

where $\vec{r}_{CL}$ is the vector from the cell centre C to the nearest point L on the vortex core line, as shown in Fig. 2.

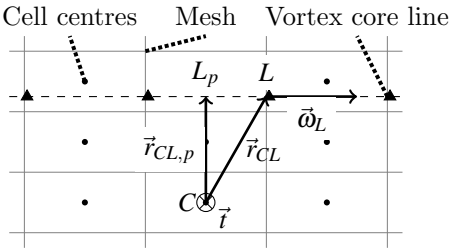

Figure 2: Discrete vortex core line (−−) on a rectilinear grid

The magnitude term q_i represents the distribution of the momentum source of method i and forces a property of the actual vortex to a user-defined reference value. Exemplarily, three methods are formulated:

$$q_{\omega,act} = A_1\,(\omega_{ref} - \omega_{act})\,v_{\theta,act}\,, \tag{7}$$

$$q_{\omega,ref} = A_2\,(\omega_{ref} - \omega_{act})\,v_{\theta,ref}\,, \tag{8}$$

$$q_v = A_3\,(v_{\theta,ref} - v_{\theta,act})\,, \tag{9}$$

where A_i is a case-dependent forcing coefficient; the case-independent procedure to obtain the optimum value for A_i is explained below.

The factor $\omega_{ref} - \omega_{act}$ accounts for the difference between the reference and actual vorticity magnitude at the vortex centre. The factor $v_{\theta,ref} - v_{\theta,act}$ denotes the difference of the actual to the reference tangential velocity profile. All three terms consider the characteristic tangential velocity profile of a vortex, represented either by the actual or the reference vortex.

For each cell, the actual tangential velocity is calculated as

$$v_{\theta,act} = \vec{t} \cdot \vec{v}_{ind}, \tag{10}$$

with direction $\vec{t}$ and the induced velocity $\vec{v}_{ind} = \vec{v} - V_\infty \vec{e}_\infty$, where V_∞ and $\vec{e}_\infty$ are velocity and unit

vector in direction of the flow specified at the velocity inlet. For this investigated case, the induced velocity is chosen in Eq. (10) instead of the velocity $\vec{v}$, because it represents the characteristic tangential velocity profile of the tip vortices more distinct. This needs not to be valid for other applications.

The reference velocity $v_{\theta,ref}$ is taken from a Lamb-Oseen vortex with reference core radius a_{ref} and reference peak velocity $v_{\theta,a,ref}$ according to Eq. (1). To determine $v_{\theta,ref}$ for any cell C, r is approximated by $r \approx |\vec{r}_{CL,p}|$ with the vector

$$\vec{r}_{CL,p} = \frac{1}{\vec{\omega}_L^2} \left(\vec{\omega}_L \times \vec{r}_{CL}\right) \times \vec{\omega}_L \,, \qquad (11)$$

which corresponds to $\vec{r}_{CL}$ projected to the plane perpendicular to the vortex axis represented by $\vec{\omega}_L$, see Fig. 2. This can be proven by the use of the triple product expansion

$$\vec{r}_{CL,p} = \vec{r}_{CL} - |\vec{r}_{CL}| \cos\sphericalangle(\vec{r}_{CL}, \vec{\omega}_L) \frac{\vec{\omega}_L}{|\vec{\omega}_L|} \,. \qquad (12)$$

Figure 3 shows qualitatively the reference and the actual velocity profiles and the distribution of the different source terms q_i. The maximum of the source terms takes place first for q_v, second for $q_{\omega,ref}$ and last for $q_{\omega,act}$ with regard to distance r. For these analytical vortices, q_v vanishes outside the core for $r \gtrsim 2\,a_{ref}$ and $q_{\omega,act}$ and $q_{\omega,ref}$ become nearly equal for $r \gtrsim 3\,a_{ref}$.

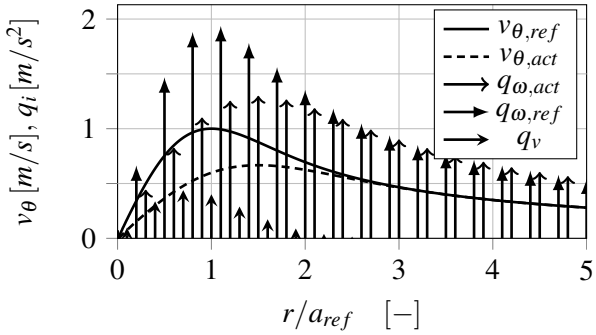

Figure 3: Distribution of the source terms q_i for a Lamb-Oseen-type vortex, with $A_1 = A_2 = 1$ and $A_3 = 1\,s^{-1}$

The reference vortex ideally represents the physically correct solution. Therefore, a realistic decay of the reference properties could be prescribed; however, this is not further considered here since the target is to evaluate the applicability of the new approaches. Referring to Eqs. (7) to (9), it becomes evident that the source terms q_i need different numbers of input parameters such as ω_{ref}, a_{ref} and $v_{\theta,a,ref}$: $q_{\omega,act}$ needs the least and requires the least computational effort, while $q_{\omega,ref}$ needs the most and is also the most complex formulation of (7) to (9).

Vortex Conservation requires the location of the vortex core line for the calculation of the source term. In STAR-CCM+, the vortex core line is determined via analysis of the eigenvalues of the velocity gradient matrix $\vec{\nabla}\vec{v}$ as described in [4] and [9], except that in this work, $\vec{\nabla}\vec{v}_{ind}$ was taken for this, since this provided a better determination of the vortex core line.

It is reasonable to restrict the effect of the new source terms by different criteria. One criterion is to define a tube like region around the vortex core line and to switch the source term off outside. Thereby the distance $|\vec{r}_{CL}|$ and/or $|\vec{r}_{CL,p}|$ is compared to a predefined distance r_T. In this work, $r_T = 1.5\,a_{ref} > |\vec{r}_{CL}|$ was used.

Another criterion is to switch the source term off in domain parts where it is obvious that no coherent vortex will appear. In this work, the source domain is restricted to vortex core lines, where the distance to the x-axis is higher than a minimum value $r_{min} = D_P/6$. Besides, it is restricted in x-direction until $x_{max} = 1.5\,D_P$, to be able to analyse the evolution of the vortices after switching the source term off.

If an actual vortex property is larger than the corresponding reference property, the source term may become negative, compare Eq. (7) to Eq. (9). This case was suppressed in this work, because the reference values were lower compared to the actual values in the vicinity of the wing tip.

In some cases it is reasonable to exclude vortices that do not originate from the wing tip from the forcing. This can be achieved by activating the source term only for those cells, for which the vorticity magnitude at the corresponding vortex core line surpasses a threshold value $|\vec{\omega}_L| > \omega_{min}$.

For the case-dependent coefficients A_i in Eqs. (7) to (9) there exists a case-independent procedure by which the optimum value for A_i can be obtained: Starting from the converged sta-

tionary or the periodic unsteady solution without vortex conservation, the source term is switched on starting with $A_i = 0$. Then A_i is gradually increased until the vortex blows up. The optimum A_i is the value below the critical blow-up value of A_i.

5 Simulation Setup

The flow around a propeller is simulated to analyse the influence of the presented vortex conservation methods on the evolution of tip vortices. The main properties of a model propeller with four blades are diameter $D_P = 0.24$ m and pitch ratio $P/D_P = 0.8$.

The advance ratio is set to $J = 0.567$, 10 % lower than the advance ratio of the maximum efficiency, and the revolutions are set to $n = 10$ Hz. Based on the homogeneous inflow, only one quarter of the propeller (one blade) is simulated using periodic boundary conditions. The domain, mesh and coordinate system are shown in Fig. 4. The x-axis indicates the direction of the inflow, the origin of the system is situated in the plane of the wing tip. The diameter of the quarter cylinder is $4D_P$, the location of the inlet and outlet boundaries are $x_{in} = -2D_P$ and $x_{out} = 5D_P$. The flow is assumed laminar and a rotating reference frame is used to model the propeller rotation.

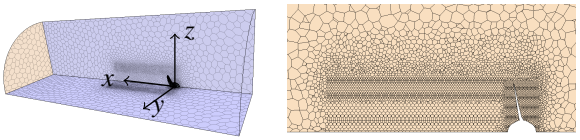

(a) Domain (b) Mesh

Figure 4: Simulation domain and mesh

In the following, the cell sizes are given in percentage of the propeller diameter. The relative cell size for the outer region is 20 %. Furthermore, the mesh is refined three times, first within a cylinder around the propeller blade to 1.6 %. For the further refinements, two cylinders around the x-axis between $x = [-0.21D_P, 1.92D_P]$ m with the radii 0.28 m and 0.16 m are used. The region inside the larger cylinder minus the region inside the smaller one is refined to 2.4 % and the region inside the smaller cylinder is refined to 4 %. Thus the mesh where the trailing vortices evolve downstream features roughly 3.5 cells across the reference vortex core region $2a_{ref} = 0.02$ m. The total number of cells is about 120000. The propeller boundary layer is not resolved since the generation of the tip vortex can be considered as a mainly pressure-driven phenomenon.

The STAR-CCM+ steady flow solver is used with all approximations based on second order. Velocity V_∞ is prescribed as homogeneous inflow, the outlet boundary is set to a pressure outlet, the lateral surface of the cylinder domain is set to a slip condition and the propeller surface is set to no-slip.

The governing equations are discretised using the finite volume method (FVM); the interpolation of variables is based on approximations of second order and for the calculation of unknown cell variables the equation system is linearised. The simulations are conducted using the implicit steady segregated solver in STAR-CCM+. The SIMPLE method is used for the correction of the pressure field, the convective terms are approximated by a second order upwind scheme. The under-relaxation factors are 0.7 for velocity and 0.3 for pressure.

In the following, the settings of the vortex conservation and VC methods are specified. The same reference vortex is used in all simulations. For this, q_v is evaluated with the parameters $v_{\theta,a,ref} = 0.2$ m/s and $a_{ref} = 0.01$ m. The resulting vorticity magnitude is $|\vec{\omega}_L| \approx 60$ 1/s, hence $\omega_{ref} = 60$ 1/s is set for $q_{\omega,act}$ and $q_{\omega,ref}$. Further restrictions of the source terms are described in Sec. 4. The minimum vorticity magnitude on the vortex core line for the source term to be active is set to $\omega_{min} = 0.5\,\omega_{ref}$ for $q_{\omega,ref}$ and q_v. For the existing VC method H, the non-dimensional wall distance is set to 1000 and the coefficient ε was varied.

The simulation without momentum source terms converged after 600 iterations. Starting from this point, the VC method H or one of the source terms according to Eqs. (7) to (9) is activated. The resulting optimum forcing coefficients for this case are: $A_1 = 30$, $A_2 = 40$, $A_3 = 2000\,1/s$. The source terms q_i are faded in linearly within 20 iterations. The simulation results are evaluated after 1000 further iterations for a steady state solution and compared to each other in the next section.

6 Results

Figure 5 shows the evolution of the vortex and the distribution of the source terms for the situation when the momentum source terms are activated. The abscissa represents a cut through the vortex at $x = 0.08 D_P$ along the z-axis, indicated by the cut A-A in Fig. 7a; $2z_L/D_P = 0.975$ indicates the location of the vortex core line L. The upper image shows the

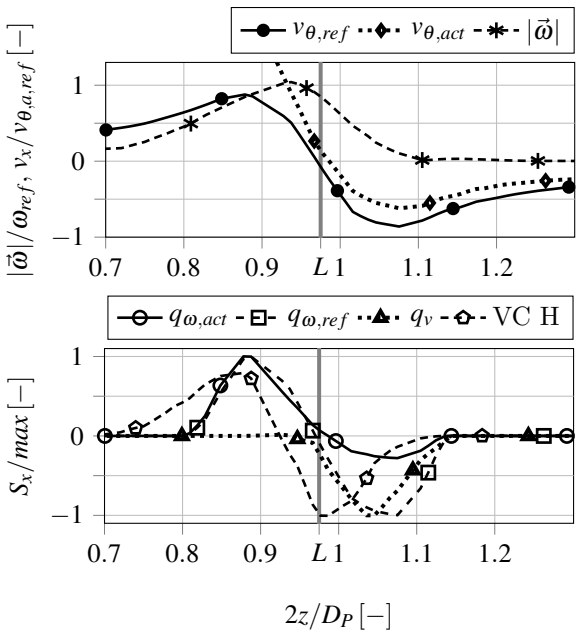

Figure 5: Converged solution without momentum source; upper figure: vorticity magnitude and x-component of the tangential velocity; lower figure: x-component of the momentum source

x-component of both the actual and reference velocity and further the vorticity magnitude. The actual velocity profile indicates the high velocities in the propeller jet for $z < z_L$ and the backflow outside, hence the tip vortex flow swirls. The vorticity magnitude distribution indicates the vortex core region; it shows further that the local maximum lies about a half core radius in z-direction $\Delta z \approx 0.5\,a$ next to the identified vortex centre z_L, which marks the centre of the rotating induced velocity field.

The lower image shows the x-component of the momentum source terms $\vec{S}$. For all q_i, it is zero at the vortex core z_L as well as from a distance of about $2a_{ref}$ to the vortex centre. Of the q_i terms, $q_{\omega,act}$ considers the actual vortex flow most, while $q_{\omega,ref}$ considers it least. Thus for $q_{\omega,ref}$ and q_v, disturbances in form of weak vortices may occur close to the tip vortex when rapidly switching on the source term. However, due to the linear fading their core vorticity is below ω_{min}, so these disturbances are not supported by the source terms and vanish with the convergence of the flow solution.

In contrast, the distribution of the source terms for VC method H in Fig. 5 shows clear discrepancies to the actual tangential vortex flow: Within $2z/D_P = [0.925, 0.975]$ the momentum source acts against the tangential velocity. This inconsistency concerns all methods mentioned in Tab. 1, because the direction of $\vec{S}$ is given by the same vector $\vec{s}$.

Figure 6 shows the evolution of the vorticity magnitude at the vortex core line $|\vec{\omega}_L|$. Without a momentum source, the vortex core vanishes after about 1/6 revolutions. The vorticity for all vortex conservation methods converges to the intended reference value in the specified domain parts. In the domain parts where the source term is inactive ($x > x_{max} = 1.5 D_P$), the vorticity decays exponentially; both effects can be seen in Fig. 7 as well.

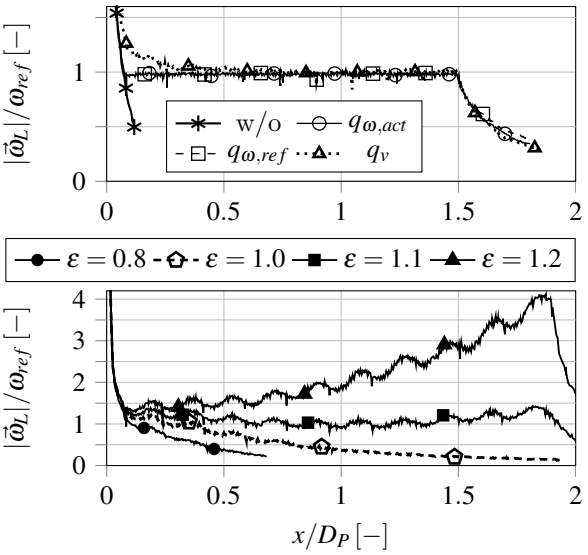

Figure 6: Evolution of the vorticity magnitude at the vortex core line $\vec{\omega}_L$; upper figure: without a source term (w/o) and with methods $q_{\omega,act}$, $q_{\omega,ref}$ and q_v; lower figure: VC method H from Tab. 1 for different ε

For the present case, the most reasonable value for VC method H is $\varepsilon = 1$, where the

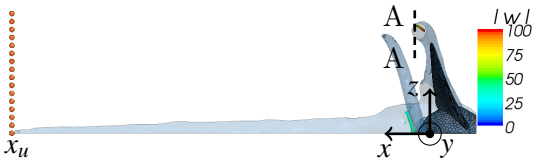

(a) Without a momentum source term ($\vec{S} = \vec{0}$), A-A shows the cutting plane for Fig. 5

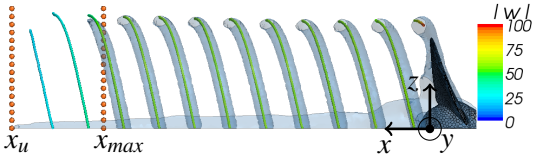

(b) With Vortex Conservation, $q_{\omega,act}$

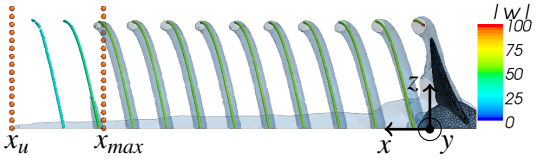

(c) With Vortex Conservation, $q_{\omega,ref}$

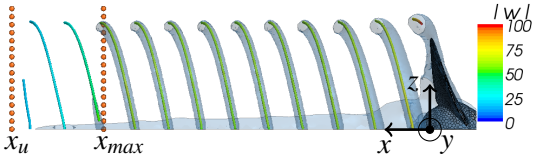

(d) With Vortex Conservation, q_v

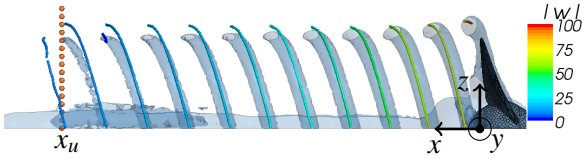

(e) With VC method H, $\varepsilon = 1$

Figure 7: Evolution of tip vortices: vortex core line coloured with $|w| = |\vec{\omega}_L|$; isosurface with $|\vec{\omega}| = 50\,\mathrm{s}^{-1}$; x_{max} end of the source domain for $q_{\omega,act}$, $x_u = 1.92\,D_P$ end of the refined mesh

vorticity decays exponentially (refer as well to Fig. 7). An increase to $\varepsilon = 1.1$ leads to an unphysically strong increase. For $\varepsilon = 0.8$ the forcing is too weak and for $\varepsilon = 1.2$ the vortex blows up. Hence, a vortex as strong as the one gained with any q_i cannot be maintained with the VC method H. All vortices disappear for $x > x_u = 1.9\,D_P$ since the mesh size increases from there on to more than one cell per vortex core diameter.

7 Summary

Vortex conservation methods were presented and applied successfully to the simulation of propeller tip vortices on a relatively coarse mesh. They enable the conservation of a constant prescribed vorticity magnitude at the vortex core line. Besides, a comparison of the momentum source terms with the tangential vortex velocity shows that the vortex conservation methods are consistent in contrast to the analysed existing VC methods. From the vortex conservation methods, $q_{\omega,act}$ considers the actual vortex flow most and requires the least restrictions. However, all terms q_i are consistent with tangential vortex flow characteristics and lead to the same vorticity magnitude, no method is preferable for the investigated case.

The appropriate choice of the reference vortex properties and the interaction of the new source terms with turbulence models may be part of further research.

References

[1] J. Burgers. A mathematical model illustrating the theory of turbulence. *Advances in Applied Mechanics*, 1, 1948.

[2] N. Butsuntorn and A. Jameson. Time spectral method for rotorcraft flow. *AIAA Paper*, 2008-0403, 2008.

[3] R. Fedkiw, J. Stam, and H. W. Jensen. Visual simulation of smoke. In *Proceedings of the 28th annual conference on Computer graphics and interactive techniques*, Los Angeles, USA, 2001.

[4] R. Haimes and D. Kenwright. On the velocity gradient tensor and fluid feature extraction. *AIAA Paper 1999-3288*, 1999.

[5] H. Lamb. *Hydrodynamics*. University Press, Cambridge, 6 edition, 1932.

[6] R. Löhner, C. Yang, and R. Roger. Tracking vortices over large distances using vorticity confinement. In *Proceedings of the 24th Symposium on Naval Hydrodynamics*, Fukuoka, Japan, 2002.

[7] M. Robinson. Application of vorticity confinement to inviscid missile force and moment prediction. *AIAA Paper 2004-0717*, 2004.

[8] J. Steinhoff, W. Yonghu, T. Mersch, and H. Senge. Computational vorticity capturing: Application to helicopter rotor flow. *AIAA Paper 1992-0056*, 1992.

[9] D. Sujudi and R. Haimes. Identification of swirling flow in 3-d vector fields. *AIAA Paper 1995-1715*, 1995.

Numerical Investigation of Aerodynamics Behavior of Dynamic Stall, with Application to Stabilizer Fins of Ships

G. Fernandes[1a], G. Kapsenberg[b], M. Kerkvliet[b] & F. van Walree[b]

[a]MARIN Academy; [b]MARIN, Wageningen, The Netherlands

1. Introduction

The accurate study of unsteady forces on lifting surfaces is important to many applications. Additionally, the phenomena of dynamic stall, in particular, is pertinent to not only engineering topics such as horizontal and vertical axis wind turbines, helicopter blades and is also relevant to the flight of insects and birds. Dynamic stall is usually described with a wing or wing section pitching at some significant rate. Contrary to a static case, the angle of attack can be increased significantly past the static stall angle (Leishman 1990). One of the earliest documentations of this is in (Kramer 1932).

Several approaches to study this intriguing fluid mechanics behaviour have been made theoretically, experimentally and numerically, several of which are listed in (Lee and Gerontakos 2004). Widely known and cited are the experimental work performed in the NASA wind tunnels at helicopter design conditions in (Carr, McAlister, and McCroskey 1977). Their findings on the topic still set the benchmark for many current projects, specifically the sequence of events typically seen in the dynamic stall phenomena. Specific to studies with a NACA 0012 at moderate Reynolds numbers (50 -150 x10^3) and airfoil pitching amplitudes in "deep stall" and reduced frequencies (k) = 0.1 include (Lee and Gerontakos 2004) where authors studied experimentally in a low-speed, suction-type wind tunnel in the Aerodynamics Laboratory at McGill University. The wing section was instrumented with multiple hot-film sensor arrays and surface pressure measurements and along with smoke-flow visualisations, the spatial-temporal progression of the locations of the boundary-layer transition and separation, and reattachment and relaminarization points, compared to the static values, for a range of oscillation frequency and amplitude both prior to, during and after the stall. This study has been widely used as validation material.

Numerical investigations studies using a commercial computational fluid dynamics (CFD) code have been carried out by (Wang et al. 2010), where the k-ω SST with low-Reynolds number corrections have been employed, using a 2D grid with a dynamic mesh. The time history of the lift force was found to be "aperiodic or quasi-periodic" but that "aerodynamic forces agree well with the experimental data, fluctuating around the measured data". These fluctuations were attributed to the specified free stream turbulence level, and by increasing this value would "improve the stability of the predicted forces on the blade" and also increases the stall delay at larger incidences. To explain the oscillations seen at lower incidences where the flow is usually attached, authors claim the k-ω SST "is very sensitive in the present unsteady low turbulence intensity flow application". Similarly, using the same code and turbulence model but with a higher quality mesh, (Gharali and Johnson 2013) also computed this case for validation. Results here compare well to the experimental data and explain small oscillations on the down stroke as "a result of reattachment and relaminarization and are not related to the mesh quality". Rather than observing an aperiodic behaviour, a periodic cycle is seen after the first pitching cycle. This is consistent with the conclusions from the DESider project with RANS based turbulence closure models. Using Large-Eddy Simulation with a mixed-time-scale subgrid-scale model and a dynamic mesh, (Kim 2013) studied the influence of inlet turbulence on the aerodynamics of wind turbines, including the dynamic stall. Validation of the pitching airfoil was attempted with (Lee and Gerontakos 2004) for a range of k, and good agreement was found for k = 0.025 and 0.05. For the current case of interest k = 0.1 however, non-trivial and noteworthy discrepancies were seen, namely: 1) Cl loop has a larger area and 2) the maximum lift is lower for the calculations than those for the experiments. Having discussed the experimental uncertainties

[1] *Correspondence author, email:* g.fernandes@academy.marin.nl

with the respective authors, it was concluded that "it would be challenging to measure the surface pressure with the leading edge vortex is very strong during the downstroke in experiments", which appears to be the case for this particular reduced frequency. This instrumentation related limitation is not present in the conducted numerical simulations. Using appropriately studied phase-average values to obtain the statistical data, and along with the mesh convergence tests, these LES simulations were deemed to be reliable (Kim 2013). Figure 1 shows the results available in the literature for the chosen case of k=0.1 and $\alpha(t) = 10\,° + 15\,° \sin \omega t$.

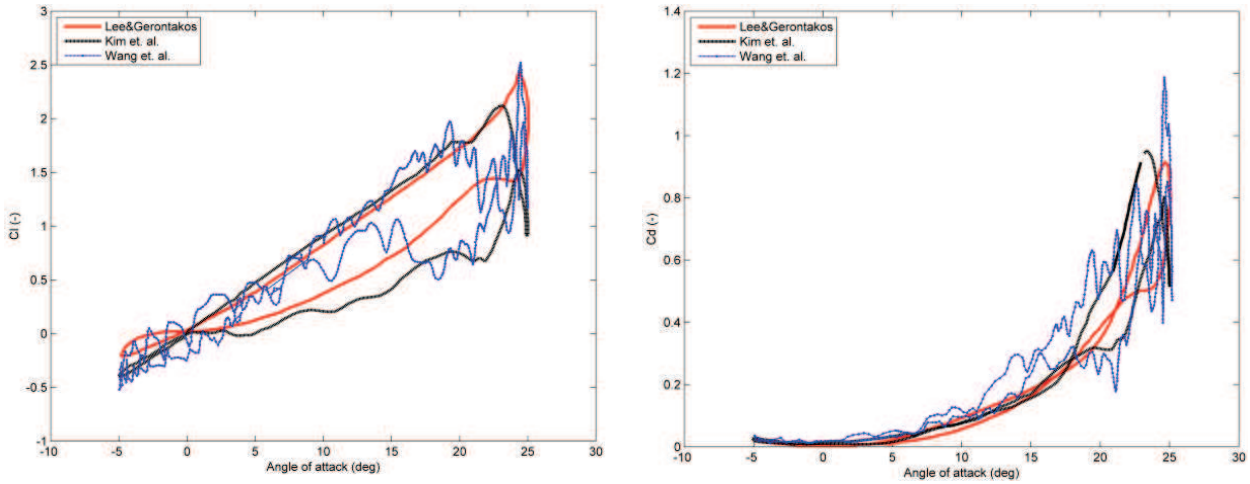

Figure 1: Results from literature

The objective of this current work is to simulate the flow conditions seen at model scale experiments, Re ≈ 65,000 for moving airfoils, and from this knowledge comprehend the applicability of stabilizer fins to ships, typically yacht-type ships. Given the spread in the literature using similar methods shown above, arriving at accurate and reliable results for the design conditions is crucial. This paper will show the step of verification and validation of a two-dimensional static NACA 0012 at various angles of attack. Several parameters will be examined (space and temporal refinements, turbulence modelling, and inlet boundary conditions). First, a comparison will be made to the available static data in (Lee and Gerontakos 2004), and repeated at the design Reynolds number.

2. Methodology

The code used for the current calculations was ReFRESCO. The unsteady for of the incompressible flow equations with turbulence models are discretized using a finite-volume approach with cell-centred collocated variable, in strong-conservation form, and a pressure-correction equation based on the SIMPLE algorithm is used to ensure mass conservation. Time integration is performed with an implicit Euler scheme. The convective fluxes are discretized with the QUICK scheme for the momentum equations and a first order upwind discretization is used for the turbulence equations. Closure of the RANS equations is achieved with the Spalart-Allmaras (Spalart and Allmaras 1994), $\kappa - \omega$ SST (F R Menter 1994) and $\kappa - \sqrt{\kappa l}$ models (F. R. Menter, Egorov, and Rusch 2006). Additionally, a model incorporating transition was also used in the form of the LCTM model (Langtry and Menter 2009). The boundary conditions applied were: no-slip for the airfoil, symmetry for the sides of the domain and a combination of inflow, pressure and outflow (Neumann) on the region of the circular domain (Toxopeus 2011). The various incidence angles were simulated by varying the inflow angles. The convergence was set to 1E-5 in the infinity norm (worst case) for most cases for all variables, or 1E-8 in some cases.

The grid was generated using the commercial code GridPro. This code allows the generation of multi-block o-type meshing strategy and also permits the generation of geometrically similar grids. The airfoil's trailing edge was closed with a circular section with the radius of ~0.3% of the chord, helping the meshing algorithm to converge. A circular domain was used and given the symmetry of the airfoil, the grid was mirrored about the chord to ensure symmetry. In total 11 grids were created, between 368k and 22k cells. The grid quality was checked, showing a maximum equiangle skewness of 0.5 in a few cells due

to the algorithm used in GridPro away from the airfoil. The aspect ratio in the region around the airfoil was ~50, and the airfoil's surface with the finest grid had ~2350 cells.

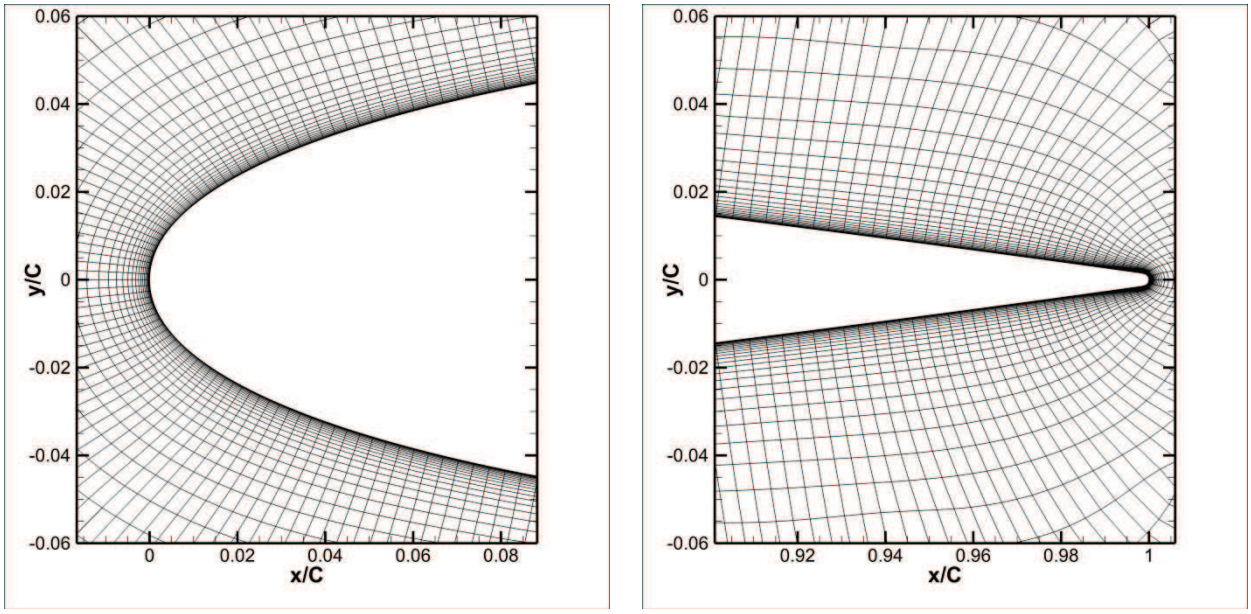

Figure 2: Close up of the coarsest grid, leading (left) and trailing (right) edge

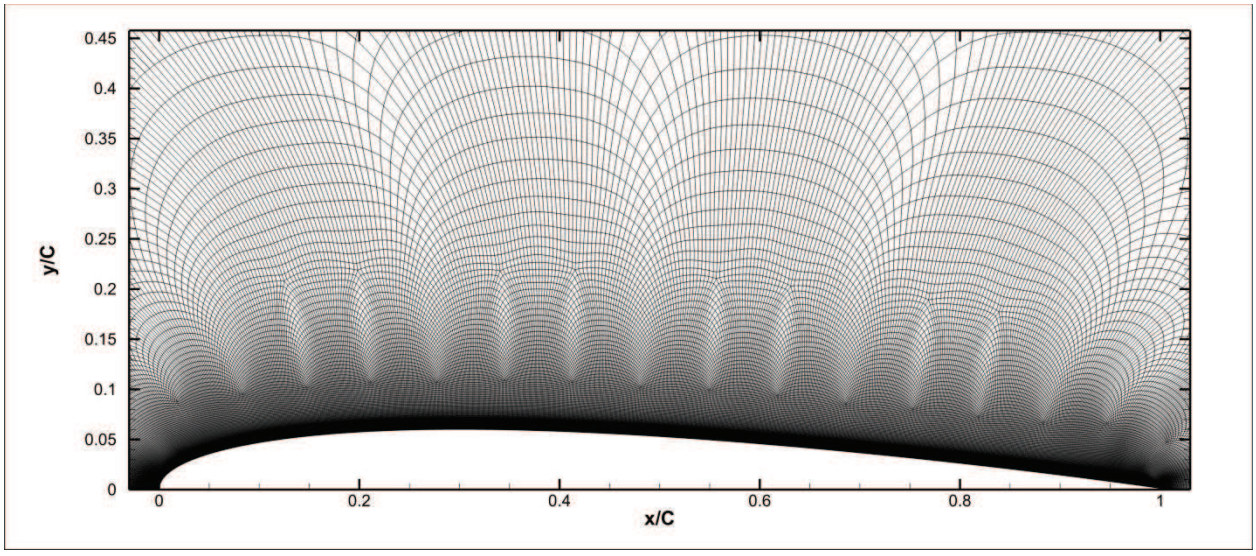

Figure 3: Upper half of the airfoil finest grid

3. Results – Re=135,000

All simulations in this Reynolds regime were found to be statistically stationary, even though at incidences above 8 degrees the time dependent RANS equations were employed. Even at higher angles, the solution arrived at a time-independent solution (or indeed with other relaxation parameters with the steady solver), this is shown by the steady state residuals. The forces were shown not to change in time, even with transient residuals.

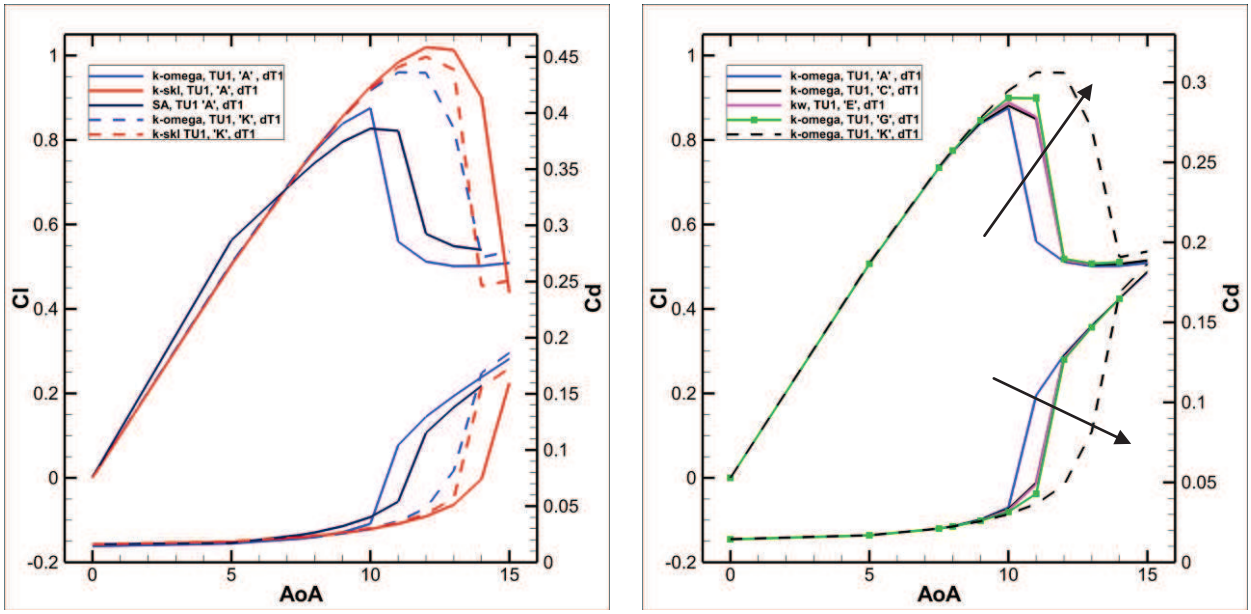

Figure 4: Lift and drag coefficients. Left figure compares finest grid and coarsest grids varying turbulence model. Right figure shows the influence of coarsening the grid using the k-omega turbulence model; arrow shows direction of grid coarsening.

Results – Re=65,000

Calculating the flow at this lower Reynolds number was found to be significantly more challenging, given the instabilities in the flow. At 15 degrees of incidence, the flow was found to be very unsteady. Moreover, the forces were found to be very sensitive to the grid employed.

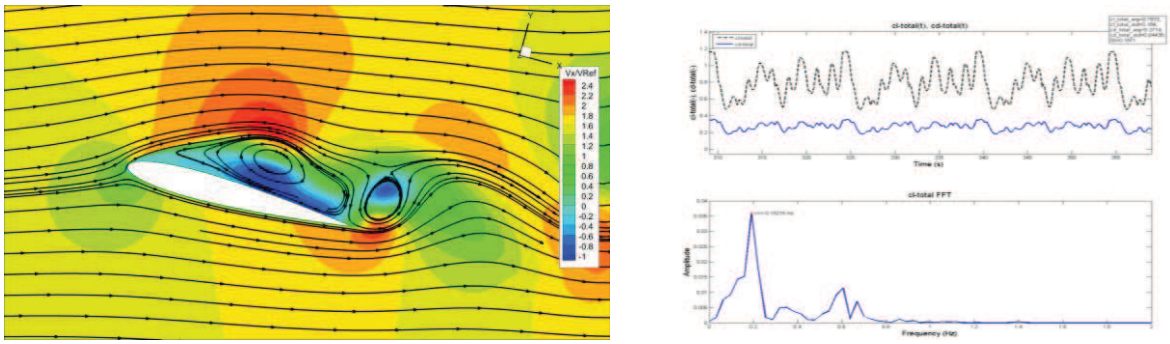

Figure 5: Flow field (left) for angle of attack = 15 degrees, using the k-omega turbulence model. Force variation (right, upper) and spectral analysis (right, lower).

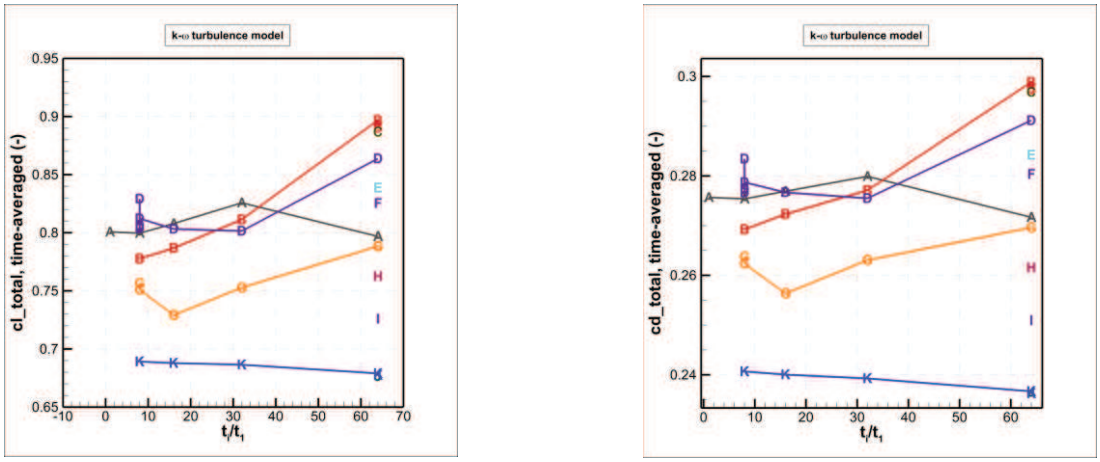

Figure 6: Spread of lift (left) and drag (right) for the k-omega turbulence model using a series of 11 geometrically similar grids.

References

Carr, L W, K. W. McAlister, and William J. McCroskey. 1977. "Analysis of the Development of Dynamic Stall Based on Oscillating Airfoil Experiments."

Gharali, Kobra, and David a. Johnson. 2013. "Dynamic Stall Simulation of a Pitching Airfoil under Unsteady Freestream Velocity." *Journal of Fluids and Structures* 42: 228–244.

Kim, Yusik. 2013. "Wind Turbine Aerodynamics in Freestream Turbulence."

Kramer, Max. 1932. "Increase in the Maximum Lift of an Airplane Wing due to a Sudden Increase in Its Effective Angle of Attack Resulting from a Gust." *National Advisory Committee for Aeronautics*. http://hdl.handle.net/2060/19930094738.

Langtry, Robin B., and Florian R. Menter. 2009. "Correlation-Based Transition Modeling for Unstructured Parallelized Computational Fluid Dynamics Codes." *AIAA Journal* 47 (12) (December): 2894–2906.

Lee, T., and P. Gerontakos. 2004. "Investigation of Flow over an Oscillating Airfoil." *Journal of Fluid Mechanics* 512 (July 23): 313–341.

Leishman, J G. 1990. "Dynamic Stall Experiments on the NACA 23012 Aerofoil." *Experiments in Fluids* 9: 49–58.

Menter, F R. 1994. "Two-Equation-Eddy-Viscosity Turbulence Models for Engineering Applications." *AIAA Journal* 32 (8): 1598–1605.

Menter, F. R., Y. Egorov, and D. Rusch. 2006. "Steady and Unsteady Flow Modelling Using the K-skL Model." *Proceedings of the International Symposium on Turbulence, Heat and Mass Transfer*: 403–406.

Spalart, P R, and S R Allmaras. 1994. "A One-Equation Turbulence Model for Aerodynamic Flows." *Recherche Aerospatiale* No. 1: pp. 5–21.

Toxopeus, Serge. 2011. "Practical Application of Viscous-Flow Calculations for the Simulation of Manoeuvring Ships." Delft University of Technology.

Wang, Shengyi, Derek B. Ingham, Lin Ma, Mohamed Pourkashanian, and Zhi Tao. 2010. "Numerical Investigations on Dynamic Stall of Low Reynolds Number Flow around Oscillating Airfoils." *Computers & Fluids* 39 (9) (October): 1529–1541.

CFD Validation of a Container Ship in Calm Water and Head Seas

Inno Gatin[1], Vuko Vukčević[1] and Hrvoje Jasak[1]

[1] *University of Zagreb, Zagreb/Croatia, inno.gatin@stud.fsb.hr, {vuko.vukcevic, hrvoje.jasak}@fsb.hr ,*

1 Introduction

Added resistance of ships in waves is one of increasingly important problems in naval engineering due to energy efficiency regulations. In this work, validation of the Naval Hydro pack in OpenFOAM is performed by conducting simulations of a KRISO container ship (KCS) in calm water and head waves. Steady resistance and dynamic sinkage and trim at different Froude numbers are compared to experimental data. Mesh refinement study has been carried out for design Froude number in order to asses numerical uncertainty. Seakeeping simulations of the ship in head waves are carried out for a number of different wave parameters at design Froude number. Added resistance is compared with experimental results. All simulations are performed with fully non–linear, turbulent, two–phase CFD solver. Wave modelling is performed using Spectral Wave Explicit Navier–Stokes Equations (SWENSE) [1] with implicit relaxation zones [5] that are used to prevent wave reflection. In addition to the validation runs, 3-D freak wave simulation encountering a KCS has been performed using the SWENSE solver coupled with a directional Higher Order Spectrum (HOS) [2] method for nonlinear wave propagation.

2 Mathematical model

In this section mathematical model of incompressible two-phase flow is presented. Two–phase model is based on a single set of mixture equations taking into account jump conditions at the free surface implicitly [4]. Volume of Fluid (VOF) method will be used for interface capturing [9] in calm water simulations, while the Level Set (LS) method will be used for head waves simulations, where SWENSE procedure is employed.
Three sets of governing equations are used to model the two phase flow: continuity equation, momentum equation and interface capturing equation. The continuity equation, used to formulate dynamic pressure equation, states:

$$\nabla_{\bullet}\mathbf{u} = 0. \tag{1}$$

Mixture momentum equation reads:

$$\frac{\partial \mathbf{u}}{\partial t} + \nabla_{\bullet}(\mathbf{u}\mathbf{u}) - \nabla_{\bullet}\left(\nu_e \nabla \mathbf{u}\right) = -\frac{1}{\rho}\nabla p_d \,, \tag{2}$$

where ν_e stands for effective dynamic viscosity, allowing for the general turbulence models [11]. Interface capturing equations used in the calculations can be found in Rusche (2002) [7] for VOF method, and in Sun & Beckermann (2007) [8] for LS method.
Apart from the governing equations, special attention is given to the jump conditions at the free surface. In the present model, normal stress balance is modelled exactly, while the tangential stress is taken into account approximately. Surface tension is neglected. This approach is justified for large scale two–phase problems encountered in naval hydromechanics. Normal stress balance yields two free surface jump conditions [4]. First condition prescribes the dynamic pressure jump across the free surface:

$$p_d^- - p_d^+ = -(\rho^- + \rho^+)\mathbf{g}\bullet\mathbf{x}\,, \tag{3}$$

where superscript "+" denotes the heavier fluid (water), while superscript "−" denotes the lighter fluid (air). Second condition prescribes the jump of dynamic pressure gradient over density to be zero:

$$\frac{1}{\rho^-}\nabla p_d^- - \frac{1}{\rho^+}\nabla p_d^+ = 0. \tag{4}$$

Jump conditions are used to discretize dynamic pressure terms (pressure gradient and laplacian) at the free surface.

3 Numerical model

Numerical model is based on second–order accurate polyhedral FV method used in foam–extend. Rigid body motion is solved using quaternion based six degrees of freedom (6DOF) equations. Mesh is modelled as a rigid body with special boundary conditions. Coupling of pressure, velocity, free surface and 6DOF equations is performed in a segregated manner using PIMPLE algorithm.

4 Numerical simulations

In this section simulation results regarding KCS model are compared to experimental data. Steady state resistance with dynamic sinkage and trim is simulated for a range of Froude numbers. Seakeeping simulations are performed in regular head waves with different incident wave parameters at design Froude number. Finally, a simulation of a freak wave encountering a full scale KSC is shown.

4.1 Steady resistance, simulations with dynamic sinkage and trim

CFD results computed on 4.6 million cells unstructured mesh are compared with experimental data for following Froude numbers: 0.1516, 0.1949, 0.2274, 0.2599 and 0.2816. KCS model particulars and experimental settings details are available at Tokyo Workshop On CFD in Ship Hydrodynamics website [6]. Symmetry boundary condition is used at the central vertical longitudinal plane, and only half of the domain is simulated. Average mesh non–orthogonality is 6.6 degrees while the maximum is 76.1 degrees. Results comparison for total resistance coefficient is shown in Figure 1. Dynamic sinkage and trim comparison is shown in Figure 2 and Figure 3, respectively.

Grid convergence study is performed for 0.282 Froude number. Table 1 shows the total resistance coefficient, sinkage and trim obtained with different grid sizes. Relative error compared to experimental result is also presented. Relative error is calculated as $\epsilon = (C_{tEFD} - C_{tCFD})/C_{tEFD}$. Calculated order of spatial accuracy for total resistance [10] is $p = 3.98$ for three finest grids, while grid uncertainty is 0.029×10^{-3}.

4.2 Seakeeping simulations in regular head waves

Added resistance is compared with experimental data for various incident wave parameters. Simulations are performed for design Froude number and head waves. Comparison is performed in Fourier space, comparing individual harmonic amplitudes to experimental data [6]. KCS model particulars can be found on Tokyo Workshop On CFD in Ship Hydrodynamics website [6]. Figure 4 shows comparison of mean, first and second order of total resistance coefficient for different incident wave parameters (λ/L_{pp}).

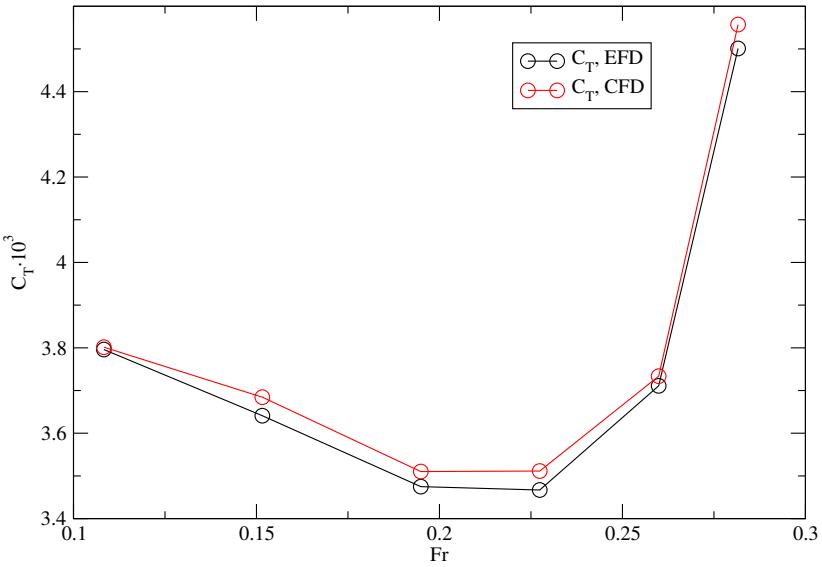

Figure 1: Comparison of total resistance coefficient for a range of Froude numbers.

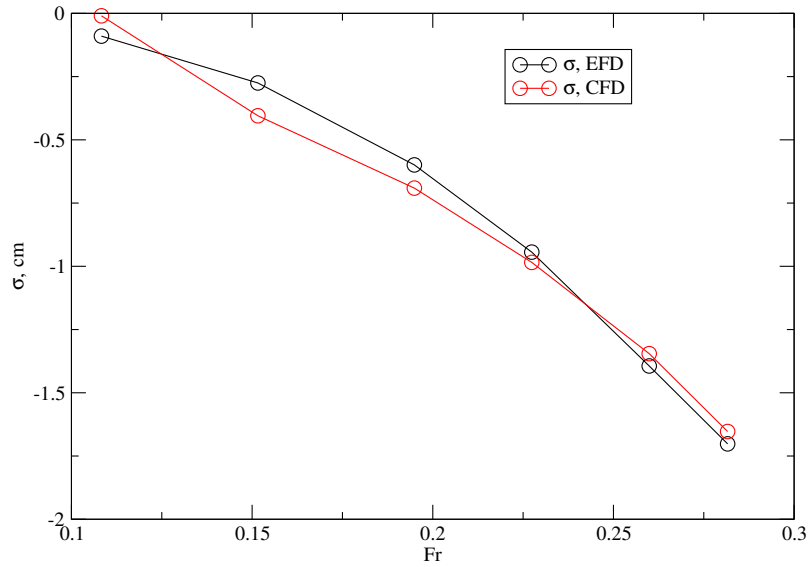

Figure 2: Comparison of dynamic sinkage for a range of Froude numbers.

Table 1: Grid convergence study results.

Grid No.	1	2	3	4	EFD
$C_t \times 10^3$	4.837	4.736	4.608	4.560	4.501
$\epsilon_{C_t}, \%$	-7.476	-5.234	-2.381	-1.313	/
σ, cm	-1.665	-1.650	-1.655	-1.653	-1.702
$\epsilon_\sigma, \%$	2.194	3.067	2.756	2.867	/
$\tau, ^o$	-0.145	-0.147	-0.147	-0.146	-0.159
$\epsilon_\tau, \%$	8.813	7.264	7.847	7.974	/

It can be seen in Figure 4 that the trend of all the curves is well captured. Mean values obtained with CFD generally overshoot the experimental data, which is consistent with the

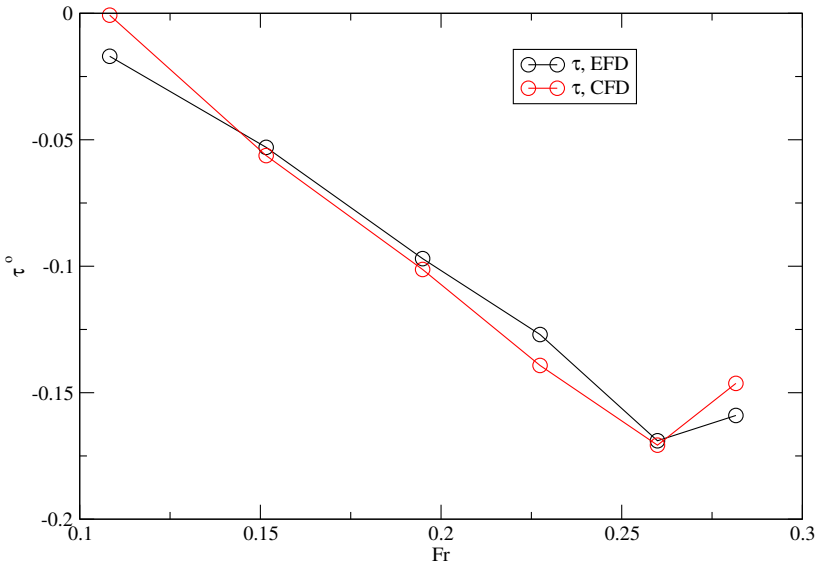

Figure 3: Comparison of dynamic trim for a range of Froude numbers.

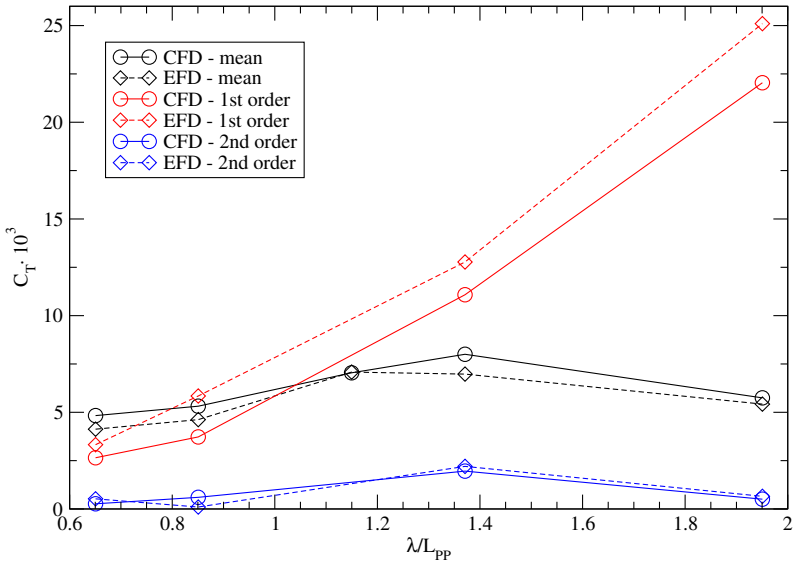

Figure 4: Comparison of total resistance coefficient for various incident wave parameters.

steady state resistance simulations. First order resistance is undershot for all cases.

4.3 Freak wave impact on a full scale floating KCS

A three-dimensional, realistic freak wave is initialized using long time evolution of wave spectrum with Higher Order Spectrum (HOS) potential nonlinear wave theory [2] implemented in Naval Hydro pack. Initial condition used for HOS simulation is JONSWAP directional spectrum. Wave spectrum parameters are: $H_s = 10.5$ m, $T_p = 9.5$ s, and directionality constant $n = 8$ [3]. Freak wave height is $H = 21.8$ m. Simulation is performed for full size KCS, Table 2. Figure 5 sequentially shows the encounter of the freak wave on the KCS.

Table 2: Full scale KCS characteristics.

L, m	B, m	D, m	T, m	x_G, m	y_G, m	KG, m	r_x, m	r_y, m	r_z, m
230	32.2	19	10.8	111.6	0	14.32	12.9	57.5	57.5

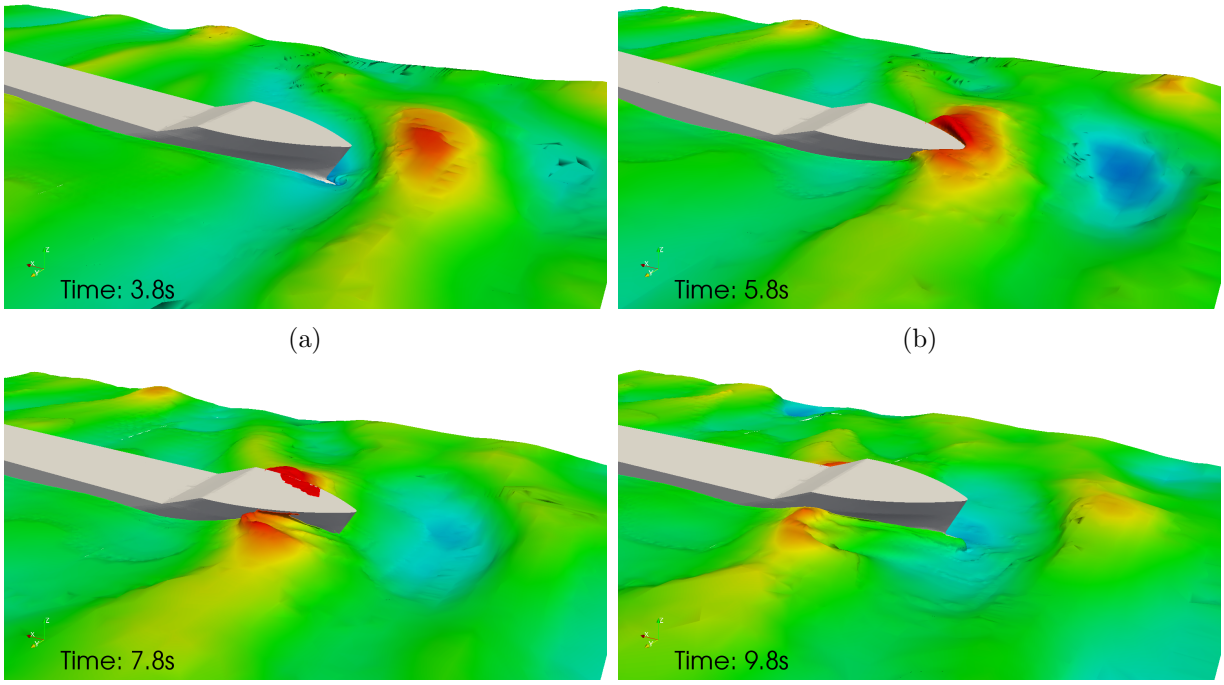

(a) (b)

(c) (d)

Figure 5: Three–dimensional freak wave encountering a full scale KCS.

5 Conclusion

Simulations of KCS in calm water and head waves are carried out and the results are compared with experimental data. Steady state simulations show good agreement for resistance and dynamic sinkage and trim. Larger discrepancies of dynamic sinkage and trim for lower Froude numbers are caused by coarse mesh considering the absolute values of sinkage and trim. Preliminary results of added resistance in head waves are compared to experimental data, being an important design criteria. Comparison showed that added resistance can be predicted fairly accurately. Finally, an example of three–dimensional freak wave simulation is performed to show the capability of the HOS wave theory coupled with CFD simulation using SWENSE method.

References

[1] Ferrant, P. and Gentaz, L. and Le Touzé, D. A new ranse/potential approach for water wave diffraction. *Proc. Numerical Towing Tank Symposium*, 2002.

[2] I. Gatin. Master Thesis; Implementation and validation of the Higher Order Spectrum (HOS) method for Simulation of Surface Waves. *Faculty of Mechanical Engineering and Naval Architecture, Zagreb*, 2015.

[3] L. H. Holthuijsen. *Waves in Oceanic and Costal Waters*. Delft University of Techonlogy and UNESCO-IHE, 2007.

[4] J. Huang, P. M. Carrica, and F. Stern. Coupled ghost fluid/two–phase level set method for curvilinear body–fitted grids. *Int. J. Numer. Meth. Fluids*, 44:867–897, 2007.

[5] H. Jasak, V. Vukčević, and I. Gatin. Numerical Simulation of Wave Loads on Static Offshore Structures. In *CFD for Wind and Tidal Offshore Turbines*, pages 95–105. Springer Tracts in Mechanical Engineering, 2015.

[6] National Maritime Reasearch Inistitute (NMRI). Tokyo 2015: A Workshop on CFD in Ship Hydrodynamics. `http://www.t2015.nmri.go.jp/`, 2015. [Online; accessed 20 August 2015].

[7] H. Rusche. *Computational Fluid Dynamics of Dispersed Two - Phase Flows at High Phase Fractions*. PhD thesis, Imperial College of Science, Technology & Medicine, London, 2002.

[8] Y. Sun and C. Beckermann. Sharp interface tracking using the phase–field equation. *Journal of Computational Physics*, 220:626–653, 2007.

[9] O. Ubbink and R. I. Issa. A method for capturing sharp fluid interfaces on arbitrary meshes. *Journal of Computational Physics*, 153:26–50, 1999.

[10] H. K. Versteeg and W. Malalasekera. *An introduction to Computational Fluid Dynamics: The finite volume method*. Pearson Education Limited, 1995.

[11] D. C. Wilcox. *Turbulence Modeling for CFD*. DCW Industries, 1993.

Resistance Analysis of a Benchmark Ship – A Computational Application

Metin Kemal Gokce, Seyfettin Bayraktar, Omer Kemal Kinaci, Yildiz Technical University, Istanbul/Turkey, mkgokce@yildiz.edu.tr , sbay@yildiz.edu.tr , kinaci@yildiz.edu.tr

1. Introduction

Ship powering prediction is a substantial part of the ship design process. Model tests provide reliable data for total resistance of a scaled ship but this method is costly and inconvenient. As a result of the technological developments in computer science and its proportionally low cost, utilization of computational fluid mechanics (CFD) methods to solve for any type of flow became handy. Ships have complex geometries and the computational flow around a ship hull is one of the troublesome areas in CFD. Comparison with the benchmark ships is a common way for validating the numerical results and provides a useful first step to start solving flows around ships. This study covers the steady state numerical hydrodynamic flow analyses of a Post Panamax Container Ship – Duisburg Test Case. The resistance characteristics of the ship and the free surface deformations are investigated with a multiphase analysis using the Volume of Fluid (VOF) method for the fixed condition of the hull in the flow. A hybrid meshing strategy is implemented for easier meshing due to the complex geometry of the ship hull. The capability of fixing the ship to obtain resistance characteristics of the vessel in a range of Froude numbers is discussed.

2. Hydrostatics of the Ship Hull

DTC container ship has a bulbous bow, large stern and a transom. It is a model developed for benchmarking purposes to be used for computational applications. No actual ship exists and the experimental results are given in the reference article by (El Moctar et al., 2012). Principal particulars of the model ship and full scale ship can be seen in Table 1.

Table 1. Principal particulars of model and full scale ship (El Moctar et al., 2012).

	Model	Full Scale
L_{PP} (m)	5.976	355.0
B_{wl} (m)	0.859	51.0
T_m (m)	0.244	14.5
V (m^3)	0.827	173467.0
S_w (m^2)	6.243	22032.0
v_d (knots)	3.244	25.0

The present study covers the numerical analyses of the DTC ship in fixed condition including free surface effects. The model scale used in experiments is implemented in numerical analyses to be compatible with the reference study. A CAD model of the ship is given in figure 1.

3. Numerical Implementation

3.1. Grid Structure

Seo et al. (2010) have proposed a hybrid meshing strategy for practical purposes to represent the ship hull and the fluid domain. They have meshed the complex parts of the ship (like the bow and the stern of the ship) with tetrahedral elements while using hexahedral elements for the rest of the domain. A similar approach was used in this study. The ship hull and its close surrounding were separated from the rest of the fluid domain. Tetrahedral elements were used in the inner domain while for the rest of the domain, hexahedral elements were used. The two domains were constructed by 3.5 million

elements in total. The width, length and depth of the fluid domain are in accordance with the recommended procedures and guidelines by the ITTC for ship CFD applications (ITTC 7.5 – 03). The grid structure on the ship hull is given in figure 2.

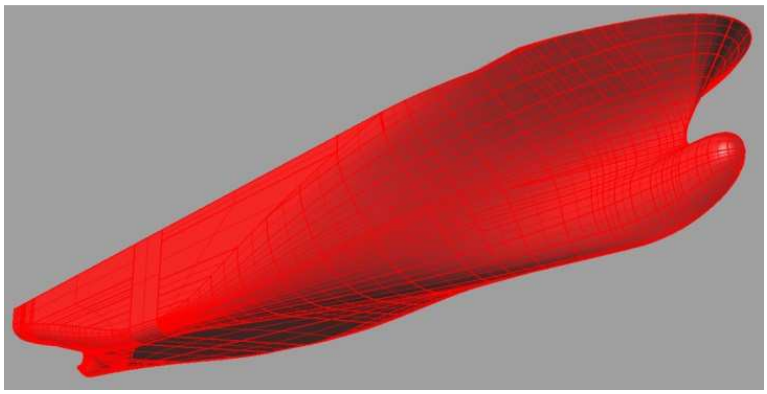

Figure 1. An overall CAD view of the DTC Container Ship.

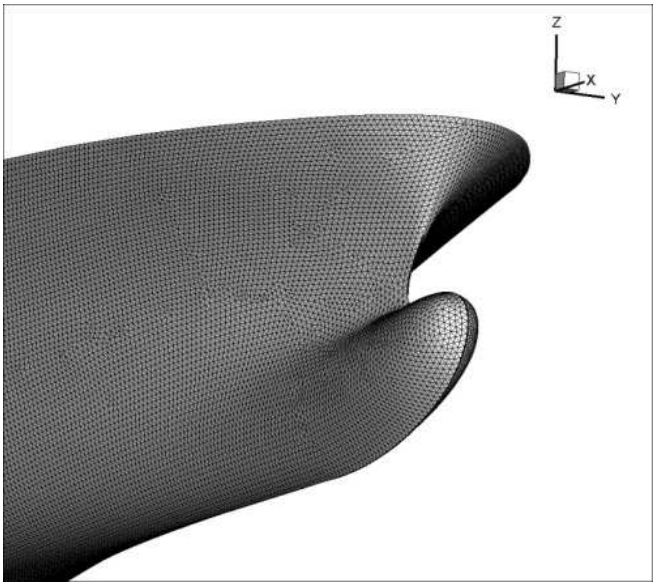

Figure 2. The grid structure on the ship hull.

3.2. CFD Setup

For all the analyses involved in the present study, a steady state solution approach was implemented and $k-\varepsilon$ turbulence model is used with a RANSE based CFD. $k-\varepsilon$ model is a two equation turbulence model which generates satisfactory results for slender bodies like ships. It is extensively used in solving numerically the flows around ships and one example is present in the work by (Kinaci et al., 2013). The Froude number range to obtain the ship resistance was varied between 0.17 and 0.22. The general properties of the simulations can be seen in table 2.

Table 2. The properties of the simulation

Type of mesh	Hybrid (Tetrahedral and quadrilateral)
Number of elements	Approximately 3.5 millions
Domains	Multiphase; homogenous water and air
Timescale	Steady
Convergence criteria	10^{-6}
Multiphase method	Volume of Fluid (VOF)
Processing	Parallel (24 partitions run on 2x8 core with 64 GB RAM)

4. Results

Total resistance data for the Duisburg Container Ship model were obtained from the experiments (El Moctar et al., 2011). The towing tank tests were simulated by CFD approach for six Froude numbers for the fixed condition of the ship.

The resistance values of the ship model are estimated for calm water conditions without the appendages (the rudder and the propeller). The total resistance coefficient C_T is determined by;

$$C_T = \frac{R_T}{\frac{1}{2}\rho {V_m}^2 S_m}$$

R_T is the total resistance value, ρ is the density of water, V_m is the model ship velocity and S_m is the wetted surface area of the model ship. The model ship velocity is given in the reference study by (El Moctar et al., 2011) and they have used the Froude similarity to go back and forth between the actual ship and its model.

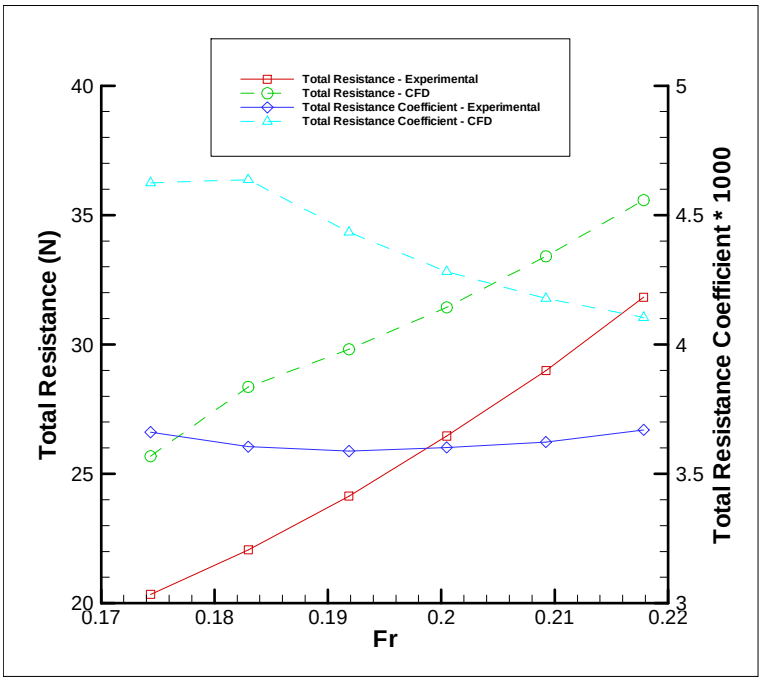

Figure 3. Comparison of CFD results with the experiments.

The CFD generated results are compared with the experimental values and this comparison is given in figure 3. The discrepancy between the results is quite noticeable in lower Froude numbers while the compatibility is getting better as the Froude number increases. The difference in the results (especially at lower Froude numbers) is accounted to the ship being fixed at its primary position. The ship hull is forced to stay stationary and this enforcement restricts the hull to escape from the high pressure regions inside the fluid. This, in return, results in higher calculated resistance.

The wave elevations along the hull at higher Froude numbers are usually established and do not vary in time. Therefore it becomes possible to solve the flow around the hull with a steady approach at the vessel's service speed. However, steady state solution approach may not be suitable at lower Froude numbers because the wave system in the fluid domain is subject to change with respect to time. Fixing the ship hull and implementing the steady state solution create a bias of results obtained by CFD when

compared with the experiments. This is the underlying reason of the difference between CFD and experiments at lower Froude numbers in figure 3.

The experimental and computational wave resistance coefficients as calculated by the Froude approach are given in figure 4. The frictional resistance coefficient (C_F) is calculated by the ITTC correlation line which is given as (ITTC, 2011);

$$C_F = \frac{0.075}{(\log Re - 2)^2}$$

where Re is the Reynolds number. Wave resistance coefficient is calculated by:

$$C_W = C_T - C_F(1 + k)$$

and k in this equation represents the ship form factor. Figure 4 supports the idea that the wave system around the ship is not well established in lower Froude numbers. The wave resistances are high computationally because the hull cannot escape the high pressure zones in the fluid whereas this is not the case experimentally. The pressure coefficient distribution around the underwater hull without the effect of the hydrostatic pressure is given in figure 8. A better numerical simulation should include the motions of the hull in response to the wave system that is formed around it which, in return, is expected to generate more accurate results. Free surface deformations and the wave profiles along the hull and in the fluid domain at $y = 0$ are given in Figures 5, 6 and 7.

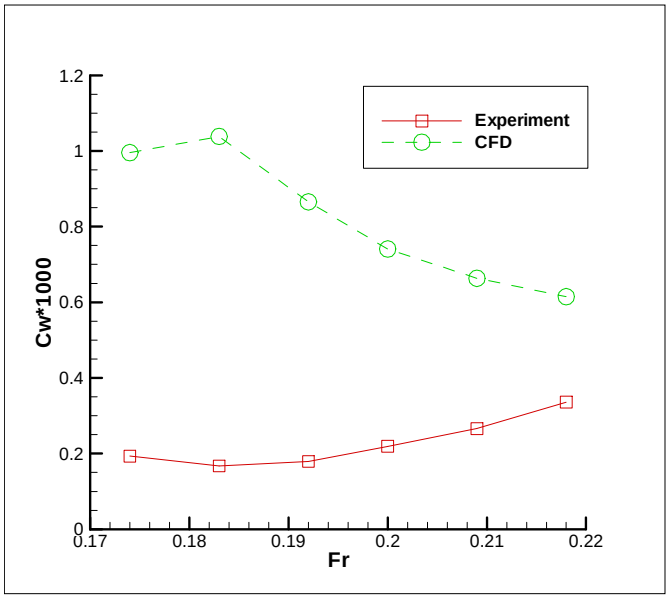

Figure 4. Nondimensional wave resistance coefficients of the model ship.

At lower velocities, the fluid-structure interaction is an important component of the flow around the ship due to significant heave and pitch motions of the vessel. However at higher velocities the heave motion is dominated by the surge motion and the share of heave and pitch in ship motions reduces. Fixing the ship inside the fluid and only towing the hull in the surge direction eliminates any possible contributions that heave and pitch make to the total resistance of the ship. Therefore, the discrepancy at lower Froude numbers is higher when compared with the difference at higher Froude numbers.

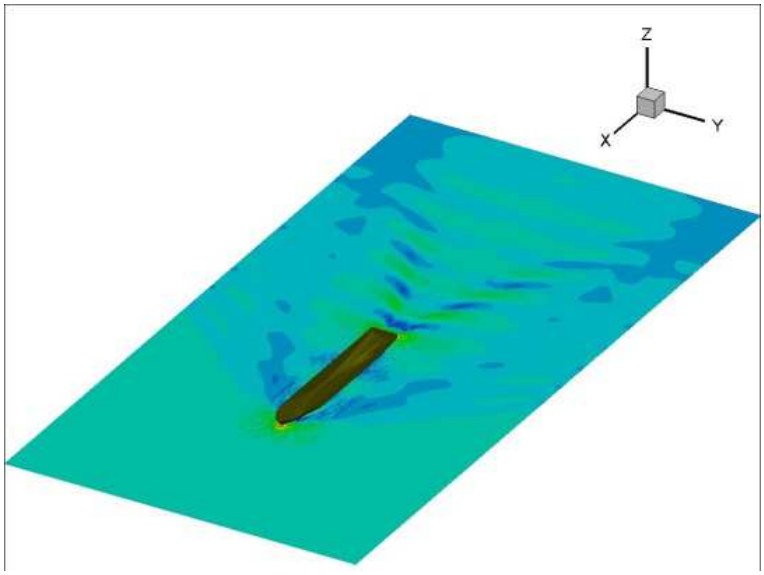

Figure 5. Free surface deformation of the model ship.

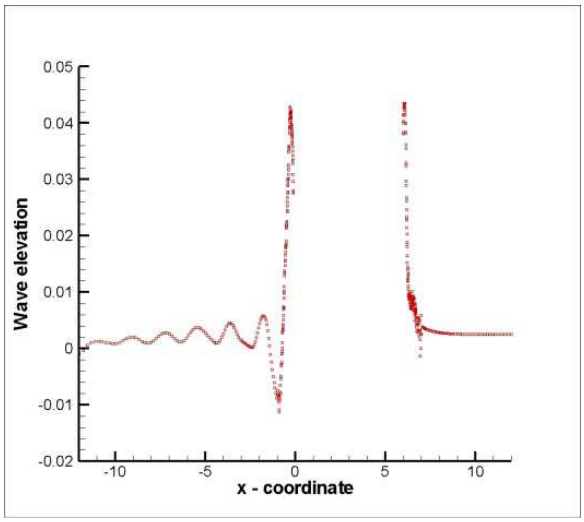

Figure 6. Wave heights for Fr=0.218 at y=0 plane

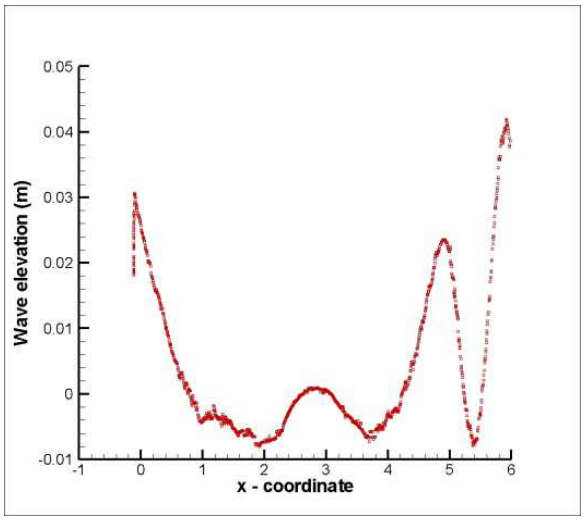

Figure 7. Wave heights along the ship hull at Fr=0.218

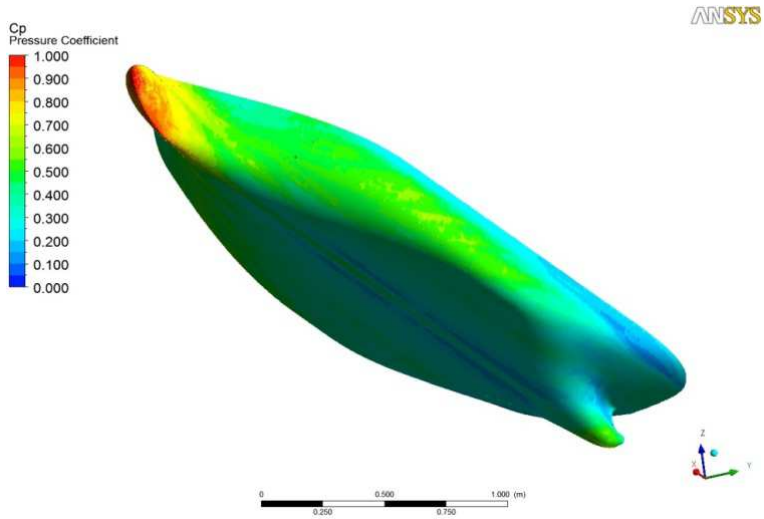

Figure 8. Pressure coefficient distribution along the underwater hull for Fr=0.218. Hydrostatic pressure is not included.

5. Conclusions

In this study, resistance characteristics of a post-panamax container ship (Duisburg Test Case) are investigated with a RANSE based CFD approach. A steady state solution approach is implemented and the ship hull is fixed in the fluid to restrict its motions. It was found out that total resistance was better approximated at higher Froude numbers. The wave system in the fluid domain is not established at lower Froude numbers and fixing the ship hull inside the flow dispossesses its ability to escape from high pressure zones in the fluid. This results in exaggerated values of wave resistance at lower Froude numbers. At higher velocities, heave motion is dominated by the surge motion. Therefore, the fluid-structure interaction becomes less important at higher Froude numbers and the results are in better accordance.

A better approximation of the flow around a ship should at least include a two degree-of-freedom (2-DOF) motion of the ship hull to include heave and pitch motions of the vessel. A time-dependent solution approach, when combined with a free to sink and trim vessel, is expected to generate more accurate results for the whole Froude number range.

References

El Moctar O, Shigunov V, Zorn T. Duisburg Test Case: Post-Panamax Container Ship for Benchmarking, *Ship Technology Research* 2012; 59(3): 50-64.

ITTC 7.5-02-03-01.4, 2011. Recommended Procedures and Guidelines, 1978 ITTC Performance Prediction Method, Revision 02.

ITTC 7.5-03-02-03, 2011. Recommended Procedures and Guidelines, Practical Guidelines for Ship CFD Applications.

Kinaci OK, Kukner A, Bal S. On propeller characteristics of DTC Post-Panamax Container Ship, *International Journal of Ocean System Engineering* 2013; 3(2): 77-89.

Seo JH, Seol DM, Lee JH, Rhee SH. Flexible CFD meshing strategy for prediction of ship resistance and propulsion performance, *International Journal of Naval Architecture and Ocean Engineering* 2010; 2(3): 139-145.

Development and Verification of an Open Source Overset Grid Library

Andreas Groß

Chair for Modelling and Simulation, University of Rostock, 18055 Rostock, Germany

Lars Greitsch and Tom Goedicke

Mecklenburger Metallguss GmbH, 17192 Waren, Germany

1. Introduction

Mesh generation is an important and time consuming step in Computational Fluid Dynamics (CFD) especially for complex geometries like the flow around a ship with appendages. The quality of the spacial discretisation of the computational domain is the primary criterion for the grade and reliability of the solution. Ease of mesh generation can save time and money as well as help to ensure a constant high level of the achieved results. Several mesh generation methods are used for creation computational meshes for different applications, which include unstructured as well as structured meshes, both single and multi-block. To combine different mesh parts methods like DRAGON grids or overset grid schemes may be used. While the first method demands for remeshing of a part of the domain, overset grid schemes allow combining several mesh regions without changing the mesh topology and quality.

In this work we present the development and validation of an overset grid scheme to be used with the OpenFOAM CFD software package, which is widely used in both industry and academia.

2. Governing equations

A short overview over the underling mathematical modelling and the numerical procedures will be given. Some parts will be discussed in detail as they are required later in the description and evaluation of the developed overset scheme. This section will include the following topics:

- Incompressible Navier-Stokes-Equations
- Discretisation of the equations and creation of a linear system of equations
- Solution strategies like pressure correction and domain decomposition
- Used turbulence models including RANS, closure models and LES

3. Overset grid algorithm

When conduction simulations of flows around arbitrary bodies of any number or shape, generation of a spacial discretisation that fits all surfaces may be challenging. The main idea of the overset grid method is to provide a simple body-fitted mesh for each feature of the geometry rather then generation a single mesh which fits all geometry features. This simplification allows for easy mesh generation and high mesh quality but leading to a number of separate meshes without explicit connection. This connection has to be provides by the overset grid scheme by interpolation of fields variables from one mesh region to another.

As a simple example the two dimensional flow around an cylinder can be considered as shown in Fig. 1. For the overset region a radial mesh fitted to the cylinder with an fine mesh at the cylinder surface to resolve the boundary layer is used. A cartesian mesh is utilised as background region for calculation of the far field and the wake. The cells in both regions are divided into one of the following categories:

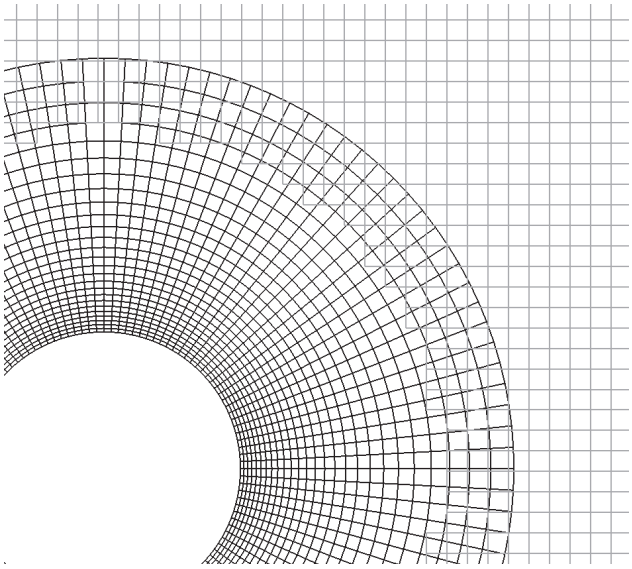

Figure 1. Grid arrangement for flow around cylinder.

- **Live cells**: Used for discretisation of the governing equations, field values are solved for
- **Acceptor cells**: Cells without neighbour cells or physical boundary on all sides, values are interpolated from overlapped grid
- **Primary donor cells**: Cells containing the the centre of an acceptor cells, primary donor for interpolated value, values are are solved for
- **Extended donor cells**: Neighbours of primary donor cells, used for interpolation of the acceptor cells value.
- **Hole cells**: Cells overlapped by an overset grid not needed for interpolation, values are not solved for.

Primary and extended donor cells may be called donor cells and can neither be hole nor acceptor cells. The developed overset grid algorithm categorises the cells of the different meshes according to these categories, collects the overset interpolation information (OII) and handles the implicit coupling of the mesh regions. The discretisation matrices created by the framework for any continuum problem can be handles regardless of the underling equation or its temporal or spacial discretisation.

3.1. Donor Cell Identification

The first step for creating the OII is the identification of donor cells for each acceptor cell. A donor cell identification algorithm has to find the cell containing a given point, the acceptor cell centre e. g., in an efficient and robust way, that is capable of domain decomposition used for parallel computations.

The implemented search algorithm is an variation of the gradient search algorithm proposed by Benek et al.[?] Starting at a seed cell, the current cell is tested for containing the centre of the acceptor cell. If the point is not found, the algorithm moves on the neighbour cell of the seed cell that lies in the direction of the acceptor cell centre.

When the search path hits a domain boundary, special treatment is needed. One possible way is to restart the search from a different seed. If the boundary is a processor boundary, i.e. the donor cell might be on a different processor, the search has to continue on this processor. Therefore a search kernel containing the position of the acceptor cell as well as and identification index and the index of the processor domain is passed to the other processor domain and the search algorithm continues there.

Cells found by the gradient search algorithm are primary donor cells by definition. Extended donor cells are determined by the interpolation method used for inter-grid interpolation.

3.2. Interpolation Methods

The connection of the different regions is handled using a interpolation function I_A^B to interpolate the field value Φ from region A to B:

$$\Phi^B = I_A^B = \sum_n w_i {\Phi^A}_i \tag{1}$$

where w_i is the weight if the i-th donor for the current acceptor.

Classical overset grid schemes are implemented for block structured meshes and therefore have access to information like left/right and upper/lower neighbours. Therefore it is possible to perform linear interpolation in space. On an unstructured grid these information is not available and different interpolation methods are used.

Within this work three different interpolation methods are used:

1. **Direct**: The value of the primary donor cell is directly transferred.

   $$I_A^B = \Phi_{pd}$$

   where Φ_{pd} denotes the value of the primary donor cell.
   This method is of first order accuracy and bounded.

2. **Gradient correction**: The value of the primary donor cell is corrected using an implicit formulation the Green-Gauss theorem for calculation of the gradient:

   $$I_A^B = \Phi_{pd} + \vec{\delta} \cdot \nabla(\Phi_{pd}) = \Phi_{pd} + \frac{\vec{\delta}}{\Omega} \sum_f \Phi_f \vec{S}_f = \Phi_{pd} + \frac{1}{\Omega} \sum_f (\lambda_f \Phi_n + (1 - \lambda_f)\Phi_{pd}) \vec{\delta} \cdot \vec{S}_f$$

   where $\vec{\delta}$ is the distance vector from the primary donor centre to the acceptor cell centre, f denotes the faces of the primary donor cell and $\vec{S}_f$ the surface normal vector with the magnitude being equal to the face size. The face weight λ_f is defined by the discretisation and used to interpolate the value of the primary donor cell and the neighbour cell value Φ_n to the value on the face Φ_f. The sum of the face areas is written as $\Omega = \sum_f \left| \vec{S}_f \right|$
   This method is of second order accuracy and unbounded.

3. **Inverse distance**: The cell is decomposed in tetrahedra using the cell centre as apex a and triangles created by splitting the faces. Each triangle is made up by the face centre f, a midpoint of a face edge m and one vertex of the edge v. All cells C connected to v that share a face with the primary donor cell are then used to interpolate the acceptor value by applying inverse distance weighting:

   $$I_A^B = \frac{1}{S} \sum_{c \in C} \frac{1}{\delta_c} \Phi_c$$

   where δ_c is the distance from the cell centre of cell $c \in C$ and the acceptor cell and S is the sum of all weights $S = \sum_{c \in C} \frac{1}{\delta_c}$.
   This method is between first and second order accuracy and bounded.

3.3. Hole Cutting

After identification of donor and acceptor cells the hole cells can be determined. Hole cells a cell, which are overlapped by other cells with an better mesh quality. The values in these locations are calculated in other cells and therefore not needed for the solution. Additionally hole cells are not needed for inter-grid interpolation and are be blanked out.

The hole boundary for the background region is defined by the faces between donor cells and live cells of the overset domain. All cells within this hull face are hole cells if they are not marked as donor or acceptor cells. Hole cells are blanked implicitly in the discretisation matrix by setting off-diagonal coefficients to zero and diagonal coefficients to one or are removed from the mesh a prior.

3.4. Bulk Correction

A common issue of overset grid schemes is a lake of mass conservation across the overset interfaces. This imbalance of the mass flow leads to not physical disturbances in the pressure correction step of the solution algorithm and may cause a defect an preserved quantities. A bulk correction may be applied to ensure the overall conservation of the mass flux across the overset boundary.

4. Validation

Several test cases with either analytical or experimental validation data have been used for validation of the presented method.

4.1. Advection Test

A laminar flow in a two dimensional channel at a Reynolds number of $\mathrm{Re} = \frac{HU_b}{\nu} = 66$ based on the channel height H and the bulk velocity U_b has been used to study the influence of different parameters on the quality of the solution. The profile of the normalised velocity U for a laminar flow can be expressed as:

$$U_a(h) = 1 - 4(h - 0.5)^2 \tag{2}$$

where $0 \leq h \leq 1$ is the non-dimensional height of the channel.

The studied variants include application of the described interpolation methods, variation of the mesh density and different cell types, i.e. quadrilateral, triangular and polygonal cells. For comparison all mesh types and densities have been compared to a monolithic mesh. In addition to the flow profile the transport of a scalar Φ has been calculated to analyse the mass conservation errors. Therefore a given quantity has been placed in the fluid and transported across the interface by pure convection for a fixed time $T\frac{U_b}{H} = 1$. From the given velocity profile the final shape of the scalar distribution can be found analytically. The shape is compared to the achieved numerical results.

Perfect Matching

As a first test a perfectly matching quadrilateral overset grid has been used. As cell centres of donor and acceptor cells align perfectly there is no influence of the interpolation method as the weights of the extended donor cells become zero for this setup and the overset scheme become equivalent a monolithic mesh. As shown in Fig. 2 the deviation from the analytically derived velocity U_a along the channel height is below 2% for the most coarse grid and decreases monotonically, when the grid is refined further. With $N = 50$ cells the maximum discretisation error is below 0.1%. These results suggest, that a refinement of 50 cells should give good resolution of the flow characteristics and therefore for the scalar transport. The distribution of the transported scalar is visualised by the a constant level of $\Phi = 0.5$ in Fig. 2. The shape of the scalar distribution shows good agreement with the analytical distribution for meshes with 50 cells and above.

Shifted Grid

When the grid is shifted in axial and transverse direction of the flow, donor and acceptor cells do not align and values have to be interpolated. This setup is used to study the influence of the interpolation methods. Results show, that the gradient correction interpolation method converges faster then the inverse distance weighted method while giving unbounded results for the transported scalar. The direct interpolation method is strongly grid dependent and therefore the interpolation error converges linear with the resolution.

Different Mesh Types

The influence of the cell type was studied using quadrilateral, triangular and polygonal cells for the channel flow using the distribution and the conservation error of the transported scalar. Influence of the mesh types on the accuracy of the solution will be highlighted.

4.2. Flow Around Wings

The two- and three-dimensional flow around a NACA 0012 was calculated to validate the developed method for technically relevant flows around lifting surfaces against experimental results. For the two dimensional

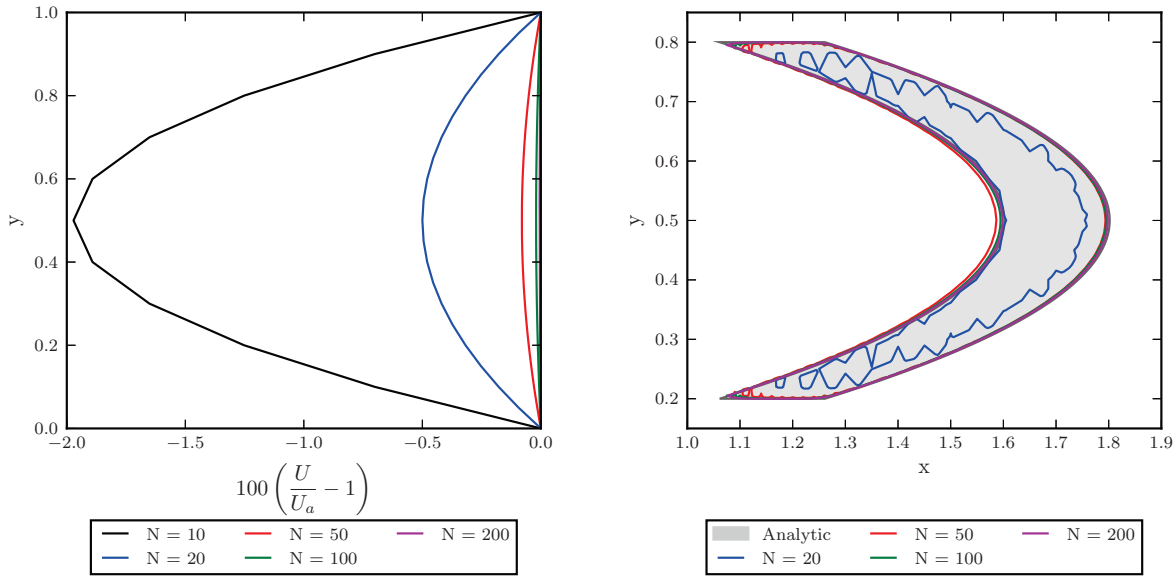

Figure 2. Influence of grid resolution on velocity profiles (left) and scalar distribution (right) with perfectly aligned grid.

flow around the profile at Re = $2.88 \cdot 10^6$ the profile lift and drag are compared as well as the pressure distribution at the cylinder surface for three angles of attack α. The pressure distribution for $\alpha = 10°$ is shown in Fig. 3.

4.3. Turbulent Flow around a Cylinder at a moderate Reynolds Number

Vortex structures behind bluff bodies like a cylinder need to be well resolved to ensure accuracy of the simulation. The flow around a circular cylinder at Re = 3900 was calculated using three mesh resolutions to evaluate the suitability of the overset grid scheme for turbulent flows and verify that turbulent flow is not influenced by the transition of these structures from one grid to another. In contrast to the three dimensional wing the vortex structures behind the cylinder are not perpendicular to the overset grid interface and are more sensitive to the interpolation between the grids.

The results show good comparison of time averaged and statistical values like mean drag and mean and rms velocity distributions without reproduction of the interface within the results. As an example of the attained results the average velocity profile behind the cylinder is compared to experimental results in Fig. 3.

4.4. Surface piercing cylinder

The deformation of the free surface between different flow phases is a typical aspect of ship hydrodynamics. The surface piercing test case shows the suitability of the developed method for multiphase flows with inhomogeneous density. The free surface evaluation around the cylinder is calculated and compared to experimental results. Further more the sectional resistance coefficient is compared to measurements.

5. Application

As example application we will present the result from a self propulsion test using a frozen rotor approach. For development of a propeller self propulsion test a used to test the propeller performance in the wake of the ship. To save computational resources steady state simulations utilizing a moving reference frame at different rotation angles of the propeller are used. Generating a mesh for this setup involves introducing a circular interface between the fixed and the moving mesh region as the normal vectors of mesh faces between these regions have to intersect to the axis of rotation. This interface has to be introduced to the mesh domain containing the ship.

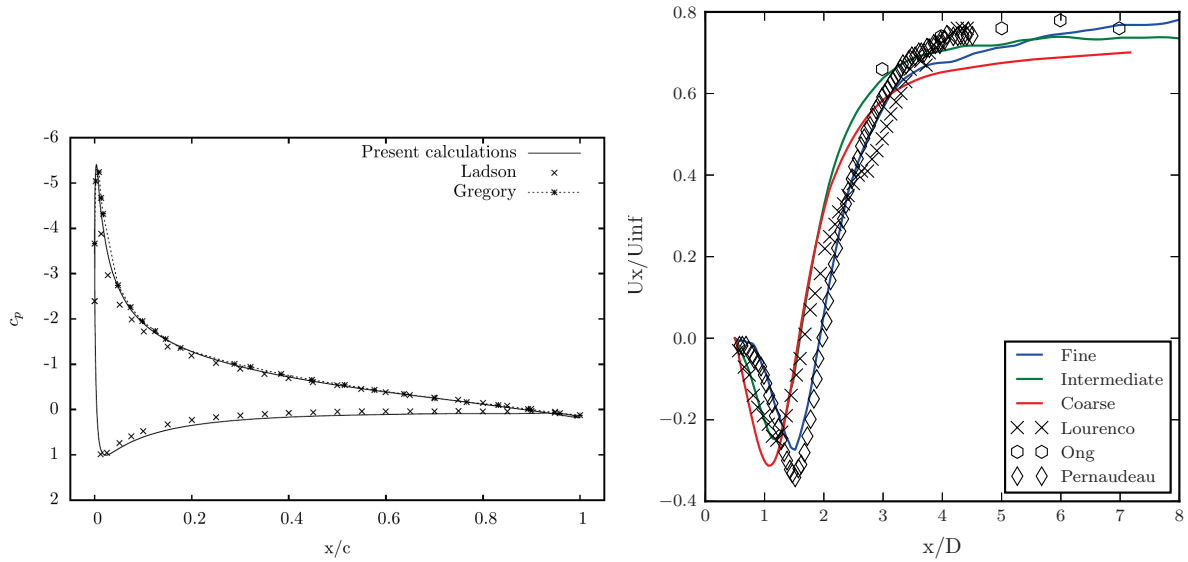

Figure 3. Pressure distribution for NACA 0012 profile at $\alpha = 10^\circ$ (left) and average velocity profile behind a circular cylinder at $\mathrm{Re} = 3900$ **(right).**

As an alternative we use the overset grid scheme to connect the rotor domain containing the rotating parts with the stator domain containing the ship and other appendages. Therefore the discretisation for the stator domain is not required to satisfy any restrictions caused by the frozen rotor approach. For the rotor domain the common meshing strategies are be applied.

6. Conclusions

An overset grid scheme for the OpenFOAM framework was developed and validated against different test cases. The results were shown to be in good agreement with measurements for miscellaneous flow problems. The method was applied to a frozen rotor propulsion test case reducing the meshing generation procedures while maintaining the quality of the spacial discretisation.

Numerical simulation of pressure fluctuation induced by cavitating propellers in wake flow

Nobuhiro Hasuike*, Taro Kajihama* and Kenichi Fukuda*
*Nakashima Propeller Co., Ltd.
688-1, Joto-Kitagata, Higashi-ku, Okayama 709-0625, Japan
E-mail: nobuhiro@nakashima.co.jp, web page: http://www.nakashima.co.jp/

Background

The pressure fluctuation has been examined from viewpoints of the structure of the hull and the comfort for crews in the propeller design. Several times, the 1st to the 4th order components were objects of the discussion in a general merchant ships in constructional. However, the influence of the noise pollution to the marine life is now discussed, and even the cavitation noise of the higher-order components becomes the object of the discussion.

Target of this research

In the propeller noise guideline of IMO, calculation that combines CFD with FEM is also introduced as a practical tool for full scale noise prediction. Thereby importance of reliable simulation method of pressure fluctuation is focused. It will be promising way to approach the full scale tip vortex cavitation. Therefore, development of the reliable CFD simulation method is highly expected. For such purpose, fundamental investigation of the relation between cavity volume variation and the pressure fluctuation was investigated in the present study. To specify the relation between cavitation dynamics with pressure fluctuation, time history of pressure near the cavity was investigated by wavelet analysis.

1 NUMERICAL SIMULATION OF CAVTATION PATTERN AND PRESSURE FLUCTUATION

In this research, cavitation flows around 20 propellers were simulated using SOFTWARE CRADLE SCRYU/Tetra V10 software, which was based on a finite volume method with an unstructured grid.

Cavitation flow simulation

The full Cavitation model(Singhal et al., See formulae(1) to (6)) was used in the calculation. NCG was set to 1ppm and the empirical constants C_e and C_c were set to 0.02 and 0.01 respectively. In this study, wall was not included in the computational domain. Pressure wave was calculated on the flow field.

Numerical grids

The computational domain was composed of the inner rotational part including the propeller and the outer stationary part(Fig.1). Unsteady propeller simulation in the wake uses the sliding mesh methodology. The numerical mesh was an unstructured grid, and basic cells were tetrahedral and prismatic cells were applied to near the blade surface for resolving the boundary layer (Fig. 2). The first layer thickness of the prism layer was set to a non-dimensional wall distance for a wall-bounded flow (y^+ in short) =50.

In this analysis, the axial wake distributions are given as an inlet boundary condition. K_T was adjusted to already-known K_T same as the model test condition. The propeller is rotated 1800deg. by 1deg per cycle to develop flow field, after that 0.3deg. per cycle is adopted during the final time step. The second order accuracy of the convective term was adapted. In this study, wall was not included in the computational domain. Pressure wave was calculated on the flow field. Solid boundary factor 2 was used as the pressure value on the wall.

Investigation of boundary condition

Boundary condition was firstly investigated. The inlet boundary was adjusted from the propeller center to the position of 0.7D to remove the influence of decrease of the velocity gradient of the wake. It was confirmed that the radius of the outer stationary cylinder was necessary to be more than 10D and the propeller downstream boundary was necesassary to be more than 30D from the propeller center. Finally, the radius of the outer stationary cylinder and the outlet boundary of the outer stationary part were adjusted from the propeller center to the position of 0.7D, 30D and 60D.

Investigation of turbulence model on tip vortex cavitation

SST-SAS model and Realizable k-ε model were compared in Fig.4. Realizable k-ε model showed stronger tip vortex cavitation was reproduced and well agreed with experiments. This tendency seemed to be preferable to estimate higher order pressure fluctuation. Finally Realizable k-ε model was selected for this study.

$$\frac{1}{\rho}=\frac{f_v}{\rho_v}+\frac{f_g}{\rho_g}+\frac{1-f_v-f_g}{\rho_l} \quad (1)$$

$$\frac{\partial}{\partial t}(\rho f)+\nabla\bullet(\rho\vec{v}f)=\nabla\bullet(\gamma\nabla f)+R_e-R_c \quad (2)$$

$$R_e=C_e\frac{\sqrt{k}}{\sigma}\rho_l\rho_v\sqrt{\frac{2(p_v-p)}{3\rho_l}}(1-f_v-f_g) \quad (3)$$

$$R_c=C_c\frac{\sqrt{k}}{\sigma}\rho_l\rho_l\sqrt{\frac{2(p-p_v)}{3\rho_l}}f_v \quad (4)$$

$$P_v=(P_{sat}+P'_{turb}/2) \quad (5)$$

$$P'_{turb}=0.39\rho k \quad (6)$$

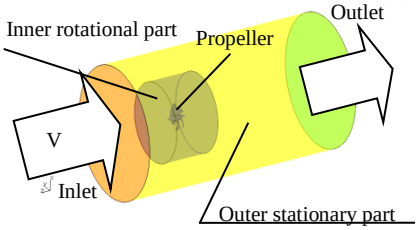

Figure 1: Computational domain

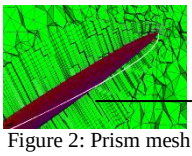

Figure 2: Prism mesh arrangement near blade surface

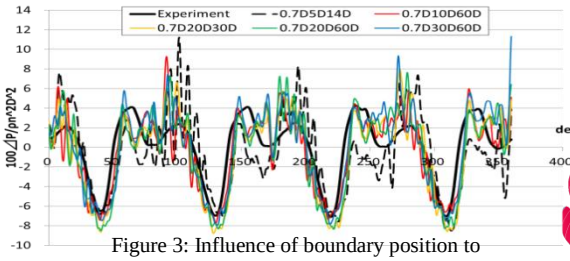

Figure 3: Influence of boundary position to the pressure fluctuation

Table 1: Principal particulars of 20 propellers

Index	Type of ship	Z	Ae(abt.)	P/D(abt.)	Skew(abt.)
Propeller A-1	Low speed	5	0.6	0.8	20
Propeller A-2	Low speed	5	0.7	0.8	40
Propeller A-3	Low speed	4	0.4	0.9	20
Propeller A-4	Low speed	4	0.4	0.8	20
Propeller A-5	Low speed	4	0.4	0.8	30
Propeller A-6	Low speed	4	0.5	0.7	30
Propeller A-7	Low speed	4	0.5	0.7	20
Propeller A-8	Low speed	4	0.4	0.8	30
Propeller A-9	Low speed	5	0.5	0.8	30
Propeller A-10	Low speed	5	0.5	0.8	30
Propeller A-11	Low speed	4	0.5	0.7	30
Propeller A-12	Low speed	4	0.4	0.7	30
Propeller B-1	High speed	6	0.7	1.0	30
Propeller B-2	High speed	5	0.6	1.0	30
Propeller B-3	High speed	6	0.8	1.1	30
Propeller B-4	High speed	6	0.6	0.9	30
Propeller B-5	High speed	6	0.8	1.1	30
Propeller B-6	High speed	6	0.8	0.8	30
Propeller B-7	High speed	6	0.8	0.8	30
Propeller B-8	High speed	6	0.8	0.9	40

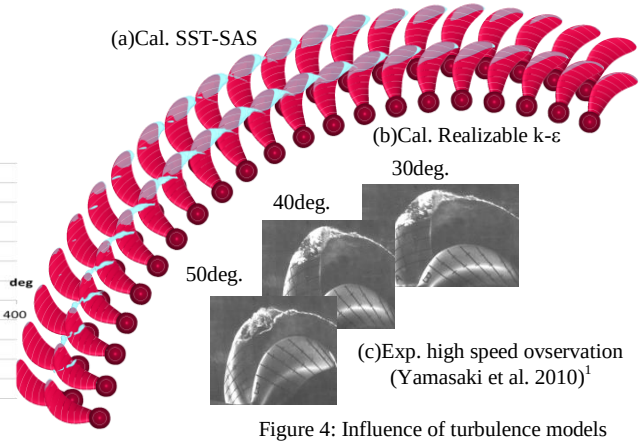

Figure 4: Influence of turbulence models (Propeller A-8)

2 CAVITATION PATTERN AND PRESSURE FLUCTUATION

Cavitation pattern

Cavitation patterns of 20 propellers were compared with model experiments(Fig.5). Principal particulars of model propellers are shown in Table 1. These 20 propellers are designed for different ships and tested at different model basins. Propellers in the group A were designed for the low speed ships(VLCC, tanker and bulk carrier) and the propellers in group B were designed for high speed ships(Container, Ro-Ro and LNG). Fig. 5 shows the contour of 10% cavity void fraction and the sketch of cavitation pattern by model experiments. As for propeller A-1 and A-2, the load at tip radius is comparatively higher than it of mid radius. Cavitation inception at leading edge at 90% radius was confirmed by the model test. Simulation results well captured this cavitation pattern. Moreover, tip vortex cavitation was strong. Simulation results well captured this cavitation pattern. As for the propeller B-1, further stronger tip loading with smaller blade area ratio was adopted for higher propulsive efficiency. In this case, sheet cavitation was smoothly merged into tip vortex cavitation and smoothly disappeared without erosion risk. On the other hand, the 2nd order pressure fluctuation was comparatively high. As for propeller B-3, the load at the mid radius position is larger in comparison with it of tip radius. Cavitation inception at leading edge at 60% radius was confirmed by the model test. In this case, pressure pulse amplitude was enough low. As for propeller A-7, further tip unloading was adopted. For this case, pressure pulse amplitude was enough low, but some erosive cavitation pattern was confirmed. Simulation results well captured this cavitation pattern. In these comparisons, it was confirmed current simulation captured cavity extent and disappearance with enough accuracy.

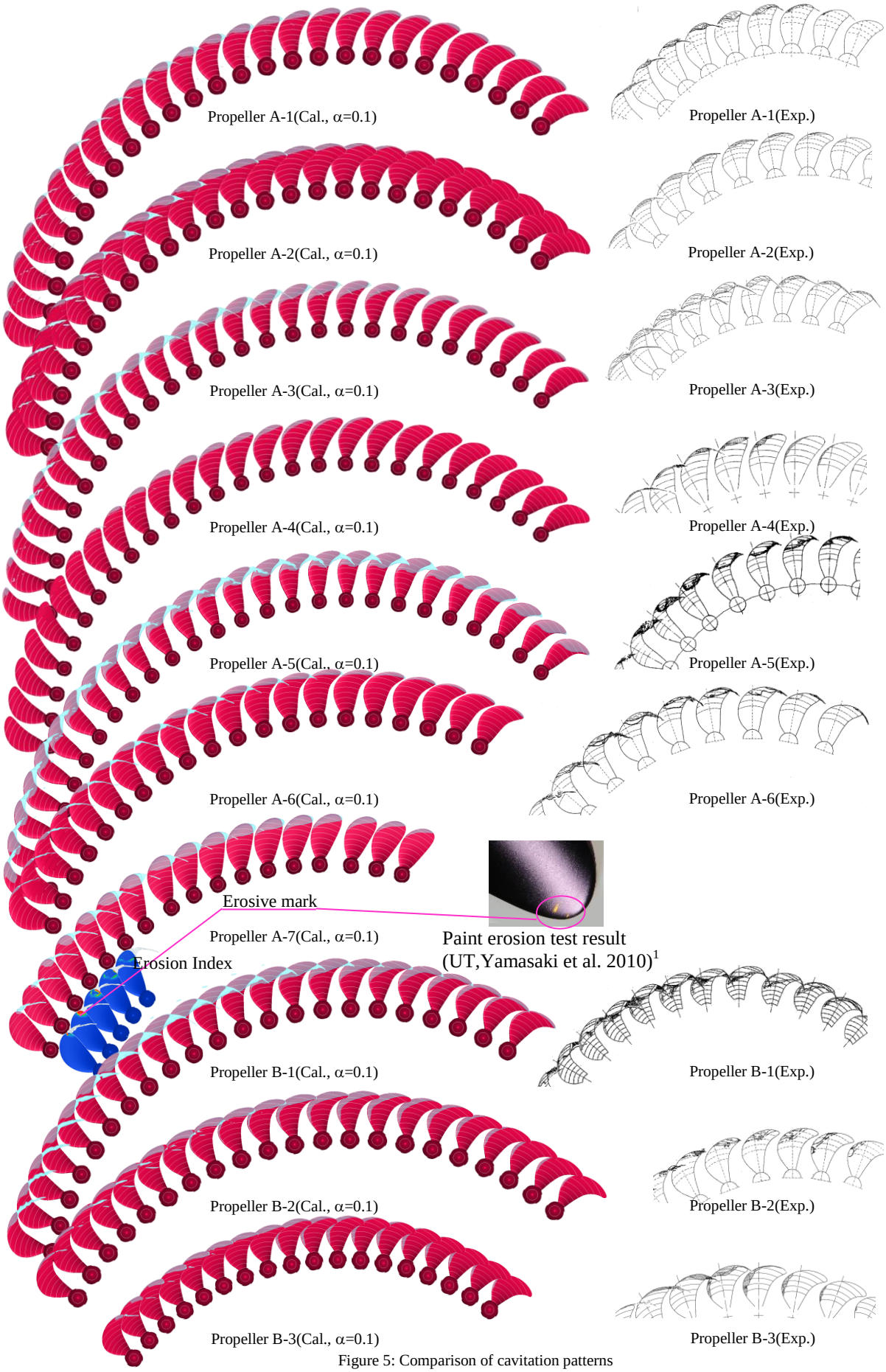

Figure 5: Comparison of cavitation patterns

Pressure fluctuation

In this study, the deviations of measurement result of pressure fluctuation at different test facilities were firstly investigated. The experimental result includes the test results by three different model basins with using the same model propeller (Propeller A-8). The deviations of the 1st and the 2nd order component were -24% to 17% based on averaged value. On the other hand, the deviations of the 2nd order component were -52% to 62% (Table 2). These deviations were mainly caused by the difference of gas nuclei distribution, methodology of promoting turbulence and stiffness of transducer. From these situations, it is preferable to validate the pressure fluctuation calculation from not only the comparison with a single experimental data but also more model experimental results. Then, the comparisons of 20 propellers with the model experiment were conducted in the present study. The 1st order blade frequency components of pressure fluctuation at the propeller top position were compared with model experiments as shown in Fig.6. Experimental pressure fluctuation was measured with transducer on the wall. However, simulations were conducted without plate. For considering this difference, product of simulated pressure and solid boundary factor 2 was used for comparison. The 1st order component of the pressure fluctuation roughly corresponds to the model experiment result within ±25% and is thought to be enough practicable level. Next, the 2nd order component is shown in Fig.7. It was confirmed that numerical simulation underestimated the 2nd order components in almost of the cases. Fig.8 shows the comparison of the wave pattern of pressure fluctuation of propeller A-8. Experimental result shows clear peak related to the 2nd order component. On the other hand, clear peak was not reproduced by the direct simulation of the pressure field of the propeller top position.

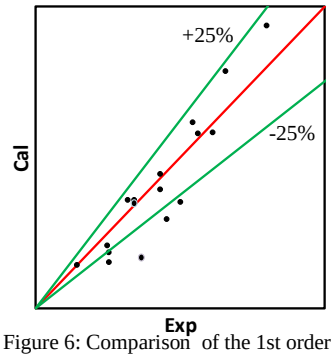

Figure 6: Comparison of the 1st order components of pressure fluctuation

Table 2: Deviations of measurement results of pressure fluctuation at 3 different model basins(Propeller A-8)

Model basin	A	B	C
1st order	7%	-24%	17%
2nd order	-10%	-52%	62%
3rd order	17%	-56%	39%

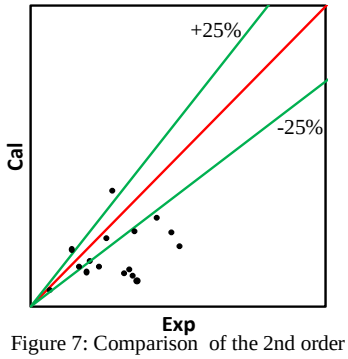

Figure 7: Comparison of the 2nd order components of pressure fluctuation

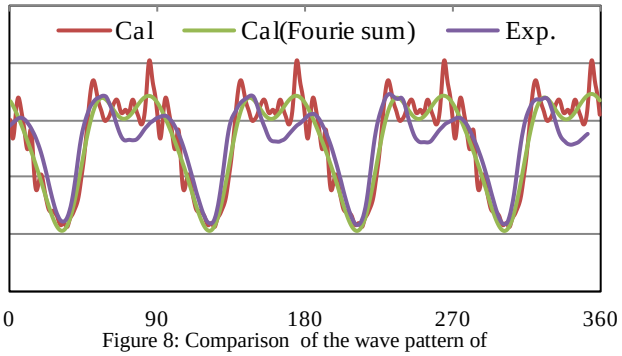

Figure 8: Comparison of the wave pattern of pressure fluctuation(Propeller A-8)

Relation between cavity dynamics and pressure fluctuation

The pressure fluctuation is thought to be related to the 2nd order time differential of cavitation volume. The computed wave shape of the 2nd order time differential of cavitation volume were compared with the computed wave patterns of pressure fluctuation in Fig.9. In comparison with pressure fluctuation by direct numerical simulation, wave peak position is corresponding well. On the other hand, depth of peak was more than that of direct numerical simulation of pressure field at propeller top position. Fig. 10 shows comparison result of wave patterns including experimental result. The wave shape of the 2nd order time differential of cavitation volume shows fairly well agreement with pressure fluctuation wave by the model test. In the case of direct simulation, there may be some numerical diffusion in pressure propagation from the cavitation position to the receiving pressure position. Especially, it is thought that this influence is remarkable in the propagation of the pressure wave of the higher order blade frequency component, and is thought that it is one of the causes of the difficulty of prediction of the 2nd or higher order blade frequency component. To solve this difficulty in practically, combination of the 1st order component by direct simulation of pressure field with the wave pattern of the 2nd order time differential of cavity volume is one of the practical approaches to solve the higher order components. The amplitude ratio of the 2nd order component versus the 1st order component is expected to be

derived from the Fourier analysis of the wave pattern of the 2nd order time differential of cavity volume. The 2nd order component is estimated by the product of the 1st order simulation result with the amplitude ratio of the 2nd order from cavity volume analysis. Indirect method by using simple formulae (7) was suggested for the prediction of the 2nd order blade frequency component of pressure fluctuation. Fig.11 shows the comparison result. The predicted amplitudes of the 2nd order component were increased from the direct numerical result and the accuracy was improved.

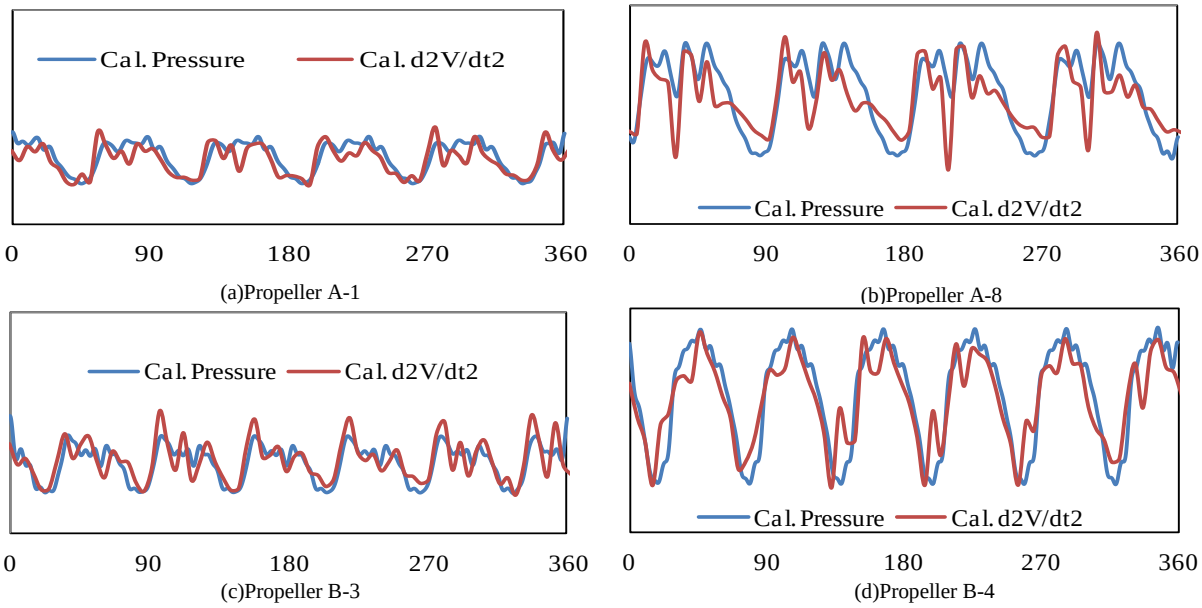

(a)Propeller A-1 (b)Propeller A-8

(c)Propeller B-3 (d)Propeller B-4

Figure 9: Comparison of the pressure wave with the 2nd order time differential of cavitation volume

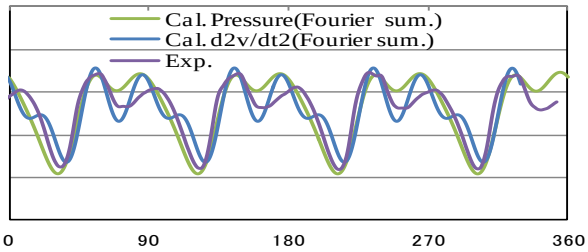

Figure 10: Comparison of the pressure wave(Cal. and Exp.) with the 2nd order time differential of cavitation volume(Propeller A-8)

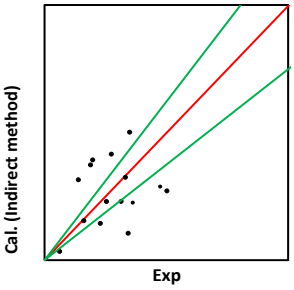

Figure 11: Comparison of the 2nd order components of pressure fluctuation

$$\Delta P_{2nd\ order} = \Delta P_{1st\ order} \times \frac{A_2}{A_1} \qquad (7)$$

Where,

A_1 is the 1st order blade frequency component of Fourier coefficient of the 2nd order time differential of cavity volume

A_2 is the 2nd order blade frequency component of Fourier coefficient of the 2nd order time differential of cavity volume

Wavelet analysis of cavitation surface pressure

Fujiyama (2015) [2] suggested discrete wavelet transform to the time history of pressure on the cavitation surface. Gabor Wavelet, written in Eq. (8), was used as the mother wavelet.

$$\psi(t) = \frac{1}{\sqrt{2\pi\sigma^2}} e^{-t^2/2\sigma^2} e^{i\omega t} \qquad (8)$$

where ω is the angular rate. σ is a parameter which affect the frequency resolution.σ = 8 was used. In this study, Fujiyama's method was adopted to the propeller B-5.The wavelet transform results of the 1st to the 4th order component of pressure fluctuation on the cavitation surface are shown in Fig.12. The 1st and the 2nd order component were related to the seat cavitation that expands from the leading edge. On the other hand, the 3rd order component was related to the behavior of rear part of the sheet cavitation and the super cavitating region., which seemed to be also related to the gradient of velocity of the ship wake in rotational direction. The 4th order component was related to the disappearance behavior of tip vortex cavitation.

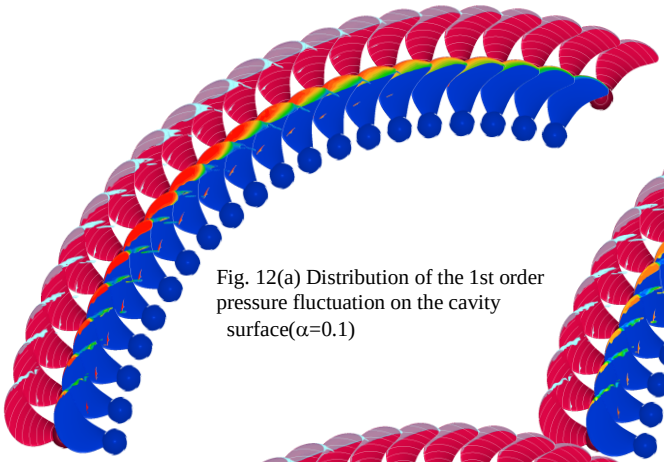

Fig. 12(a) Distribution of the 1st order pressure fluctuation on the cavity surface(α=0.1)

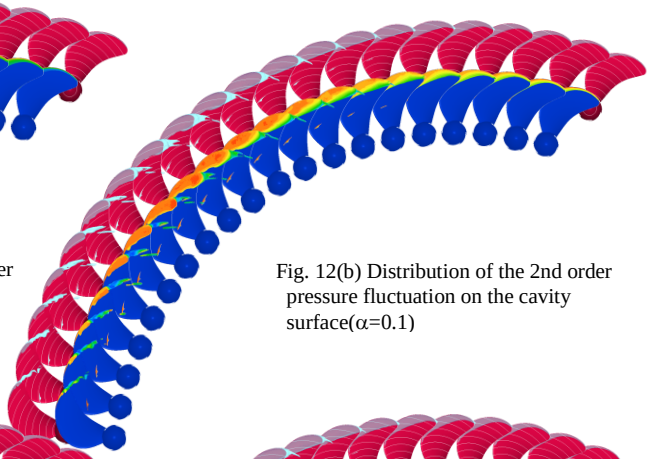

Fig. 12(b) Distribution of the 2nd order pressure fluctuation on the cavity surface(α=0.1)

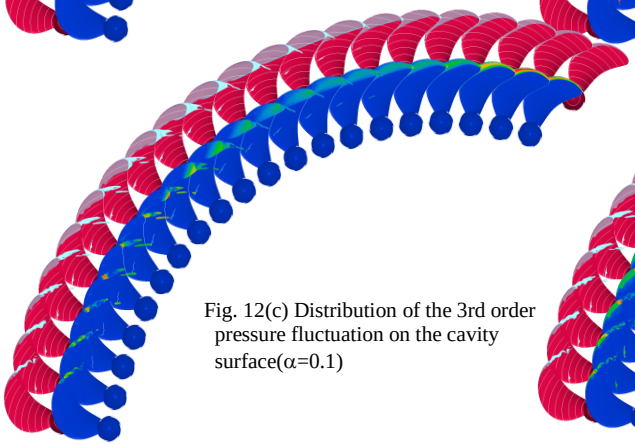

Fig. 12(c) Distribution of the 3rd order pressure fluctuation on the cavity surface(α=0.1)

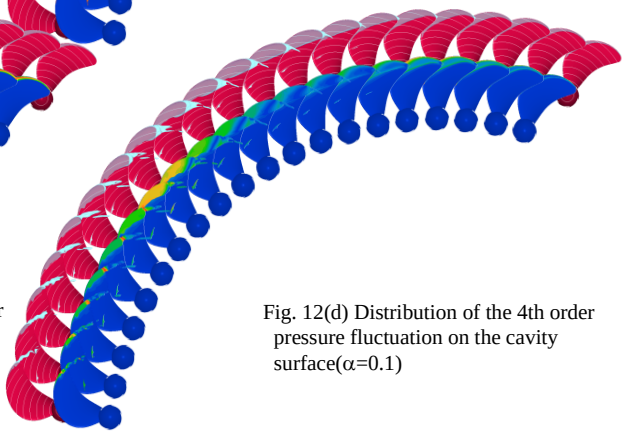

Fig. 12(d) Distribution of the 4th order pressure fluctuation on the cavity surface(α=0.1)

3 CONCLUSIONS

Numerical simulation of cavitation patterns and pressure fluctuation of 20 propellers were compared with experimental results. Time history of pressure on the cavitation surface was investigated by wavelet transform.

- It was confirmed that prediction accuracy of cavitation pattern and the 1st order blade frequency component of pressure fluctuation was enough practical level.
- The 2nd order component of pressure fluctuation was underestimated by the direct simulation of the pressure field at propeller top position. Further improvement is necessary.
- The shape of waves of the 2nd order time differential of the cavitation volume showed a similar shape of waves of fluctuating pressure by experimental results.
- Simple indirect method by combination of the 1st order component by direct simulation of the pressure field at propeller top position with the wave pattern of the 2nd order time differential of cavity volume was suggested.
- The 1st and the 2nd order component were related to the seat cavitation that expands from the leading edge. On the other hand, the 3rd order component was related to the behavior of rear part of the sheet cavitation and the super cavitating region. The 4th order component was related to the disappearance behavior of tip vortex cavitation.

NOMENCLATURE

D Propeller diameter
K_T Thrust coefficient ($=T/\rho n^2D^4$)
y^+ A non-dimensional wall distance for a wall-bounded flow ($=u^*y/\nu$)
y Distance to the nearest wall
u* Friction velocity
ν Kinematic viscosity (m^2s^{-1})
σ_n Cavitation number ($=2(P-P_V)/\rho n^2$)
ρ Density (kgm^{-3})
α cavity void fraction
k Kinetic turbulence energy

REFERENCES

[1] Yamasaki, S., Okazaki, A., Katayama, K., Himei, K., Mishima, T. and Hasuike, N., "High Efficiency Propellers – NHV (Non Hub-Vortex) Propeller with Smallest Blade Area, IPS'10, Okayama, Apr., (2010).

[2] Fujiyama K., "Numerical Simulation of Ship Hull Pressure Fluctuation Induced by Cavitation on Propeller with Capturing the Tip Vortex", Fourth International Symposium on Marine Propulsors SMP'15, June 2015

Systematic Assessment of Model Errors in CFD Ship Resistance Simulations

Ole Hympendahl, DNV GL, Hamburg/Germany, ole.hympendahl@dnvgl.com
Cosmin Ciortan, DNV GL, Høvik/Norway, cosmin.ciortan@dnvgl.com

1 Background

DNV GL's Maritime Advisory has a global presence in fluid dynamics. As part of the daily work the fluid dynamics sections compute ship resistance using RANS methods; several solvers are used. To evaluate the accuracy of these computations as part of a research project DNV GL performed systematical simulations. Two well-known test cases have been chosen for this project: Moeri's (ex KRISO) Container Ship, KCS is chosen as reference case for relatively slender vessels running at high speeds. It is not a very recent design (1997) and running at higher speeds than today's vessels, but it is fairly well documented and the model test data are considered reliable. As representative for a blunt ship Moeri's Very Large Crude Oil Carrier version two KVLCC2 has been chosen for the same reasons. Simulations have been run using the solvers Star-CCM+, FineMARINE and OpenFOAM, all including free surface and considering dynamic trim and sinkage. In a first step the mesh density has been varied. All simulations have been run in the same scale and conditions as the model experiments to identify the errors from CFD and not the errors of the extrapolation method.

1.1 Wall functions and non-dimensional wall distance y+

The velocity profile close to the wall can be divided into three layers: The viscous sub-layer, the logarithmic region and the wake region. For this purpose the wall distance and the velocity are made non-dimensional as y+ and u+:

$$y^+ = \frac{y u_\tau}{\nu} \quad \text{and} \quad u^+ = \frac{u}{u_\tau}$$

With:

$$u_\tau = \sqrt{\frac{\tau_w}{\rho}}$$

U – velocity parallel to the wall, y – distance to the wall, ν – kinematic viscosity, τ_w – wall shear stress, ρ – density

The velocity profile in the viscous sub-layer and the logarithmic layer are shown in Fig.1.

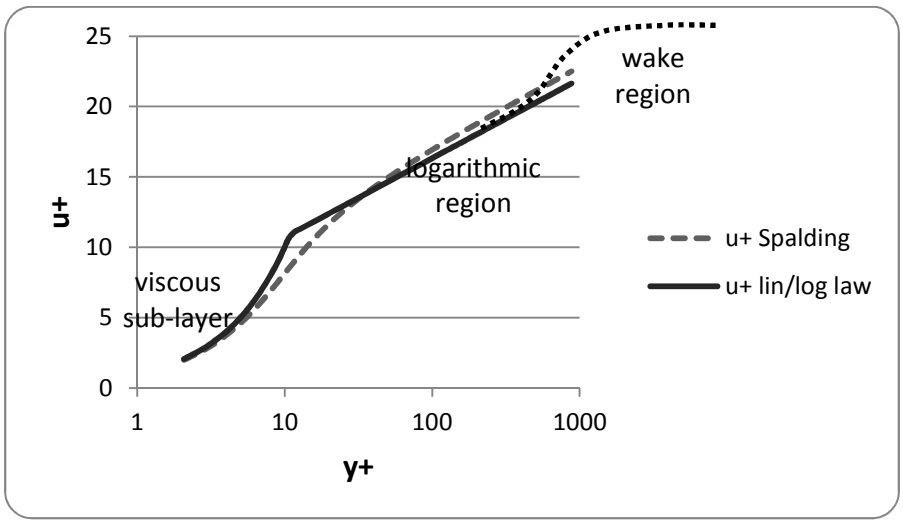

Figure 1 - Velocity profile close to the wall

Below y+=11 the velocity profile follows a linear correlation $y^+ = u^+$; then follows the logarithmic region $u^+ = \frac{1}{k}\ln y^+ + C^+$, due to the logarithmic scale visible as straight line. At some point the velocity profile leaves the logarithmic correlation into the wake region. This point depends on the nature of the flow outside the boundary layer and on the Reynolds number. The larger the Reynolds number, the larger the y+ where the logarithmic law becomes invalid.

When applying this to CFD simulations there are two options how to accurately resolve the velocity profile close to the wall. One option would be to geometrically resolve the boundary layer with a sufficient number of grid nodes. In this case the first grid node is required well in the viscous sub-layer, thus at a y+ of approximately 1. Because this may require quite large numbers of cells for technical applications, most commercial solvers have implemented wall functions which model the viscous sub-layer and require the first mesh node in the logarithmic region, this means well above y+=20. This is commonly used for applications at high Reynolds numbers.

Figure 1 shows also an approximation by Spalding for both the viscous sub-layer and the logarithmic region. Many wall functions in commercial solvers have implemented such an approximation to allow the first mesh node to be at any wall distance in this region. Spalding's formula for velocity distribution is presented next:

$$y^+ = u^+ + 0.1108\left\{e^{0.4u^+} - 1 - 0.4u^+ - \frac{(0.4u^+)^2}{2!} - \frac{(0.4u^+)^3}{3!} - \frac{(0.4u^+)^4}{4!}\right\}$$

[D.B. Spalding, A Single Formula for the "Law of the Wall", *J. Appl. Mech* 28(3), 455-458 (Sep 01, 1961)]

2 Results Mesh Study

2.1 Star-CCM+

For the ship KVLCC2 two meshes were generated and run with Star-CCM+ to check for mesh convergence.

Mesh	Number of cells	Resistance CFD [N]	Resistance exp [N]	Difference to exp [%]
1 w/o rudder	1M	19.232	18.129	6.08
2 w/o rudder	3.8M	18.874	18.129	4.11

Both simulations had been performed without a rudder. As the model tests included a rudder, the second simulation (fine mesh) was repeated including the rudder.

Mesh	Number of cells	Resistance CFD [N]	Resistance exp [N]	Difference to exp [%]
2 w rudder	4M	19.2	18.129	5.91

While this is not a comprehensive mesh study it is nevertheless an indication on the magnitude of error introduced by the mesh density. As shown in paragraph 3.1 the absolute error is relatively large due to a too small y+-value.

2.2 Fine/Marine

For each ship three meshes have been generated. The meshes have 2.6M, 4.9M and 8.3M cells for KCS and 3.3M, 4.4M and 6.1M cells for KVLCC2.
The diagrams Figure 2 and Figure 3 show the results (difference to model test) for the mesh study.

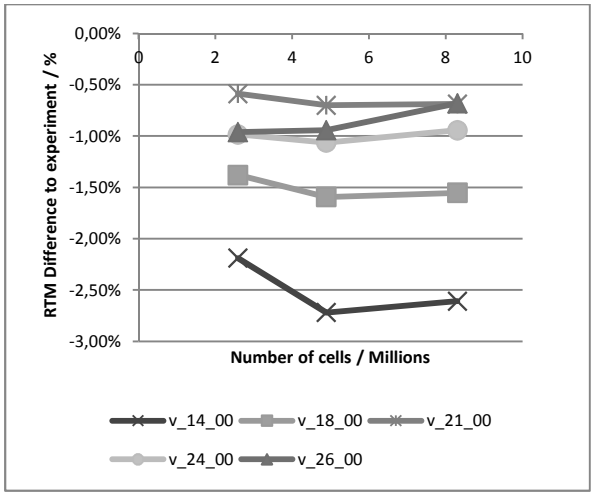

Figure 2 - Mesh convergence KCS - Fine/Marine

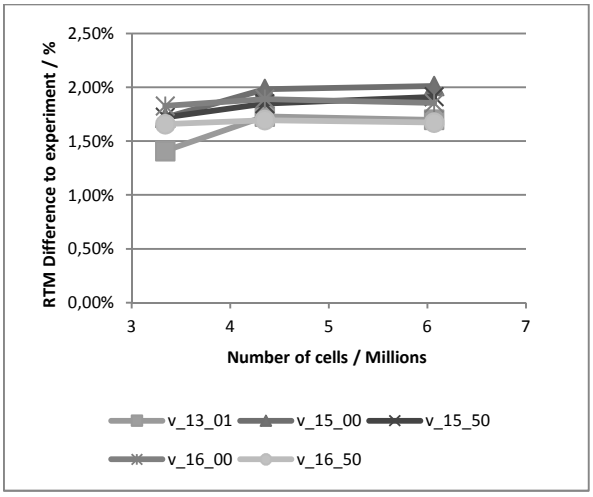

Figure 3 - Mesh convergence KVLCC2 - Fine/Marine

The diagrams show already for the coarser meshes relatively small scatter due to mesh size. The results on the two fines meshes are nearly identical, thus mesh convergence has been achieved.

2.3 OpenFOAM

For each ship three meshes have been generated. Cell numbers are 1.6M, 3.0M, 4.9M for KCS and 2.0M, 3.7M and 6.2M for KVLCC2.
The results are shown in Figure 4 and Figure 5.

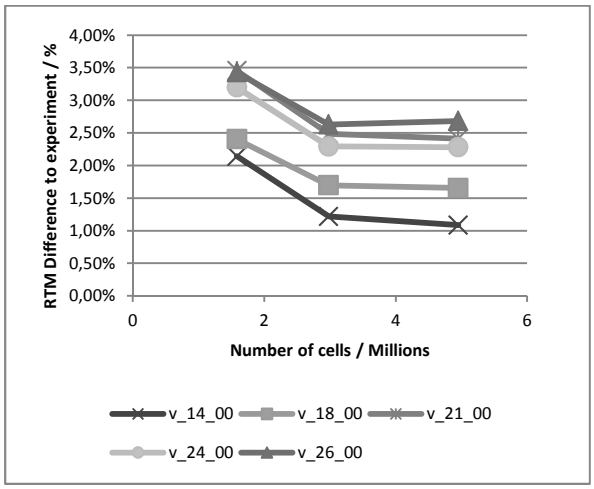

Figure 4 - Mesh convergence for KCS, OpenFOAM. Colors: Speed in knots, full scale

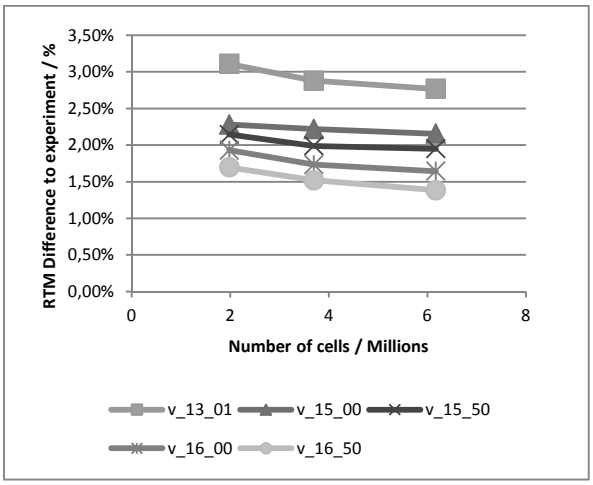

Figure 5 - Mesh convergence for KVLCC2, OpenFOAM. Colors: Speed in knots, full scale

The results on the coarsest mesh deviates for both ships from the results on the finer meshes, thus this mesh is considered too coarse. For the two finer meshes mesh convergence is achieved.

3 Variation of Non-Dimensional Wall Distance Y+

A conclusion from the mesh study was that the mesh influence is small for meshes with reasonable and feasible numbers of cells. But all solvers showed quite a significant influence of the ship speed. As all speeds were calculated on the same mesh, it was assumed that this speed dependency originates in the different y+ values of the first layer close to the wall. In all setups this cell thickness is chosen in order to maintain a desired y+ value on a medium ship speed. It was decided to further investigate

the y+ influence on the results. Y+ studies have been performed with FineMarine and OpenFOAM. In order to save computational effort, only the coarse meshes (except for: KVLCC2 - OpenFOAM - medium sized meshes) have been used and only three velocities have been investigated. In the following diagrams the difference in total resistance (model scale) to the experimental results is shown. Each thick line connects the results for the same speed on different meshes; and each thin line connects the results for different speeds on the same mesh.

3.1 Results of y+ study Star-CCM+

With Star-CCM+ only KVLCC2 at only one speed was checked against y+ variation.

Simulation	Approx. y+	Resistance CFD [N]	Resistance exp [N]	Difference to exp [%]
2	20	19.2	18.129	5.91
3	40	18.462	18.129	1.84
4	50	18.426	18.129	1.64

The study shows that with an appropriately chosen y+-value the error is within the expected accuracy. The mesh settings for an y+ of approximately 50 have been applied to both test ships at different speeds. The results are listed in the tables below. They show a good agreement with the experiments.
KVLCC2:

Fr / velocity [m/s]	RT experiment [N]	RT CFD [N]	Difference [%]
0.1423 / 1.0469	18.129	18.526	2.190
0.1515 / 1.1146	20.453	20.94	2.383

KCS:

Fr / velocity [m/s]	RT experiment [N]	RT CFD [N]	Difference [%]
0.195 / 1.6469	44.978	45.05	0.151
0.282 / 2.3795	121.618	120.3	-1.083

3.2 Results of y+ study FineMarine

In the following diagrams the difference in total resistance (model scale) to the experimental results is shown. Each thick line connects the results for the same speed on different meshes; and each thin line connects the results for different speeds on the same mesh. ‘v_10_00’ denotes a ship speed corresponding to 10 knots full scale. ‘gp2-20’, ‘gp2-40’,etc. denote meshes with a target y+ of 20,40,...

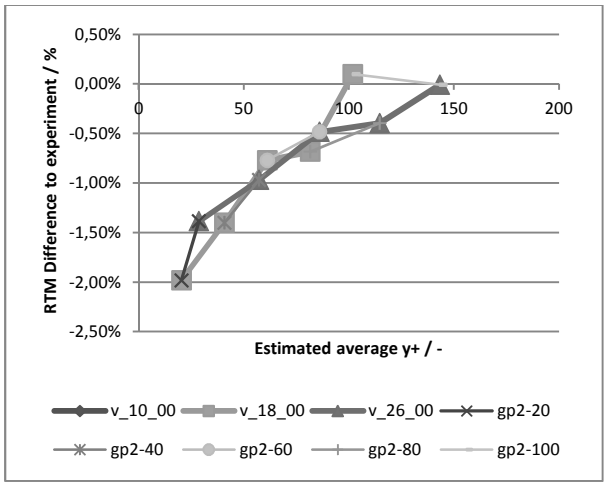

Figure 6 – KCS - Results y+ study FineMarine

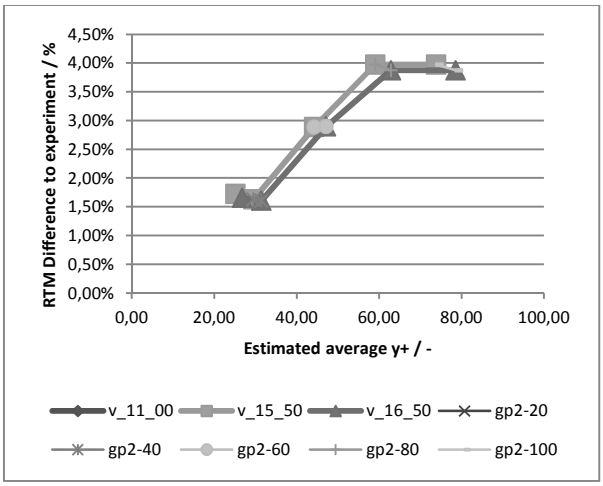

Figure 7 -KVLCC2-Results y+ study FineMarine

The results show a significant influence of the target y+. With a target y+ of about 40 the error is within +/- 2%.

3.3 Results of y+ study OpenFOAM

In the simulations with OpenFOAM two wall functions have been applied. One set of simulations has been done with a wall function with uses Spalding's approximation and thus should be relatively y+-independent. A second set of simulations has been done with the standard 'nutk' wall function. This wall function requires the first mesh node to be in the logarithmic region. The results of both sets of simulations are shown in the following diagrams.

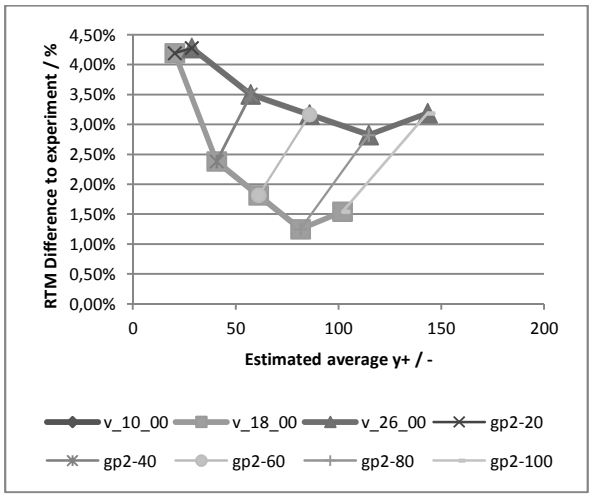

Figure 8 - KCS - Results y+ study OpenFOAM - Spalding wall function

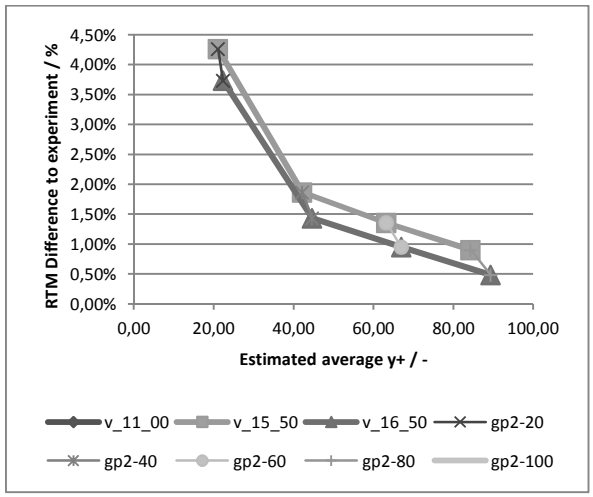

Figure 10 - KVLCC2 - Results y+ study OpenFOAM - Spalding wall function

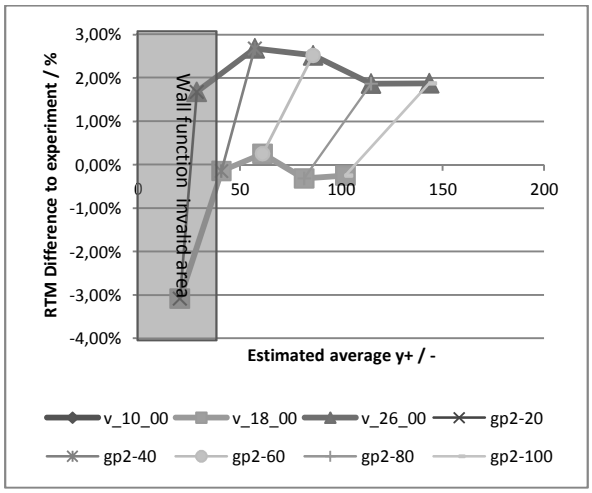

Figure 9 - KCS - Results y+ study OpenFOAM – nutk wall function

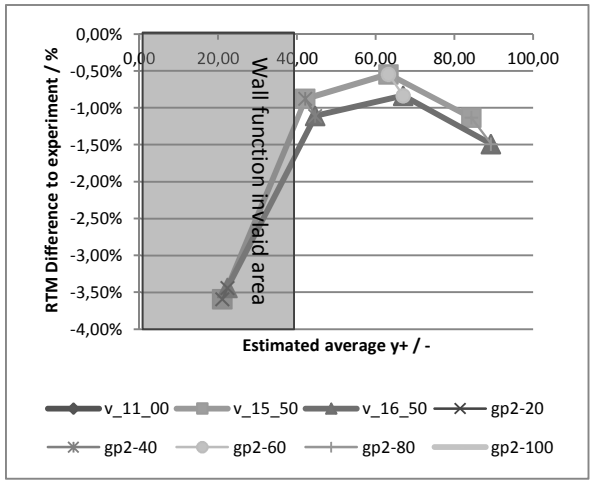

Figure 11 - KVLCC2 - Results y+ study OpenFOAM - nutk wall function

As expected from theory the 'nutk' wall function shows large errors if the y+ is chosen too small. With an appropriately chosen first cell height the results are very close to the experimental data. But also the Spalding wall function shows a dependency of the first cell height. It is smaller than for the 'nutk' wall function but at the expense of a slightly lower overall accuracy (when looking only at these two vessels).

4 Conclusions

CFD ship resistance simulations have been performed for two ships. A mesh convergence study and a time step convergence study have been performed; the results of the former have been shown here. With sufficiently fine mesh and small time step the influence of both is sufficiently small. The remaining scatter in the results is considered to originate from secondary effects such as differing numbers of prism layers.
The studies confirmed DNV GL's experience that the necessary cell numbers and time steps can be well handled with today's solvers and hardware within reasonable computational time to run such simulations on an industrial scale. The discretization errors need not be an issue any more if properly considered.
But the following study with varied distance of the first mesh node from the wall showed that the errors introduced due to model assumptions such as wall functions are a multiple of the remaining discretization errors. When comparing the results on the meshes generated with desired average y+-values of 20 to 60 there was a surprisingly large influence of the height of the first wall cell. This could be expected from theory for the 'nutk'-wall function which requires the y+ to be above 20 (and this means everywhere at the hull!), but the effect was visible also for the wall functions of all solvers which include some empirical formulae for the velocity distribution in the boundary layer.
The diagrams indicate that our target y+-value of about 40 for standard meshes (ship model scale Reynolds numbers) may be chosen too low and could be changed to a higher value. But this is dangerous, as higher y+-values lead to larger cells in the boundary layer and this may lead to insufficient mesh resolution to capture the flow accurately, especially if flow separation could be an issue. This is illustrated by Figure 12 showing the results for KVLCC2 on a (too) coarse mesh. With larger distance of the first mesh node the results are far off.

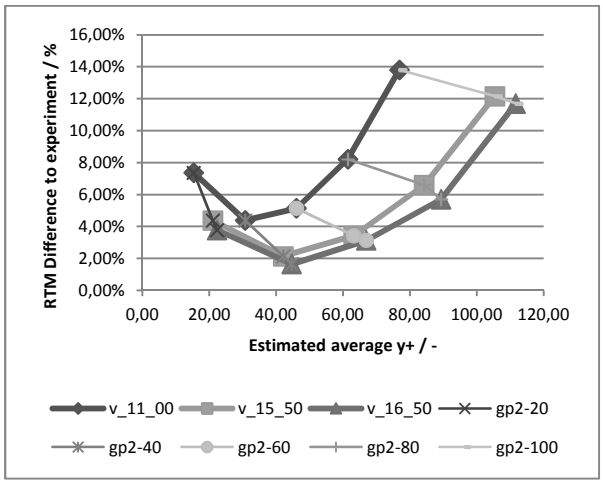

Figure 12 - Results KVLCC2 - OpenFOAM - Spalding wall function - coarse mesh - insufficient resolution of boundary layer

Thus the main conclusion from the y+-study is that it is still of utmost importance to ensure exactly the same first mesh node distance when comparing different simulations.
Regarding the comparison of the three solvers it can be concluded that similar results are obtained independent of the chosen code.

Numerical Study on Flow Field around the Aft Part of Hull Form Series in a Steady Flow

Yasuo Ichinose, Yusuke Tahara, Yoshikazu Kasahara
National Maritime Research Institute (NMRI), Mitaka, Tokyo/Japan
ichinose@nmri.go.jp tahara@nmri.go.jp kasahara@nmri.go.jp

1. Introduction

Design of the aft part of hull form yields optimum trade-off problem between resistance performance and propulsive efficiency. Especially for full hull forms, such as tankers or bulkers, control of bilge vortices and velocity distribution at propeller plane has a crucial impact on maximization of hull form performance and enhancement of ESDs performances. Kjellgerg and Janson (2009) optimized "VIR-TUE" tanker with multi-objective function, resistance and wake quality for cavitation using FRIENDSHIP-Framework for hull form modification. Van der Ploeg (2014) added self-propulsion performance for optimization of "STREAMLINE" chemical tanker using GMS-Merge tool. These works made good results to generate hull forms with well-performed in objective functions. Meanwhile, for the purpose to explain the principal character of hull form to effect propulsion performances, these data are not enough to be suited.

The main objective in the present study is an investigation on salient features of the generation and the deformation of bilge vortices depending on hull-form changes. In particular, a series of relatively continuous hull forms modifying from U-type to V-type frame-lines has been investigated by numerical analysis using NMRI RANS-solver NEPTUNE on model and full scale. The aft parts of 33,000 DW chemical tanker and 82,000 DW bulk carrier, hereafter referred to as 33CT and 82BC, respectively, are modified by structured-grid-blending technology using the two basic hull forms, which are characterized by U-shape and V-shape frame-lines. The animated figures created from more than 200 steady-flow series results show significant changes in generations and deformations of bilge vortices.

2. Modification method of hull forms and Computational Method

Hull form series is generated by hull-form interpolation between the two basic hull forms designed with NAPA. This hull-form (or structured grid) interpolation method, called hull-form-blending, was confirmed by Tahara (2011). Basic structured grids with same structures and grid points for all i, j, k directions were generated with semi-automatically grid generator AutoDes developed by NMRI and ACT. The grid-blending operation for two basic grids is expressed as follows:

$$\vec{P} = a_1\overrightarrow{P_1} + a_2\overrightarrow{P_2} \quad \text{where} \quad a_1 = \alpha \quad , a_2 = (1-\alpha) \tag{1}$$

Where $\overrightarrow{P_1}$ and $\overrightarrow{P_2}$ are grid points for the two basic forms, and $0 \leq \alpha \leq 1$ is design variables.

The governing equations are the continuity equation and Reynolds-averaged Navier-Stokes (RANS) equation. The artificial compressibility form of these equations based on a cell-centered finite-volume formulation is solved by structured grid based solver, NEPTUNE ver.6.41 developed at NMRI (Hirata 2000). The turbulence model used in the present work is modified Spalart-Allmaras (MSA) one-equation model (Hirata and Hino 2000) without wall function. An arbitrary constant parameter, Cvor in MSA, set as 10 in all cases of the present work. The presence of rotating propeller is represented by simplified body-force model based on an infinitely bladed-propeller theory. This solver and turbulence model are normally used for hull form design at NMRI to estimate model-scale performance. The full-scale simulation used this solver and turbulence model is validated with full-scale measurement data of 200,000DWT tanker “Ryuko-maru” worked by Hirata and Hino (2007).

3. Computational Setup and Validation of the flow computations

The two hull forms with same fore parts for each 33CT and 82BC were designed as practical hull forms with principal dimensions on Table 1. Fig. 1 shows aft-part frame-lines of each case. The differences of displacements and wetted surface areas from blue line (U-type) and green lines (V-type), Disp. diff. and WSA diff., respectively, are shown on Table 1. The blue line hull forms of each case, generally called U-shape frame-lines, are built as model ships with ~7m ship lengths. The tank test results show EEDIs for both ships with energy saving devices achieved phase 2 at design stage.

Table 1 Principal Dimensions

	Length[m]	Breadth[m]	Draft[m]	C_b	Disp. diff.	WSA diff.
33CT	170.50	27.70	10.00	0.79	-0.5%	-0.2%
82BC	222.00	32.26	12.20	0.87	0.3%	-0.2%

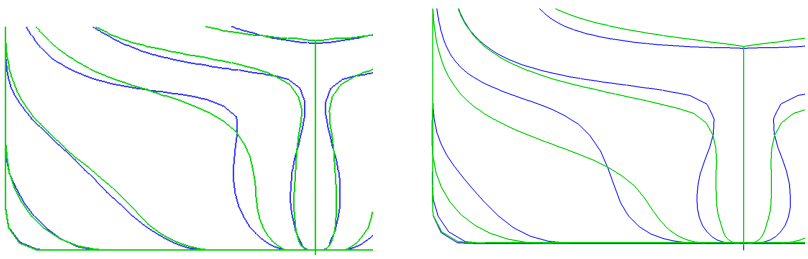

Fig. 1 Aft Part Frame-Lines (Left: 33CT, Right: 82BC)

The calculation grids of the basic hull forms without any appendages at full-load and even-keel were generated with HO topology, 1.6 million cells (i x j x k = 209 x 97 x 81: both sides) for model scale of both cases. The grids for full scale are composed with OO topology, 2.4 million cells (i x j x k = 321 x 73 x 105) and 2.2 million cells (i x j x k = 321 x 73 x 97) for 33CT and 82BC, respectively. The minimum spacing normal to wall is set to be y^+= 0.75 for model and full scale. The effect of free surface

is considered to be small and ignored in all cases.

Table 2 shows comparisons of calculation results and tank test results of U-type hull forms (the blue lines in Fig. 1). For 82BC case, the discrepancy between computed and measured 1+k is not ignorable, which may be due to limited size of total cell number, prepared for the time consuming optimization calculation. Otherwise, the flow field results appear to be accurate enough for the present analyses, with main focus placed more on comparison of flow field characteristics. Fig. 2 presents wake comparisons between tank test measurements and computational results. In both cases, the computational results agree well to the tank test measurements and show very obvious hook shapes generated by bilge vortices.

Table 2 Tank Test Measurements and Computational Results in Model Scale

	33CT			82BC		
	EFD	CFD	Error	Exp.	CFD	Error
1+k	1.246	1.208	-3.0%	1.310	1.227	-6.3%
1-t	0.835	0.831	-0.5%	0.842	0.837	-0.6%
1-wt	0.659	0.646	-2.0%	0.542	0.582	7.4%

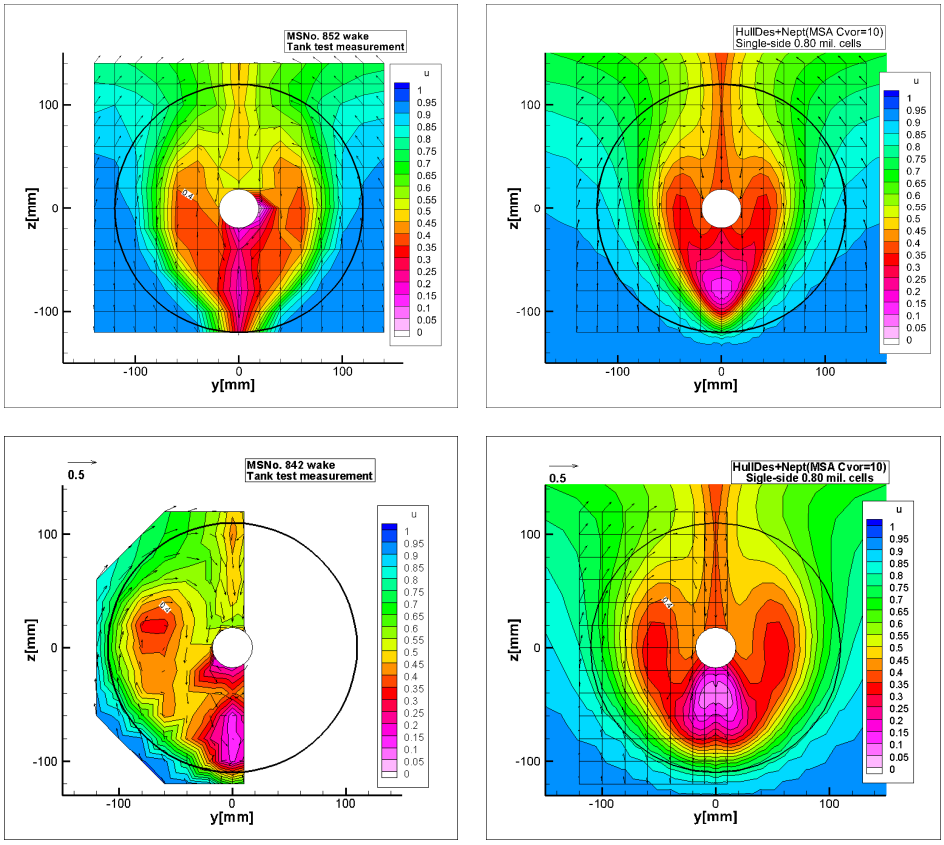

Fig. 2 Tank Test Measurements and Computational Results in Model Scale
(Left: Measurements, Right: Computational Results, Top: 33CT, Bottom: 82BC)

4. Results

Fig. 3 presents limiting streamlines and axial vorticity distributions for 33CT in model and full scale. The vorticity contour lines show generation of bilge vortices and relation of limiting streamlines to bilge vortices clearly.

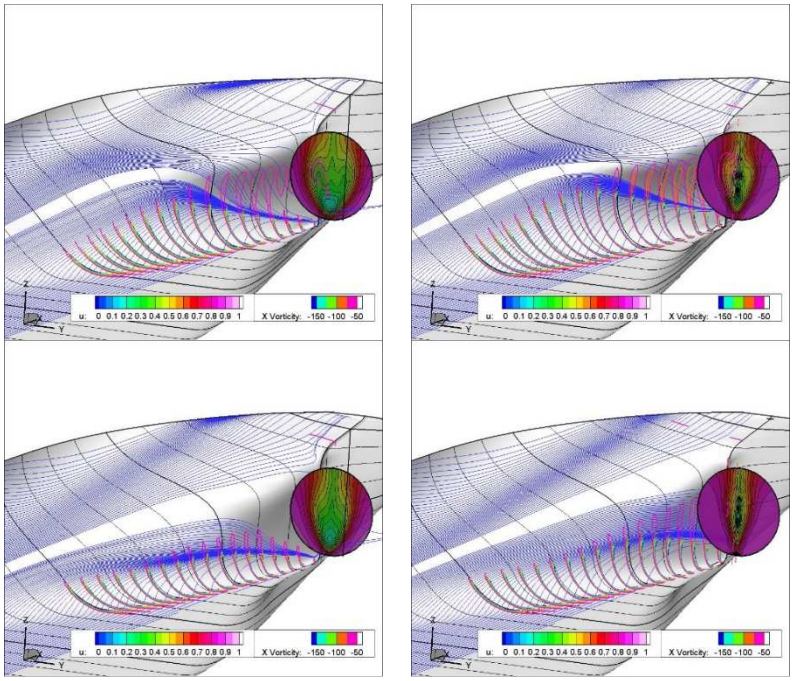

Fig. 3 Limiting Streamlines and Axial Vorticity Distribution for 33CT
(Left: Model Scale, Right: Full Scale, Top: U-type Lines, Bottom: V-type Lines)

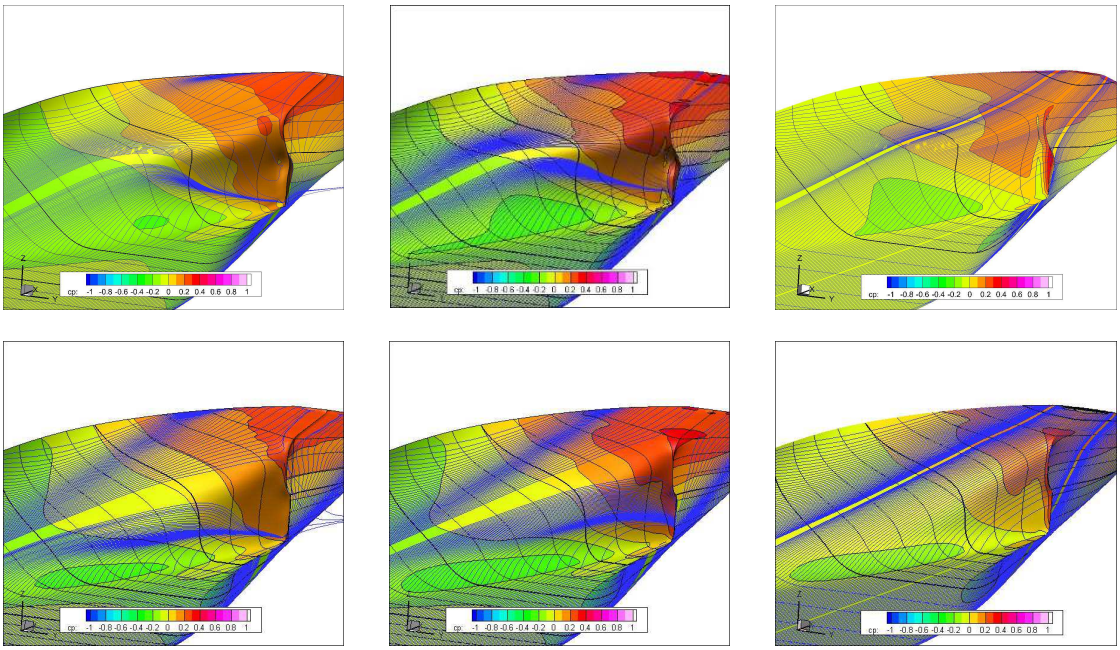

Fig. 4 Pressure Distributions and Limiting Streamlines for 33CT (Left: Model Scale, Middle: Full Scale, Right: Potential flow, Top: U-type Lines, Bottom: V-type Lines)

The hull form with U-type frame-lines generates bilge vortices strongly in model and full scale. The V-type form is unable to supply enough vorticity to build obvious hook shapes at propeller plane in model scale. In full scale, vorticity is stronger than that in model scale due to shrinkage of boundary layers. The transition of bilge vortex from V-type to U-type hull forms is clearly confirmed on animated figures made by 200 simulations for interpolated hull forms.

Fig. 4 shows pressure distributions for 33CT in model-, full-scale and potential flow. The pressure distributions in full scale are closer to those of potential flow. Re effects on surface flow field are seen to be different for the different hull-form types. This appears to be related to characteristics of form factor 1+k. The difference of form factor 1+k between U-type and V-type hull forms is 2.9% based on U-type hull form result for model scale, and that for full scale is 4.3%.

Fig. 5 presents limiting streamlines and vorticity distributions for 82BC in model and full scale. Similarly for 33CT, near-wall flow indicates weaker secondary motion like potential flow in full scale, and the shrinkage of boundary layer enhances axial vorticity in full scale. Fig. 6 shows pressure distributions for 82BC in model scale, full scale and potential flow. The difference of form factor 1+k between U-type and V-type hull forms is 2.4% and 6.2% for model and full scale, respectively.. This is the same trend for 82BC and 33CT, where the difference of 1+k for hull forms in full scale is larger than that in model scale.

5. Concluding Remarks

Simulations for hull-form series present the following flow field characteristics around aft parts of the ships. 1) The U-type hull form generates bilge vortices strongly in model and full scale and axial vorticity is stronger in full scale due to the shrinkage of boundary layers. 2) The pressure distributions in full scale are closer to those of potential flow. 3) Re effects on surface flow filed are different for the different hull form types. Our future work involves, detailed investigation for scale effect in hull form manner, detailed turbulence model study, and comparison of measurement in actual sea.

References

1. M. Kjellgerg, C-E. Janson, 2009, Numerical optimization of resistance and wake quality for a VLCC, 12th Numerical Towing Tank Symposium.
2. A. van der Ploeg, 2014, Optimization of the STREAMLINE tanker using RANS/FS computations, 17th Numerical Towing Tank Symposium.
3. Y. Tahara, D. Peri, E. F. Campana, F. Stern, 2011, Single- and multi-objective design optimization of a fast multihull ship: numerical and experimental results, J. Marine Science and Technology, Vol.16, No. 4, pp.412-433.
4. N. Hirata, T. Hino, 2000, A comparative study of zero- and one-equation turbulence models for ship flows, J. Kansai Society of Naval Architects, Japan, No.234, pp.17-24.

5. N. Hirata, T. Hino, 2000, An Efficient Algorithm for Simulating Free-Surface Turbulent Flows around an Advancing Ship, J. Society Naval Architect. Japan, Vol.185, pp.1-8
6. N. Hirata, T. Hino, 2007, Numerical computations of ship flows in full scale, Computational Methods in Marine Engineering, Barcelona.

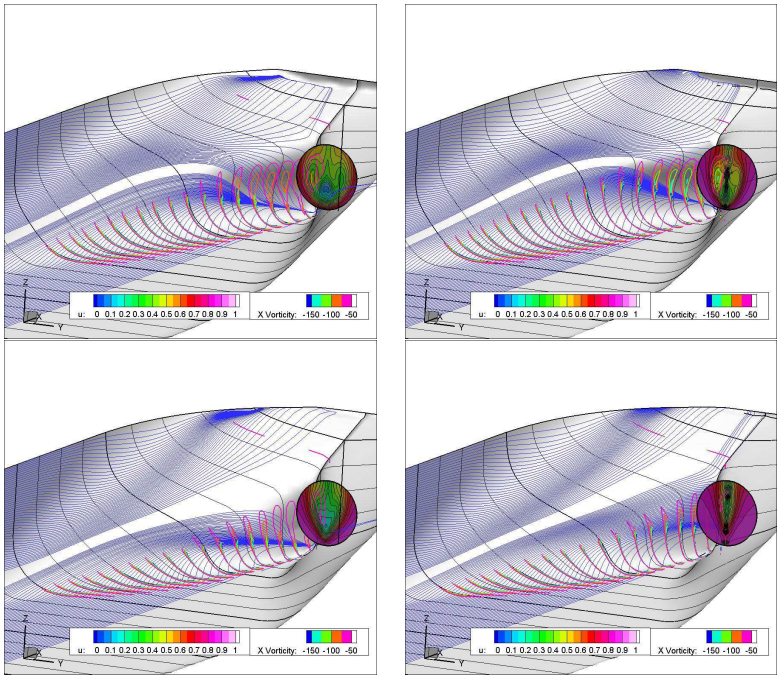

Fig. 5 Limiting Streamlines and Axial Vorticity Distribution for 82BC
(Left Side: Model Scale, Right Side: Full Scale, Top: U-type Lines, Bottom: V-type Lines)

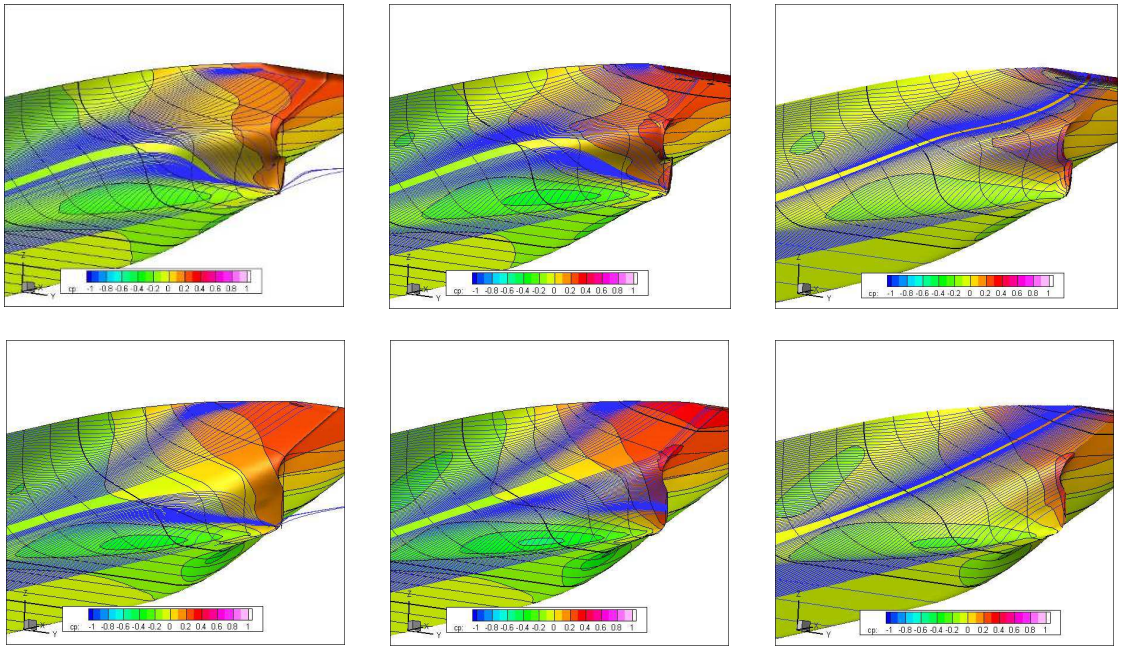

Fig. 6 Pressure Distributions and Limiting Streamlines for 82BC (Left: Model Scale, Middle: Full Scale, Right: Potential flow, Top: U-type Lines, Bottom: V-type Lines)

Towards Fluid-Structure Interaction Simulations in a Finite-Volume Flow Solution Method

Sietse Jongsma *[1] and Jaap Windt[2]

[1]MARIN Academy, Wageningen, The Netherlands
[2]MARIN, Wageningen, The Netherlands

1 Introduction

When CFD simulations are performed, objects embedded in the flow are often considered rigid. In some cases however, this assumption is not valid and the interaction between the fluid and the structure should be taken into account. The aim of this research is, to develop such a method.

This paper starts by presenting the planned approach, describing the required steps. Subsequently, the current status of the implementation is discussed. Then a test case is described, which is a general benchmark for fluid-structure interaction (FSI), and the results obtained using the present method will be shown. Finally, some concluding remarks and directions for future research will be given.

2 Objective and approach

The objective of the present research is to extend the capabilities of an in-house flow solution method to be able to perform fluid-structure interaction simulations. It was decided to follow the partitioned approach, which means that the fluid and solid-problem will be solved independently. Hence, for modelling and discretisation of the structural part of the problem, an external finite-element solver will be used. For the interface between the fluid and the structure, non-conforming meshes should be allowed. This means a disjoint discretisation of the fluid-structure interface, such that the method is sufficiently flexibile for general application.

In the present implementation, conforming meshes are used; a non-conforming mesh method will be implemented in the near future. An important aspect of the present research is the temporal coupling algorithm, an essential ingredient of a partitioned approach. In the first place, this algorithm must be robust. Moreover, since fluid-structure interaction problems often have an unsteady nature, the coupling algorithm should be efficient too. In the remainder of this paper the most important aspects of the fluid-structure interaction method will be explained.

2.1 Flow solution method

The starting point for the present research is to use ReFRESCO for solving the flow equations. ReFRESCO is a viscous-flow solution method that simulates multiphase unsteady flows modelled by the Navier-Stokes equations for incompressible flow, complemented with turbulence models, cavitation models and volume-fraction transport equations for different phases [9]. The equations are discretised using a finite-volume approach with cell-centred collocated variables, in strong-conservation form, and a pressure-correction equation — based on the SIMPLE algorithm — is used to ensure mass conservation [4]. Time integration is performed implicitly with first or second-order backward schemes. At each implicit time step, the non-linear system for velocity and pressure is linearised with Picard's method and either a segregated or coupled approach is used. In the latter case, the coupled system of linear equations is solved with a matrix-free Krylov subspace method, using a SIMPLE-type preconditioner. A segregated approach is always adopted for the solution of all other transport equations. The implementation is face-based, which permits grids with elements consisting of an arbitrary number of faces and hanging nodes. State-of-the-art CFD features such as: sliding interfaces, moving and deforming grids, as well as automatic grid refinement [10, 11] are available. For turbulence modelling, RANS/URANS, SAS and DES approaches can be used.

*e-mail: s.h.jongsma@academy.marin.nl

2.2 Structural model

For fluid-structure interaction simulations, a coupling must be realised between the flow solution method and a method for modelling a deformable object and solving the corresponding equations of motion. The structure deforms due to forces exerted by the fluid. Methods based on a finite-element discretization of the structure are typically used for this purpose. In the present research, structures are modelled using a linear elastic material model. The discretisation of the structure is done in ANSYS Mechanical, from which the corresponding mass and stiffness matrix — denoted by $\underline{\underline{M}}$ and $\underline{\underline{K}}$, respectively — are exported. Subsequently, this data is imported in the flow solution method and used for solving the equations of motion for the deformable object.

2.3 Grid deformation

The flow solution method uses body fitted grids. So, when the body deforms, the volume grid has to be modified too. For this purpose, two different grid deformation methods have been implemented in ReFRESCO, i.e. the inverse distance weighting method [12] and the radial basis function interpolation method [2, 7]. Either of them can be used for deforming the field grid of the flow domain, such that the discretised flow domain matches the shape of the deformed object.

2.4 Partitioned approach

To limit the influence on the existing solution algorithms for the flow equations, the choice has been made to use a partitioned approach [5] for solving the fluid-structure interaction problem. This approach has the advantage that the existing solution method for the flow equations does not need to be changed. Moreover, it satisfies the requirement of permitting to use a different discretisation for the fluid and the structural part of the domain. Typically, an accurate discretisation of the structure requires a coarser grid than what is required for accurately resolving the flow.

3 Present implementation

3.1 Strong coupling

Because the fluid is modelled in ReFRESCO as incompressible and the choice was made to employ a partitioned approach for the fluid-structure interaction coupling, special care must be taken for the coupling [13]. In order to create a robust algorithm, a so-called strongly-coupled approach is adopted in the present research. With the strongly-coupled approach the solution for both the flow and the structural domain are exchanged multiple times per time step, until a converged solution has been obtained. For a so-called loosely-coupled or staggered approach the coupling is performed only once per time step. Especially for incompressible flows the latter approach can present serious stability issues [1, 3]. Therefore, the choice has been made to adopt the former approach.

The flow chart in figure 1 depicts the solution procedure for a single time step. First, the forces — denoted by $\boldsymbol{F}$ — acting on the object are computed. These forces can comprise of forces that are exerted by the flow — due to pressure and shear stress — but also external forces, such as gravity. Subsequently, the equations of motion for the deformable object are solved. The solution is used to compute an update for the vertices of the CFD grid at the fluid-structure interface. The deformation of the interface is then transferred to the internal vertices of the field grid, by means of the grid deformation method. Next, an update for the flow solution is computed. This whole procedure is repeated, until the convergence criteria for the flow solution method have been met. In that case the solution method can proceed to the next time step.

3.2 Time integration equations of motion

For the integration of the equations of motion in time, the Newmark integration scheme [6] is used, which reads

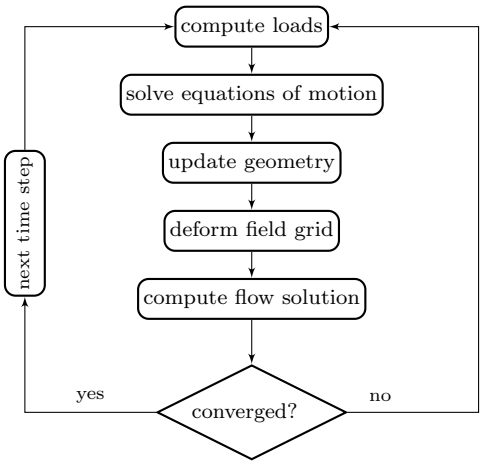

Figure 1: Flow chart for a time step of the fluid-structure interaction simulation.

Table 1: Properties for the fluid-structure interaction test case.

property	value	
$\mathrm{Re_D}$	200	
$\rho_\mathsf{s}/\rho_\mathsf{f}$	1	
E	5.6	MPa
ν	0.40	
$\bar{t}$	0.02	m
D	0.10	m
H	0.41	m
L	0.35	m

$$\left(\frac{1}{\alpha\Delta t^2}\underline{\underline{M}} + \underline{\underline{K}}\right)\boldsymbol{u}^{\mathrm{n}+1} = \boldsymbol{F}^{\mathrm{n}+1} + \underline{\underline{M}}\left(\frac{1}{\alpha\Delta t^2}\boldsymbol{u}^{\mathrm{n}} + \frac{1}{\alpha\Delta t}\dot{\boldsymbol{u}}^{\mathrm{n}} + \left[\frac{1}{2\alpha} - 1\right]\ddot{\boldsymbol{u}}^{\mathrm{n}}\right), \tag{1}$$

where $\boldsymbol{u}^{\mathrm{n}}$ is the vector of displacements of the vertices of the structural grid with respect to the initial shape $\boldsymbol{x}^0$, for time level n, Δt is the time increment, and α is an integration parameter. Vectors $\dot{\boldsymbol{u}}$ and $\ddot{\boldsymbol{u}}$ denote the corresponding displacement velocity and acceleration, respectively. Using the displacement computed for the next time level, the acceleration is subsequently computed:

$$\ddot{\boldsymbol{u}}^{\mathrm{n}+1} = \frac{1}{\alpha\Delta t^2}\left(\boldsymbol{u}^{\mathrm{n}+1} - \boldsymbol{u}^{\mathrm{n}}\right) - \frac{1}{\alpha\Delta t}\dot{\boldsymbol{u}}^{\mathrm{n}} - \left[\frac{1}{2\alpha} - 1\right]\ddot{\boldsymbol{u}}^{\mathrm{n}}. \tag{2}$$

The acceleration can then be used to compute the displacement velocity:

$$\dot{\boldsymbol{u}}^{\mathrm{n}+1} = \dot{\boldsymbol{u}}^{\mathrm{n}} + \Delta t\left[1 - \delta\right]\ddot{\boldsymbol{u}}^{\mathrm{n}} + \delta\Delta t\ddot{\boldsymbol{u}}^{\mathrm{n}+1}, \tag{3}$$

where δ is a different integration parameter. For the integration parameters, the following values are used: $\alpha = \frac{1}{4}$ and $\delta = \frac{1}{2}$, for which the Newmark integration scheme is second-order accurate.

3.3 Update of interface vertices

The present implementation is limited to handling point matching configurations only. With this approach, no interpolation is required to transfer the displacement of the vertices of the finite-element mesh to the vertices at the fluid-structure interface of the grid for the flow domain. The displacement of these interface vertices is based on the solution of the equations of motion. For light constructions — relative to the density of the fluid — however, this solution cannot be directly applied, for stability reasons. In that case, under-relaxation of the interface vertices is applied to achieve a stable algorithm, with a fixed under-relaxation factor $0 \leq \theta \leq 1$:

$$\boldsymbol{x}_{\mathrm{i}+1}^{\mathrm{n}+1} = \boldsymbol{x}_{\mathrm{i}}^{\mathrm{n}+1} + \theta\left(\boldsymbol{x}^0 + \boldsymbol{u}_{\mathrm{i}+1}^{\mathrm{n}+1} - \boldsymbol{x}_{\mathrm{i}}^{\mathrm{n}+1}\right). \tag{4}$$

In this equation subscript i denotes the iteration of the iterative procedure inside a time step. Moreover, for the initial value $\boldsymbol{x}_0^{\mathrm{n}+1}$ the shape of the interface for the present time step is used, i.e. $\boldsymbol{x}_0^{\mathrm{n}+1} = \boldsymbol{x}^{\mathrm{n}}$. Note, that the displacement is specified with respect to the initial geometry at $t = 0$, which is permitted because a linear material model is used.

4 Test case

To check the implementation of the fluid-structure interaction simulation method, a benchmark test case has been chosen. Before this FSI test was considered, the structural part was verified by computing the periodic oscillation of a beam in a vacuum clapped on one side, subject to a uniform distributed load. The FSI test case concerns the laminar flow through a 2D channel. A rigid circular cylinder of diameter $D = 0.10$ m with a flexible flap — of length $L = 0.35$ m, thickness $\bar{t} = 2.0$ cm, Young's modulus $E = 5.6 \cdot 10^6$ Pa and Poisson ratio $\nu = 0.40$ — attached to its downstream side has been placed inside the channel, with its centre at $(x, y) = (0.20, 0.20)$. A graphical representation of the flow domain is depicted

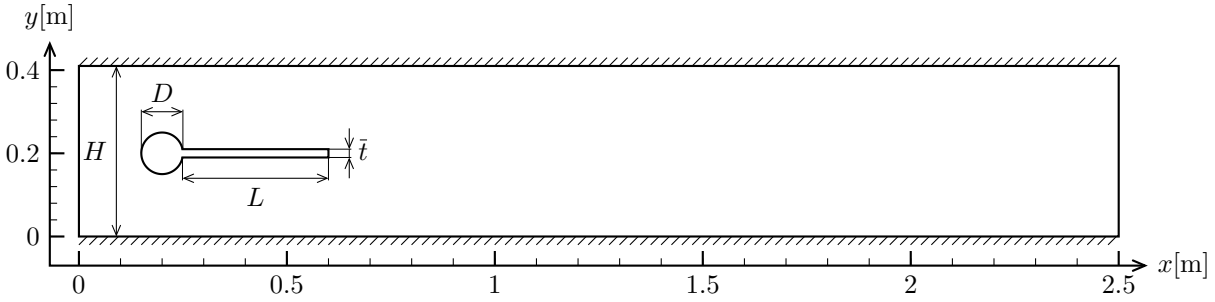

Figure 2: Flow domain used for the fluid-structure interaction test case.

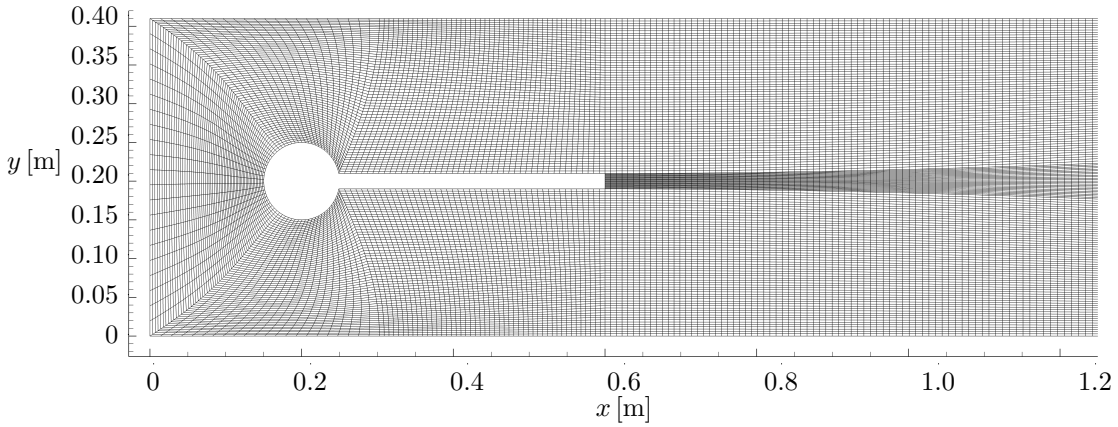

Figure 3: Part of the grid used for the fluid-structure interaction simulation.

in figure 2. Note, that the positioning of the object in the channel is intentionally non-symmetric. The original description of this test case has been given by Turek [8]. Table 1 lists the relevant properties for this test case. Note, that the Reynolds number is based on the mean inflow velocity $\overline{U}$.

4.1 Boundary and initial conditions

At the inflow boundary the velocity is prescribed by means of a parabolic velocity profile for the flow in the x-direction, i.e.

$$v_{\mathrm{x}}(y,0) = \frac{6\overline{U}y}{H^2}(H-y), \tag{5}$$

where H is the height of the channel. At the outflow boundary the pressure is prescribed, which is equal to zero. At the bottom and top wall of the channel, as well as at the object in the channel, a no-slip boundary condition is imposed.

Initially, the flow is at rest and the static pressure is zero. During the first two seconds of the simulation, the prescribed inflow velocity is increased to its full magnitude, using a smooth start-up function, defined by

$$v_{\mathrm{x}}(y,t) = \begin{cases} v_{\mathrm{x}}(y,0)\,\frac{1-\cos\left(\frac{\pi}{2}t\right)}{2} & \text{if } t \leq 2, \\ v_{\mathrm{x}}(y,0) & \text{otherwise.} \end{cases} \tag{6}$$

4.2 Discretisation

For the discretisation of the flow domain a multi-block structured grid, depicted in figure 3, has been used consisting of 38 667 hexahedral control-volumes — the number of cells in the third direction is equal to 1. For the flexible beam the discretisation is uniform in both x and y-direction using 47×24 8-node quadrilateral solid elements, respectively, resulting in a total of 1 128 elements. For the discretisation in time, a time increment of $2.5 \cdot 10^{-3}$ s is used.

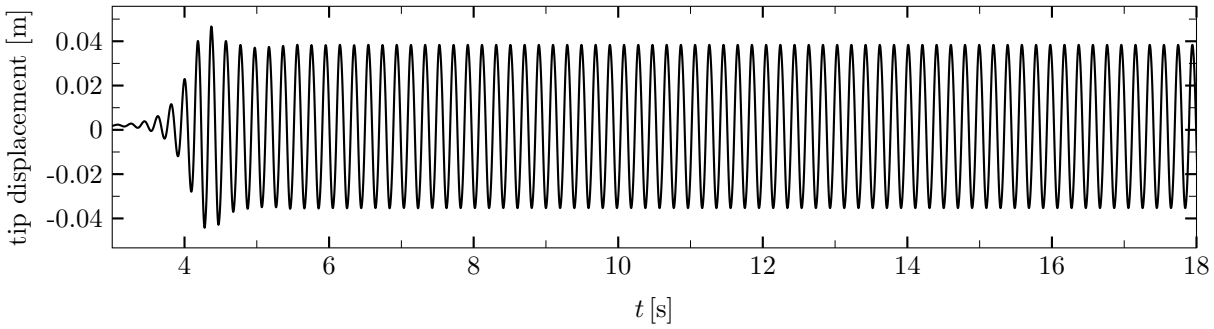

Figure 4: Vertical tip displacement as a function of time.

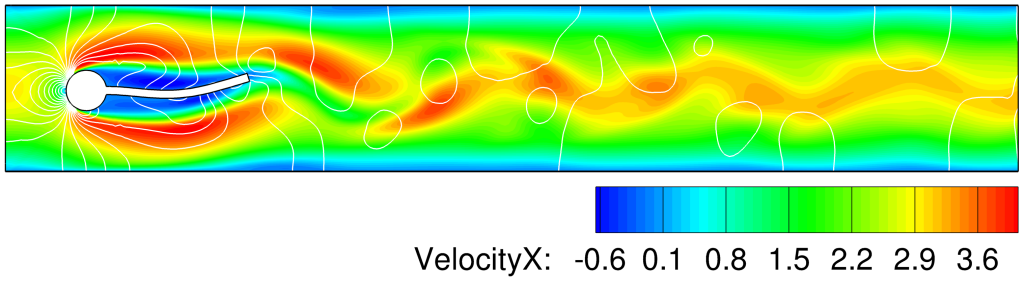

Figure 5: Snap-shot of the flow solution at $t = 7.5425$ s. The white lines represent iso-pressure contours.

4.3 Preliminary results

Figure 4 shows the displacement of the centre of the end of the flap in y-direction as a function of time. A snap-shot of the flow solution is depicted in figure 5. Table 2 presents a number of quantities, that have been computed based on these results, together with the ones presented in the literature [8]. The results for the present implementation are already in reasonable agreement with the results from the literature. The most notable difference is in the amplitude and mean of the displacement in x-direction. The considerably smaller magnitude is probably caused by the destructive interference of a second deformation mode, as can be observed for the time evolution depicted in figure 6. Results from the literature do not show the presence of a second harmonic function in the displacement in the x-direction. Other differences in the results can stem from the difference in the material model used; for the reference result a non-linear material model was used. Moreover, the discretisation in both time and space for the present results is coarse compared to those used for the reference results. A proper verification study will be done in the future.

5 Concluding remarks

A method for the simulation of fluid-structure interaction phenomena has been presented. The results of a test case have been shown to illustrate the capabilities of the present implementation. One of these capabilities is that it can handle configurations with a density ratio of one. Moreover, the preliminary results show reasonable agreement with the results presented in the literature.

Future work includes extending the method to allow for non-matching discretisations at the fluid-structure interface, such that an arbitrary discretisation can be used for both the fluid domain and the structural part. Moreover, coupling strategies will be investigated, that are both more robust as well as have better convergence properties than the fixed under-relaxation method presently implemented. Furthermore, the sensitivity of the coupling method regarding the density ratio is subject to further investigation. Also a more

Table 2: Displacement of the tip of the flap for the fluid-structure interaction test case.

quantity	present result		reference result	
x-direction				
mean	$-6.40 \cdot 10^{-5}$	m	$-2.69 \cdot 10^{-3}$	m
amplitude	$1.175 \cdot 10^{-4}$	m	$1.48 \cdot 10^{-3}$	m
frequency	$1.015 \cdot 10^{1}$	Hz	$1.09 \cdot 10^{1}$	Hz
y-direction				
mean	$1.526 \cdot 10^{-3}$	m	$1.48 \cdot 10^{-3}$	m
amplitude	$3.685 \cdot 10^{-2}$	m	$3.438 \cdot 10^{-2}$	m
frequency	5.089	Hz	5.3	Hz

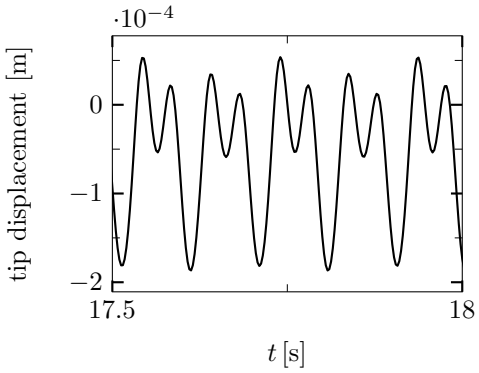

Figure 6: Horizontal displacement of the tip of the deformable flap as a function of time.

thorough comparison should be made of the results of the test case with results from different numerical methods applied to the same test case. Validation and verification of the method is also an important matter to be considered.

References

[1] Causin, P., Gerbeau, J., and Nobile, F. Added-mass effect in the design of partitioned algorithms for fluidstructure problems. *Computer Methods in Applied Mechanics and Engineering 194*, 42-44 (2005), 4506–4527.

[2] de Boer, A., Schoot, M. S., and Bijl, H. Mesh deformation based on radial basis function interpolation. *Computers & Structures 85* (2007), 784–795.

[3] Förster, C., Wall, W. A., and Ramm, E. Artificial added mass instabilities in sequential staggered coupling of nonlinear structures and incompressible viscous flows. *Computer Methods in Applied Mechanics and Engineering 196*, 7 (2007), 1278–1293.

[4] Klaij, C. M., and Vuik, C. SIMPLE-type preconditioners for cell-centered, colocated finite volume discretization of incompressible Reynolds-averaged Navier-Stokes equations. *International Journal for Numerical Methods in Fluids 71*, 7 (2013), 830–849.

[5] Matthies, H. G., and Steindorf, J. Partitioned strong coupling algorithms for fluid-structure interaction. *Computers & Structures 81*, 8-11 (2003), 805–812.

[6] Newmark, N. M. A Method of Computation for Structural Dynamics. *Journal of the Engineering Mechanics 85* (1959), 67–94.

[7] Rendall, T. C. S., and Allen, C. B. Efficient mesh motion using radial basis functions with data reduction algorithms. *Journal of Computational Physics 228* (2009), 6231–6249.

[8] Turek, S., and Hron, J. Proposal for numerical benchmarking of fluid-structure interaction between an elastic object and laminar incompressible flow. In *Fluid-Structure Interaction - Modelling, Simulation, Optimization* (2006), H. Bungartz and M. Schäfer, Eds., no. 53 in Lecture Notes in Computational Science and Engineering, Springer, pp. 371–385.

[9] Vaz, G., Jaouen, F., and Hoekstra, M. Free-Surface Viscous Flow Computations: Validation of URANS Code FreSCo. In *OMAE Conference, Honolulu* (2009), no. OMAE2009-79398.

[10] Windt, J. Adaptive Mesh Refinement in Viscous Flow Solvers: Refinement in the Near-wall Region, Implementation and Verification. In *16th Numerical Towing Tank Symposium (NuTTS), Müllheim, Germany* (2013), pp. 171–176.

[11] Windt, J., and Klaij, C. M. Adaptive Mesh Refinement In MARIN's Viscous Flow Solver ReFRESCO: Implementation And Application To Steady Flow. In *IV International Conference on Computational Methods in Marine Engineering (ECCOMAS MARINE), Lisbon, Portugal* (2011).

[12] Witteveen, J. A. S., and Bijl, H. Explicit and Robust Inverse Distance Weighting Mesh Deformation for CFD. In *19th AIAA Computational Fluid Dynamics Conference, San Antonio, TX* (2009).

[13] Wood, C., Gil, A., Hassan, O., and Bonet, J. Partitioned block-Gauss-Seidel coupling for dynamic fluid-structure interaction. *Computers & Structures 88*, 23-24 (2010), 1367–1382.

Helideck Analysis of an FPSO

Kavyashree Kalaskar, CD-adapco, London, UK
kavyashree.kalaskar@cd-adapco.com

Introduction

Helicopter landing on ships or offshore platforms is one of the most challenging tasks which presents severe unsteady flow field and requires precision tasking under confined spaces. This puts immense pressure on pilots to operate the aircraft safely and efficiently. CAP437 [1], the Standards for Offshore Helicopter Landing areas, provides guidelines for the design criteria of the helidecks to define safe operating boundaries.

This paper will investigate the helideck environment around a full scale Floating Production Storage and Offloading vessel (FPSO) using transient simulations to capture the flow field around it. Different turbulence models will be investigated against CAP437 [1] criteria to establish an effective method that is efficient in terms of time, computational resources and accuracy.

Objective and Scope of Work

It is suggested in CAP437 [1], that any helideck platform that is under the influence of environmental effects i.e. turbulence from superstructure, exhaust gases etc. should be subjected to appropriate wind tunnel testing or CFD analysis, to establish the wind environment around the helideck. According to the guidelines, a limit on the standard deviation of the vertical airflow velocity of 1.75 m/s should not be exceeded. It is suggested that the helicopter and ship operators should be informed at the earliest of any wind conditions for which this criteria is not met.

So far in the industry, wind tunnel tests are mainly used to perform such calculations. However, these results have their own drawbacks due to scaling effects and extrapolation techniques used. Hence, this paper looks at a possibility of using full scale Computational Fluid Dynamics (CFD) to calculate the turbulence levels on the helideck.

Methodology

The analysis was done in ship scale to eliminate any scaling errors. A 3D CAD model of the ship is provided in Figure 1. The flow of air around the vessel was simulated using the commercial CFD software STAR-CCM+ [2].

An overview of the computational domain is provided in Figure 2. The rectangular domain extended one ship length upwind from the bow and two ship lengths downstream of the vessel. The upstream boundary, as well as the sides and the top, were set as inlet boundaries. The downstream boundary was set as a pressure outlet and the bottom of the domain as a no-slip wall.

The simulation was run at a tail wind condition of 20 knots for stationary vessel condition. This wind condition was specifically chosen, as at tail wind, the freestream has the largest interaction with the superstructure thereby affecting the

flow field downstream on the helideck region.

The computational domain was discretised using a trimmed-cell mesh, comprising of hexahedron cells aligned with the direction of the nominal flow. This way, the mesh-induced numerical diffusion is kept to a minimum. Prism layers with wall y+ between $30 < y+ < 100$ were used on all wall boundaries, to capture the boundary layer flow. The region around the helideck and the deckhouse were further refined to capture the turbulence accurately. Figure 3 shows a view of the mesh of the entire domain and the refinement areas on the helideck.

For all the ship scale simulations, a stable atmospheric boundary layer (ABL) flow was established. The ABL was modelled using the logarithmic law [2] for sheared inflow, turbulence kinetic energy and turbulence dissipation.

The applied turbulence models are discussed in the results section of the paper. The turbulence on the helideck was monitored by using line probes at 5m, 10m and 15m height above the landing pad in both lateral and longitudinal directions as shown in Figure 4. The standard deviations of the vertical velocity was calculated at each point on the probe and measured against the CAP437 criteria of 1.75 m/s.

Results and Discussion

In order to establish a well-suited physics model for this type of problems, different turbulence models were tested to resolve the turbulence over the helideck.

Two methods were particularly investigated in this study -

1. Unsteady Reynolds Averaged Navier Stokes (URANS) with SST (Mentor) K-Omega turbulence model, and
2. Detached Eddy Simulation (DES) with SST (Mentor) K-Omega detached eddy model.

The Standard Shear Transport Mentor (SST) model was chosen as this model blends the K-Epsilon model in the far field with the K-Omega model near the wall. Three grid sizes of 2.5 mil, 5 mil and 7.5 mil were set up to compare the mesh dependency of the solution.

The results were monitored on line probes shown in Figure 4.

Comparison of drag

The first step in the study was a comparison of the drag or the resistance generated from the superstructure of the vessel.

Figure 5 shows the comparison of drag between the URANS model and the DES model for three mesh sizes. It can be seen that in all the cases, DES and URANS predicts similar resistance values with percentage differences less than 1.5%.

This confirmed that both the cases are set up correctly and the mean values are predicted accurately in the flow stream.

Comparison of Vertical Velocity

The vertical velocity for the URANS calculations were calculated by extracting the fluctuating velocities from turbulent kinetic energy. The standard deviation of these fluctuating velocities were calculated over a period of 50 sec of real time data. Similarly, for DES, time data statistics were accumulated for a period of 50 sec and the standard deviation of vertical velocity was calculated.

Figure 6 and Figure 7 shows comparison of standard deviation of vertical velocity for URANS and DES run at 7.5 mil cells. The results are shown in the lateral (Y) and longitudinal (X) direction respectively at a height of 5m and 10m above the helideck.

From the first glance itself, it is very clear that the URANS is predicting a lot lower values of velocities when compared to the DES. This trend is seen in all the cases and the percentage difference in velocities is more than 50%. The URANS model gives a time averaged result of the flow field. Because of this, the vertical velocities that are seen are of lower magnitude denoting mean values and not representing the realistic flow situation. In DES, the turbulent eddies over the helideck region are resolved with greater accuracy and hence the fluctuating velocities are captured precisely. The scalar plots in Figure 8 shows the differences between URANS and DES models, where it can be seen that URANS shows a smooth flow over the deck whereas DES shows a lot of small turbulent eddies dispersed on the helideck region.

The height of 5m above the helideck is considered to be the most crucial one as the helicopter is very close to the landing pad. It can be seen that at this height, the limit of 1.75 m/s is exceeded in some zones over the helideck on the lateral probe in Figure 6. In such cases, it is important to make the captain and the pilot aware of the data.

This shows that how important is the choice of turbulence models. URANS on one hand predicted results that were all below the safety limit whereas in DES, it was seen that the turbulence levels exceeded the limit in some zones.

The location of these exceedances match with the location of the exhaust funnel in the superstructure. The small vortices that develop from the exhaust funnels combine with the vortices dispersed from the central mast which further develop and disperse on the helideck. This is shown in a top view image in Figure 9.

Grid Independence

Three meshes were tested in the study - 2.5mil, 5mil and 7.5mil. The comparison of the three meshes is shown in Figure 10 for DES runs. The plot shows the standard deviation of vertical velocity at 5m height above the helideck.

It can be seen here that similar results are obtained for the three meshes. All the three cases predict velocities very close to each other. It is difficult to conclude at this stage as to which mesh is the optimum, as this requires detailed study of each point and the differences between them. However, this shows that with a well-designed mesh, and application of DES model, accurate results could be achieved even with a mesh size of 2.5 mil as these compare well with the case of 7.5 mil cells. Since, the solution does not change drastically between the two grid sizes, any mesh size between 2.5 mil cells and 7.5 mil cells will generate similar results.

Alternative solution of RSM

Due to the higher expense (min 20-30%) of using DES, an alternative option of URANS with Reynolds Stress Turbulence Model (RSM) was investigated. The RSM model was set up with Elliptic Blending as this is a hybrid model which blends the near wall and far field flows.

A comparison plot of standard deviation of vertical velocity is shown in Figure 11 for a case of 2.5 million cells. It can be seen here that the RSM model predicts velocities

similar to URANS k-omega model. This shows that RSM model cannot resolve the same level of turbulence as DES.

Even though the flow is solved in an anisotropic manner, the RANS solver still averages the fluctuating velocities and hence under predicts the turbulence levels in the flow field.

Conclusions

To summarise, a helideck analysis was conducted on an FPSO by applying different turbulence models and the following are the main conclusions from the study -

- Unsteady RANS with K-Omega SST model does not predict the turbulence well enough as the fluctuating velocities are time averaged and hence generate lower velocities.
- DES was able to predict the fluctuating velocities with much greater accuracy and was able to identify the zones where the velocities were exceeding the acceptable limits.
- If the mesh is correctly set up with precise refinements, then DES could predict accurate enough results on a coarser grid as seen in Figure 9.
- Unsteady RANS with RSM did not capture the same fluctuating velocities as DES. Even though RSM is solving a lot more equations and is anisotropic, RANS solver time averages the velocities thereby reducing the magnitude of fluctuations.
- It was also found from a practical stand point that DES is more robust and stable to run when compared with RSM. RSM requires a high quality mesh and can be prone to instabilities.

It can be concluded from the above study that in order to capture heavy turbulence flow fields such as helideck etc., a higher fidelity model is required. For such simulations, DES has shown to be the best option combining accurate results within reasonable timescales.

References

1. CAP 437, Standards for Offshore Helicopter Landing Areas, www.caa.co.uk
2. Star-CCM+ v10.04.011, www.cd-adapco.com

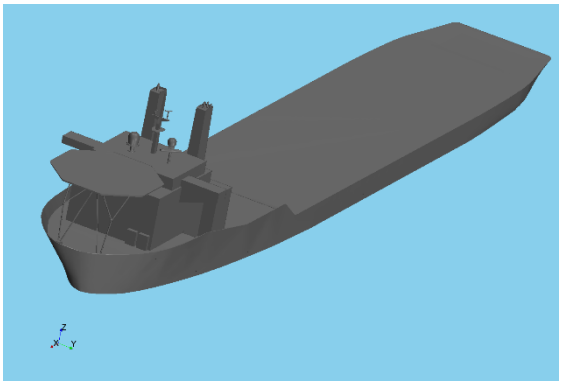

Figure 1: 3D model of the FPSO

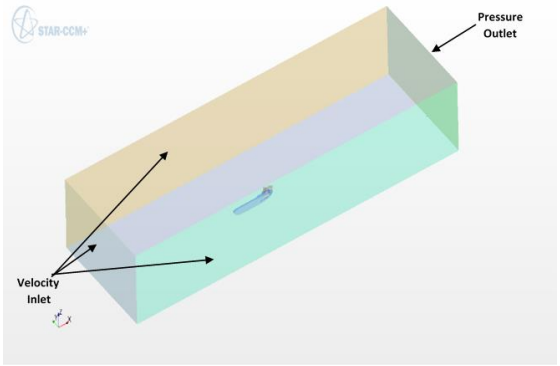

Figure 2: Domain around the vessel

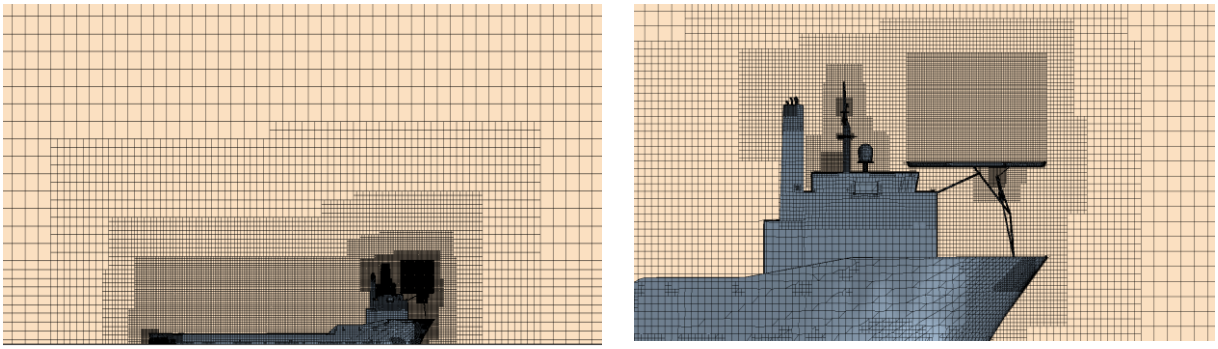

Figure 3: Trimmer mesh set up for the model with refinement around helideck region

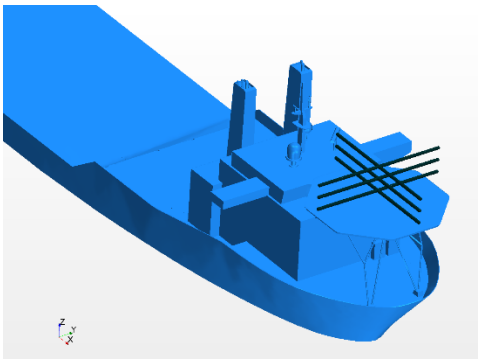

Figure 4: Line probes placed on the helideck

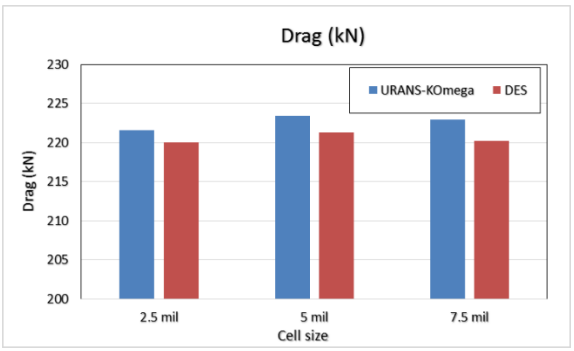

Figure 5: Drag from superstructure for URANS and DES

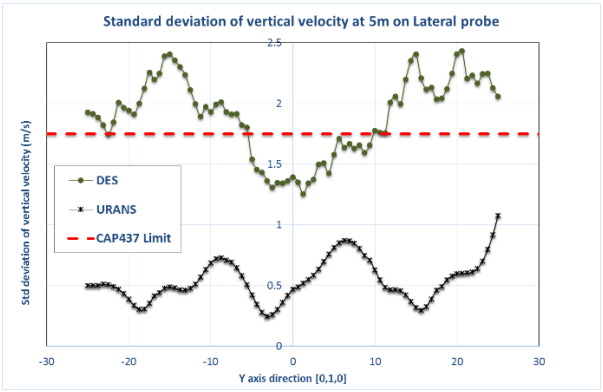

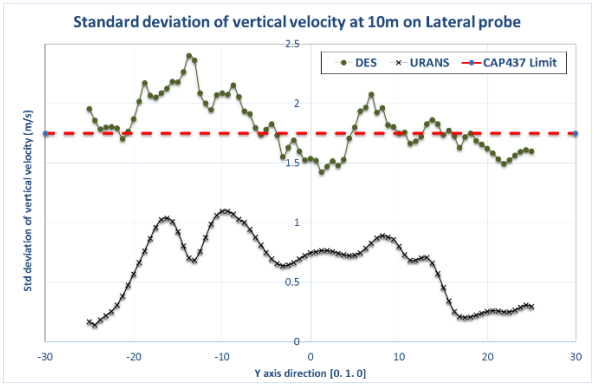

Figure 6: Standard deviation of vertical velocity on Lateral probe at 5m (left) and 10m (right) height above helideck

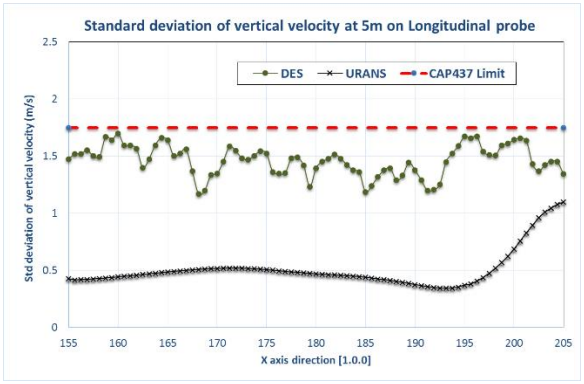

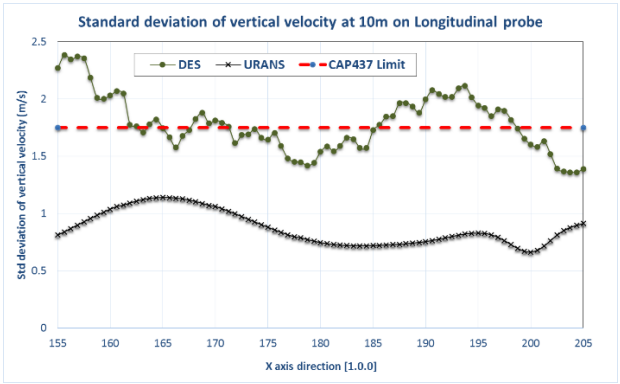

Figure 7: Standard deviation of vertical velocity on Longitudinal probe at 5m (left) and 10m (right) height above helideck

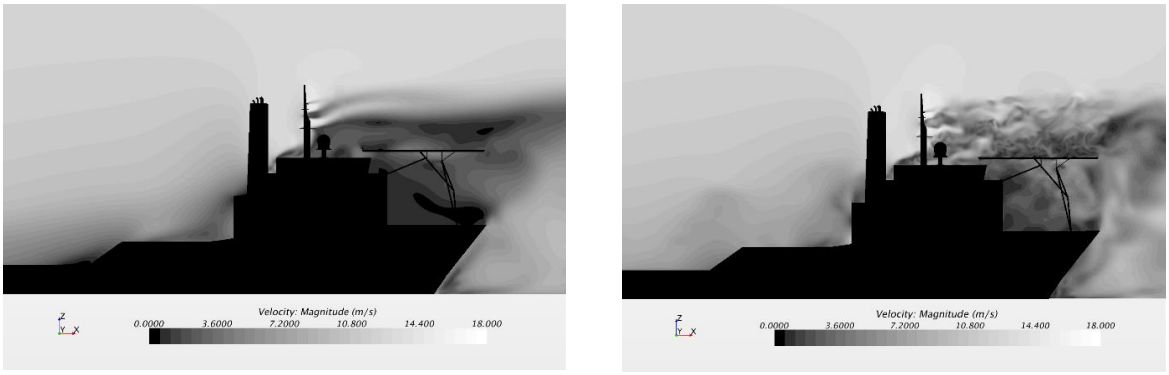

Figure 8: Velocity Magnitude from URANS (left) and DES (right) above the helideck

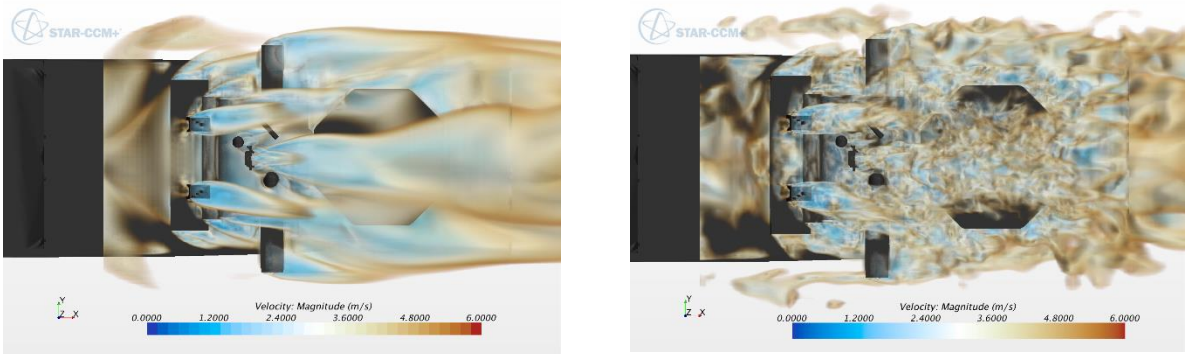

Figure 9: Flow interaction with the exhaust funnel for URANS (left) and DES (right)

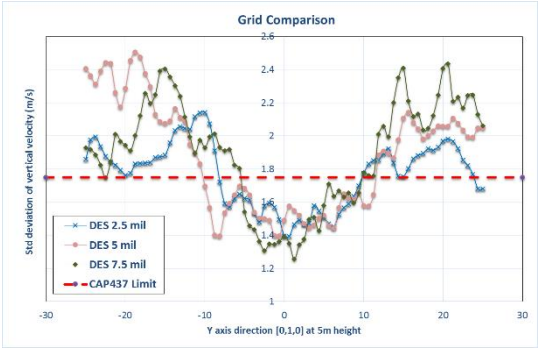

Figure 10: Grid Independence study for DES at 2.5mil, 5mil and 7.5mil mesh sizes

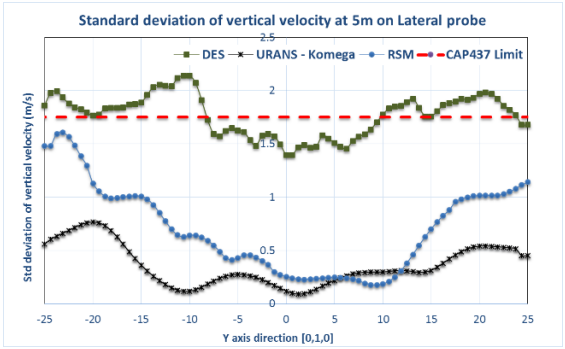

Figure 11: Comparison of DES, URANS K-Omega and RSM model for standard deviation of vertical velocity

Computational Simulations of Vortex-Induced Vibrations Using URANS

Omer Kemal Kinaci, Yildiz Technical University, Istanbul/Turkey, kinaci@yildiz.edu.tr

NOMENCLATURE

a	acceleration of the cylinder	m	oscillating mass
A	amplitude	m_a	added mass
c	mechanical damping	t	time step
D	diameter of the cylinder	U	velocity of the cylinder
$f_{n,a}$	natural frequency in air	U_{fs}	free-stream velocity of the fluid
f^*	non-dimensional frequency	U^*	reduced velocity
F	fluid force	y	displacement
k	spring stiffness		

1. Introduction

Vortex-induced vibrations are highly nonlinear and hard to numerically solve with conventional CFD approaches. The fluid-structure interaction between the oscillating cylinder and the fluid around it involves the vibration equation besides the Navier-Stokes Equations which increases the complexity of the flow. The numerical approaches are fragile and very sensitive to the implemented grid in the fluid domain. Due to the nature of the vortex-induced vibrations, dynamic meshing should be used; and the implementation of the dynamic mesh increases the computation time significantly as well as it usually obstructs the iterative convergence.

In this study, a computational approach implementing URANS is presented. This study is limited to the vortex-induced-vibrations of rigid circular cylinders on elastic supports. The cylinder is restricted to oscillate transversely to the fluid flow in a two-dimensional environment. Two-dimensional flow assumption allows fast computations and gives quantitative notion about the dynamics of the flow. The mathematical model is validated with a benchmark experimental study and the obtained results are evaluated accordingly.

2. Mathematical Approach

The vibration equation of a cylinder attached with springs subjected to a steady fluid flow is given as;

$$m\ddot{y} + c\dot{y} + ky = F \tag{1}$$

This is the forced oscillation equation. The left hand side deals with the vibration while the right hand side deals with the force applied to the cylinder by the fluid.

Leaving the acceleration term $\ddot{y}$ alone, equation (1) becomes;

$$\ddot{y} = \frac{F - c\dot{y} - ky}{m} \tag{2}$$

When the acceleration of the cylinder is known, its velocity and displacement can be calculated by;

$$\int dy = \int \dot{y}\, dt = \iint \ddot{y}\, dtdt \tag{3}$$

Rewriting equation (3) in a numerical sense;

$$y_{t+1} = y_t + U_{t+1} \cdot \Delta t \tag{4}$$
$$U_{t+1} = U_t + a_{t+1} \cdot \Delta t \tag{5}$$

The displacement of the cylinder in VIV can therefore be given as;

$$y_{t+1} = y_t + U_t \Delta t + a_{t+1} \cdot (\Delta t)^2 \tag{6}$$

a_{t+1} in equation (6) is calculated from equation (2). So writing it in numerical form;

$$a_{t+1} = a_t + \frac{F_{t+1} - cU_t - ky_t}{m} \tag{7}$$

Returning back to equation (6) and rewriting the numerical displacement equation will read;

$$y_{t+1} = y_t + U_t \Delta t + (a_t + \frac{F_{t+1} - cU_t - ky_t}{m}) \cdot (\Delta t)^2 \tag{8}$$

Equation (8) gives the displacement of the cylinder at each time step. The force F, applied by the fluid will commence the oscillatory movement of the cylinder. The cylinder is assumed to be at the origin ($y = 0$) and stable at $t = 0$. The initial conditions in mathematical terms are;

$$y_0 = U_0 = a_0 = 0 \tag{9}$$

Just after the flow starts, the displacement of the cylinder will therefore be;

$$y_1 = y_0 + U_0 \Delta t + \left(a_0 + \frac{F_1 - cU_0 - ky_0}{m}\right) \cdot (\Delta t)^2 = \left(\frac{F_1}{m}\right) \cdot (\Delta t)^2 \tag{10}$$

VIV involves a two-way fluid structure interaction (FSI) problem. At each time step, the flow around the cylinder is solved to find the vertical lift force acting on it *as if it is not moving*. This force is then used to find the new displacement at the next time step. This is the first part of the FSI. As the cylinder moves, it also moves the fluid nearby. Therefore, the flow also gets affected by the cylinder's movement. This is the second part of the FSI. So the cylinder gets excited by the fluid and in return, the flow is affected by the cylinder's movement. This will alter the applied fluid force but it must be indicated here that the change in this force F is not visible in equation (8). F is completely solved by the Navier-Stokes Equations and it is used to find the new displacement in equation (8). To identify how the fluid force F is affected by the movement of the cylinder, the Navier-Stokes Equations have to be written down.

The pressure distribution along the cylinder can be calculated from the Navier-Stokes Equations and in two-dimensional form they are given as;

$$\frac{\partial p}{\partial x} = \mu\left(\frac{\partial^2 u}{\partial x^2} + \frac{\partial^2 u}{\partial y^2}\right) - \rho\left(\frac{\partial u}{\partial t} + u\frac{\partial u}{\partial x} + v\frac{\partial u}{\partial y}\right) \tag{11}$$
$$\frac{\partial p}{\partial y} = \mu\left(\frac{\partial^2 v}{\partial x^2} + \frac{\partial^2 v}{\partial y^2}\right) - \rho\left(\frac{\partial v}{\partial t} + u\frac{\partial v}{\partial x} + v\frac{\partial v}{\partial y}\right) \tag{12}$$

Here, x and y denote the Cartesian coordinate system axes. When the cylinder moves in a direction, the horizontal and vertical velocities u and v in the fluid domain also change. This results in a different pressure distribution and so a different fluid force F on the cylinder. The cylinder has one degree-of-freedom and therefore in this work, the vertical lift force F is calculated by;

$$\int dF = \int pdy \tag{13}$$

3. Numerical Implementation

The numerical solution to VIV in this paper is based on Finite Volume Method (FVM) implementing URANS as the solution approach. Structured grid in the near-cylinder and wake regions is implemented to return better contours around the cylinder. Quadrilateral elements are used near the cylinder and triangular elements are preferred for the outer domain. Near-cylinder region is meshed with an O-grid type of meshing. The grid in the whole fluid domain and a close-up view in the near-cylinder region are provided in figure 1.

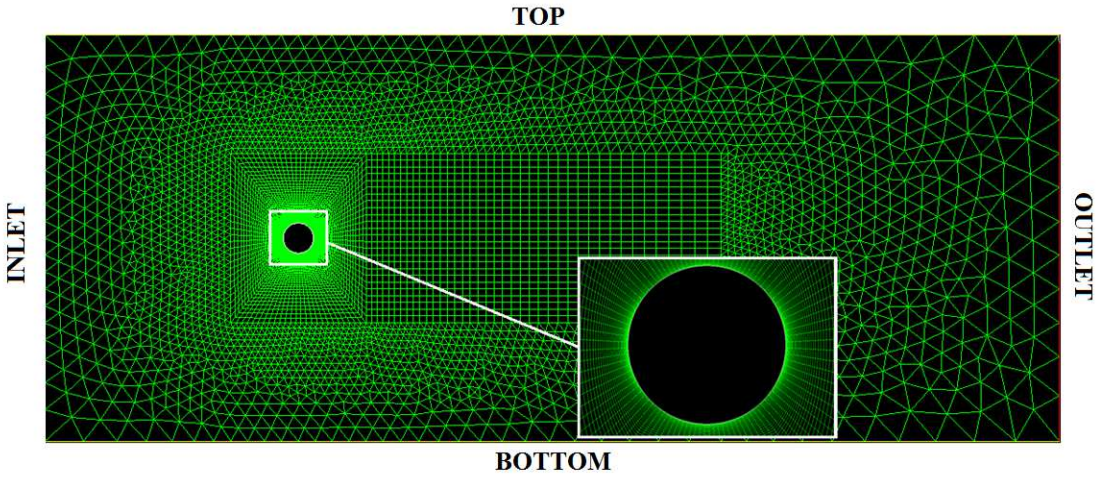

Figure 1. The mesh structure in the fluid domain.

Table 1 gives the boundary conditions. The *velocity inlet* boundary condition is selected for the inlet because it allows imposing the fluid velocity directly. The top and bottom of the fluid domain is selected to be a *symmetry* plane to allow the cylinder to move in the flow without any boundary layer effects.

Table 1. Boundary conditions.

INLET	Velocity Inlet
OUTLET	Pressure Outlet
TOP	Symmetry
BOTTOM	Symmetry
CYLINDER	Wall

The grids in the near region of the cylinder and its wake are moving with the cylinder and these elements are not deforming. On the other hand, the outer region is fixed in space but the elements are allowed to deform to permit re-meshing when the cylinder is moving up and down in the fluid.

The $k-\omega\ SST$ turbulence model is selected to solve for the flow around the cylinder in oscillation. $k-\omega\ SST$ uses the standard $k-\omega$ model inside the boundary layer and switches to the $k-\varepsilon$ model in the outer region (Menter, 1994). This turbulence model is especially useful to solve for the flow around bluff bodies where adverse pressure gradients are high. Separation of the boundary layer is

accurately calculated by this turbulence model as stated by (Wilcox, 2008) which is a key point to accurately simulate the flow.

There are a couple of researchers who used $k-\omega\ SST$ turbulence model to solve vortex-induced vibration problems. The closest papers to this study are authored by (Pan et al., 2007) and (Guilmineau and Queutey, 2002). They both validated their computational approaches by the experimental results of (Khalak and Williamson, 1996). The results computationally obtained in this study is also compared with their experimental benchmark study and it is presented in the next section.

4. Results

The CFD results implementing $k-\omega\ SST$ turbulence model of URANS approach are compared with the experiments of (Khalak and Williamson, 1996). The comparison is given in figure 2 along with the results obtained by other researchers in the field, using the same turbulence model. The results are obtained by starting the cylinder from rest at each reduced velocity. The reduced velocity, U^* and the non-dimensional frequency, f^* in figure 2, is calculated as:

$$U^* = \frac{U_{fs}}{f_{n,a} \cdot D} \tag{14}$$

$$f^* = \frac{f_{osc}}{f_{n,a}} \tag{15}$$

where $f_{n,a}$ is

$$f_{n,a} = \frac{1}{2\pi}\sqrt{\frac{k}{m}} \tag{16}$$

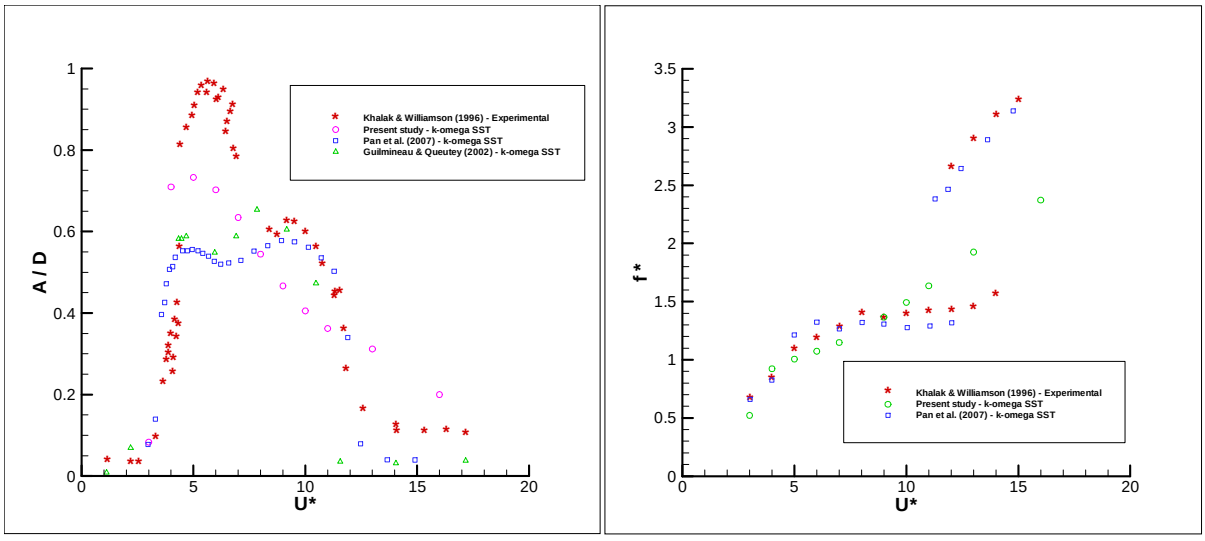

Figure 2. Comparison of computational results with the experiments. Amplitude response (left), frequency response (right).

The initial branch of the amplitude response of the cylinder is captured accurately in all computational results when compared with the experiments. The upper branch which is around $5 < U^* < 7$ in the experiments is partially captured in this study when compared with the other computational results. (Pan et al., 2007) and (Guilmineau and Queutey, 2002) were unable to capture the upper branch. How-

ever, the transition to de-snychronization regime from the lower branch which is after $U^* > 11$ is somewhat shadowy with the implemented approach in this paper. The other computational results more accurately reveal this transition.

The problem in the transition to de-synchronization regime can also be seen from the frequency response obtained in the present study. There is an intermittency in the experimental results which is also captured by (Pan et al., 2007). This sudden jump of amplitude and frequency response obtained experimentally could not be captured in this work. The transition from VIV to galloping is also a problematic issue in numerical solutions to fluid-induced motions. Similar problems were also encountered by (Wu et al., 2014) and (Kinaci et al., 2015).

5. Conclusions

URANS is a powerful tool to understand fluid-induced motions and can return fast and accurate results when used correctly. Quantitative data for practical purposes like the amplitude and frequency responses of the cylinders can be obtained quickly. In this paper, the author's approach to solve for the vortex-induced vibrations of rigid circular cylinders is presented. The obtained results are compared with the results from the literature and satisfactory accordance is found with the experiments overall. In comparison with some other researchers' results; the upper branch response of VIV is partially captured but on the other hand, the transition to de-synchronization from the lower branch was inadequately represented. Along with the other results from the literature, the intermittency in the experimental results between the upper and lower branches was not seen in computational results either. The effects of grid structure, time step size, turbulence model and three dimensionality of the flow may be some of the factors that might be playing an important role in capturing these VIV-specific phenomena and will be investigated in the following papers.

Acknowledgments

The financial support of The Scientific and Technological Research Council of Turkey (TUBITAK) is gratefully acknowledged.

References

Guilmineau, E., & Queutey, P. (2002). A numerical simulation of vortex shedding from an oscillating circular cylinder. *Journal of Fluids and Structures*, 773-794.

Khalak, A., & Williamson, C. (1996). Dynamics of a hydroelastic cylinder with very low mass and damping. *Journal of Fluids and Structures*, 455-472.

Kinaci, O. K., Lakka, S., Sun, H., & Bernitsas, M. M. (2015). Computational and experimental assessment of turbulence stimulation on flow induced motion o circular cylinder. ASME *34th International Conference on Ocean, Offshore and Arctic Engineering*. Canada.

Menter, F. (1994). Two-equation eddy-viscosity turbulence models for engineering applications. *AIAA Journal*, 1598-1605.

Pan, Z., Cui, W., & Miao, Q. (2007). Numerical simulation of vortex-induced vibration of a circular cylinder at low mass-damping using RANS code. *Journal of Fluids and Structures*, 23-37.

Wilcox, D. (2008). Formulation of the k-ω turbulence model revisited. *AIAA Journal*, 2823-2838.

Wu, W., Bernitsas, M. M., & Maki, K. (2014). RANS simulation versus experiments of flow induced motion of circular cylinder with passive turbulence control at 35,000<Re<130,000. *Journal of Offhsore Mechanics and Arctic Engineering*, 041802.

Importance of the Free Surface for the Drift-Induced Forces on a Ship-Like Foil

Jarle Andre Kramer, Sverre Steen,
Norwegian University of Science and Technology (NTNU), Trondheim/Norway,
jarle.a.kramer@ntnu.no

1 Introduction

A ship or a boat that uses sails for propulsion will experience some amount of side force, in addition to thrust, from the sails. The ship hull must balance this side force in order to have a steady traveling direction. For a normal ship hull, this happens by traveling with a drift angle. The drift angle makes the hull and potential appendages on the hull, a lifting surface, where the "lift" is the side force. As with all lifting surfaces, the lift also creates lift induced drag. In order to evaluate a specific hull design, in a context where the ship is supposed to have sails, the drift-induced effects on the global forces must be determined. The amount of drift angle necessary in order to balance the side forces, as well as how much added resistance this drift angle creates are of interest. Many configurations must be tested in a design process and it is therefore beneficial to optimize the simulation process in regards to time as much as possible. A ship hull traveling with a drift angle is a highly viscous phenomenon, and viscous Computational Fluid Dynamics (CFD) is the only practical way to simulate this case. However, CFD comes in many forms. Steady state Reynolds-averaged Navier Stokes (RANS) based CFD without free surface modeling is considerably faster than CFD with free surface modeling. As an example, the steady state simulations performed in this case could converge after just 20 minutes, while the same case took an entire day (24 hours) with free surface modeling, on the same computer. This is because free surface modeling needs an unsteady approach, and more mesh cells. The unsteady approach is necessary in order to let the waves develop around the hull and more mesh cells is necessary in order to discretize the air above the free surface. It is natural to think that the free surface could have an effect on the drift-induced forces on a ship. A deformed free surface does affect the velocity and pressure, and ventilation is known to reduce transverse forces [4]. However, as neglecting the free surface would be convenient, the following hypothesis will be explored

Free surface effects are not important for the global drift induced forces on a ship.

This is not to say that the free surface is not important for the global forces, as wave resistance is a well-known phenomenon. The hypothesis is rather that the wave resistance is independent of drift angle, and that the drift induced resistance as well as the drift induced lift, is independent of the free surface. This would obviously be true if the Froude number is low enough, as low Froude number means no free surface deformation. It also seems unreasonable to assume that this hypothesis can be true for any Froude number, or any geometry. The question is whether it is true for normal Froude numbers and ship geometries. If this is the case, one could find the wave resistance with one free surface simulation, and then find the drift induced effects with steady state, double body, simulation. Even if this hypothesis is not perfectly true, it could be a convenient strategy to make rough estimations of the performance of sailing ships. Reference [8] suggest that this hypothesis could be true. There, a flat plate with a drift angle is studied numericaly, and the side force is seen to vary very little for Froude number below 1. The same tendency can be seen by inspecting the experimental results from reference [6]. In this paper, the ship "Series 60" is towed in a towing tank with several drift angles, and Froude numbers.

2 Test case

In order to see the effect of the free surface, a ship like geometry has been simulated with, and without free surface. Three factors have been varied, based on the assumption that they could have an importance for the results:

- Drift angle (α). The angles 0, 2.5, 5 and 10 degrees have been tested. These angles should cover normal sailing drift angles [3].
- Froude number (Fr). Fr equal to 0.2, 0.25 and 0.3 have been tested. These Froude numbers are large enough that wave resistance is important, and within the range of normal Froude numbers for cargo ships. For instance, a 100 m long ship, traveling at 15 knots would have Fr = 0.246
- Depth to length ratio, or aspect ratio (Asp). A deep ship will have more of its body far beneath the free surface, and the global forces might therefore be more independent of the free surface than a shallow ship. Depth to length ratios of 0.05 and 0.1 have been tested. For comparison, the KVLCC2 tanker has a depth to length ratio of 0.064, while the KCS container ship has a depth to length ratio of 0.047.

As the depth of the ship is a variable in this test case, a special geometry have been chosen. Rather than using a ship geometry, a modified symmetrical foil geometry have been used. The foil is representing a ship, with the special property of having straight sides, such that the water plane shape does not change when the depth changes. This geometry is also currently being used for CFD validation experiments at NTNU (too be published later). The foil shape is called "Eppler E386", and the shape can be downloaded from reference [1]. The thickness of the foil is scaled up to 16%, in order to be closer to typical ship length to width ratios. The original thickness of the foil is 12.6%. The simulation is done in model scale, where the length of the model is 4.4 m. The rest of the geometry can be seen in figure 1

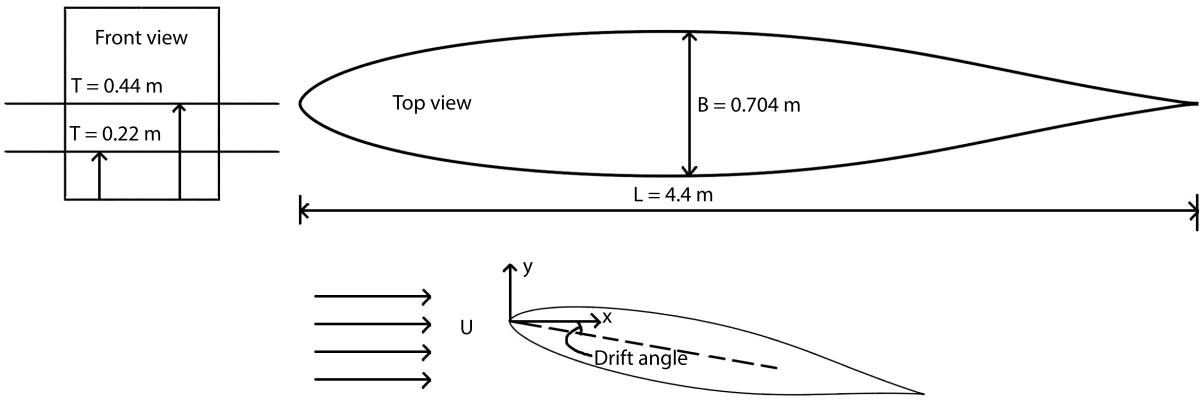

Figure 1: Shape, dimensions and coordinate system of the tested geometry. The Foil shape is "Eppler E386", with scaled up thickness to 16%

The result from the simulations will be presented as coefficients. The representative area of the foil (A) is chosen to be length multiplied by depth of the model ($A = L \cdot T$), rather than the wetted surface. The coordinate system has the x-axis pointed along the ship axis when the drift angle is zero, as is illustrated in figure 1. The drift induced drag coefficient (C_{Di}) is the important drag coefficient, as only the drift induced effects are of interest. The coefficients are defined as follows:

$$C_L = \frac{F_y}{0.5\rho A U^2} \tag{1}$$

$$C_D = \frac{F_x}{0.5\rho A U^2} \tag{2}$$

$$C_{Di}(\alpha, Fr) = C_D(\alpha, Fr) - C_D(\alpha = 0, Fr) \tag{3}$$

3 Numerical Setup

All of the simulations presented in this paper is done with the open source CFD software "OpenFOAM" [2]. Two different setups are used: one for the free surface simulations, and one for the steady state, double body simulations. As the point of this study is to quantify the difference between the two simulation strategies, the setups are kept as similar as possible.

3.1 Solvers

Two solvers are used: "simpleFoam" for the steady state simulations without free surface, and "interFoam" for the free surface simulations. simpleFoam is a steady state solver, that is using the SIMPLE algorithm [9] to find a steady state solution. interFoam is using the PISO algorithm [5] to do time marching, with the opportunity to do additional iterations on each time step with the SIMPLE algorithm. interFoam simulates the free surface between water and air by using the Volume of Fluid (VOF) method. The same spatial numerical discretisation schemes is used for the two different simulation cases. The convective term of the Navier-Stokes equation was done with a linear upwind scheme, while all the other terms were done using linear central difference. The k-ω SST turbulence model [7] were used, together with wall functions.

3.2 Boundary conditions

The inlet velocity is kept constant and equal to 1.642 m/s for all the simulations. The kinematic viscosity (ν) is equal to 1.19e-6, giving a Reynolds number equal to 6071261. The velocity was kept constant in order to eliminate changes in the results due to Reynolds number effects. In order to change the Froude number when the velocity is a constant, the acceleration of gravity was changed. For Froude numbers equal to 0.2, 0.25 and 0.3, the acceleration of gravity was set to 15.32 m/s^2, 9.81 m/s^2 and 6.81 m/s^2 respectively. The turbulent quantities k and ω at the inlet was calculated based on the following equations:

$$k = \frac{3}{2}(I \cdot U)^2 \tag{4}$$

$$\omega = \frac{k}{\nu}\frac{\mu_t}{\mu}^{-1} \tag{5}$$

I is the turbulent intensity, set equal to 0.01, and $\frac{\mu_t}{\mu}$ is the turbulent viscosity ratio, set equal to 1.

The boundary condition used at the water plane in the steady state simulation setup was symmetry plane.

3.3 Mesh and time step

The OpenFOAM mesh generators "blockMesh" and "snappyHexMesh" was used to create the mesh. The mesh was refined close to the ship walls, as well as in the expected kelvin wave wake. Since wall functions were used, the average y+ values were set to be around 30. The cell length closest to the ship hull was set to 0.002 m. The mesh cells in the refined wake had an approximate cell length of 0.03125 m. For the free surface simulation setup, a custom "free surface refinement tool" was used to generate anisotropic refinements close to the free surface. This was done in order to keep the height of the cells small, which allows the VOF method to capture an almost sharp free surface. The height of the cells in the free surface area was equal to 0.0039 m. This was the only difference between the mesh designs for the double body setup and the free surface setup. Although the refined wave wake is probably unnecessary for the double body case, it was kept in order to avoid differences due to discretization. An overview of the mesh design can be seen in figure 2

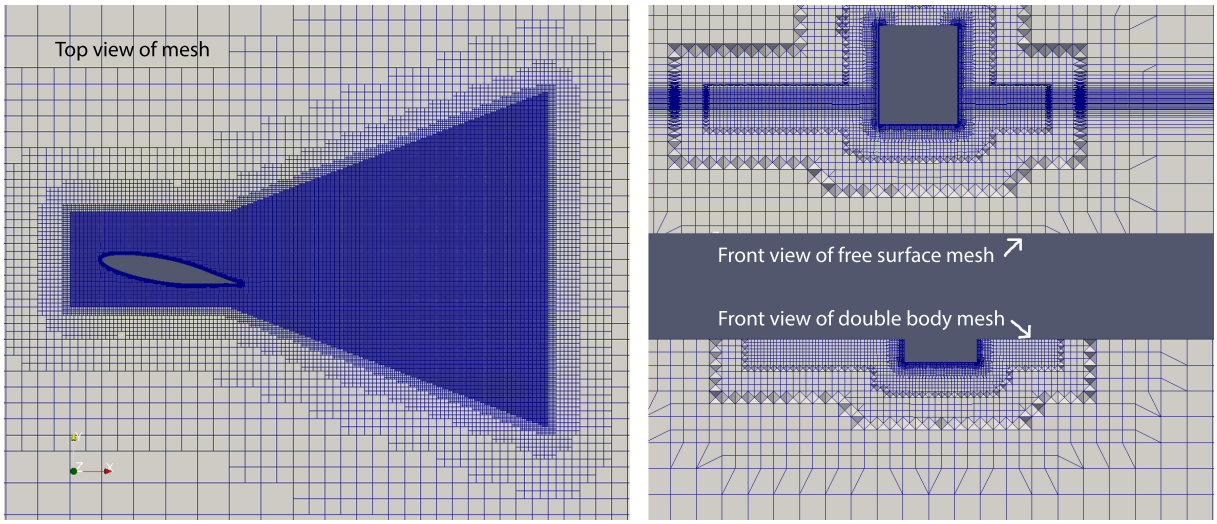

Figure 2: Overview of the mesh design used for the simulations. Foil angle for this mesh is 10 degrees.

The mesh described above was the mesh used for the final result. A coarser and finer version of the above mesh design was also tested in order to check for mesh independence. This was done using the double body simulation setup. A factor of two was used to adjust the cell local lengths in the mesh design. The result from this mesh test can be seen in table 1

Table 1: Result from mesh resolution test

Mesh name	coarse	medium	fine
background mesh cell length	2	1	0.5
finest level cell length	0.00781	0.00391	0.00195
number of cells	542508	1756011	5823685
Lift coefficient, C_L	1.336E-1	1.359E-1	1.357E-1
Drag coefficient, C_D	4.692E-2	4.744E-2	4.666E-2

For the free surface simulations, the time step is an important parameter. Several simulations with varying time step have been done. The result can be seen in figure 3. The chosen time step for the simulations was 0.005 s.

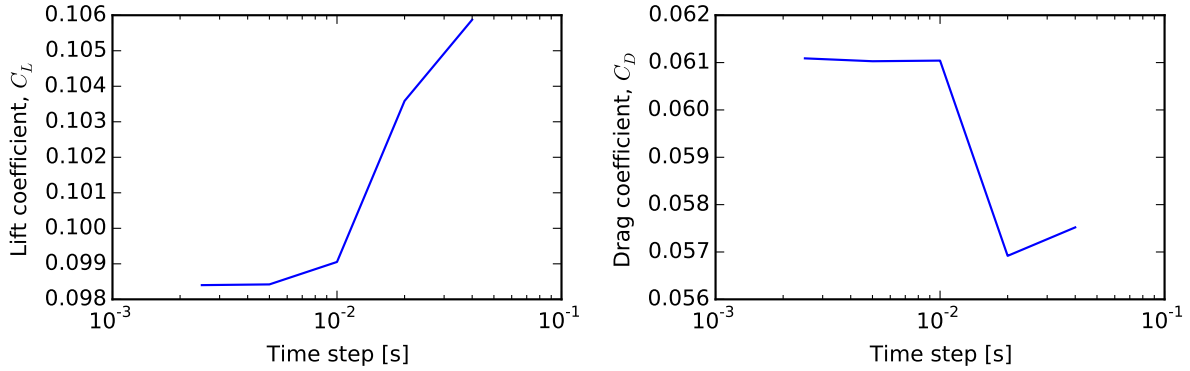

Figure 3: Effect of varying the time step on the resulting forces

4 Results

Plots of the result from the CFD simulations can be seen in figure 4 and 5. The lines connecting the dots for the lift coefficients are "least squared" fitted second order polynomials. Second order polynomials are used due to the possibility of non linear cross flow lift. The lines connecting the dots for the drag coefficients are fourth order polynomials, as lift induced drag is generally proportional to the lift squared. The free surface simulations are assumed to give the correct value, and the values at drift angle = 10 degrees are compared with each other. The maximum error in the lift from the steady state simulations happens for Fr = 0.3 and Asp = 0.1, where the error is 5.8%. For Asp = 0.05, the maximum error is for Fr = 0.25, where the error is 2.4%. For the drift induced drag the error is largest for Fr = 0.25 for both aspect ratios. For Asp = 0.1, the error is 9.9%, while for Asp = 0.05, the error is 7.6%.

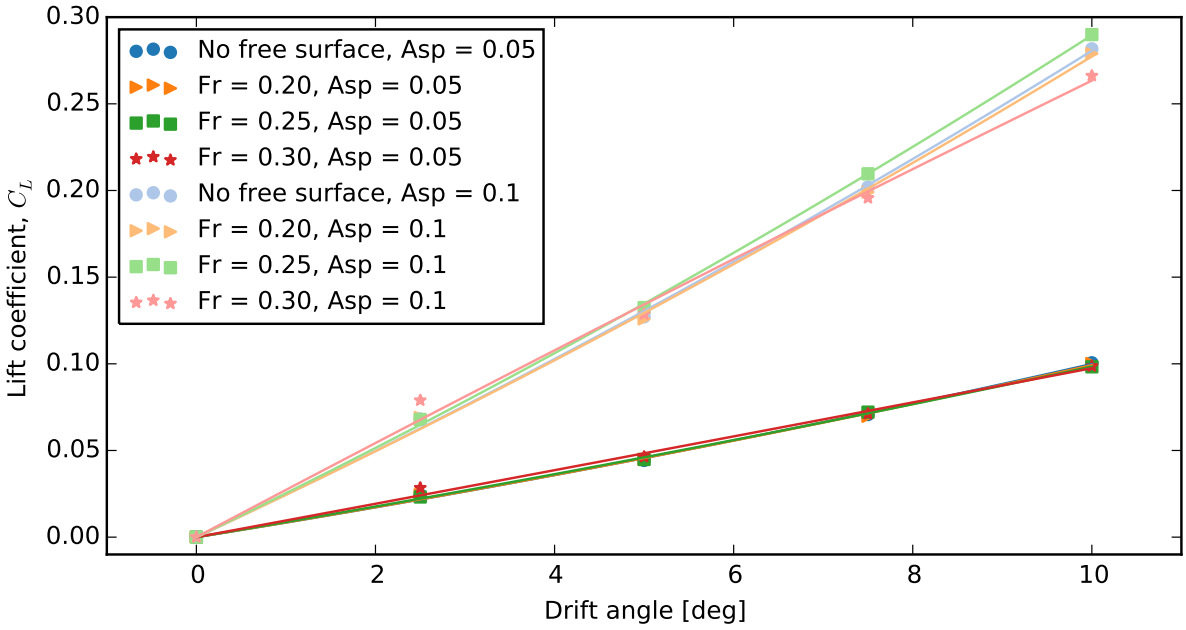

Figure 4: Lift coefficient calculated for different Froude numbers and aspect ratios

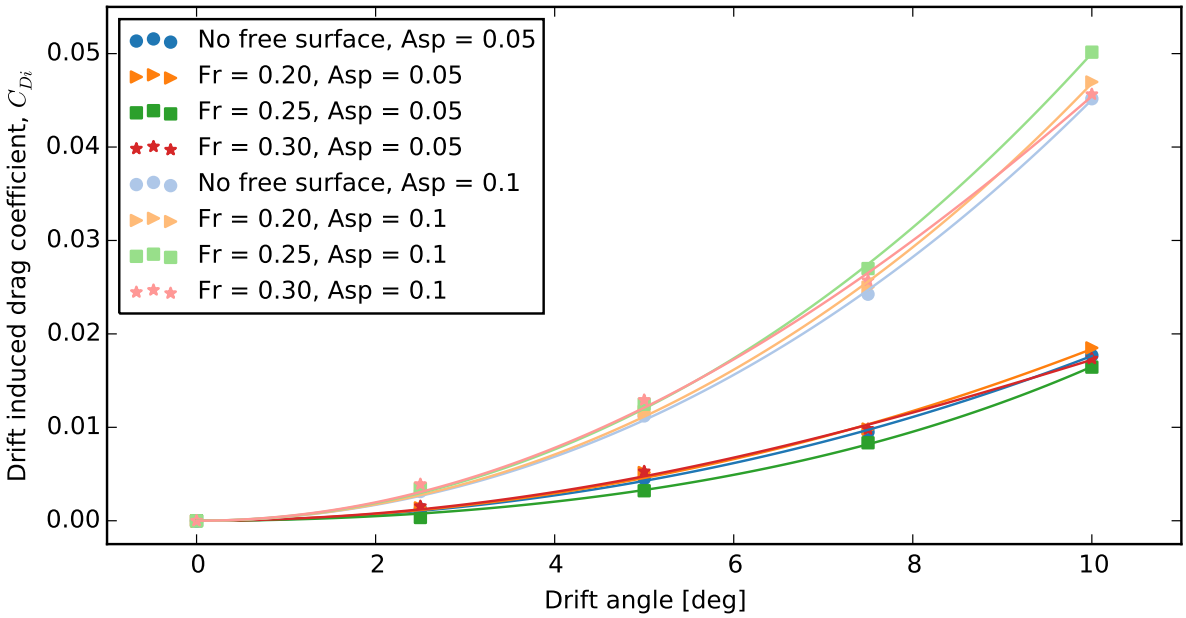

Figure 5: Drift induced drag coefficient calculated for different Froude numbers and aspect ratios

5 Conclusion

The free surface does have an effect on the forces, but the largest error in the drift induced effects is below 10%, and for most of the cases, the error is below 5%. Depending on the situation, this could be a small enough error, and steady state double body simulations could be a viable simulation strategy. It is also interesting to note that there is no general trend in the error. It is not so that Fr = 0.3 always gives a larger error than the smaller Froude numbers, and the error for Asp = 0.1 seems to be larger than the errors for Asp = 0.05. The results from the steady state simulations are between the free surface simulations, and not always above or below. That is, there does not seem to be a general direction of the error. The result from a simulation that neglects the free surface can be both too large and too low. The error could also be numerical in nature, and some of the "scatter" could result from this. Although it might not always be appropriate to neglect the effect of the free surface completely, it does seem that the effect is secondary. This simulation strategy could for instance be appropriate if one is interested in evaluating a new design of a ship hull, for instance in an optimization process. The exact values of the forces might not matter, but the difference between the old and the new design is important.

References

[1] Airfoiltools.com, eppler e836 hydrofoil airfoil. `http://airfoiltools.com/airfoil/details?airfoil=e836-il`.

[2] The openfoam foundation. `http://www.openfoam.org`.

[3] Juan Baader. *The sailing yacht*. Adlard Coles Nautical, 1979.

[4] Odd M Faltinsen. *Hydrodynamics of high-speed marine vehicles*. Cambridge university press, 2005.

[5] Raad I Issa. Solution of the implicitly discretised fluid flow equations by operator-splitting. *Journal of computational physics*, 62(1):40–65, 1986.

[6] J Longo and F Stern. Effects of drift angle on model ship flow. *Experiments in fluids*, 32(5):558–569, 2002.

[7] Florian R Menter. Two-equation eddy-viscosity turbulence models for engineering applications. *AIAA journal*, 32(8):1598–1605, 1994.

[8] Babak Ommani and Odd M Faltinsen. Viscous and potential forces on an advancing surface-piercing flat plate with a fixed drift angle. *Journal of Marine Science and Technology*, pages 1–14, 2014.

[9] Suhas Patankar. *Numerical heat transfer and fluid flow*. CRC Press, 1980.

Implementation of the Ffowcs Williams - Hawkings Equations into OpenFOAM for Hydro-Acoustic Ship Evaluation

Christian Krüger, Nikolai Kornev

Chair of Modeling and Simulation
University of Rostock, 18059 Rostock, Germany

christian.krueger@uni-rostock.de

Notation

A_S	amplitude of sphere pulsation
B	denotes the ships breadth
C_B	block coefficient of the ship
C_F	viscous friction coefficient
C_P	pressure resistance coefficient
C_R	total resistance coefficient
c	sound speed in quiescent medium
d_P	propeller diameter
d_S	distance between sphere center and free-surface Θ
$F = 0$	$[f(y,\tau)]_{ret} = f(y, t - r/c)$
Fn	Froude number
f_S	frequency of sphere pulsation
$f = 0$	function that describes the ships surface
g	$\tau - t + r/c$
L_{PP}	denotes the length between perpendiculars of the ship
l_i	components of local force intensity, that acts on the fluid $l_i = P_{ij} n_j$
l_r	$l_i \hat{r}_i$
$\dot{l}_r$	$\dot{l}_i \hat{r}_i$
M	magnitude of local Mach number vector of source
M_r	Mach number of source in radiation direction, $M_i \hat{r}_i$
N	number of event horizons, $r_\Delta/(ct_\Delta)$
m	density relation at the free-surface, ρ_1/ρ
n	sound speed relation at the free-surface, c/c_1
P_{ij}	compressive stress tensor
p'	acoustic pressure, $p - p_0$ in undisturbed medium; $c^2 - \rho'$ in FW-H equations
R	reflection coefficient
r	distance between observer and source, $r = \lvert x - y \rvert$
r_Δ	maximum domain extension with respect to the observer
$\hat{r}$	unit vector in the radiation direction, with components $\hat{r}_i$, $\hat{r} = (x - y)/r$
dS	element of the ship surface
T_{ij}	Lighthill stress tensor, $\rho u_i u_j + P_{ij} - c^2 \rho' \delta_{ij}$
T_{rr}	$T_{ij} \hat{r}_i \hat{r}_j$
T	denotes the ships draught
t	observer time
t_{KVLCC2}	thrust deduction number
t_Δ	simulation timestep
u	instantaneous fluid velocity with respect to the observer x
v	local velocity of the surface
v_n	local normal velocity of source surface
$v_{\dot{n}}$	$v_i \dot{\hat{n}}_i$
$\dot{v}_n$	$\dot{v}_i \hat{n}_i$
x	observer position vector, with components x_i
y	source position vector, with components y_i

Greek symbols:

δ_{ij}	Kronecker delta, $\delta_{ij} = 1$ for $i = j$ and otherwise $\delta_{ij} = 0$
Θ	free-surface plane
θ	angle between incident wave and surface normal
ρ_0	density of quiescent medium
ρ'	density perturbation, $\rho - \rho_0$
τ	source time
$d\Omega$	element of surface area of the collapsing sphere $g = 0$

Subscripts:

FS	denotes parameters reflected at the free-surface
ret	quantity is evaluated at the retarded time, $\tau = t - r/c$
0	denotes fluid variable in quiescent medium
1	denotes the outer fluid at the free-surface
obs	denotes the individual observer
L	loading noise component
T	thickness noise component
Q	quadrupole noise component

Introduction

The protection and conservation of marine flora and fauna is in the longtime focus of the public authorities. Tightening regulations for ship emissions, narrowed to sewage disposal and water pollution in the past, start to extend to hydro-acoustic limits for merchant shipping. To fulfill the requirements, arising from those regulations, the ship designer requires robust and efficient methods, that deliver reliable information about the acoustic signature of the projected vessel.
The Computational Aero Acoustic (CAA) contain a wide range of acoustic analogies, that are applicable for ship hydrodynamics. Especially the integral form of Ffowcs Williams - Hawkings (FW-H) equation delivers high potential for moving hull systems with low Mach numbers. Within the FW-H method the hydro-acoustic problem splits into a hydrodynamic and an acoustic part: While the hydrodynamic field is calculated on a typical computational grid, the acoustic sources can be derived directly from the instantaneous flow field. By solving the wave equation for this acoustic field, the acoustic pressure can be calculated for arbitrary observers inside and outside of the numerical domain. Derived in the form of Farassat 1A [1], the FW-H equations read:

$$
\begin{aligned}
4\pi p'_T(x,t) &= \int_{f=0} \left(\frac{\rho_0 \left(\dot{v}_n + v_{\dot{n}} \right)}{r \left(1 - M_r\right)^2} \right)_{ret} dS + \int_{f=0} \left(\frac{\rho_0 v_n (r\dot{M}_r + c(M_r - M^2))}{r^2 \left(1 - M_r\right)^3} \right)_{ret} dS \\
4\pi p'_L(x,t) &= \frac{1}{c} \int_{f=0} \left(\frac{\dot{l}_r}{r \left(1 - M_r\right)^2} \right)_{ret} dS + \int_{f=0} \left(\frac{l_r - l_M}{r^2 \left(1 - M_r\right)^2} \right)_{ret} dS \\
&\quad + \frac{1}{c} \int_{f=0} \left(\frac{l_r (r\dot{M}_r + c(M_r - M^2))}{r^2 \left(1 - M_r\right)^3} \right)_{ret} dS \\
4\pi p'_Q(x,t) &= \frac{1}{c^2} \int_{F>0} \frac{1}{r} \left[\ddot{T}_{rr} \right]_{ret} c d\tau d\Omega + \frac{1}{c} \int_{F>0} \frac{1}{r^2} \left[3\dot{T}_{rr} - \dot{T}_{ii} \right]_{ret} c d\tau d\Omega \\
&\quad + \int_{F>0} \frac{1}{r^3} \left[3T_{rr} - T_{ii} \right]_{ret} c d\tau d\Omega
\end{aligned}
$$

Implementation

The FW-H method was implemented into the OpenFOAM framework in forms of a function-object. This approach supports a solver-independent method, flexible on-the-run adjustments as well as multiple hydro-acoustic evaluations within a single hydrodynamic calculation. The implementation itself is straight forward, as the geometric information and fields used for the calculation of the monopole, dipole and quadrupole source fields are provided by the hydrodynamic solver or can be derived directly. With respect to the turbulence models, it is necessary to provide the Reynolds stress tensor for calculation of quadrupole source field. Alternatively it is possible do restrict the calculation of the Lighthill stress tensor to $T_{ij} = \rho u_i u_j$, as the contribution from the nonlinear source term is comparably small. To take into account the compressibility effects on the sound propagation, a forward-time-stepping approach was implemented: Depending on the simulation time step and sound speed of the considered fluid, the computational domain splits into N_{obs} spherical event horizons for every observer. Integrating the spatially distributed acoustic sources in observer direction over those individual event horizons at observer time τ, creates a scalar list with the specific acoustic pressure fluctuations within every spherical structure. The concentric sound propagation in observer direction is presented by moving all list elements one step closer to the observer for the next time step $\tau + t_\Delta$ and adding the integrated acoustic pressure again. Once, the outermost list elements have reached the observer, the hydro-acoustic analysis can be started. By updating the cell position in every single time step, this technique can be used with every grid-motion based solver. One of the biggest benefits form this list-based technique is, that there is no storage of previous flow fields needed, as the retardation time is calculated on the fly, so there are no additional storage nor memory demands for the acoustic analysis.
The free-surface effects on the hydro-acoustic field are well known [2], [3], and can not be neglected within the maritime context. While the observer positions within the FW-H equations may take place well outside of the hydrodynamic domain, the acoustic reflection at the free-surface needs to be modeled independently of the free-surface position within the hydrodynamic solution. Therefore a mirroring technique was implemented: An arbitrary plane Θ can be specified by a test point and its normal vector. This plane in an optimal way, but not necessarily, is identical with the hydrodynamic position of the free-surface. If Θ is known, the reflected acoustic source field is calculated using the new observer positions

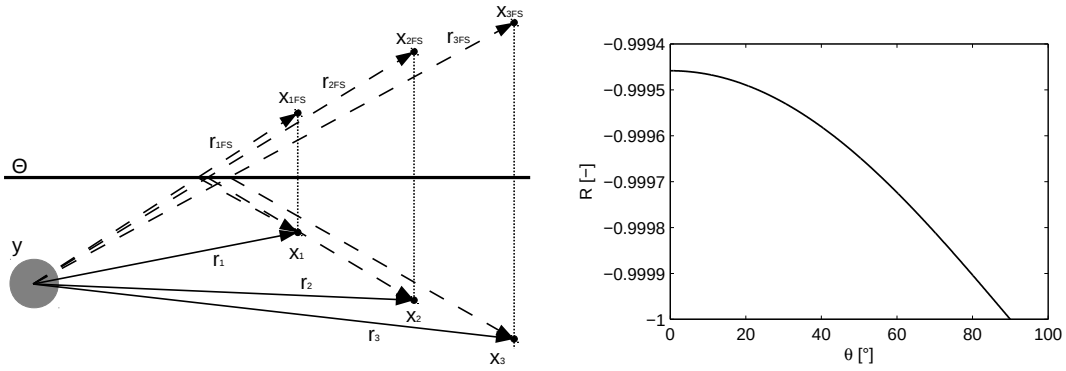

Figure 1: Scheme of free-surface implementation (left) and reflection coefficient R as a function of incident wave angle θ (right)

x_{FS}, reflected at Θ. To take into account the impedance of the water-air density-step, the acoustic pressure is scaled by the reflection coefficient:

$$R = \frac{m \cdot cos\theta - n\sqrt{1 - \frac{sin^2\theta}{n^2}}}{m \cdot cos\theta + n\sqrt{1 - \frac{sin^2\theta}{n^2}}}.$$

As the mirrored observer positions imply new position vectors and radiation distances, the lists of the forward-time-stepping implementation need to be updated in length as well. From there on, mirrored and direct acoustic emissions sum up in their respective event horizons. Due to the phase shift and the reflection coefficient with values of $R \approx -1$ for the water-air-interface, the typical acoustic interference structures show up, depending on the observer position. As mentioned, the plane Θ introduced does not necessarily need a hydrodynamic free-surface nor match their hydrodynamic position. This leads to a number of benefits: Firstly, the calculation of a ship can be performed using the single-face double body configuration. This allows more stable calculations and drastically reduced computational costs. Secondly, the hydro-acoustic calculation for different free-surface positions can be achieved within one single hydrodynamic calculation. And thirdly, the observer positions are not limited to an outermost reflection point within the hydrodynamic domain.
Speaking of computational cost, the code was implemented to work in complete parallel up to the latest steps of acoustic calculations. As the computational effort for the FW-H method needs to be investigated further, no reduction in calculation performance can be noticed at the actual point of development.

Numerical Model

Pulsating Sphere Test Case

To validate the FW-H implementation the pulsating sphere test case was selected, as the acoustic pressure can be calculated analytically for arbitrary observer points with or without a free-surface. As there is no solver functionality given for a pulsating sphere in OpenFOAM, a new motion law was implemented for the pimpleDyMFoam Solver, providing a harmonic concentric mesh motion. With a diameter of $D_S = 1m$ the sphere is located at the origin, surrounded by a spherical domain with a diameter of $10D_S$ and 2.88 million hexahedron cells. The sphere pulsates in radial direction around the origin with a frequency of $f_S = 10Hz$ and an amplitude of $A_S/D_S = 0.01$. The free-surface is located at the test point of Θ_t/D_S =(0 -10 0) with a normal vector of Θ_n =(0 1 0). All CFD calculations were performed using water as single-phase ($\rho = 998.21kg/m^3; c = 1484m/s$), however, within the free-surface acoustic calculations the outer fluid was specified as air ($\rho_1 = 1.2041kg/m^3; c_1 = 343m/s$). The investigated observer points are listed in table 1.

KVLCC2 Tanker Propulsion Test Case

For validation in a more maritime context, the KRISO tanker KVLCC2 with the scale of $\lambda = 1/58$ was selected in double body configuration, since it is widely used in the shipbuilding community [6]. The model has a length of $L_{PP} = 5.517m$, a breadth of $B = 1m$, a draught of $T = 0.359m$ and a block

Table 1: Observer positions for the pulsating sphere test case

	x_1	x_2	x_3	x_4	x_5	x_6	x_7	x_8	x_9
x/D_S	(1 0 0)	(2 0 0)	(4 0 0)	(8 0 0)	(16 0 0)	(32 0 0)	(64 0 0)	(128 0 0)	(256 0 0)

coefficient of $C_B = 0.8098$. The study of the model is performed for a constant velocity of $v = 1.047m/s$ corresponding to the Reynolds number of $\mathrm{Re} = 5 \cdot 10^6$. While the Froude number of $Fn = 0.142$ is comparably small, free-surface deformation effects can be neglected. The five-bladed propeller P1356 used in this case, provides a diameter $D_P = 0.17m$, a pitch ratio of $P/D = 0.996$, an expended area ratio of $A_E/A_0 = 0.8$, a hub diameter of $D_{hub}/D = 0.18$, a maximum skewness of 32° and a propeller frequency of $n = 9.35s^{-1}$ rotations per second. The computational domain of 22 million hexahedron cells extends $(-2.88 \leq x \leq 1.73)L_{PP}$ in flow direction, $(-7.96 \leq y \leq 7.96)B$ in horizontal cross-flow direction and $(-2.8 \leq z \leq 1)T$ in vertical cross-flow direction with the aft perpendicular positioned at the origin. Due to the comparably small grid size, the pimpleFoam Solver with an IDDES turbulence model was used. For direct comparison of free-surface and double-body configuration, the acoustic setup included both cases in within the hydrodynamic calculation. The acoustic free-surface plane was placed directly on top of the domain at Θ_t =(0 0 T) with an normal vector of Θ_n =(0 0 1).

Results

Pulsating Sphere Test Case

The results show, that for this basic test case a very good agreement between FW-H and analytical solution can be achieved. Comparing the acoustic pressure fluctuations for the single-phase setup as well as for the free-surface configuration, all curves, independent of observer distance, are nearly identical (fig. 2). As expected, the pressure fluctuations decrease with increasing distance to the sphere by r^{-1} and r^{-2}. It can be noticed, that for the free-surface configuration the decrease of the pressure fluctuations is even stronger than for the single-phase case. This is a direct result of interference between direct and reflected acoustic emission, as all observers are aligned directly beneath the free-surface. While the reflection coefficient is $R \approx -1$, direct an reflected contribution start to cancel out each other where the relation between direct and reflected observer distance go to $r/r_{FS} \to 1$. Calculating the acoustic pressure map around the free-surface sphere, the typical interference structures show up, presenting an acoustic field between perfect cancellation and amplification by the factor of two (fig. 3).

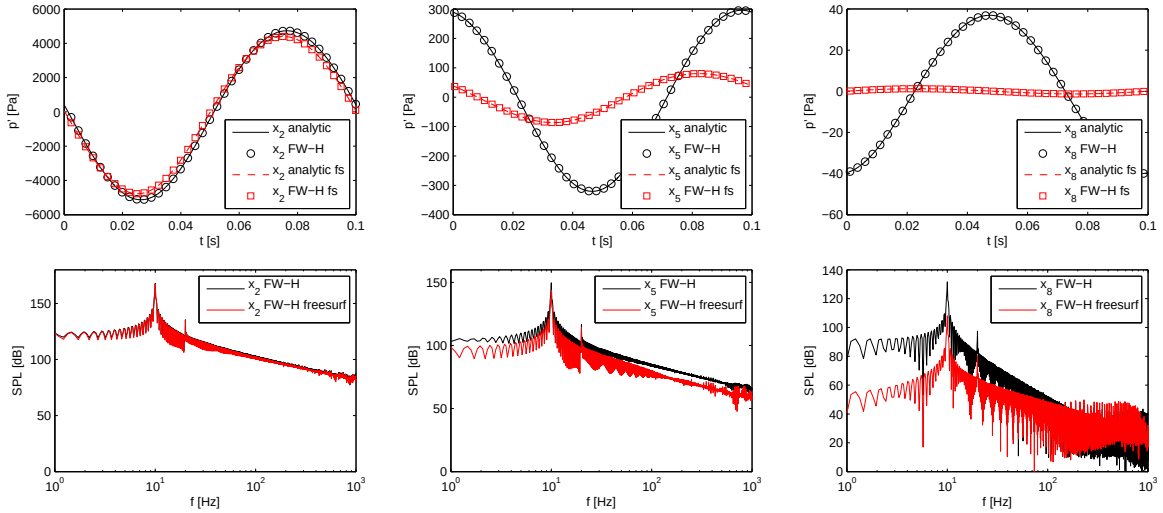

Figure 2: Acoustic pressure fluctuations (top) and spectra of sound pressure level (bottom) at observer x_2 (left), x_5 (center) and x_8 (right) for a pulsating sphere with and without free-surface

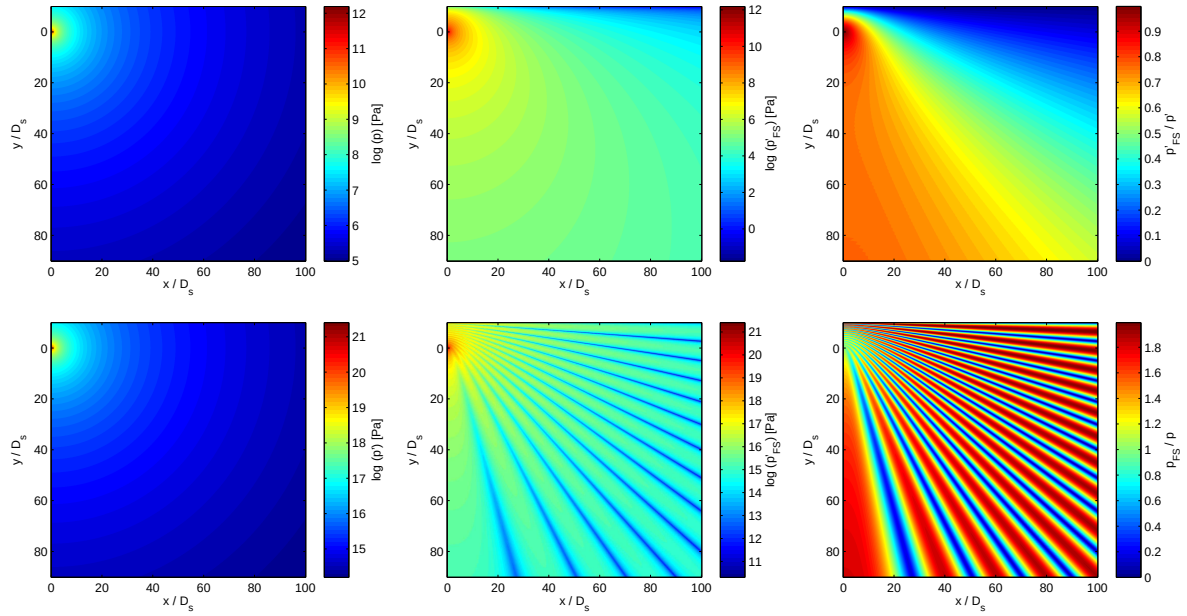

Figure 3: Free-surface effect: Acoustic pressure fluctuations of a pulsating sphere for single-phase (left), with free-surface (center) and in normalized form (right) for $f_s = 10Hz$ (top) and $f_s = 1000Hz$ (bottom)

Table 2: Observer positions for the KVLCC2 test case

	x_1	x_6	x_7
(x y z) [m]	(0.0 2.1 0.35)	(0.1 0.1 0.22)	(0.1 0.0 0.22)

KVLCC2 Tanker Propulsion Test Case

Investigating the integral values for the KVLCC2 test case, a mean total resistance coefficient of $C_R = 5.27 \cdot 10^{-3}$ was calculated for the propulsion test case. For comparison with the KRISO towing-tank experiments, the total resistance was corrected by the thrust deduction number of $t_{KVLCC2} = 0.190$ measured by Kim et al. [4], leading to an error of $\Delta_{CR} = +3.92\%$ (KRISO experiments $C_R = 4.11 \cdot 10^{-3}$). Using the thrust deduction number for correction of the pressure resistance only, results in a relation of friction to total resistance of $C_F/C_R = 0.764$ and a relation of pressure to total resistance of $C_P/C_R = 0.236$. This discrepancy to the experimental data (KRISO exp. $C_F/C_R = 0.85$, $C_P/C_R = 0.15$), presenting an overestimation of the pressure resistance, seems to be typical for hybrid URANS-LES turbulence models [5].
Because the acoustic measurements in the towing tank are still in progress, the hydro-acoustic results are compared with pressure results from the hydrodynamic calculation. It can be noticed, that the hydro-acoustic pressure fluctuations from FW-H are smaller than the pressure fluctuations resolved within the CFD calculation in all cases. The discrepancy is dependent on the observer position. While observers, placed within a short distance to the propeller, show comparably good agreement with the calculated pressure fluctuations from CFD, the relative discrepancy increases while the distance to the active hydro-acoustic sources like propeller and hull increases (fig. 4). It is interesting to see, that for this particular case there is no significant difference in the hydro-acoustic results between free-surface and one-phase calculation. This could be due to the fact, that for validation purposes all observer were positioned well within the computational domain, where the direct contribution from the acoustic sources dominates the acoustic fluctuations. Only for observer points placed directly beneath the free-surface, a difference between one-phase and free-surface calculations can be distinguished, even though there is a large amount of white noise.

Conclusion

The Ffowcs-William Hawkings equations have been implemented into OpenFOAM to allow hydro-acoustic flow evaluations inside and outside of the hydrodynamic domain. The function object allows for a wide

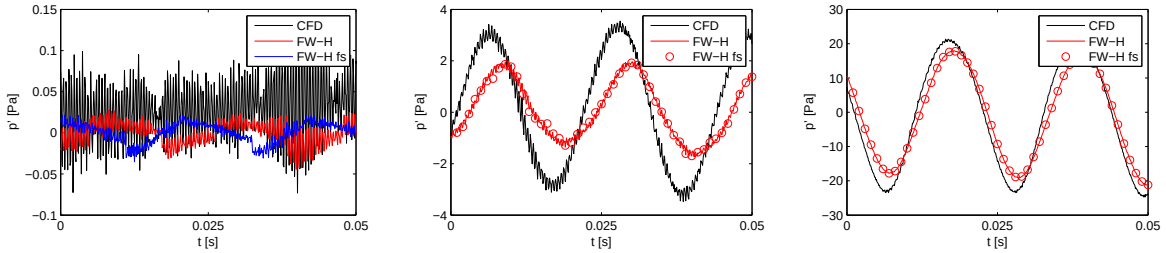

Figure 4: Pressure fluctuations for the KVLCC2 propulsion test case: x_1 - portside beneath the free-surface (left); x_6 - in the propeller plane at the portside of the propeller well (center); x_7 - in the propeller plane at top dead position in the propeller well (right)

range of hydrodynamic solvers and flexible on-the-run adjustability. To represent the retarded time effects, a forward-time-stepping procedure was developed, providing low system requirements even in hydro-acoustic multithreading. While this project is targeting on the evaluation of maritime hydro-acoustic emissions, the FW-H model was extended by a mirroring technique to take free-surface effects into account. First results for the pulsating sphere test case show an impressive agreement between the pressure fluctuations from the implemented FW-H model and the analytic solution. The free-surface effects are presented with very good agreement as well, showing an strong interference in the surrounding fluid. For the more complex case of the self-propelled KVLCC2 tanker in model scale, the FW-H results are in qualitatively good agreement with the CFD pressure, but show to be sensitive on the observer position. For the investigated case the free-surface effect for all observers was rather small. Based on the results of the pulsating sphere test case, this effect is expected to increase with increasing distance to the radiation source. At the present state, the implemented model showed to be very robust and flexible as well as light on the computational resources. Further investigations are needed to improve the agreement for more complex flow simulations.

References

[1] F Farassat. Derivation of formulations 1 and 1a of farassat. *NASA TM*, 214853:2007, 2007.

[2] Oleg A Godin. Anomalous transparency of the water/air interface for low-frequency sound. *The Journal of the Acoustical Society of America*, 119(5):3253–3253, 2006.

[3] Paula Kellett, Osman Turan, and Atilla Incecik. A study of numerical ship underwater noise prediction. *Ocean Engineering*, 66:113–120, 2013.

[4] WJ Kim, SH Van, and DH Kim. Measurement of flows around modern commercial ship models. *Experiments in Fluids*, 31(5):567–578, 2001.

[5] N Kornev, A Taranov, E Shchukin, and L Kleinsorge. Development of hybrid urans–les methods for flow simulation in the ship stern area. *Ocean Engineering*, 38(16):1831–1838, 2011.

[6] Lars Larsson, Frederick Stern, and Volker Bertram. Benchmarking of computational fluid dynamics for ship flows: the gothenburg 2000 workshop. *Journal of Ship Research*, 47(1):63–81, 2003.

CFD Prediction of Shallow-Water Performance of a Trailing Suction Hopper Dredger Validated with Full-Scale Measurements

Alex Kruijswijk, Royal IHC, Kinderdijk/The Netherlands, AB.Kruijswijk@ihcmerwede.com

In dredging projects like harbor maintenance and land reclamation, the trailing suction hopper dredger (TSHD) is used in different ways. Such dredging projects are almost always near shore, and therefore the TSHD is often sailing in very shallow water (up to half the draught under the keel or less). The speed of a TSHD in shallow water influences its production performance (costs per cubic meter) but also affects its sustainability performance (fuel consumption). Up to now the estimation of ship velocity in shallow water is done with basic regression formulas which are a correction related to the deep water performance. During sea trials of several TSHDs the performance in shallow water appeared to be better than predicted. This paper focuses on whether CFD simulations can predict the shallow water performance of a TSHD with higher accuracy than current prediction methods.

Sea trials show that ship velocity in shallow water is not correctly predicted. The current empirical correction method for shallow water is too conservative and can under-predict the velocity. The model-tests show that the shallow water performance is not predicted correctly. This is due to scale-effects and likely due to interaction with the tank wall.

In the project presented in this paper steady-state CFD simulations are done with a commercial software package (FineMARINE, NUMECA). The simulation has a fully appended ship with propeller action and free-surface. Openings like bow thruster tunnel and suction tube inlet are omitted. From the computation the torque is compared with the full-scale measured torque. Measurements are available for deep water and several shallow water depths and also for different ship velocities. All measurements are in loaded draught.

The most commonly used correction methods for ship velocity in shallow water are Schlichting and Lackenby. CFD results are compared with currently used correction method and full-scale measurements and from the CFD results conclusions are drawn about the wake fraction and the thrust deduction factor.

Current prediction method shallow water performance

A first correction method for shallow water performance is presented in (Schlichting, 1934) . This is a empirical correction method based upon model tests. It corrects the resistance curve for shallow water effect. The second method is presented in (Lackenby, 1963). This is also an empirical correction method, but it proposes a correction on the power curve with two parameters *sqrt(Am/H)* and *FnH*. This method is currently the most used and is recommended by ITTC when trial results must be corrected for shallow water. It may be applied when :

the conditions meet one of these	and as long these conditions are met
$H < 2.75\frac{v^2}{g}$, $FnH > 0.6$ $H < 3.0\sqrt{B \cdot T}$, $\frac{Am}{H^2} > 0.111$	$H > 2.0\frac{v^2}{g}$, $FnH < 0.7$ $H > 2.0\sqrt{B \cdot T}$, $\frac{Am}{H^2} < 0.25$

For this full-scale test program this means that the correction method of Lackenby is limited to H >22.6. The Lackenby correction method to estimate the ship velocity loss in shallow water is:

$$\frac{\Delta v_s}{v_s} = 0.1242\left(\frac{Am}{H^2} - 0.05\right) + 1.0 - (\tanh\left(\frac{gH}{v_s^2}\right))^{1/2}$$

With:

FnH = Froude number based on water depth [-]
Am = midship section area under water [m2]
g = gravitational acceleration [m/s2]
H = water depth [m]
Vs = ship velocity
Δv_s = loss of speed due to shallow water [m/s]

Full-scale test setup

In cooperation with MARIN a trailing suction hopper dredger named HAM317 was tested in shallow water. The ship is built by Royal IHC and operated by van Oord. The ship main dimensions are: Lpp = 84.95 m, B = 18.4 m, T =7.12 m and Cb = 0.88-. The highest Froude number during the trials is Fr = 0.22-. This ship is fitted with a controllable pitch propeller (CPP).

The water depths chosen are H=40 m for deep water and H=25 m for shallow water depth, so Lackenby can be applied. Also, two shallow water depths are added to the program, H= 18 m and H = 12m. These very shallow water depths are especially relevant for a hopper dredger.

In the speed trials report of MARIN the conditions are described as: light to moderate wind conditions, calm wave conditions (wave height less than 0.2 m), and wave direction which either could not be determined or was from the side. No wave correction was done for the measurements.

During the trials the measurement system recorded the torque and rotational rate of the propeller shaft., as well as the trim, altitude , speed, heading, course and speed over ground of the ship. Relative wind speed is also logged.

CFD setup

Geometry

The 3D model of the ship is a parasolid format. This format contains solids with surface definition. The surfaces of the solids are redefined such that the surfaces which are smaller can have higher refinement and surfaces with more curvature are checked so that geometry is properly captured by the mesh.

The domain dimensions are based upon the Lpp of the ship: L×B×H= 5Lpp × 2Lpp × 2.5Lpp, with 1Lpp in front of the ship, portside of the ship only and 2Lpp beneath ship keel. For shallow water the bottom of the domain is at water depth.

Two different setups are used for the ship geometry. First, a basic model without nozzle and rudder is used for resistance and wake fraction. Second, an appended hull with nozzle and rudder is used together with an actuator disk (AD) for (simple) propulsion analysis.

Mesh

The mesh is constructed by following the 5 steps in HEXPRESS: initial mesh, adaptation, snapping, optimization, and viscous layer insertion. The snapping and optimization steps are usually done with

standard settings and don't require additional input. The other 3 steps define the final mesh size and quality and are kept the same for all setups as much as possible. But always such that mesh quality is good and mesh size is less than 9 million cells.
In the viscous layer insertion step all surfaces are refined for the wall function approach, except for the deck, which has a slip condition. The first layer thickness is calculated with a y+ value of 200, and the highest velocity for each water depth. For the shallow water setup the bottom of the domain has a slip condition instead of a normal boundary condition.
The free surface is made with a surface which spans the entire domain, and with a target cell size of dx×dy×dz = 10m×10m×0.1m (based on Lpp). The geometry is meshed with initial trim and thus extra dynamic trim due to shallow water effect should be small enough such that the free surface near the ship stays in the refinement location of the free surface.

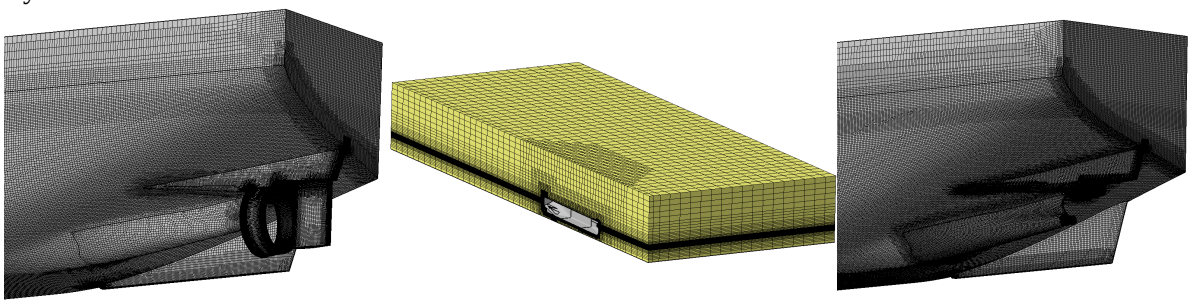

Aftship mesh with nozzle/rudder – domain for shallow water (H12) – aftship without nozzle/rudder

Computations for shallow water
In a normal deep water condition the boundary condition on the bottom of the domain is prescribed pressure, but for (very) shallow water the b.c. is set to slip. The viscous part is omitted in order to avoid numerical instability, the need for a lot of extra cells and over-prediction of viscous forces.
Due to dynamic sinkage and trim the mesh will deform between the ship and the bottom of the domain. This deformation must not be too large because mesh quality can become very poor. To avoid this, the ship is given a pre-squat so that dynamic sinkage and trim will not deform the mesh very much. The pre-squat is taken from the deep water and highest velocity CFD calculation. Also a special bottom mesh management option is set in the FineMARINE options which also helps with the deformation.
First a computation is done with a fixed ship and only accelerated to its imposed forward velocity. After that, the ship heave and pitch motions are solved with a re-start on the first run.

Propeller action with Actuator Disk
To be able to make a first comparison between the CFD results and the full-scale measurements, the propeller action is modeled in FineMARINE. With the actuator disk (AD) the flow at the aftship is better estimated than without nozzle and AD. The AD also gives a simplified model with less cells than a sliding grid. This model cannot estimate the torque on the shaft, and a direct comparison with measurements is not possible.
The dimension of the AD are based on the propeller diameter (Dp): outer radius = propeller radius (r_{prop}), inner radius = $0.25r_{prop}$ and thickness = 0.1Dp. The initial thrust is taken from a previous trimmed calculation, and the AD calculation is a re-start. There are no tangential forces modelled (no torque) and the distribution is uniform. Every time-step the body force is updated.

Computational setup
The computations are steady state and water properties are taken from the full-scale tests. In the flow model the k-omega (SST-Menter) turbulence model is used, and Reynolds numbers are ranging from 2.31E+08 to 4.54E+08 for full-scale calculation. A quasi-static approach is used to calculate the equilibrium position of the ship. The method consists of a time-marching scheme with sub-cycling. This means that when steady-state is reached the solution is physically correct.

Results

Dynamic sinkage and trim CFD

Due to forward velocity of the ship there is dynamic sinkage and trim. The increased velocity under the hull reduces the hydrodynamic pressure, and therefore the ship will have increased squat with increasing velocity. The results are for appended hull with nozzle, rudder and AD.

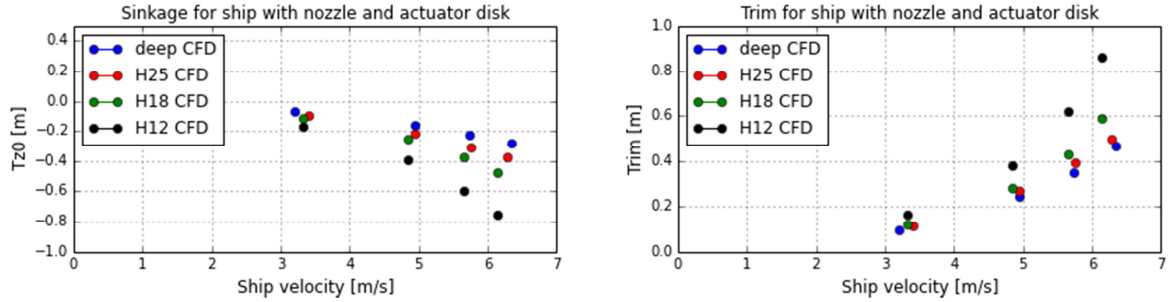

The sinkage (Tz0) is the sinkage of the initial KG=7.12m. The trim is defined as the difference in forward and aftship draught, with positive trim as bow down. When sailing in shallow water the velocity under the hull is even more accelerated and the pressure is decreasing more. The increased sinkage and trim for shallow water is expected.

CFD Resistance & Thrust

The resistance and the thrust are calculated from the steady-state time signal. A mean value is taken over the last 50 seconds of the simulation. The convergence is checked with a relative error and standard deviation over the same period.

The resistance of the appended ship is calculated for the model without nozzle and rudder. The nozzle is replaced with an elongated tunnel. The steady-state results are plotted for a trimmed ship with imposed forward velocity.

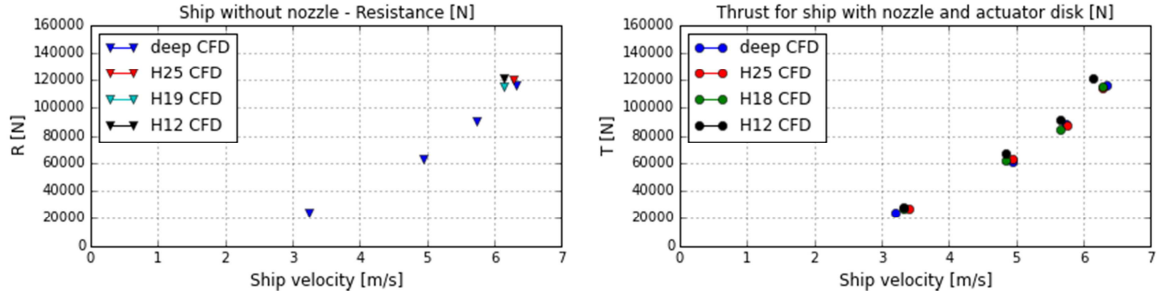

The thrust is calculated for the model with nozzle and rudder, and the actuator disk is added to model propeller action. The results are also steady-state and with trim and imposed forward velocity. The thrust of the actuator disk is based on the resistance of the ship, and is updated every time-step.

Thrust calculations show that for H25 and H18 the effect of shallow water is minimal. For H12 the thrust is increased for slight lower ship velocity. Comparison between the thrust coefficient show that for the highest velocity H12 is 11% higher than deep water.

Full-scale test results compared with CFD

In the full-scale test the torque (Q) and rotational rate of the propeller (n_prop) are measured, which gives the shaft power. If we want to compare this with CFD we have to calculate the torque on the propeller in CFD, which is only possible if a rotating propeller is modeled in the computation. For now the propeller is modeled with an actuator disk, and the CFD results give the thrust.

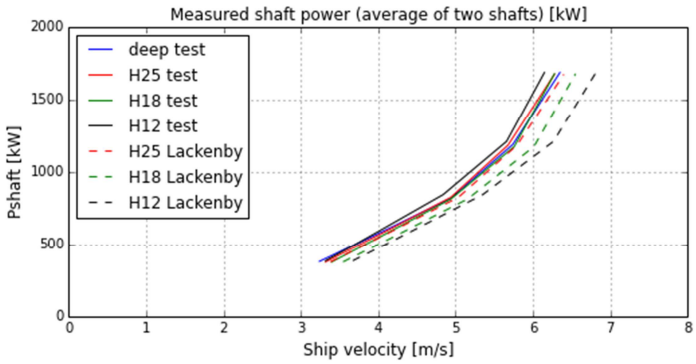

In the figure the black line represents the most shallow water (H12). The dotted lines are the corrected values for equal shaft power (Lackenby), which are corrected to deep water. Corrections with Lackenby are too large. For the highest velocity and H12, the drop in velocity is 0.2 m/s (0.4 kn) for equal shaft power.

In the full-scale tests the thrust (T) on the shaft is not measured. This means that a direct comparison with the calculated thrust from CFD is not possible. If we want to compare these results, an open water diagram of the propeller can be used. However, the pitch of the propeller (CPP) is given in percentage of the maximum pitch. The real geometrical (maximum) pitch is not known at the moment. This makes it difficult to calculate the true operating point of the propeller. This is demonstrated by the following calculations of the propulsion parameters where the propeller pitch is varied.

In the table the pitch is varied for deep water and highest ship velocity. Torque and rotational rate are taken from the tests and the relative rotative efficiency is assumed to be 1.0-.

Measurements				
10Kq	0.556			
P/D	J	10Kq	Kt_tot	T [kN]
1.25	0.450	0.552	0.396	235.6
1.258	0.466	0.553	0.390	232.3
1.29	0.530	0.556	0.368	219.1
1.3	0.550	0.557	0.361	215.0
1.4	0.750	0.569	0.292	174.0

From the table it is clear that small changes in propeller pitch(P/D) can lead to significant changes in thrust. Because the exact propeller pitch is not measured, it is not possible to use the open water data to calculate the thrust for the measured torque.

For the same deep water condition and highest ship velocity the thrust from the CFD calculation, T = 116.26 kN, and Kt= 0.195 [-]. This is not close to the thrust values calculated with the open water data (see table), from the measured torque.

The actuator disk used in the CFD computation has a uniform distribution. This is a general setting which can be used for wake field calculations. Previous in-house studies have shown that this setting for the AD show good resemblance with full-scale measured wake field in front of the propeller, but for speed-power predictions the uniform distribution does not properly model the flow in the nozzle.

	Nozzle thrust [N]	Kt,nozzle [-]
Deep water	4407	0.007
H12 shallow	4316	0.007

The thrust of the nozzle is underestimated in the calculation with AD and uniform distribution. In the open water test of the stock propeller and nozzle, the thrust coefficient of the nozzle alone is around 0.11.

Propulsion efficiency in wake fraction and thrust deduction factor
In normal design practice the nominal wake field for propeller design is determined for a ship without nozzle. The part where the nozzle is attached to the hull or headbox, is smoothed by elongation of the tunnel. From the results of this setup the wake fraction is compared for different water depths.

	H= 40 m	H = 25 m	H = 18 m	H = 12 m
Wake fraction	0.108	0.106	0.109	0.161

The wake fraction is expected to be higher for shallow water. The relative axial velocity is lower because in shallow water, the water is decelerated between the keel and bottom. Lower wake fraction means that the hull efficiency can increase, as long as the thrust deduction factor stays at least the same.

Normally the thrust deduction factor is determined by CFD calculation of ship with propeller (WIP) and without propeller (WOP). However, in this case the ship has a nozzle, which in design stage is taken into account in the open water diagram of propeller and nozzle. The determination of the thrust deduction factor can be performed between WOP = ship without nozzle and rudder vs. WIP = ship with nozzle and rudder, but the differences between these two setup in Fx, is within the relative error of the computations (approx. 1%).
As an alternative the thrust deduction factor is determined between WIP = ship+nozzle+AD and WOP = ship+nozzle. This resulted in negative factors, which for more shallow water are decreasing.

Conclusions

The recommended correction method for shallow water, Lackenby, is too conservative. Both the full-scale measurements and the full-scale CFD show that the performance of the ship is only affected in very shallow water: water depth is 12 m with T = 7.12 m.
Measured torque of the propeller shaft cannot be used to calculate the thrust, because the exact propeller pitch is not known, and therefore data of the open water diagram cannot be used.
The uniform distribution in the actuator disk showed good wake field prediction in previous studies, but for a good speed-power prediction for a propeller in a nozzle, a use defined distribution should give better results. The uniform distribution clearly showed a too low thrust of the nozzle.
Wake fraction does increase in shallow water, and the thrust deduction factor is decreasing, although it is not clear on how to define the factor for propeller in nozzle. With the current prediction the results show a increase in hull efficiency.
The results show that for more shallow water the ship will have increased sinkage and trim. Also the amount of sinkage and trim seem to be in line with previous estimated numbers (potential theory and model-tests).

Recommendations

- User defined actuator disk distribution for propeller in nozzle
- Computations with a moving propeller. In FineMARINE it is possible to use a sliding grid method to model the propeller completely. The calculated moment on the body of the rotating propeller can be compared with the measured torque form the full-scale.
- It would be more accurate to use the measured thrust, so that the propeller efficiency can also be checked. The propeller is an older model and is already in service for a longer period. Damages to the propeller can cause changes in efficiency and thus in required torque. This is also important when a rotating propeller is used in CFD.

Progress in Predicting Pressure Pulses and Underwater Radiated Noise Induced by Propeller with Pressure Side Cavitation

Da-Qing Li (da-qing.li@sspa.se), Jan Hallander (jan.hallander@sspa.se) and Roger Karlsson (roger.karlsson@sspa.se)

SSPA Sweden AB, Göteborg, Sweden

Introduction

The steady increase of maritime shipping has contributed to a significant increase of underwater radiated noise (URN) and caused a great concern by the authorities, policy makers and ship operators. e.g., International maritime organization (IMO) has expressed their concerns about the increased ocean noise due to shipping activities. Excessive URN pollutes ocean environment and threatens marine life. It is no doubt important to understand the ship generated noise and its radiation characteristics. Equally important is development of computational tools to reliably predict the noise level generated by ships at various operating conditions. Among the noise sources generated by a propeller-driven ship, the propeller is recognized as a dominant source contributing to URN in the low frequency spectrum. Cavitation on propellers can further augment the noise level over a wide frequency range. Cavitation noise occurs when the cavity volume changes (e.g. the creation, growth and collapse of cavitation).

The EU project AQUO (Achieve QUiter Oceans by shipping noise footprint reduction) aims to provide support to policy makers with practical guidelines to reduce shipping noise for a quieter ocean and to investigate design improvement solutions and mitigation measures to manage ship generated URN and its impact on the marine fauna. SSPA is engaged in the model testing, full scale measurement and numerical simulation of a coastal tanker equipped with a controllable pitch propeller (CPP). Ships operating on short routes along coast lines are often equipped with a CPP propeller with an engine running at constant RPM, and the engine RPM is usually optimized at NCR (nominal continuous rating). When sailing at a reduced (off-design) speed, a natural choice of operation is to reduce propeller pitch while keeping the engine at fixed RPM. However, is this always a beneficial operation with regard to underwater radiated noise and fuel saving? The model tests for the coastal tanker in AQUO reveals that this is not always the case, as compared with the option of reducing RPM instead of lowering pitch.

As a follow-up of our previous study of design loading (LC2) in NuTTs2014 (Li et al. 2014), the present paper addresses the numerical results for the tanker running at reduced pitch and nominal constant RPM (loading condition LC6) at a low ship speed 11 kn. We studied the cavitation behaviour, pressure pulses and radiated noise level for LC6 at model scale. The simulation was carried out with a hybrid method using a Delayed Detached Eddy Simulation (DDES) solver for flow resolution and an acoustic analogy based on Ffowcs Williams-Hawkings (FW-H) permeable surface integration for prediction of far field noise. The commercial software ANSYS FLUENT 15.0 was used.

Compared with the model test data, the numerical results confirmed that the inefficiency of propulsion setup and a pronounced pressure side cavitation with rather unstable shedding behaviour are the main reasons for a noise level almost as high as that in LC2.

Model Test Campaign

A comprehensive experiment campaign was carried out in SSPA's towing tank and cavitation tunnel [1]. Cavitation observation, pressure pulse and noise measurement were performed at six loading conditions. Figure 1 shows a photo of the ship model inside the cavitation tunnel (left), a sketch of transducer locations for pressure pulse measurement (mid) and a sketch of the hydrophone locations for noise measurement (right).

The subject ship M/T Olympus is a 116.9 m long and 18 m wide coastal tanker, kindly provided by Sirius Shipping (http://siriusshipping.eu/) for study in AQUO project. The CPP propeller has a diameter 4.8 m, blade area-ratio 0.45 and design pitch ratio of P/D=0.87. The loading used in the simulations corresponds to loading condition LC6 defined in [1], i.e. ship speed at 11 kn and the propeller rotating at 120 rpm with a reduced pitch of P/D=0.52. The estimated thrust coefficient is $K_T \approx 0.087$ and the cavitation number becomes $\sigma_n = 2.85$ at ballast draught.

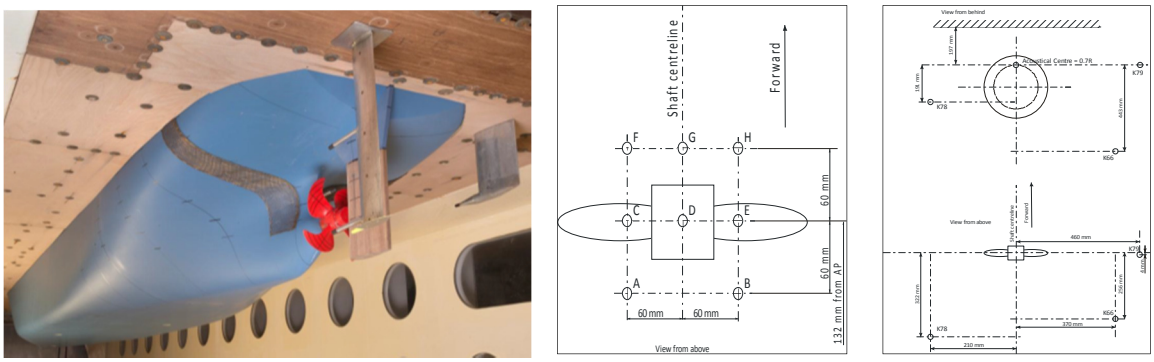

Figure 1 Model setup (left), sketch of transducer locations (mid) and hydrophone locations (right)

Numerical Methods

The numerical solution consists of two steps. First, it resolves the flow field around the ship hull with a DDES method. DDES is essentially a hybrid solution technique that combines and switches between a RANS method and an LES (Large Eddy Simulation) method depending on the local grid resolution. Namely, RANS method is used to solve the flow region inside the attached boundary layer and LES is employed in the regions of separated flow or wake where the grid is fine enough. In region farther away from the hull where the grid becomes coarse, flow field is solved by the RANS method too. For turbulent viscosity modelling, the two-equation SST k-ω model is employed. Secondly, the noise propagated from the sources to any arbitrary receiver location is determined by solving a pressure wave equation. In the present work, the solution for acoustic pressure is obtained by numerical integration of Ffowcs Williams-Hawkings (FW-H) equation over prescribed permeable surfaces. As regard to cavitation prediction, the multiphase mixture flow DDES solver and Zwart's cavitation model are employed. Moreover, Reboud's correction on turbulent viscosity is implemented in the SST k-ω model. The correction is active in the mixture region to prevent the otherwise too high eddy viscosity in the region. The used numerical schemes are as follows:

- Multiphase mixture flow incompressible solver
- Pressure and velocity solved in a coupled manner
- Bounded 2nd order central difference for convection terms in momentum equations
- QUICK scheme in other transport equations
- Propeller rotation handled by sliding mesh technique
- Bounded 2nd order implicit scheme for time-derivative
- Time-step is 4.42x10^{-5} [s] at model scale

A rectangular computational domain is defined around the hull (Figure 2). The inlet boundary is located at 1 L_{pp} distance from FP and the outlet at 1.5 L_{pp} aft of AP. The two sides and the bottom of the domain are placed 1 L_{pp} away from the central line. A smaller rectangular domain that closely surrounds the hull is also visible in Figure 2. It has two roles: grid refinement is focused in this domain to facilitate an LES solution; the domain boundaries serve as the permeable integral surfaces later in the FW-H acoustic analysis. The meshes are of hexahedral type. The grid lines are refined not only in the wall normal direction to achieve a y^+=1, but also in the streamwise and girthwise direction to fulfil grid requirement for DDES method, i.e. about 10 nodes in the streamwise direction and 20 nodes in the girthwise direction per boundary layer thickness. A grid cut-off at the central plane is shown in Figure 2 (right). The black region that embraces the propeller is the rotating mesh block. The total number of grid cells is 35 million.

Constant velocity, turbulence intensity and viscosity ratio are specified at the velocity inlet boundary, whereas a constant pressure is set at the outlet boundary to ensure correct cavitation number. The free surface, side and bottom boundaries are treated as slip walls.

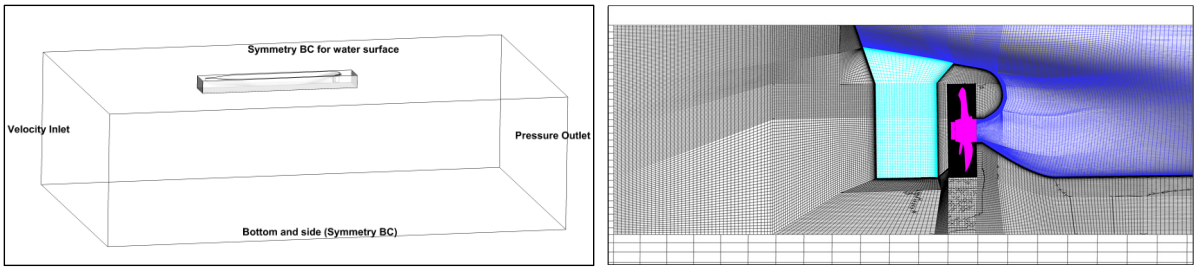

Figure 2 Computational domain (left) and surface mesh on propeller, rudder and stern (right)

Results and Discussions

The results are presented in the following formats: Iso-surface of vapor volume fraction α_v=0.5 is used to visualize cavitation surface. Turbulence vortex structure is represented by the iso-surface of Q-criterion, defined as Q=½(Ω^2-S^2) [s^{-2}], with S being the strain rate and Ω the vorticity rate magnitude. Pressure pulses are expressed as K_p coefficient defined by $K_p = 2P_M/(\rho(nD)^2)$, with P_M being the single amplitude of pressure signal. No windowing scheme is applied in post-processing pressure signal. The noise is presented as sound pressure level of Power Spectra Density (L_{PSD}). The source level radiated noise (URN) is derived by scaling to 1 m distance away from the acoustic centre.

Flow field. The total wake (V_x=u/U_o) at the propeller plane is shown in Figure 3 (left). Note that the total wake was calculated by SHIPFLOW, with the propeller effect modelled by a lifting-line analysis program. The turbulence vortex structures at the stern are presented in Figure 3 (right) by the iso-surface of Q=3000 (s^{-2}), coloured by the turbulent viscosity ratio. As seen in the figure, the tip vortices and the wake structures behind the hull and rudder are captured well in a near downstream region about 2 propeller diameters downstream the propeller plane. Farther downstream the vortices disappear due to insufficient grid resolution. The small pitch angles of the tip vortices correlate well with the lightly loaded propeller (reduced pitch) in LC6.

Cavitation behaviour. The predicted cavitation is compared with that observed in the cavitation test at three blade positions in Figure 4. Note that the view angle is different for the model test and the simulation. In the test the pressure side blade was viewed through the bottom window of the cavitation tunnel. No cavitation on the suction side was present in LC6. Starting from r/R≈0.7, an unsteady and thin sheet cavity was formed along the leading edge on the pressure side. The cavity turned into a Leading Edge Vortex Cavity (LEVC) when it developed further towards the tip region. In the model test, Tip Vortex Cavitation (TVC) was occasionally seen but it didn't survive longer. In the simulation, no TVC could be identified. The formation and development of LEVC were very similar with that in the experiment. However, the predicted cavity exhibited more dynamic shedding and break-off (possibly a consequence of using Reboud's correction). Moreover, the LEVC at the outer radii was raised up above the blade surface, see Figure 5.

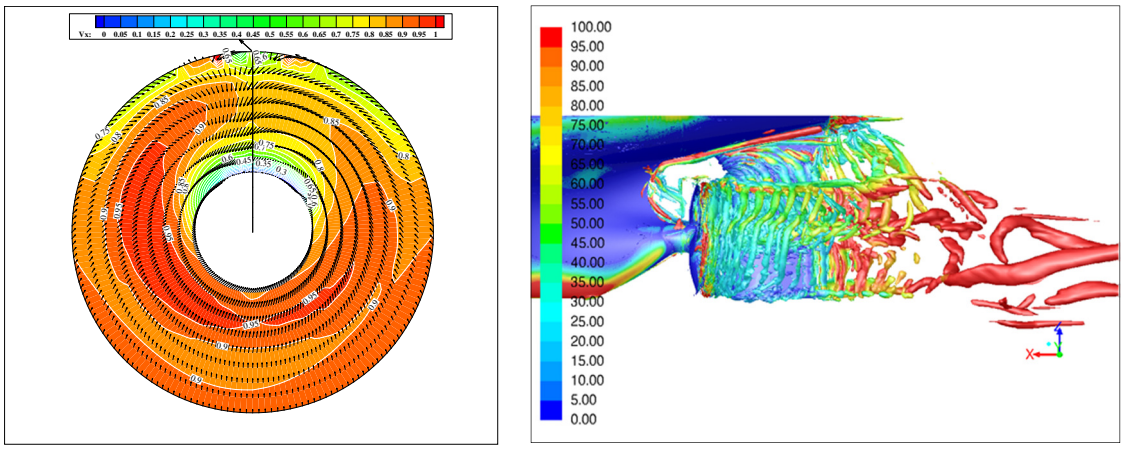

Figure 3 The total wake (left) and the vortical flow structures (right) in the hull and propeller wake

Pressure pulses. The measured pressure pulses are compared with the predicted ones at 8 transducer locations in Figure 6. Due to the light loading, the pressure fluctuations are at moderate level. The agreement with the measured K_p at the 1st harmonics is quite good except at transducer D. At 2nd ~5th harmonics, the measured K_p are practically zero whereas the computed K_p reveal higher values. The discrepancy is suspected to have something to do with the over-predicted shedding dynamics.

Noise signature. The noise signal measured at hydrophone K66 and K78 is compared with the predicted one in Figure 7. The vertical grid lines in the diagrams are drawn at harmonics of Blade Passing Frequency (BPF) with a blade rate (BR) fundamental at 125.8 Hz. Figure 8 compares the measured and computed URN at source level over the entire achievable frequency domain. Due to the lower speed and reduced pitch in LC6 (compared with LC2 loading in [1][2]), the shaft power is substantially lower, thus the contribution of blade loading to the tonal noise (and pressure pulses) is limited to the low frequency region with a low-to-medium noise level. This is why only the tonal noise at the first two harmonics is distinguishable from the measured data in Figure 7. There is a plateau of significantly high noise level (appearing mainly as broadband noise) in the frequency range 500-2000 Hz, almost comparable to the tonal noise in the low frequency range. This part of spectra is primarily caused by the LEVC and its shedding and collapse behaviour. The unfavourable pressure side cavitation is clearly a consequence of reduced pitch. Compared with the measured noise spectra, the tonal noise at the first two BPF harmonics is under-predicted and the noise in the range 500-2000 Hz is somewhat over-predicted (with a maximum difference about 28 dB at the frequency ~670 Hz.). The over-prediction tendency correlates well with the over-prediction of the pressure pulses. Both are believed to be associated with the over-predicted shedding dynamics of LEVC. More analysis is needed to clarify this.

Conclusions

A multiphase DDES method coupled with FW-H's acoustic analogy is applied to predict the cavitation, pressure fluctuations and underwater radiated noise of a coastal tanker with a cavitating propeller. The calculation confirmed the same finding as the model testing: a pronounced leading edge vortex cavity (LEVC) was developed on the pressure side of propeller blades, contributing to a significantly high level of noise in the frequency range 500-2000 Hz. The volume and shedding dynamics of LEVC was however somewhat over-predicted in the simulation. As a result, the radiated noise in the relevant frequency range became higher than the measured one. Similar prediction difference is observed for the pressure pulses. The work demonstrated for another loading condition LC6, the fairly good agreement between the measured data and the result predicted by the hybrid method.

Acknowledgements

This work was carried out within the collaborative project AQUO (Achieve QUieter Oceans by shipping noise footprint reduction), funded by the European Commission within the Call FP7 SST.2012.1.1-1: Assessment and mitigation of noise impacts of the maritime transport on the marine environment, Grant agreement No. 314227, coordinated topic "The Ocean of Tomorrow". The content of this paper does not reflect the official opinion of the European Union. Responsibility for the information and views expressed in the paper lies entirely with the authors.

References

[1] "Propeller noise experiments in model scale". AQUO Deliverable D2.4, European Commission FP7 - Collaborative Project n° 314227, 2014.

[2] Da-Qing Li, Jan Hallander, Torbjörn Johansson and Roger Karlsson, "Cavitation dynamics and underwater radiated noise signature of a ship with a cavitating propeller", VI Int'l Conference on Computational Methods in Marine Engineering, MARINE 2015, Rome, Italy, 2015.

[3] ANSYS FLUENT 15.0, 2013, "FLUENT User Manual".

[4] Johansson, T., Hallander, J., Karlsson, R. Långström, A. and Turesson, M. (2015), "Full scale measurement of underwater radiated noise from a coastal tanker". OCEANS' 15, Genova, Italy.

[5] J. Hallander, R. Karlsson and A. T. Johansson, (2015), "Assessment of underwater radiated noise, cavitation and fuel efficiency for a chemical tanker", OCEANS' 15, Genova, Italy.

[6] Li, D.Q., Hallander, J. and Karlsson R., 2014, “Study of underwater noise signature from a tanker with a cavitating propeller using a DDES and acoustic analogy method”, NuTTs 2014, Marstrand, Sweden.

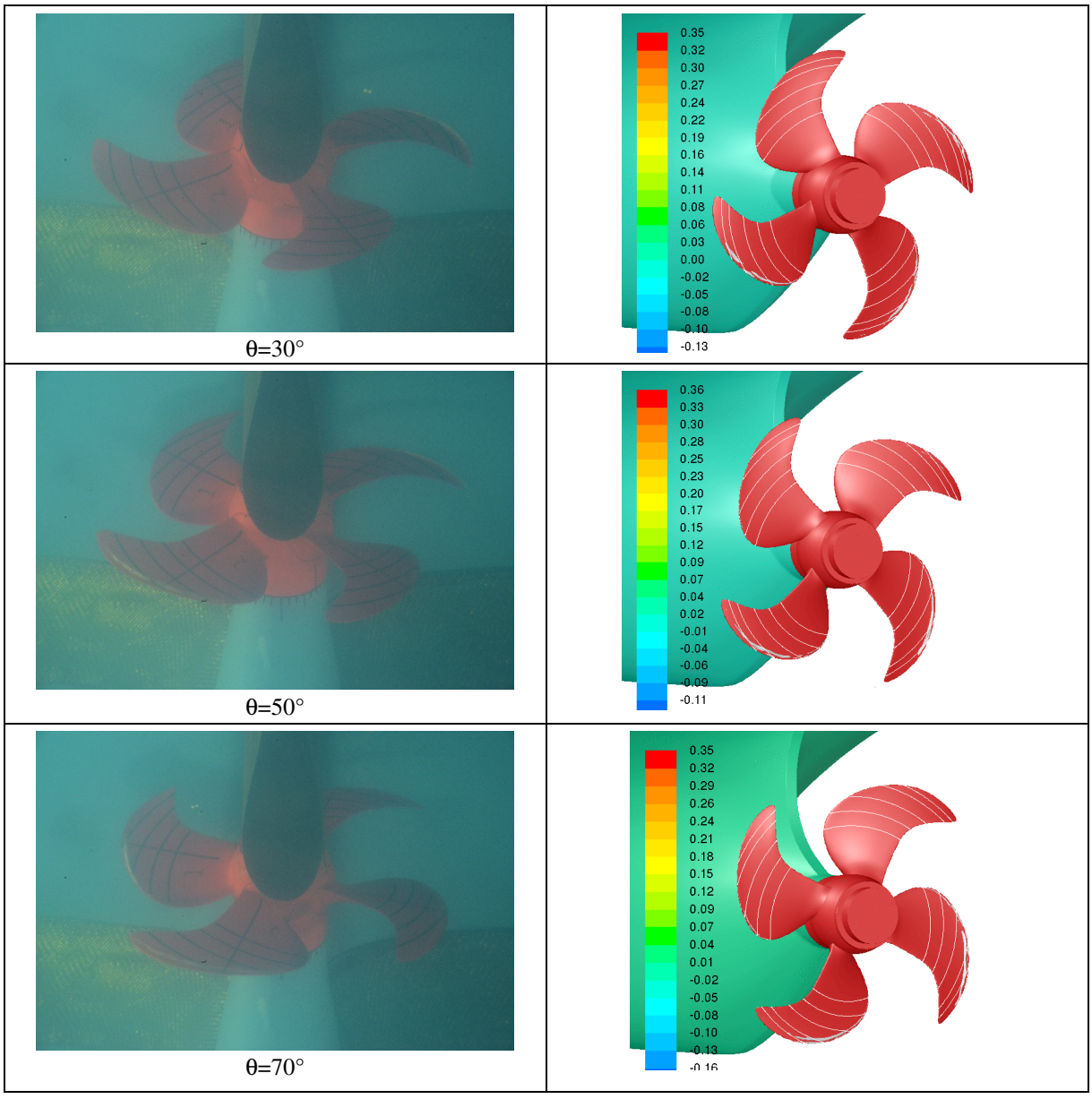

Figure 4 Cavitation patterns, experiment observations vs. DDES prediction

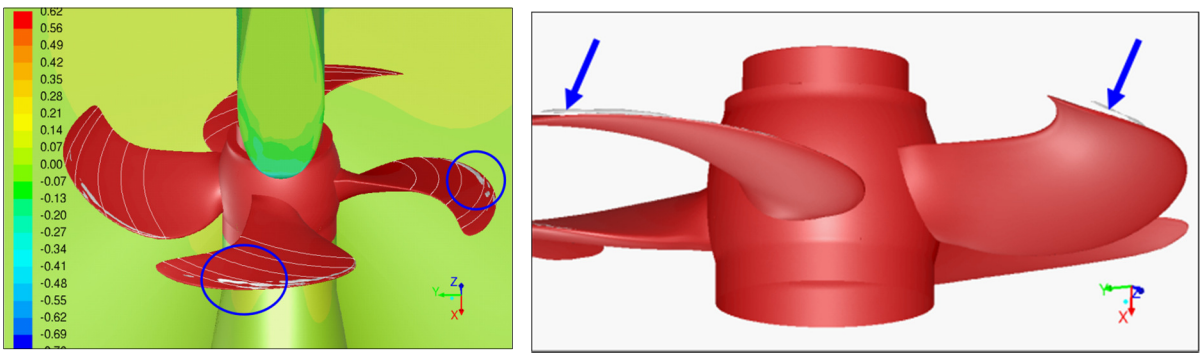

Figure 5 The shedding and raise up of LE cavity

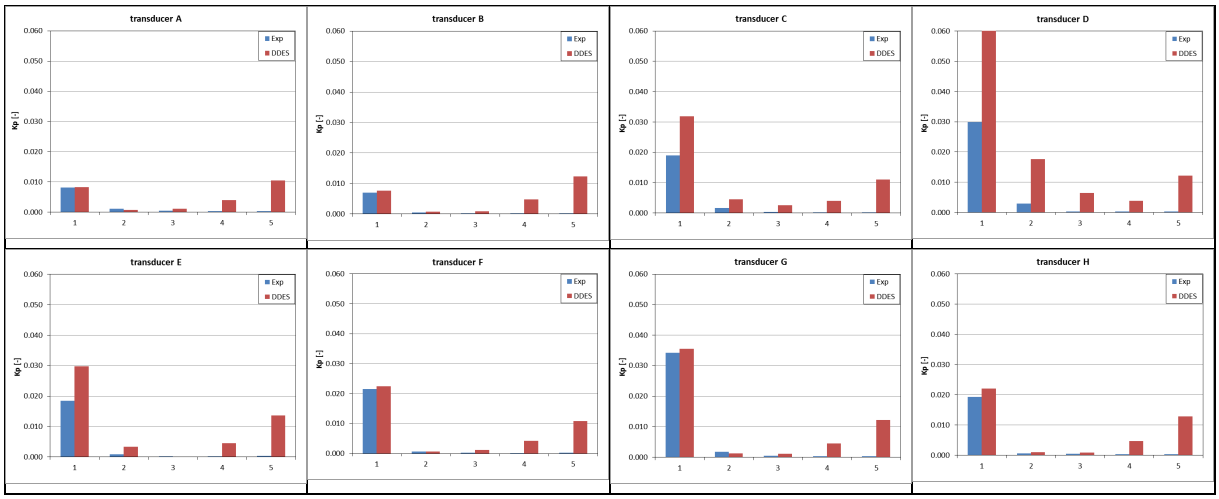

Figure 6 Pressure pulses at harmonic modes, Exp. vs. DDES

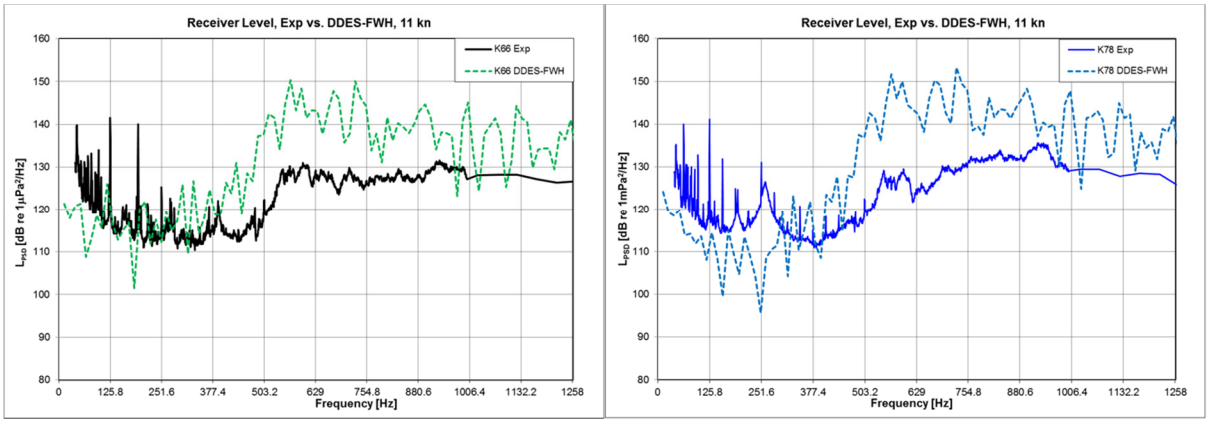

Figure 7 Receiver level noise at hydrophone K66 (left) and K78 (right), Exp. vs. DDES

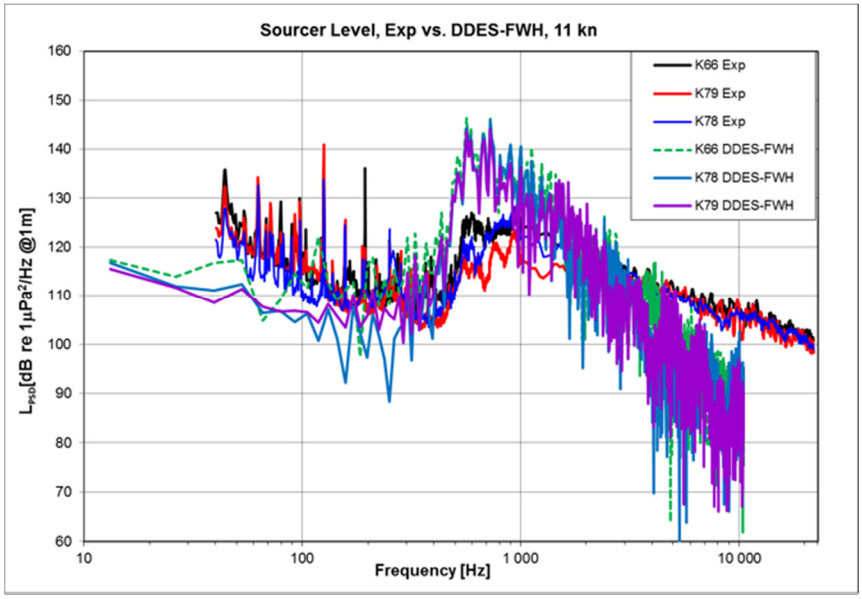

Figure 8 Source level URN, Exp. vs. DDES

Using the FW-H equation for hydroacoustics of propellers

Thomas P. Lloyd[a,b], Artur K. Lidtke[b], Douwe R. Rijpkema[c], Erik van Wijngaarden[c], Stephen R. Turnock[b], Victor F. Humphrey[d]

[a]MARIN Academy, Wageningen, NL (t.lloyd@marin.nl); [b] FSI Group, University of Southampton, Southampton, UK; [c]MARIN, Wageningen, NL; [d] ISVR, University of Southampton, Southampton, UK;

1 Introduction

Marine propeller noise and vibration has been studied in order to reduce acoustic signature, improve fatigue life and comfort onboard, and, more recently, to quantify the impact of maritime noise on the environment. Therefore the importance of acoustic measurements and simulations has increased. Acoustic simulations offer the advantages of avoiding vibration effects on measurement data, as well as the free placement of probes. These are not without difficulty however, and require robust verification, especially in the maritime field, where hydroacoustic computations are relatively uncommon.

An attractive approach for making hydroacoustic predictions is an *acoustic analogy*, such as that of Ffowcs Williams and Hawkings (1969). The processes of sound generation and propagation are then conveniently separated, and acoustic predictions may be made as a post-processing of a hydrodynamic simulation. Since the precise location of the acoustic sources, such as cavitation and non-linear wake flow, are not known *a priori* in maritime applications (unlike in aeronautical applications, where, at low Mach number, they are assumed coincident with the blade surfaces), the *porous* formulation of the Ffowcs Williams-Hawkings (FW-H) equation is typically preferred (Di Francescantonio, 1997). In this case, the propeller is surrounded by a porous data surface (PDS) upon which velocity and pressure fluctuations representing the acoustic sources are extracted from a computational fluid dynamics (CFD) simulation.

Uncertainty remains, however, regarding how best to use this method in practice. This is motivated by research showing that the propeller tip vortex may be a non-negligible noise source for non-cavitating conditions (Ianniello *et al.*, 2013; Felli *et al.*, 2015). Ianniello *et al.* (2013) and Lloyd *et al.* (2015) used an open-ended PDS to avoid the wake penetrating the downstream end cap, but did not investigate the effect of this. While similar studies have been performed in the aeroacoustics community for jet flows *e.g.* see Rahier *et al.* (2004), general experience of using such methods for marine propellers is not widespread (Ianniello and De Bernardis, 2015; Lloyd *et al.*, 2014; Lidtke *et al.*, 2015).

In this paper we detail a study into appropriate use of the FW-H acoustic analogy for making hydroacoustic predictions of marine propellers. Two CFD codes (ReFRESCO and OpenFOAM®) are used in order to provide additional verification. We focus on issues from the literature resulting from the simulation of a realistic propeller flow (*e.g.* Ianniello and De Bernardis, 2015), addressing two main questions, namely: how does closure of the PDS in the propeller wake affect the acoustic pressure prediction?; and what is the effect of the axial extent of the PDS in the downstream direction?

2 Theoretical and numerical background

The numerical approach involves solving the Ffowcs Williams-Hawkings equation for the acoustic pressure using source data derived from an unsteady, incompressible Reynolds-averaged Navier-Stokes (RANS) computation. The solution to the FW-H equation, assuming free-field propagation, negligible density fluctuations and a stationary porous data surface may be written as

$$4\pi p'(\boldsymbol{x},t) = \underbrace{\int_S \frac{\rho_0 \dot{u}_n}{r} dS(\boldsymbol{y})}_{\text{monopole, } p'_0} + \underbrace{\int_S \frac{\dot{p}\hat{\boldsymbol{n}}\cdot\hat{\boldsymbol{r}}}{c_0 r} dS(\boldsymbol{y})}_{\text{dipole, } \dot{p}'_1} + \underbrace{\int_S \frac{p\hat{\boldsymbol{n}}\cdot\hat{\boldsymbol{r}}}{r^2} dS(\boldsymbol{y})}_{\text{dipole, } p'_1} + \underbrace{\int_S \frac{\rho_0(u_n\dot{u}_r)}{c_0 r} dS(\boldsymbol{y})}_{\text{non-linear, } \dot{p}'_2} + \underbrace{\int_S \frac{\rho_0 u_n u_r}{r^2} dS(\boldsymbol{y})}_{\text{non-linear, } p'_2}, \tag{1}$$

where p' is the pressure fluctuation at the receiver location $\boldsymbol{x}$, the porous data surface S is located at $\boldsymbol{y}$ and r is the source-receiver distance; ρ_0 and c_0 are the fluid density and sound speed; p and u are pressure and velocity, while $\dot{()}$ indicates a time derivative. The subscripts n and r denote dot products with the unit vectors in the normal ($\hat{\boldsymbol{n}}$) and radiation ($\hat{\boldsymbol{r}}$) directions respectively. The terms on the *r.h.s.* are referred to using their multipole order *i.e.* p'_k where 2^k gives the multipole order. Equation 1 has been implemented into ReFRESCO and OpenFOAM® as a run-time post-processing module.

For brevity, we include only brief details here of our hydrodynamic simulation setup; full details may be found in our previous papers (Lidtke *et al.*, 2015; Lloyd *et al.*, 2014, 2015). We used structured grids, designed to better resolve pressure fluctuations. Discretisation schemes were all second-order, apart from turbulence model variables, where a first-order scheme was used. The $k-\omega$ *SST* 2003 model has been used to account for the effect of turbulence.

3 Results for canonical sources

In order to allow controlled investigation of the behaviour of the porous data surface, simulations of canonical monopole and dipole sources were performed. Thus the effect of removing PDS panels could be investigated by comparison to an analytical solution. A chosen pressure amplitude was achieved by prescribing appropriate expressions for pressure and velocity fluctuations inside a cubic domain. Within *OpenFOAM*, values are specified inside every cell, while for *ReFRESCO* time-dependent boundary conditions are used to solve for the field values. These data are then supplied to the PDS in order to make FW-H acoustic predictions. Different porous data surfaces were used in each code: a spherical one of radius 0.1 m in *OpenFOAM* with data extracted directly from cell faces; and a cubic one of side length 0.2 m in *ReFRESCO*, with values interpolated from the flow solution. The simulations used a source frequency of 100 Hz and receiver distance of $r = 1$ m, which were chosen as typical values for propeller near-field pressure fluctuations (as reported in the next section).

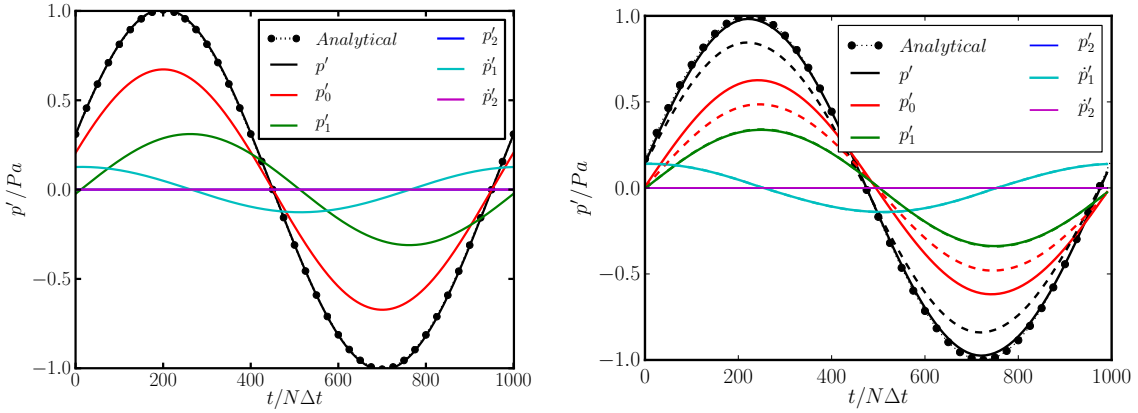

(a) *OpenFOAM®* (b) *ReFRESCO*

Figure 1: FW-H prediction of pressure due to dipole source, compared to analytical solution: relative integrated contributions from each acoustic analogy source term for frequency $n = 100$ Hz and receiver at $|\mathbf{r}| = 1$ m. See Equation 1 for source term definitions. Maximum pressure amplitude is $|p'| = 1$ Pa.

Figure 1 shows examples of the computed pressure signals for both *OpenFOAM®* (left) and *ReFRESCO* (right) sources. In both cases, an almost perfect agreement with the analytical value is achieved. Thus differences in the numerical approach between the two codes have not have a significant effect on the results. We observe that the signal consists of contributions from both dipole terms (p'_1 and $\dot{p}'_1$) as well as the monopole. By contrast, a monopole source (not shown) is modelled numerically as a pure monopole (p'_0 only). The non-linear terms are zero, as expected. Changes in the relative contributions of the FW-H terms were also seen for increasing source frequency and receiver distance, *i.e.* moving from acoustic near-field to far-field, for both monopole and dipole sources. This highlights the fact that sources become modelled by a combination of terms when using the porous FW-H method.

More relevant to the current study is the effect of removing panels from the PDS on the computed pressure signals. To illustrate this, in Figure 1b, we also include data from a simulation using an open PDS. The "missing" panels are those with $\hat{n}_z = \pm 1$ while the receiver is located at $\hat{r}_x = 1$. This setup offered some similarity to the true propeller configuration (see Section 4) where receivers are located above the wake region and the downstream end of the PDS left open. Note also that the "line-of-sight" between source and receiver *does* intersect the PDS.

The result is a reduction in the computed pressure amplitude due to the inadequate numerical representation of the source. More interesting is the fact that this under-prediction is associated entirely with the p'_0 term of the FW-H equation. We can explain this by examining Equation 1, where it is easily observed that p'_0 is the only term to not contain any dependency on $\hat{\boldsymbol{r}}$. Thus, while a dipole or non-linear source could be accurately represented using an open surface as long as the source-receiver line-of-sight intersects the PDS, this is not the case for a monopole, where the total integrated velocity flux on the PDS must equal the source strength. This finding is different from that of Freund *et al.* (1996), who concluded that a line-of-sight intersecting the PDS was sufficient. This simple observation has a significant implication when designing a PDS in more realistic scenarios, as addressed in the next section. We note however the fact that the propeller noise sources do not possess the same simple directionality as those treated here, meaning the "missing" panels may have less or more effect depending on their orientation.

4 Results for a marine propeller

Computations followed the setup of Lloyd *et al.* (2015), for the E779A propeller in open-water at an advance ratio of 0.88. Based on the findings of Lloyd *et al.* (2015), a single grid of 13 million cells was used, both for *ReFRESCO* and *OpenFOAM®* computations. The main difference between the solution approaches within the two codes is in the linear equation coupling. *OpenFOAM®* adopts a PISO-type algorithm, which uses a low number of predictor-corrector loops and a time step equivalent to 0.045 degrees rotation. *ReFRESCO* on the other hand uses the SIMPLE-type algorithm, which permits much higher time steps (three degrees was used in this study) but requires a higher number of loops.

Lloyd *et al.* (2015) showed that the pressure predicted by RANS and FW-H agreed well for probes located directly above the propeller; they did not evaluate probes above the wake however, which are addressed here. We also used a PDS closed at both ends; this results in the propeller wake penetrating the downstream *end cap*. Figure 2 shows the positions of the probes used and porous data surface configurations. These were chosen in order to elucidate how the end cap affects the acoustic prediction, and how this changes with probe location. Probes directly above the propeller were not affected by the chosen variations in PDS design, since here the noise is dominated by the rotating propeller blades.

Firstly, the flow solution from the two codes is compared in Figure 3. We show iso-surfaces and slices of vorticity magnitude as a means to visualise the wake flow. While the solutions are similar, it is noticeable that the tip vortex resolved using *OpenFOAM* propagates slightly further downstream than in *ReFRESCO*. In addition, higher levels of vorticity are seen in the wake. This is primarily due to the different time steps used, since most other setup parameters are the same. It is expected that this difference in the hydrodynamic solution may have an effect on the acoustic prediction, especially where the flow intersects the downstream end cap. We expect the tip vortex to be more important than the wake however, since the former provides the dominant contribution from non-linear sources (Felli *et al.*, 2015).

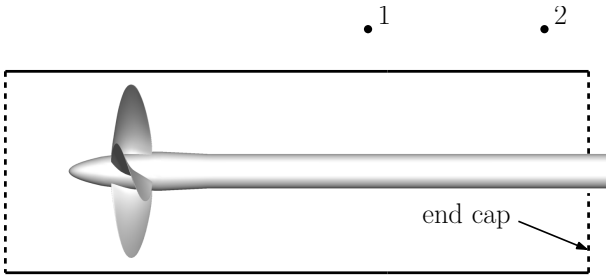

Figure 2: Layout of porous data surfaces and probe positions: solid - baseline; dashed - end caps. Inflow from the left. Probes located on $y = 0$ plane, at $x/D_P = -1.15$ and 2.00.

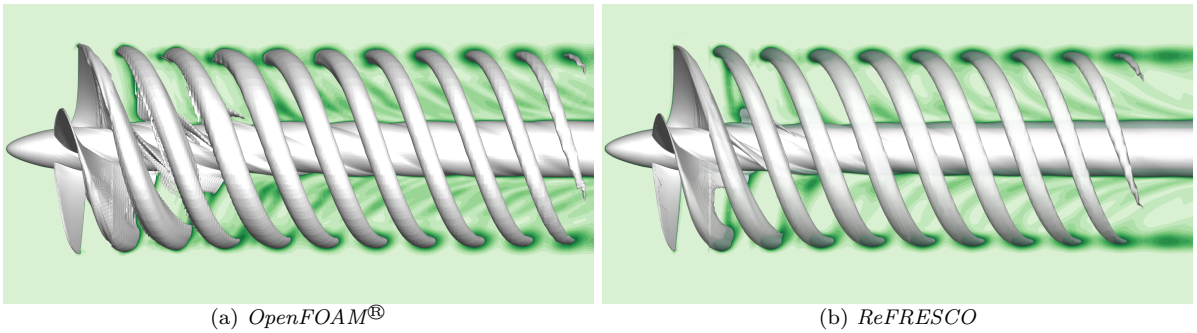

(a) *OpenFOAM®* (b) *ReFRESCO*

Figure 3: Propeller wake visualisation: iso-surface of normalised vorticity magnitude $|\omega|^* = |\omega|/n = 4$; and $y = 0$ slice of $|\omega|^*$ in range 0 (light) to 4 (dark) with an increment of 0.4.

Figures 4 shows the contribution from each PDS panel to the total pressure signal at Probe 2, for each of the FW-H source terms ($\dot{p}'_1$ and $\dot{p}'_2$ are almost zero and therefore not shown). Although the tip vortices have been resolved up to the axial location of the probe, the wake flow is not fully captured using the RANS approach, and DES may be preferable if probes further downstream are of interest (Ianniello and De Bernardis, 2015). The monopole source shows a contribution from the blades, even at two diameters downstream (Figure 4). Traces of the tip vortices (and wake) are also seen, both on the cylinder and end cap. The dipole term gives only a very localised contribution, and is small compared to other two terms shown. The non-linear source shows a different distribution (Figure 4), concentrated close to the probe. Especially notable is the high source level on the end cap, which is stronger at the top due to the close proximity to the chosen probe location. The combined effect of the sources can be seen in Figure 4. Here the contribution from the blade monopoles is still seen, while both the monopole and non-linear terms are evident on the end cap.

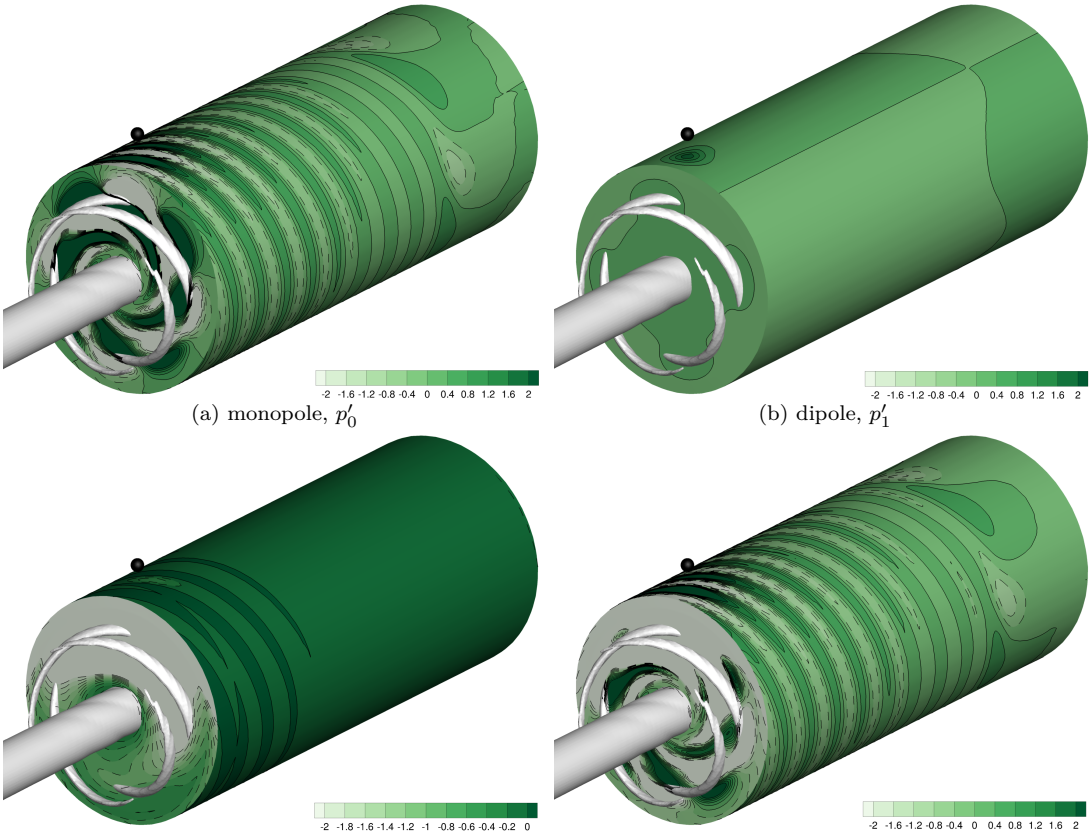

(a) monopole, p'_0 (b) dipole, p'_1

(c) non-linear, p'_2 (d) total source, p'

Figure 4: Tip vortices and acoustic sources: iso-surface of $\omega^* = 4$; instantaneous acoustic sources on closed porous data surfaces (contribution per panel for Probe 2). Probe location shown as black dot.

We now show time traces and harmonic components of the signals at Probes 1 and 2, for Open and Closed surfaces (Figure 5). Each plot contains a comparison between *ReFRESCO* (black) and *OpenFOAM®* (green) results. For each subfigure, the left plot contains harmonic components and time traces of the RANS and FW-H signals; the right plot shows a breakdown of the FW-H terms.

Beginning with Probe 1, the *OpenFOAM®* results are clearly more affected by numerical noise than *ReFRESCO*, and do not exhibit a periodic behaviour. A difference in the pressure amplitude is also seen between the two data sets, both for FW-H and RANS results, although the FW-H consistently over-predicts compared to the RANS. The increase in the *ReFRESCO* FW-H pressure amplitude between Figures 5a and 5b is attributed to a high non-linear contribution due to the surface end cap.

For the Probe 2 (Figure 5c), the time traces look quite different. Here the expected pressure amplitudes are smaller than at Probe 1, hence numerical effects become more evident. The *OpenFOAM®* time-trace shows a large monopole source. While this does not appear directly in the harmonic components, due to its lower frequency, it suggests the simulation is not fully converged. For *ReFRESCO*, the Open surface is monopole dominated, with little non-linear contribution. In this case, the FW-H and RANS results lie close to one another. The Closed surface (Figure 5d) gives large ($\pm 15\ Pa$) anti-phase fluctuations of p'_0 and p'_2 due to the tip vortices penetrating the end cap. Here *OpenFOAM®* and *ReFRESCO* show very similar behaviour. This cannot be viewed as physical, and results in a much higher FW-H pressure amplitude than the RANS value. It seems that both monopole and non-linear sources are incorrectly represented when the end cap cuts the vortical wake, as seen in Figure 4. This is similar to the finding of Rahier *et al.* (2004), who observed that quadrupoles were over-predicted if the surface was not extended far enough downstream.

This behaviour is different from Figure 5b, where the probe is located further from the end cap, which reduces the contribution from the non-linear term. The monopole term then gives the largest contribution, since it only decays as $1/r$ compared to $1/r^2$ for the other terms. The Open surface (Figure 5c) removes the unphysical sources but underpredicts the pressure amplitude due to the "missing" part of the monopole source, as shown in Section 3.

5 Concluding remarks

The focus of this study was on noise prediction using an acoustic analogy, for probes above the wake of an open-water propeller. Canonical sources were also used to investigate the effect of removing parts of the porous data surface. It was found that the monopole term is underpredicted in this case, while the other terms would only be affected if panels intersecting the source-receiver line-of-sight were removed.

Unlike other studies in this area (Ianniello and De Bernardis, 2015), we also use visualisation of the acoustic source information in conjunction with pressure time traces (and harmonic analyses) to evaluate the dominant effects. It was found that probes located closer to the downstream end of the porous data surface were more sensitive to the inclusion of a closing end cap. In this case, the vortical wake directly enters into the acoustic source representation, contradicting the theoretical formulation, which is the typical justification for omitting the end cap (Ianniello and De Bernardis, 2015).

Comparison of two CFD codes revealed the sensitivity of acoustic predictions to numerical noise, as particularly seen in *OpenFOAM®*, since the pressure amplitudes for probes in the wake region are typically small compared to those above the propeller. The numerical convergence of the *OpenFOAM®* results could be improved if a longer simulation time were possible. This is somewhat restricted by the small timestep imposed by the PISO algorithm.

It remains unclear whether the contribution to the pressure signal at such locations is purely due to nonlinear sources, as previously claimed (Ianniello *et al.*, 2013). We find that, for open surfaces, the largest contribution to the computed pressure signals is *modelled numerically* by the monopole term of the FW-H equation. In addition, visualisation of the source data clearly showed contributions from the blades themselves, as well as the tip vortices (which could be separated in future computations). This finding will have implications when simulating cavitating conditions, since omitting the surface end caps may then result in incomplete modelling of this monopole-type source.

References

Di Francescantonio, P. (1997), A new boundary integral formulation for the prediction of sound radiation. *Journal of Sound and Vibration*, **202**(4): pp. 491–509, doi:10.1006/jsvi.1996.0843.

Felli, M., Falchi, M. and Dubbioso, G. (2015), Hydrodynamic and hydroacoustic analysis of a marine propeller wake by TOMO-PIV. In: *Proceedings of the 4th Symposium on Marine Propulsors*, 31st May-4th June, Austin.

Ffowcs Williams, J.E. and Hawkings, D.L. (1969), Sound generation by turbulence and surfaces in arbitrary motion. *Philosophical Transactions of the Royal Society A: Mathematical, Physical and Engineering Sciences*, **264**(1151): pp. 321–342, doi:10.1098/rsta.1969.0031.

Freund, J.B., Lele, S.K. and Moin, P. (1996), Calculation of the radiated sound field using an open Kirchhoff surface. *AIAA Journal*, **34**(5): pp. 909–916, doi:10.2514/3.13167.

Ianniello, S. and De Bernardis, E. (2015), Farassat's formulations in marine propeller hydroacoustics. *International Journal of Aeroacoustics*, **14**(1-2): pp. 87–104, doi:10.1260/1475-472X.14.1-2.87.

Ianniello, S., Muscari, R. and Mascio, A. (2013), Ship underwater noise assessment by the acoustic analogy. Part I: nonlinear analysis of a marine propeller in a uniform flow. *Journal of Marine Science and Technology*, **18**(4): pp. 547–570, doi:10.1007/s00773-013-0227-0.

Lidtke, A.K., Turnock, S.R. and Humphrey, V.F. (2015), Use of acoustic analogy for marine propeller noise characterisation. In: *Proceedings of the 4th Symposium on Marine Propulsors*, 31st May-4th June, Austin.

Lloyd, T.P., Rijpkema, D. and van Wijngaarden, E. (2014), Implementing the Ffowcs Williams-Hawkings acoustic analogy into a viscous CFD solver. In: R. Bensow (ed.), *17th Numerical Towing Tank Symposium (NuTTS)*, 28-30th September, Marstrand, Sweden.

— (2015), Propeller acoustic modelling: comparing CFD results with an acoustic analogy approach. In: *Proceedings of the 4th Symposium on Marine Propulsors*, 31st May-4th June, Austin.

Rahier, G., Prieur, J., Vuillot, F., Lupoglazoff, N. and Biancherin, A. (2004), Investigation of integral surface formulations for acoustic post-processing of unsteady aerodynamic jet simulations. *Aerospace Science and Technology*, **8**(6): pp. 453–467, doi:10.1016/j.ast.2004.04.005.

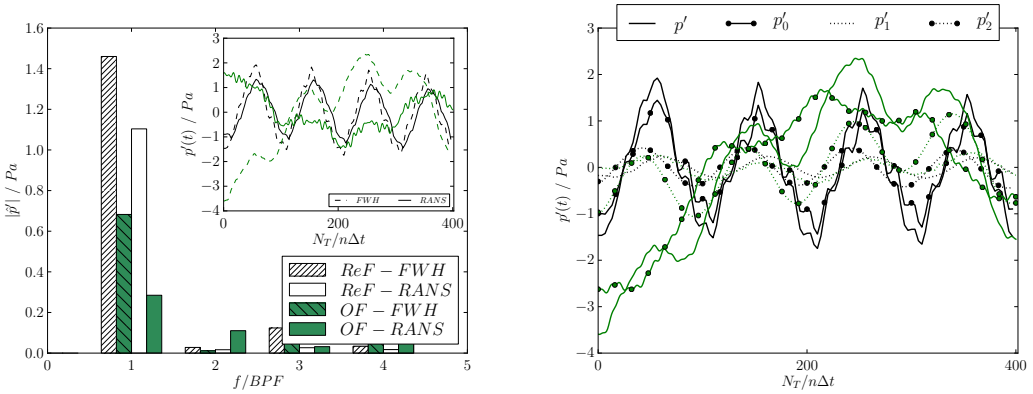

(a) Open, Probe 1

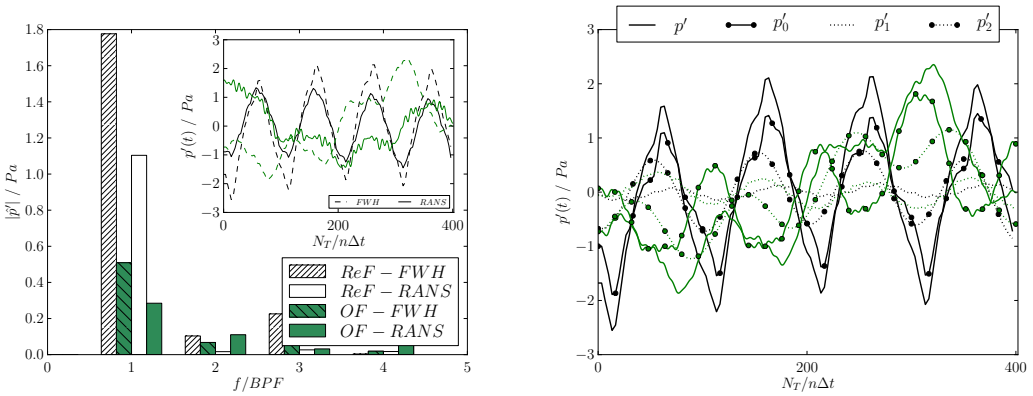

(b) Closed, Probe 1

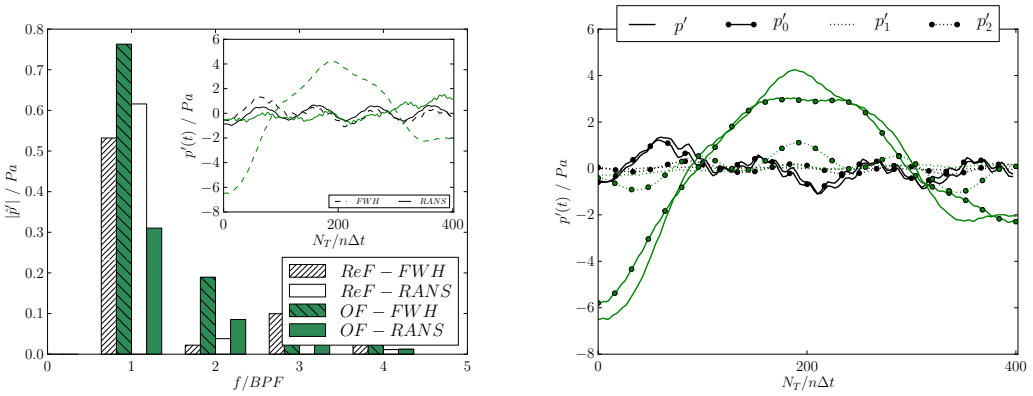

(c) Open, Probe 2

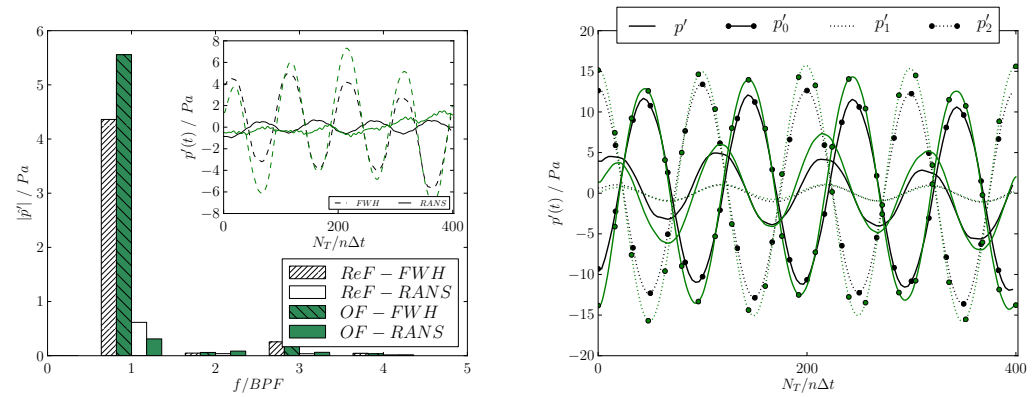

(d) Closed, Probe 2

Figure 5: FW-H pressure signals compared to RANS data for different PDS setups and probe locations: harmonic components and total signal (left column) and FW-H components (right column). *OpenFOAM*® results shown in green, *ReFRESCO* in black.

Adaptive Mesh Technology in Marine CFD Simulations

Benoit Mallol, **Barbara D'Aube**, NUMECA International, Brussels/Belgium,
benoit.mallol@numeca.be

The global objective of each numerical scheme is to obtain a sufficiently good overall result with the least computational effort. Numerical adaptivity in CFD describes techniques and procedures to adapt the local flow solution scheme only in regions where it matters. But how does the CFD code know how accurate it has to be at which location? It is the gradients that matter. Gradients can be spatial gradients, e.g. regions in the flow field where severe changes in the flow quantities take place within a very limited spatial region. Examples for high spatial velocity gradients are the boundary layer around the ship hull or on the propeller blades, where the flow velocity changes from zero on the wall to full speed within a very small distance. Another example is the density gradient at the free surface. Similar to spatial gradients, temporal gradients exist in unsteady flow fields, e.g. impact investigations or sliding grid propeller simulations.

The most important factors of numerical accuracy are mesh resolution (and quality) and the order of the numerical scheme. Consequently, we use these two key factors in order to improve or reduce the local accuracy. In most people's mind, adaptation refers to refinement, but adaptation also means de-refinement in regions or in times where a high resolution is not necessary.

Grid adaptation works by modifying the numerical grid, hence the local resolution of the discretization scheme according to the gradients of the flow as discussed above. There are two different methods for grid adaptation:

1. Redistribution, also called r-adaptation. Here, the mesh distribution is modified in accordance with the flow gradients. Number of mesh nodes, mesh topology and connectivity remain unchanged. The redistribution is achieved by moving grid points or lines around, following the flow gradients. This method is limited, since a refinement in one area may result in excessive coarsening in another. An advantage is that r-adaptation can in principle be applied for structured grids also, while most other methods only work for unstructured grids. Grid quality however, might be difficult to control or maintain.

2. h-adaptation adds or removes mesh points. Number of nodes, node distribution and mesh topology generally change. Various strategies exist for h-adaptation. Simple procedures subdivide cells, more complex strategies insert or remove cells. h-adaptation requires un-structured grids.

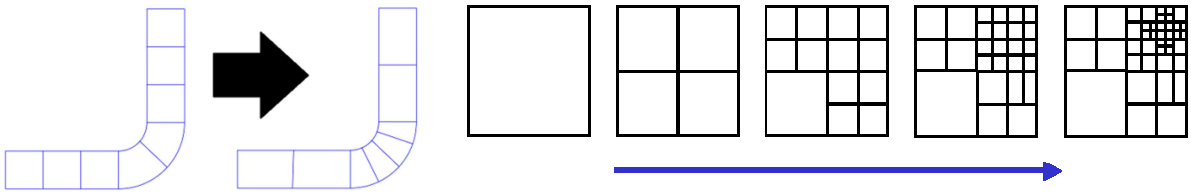

Fig.1: Simple r-adaptation (left), *CFD Online (2012)*, and h-adaptation (right), *Mevis Research*

Adapting the resolution of the numerical scheme to the flow gradients (p-adaptation) can also be achieved by changing the polynomial order of the numerical scheme. Most CFD solvers today are (theoretically) second order in space. However, this only holds true for smoothly varying grids. And most practical grids are definitely not smoothly varying. p-adaptation may increase from second order to higher orders. Consequently scheme "coarsening" can be accomplished by reducing the order.

Mesh and scheme adaptation procedures can also be combined. These techniques are then called e.g. hp-adaptation.

All applications of technical adaptivity presented in the frame of this paper are performed using FINE™/Marine, e.g. *Visonneau et al. (2012).* It incorporates the following modules:

1. Mesh generator HEXPRESS™: A full hexahedral unstructured mesh generator, capable of solver driven mesh refinement and coarsening (h-adaptation). It features body fitted meshes with a high quality boundary layer resolution. Grid refinement and coarsening, during the initial generation process as well as in later adaptations is achieved by means of hanging nodes, Fig. 2. Fig. 3 shows an example of a HEXPRESS™ mesh of ship hull appendages.

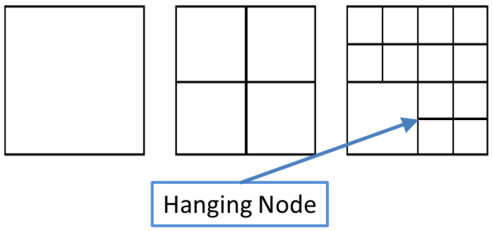

Fig. 2: Hanging Node, *Mevis Research*

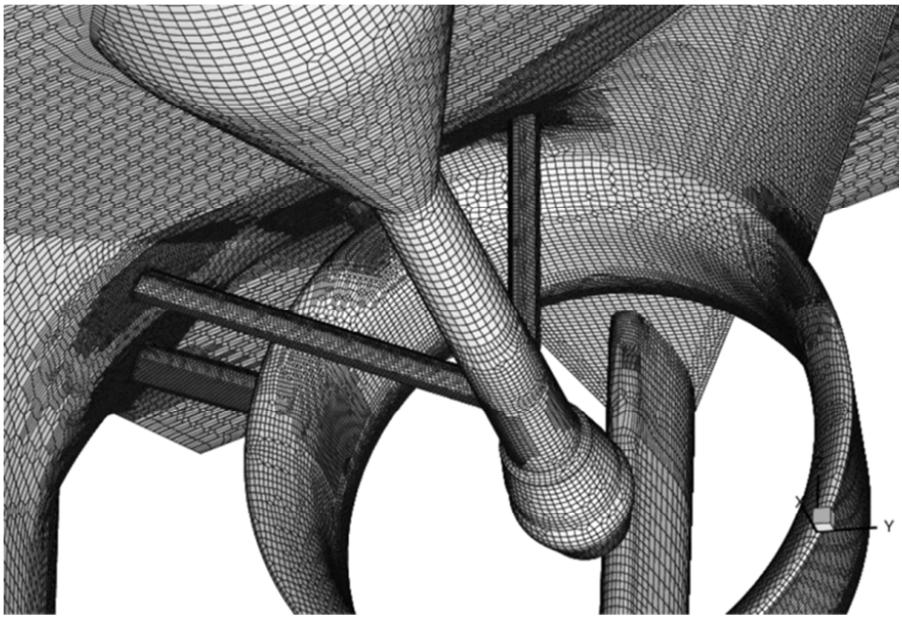

Fig. 3: HEXPRESS™ mesh

2. The flow solver inside FINE™/Marine (ISIS-CFD) is a steady and unsteady incompressible free-surface RANS-Code (Reynolds-Averaged-Navier-Stokes) presented in detail by *Duvigneau et al. (2003)*, *Queutey and Visonneau (2007)*. The spatial discretisation of the transport equations is accomplished by a finite volume method. The velocity field is obtained from the momentum conservation equations and the pressure field is extracted from the mass conservation constraint, or continuity equation, transformed into a pressure equation, *Schrooyen et al. (2014)*. Pressure-velocity coupling is obtained through a Rhie & Chow SIMPLE type method. No specific requirements for the topology of the cells are imposed. The grid can be completely unstructured and cells with an arbitrary number of arbitrarily-shaped faces are accepted. Several turbulence models ranging from relatively simple one-equation Spalart-Almaras to advanced EARSM (Extended Algebraic Reynolds Stress) models, *Duvigneau et al. (2003)*, are implemented. Free-surface flow is represented by a VOF (Volume of Fluid) technique with an interface capturing approach. Both non-miscible flow phases (air and water) are modelled through a conservation equation for a volume fraction of phase. The free-surface location corresponds to the iso-surface with a volume fraction of 0.5. To avoid smearing of the interface, the volume fraction transport equations are discretized with a specific discretization scheme, which ensures the accuracy and sharpness of the interface, *Queutey and Visonneau (2007)*. Furthermore, the flow solver features 6 DOF motion for the simulation of freely moving ships, *Leroyer and Visonneau (2005)*. Parallelisation is based on domain decomposition.

3. Flow visualisation system CFView™: This system incorporates also marine specific plug-ins. The visualisation of characteristic features such as wave patterns, the free surface, wetted surface as well as the calculation of forces, momentum and angles is done by a mouse-click.

FINE™/Marine incorporates adaptive grid refinement (AGR). When a flow simulation with adaptive grid refinement is launched, the refinement procedure is called every *n* time steps in order to keep the grid adapted to the evolving flow solution. Usually, the flow solver is first run on the initial mesh for a given number of times steps, after which the adaptation algorithm is activated. The existing flow solution is then evaluated and in case one or several adaptation criteria indicate the mesh is too coarse at certain locations, the cells in question are refined, or cut. The flow solution of the previous step is then interpolated on the refined (=adapted) grid and the flow solver continues for a given number of iterations. Thereafter, the adaptation procedure is called again, and the adaptation criteria are applied. In addition to the first step, all further adaptation steps may refine or de-refine. This cycle is then repeated a number of user defined time steps. This technique is described in more detail e.g. in *Wackers et al. (2010a,b,2011)*. It is designed with a broad range of applications in mind and written in an as general way as possible, *Visonneau et al. (2012).* To ensure even processor loads with adapting meshes, the newly created cells are distributed automatically between the partitions by the flow solver. Hence the total number of cells on each processor is comparable and an efficient usage of all processors is achieved. Several refinement criteria are available and can be selected separately, combined or in succession of each other according to the task at hand. Examples are:

- Free surface criterion: Since the free surface is clearly characterised by the gradient of the volume fraction normal to the surface, the refinement is employed to refine the grid in the direction normal to the surface only. In large regions of the flow domain this directional (= anisotropic) refinement will be applied in order to keep the number of additional grid points as low as possible. The resulting zone of directional refinement includes the undisturbed water surface, as well as smooth wave patterns. Only in cases where the free surface seriously deviates from the main grid directions, such as breaking waves, isotropic refinement is used, *Wackers et al. (2010a)*.

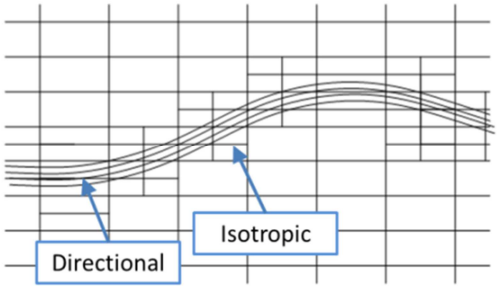

Fig. 4: Directional and isotropic refinement at the free surface, *Wackers et al. (2010a*)

- Gradient criteria: A second group of refinement criteria is based on the absolute values of the gradients of solution quantities in each cell. These criteria detect the regions where the flow field changes rapidly; they react to most features of a flow and are thus more general than the free-surface criterion. Also, they are obviously not restricted to the vicinity of the free surface and can refine in the whole computational domain. Three gradient criteria are available in FINE™/Marine: Pressure gradient, velocity gradient and vorticity gradient.

- Hessian based criteria: This criterion works with the second spatial derivative of the pressure. It is a very robust refinement criterion, yielding good results for a variety of applications. In contrast to velocity based gradients, it does not introduce any unnecessary refinement into the already refined boundary layer, *Wackers et al. (2014)*.

Fig. 5 shows the effect of mesh adaptation for an impacting cone probe, with splashing free surface and adapted mesh.

Fig. 6 highlights the efficiency of adaptive mesh refinement. In this case, the adapted mesh has only about 40% more cells than the initial mesh; still the surface wave pattern is considerably more detailed showing features which do not appear in the original mesh. Numerical experiments have shown, that similar or even better resolution of flow features can be obtained on properly adapted grids, having not even a fifth of the mesh count compared to a fine mesh without adaptation.

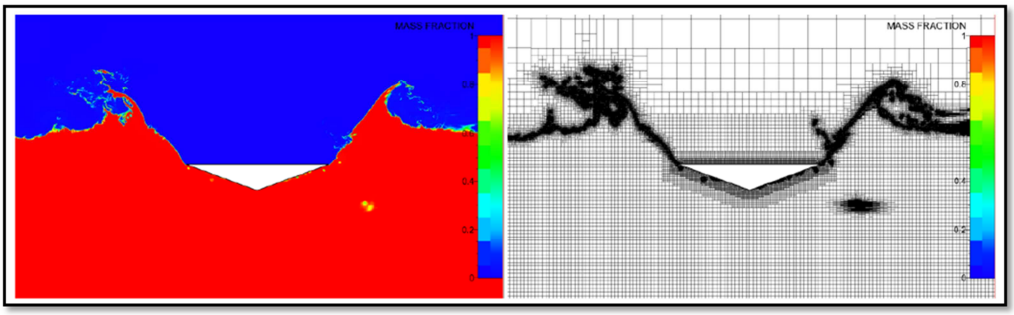

Fig. 5: Impacting probe and adapted mesh

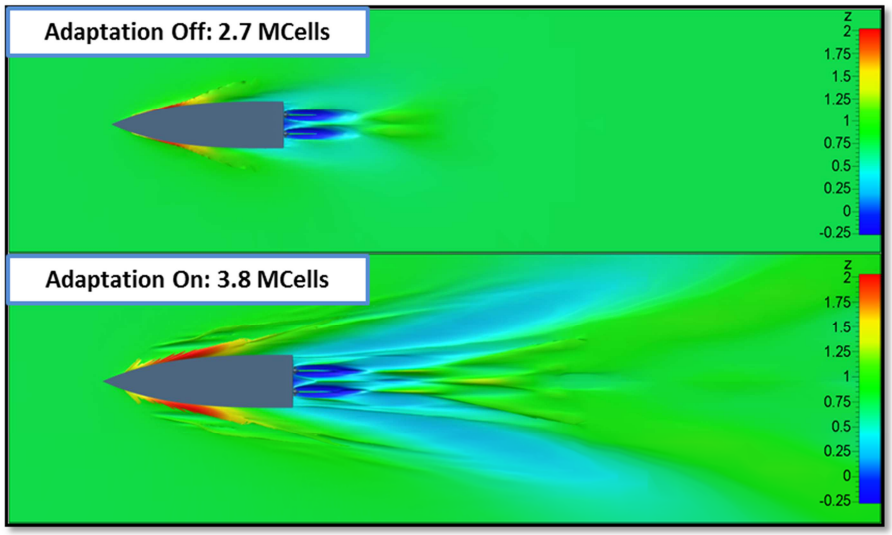

Fig. 6: Wave pattern without (top) and with (bottom) mesh adaptation

Despite all the intelligent features which increase the efficiency of computations, many CFD applications call for extreme computing power. Full (or more realistically nearly full) and automatic parallelisation is therefore important. But parallelisation of adaptive grids is not obvious. In non-adaptive calculations, usually a domain-decomposition is performed before the computation is initialised. The decomposed regions (partitions) of the grid are then distributed over the available cores, which may even have different individual performances. The number and size of the decomposed regions depend on the number and performance of the computing nodes. Each domain is then put on one core. The communication is ensured by parallel libraries, in the case of FINE™/Marine MPI (Message Passing Interface). For adaptive grids, the initially decomposed regions will not remain constant in size. The refinement (or coarsening) algorithm will alter the number of nodes in one partition. Keeping the original decomposition constant, would mean a severe degradation of computational performance due to load imbalance between the processors. So, a new decomposition and redistribution over the parallel hardware becomes necessary after each adaptation step. In FINE™/Marine the grid refinement is capable of dealing with massively parallel hardware. It includes an automatic dynamic load balancing which redistributes the refined grid over the already allocated cores when some regions have been refined or coarsened.

References

CFD Online (2012), http://www.cfd-online.com/Wiki/Mesh_adaptation

DUVIGNEAU, R.; VISONNEAU, M.; DENG, G.B. (2003), *On the role played by turbulence closures in hull shape optimization at model and full scale*, J. Marine Science and Technology 8/1, pp.1-25

LEROYER, A.; VISONNEAU, M. (2005), *Numerical methods for RANSE simulations of a self-propelled fish-like body*, J. Fluid & Structures 20/3, pp.975-991

MEVIS RESEARCH, http://www.mevis-research.de/~tp/LargeScaleFE

QUEUTEY, P.; VISONNEAU, M. (2007), *An interface capturing method for free-surface hydrodynamic flows*, Computers & Fluids 36/9, pp.1481-1510

SCHROOYEN, I.; RANDLE, K.; HERRY, B.; MALLOL, B. (2014), *A methodology for quick and accurate CFD calculations of self-propelled ships using sliding grids and dynamic RPM control*, 13th Conf. Computer and IT Appl. Maritime Ind. (COMPIT), Redworth, pp.49-59

VISONNEAU, M; QUEUTEY, P; DENG, G.B; WACKERS, J; GUILMINEAU, E; LEROYER, A; MALLOL, B, (2012), *Computation of free-surface viscous flows around self-propelled ships with the help of sliding grids*, 11th Conf. Computer and IT Appl. Maritime Ind. (COMPIT), Liege, pp.344-358

WACKERS, J.; AIT SAID, K.; DENG, G.B.; MIZINE, I.; QUEUTEY, P.; VISONNEAU, M. (2010a), *Adaptive grid refinement applied to RANS ship flow computation*, 28th ONR Workshop on Naval Hydrodynamics, Pasadena

WACKERS, J.; DENG, G.B.; VISONNEAU, M. (2010b), *Tensor-based grid refinement criteria for ship flow simulation*, 12th Numerical Towing Tank Symp. (NuTTS), Duisburg

WACKERS, J.; DENG, G.B.; VISONNEAU, M. (2011), *Combined tensor-based refinement criteria for anisotropic mesh adaptation in ship wave simulation*, ADMOS 2011, Paris

WACKERS, J.; DENG, G.B.; GUILMINEAU, E.; LEROYER, A.; QUEUTEY, P.; VISONNEAU, M. (2014), *Combined refinement criteria for anisotropic grid refinement in free-surface flow simulation*, Computers & Fluids 92, pp.209–222

Developing Tools for Assessing Bend-twist Coupled Foils

Laura Marimon Giovannetti, Joseph Banks, Stephen R. Turnock, Stephen W. Boyd,
University of Southampton, Southampton/UK, L.Marimon-Giovannetti@soton.ac.uk

1 Introduction

For many applications, the ability of a foil to passively adapt to the experienced fluid loading could be advantageous, Nicholls-Lee & Turnock (2007): e.g. wind or tidal turbine blades, hydrofoils for sailing yachts, or marine propellers. Composite materials provide the opportunity to tailor the bend twist coupling of a structure to achieve these goals, Veers & Bir (1998). To allow such foils to be designed and assessed, numerical tools such as finite element analysis (FEA) and computational fluid dynamics (CFD) will need to be coupled together in fluid-structure interaction (FSI) simulations. Currently, there is a lack of experimental validation data for FSI investigations. This paper details experiments conducted on a flexible NACA0015 foil.

2 Experimental Data

The experiments were conducted in the 3.5 m x 2.4 m RJ Mitchell wind tunnel at the University of Southampton, Fig.1. This closed circuit tunnel operates at wind speeds of 4 to 40 m/s with less than 0.2% turbulence. A six-component Nutem load cell balance is mounted on a turntable in the tunnel roof. This allows forces and moments to be measured in the turntable axis system about the balance centre 1.27 m below the tunnel roof. The aluminium beam protruding from the foil is attached to the overhead balance using a rigid clamping structure.

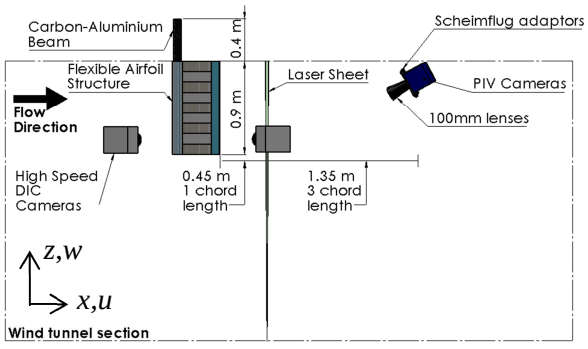

Fig.1: Schematic of experimental set up

Digital Image Correlation (DIC), Giovannetti et al. (2014), measured the full field deflection at the board tip. Particle Image Velocimetry (PIV) captured the position and strength of the tip vortex. Preliminary FSI simulations are compared to this data. Fig.2 shows the investigated NACA0015 foil.

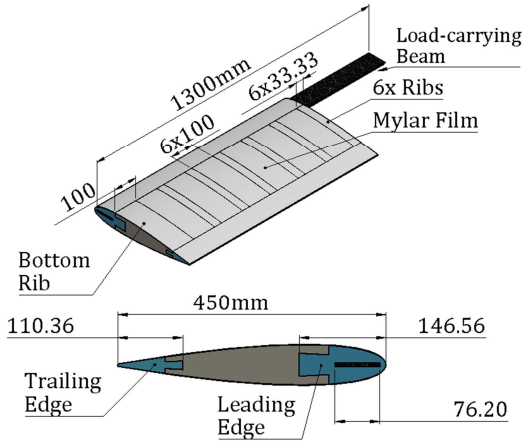

Fig.2: Tested foil design

The forces were measured at 1kHz and converted into the tunnel axis system to provide sideways lift coefficient (C_L), vertical force coefficient (C_Z) and drag coefficient (C_D).

A stereo DIC system was set up in the wind tunnel allowing 3D deflection data to be captured within a 0.5x0.5m field of view at the board tip. Fig.3 shows the DIC and PIV systems working simultaneously in the wind tunnel.

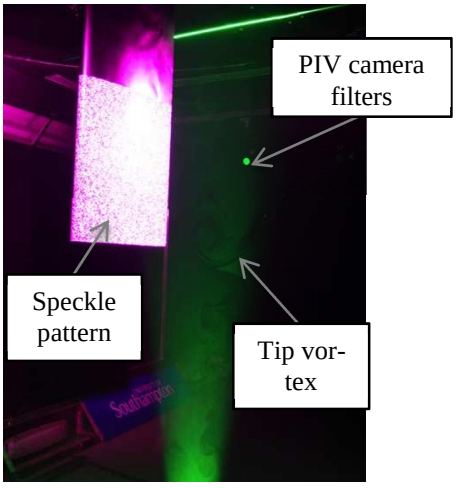

Fig.3: DIC and stereo-PIV set up

2.1 Flow field measurement

A PIV laser sheet was set up one chord (0.45m) behind the trailing edge of the foil and perpendicular to the flow direction. Two 29 MP cameras were positioned behind the board tip, with a 100mm Nikon lens providing a 0.4x0.11m area of interest. Seeding particles were introduced into the tunnel using a smoke machine on a timer. The time between the two image frames was set to ensure that most particles were observed in both frames. Then a series of 120 pairs of images were taken at a constant frame rate of 2Hz.

The angle of attack was set to 15°, and a range of wind tunnel speeds were tested. The images were processed using the LaVision software DaVis.

3 Numerical Simulations

A numerical model of the generic aerofoil structured tested in the wind tunnel is developed. The aim is to provide a numerical prediction of this structure to fluid loading validated with experiments. The numerical analysis has been approached systematically, firstly assessing the validity of the FEA model from a simple beam, building the geometry complexity to its final shape, containing the foam-rib structure as well as the Mylar sheet. Moreover, the coupling scheme between FEA and CFD solvers was investigated. The software used are ABAQUS 6.13 for the structural solver and Star-CCM+ 8.04 for the fluid solver.

In an FSI simulation, such as the one encountered, the sets of differential equations and boundary conditions associated with the fluid and structure domains must be satisfied simultaneously. The two domains are interconnected using the SIMULIA Co-simulation Engine (CSE) through a common physical interface surface that comprises of the aerofoil and 50 mm of the load-carrying beam, as in the wind tunnel experiments. In the co-simulation the nodal displacements are exported in the global coordinate systems from the FEA solver and the pressure normal to the element surfaces are imported back in the CFD environment.

3.1 Finite Element Analysis domain

In order to correctly reproduce the tested geometry in ABAQUS 6.13 it was necessary to model accurately the contact surfaces, joining them so that there was no relative motion between them.

Solid second order elements were chosen to represent the load-carrying beam as well as the foam structures and quadratic shell element were used to represent the Mylar sheet. Second-order element were chosen to avoid shear locking (i.e. occurring to first order elements subject to bending where parasitic shear are created) and hourglassing effects (i.e. occurring to first-order reduced integration elements in stress-displacement studies where the strains calculated at the integration points results as being zero).

The load-carrying beam was modelled as a solid composite section with one element through thickness as in composite sections each element contains the number of plies defined in the section (ABAQUS Simulia, 2013). In order to increase the accuracy of the results for the calculation of stresses and strains the number of integration points is increased to 21. This allows a smooth stress and strain distribution to be captured for each ply in the through thickness direction. Fig.4 shows the load-carrying beam with the aluminium section in the core, the two carbon plies as skin elements and the 21 integration points (i.e. blue dots within each material).

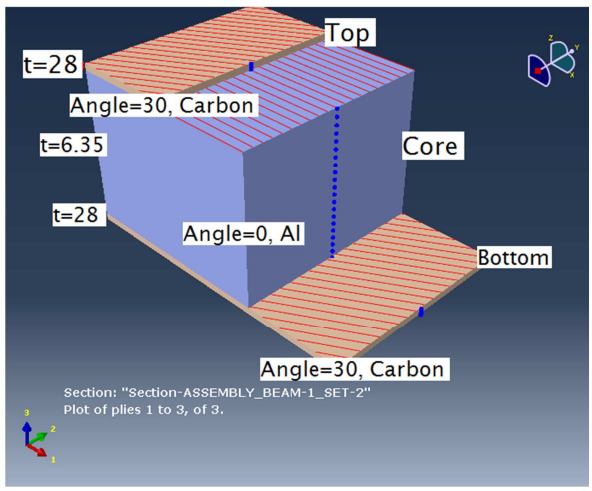

Fig.4: Composite beam structure representation for a ply angle of 30°.

Each element of the flexible aerofoil is meshed separately but consistency in nodes position was assessed, constraining the mesh size at the boundaries between each different structural element, so to ensure that the same number of nodes was kept at the interfaces.

Fig.5 shows a view of the complete wind tunnel geometry represented in ABAQUS. The boundary conditions set in the FEA environment replicate the ones encountered in the wind tunnel, fixing in translation and rotation the first 350 mm of the load-carrying beam. This region is therefore not modelled in the CFD as it is out-side the domain walls.

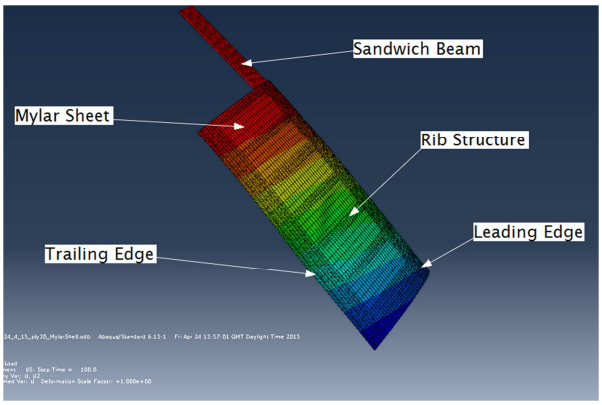

Fig.5: FEA structure comprising of the load-carrying beam, the foam and the Mylar structures

Table 1 shows the material properties used in the FEA model. The carbon and foam properties are anisotropic and aluminium and Mylar are considered isotropic materials.

Table 1: Material properties used in FEA model

Material	Property	Value
Aluminium	ρ	2.7 e^{-9} tonne mm^{-3}
	E	55000 MPa
	ν	0.35
Carbon	ρ	3 e^{-9} tonne mm^{-3}
	E_1	117940 MPa
	E_2	7840 MPa
	E_3	7840 MPa
	ν	0.25
	G_{12}	4400 MPa
	G_{13}	3600 MPa
	G_{23}	4400 MPa
Foam	ρ	3.6 e^{-12} tonne mm^{-3}
	E_1	10.4 MPa
	E_2	10.4 MPa
	E_3	10.4 MPa
	ν	0.3
	G_{12}	10.14 MPa
	G_{13}	10.14 MPa
	G_{23}	10.14 MPa
Mylar	ρ	1.39 e^{-9} tonne mm^{-3}
	E	283.509 MPa
	ν	0.35

3.2 CFD domain

We used the finite-volume RANSE solver Star-CCM+ 8.0.4 with the k-ω SST turbulence model. A dynamic implicit solution is chosen given the strong physical coupling deriving from the highly flexible specimen. In the implicit iterative approach the fields are exchanged multiple times per coupling step until an overall equilibrium is achieved prior to advancing to the next coupling step. The coupling step size need to be specified in the two solvers and define the period between the two consecutive exchanges, therefore the frequency of exchange between the analyses. Using a constant coupling size allows both analyses to advance while exchanging data at set target points according to:

$$t_{i+1} = t_i + \Delta t_c \qquad 3\text{-}1)$$

Δt_c is a value that defines the coupling step size to be used through the coupled simulation, t_{i+1} is the target time and t_1 is the time at the start of the coupling step, here 0.0025 s in both solvers.

The fluid domain was set as a box-section 10.7x3.5x2.4 m replicating the wind tunnel dimensions to correctly capture the fluid behaviour. The aerofoil was positioned 4 m downstream of the inlet, attached to the domain roof and centred in the cross-domain direction, as in the working section during the experiments.

The trimmer mesh with mesh morpher scheme was selected to allow the mesh to follow the nodal displacement given by the solid solver. Twelve prism layers were set along the aerofoil; the first prism layer thickness was set to y=6.55x10^{-4}m assuming y^+=50 for a base wind speed V_S=25 m/s. Mesh refinement regions were set around the aerofoil, especially around the leading edge, the root and tip as well as the root and tip vortices regions, Fig.6. The final mesh of the fluid domain had 2,500,000 cells.

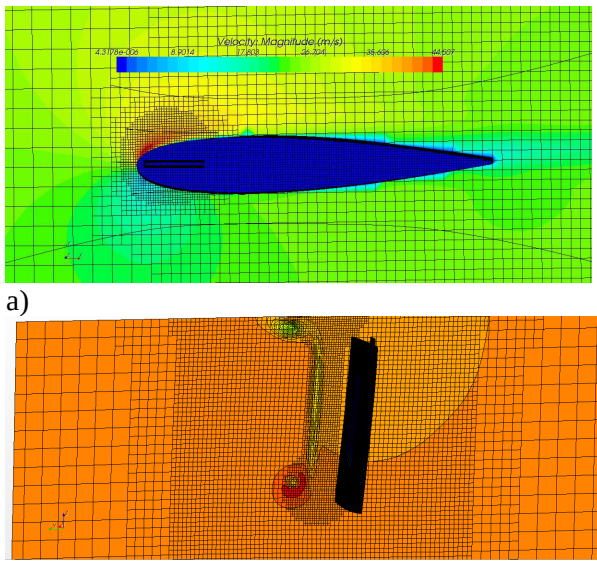

a)

b)

Fig.6: Mesh around the aerofoil and at a plane 1 chord downstream of the trailing edge - PIV laser sheet position.

4 Experimental Results

Fig.7 presents the results for the aerofoil tip deflection in the wind tunnel at different wind speeds for a steady angle of attack of 15°. Note the small discrepancies in measures for DIC-only runs and coupled DIC-PIV runs.

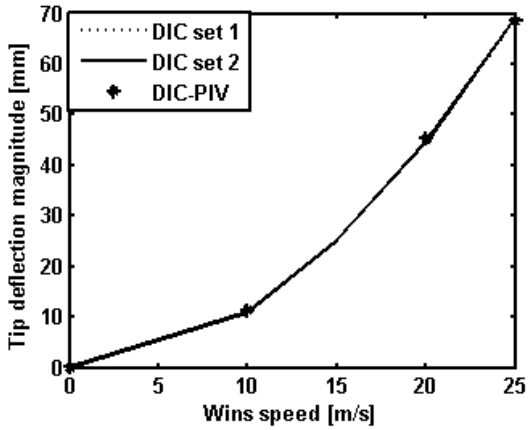

Fig.7: Tip deflection measured with DIC at different wind speeds

4.1 Flow field

The basic VORTFIND algorithm, Pemberton et al. (2002), was used to locate the centre of the tip vortex in the 120 vector fields produced for each experimental configuration. The algorithm finds the in-plane vectors closest to a vortex centre using criteria defined in Phillips & Turnock (2013). The average position of the 10 closest vectors was then taken as the vortex position for each vector field.

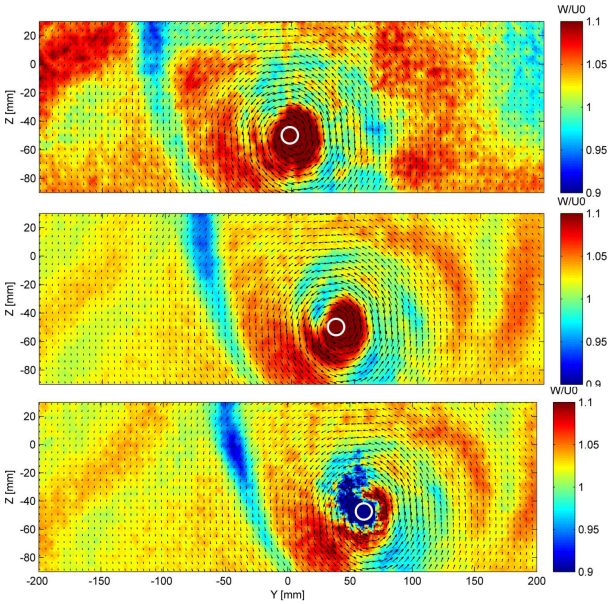

Fig.8: Time averaged axial velocity distribution relative to the free stream velocities: 10, 20 and 25 m/s (from top to bottom). The in-plane velocity field is represented as vectors. The vortex centre calculated from the mean velocity field is represented by a white circle.

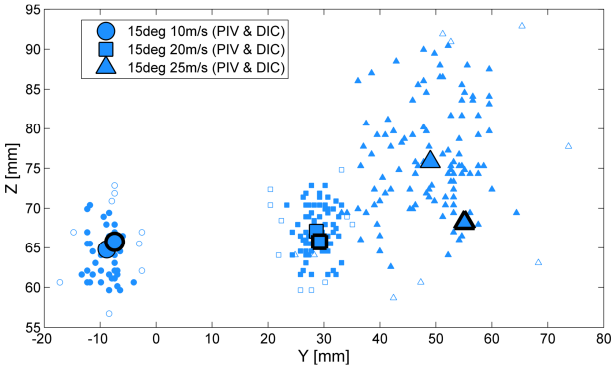

Fig.9: Instantaneous vortex positions from 120 images in-plane vector fields for different free stream velocities. The mean value of these positions is indicated by a large marker with a thin boarder. The vortex position obtained from the time averaged velocity field is indicated by a large marker with a bold border.

5 Numerical Results

The first five modes natural frequencies were initially investigated in FEA. Results were validated against impact tests performed on the wind tunnel structure, Table 2, showing good agreement. This allowed assessing the validity of the material properties selected in the FEA simulations.

Table 2: First five mode natural frequencies of the flexible aerofoil in experiments and FEA

Mode number	Numerical	Experimental
1	4.20 Hz	4.44 Hz
2	15.21 Hz	15 Hz
3	30.03 Hz	24.99 Hz
4	34.18 Hz	35 Hz
5	41.74 Hz	45 Hz

In order to build confidence on the FEA model, the structure was tested initially with different geometries (i.e. foam as a full-solid section, the foam as a rib-structure without the Mylar sheet and finally the whole wind tunnel model). Furthermore the initial load was applied at the centre of effort location and then a constant pressure load was applied to the FEA surface. Fig.11 compares experiments and initial FEA. Note how the tip displacement increases for the only-rib structure. The results obtained with the final FEA

model (i.e. Mylar structure) are very close to the ones measured with DIC. Fig.12 compares qualitatively between the DIC, FEA only and coupled FSI displacements. Note how the aerofoil experiences higher deflections near the tip and toward the trailing edge, as expected.

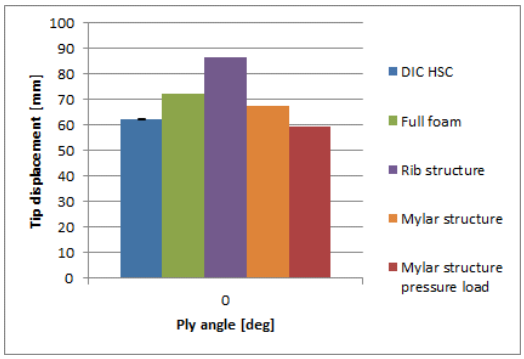

Fig.10: Tip displacement comparison between DIC and different FEA configurations

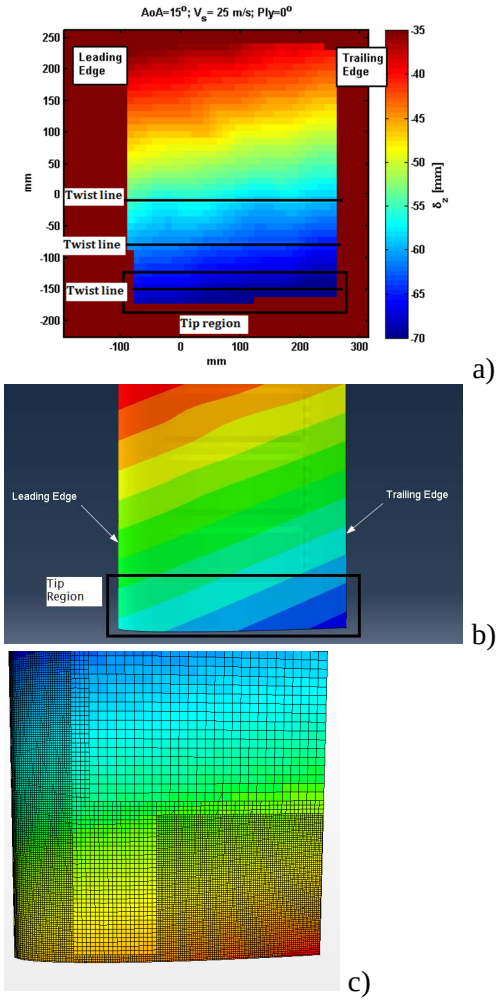

a)

b)

c)

Fig.11: DIC, FEA and FSI out-of-plane displacements for AoA=15° and Vs=25 m/s (scale 30-80 mm)

Fig.12a shows the axial velocity at a plane one chord downstream of the trailing edge (the location of the laser sheet in the PIV experiments). Note the deflected aerofoil in the CFD environment.

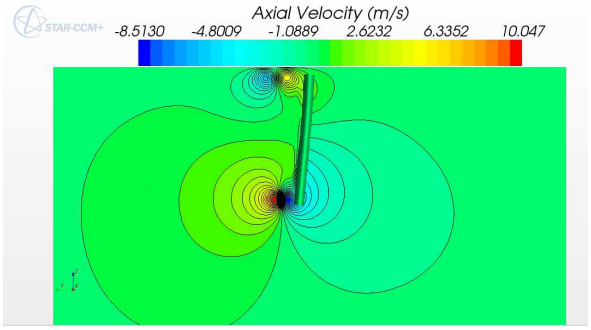

a)

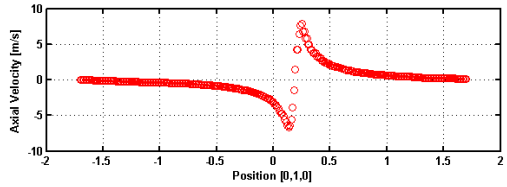

b)

Fig.12: Axial velocity at a plane one-chord downstream of the aerofoil

Fig.12b shows that the tip vortex is located at the maximum axial velocity perturbation, where the free-stream velocity changes with a maximum at the vortex centre location.

Acknowledgements

We would like to thank the help of the TSRL team, Dave Hollis from LaVision, the RJ Mitchell wind tunnel staff and the research funding from the EPSRC (grant number EP/009876/1).

References

Giovannetti, L. M., Banks, J., Soubeyran, X., Turnock, S. R., & Boyd, S. W. (2014). Full-field deformation response of a high performance foil under fluid loading using Digital Image Correlation. *Ready for submission*.

Nicholls-Lee, R. F., & Turnock, S. R. (2007). Enhancing Performance of a Horizontal Axis Tidal Turbine using Adaptive Blades. In *OCEANS 2007 - Europe* (pp. 1–6). Aberdeen: Ieee. doi:10.1109/OCEANSE.2007.4302437

Veers, P.; Bir, G. (1998). Aeroelastic tailoring in wind-turbine blade applications. *Windpower'98,*

American Wind Energy Association Meeting and Exhibition. Bakersfield, California. http://windpower.sandia.gov/other/AWEA4-98.pdf

Pemberton, R.; Turnock S.; Dodd, T.R.E. (2002). A novel method for identifying vortical structures. *J. Fluids and Structures*, *16*(23), 1051–1057.

Phillips, A., Turnock, S. (2013). Application of the VORTFIND algorithm for the identification of vortical flow features around complex three-dimensional geometries. *Int. J. for Numerical Methods in Fluids*, *71*(11), 1461–1474. doi:10.1002/fld.3720

Interface capturing methods on DTC Post-Panamax hull

Sankar Menon CP, Rickard Bensow, Claes Eskilsson
Chalmers Technical Univeristy, Göteborg, Sweden
menon@chalmers.se

A simple coupled Volume of Fluid (VOF)[1] and Level Set (LS) method is produced and compared with standard VOF solver in OpenFOAM® (OF). The coupling implemented has two different alternatives. One in which the surface tension is improved with the LS and other one where viscosity and density in addition to surface tension are corrected by the coupled VOF - Level Set (CLSVOF)[2] method. In standard OpenFOAM solver, volume fraction is advected through an compression scheme. In the VOF method, surface tension is implemented as source term and generally calculated using Continuous Surface Force Model (CSF) [3]. Here the interface curvature is calculated from the gradient of volume fraction which cannot be accurate. This approximation is known to create non-physical spurious currents at the interface [4] [5] [6]. The LS method provides a sharper interface and smooth transition across the interface. But, it cannot be completely stated that these parasite currents reduces in CLSVOF method [7]. Gerlach et al.[8] have studied three different models (PROST,Kernel and CLSVOF) using several tests in which the least spurious currents were obtained for PROST method. But, CLSVOF methods was shown to be less computationally expensive.

Most studies were focussed on bubble dynamics and formation, but little on wave making and breaking. Here is an attempt to understand the surface tension correction effects with CLSVOF on differences in wave profiles generated from the hull. Also, alternative model corrects the viscosity and density to see if there is any change in the friction resistance predicted on the hull. The paper will have validation on mesh sensitivity on these proposed models. Comparison was carried on solver provided Duisburg Tutorial Test Case (DTC) provided in the version OF2.3, which is a hull design of a modern 14000 TEU post-panamax container carrier.

References

[1] C. Hirt and B. Nichols, "Volume of fluid (vof) method for the dynamics of free boundaries," *Journal of Computational Physics*, vol. 39, no. 1, pp. 201 – 225, 1981.

[2] A. Albadawi, D. Donoghue, A. Robinson, D. Murray, and Y. DelaurÃ©, "Influence of surface tension implementation in volume of fluid and coupled volume of fluid with level set methods for bubble growth and detachment," *International Journal of Multiphase Flow*, vol. 53, no. 0, pp. 11 – 28, 2013.

[3] J. U. Brackbill, D. B. Kothe, and C. Zemach, "A continuum method for modeling surface tension," *J. Comput. Phys.*, vol. 100, pp. 335–354, June 1992.

[4] B. Lafaurie, C. Nardone, R. Scardovelli, S. Zaleski, and G. Zanetti, "Modelling merging and fragmentation in multiphase flows with {SURFER}," *Journal of Computational Physics*, vol. 113, no. 1, pp. 134 – 147, 1994.

[5] Y. Renardy and M. Renardy, "Prost: A parabolic reconstruction of surface tension for the volume-of-fluid method," *Journal of Computational Physics*, vol. 183, no. 2, pp. 400 – 421, 2002.

[6] D. Harvie, M. Davidson, and M. Rudman, "An analysis of parasitic current generation in volume of fluid simulations," *Applied Mathematical Modelling*, vol. 30, no. 10, pp. 1056 – 1066, 2006. Special issue of the 12th Biennial Computational Techniques and Applications Conference and Workshops (CTAC-2004) held at The University of Melbourne, Australia, from 27th September to 1st October 2004.

[7] D. J. E. Harvie, M. Rudman, and M. R. Davidson, "Parasitic current generation in combined level set and volume of fluid immiscible fluid simulations," in *Proceedings of the 13th Biennial Computational Techniques and Applications Conference, CTAC-2006* (W. Read, J. W. Larson, and A. J. Roberts, eds.), vol. 48 of *ANZIAM J.*, pp. C868–C884, Jan. 2008. http://anziamj.austms.org.au/ojs/index.php/ANZIAMJ/article/view/130 [January 11, 2008].

[8] D. Gerlach, G. Tomar, G. Biswas, and F. Durst, "Comparison of volume-of-fluid methods for surface tension-dominant two-phase flows," *International Journal of Heat and Mass Transfer*, vol. 49, no. 3-4, pp. 740 – 754, 2006.

Propeller Particulars and Scale Effect Analysis of ECO-Cap by CFD

Masafumi Okazaki, Taro Kajihama, Kenta Katayama, Yoshihisa Okada,
Nakashima Propeller Co.,Ltd. Okayama/Japan**,** m-okazaki@nakashima.co.jp

List of symbols

D	Propeller diameter	J	Advance coefficient	$J=\frac{V}{nD}$	ΔK_T	K_T ECO-Cap/K_T normal cap
V	Velocity of the flow	K_T	Thrust coefficient	$K_T=\frac{Thrust}{\rho n^2 D^4}$	ΔK_Q	K_Q Eco-Cap/K_Q normal cap
n	Propeller shaftspeed	K_Q	Torque coefficient	$K_Q=\frac{Torque}{\rho n^2 D^5}$	$\Delta\eta$	η ECO-Cap/η normal cap
ρ	Density	η	Propeller efficiency	$\eta=\frac{J\cdot K_T}{2\pi K_Q}$	K_T	$K_T$blade + K_T boss + K_T cap
ν	Kinematic viscosity	$R_{n\ Kempf}$	Reynolds number		K_Q	K_Q blade + K_Q boss + K_Q cap
$l_{0.7R}$	Chord length at 0.7R	$R_{n\ Kempf}=\frac{l_{0.7R}\sqrt{V^2+(\pi n\cdot 0.7D)^2}}{\nu}$				
C_{pn}	Pressure Coefficient	$C_{pn}=\frac{Pressure}{\rho n^2 D^2}$				

1. Introduction

In recent years, Energy Saving Devices (ESD) for ships have gained attention. Among them are the propeller caps with fins. Their characteristics are easy to attached, so they are suitable for retrofitting. The most famous caps with fins are Propeller Boss Cap Fins (PBCF). The research and development of PBCF were originally carried out by Ouchi[1)] et al. and concluded that it can gain the propulsion efficiency about 2.1% on the model and about 4% on the actual ship. ITTC referred the results and mentioned that the full scale improvement rate of propulsion efficiency is 2 to 3 times greater than the model scale prediction in their guidance[2)]. But the effect of the difference of propeller particulars like as pitch, number of blades are not mentioned. Kawamura[3)] et al. researched PBCF by CFD and the scale effect was confirmed.

The authors also developed a new propeller cap with fins which was named ECO-Cap[4)5)]. Fig.1 shows the ECO-Cap attached to the actual ship. In our research, ECO-Cap gained the propulsion efficiency about 1.28% in the six blades propeller for the container vessel and about 0.69% in the five blades propeller for the bulk carrier on the model scale. And it reduced the fuel oil consumption about 2.8% in the four blades propeller for the twin-screw car ferry on the actual ship. It looks like same scale effect as PBCF. The purpose of this paper is to predict the effect of the difference of the propeller particulars and scale of ECO-Cap by CFD.

Fig.1 ECO-Cap attached to the actual ship

2. Analysis by CFD

2-1. Propeller particulars and analysis models

Analysis carried out using the six propellers which are designed for large container vessel. Table1 shows the propeller particulars and Fig.2 shows pitch distribution of propellers.Fig.3 shows the propeller particulars and profiles. The feature of ECO-Cap compared with normal cap is attaching the seven fins for recovering energy loss caused by generating hub vortex.

Table.1 Propeller particulars

	MPNo.1	MPNo.2	MPNo.3	MPNo.4
Number of blades	6			5
Diameter(mm)	250(model)/9500(actual)			
Exp. Area ratio	0.89			0.85
Pitch distribution	constant	tip loaded	tip unloaded	constant
Pitch ratio at 0.7r/R	0.994	1.007	0.981	1.039

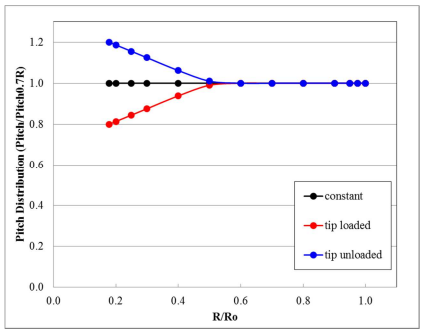

Fig.2 Pitch distribution

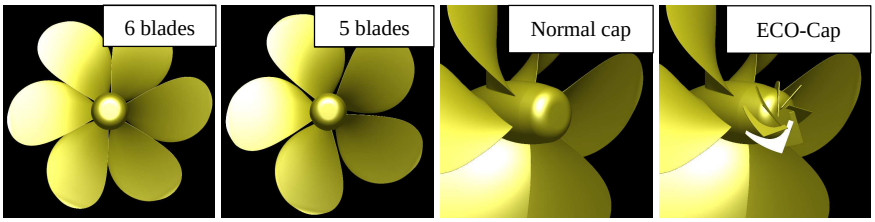

Fig.3 Propeller and cap profiles

RANS calculations are performed by SOFTWARE CRADLE SCRYU/Tetra Ver.10 which is a commercial CFD code based on a finite volume method with an unstructured grid. The k-kl-ω model is applied as turbulence model. The authors simulated the flow field around a propeller in uniform wake flow. The computational domain is composed of the inner rotational part including the propeller and the outer stationary part. The stationary part and the rotational part are connected discontinuously. Constant velocity and zero pressure are prescribed at the inlet and the outlet boundary, respectively. Fig.4 shows the computational domain. The numerical mesh is an unstructured grid, and basic cells are tetrahedral and prismatic cells are applied to near the blade surface for resolving the boundary layer. Table.2 shows conditions for the CFD model.

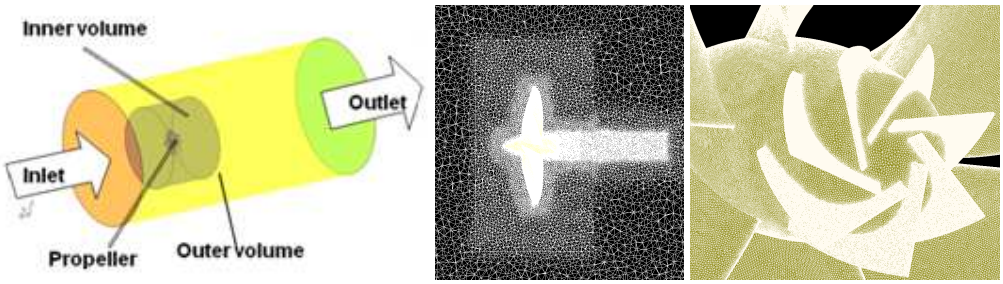

Fig.4 Numerical grids for CFD

Table.2 Conditions of CFD model

	Model scale		Full scale	
	Normal cap	ECO-Cap	Normal cap	ECO-Cap
$R_{nKempf}/10^5$	6.0		860.0	
y+	1.0			
Total thickness(mm)	3.0			
Prism layer	18		32	
Growth ratio	1.40		1.41	
Number of cells/10^7	2.2	2.9	3.6	4.8

2-2. Model scale analysis of difference of propeller pitch distribution

The authors calculated the MPNo.1-3 with normal cap in model scale. Fig.5 shows the distribution of pressure coefficient C_{pn} behind the normal cap at J=0.72. The blue part represents low pressure caused by the hub vortex. The low pressure was found for each propeller, but MPNo.2 is the smallest and MPNo.3 is biggest. Fig.6 shows pressure distribution behind the ECO-Cap at J=0.72. The recovery of pressure by ECO-Cap is found in each case. The tendency of extents of remaining blue part is same as the results of normal cap.

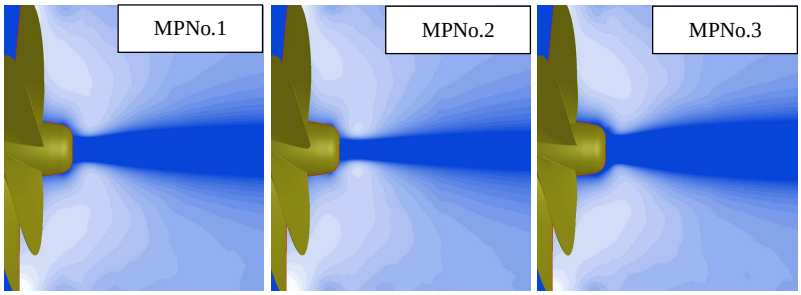

Fig.5 C_{pn} distributions behind the normal cap

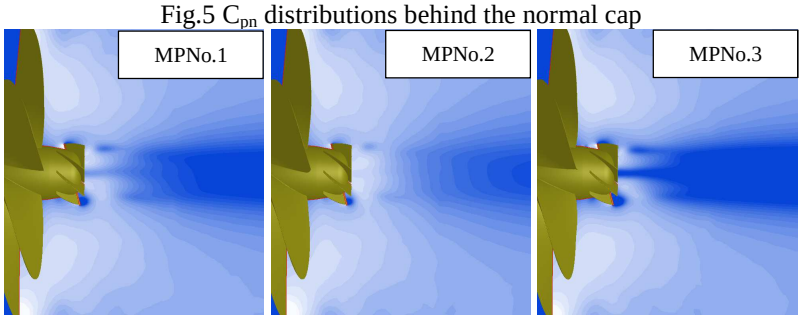

Fig.6 C_{pn} distributions behind the ECO-Cap

Fig.7 shows the comparison of propeller characteristics of MPNo.1-3 equipped with the normal cap and ECO-Cap. Each propeller equipped with ECO-Cap improves propeller efficiency $\Delta\eta_O$ by gaining ΔK_T and reducing ΔK_Q. Efficiency of MPNo.3 is improving most. The lower pressure behind the cap is, the more the propeller efficiency is improved by ECO-Cap.

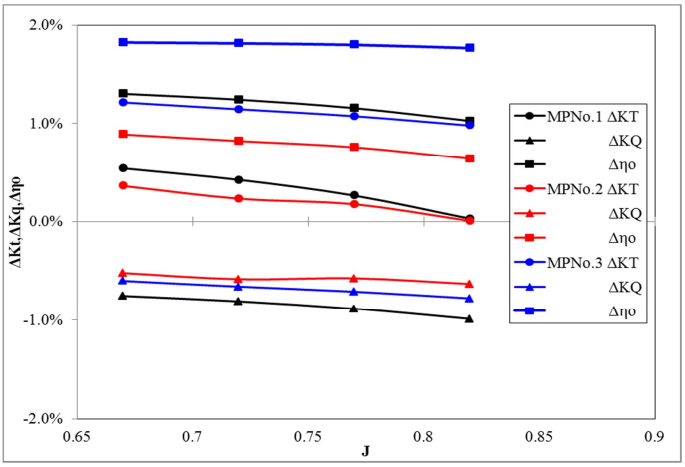

Fig.7 Comparison of propeller characteristics (with ECO-Cap/with normal cap)

2-3. Model scale analysis of difference of blade number

The authors calculated the normal cap and ECO-Cap about MPNo.4 which has five blades in the model scale. Fig.8 shows the streamline behind the normal cap at J=0.72. The colour of the streamline depends on C_{PN}. Each streamline swirls behind the cap and the direction is same as the propeller rotation. It looks like that the streamline of MPNo.1 is more swirly than that of MPNo.4. Fig. 9 shows the streamline behind the ECO-Cap at J=0.72. Each streamline was disturbed by fins and the pressure was recovered and the streamline direction was directed opposite direction of the propeller rotation by fins.

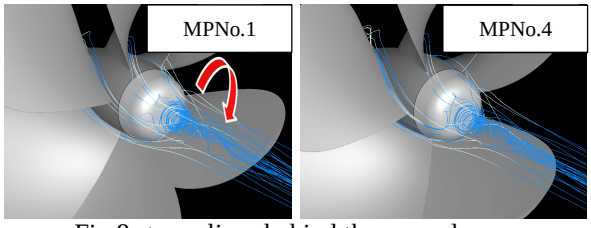

Fig.8 streamlines behind the normal cap

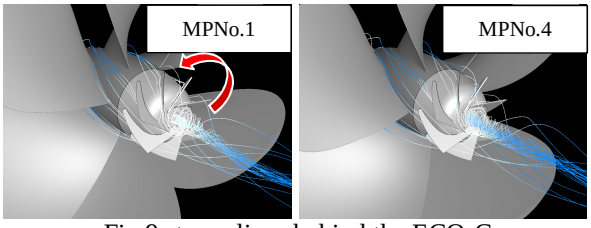

Fig.9 streamlines behind the ECO-Cap

Fig.10 shows the comparison of propeller characteristics of MPNo.1 and MPNo.4 equipped with the normal cap and ECO-Cap . $\Delta\eta_O$ of MPNo.1 is higher than MPNo.4 because of the difference of ΔK_T and the gap widens at the high J.

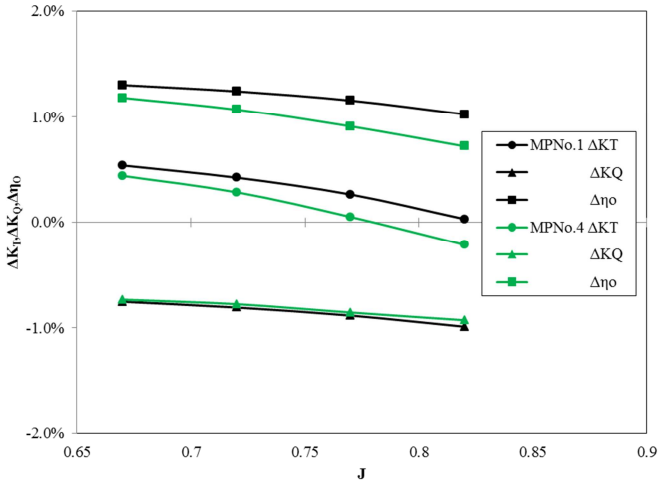

Fig.10 Comparison of propeller characteristics

2-4. Analysis of scale effect

The authors calculated the normal cap and ECO-Cap in model scale and full scale. The reynolds number R_{nKempf} is 6.0 x 10^5 in model scale and 860.0 x 10^5 in full scale. Fig.11 and Fig.12 show the C_{pn} distribution behind the normal cap and the ECO-Cap attached to MPNo.1. Each figure indicated that the C_{pn} distribution in model scale was different from that in full scale. Especially, low pressure remained behind the ECO-Cap in full scale against the result in model scale.

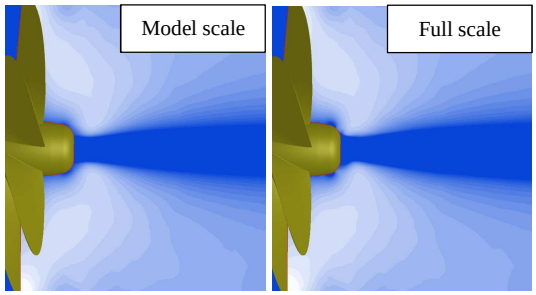

Fig.11 C_{pn} distributions behind the normal cap attached to MPNo.1

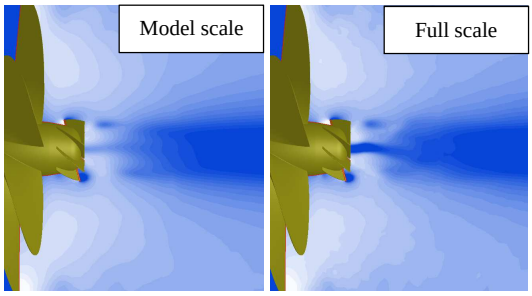

Fig.12 C_{pn} distributions behind the ECO-Cap attached to MPNo.1

Fig.13 shows the comparison of propeller characteristics of MPNo.1 equipped with the normal cap and ECO-Cap in model scale and full scale. Propeller characteristic of full scale is improved compared with model scale. Table.3 is the comparison of $\Delta\eta_O$ of model and full scale about MPNo.1-4 at design point. The full-scale improvement rate of propulsion efficiency is 1.5 to 3.2 times greater than the model scale.

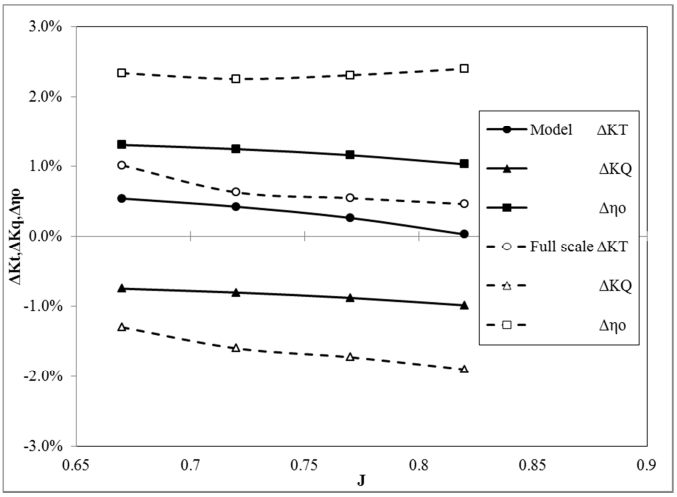

Fig.13 Comparison of propeller characteristics MPNo.1

Table.3 comparison of $\Delta\eta_O$ of model and full scale

MPNo.	$\Delta\eta_O$		$\frac{\Delta\eta_{o\,full}}{\Delta\eta_{o\,model}}$
	model scale	full scale	
1	1.27%	2.27%	1.8
2	0.52%	1.68%	3.2
3	1.89%	2.76%	1.5
4	1.07%	1.88%	1.8

3. Conclusion

The authors confirmed the following by CFD analysis.

1) Propeller particulars such as pitch distribution and blade number affected pressure distributions behind the propeller cap. Reynolds number also affected pressure distributions behind the propeller cap.
2) The lower pressure behind the cap is, the more propeller efficiency is improved by ECO-Cap.
3) The full-scale improvement rate of propulsion efficiency is changed by propeller particulars, and it is 1.5 to 3.2 times greater than in model scale. It is nearly the same as ITTC's guidance.
4) The full-scale improvement rate of propulsion efficiency is expected because of the difference of pressure distribution that cannot reproduce in the model test.

References

1. K. Ouchi, T. Kawasaki, M. Tamashima, H. Koizuka, "Research and development of PBCF(Propeller Boss Cap Fins)", J.S.N.A. Japan, Vol.163, 165, 1989.
2. N. Bose et al., "Final Report and Recommendations to the 22nd ITTC", The specialist Committee on Unconventional Propulsors, 1989.
3. T. Kawamura, "Model and full scale CFD analysis of propeller boss cap fins (PBCF)", J. Marine Science and Technology 17, 2012.
4. Y. Okada, K. Katayama, A. Okazaki "Numerical Analysis of the Propeller with Economical Cap by CFD", 16th Numerical Towing Tank Symp., 2013.
5. K. Katayama, Y. Okada, A. Okazaki "Optimization of the Propeller with ECO-Cap by CFD", 4th Int. Symp. Marine Propulsors, 2015.

Structural and Hydrodynamic Characterization of a NACA 0009 Hydrofoil by Finite Elements

Riccardo Pellegrini[1,2], Cecilia Leotardi[1], Umberto Iemma[2], Emilio F. Campana[1], Matteo Diez[1]

[1]CNR-INSEAN, Natl. Research Council-Marine Technology Research Inst., Rome, Italy

[2]Roma Tre University, Dept. of Engineering, Rome, Italy (riccardo.pellegrini@uniroma3.it)

1 Introduction

Simulation-based design optimization (SBDO) assists the designer in the design process of complex engineering systems. Design goals and requirements of the SBDO are often multidisciplinary, such as in aerial (*e.g.* aerodynamics, structures, flight mechanics, aeroacoustics), ground (*e.g.* aerodynamics, structures, engines) or maritime (*e.g.* hydrodynamics, structures, propulsion) applications. Multidisciplinary design optimization (MDO) refers to the identification of the best solution with respect to optimality criteria, whose definition involves a number of disciplines mutually coupled and interconnected. Deterministic MDO methods have been successfully applied in ship design for fluid-structure interaction (FSI) applications (Campana et al, 2006), including composite materials (*e.g.* Liu and Young 2007; Volpi et al 2015). Realistic applications are affected by uncertainty, both on the operating (*e.g.* speed) and environmental (*e.g.* sea state) conditions. Therefore, uncertainty quantification (UQ) methods (He et al 2013; Mousaviraad et al 2013; Diez et al 2014) are required in the optimization process, leading to multidisciplinary robust design optimization (MRDO) formulations (*e.g.* Diez et al 2012; Leotardi et al 2014).

Within this context, the objective of this work is the preliminary structural and hydrodynamic characterization of a NACA 0009 hydrofoil, including a comparison with numerical and experimental data from Brandner and Pearce (2012). This represents a first step towards a simulation-based MRDO of the hydrofoil. The characterization is performed with numerical (structural and hydrodynamic) simulations by finite element method (FEM). A grid convergence analysis using different shape functions is presented to determine the dry eigenfrequencies and modes; a comparison with experimental data is shown. Wet modes and eigenfrequencies are computed using a structural-acoustic multi-physics approach. A comparison with a 2D potential strip-theory method (the results are taken from Brandner and Pearce 2012) is also shown. The hydrodynamic characterization is performed, including grid convergence analysis and comparison with experimental data. The numerical simulations are performed with the commercial finite element code *COMSOL Multiphysics*^{TM}.

2 Structural and hydrodynamic characterization of the hydrofoil

The geometry of the hydrofoil, defined in Brandner and Pearce (2012), is an unswept trapezoidal fin with a NACA 0009 section profile. The root, mid and tip chords are 0.12 m, 0.09 m and 0.06 m long, with a span length of 0.3 m. The resulting aspect ratio is 3.33. According to Brandner and Pearce (2012), a stainless steel with a density of 7900 kg/m^3, a Young modulus of 193 GPa and a Poisson modulus of 0.3 is chosen to perform numerical structural simulations.

2.1 Dry modes

The partial differential equations solved to compute the dry eigenfrequencies and modes are the Cauchy equations for solid continuum. A fixed (clamped) boundary condition is imposed at the root section of the hydrofoil.

The hydrofoil geometry is discretized with a structured mesh. Three different grids (G1, G2, G3), with a $\sqrt{2}$ refinement ratio, are used to evaluate the convergence of the first six modes. A convergence analysis is performed considering three different shape function order for each grid. Lagrange polynomials of first, second and third order (namely P1, P2 and P3) are used as shape functions. These are defined as tensor product of one-dimensional polynomials of order $n-1$:

$$\phi_N^{(e)}(\xi) = L_N = \prod_{M=1, M\neq N}^{n} \frac{\xi - \xi_M}{\xi_N - \xi_M} \tag{1}$$

where n is the number of nodes of the element e, N is the current node and ξ is the non-dimensional coordinate defined as $\xi = x/h$, with h the length and x the dimensional coordinate of the element. The characteristics of the three grids are summarized in Tab. 1, whereas the mesh is represented in Fig. 1(a).

The MUltifrontal Massively Parallel Solver (MUMPS) is used as numerical solver. It is a direct solver for linear equations systems $\mathbf{Ax} = \mathbf{b}$, where $\mathbf{A}$ is a symmetric or asymmetric square sparse matrix.

Table 1: Domain discretization and shape functions

Simulation type	Dry modes			CFD			CFD, Wet modes		
Polynomial	Lagrange 1^{st}, 2^{nd}, 3^{rd}			Lagrange 1^{st}			Lagrange 2^{nd}		
Mesh	G1	G2	G3	G1-P1	G2-P1	G3-P1	G1-P2	G2-P2	G3-P2
No. elements	15.6 k	5.6 k	1.9 k	972.0 k	369.9 k	121.5 k	195.3 k	71.4 k	29.6 k
No. DoFs	(P1) 52.9 k	19.8 k	7.42 k	6.00 M	2.31 M	774 k	8.22 M	3.03 M	1.05 M
	(P2) 400 k	146 k	52.9 k						
	(P3) 1.32 M	480 k	172 k						

2.2 Wet modes

In order to compute the wet eigenfrequencies and modes, a multi-physics approach is chosen. The equations of the structure are coupled with the equations of acoustics through the boundary conditions between the hydrofoil and the surrounding fluid domain:

$$\begin{cases} -\mathbf{n}\cdot\left(-\left.\frac{\nabla p_t}{\rho_c}\right|_1\right) = \mathbf{n}\cdot\mathbf{a} \\ -\mathbf{n}\cdot\left(-\left.\frac{\nabla p_t}{\rho_c}\right|_2\right) = -\mathbf{n}\cdot\mathbf{a} \\ \mathbf{F_A} = (p_{t,1} - p_{t,2})\,\mathbf{n} \end{cases} \tag{2}$$

where $\mathbf{n}$ is the surface normal, p_t is the total acoustic pressure, $\rho_c = \rho\left(1 + i\omega b/\rho c^2\right)^{-1}$, ω is the eigenfrequency, ρ is the fluid density, c is the speed of sound, $b = (4/3\mu + \mu_B)$, μ is the dynamic viscosity, μ_B is the bulk viscosity, a is the structural acceleration and $\mathbf{F_A}$ is the load experienced by the structure. The subscripts 1 and 2 in equation 2 indicates the two sides of the interface (solid and fluid respectively).

Hence, the computational domain needs to include both the hydrofoil structure and an appropriate surrounding fluid volume. To the aim of using the same domain and/or topology for both wet modes and later hydrodynamic calculations, a *C*-type domain is chosen. Its dimensions are selected in view of the hydrodynamic analysis: four mid-chords (Cm) are used as radius of the *C*, the total height of the domain is twice the span of the hydrofoil and the domain length is 7 times the mid-chord length, see Fig. 1(b).

The domain is discretized with a structured mesh and the distribution of the elements in the rear region is intentionally refined to guarantee the finest discretization of wake flow for each angle of attack of the hydrofoil (for later hydrodynamic simulations). The grid is also refined in critical regions such as the root and the tip of the hydrofoil (Fig. 1(b)). The grid size is reported in Tab. 1, namely G2–P2.

According to Fig. 1(c), the boundary conditions are set considering sound soft (*i.e.* null impedance) on blue and green faces, and sound hard (*i.e.* infinite impedance) on gray face, in order to reproduce the conditions of an experimental test room.

The MUMPS solver is used also to compute the wet modes.

2.3 Stationary hydrodynamic analysis

The hydrodynamic characterization of the hydrofoil is performed by solving the Navier-Stokes equations for an incompressible, stationary flow. The hydrofoil is modeled as a rigid wall, therefore the deformation effects of the fin are not taken into account in this preliminary calculations.

Two sets of three grids, both with a refinement ratio equal to $\sqrt{2}$, are defined in order to determine the most effective compromise between the number of elements and the shape function order. Two different orders of Lagrange polynomial are investigated: the first order for all the variables (*i.e.* velocity, pressure, turbulent kinetic energy and turbulent dissipation rate) and second order only for velocity, turbulent kinetic energy and turbulent dissipation rate.

Furthermore, a domain size convergence is performed on the mid grid refinement (G2) with the second order shape function (P2) varying the wake length (5, 7 and 10 times the mid-chord length). For each domain extension the element size is kept constant. The characteristics of the grids are reported in Tab. 1.

Referring to Fig. 1(c), the boundary conditions are set considering an inlet/undisturbed flow on the green face, a wall on the gray face and an outlet on the blue face for the hydrodynamic load convergence analysis.

The $k-\varepsilon$ turbulence model is used with standard coefficients (Jones and Launder, 1972) and wall function. The non-linear stationary problem is solved with a dumped Newton method through linear step (Deuflhard, 1974). Due to the increased complexity of the problem, resulting in more elements and more degrees of freedom than the

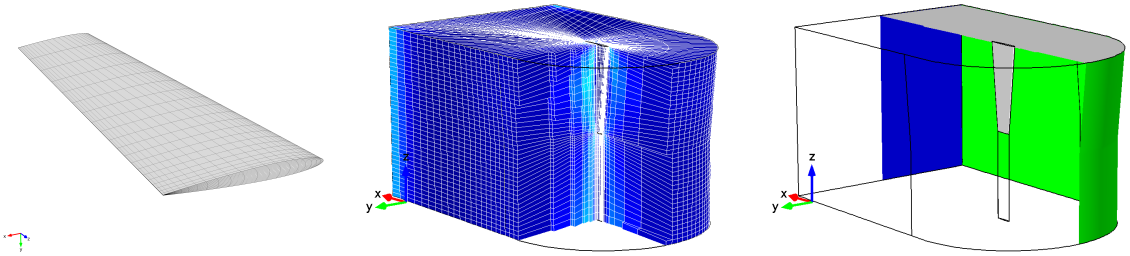

(a) Hydrofoil mesh for structural analysis (G2)

(b) G2-P2 section of the C domain discretization for acoustic-structure and hydrodynamic analyses. 7 mid-chord length

(c) Domain for acoustic-structure and hydrodynamic loads convergence analyses

Figure 1: Structural and hydrodynamic domains and grids

structural simulations, a direct solver is no longer suitable for the linearized problem. Consequently, a segregated iterative solver is applied in order to reduce the problem dimension. Specifically, two segregated groups are defined: the first for velocity and pressure and the second for turbulent kinetic energy and turbulent dissipation rate. While performing the simulations on the first grid triplet, associated to first order Lagrangian polynomial (see Tab. 1), both segregated groups are solved using the Generalized Minimal Residual Method (GMRES) (Saad and Schultz, 1986), preconditioned with a Symmetrical Coupled Gauss-Seidel (SCGS) scheme. Otherwise, while performing the simulations on the second grid triplet, associated to the second order Lagrangian polynomial (see Tab. 1), both segregated groups are solved using the Flexible Generalized Minimal Residual Method (FGMRES) (Saad, 1993), preconditioned with GMRES.

Moreover, a pseudo time-stepping is introduced to increase the simulation stability. The Courant-Friedrichs-Lewy (CFL) number adjusts the local time-step according to $\Delta t_{loc} = CFL_{loc}h/U$, where h is the longest cell edge, and U is the magnitude of the local fluid flow velocity. For all the simulations the CFL is set equal to 1.

3 Numerical results

In this section, the results pertaining to the structural modal analyses and the hydrodynamic characterization are presented.

3.1 Dry modes and frequencies

In Fig. 2, the dry modes and the corresponding eigenfrequencies are presented.

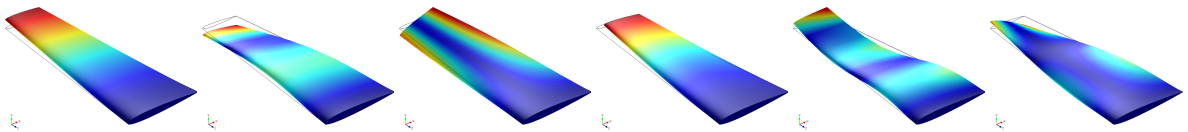

(a) $f = 106$ Hz (b) $f = 442$ Hz (c) $f = 781$ Hz (d) $f = 1075$ Hz (e) $f = 1080$ Hz (f) $f = 1635$ Hz

Figure 2: Dry modes

Figure 3 shows the convergence of the six eigenfrequencies on the grid triplet for each shape function order. The results obtained using P1 show a poor convergence in comparison with the corresponding results evaluated using P2 and P3 (Fig. 3(a), 3(b), 3(d) and 3(e)). The frequencies associated to modes with a significant torsion show a better convergence (Fig. 3(c) and 3(f)). The results obtained using the second and the third order Lagrange polynomials show small differences for G1, G2 and G3. The eigenfrequencies associated to P2 and P3 are grid convergent. It could be noted that a better convergence is achieved using P3, with the highest computational cost.

A comparison between experimental data available in air and the numerical results is performed. The experimental frequency of the first mode in air equals to 100 Hz, whereas the corresponding numerical eigenfrequency in vacuum equals to 106 Hz. The difference is 6%.

3.2 Wet modes and frequencies

The wet modes and the corresponding eigenfrequencies are presented in Fig. 4. Experimental eigenfrequencies in water are not available. Nevertheless, Brandner and Pearce (2012) present a numerical estimation, based on a

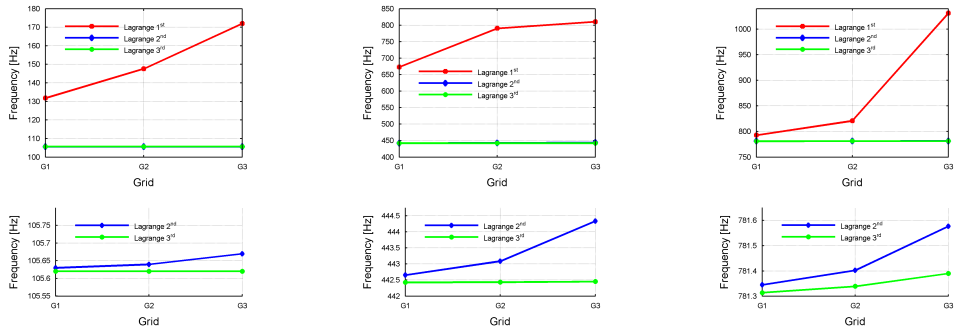

(a)1^{st} Eigenfrequency and detail (b) 2^{nd} Eigenfrequency and detail (c) 3^{rd} Eigenfrequency and detail

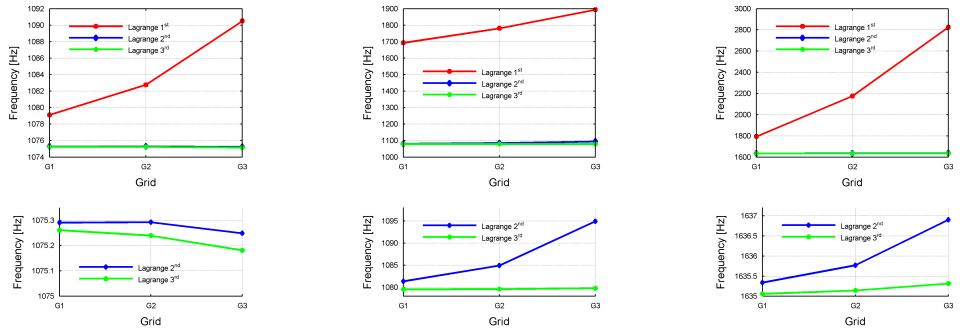

(d) 4^{th} Eigenfrequency and detail (e) 5^{th} Eigenfrequency and detail (f) 6^{th} Eigenfrequency and detail

Figure 3: Dry eigenfrequencies convergence

2D potential strip theory method. The first wet frequency equals to 62 Hz, whereas the current FEM approach provides a frequency of 69 Hz, resulting in a difference of about 11%.

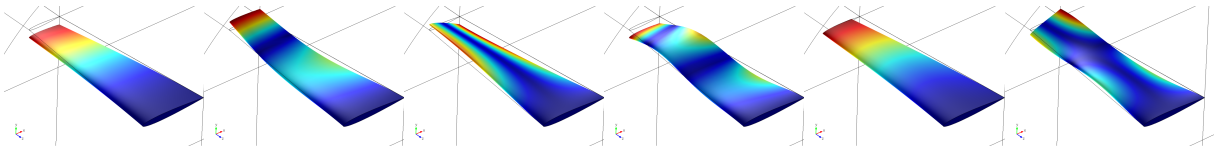

(a) $f = 69$ Hz (b) $f = 297$ Hz (c) $f = 564$ Hz (d) $f = 744$ Hz (e) $f = 1070$ Hz (f) $f = 1196$ Hz

Figure 4: Wet modes

3.3 Hydrodynamic loads

The hydrodynamic simulations conditions are set according to Brandner and Pearce (2012). Specifically, the mid-chord based Reynolds number (Re) is 0.6E6, the angle of attack (AoA) is 3 deg, the absolute pressure equals to 201.13 kPa, the absolute temperature is 293.15 K, the density of water is set to 999 kg/m^3 and the dynamic viscosity to 1.1545E–3 Pa·s.

The convergence of the hydrodynamic loads (in terms of lift and drag) is shown in Fig. 5. Second order Lagrange polynomials provide a better convergence than first order Lagrange polynomials, in this case (see Fig. 5(a) and 5(c)). A domain extension of 7 mid-chord length guarantees the convergence of the wake effects, in this case (see Fig. 5(b) and 5(d)).

The agreement with the experimental data is within 5% error for the first order shape functions and the finest grid G1–P1 (Fig. 5(a)), and within 9% error for the second order shape functions and the finest grid G1–P2 (Fig. 5(a)).

The domain size of 10 mid-chords and boundary conditions of Fig. 1(c) are chosen to identify the lift and drag coefficient curve versus AoA in Fig. 6(a). Finally Figs. 6(b) and 6(c) show respectively the pressure distribution on a XY-plane located at 90% of the span and the non-dimensional velocity (U/U_0) on the same plane.

4 Conclusions and future work

The structural and hydrodynamic characterization of a NACA 0009 hydrofoil has been performed using a commercial finite element code, *COMSOL Multiphysics*^{TM}.

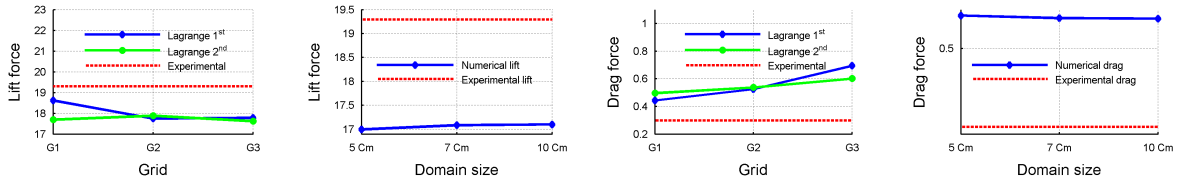

(a) Lift force convergence with respect to the shape function order

(b) Lift force convergence with respect to the domain size expressed in function of mid-chord (Cm)

(c) Drag force convergence with respect to the shape function order

(d) Drag force convergence with respect to the domain size expressed in function of mid-chord (Cm)

Figure 5: Hydrodynamic forces convergence

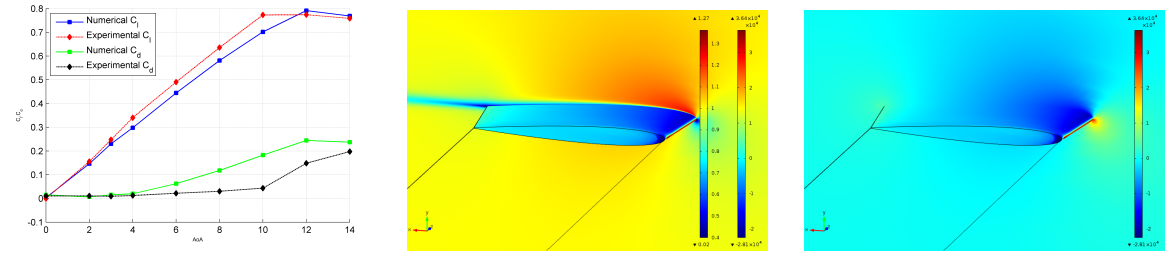

(a) Polar curves of lift and drag coefficients

(b) Non-dimensional velocity contour on the XY-plane at 90% of the span and pressure on fin surface

(c) Pressure contour on the XY-plane at 90% of the span and pressure on fin surface

Figure 6: Hydrodynamic analysis of the hydrofoil, (AoA = 3 deg; Re = 0.6E6)

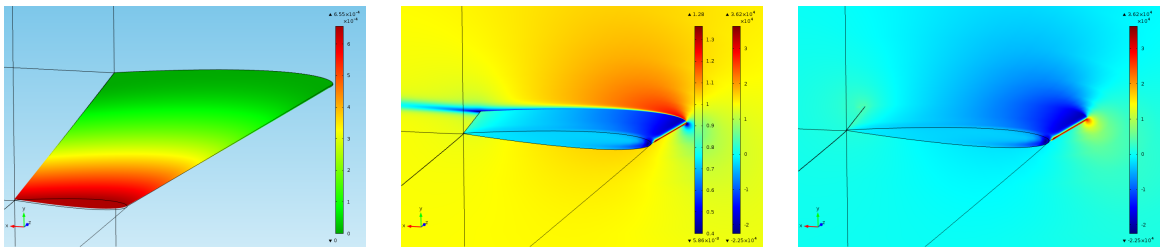

(a) View of the total displacement of the hydrofoil

(b) Non-dimensional velocity contour on the XY-plane at 90% of the span and pressure on fin surface

(c) Pressure contour on the XY-plane at 90% of the span and pressure on fin surface

Figure 7: FSI analysis of the hydrofoil, (AoA = 3 deg; Re = 0.6E6)

The structural characterization included the numerical evaluation of both dry and wet modes. A convergence analysis of the dry eigenfrequencies has been performed using three grids with a $\sqrt{2}$ refinement ratio, and using three shape function order. Figure 3 shows that the choice of a third order shape function does not lead to appreciable improvement on solution accuracy, but induces a consistent increase of the computational cost. The choice of G2 with P2 is a good trade off between computational cost and accuracy for the identification of dry eigenfrequencies and modes. The difference between the numerical and experimental eigenfrequency is close to 6%, likely due to added mass effects in air versus vacuum.

The multi-physic coupling of acoustics and structure (used to determine the wet eigenfrequencies and modes) lead to reasonable results, comparable with other approaches such as the 2D potential strip theory method used in Brandner and Pearce (2012). The difference between the two approaches for the current problem is about 11%.

The hydrodynamic study shows a poor convergence of the lift force, whereas the drag force has been found grid convergent. The lift curve is in reasonable agreement with the experiments, whereas the drag curve shows a significant error versus the experimental values, as the AoA increases.

Future work includes the verification of the wet eigenfrequencies by grid-convergence analysis. A parametric study of lift and drag versus the turbulence model will be also conducted. Finally, a UQ analysis considering stochastic operating conditions (*e.g.* AoA and Re) will be conducted on steady fluid structure interaction (FSI) simulations. MRDO will be then performed, aiming at increasing the efficiency of the hydrofoil. A preliminary two-way FSI study is shown in Fig. 7, for a AoA equal to 3 deg and Re equal to 0.6E6. The maximum displacement,

Fig. 7(a) at the hydrofoil tip equals 6.55E–4 m. The corresponding (interpolated) experimental value is 9.4E–4 m.

Acknowledgements

The present research is partially supported by the US Navy Office of Naval Research, NICOP grant N62909-11-1-7011, under the administration of Dr Ki-Han Kim and Dr Woei-Min Lin, and by the Italian Flagship Project RITMARE, coordinated by the Italian National Research Council and funded by the Italian Ministry of Education, Research Program 2011-2013.

References

Brandner P, Pearce B (2012) Experimental modelling of steady hydrofoil fluid-structure interaction. In: Proceedings of the 18th Australasian Fluid Mechanics Conference, pp 3–7

Campana EF, Fasano G, Peri D (2006) Issues on nonlinear programming for Multidisciplinary Design Optimization (MDO), in ship design frameworks. In: III European Conference on computational mechanics solids, structures and coupled problems in engineering. Lisbon, Portugal

Deuflhard P (1974) A modified newton method for the solution of ill-conditioned systems of nonlinear equations with application to multiple shooting. Numerische Mathematik 22(4):289–315

Diez M, Peri D, Fasano G, Campana EF (2012) Hydroelastic optimization of a keel fin of a sailing boat: a multidisciplinary robust formulation for ship design. Structural and Multidisciplinary Optimization 46(4):613–625

Diez M, He W, Campana EF, Stern F (2014) Uncertainty quantification of Delft catamaran resistance, sinkage and trim for variable Froude number and geometry using metamodels, quadrature and Karhunen–Loève expansion. Journal of Marine Science and Technology 19(2):143–169

He W, Diez M, Zou Z, Campana EF, Stern F (2013) URANS study of Delft catamaran total/added resistance, motions and slamming loads in head sea including irregular wave and uncertainty quantification for variable regular wave and geometry. Ocean Engineering 74:189–217

Jones W, Launder B (1972) The prediction of laminarization with a two-equation model of turbulence. International journal of heat and mass transfer 15(2):301–314

Leotardi C, Diez M, Serani A, Iemma U, Campana E (2014) A framework for efficient simulation-based multidisciplinary robust design optimization with application to a keel fin of a racing sailboat. In: OPT-i 2014 - 1st International Conference on Engineering and Applied Sciences Optimization, Proceedings, pp 1177–1193

Liu Z, Young YL (2007) Utilization of deformation coupling in self-twisting composite propellers. In: Proceedings of 16th International Conference on Composite Materials, Kyoto, Japan, pp 8–13

Mousaviraad SM, He W, Diez M, Stern F (2013) Framework for convergence and validation of stochastic uncertainty quantification and relationship to deterministic verification and validation. International Journal for Uncertainty Quantification 3(5)

Saad Y (1993) A flexible inner-outer preconditioned GMRES algorithm. SIAM Journal on Scientific Computing 14(2):461–469

Saad Y, Schultz MH (1986) GMRES: A generalized minimal residual algorithm for solving nonsymmetric linear systems. SIAM Journal on scientific and statistical computing 7(3):856–869

Volpi S, Sadat-Hosseini H, Diez M, Kim DH, Stern F, Thodal R, Grenestedt J (2015) Validation of high fidelity CFD/FE FSI for full-scale high-speed planing hull with composite bottom panels slamming. In: Proceedings of the 4th International Conference on Coupled Problems in Science and Engineering

Numerical Investigation on the Use of the Euler Overlay Method for a Floating Structure

Alessio Pistidda, Harald Ottens, Heerema Marine Contractors, Leiden/The Netherlands,
apistidda@hmc-heerema.com

INTRODUCTION

As an offshore contractor Heerema Marine Contractors is specialized in the transportation and installation of offshore structures such as jackets, topsides and subsea infrastructures. The deep water construction vessel Aegir uses a moonpool to lower pipelines and connected structures. The lowering operations are feasible only if the vessel motion and the flow conditions inside the moonpool are within workable conditions.

The vessel motion can be analysed via model test or numerically. Potential methods and viscous solvers (RANS) are used in nowadays computations. The first one is very effective to analyse wave field but it is not accurate in the surrounding of the body where viscous effect are dominant, like in the moonpool. RANS solvers are accurate around the floating body but very time consuming if used to solve the entire wave field. Based on previous considerations, the RANS approach forces the user to limit the size of the domain. The main disadvantage of a small domain is the reflection of diffracted and radiated waves at the grid boundaries, affecting the inlet conditions.

The overlay approach tries to minimize the negative side effect of the classical RANS approach dissolving diffracted and radiated waves before they reach the boundaries. In this way inlet boundary conditions are not affected by wave reflections. RANS equations are solved close to the floating body while potential/analytical solution is applied at the boundary. The area where radiated/diffracted waves are dissipated is the so called overlay area. In this work several sensitivity analyses are performed to investigate some numerical aspects regarding this approach. The effect of the overlay geometry (size and distance from the floating body) on the motion of a floating structure will be investigated. The dissipation of the radiated/diffracted waves in the overlay region is obtained using a source term in the momentum equation. The choice of the magnitude of the source term is not trivial, for that reason a study on this parameter will be also presented. As application, the moonpool response amplitude operator (RAO) using the overlay method will be derived.

Recent publications show that the overlay method is getting more and more popular [1][2]; however, several aspects of this method are still unclear and need further investigation. This work aims to analyse the numerical aspects which can have an impact on the motions of the floating structure we are interested in. The final goal of this study is to provide a guideline to perform CFD simulations using the overlay approach with confidence.

EOM METHOD

The Euler Overlay Method (EOM) used in this work consist in forcing the solutions of the RANS equations toward a specified boundary condition over some distance from the floating body. In this way the reflected waves can be damped and the size of the domain can be reduced. The boundary condition is generally the solution of inexpensive computational method (e.g. analytical solution, potential solution). The EOM is implemented introducing a source term S in the transport equations, which reads:

$$S = \mu_f(\varphi_{CFD} - \varphi_{FF})$$

The difference between the CFD (RANS) solution φ_{CFD} and the far field solution φ_{FF} is multiplied by a forcing coefficient μ_f.The source term is zero($\mu_f = 0$) in the proximity of the floating body, but increases towards the boundaries using a half cosine profile in the overlay zone [4].

$$\mu_f = \mu_0 \cos^2(\pi x^*/2)$$

μ_0 is the maximum value of the forcing coefficient and it is case dependent. x^* is the relative coordinate in the damping/transition zone. Forcing is usually applied to momentum and volume fraction of the RANS equations [5].

Fig. 1 shows two possible way to implement the forcing zone using the EOM method. In the first case the RANS domain is around the floating body only, while in the second case it extends till the outlet.

Since with 3D flows the resolution of the waves (e.g. wave length and amplitude) is likely to be deteriorated, imposing the forcing at the outlet can introduce unwanted phenomena [5] like beating waves close to the outlet, as shown in Fig. 2, where two different time frames of the same simulation show that phenomenon. All simulations presented in following sections use the approach of Fig. 1b; reflection of the waves at the outlet are avoided using the classical wave damping approach [3].

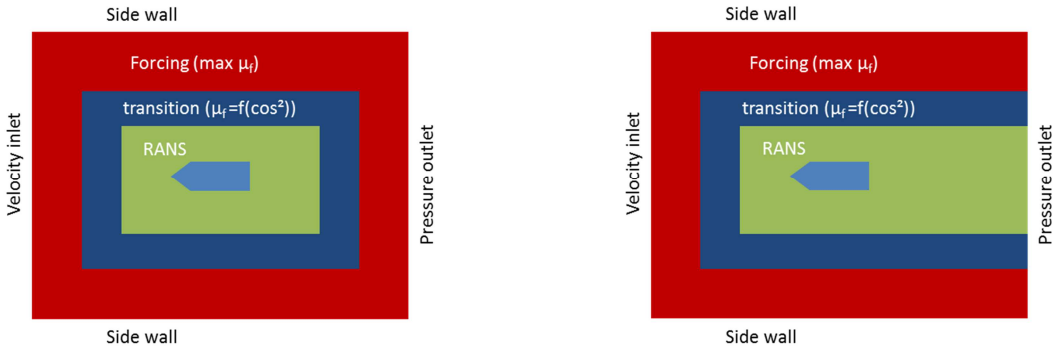

Fig. 1: computational domains using EOM to derive motions RAO

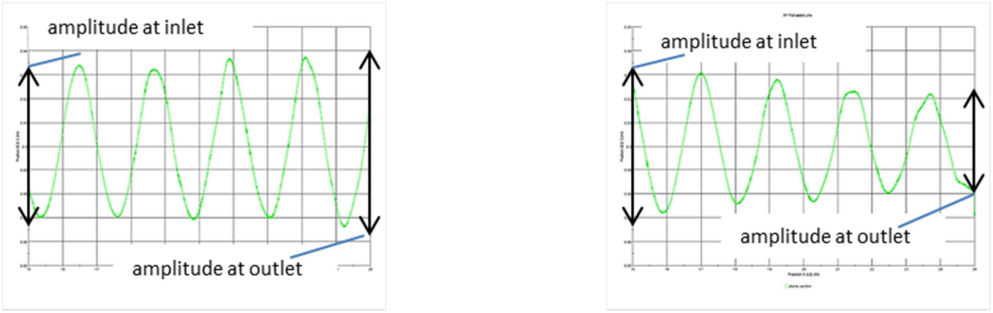

Fig. 2: wave profile propagating from left to right in a poor quality grid. Large beating is present reaching the outlet.

MODEL TEST

Experimental data of the roll RAO of a 2D barge is derived using regular waves [6]. This experiment has been selected to validate the setting of the EOM, i.e. forcing coefficient and length of the forcing zone. The barge is 0.9m long, 0.3m wide and 0.1m high. The barge is mounted on the tank walls with bars and a pair of hinges thru the CoG (0.05m above keel); the CoG is at water level. Moment of inertia of the structure in air is I=0.236 kgm^2. Test setup is shown in Fig. 3a.

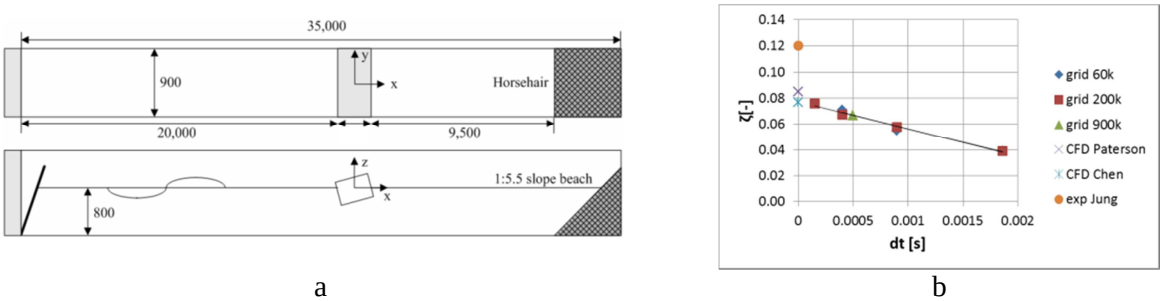

Fig. 3: model test domain (a) and roll damping for roll angle of ~10 deg (b)

During the execution of the experiment, the waves reflected and radiated by the barge travel to the inlet. If the domain is long enough, once the reflected waves start affecting the inlet, enough roll cycles are already available to derive the RAO (i.e. the RAO is not affected by corrupted waves at the

inlet). Computing the roll RAO via CFD can be very time consuming if a long domain is used. A large number of cells is required to solve the waves in proximity of the free surface. The first idea to reduce computational cost is then reducing the domain dimensions (length in this case). On the other hand, a small domain means also that the reflected waves reach the inlet earlier. Therefore, the number of roll cycles available for the RAO are strongly correlated to the domain size. A possible solution to this problem is the use of the EOM, to retain the correct inlet boundary condition (BC) removing the effect of the wave generated by the presence of the barge.

BARGE ROLL RAO WITH REGULAR WAVES

The roll RAO of a 2D barge [6] will be used to find the influence of the EOM settings. Not only the roll RAO but also a roll decay is derived in the experiments. The roll decay resulted in a roll damping of about 12% of the critical damping, from large roll amplitude (~15deg) till the motion is completely damped. Several authors [7][8] repeated via CFD the roll decay obtaining a lower damping, probably part of the damping was generated by the hinges of the barge. In this work a grid convergence study has been performed for the roll decay and, for large angle (~10 deg), results are aligned with other numerical works as shown in Fig. 3b. Only frequencies far away from the resonance will be selected for the roll RAO validation, since they are not really affected by damping. RAO will be computed using 5th order regular waves.

Even if the roll RAO is computed with regular waves, in the simulations the barge was moving not only at the wave period but also at the roll natural period. For that reason extra damping was added at the roll motion in order to damp the motion at the natural frequency. Since damping has a large impact mainly in proximity of the resonance frequency, this approach is suitable as long the frequency of interest is far from the vessel natural period.

When working in proximity of the resonance period, extra damping cannot be used since it has a large effect on the motion RAO, therefore a possible way to remove the undesired components is as follows. Perform a FFT of the vessel motion time trace to identify the frequencies present, decompose the signal in a Fourier series and keep only the component at the wave period. This approach is quite general and it can be used also far away from the natural period, but since it is more complicated than simply applying extra damping, the use of it is recommended only for wave period close to the motion resonance period.

Sensitivities have been performed on the forcing factor μ_0 and the length of the forcing zone (Fig. 4, Fig. 5 and Fig. 6). The wave tested had a period of 1.2s ($^{\omega}/_{\omega_n} = 0.768$) and a height of 0.035m. The forcing zone is one wave length long (Fig. 4). Water level has been measured just after the inlet (P1), at the point where the damping coefficient start decreasing (P2) and between the vessel and the transition zone. Fig. 5a shows that for $\mu_0 \geq 1$ no reflection from the barge are present. For $\mu_0 = 0.1$, the wave amplitude is clearly deteriorated, in other words, the wave boundary condition at the inlet is compromised. Fig. 5b shows that for $\mu_0 \geq 10$ the wave amplitude at P2 is as prescribed at the inlet. This fact suggests that if the inlet is at P2 location, the boundary condition at inlet is preserved as long as $\mu_0 \geq 10$. Fig. 5c shows that the roll angle is according to experimental results (~5 deg for a wave height of 0.035m) for $10 \leq \mu_0 \leq 100$. For the smallest μ_0 value the vessel motion is under predicted, due to the deterioration of the incident wave, while large values of μ_0 seems to generate larger vessel motion.

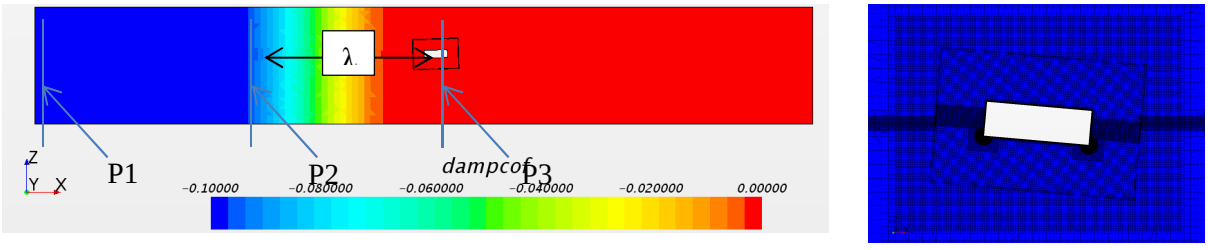

a b

Fig. 4: forcing zone location for μ_0 sensitivity with water level probes locations (a) and grid (b)

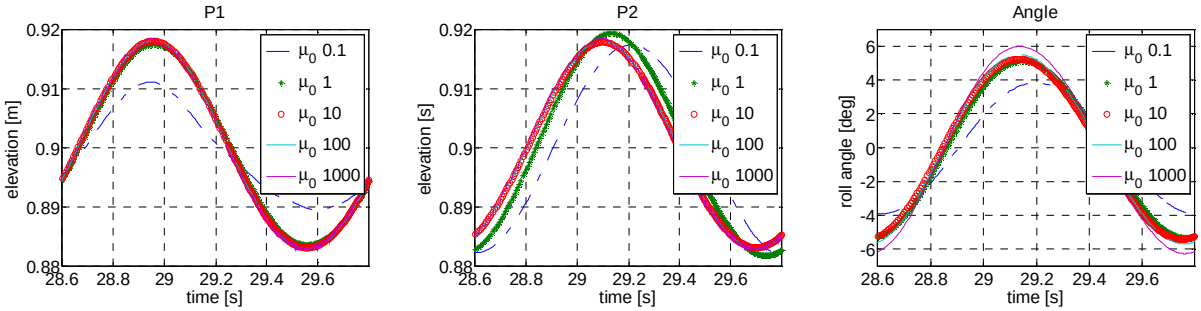

Fig. 5: sensitivity on μ_0, water level at P1, P2 and roll angle

Looking at the results of P3 in Fig. 6a, it is clear that a large value of μ_0 can create a sort of blockage effect for the reflected and radiated waves, which can be translated in more energy for the barge and therefore larger motion. Large value of μ_0 introduces also some noise in the wave profile, which is shown in Fig. 6b.

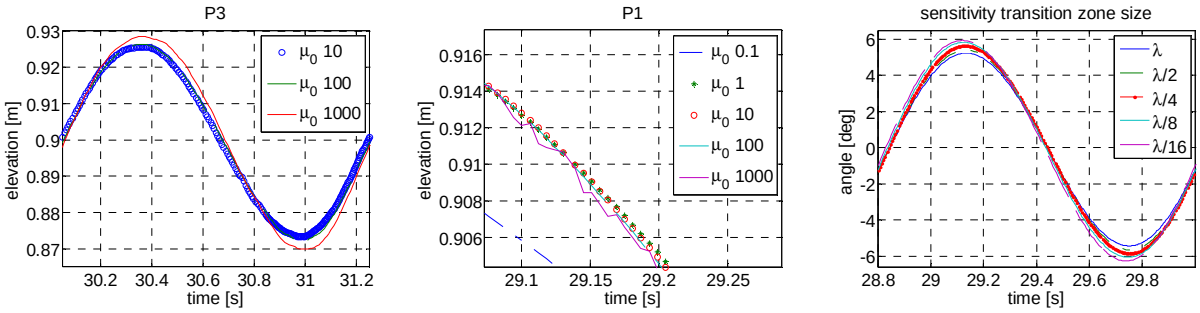

Fig. 6: results of μ_0 sensitivity (a & b) and transition length sensitivity (c)

Sensitivities have been performed also on the size of the transition zone using μ_0=10. In the base case the length of the transition zone was equal to the wave length λ (see Fig. 4). The transition zone has been decreased keeping fixed the position in front of the barge. Fig. 6c shows that decreasing the length of the transition zone the roll amplitude increases of about 13%. Possible reasons for this increase are described below.

With short transition length, the area were the wave can be dissipated because of discretization accuracy (from starting of transition zone till the barge), gets shorter. This means the incident wave on the barge has a larger amplitude and therefore a larger roll motion is generated. The incident wave amplitude, for the case with the shortest transition zone, was only 4% larger with respect to the base case (results not shown), which is not enough to justify the roll increase discussed before. Probably, with short transition zone something similar to the case with high μ_0 is taking place (see blockage effect discussed before). The results shown before suggest that not only μ_0 is important but also the length of the transition zone.

APPLICATIONS: MOONPOOL RAO

The deep water construction vessel Aegir is equipped with a pipelay tower for J-lay and reeling. The pipe and its structure are lowered to the seabed through a moonpool. The water motions inside the moonpool during installation can be described by a moonpool RAO. Deriving the moonpool RAO via CFD (RANS) for a wide range of frequency is computationally very expensive. Therefore the moonpool RAO has been computed performing CFD simulation with regular 5th order waves for the periods around the moonpool natural period while potential calculations have been performed to derive the moonpool RAO for the other frequencies. The RAO in proximity of the resonance period of the moonpool is strongly governed by viscous effect, which is why RANS calculations are required, while for the other wave periods potential calculations suffice. In this work we will focus on RANS

only. RAO will be computed with a structure inside the moonpool (structure not shown). A representation of the water surface elevation and mesh used is shown in Fig. 7. The investigated conditions for which RANS calculations have been performed were:

Wave height H = 1.0 [m]
Wave period T = 6, 8, 8.5, 9 and 10 [s]
Wave direction 150 [deg]
Vessel draught D = 10.5 m

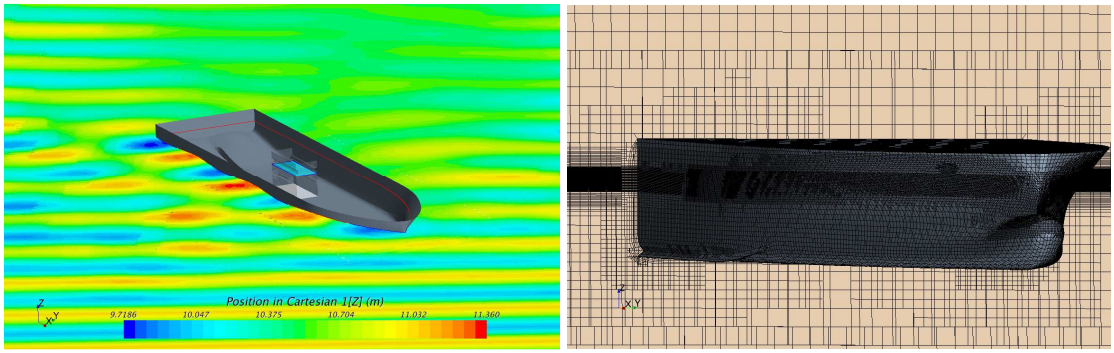

Fig. 7: CFD simulation with linear waves

The vessel motion was modelled using overset grid for the wave periods T = 6 → 9 [s]. The use of the overset grid requires the same cell size between background (domain) and overset grid (floating body) at the interfaces. This aspect can be a problem at the free-surface in presence of large movements. This was the case for wave of T = 10 [s]. For that reason it has been decided to use morphing for T = 10 [s]. A summary of the settings used for the simulations is reported in Table 1. The vessel was allowed to heave and pitch. For the wave direction used, roll motion has a minor impact on the moonpool RAO. For that reason roll motion was not modelled. Simulations were 20 wave periods long and the last 5 cycles has been used for the RAO. About 10 wave periods were required to get a steady condition in terms of vessel and moonpool motion.

Grid size	~6M	Forcing coefficient μ_0	10
Cells per wave length	~100	BL layers	5
Cells per wave height	~25	BL stretching	1.2
Time step	~T_{wave}/250	Inner loops	5
Inner loops	5	Forcing coefficient μ_0	10

Table 1: setting RANS simulations

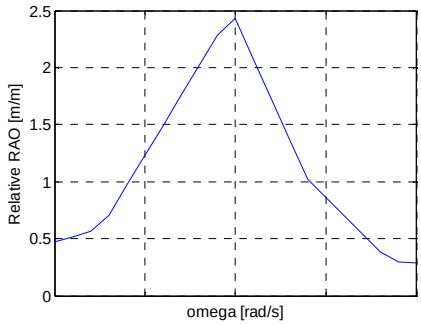

Fig. 8: relative moonpool RAO

The relative RAO is computed as the ratio between the water level fluctuation inside the moonpool w.r.t. the vessel and the undisturbed wave elevation. The water level elevation inside the moonpool has been reported with several probes and the results of the probe in the middle of the moonpool have

been used for the RAO. The undisturbed wave amplitude has been obtained from simulations without the vessel.

The relative moonpool RAO is shown in Fig. 8. CFD simulations have been performed also using $\mu_0 = 2$, and no difference in the moonpool behaviour has been found (results not shown). No sensitivity has been performed on the length of the transition zone. Nevertheless, the validation performed on the roll RAO in the previous section showed that the length of the transition zone can have an impact of about 10% on the RAO. Such an inaccuracy, from an engineering perspective, is still acceptable. The RAO shown in this section will be validated in the future with offshore measurements using a down looking radar.

SUMMARY AND CONCLUSIONS

The EOM was used to reproduce the experiments performed on a 2D barge [6]. The roll RAO has been computed and the effect of the numerical setting of the EOM has been investigated. Results showed that parameter like forcing coefficient μ_0 and the extension of the forcing zone have an impact on the simulation outcome. If μ_0 is above a certain threshold, waves radiated and reflected from the floating body are damped without interfering with the boundary conditions at the inlet. If μ_0 is too large (few order of magnitude larger than the minimum required to damp the waves), some noise is introduced in the wave profile.

The extension of the transition zone plays also an important role on the simulation outcome. On the vessel motion RAO not only the μ_0 value but also the transition zone length had some impact. Further verification is required.

The EOM has been also used to derive the moonpool RAO of the DCV Aegir at full scale. RAO has been derived for a specific wave direction with a structure inside the moonpool. Results will be validated with offshore measurements in the future using a down looking radar.

To derive motion RAO's with regular waves the EOM has been used with success. Using EOM smaller numerical domains can be used to save CPU time. In the future the EOM in combination with irregular sea-states will be investigated.

REFERENCES

[1] Ottens, H., Pistidda, A., Motion RAOs of a SSCV at deep and inconvenient draft using CFD, OMAE2015, St John's, Newfoundland, Canada.

[2] Jang Kim et al, Ringing analysis of a vertical cylinder by Euler Overlay Method, OMAE2012, Rio de Janeiro, Brazil.

[3] CD-Adapco, *User Guide STAR-CCM+*, version 9.04.009, London

[4] Kim, J. W., Kyoung, J. H., Ertekin, R. C., & Bai, K. J., 2006. Finite-element computation of wave-structure interaction between steep Stokes waves and vertical cylinders. *J. Waterway, Port, Coastal, Ocean Eng.*, vol. 132, pp. 337–347.

[5] Enger, S., Peric, M., Monteiro, H., Coupling of 3D numerical solution method based on Navier-Stokes equations with solutions based on simpler theories. CILAMCE2014, Fortaleza, Ceará, Brazil.

[6] Jung, K., J., Chang, K., Jo, H., J., February 2006. Viscous effect on the roll motion of a rectangular structure. *Journal of Engineering Mechanics*, Vol.132, pp. 190-200.

[7] L.F. Chen et al, Numerical Simulation of Wave-Induced Roll of a 2-D Rectangular Barge Using OpenFOAM, IWWWFB 2014, Osaka, Japan.

[8] E. Paterson, Multiphase and Free-Surface Flow Simulations, 3rd OpenFOAM Workshop, Milan, Italy

CFD Cavitation Model Parameters and Their Influence on Simulation Case

Dmitriy Ponkratov, Lloyd's Register, London/UK, Dmitriy.Ponkratov@lr.org

1. Introduction

With the new International Maritime Organisation (IMO) regulations MARPOL Annex VI coming into force, energy efficient propulsion systems are becoming important. The drive to increasing levels of efficiency necessitates special attention to be paid by ship and propulsion designers to cavitation issues. The traditional way to investigate and predict cavitation on marine propulsors during the design stage is a physical model experiment in a cavitation tunnel or depressurised towing tank. Even though the procedures for these tests are well established over decades of performing experiments, some principal uncertainties, such as the difference in Reynolds number between model and ship scale objects are unavoidable.

It is now practical to perform cavitation investigations using Computational Fluid Dynamics (CFD) due to recent advances in computational methods and a reduction in the cost of computer power. Carrying out a simulation in ship scale simultaneously maintains the correct Reynolds and Froude numbers, avoiding the scale effect problems associated with physical model tests. However, the numerical simulations of even non-cavitating flows have their own uncertainties related to turbulence models, mesh types, discretisation schemes etc. The influence of these general parameters has been thoroughly investigated for non-cavitation cases by researchers in various publications. For example, Li et al (2006) investigated the influence of turbulence models on propeller open water characteristic prediction. Krasilnikov (2013) investigated a similar influence on self-propelled model scale vessel.

CFD software developers continually improve their codes, introducing new parameters that can be tuned, influencing simulation results. A general purpose commercial CFD code STAR-CCM+ is one of the most widely used software programs within industry offering a choice of cavitation model parameters, such as scaling factor of cavitation rate and density of seed nuclei, which can have an influence on the simulation results (CD-Adapco, 2014). Undoubtedly, knowing the impact of these parameters on the simulation results would greatly benefit researchers working on cavitation simulation that the aim of this paper is to help enhance knowledge for this purpose.

2. Study case: hydrofoil NACA0015

Since a CFD simulation of cavitation requires a fine mesh together with a small time step, it was decided to establish a correlation between cavitation model parameters based on a model scale object. This approach facilitated the completion of the investigation within a reasonable time frame. For the study case an intensively investigated hydrofoil NACA0015 was selected. Numerical and experimental studies for this case were completed within Cooperative Research Ships (CRS) EROSION II working group, in which Lloyd's Register Technical Investigation Department (LR TID) participated (Boorsma 2010, Hoekstra 2011, Rijsbergen and Boorsma 2011). The computational settings, such as flow speed, cavitation number, and angle of attack were identical to the experiment set up. This hydrofoil was also numerically investigated by Ponkratov and Caldas (2015), Li (2012) and Li and Terwisga (2012), however, their main focus was the erosion prediction. As the hydrofoil has a well-known offset of points, the geometry was built based on these points. The size of computational domain was identical to the section of the cavitation tunnel, where the object was tested. An illustration of the computational domain is provided in Fig. 1.

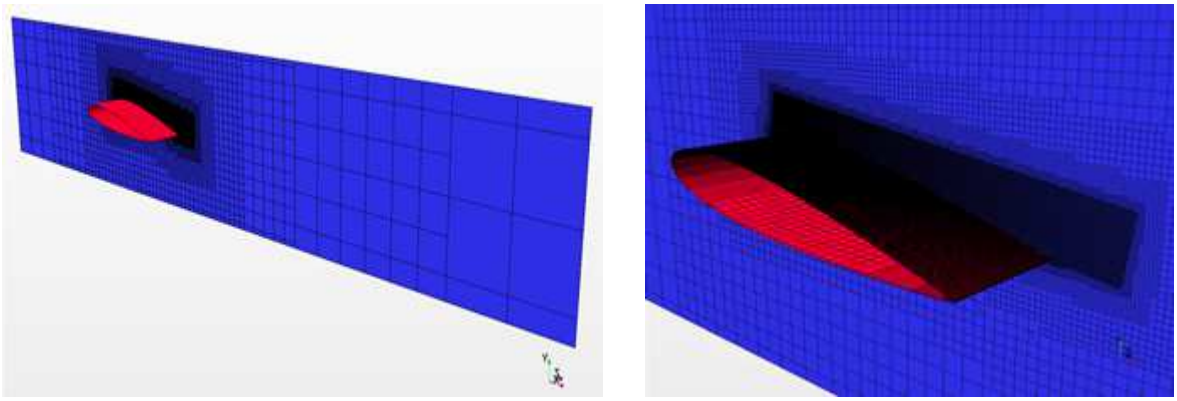

Fig. 1. Computational domain identical to cavitation tunnel working section and mesh refinement above foil

The computational domain extended to approximately two foil lengths fore of the leading edge, four lengths aft of the trailing edge and on the sides the foil was connected to the walls. The boundary condition on the sides of the computational domain (as well as on the top and bottom) were set up as a non-slip wall, replicating experimental geometry. In order to save computational time, it was decided to calculate only half of the foil, assuming that the cavitation extent is symmetrical.

A trimmed mesh methodology was used and an additional mesh refinement was made on the upper side of the foil, where the cavitation structures were expected, Fig. 1. The final computational mesh was approximately 4 million cells. Initial calculations were completed with RANS equations and closed with the k-ω SST turbulence model. However, the final calculations were completed with the Detached Eddy Simulation (DES) model.

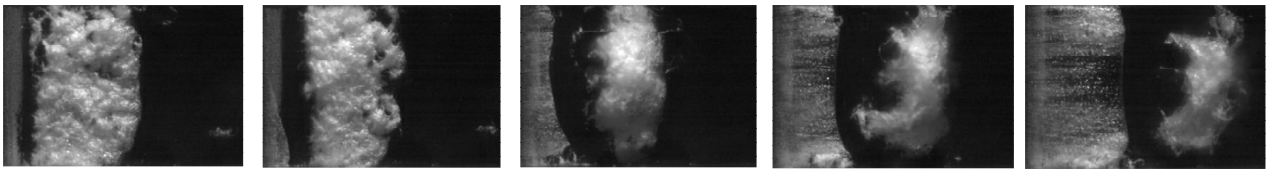

Fig. 2. Experimental observation of cavitation. Top view. Flow comes from the left.

Fig. 3. CFD prediction. Scaling factor of negative cavitation rate 0.1. Seed nuclei density 10^{14}.

Fig. 4. CFD prediction. Scaling factor of negative cavitation rate 1. Seed nuclei density 10^{14}.

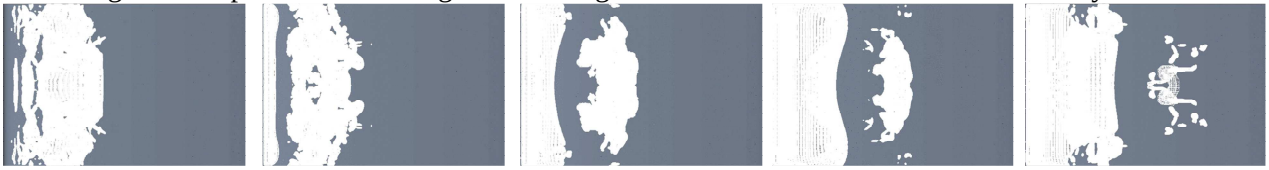

Fig. 5. CFD prediction. Scaling factor of negative cavitation rate 2. Seed nuclei density 10^{14}.

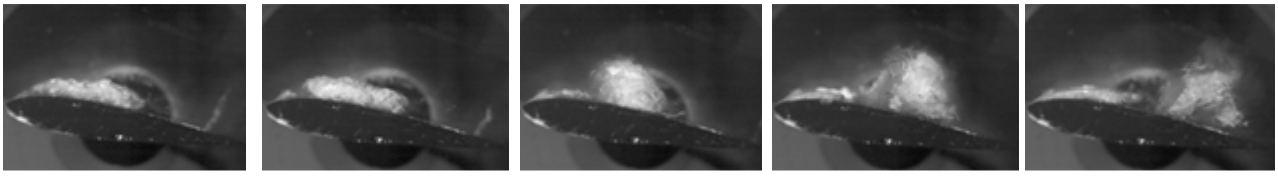

Fig. 6. Experimental observation of cavitation. Side view. Flow comes from the left.

Fig. 7. CFD prediction. Scaling factor of negative cavitation rate 0.1. Seed nuclei density 10^{14}.

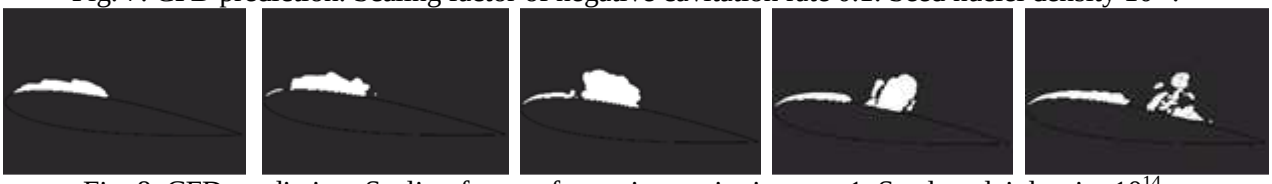

Fig. 8. CFD prediction. Scaling factor of negative cavitation rate 1. Seed nuclei density 10^{14}.

Fig. 9. CFD prediction. Scaling factor of negative cavitation rate 2. Seed nuclei density 10^{14}.

All results presented in this paper were calculated based on the DES model. As mentioned previously, the computational settings, such as flow speed, cavitation number, and angle of attack were identical to the experiment set up. The simulation strategy was as follows: at the initial stage, the flow around the hydrofoil was calculated in a steady mode. The cavitation model was active; however, the saturation pressure was set to an unphysical value to ensure that cavitation does not appear at this stage. The seed nuclei density was set to 10^{14}. Once the convergence of this stage was achieved, the simulation was switched to an unsteady mode maintaining the same unphysical saturation pressure. The time step at this stage was approximately 2.0×10^{-5} sec and the simulation was continued. As soon as the unsteady case converged, the time step was reduced to 1×10^{-6} sec and the saturation pressure was set to a physical value. As sudden development of cavitation may be unphysical, the calculation progressed to a stage when some shedding cycles are completed. At this stage the simulation file was saved, therefore the starting point of the current study was obtained. All further calculations described in this paper were progressed from this stage with different parameter settings.

The first set of results consists of the top and side views of cavitation development over the period of time. For comparison Figs. 2 and 6 show the development of cavitation extent recorded during one typical shedding cycle in the cavitation tunnel by high speed video camera. The pictures should be viewed from left to right hand side. The flow is coming from the left.

Figs. 4 and 8 show the progression of cavitation calculations within one shedding cycle, with default cavitation model settings. The cavitation is visualised in the CFD simulations by showing the extent of the 0.05 ratio of vapour volume fraction. It can be seen that the DES model generally predicts the cavitation development satisfactorily. The main sheet cavity detaches from the leading edge and transforms into a cloud, similar to model scale test observations. However, the volume of cavitation extent both in sheet and cloud are somewhat less than experiment. This could be to a number of reasons such as numerical diffusion and mesh size sensitivity.

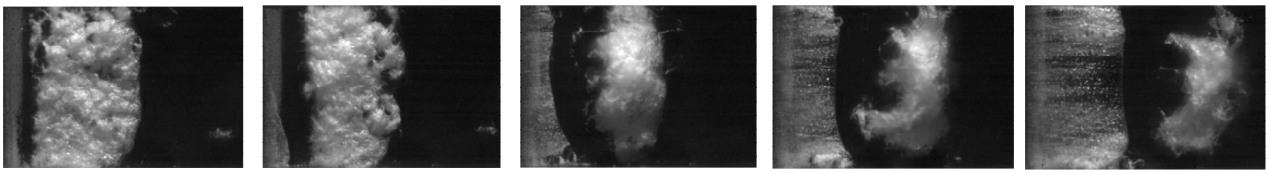

Fig. 10. Experimental observation of cavitation. Top view. Flow comes from the left.

Fig. 11. CFD prediction. Scaling factor of negative cavitation rate 1. Seed nuclei density 10^{14}.

Fig. 12. CFD prediction. Scaling factor of negative cavitation rate 1. Seed nuclei density 10^{12}.

Fig. 13. CFD prediction. Scaling factor of negative cavitation rate 1. Seed nuclei density 10^{10}.

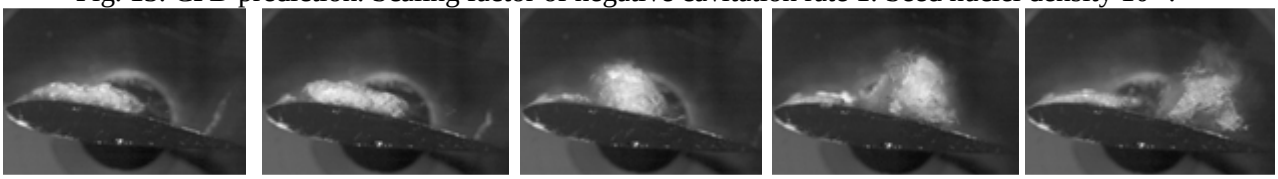

Fig. 14. Experimental observation of cavitation. Side view. Flow comes from the left.

Fig. 15. CFD prediction. Scaling factor of negative cavitation rate 1. Seed nuclei density 10^{14}.

Fig. 16. CFD prediction. Scaling factor of negative cavitation rate 1. Seed nuclei density 10^{12}.

Fig. 17. CFD prediction. Scaling factor of negative cavitation rate 1. Seed nuclei density 10^{10}.

In STAR-CCM+ there are some parameters that can improve the cavitation pattern relatively easily without any modification to the computational mesh. One of these is the scaling factor of cavitation rate which makes the development of cavitation extent slower or quicker. According to CD-Adapco (2014) the parameter called scaling factor of positive cavitation rate controls cavitation growth speed. This parameter introduces a new uncertainty since the cavitation pattern development can be artificially tuned by a user through this variable. Hence, the results can be adjusted depending on the

requirements. For this reason this parameter was set up to a default value 1 and remained unchanged for all cases described in the paper.

The second parameter called scaling factor of negative cavitation rate controls how quickly cavitation disappears. Since accurate simulations of cavitation demand a high resolution mesh, and low resolution meshes will cause artificial diffusion, an efficient modelling approach may be to use the negative cavitation rate for coarse meshes to offset the diffusion.

According to CD-Adapco (2014) a negative cavitation rate value less than 1 should delay the cavitation diffusion and consequently, a value greater than 1 should increase diffusion. Fig. 3 shows the further progression of calculation case with scaling factor of negative cavitation rate 0.1, keeping other parameters the same. Fig. 5 shows the results of the run with a rate of 2, again keeping all other parameters unchanged. Comparing Figs. 3, 4 and 5, it can be concluded that this parameter has a minor influence on the volume of cavitation sheet. The volume of developed cloud cavitation is again almost the same. However, the cloud cavitation disappears earlier in the case with a lower scaling factor. Setting the factor to 2 increases the extent of the cavitation. Figs. 7, 8 and 9 show the side view of results from the same runs.

Another parameter available for the investigation is the density of seed nuclei. It is well known that apart from the cavitation number, the number of different particles contained in the water plays a major role, as it physically triggers the cavitation. For that reason cavitation in distilled water would not be observed. Hence, the value of seed nuclei density becomes a pseudo-physical parameter, as this characteristic of water exists naturally.

The results of a set of simulations where the seed nuclei was varied are shown in Figs. 11 to 13 (top view) and Figs. 15 to 17 (side view). The base case seed nuclei results (10^{14}) are shown in Figs. 11 and 15. Figs. 12, 13, 16 and 17 show further calculations of the case, but with the nuclei density 10^{10} and 10^{12}. As shown in these figures, setting the density to a lower value of 10^{10} or 10^{12} reduces the extent of the cavitation.

The process for generating the results for the cases with nuclei density of 10^{10} and 10^{12} was changing the nuclei density after a shedding establishment period using a nuclei density of 10^{14}.

The approach implemented in this paper where cavitation was initiated with one density of nuclei and then changed may be recommended for cavitation cases with relatively high cavitation numbers where cavitation extent is expected to be small. For these cases it is suggested to set up an artificially high value of nuclei density to initiate the cavitation and then reduce the density to a realistic value.

3. Conclusions

Undoubtedly, CFD prediction of cavitation requires careful implementation of numerical meshes, calculation time step, turbulence models, cavitation models, near wall treatment, differential schemes etc. There are also some CFD code specific parameters, such as the scaling factor of cavitation rate and seed nuclei density that require consideration. During the study it was established that seed nuclei density is the most pseudo-physical parameter influencing the cavitation results. Similar to reality, changing this value can initiate the cavitation at an earlier or later stage. For the cases with a relatively high cavitation number, where the cavitation extent is expected to be small, it may be recommended to artificially increase the seed nuclei density value at an initial stage, in order to trigger cavitation. After that, the density should be reduced to a realistic value.

It is understood that the scaling factor of cavitation rate is a numerical tool which can improve the cavitation development. However, there is no guarantee that the specific value of this parameter will improve all cavitation cases. Special attention should be paid whilst working with these parameters, as it may introduce additional uncertainties.

Acknowledgement

I would like to thank my colleagues C. Craddock, T. Hall and A. Caldas for their significant support.

References

Boorsma, A., (2010) CRS Erosion II WG, Cavitation tests on a NACA 0015 Aerofoil, Quantification of Cavitation Impacts from High Speed Video and AE Signals, *TID report 6997*, November 2010.

CD-Adapco (2014) STAR-CCM+ 9.06.009 User Guide.

Hoekstra, M. (2011) Cavitation Simulations for a NACA0015 foil in a Tunnel, *CRS Report 23990-2-RD*, 2011.

Krasilnikov, V. I., (2013) Self-Propulsion RANS Computations with a Single-Screw Container Ship, *3rd Int. Symp. on Marine Propulsors, SMP'13*, Launceston, Tasmania, Australia, May 2013.

Li, D.Q., Berchiche, N. and Janson, C.E., (2006) Influence of Turbulence Models on the Prediction of Full-Scale Propeller Open Water Characteristics with RANS methods, *Proc., 26th Symp. on Naval Hydrodynamics*, Rome, Italy.

Li, Z. (2012) Assessment of Cavitation Erosion with a Multiphase Reynolds-Averaged Navier-Stokes Method, *PhD thesis*, Delft University of Technology, 2012.

Li, Z. and Terwisga, T.V. (2012) On the capability of a RANS method to assess the cavitation erosion risk on a hydrofoil, *8th Int. Symp. on Cavitation CAV2012*, Singapore, 2012.

Ponkratov, D. and Caldas, A. (2015) Numerical Prediction of Cavitation Erosion and its Validation against Model and Ship Scale Results, *4th Int. Symp.on Marine Propulsors, SMP'15*, Austin, Texas, USA, June 2015.

Rijsbergen, M.X. and Boorsma, A. (2011) High Speed Video Observations and Acoustic Impact Measurements on a NACA 0015 Foil, *CRS Report 22195-5-RD*, July 2011.

Time-Splitting Procedure for the Resolution of the Volume Fraction for Unsteady Flows

Yoann Robert, Alban Leroyer, Jeroen Wackers, Michel Visonneau and Patrick Queutey

LHEEA Lab., École Centrale de Nantes / CNRS-UMR 6598, 1 rue de la Noë, Nantes, France
yoann.robert@ec-nantes.fr

1 Introduction

Numerical simulations of multifluid flows using interface capturing schemes are highly constrained by the Courant-Friedrichs-Lewy (CFL) condition. Even with implicit codes, the Courant number Co is limited to values lower than unity in order to benefit from compressive properties of the schemes and to restrict the diffusion of the interface [6, 9]. Therefore the usable time steps become rapidly redhibitory since they are linked to the grid by the definition of Co and since, if the grid is refined, the time step must be reduced accordingly. This is particularly true when the free surface undergoes large and violent deformations, as in the case of a rowing stroke in water [3, 8] or a prism impacting a free surface [2, 10]. The equation subject to this condition is the convection equation of the volume fraction of water c.

The goal of this work is to elaborate a strategy to accelerate numerical simulations of unsteady multifluid flows while formally respecting the CFL condition. The procedure presented here is an extension of the one developed for flows reaching a steady state [4]. Manzke *et al.* have likewise worked on this topic [5] but only a few details were given for the treatment of unsteady computations. In short our method allows the use of a larger global time step for each temporal iteration and the resolution of the convection equation for c is carried out in several successive steps in which the associated time step is smaller. This compromise enables to diminish the total computation time, a priori without loss of accuracy. This approach should be even more efficient for parallel computations and especially for the fine meshes using adaptive grid refinement (AGR) [10]. In the AGR procedure, a number of layers of refined cells around the free surface, or buffer layers, can be set. This is done to ensure that the free surface stays in the refined grid area, until the next step of grid refinement. Indeed each refinement causes an extra cost in CPU time, that is why it is not performed at each temporal iteration. The combination of the AGR with the time-splitting procedure enables to carry out an indirect form of parallelisation of the temporal resolution: the use of a larger time step leads to increase the number of buffer layers, and thus the number of cells, which forces to employ more cores. Parallel computations have a problem of scaling efficiency, as there is an issue of communication between cores, in other words a maximum number of cells per core. So the use of the time-splitting procedure with a reasonable number of extra cores, keeping the same ratio of cells per core as for a regular computation, should make the number of temporal iterations decrease and will therefore reduce the total CPU time.

In the article, some explanations of the method will be given in section 2 and first results showing benefits will be exposed in section 3. Finally, section 4 will draw some conclusions and perspectives. In the remainder of the document, the term *time-splitting procedure* will be employed to indicate the described method.

2 The time-splitting procedure

2.1 Principle

The time-splitting procedure consists of cutting each original time step into N successive intervals (see figure 1), also called temporal splits or subcycles, and solving c on each of them. Hence a fraction of the original time step is associated with each temporal split and adjusted to have a Courant number satisfying the CFL condition. In this way, the global time step can be increased and the total CPU time will therefore be reduced. The global time step can in principle be set to a critical value, representing the limit not to cross in order to capture the physics with a second-order time discretisation scheme, regardless of the grid fineness. The cost of the extra resolutions for the volume fraction remains quite low because this resolution is not the most time-consuming part in RANS codes.

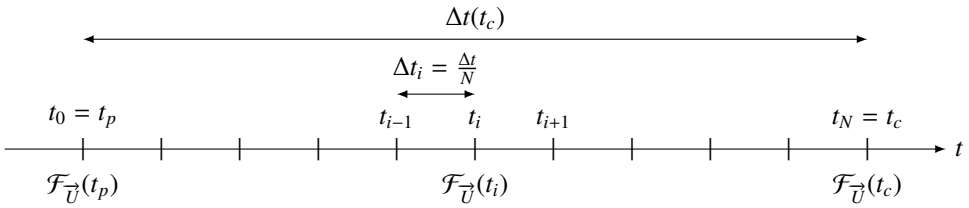

Figure 1: Temporal splitting for the equation (2).

2.2 Time-integration method

The equation to solve for the interface-capturing methods using an ALE approach is the convection equation for the volume fraction c:

$$\frac{\delta}{\delta t}\int_{\mathcal{V}} c \,\mathrm{d}\mathcal{V} + \oint_{\mathcal{S}} c\left(\overrightarrow{U} - \overrightarrow{U_d}\right)\cdot\overrightarrow{n}\,\mathrm{d}\mathcal{S} = 0\,, \tag{1}$$

where $\mathcal{V}$ is the control volume limited by a closed surface $\mathcal{S}$ of normal vector $\overrightarrow{n}$ outwardly directed and moving at a velocity $\overrightarrow{U_d}$. The time derivative following the moving grid is written $\frac{\delta}{\delta t}$.

The finite volume discretisation with the first-order backward differentiation formula leads to the following discretised equation:

$$\frac{c(t_c)\,V(t_c) - c(t_p)\,V(t_p)}{\Delta t} + \sum_{\text{faces } \mathcal{S}_f} c_f(t_c)\left(\mathcal{F}_{\overrightarrow{U}}(t_c) - \mathcal{F}_{\overrightarrow{U_d}}(t_c)\right) = 0\,, \tag{2}$$

where t_p and t_c indicate respectively the previous and current instants, $\Delta t = t_c - t_p$ the current global time step and V the volume of the cells. The reconstruction of the volume fraction at the face centre is noted c_f. The vectors $\mathcal{F}_{\overrightarrow{U}}$ and $\mathcal{F}_{\overrightarrow{U_d}}$ are respectively the flux of velocity and the flux of displacement velocity of the grid through the face $\mathcal{S}_f$. These three quantities are expressed at the current instant t_c. To shorten thereafter the equations, the variable $\mathcal{F}'$ is introduced to gather both fluxes and is defined by $\mathcal{F}' = \mathcal{F}_{\overrightarrow{U}} - \mathcal{F}_{\overrightarrow{U_d}}$. The first-order time discretisation scheme described here is not able to accurately capture unsteady phenomena for reasonable time steps because it is too diffusive. However, for computations reaching a steady state, an accurate temporal resolution is not sought, which means that this scheme can be used. On the other hand, the temporal accuracy is essential for unsteady computations. At the end of the time step, the second-order backward differentiation formula (BDF2) has to be verified:

$$e_c\,c(t_c)\,V(t_c) + e_p\,c(t_p)\,V(t_p) + e_q\,c(t_q)\,V(t_q) + \sum_{\text{faces } \mathcal{S}_f} c_f(t_c)\,\mathcal{F}'(t_c) = 0\,, \tag{3}$$

where e_c, e_p and e_q are the coefficients of the aforementioned scheme for the time derivative and t_q is the instant preceding t_p. This causes new difficulties compared to the steady case explained in [4], especially to reconstruct c_f on the global time step (detailled in section 2.2.2).

2.2.1 Resolution of the cell-centered volume fraction on a subcycle

As previously mentioned, the resolution of (1) is carried out by a succession of temporal splits on intervals $\Delta t_i = \frac{\Delta t}{N}$ (see figure 1). The fluxes $\mathcal{F}_{\overrightarrow{U}}$ and $\mathcal{F}_{\overrightarrow{U_d}}$, as well as the volumes, are interpolated between their values at the instants t_p and t_c, knowing that quantities at t_c are updated at each non linear iteration within the convergence loop. By linear combination, $\mathcal{F}'$ is calculated in the same way:

$$\mathcal{F}'(t_i) = (1-\alpha_i)\,\mathcal{F}'(t_p) + \alpha_i\,\mathcal{F}'(t_c) \quad \text{with} \quad 0 < i \leq N\,, \quad \alpha_i = \frac{i}{N} \quad \text{and} \quad t_i = t_p + \alpha_i\,\Delta t(t_c)\,. \tag{4}$$

The Crank-Nicolson scheme (5) has been chosen to maintain a second-order accuracy with a compact two-point stencil for the time discretisation on each subcycle. The discretised equation of convection for the volume fraction within each temporal split is then written:

$$\frac{c(t_i)\,V(t_i) - c(t_{i-1})\,V(t_{i-1})}{\Delta t(t_i)} + \frac{1}{2}\sum_{\text{faces } \mathcal{S}_f} c_f(t_i)\,\mathcal{F}'(t_i) = -\frac{1}{2}\sum_{\text{faces } \mathcal{S}_f} c_f(t_{i-1})\,\mathcal{F}'(t_{i-1})\,, \tag{5}$$

where the right-hand side is the source term.

The value of c at t_c is directly equal to its value at the last subcycle.

2.2.2 Reconstruction of the interfacial volume fraction at the global level

The interfacial volume fraction c_f, expressed at the time t_c, is required to compute the term $\rho\,\mathcal{F}'$ of the momentum equation. It has to be reconstructed while verifying the second-order time discretisation of (3). To do so, it is mandatory to take into account the evolution of the cell-centered value of c during the subcycles.

The sum of the N equations (5) between t_p and t_c leads to:

$$\frac{c(t_c)\,V(t_c) - c(t_p)\,V(t_p)}{\Delta t(t_c)} + \sum_{\text{faces } \mathcal{S}_f} \underbrace{\frac{1}{2\,N(t_c)} \left(\sum_{i=1}^{N(t_c)} c_f(t_i)\,\mathcal{F}'(t_i) + \sum_{i=1}^{N(t_c)} c_f(t_{i-1})\,\mathcal{F}'(t_{i-1}) \right)}_{= B_{t_p \to t_c}} = 0\,. \tag{6}$$

This first step enables to have an equation where the time-derivative part is identical to (2), hence only a first order. The term $B_{t_p \to t_c}$ can be seen as an interfacial quantity equal to the average of $c_f\,\mathcal{F}'$ over all the temporal splits between t_p and t_q. The same sum between t_q and t_p gives:

$$\frac{c(t_p)\,V(t_p) - c(t_q)\,V(t_q)}{\Delta t(t_p)} + \sum_{\text{faces } \mathcal{S}_f} \underbrace{\frac{1}{2\,N(t_p)} \left(\sum_{i=1}^{N(t_p)} c_f(t_i)\,\mathcal{F}'(t_i) + \sum_{i=1}^{N(t_p)} c_f(t_{i-1})\,\mathcal{F}'(t_{i-1}) \right)}_{= B_{t_q \to t_p}} = 0\,. \tag{7}$$

From the equations (6) and (7), it is possible to retrieve a BDF2 for (1). The second-order time discretisation of the derivative of a quantity ϕ at the time t_c, in function of t_c, t_p and t_q is:

$$\left(\frac{\delta \phi}{\delta t}\right)_{t=t_c} = e_c\,\phi_c + e_p\,\phi_p + e_q\,\phi_q\,, \tag{8}$$

with

$$e_c = \frac{2\,\Delta t(t_c) + \Delta t(t_p)}{\Delta t(t_c)\left[\Delta t(t_c) + \Delta t(t_p)\right]}\,, \quad e_p = -\frac{\Delta t(t_c) + \Delta t(t_p)}{\Delta t(t_c)\,\Delta t(t_p)} \quad \text{and} \quad e_q = \frac{\Delta t(t_c)}{\Delta t(t_p)\left[\Delta t(t_c) + \Delta t(t_p)\right]}\,. \tag{9}$$

Applying the linear combination

$$(11) \leftarrow (6) \cdot e_c \cdot \Delta t(t_c) - (7) \cdot e_q \cdot \Delta t(t_p)\,, \tag{10}$$

leads to, after simplifications, an equation with a second-order time derivative:

$$e_c\,c(t_c)\,V(t_c) + e_p\,c(t_p)\,V(t_p) + e_q\,c(t_q)\,V(t_q) + \underbrace{\sum_{\text{faces } \mathcal{S}_f} \left[e_c\,\Delta t(t_c)\,B_{t_p \to t_c} - e_q\,\Delta t(t_p)\,B_{t_q \to t_p} \right]}_{F} = 0\,. \tag{11}$$

The term F contains $B_{t_q \to t_p}$ and $B_{t_p \to t_c}$, respectively computed in the subcycles of the intervals $[t_q, t_p]$ and $[t_p, t_c]$. To fulfill (3), F has to be written under the form (12) where $\tilde{c}_f$ stands for the reconstructed value of c_f.

$$F = \sum_{\text{faces } \mathcal{S}_f} \tilde{c}_f\,\mathcal{F}'(t_c)\,. \tag{12}$$

This gives the following arbitrary expression for $\tilde{c}_f$:

$$\tilde{c}_f = \frac{1}{\mathcal{F}'(t_c)} \left[\Delta t(t_c)\,e_c\,B_{t_p \to t_c} - \Delta t(t_p)\,e_q\,B_{t_q \to t_p} \right] \tag{13}$$

where an obvious problem arises in the case $\mathcal{F}' = 0$. Until now, the division by $\mathcal{F}' + \epsilon$ (with ϵ equal to 10 times the machine precision), proved to be a functional workaround.

3 Results for the dam break with obstacle

The time-splitting procedure has been implemented in the *ISIS-CFD* code [7], developed by the DSPM (Dynamics of Marine Propulsion Systems) team of the LHEEA Lab. and available as part of the FINE™/Marine computing suite. Then it has been validated on several bidimensional test cases, for flows reaching a steady state and purely unsteady flows: simple advection of a square, submerged foil (as described in [1, 4]), dam break with an obstacle or propagation of waves. Solutions are very close (or even identical) to the ones obtained without the time-splitting procedure. In these first computations, the expected reduction of the total CPU time is confirmed: a reduction factor up to 4 has been reached. In this article, the results related to the dam break with obstacle are presented.

3.1 Test case description

One of the most interesting examples used for the validation of the simulation of free surface flows is the dam break with obstacle [9]. In the initial state (see figure 2), a rectangular water column (146 cm wide, 292 cm high) is located in the lower left corner of a square domain (side of 584 cm) whose edges are solid walls except for the top one which is in open air. The gravity makes the water column fall, the latter hits a rectangular obstacle (24 cm wide, 48 cm high).

3.2 Numerical procedure

For these simulations, a slip condition is applied to all solid walls. Since the case is two-dimensional, a mirror condition is used for the front and back faces. A Dirichlet condition is applied to the upper face: the hydrostatic pressure is imposed.

The mesh generation is performed with HEXPRESS™. Two kinds of grid have been used. In the first configuration, the grid is fixed and quite fine. In the lower half of the domain, there are 192 cells in the horizontal direction and 96 in the vertical direction. The grid becomes coarser in the upper part. The dimensions of the cells gradually get larger as the vertical coordinate increases and reach values they would have if the domain would be entirely discretised in 24 per 24 cells. In the second configuration, the AGR is used. The initial mesh is quite coarse since the domain contains only 58 cells in each direction, except in a more refined area around the obstacle. The cells around the free surface are refined during the computation every three time steps, with a target size of 1,25 mm (normal distance to the free surface) and with a given number of buffer layers of cells N_l.

The computations have been done on the same computer and with only one core. Cases with or without time-splitting procedure have been launched and different numbers N of temporal splits (as defined in section 2) have been tested. If $N = 1$, it means that the time-splitting procedure has not been used. Increasing N should make the CPU time t_{CPU} decrease although it has to be verified that the results do not degrade. For instance, the maximum value of the horizontal component of the force on the obstacle Fx_{max} is examined. Since any experimental value are available, the value of the case 4 (see table 1) is arbitrarily taken as reference. When the time-splitting procedure is used, it is necessary to increase N_l to have a sufficient safety margin. Thus the mean number of cells $N_{c,\,mean}$ is higher.

The global time step is adapted at each temporal iteration in order to have a global Courant number Co lower than a limit value. For the computations not using the time-splitting procedure, this limit is equal to 0.3 and this value is multiplied by N in the other cases.

3.3 Results

The results of six different cases are summed up in the table 1, all reaching a physical time of simulation of 0.2 s. The evolution of the simulated flow, together with the grid, between the initial instant and $t = 0.6\,s$ is represented in figure 3. The images come from the case 5, somewhat modified to avoid at best undesirable effects relative to the AGR, i.e. unnecessary and costly generations of cells after $t = 0.2\,s$ (images 3c to 3f) and to prevent the water from hitting the top boundary. So the action of the AGR is limited to a acceptable vertical coordinate and the domain is enlarged in the vertical direction. The evolution of the solution as described in [9] is reproduced. A fine layer is coming from the water column and impacts the obstacle. A tongue of water is created at the top of the obstacle, then it is directed to the right and hits the opposite wall of the domain, trapping air below itself. A secondary tongue is then created at the top right of the obstacle, imprisoning in its turn an area of air.

3.3.1 Computations with fixed grids

The first three cases use the fixed-grid configuration. As seen in figure 4, the contour lines of c at $t = 0.2\,s$, with or without using the time-splitting procedure, are very similar. The main difference is that a bigger drop is breaking away from the tongue of water in the case 3. The use of the time-splitting procedure enables to decrease t_{CPU}: a factor up to 3 has been reached in the case where $N = 10$. The cost C_{tot} of each computation can also be observed. It shows the mean total CPU time per cell. Since the number of cells does not vary for this grid, C_{tot} has the same ratio than t_{CPU}. However, Fx_{max} is slightly reduced. The global time step may have been chosen too large relatively to the physics of the flow. The use of time steps too large also has the tendency to trap air at the impact on the obstacle, which consequently reduces the force.

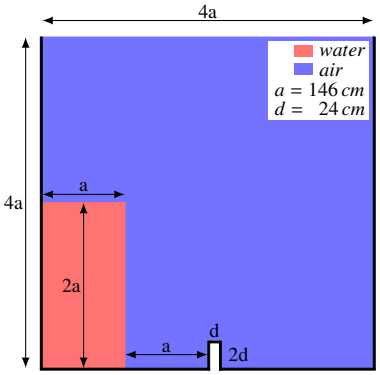

Figure 2: Initial configuration of the dam break with obstacle test case.

Case	N	AGR	N_l	t_{CPU} (s)	ratio t_{CPU}	$N_{c,\,mean}$	ratio $N_{c,\,mean}$	C_{tot}(ms/pt)	ratio C_{tot}	Fx_{max} (N)	Error Fx_{max} (%)
1	1	×	×	1905	-	20210	-	94.3	-	183	0.5
2	5	×	×	824	2.31	20210	1	40.8	2.31	179	2.7
3	10	×	×	646	2.95	20210	1	32.0	2.95	175	4.9
4	1	✓	1	3514	-	5774	-	540.9	-	184	-
5	10	✓	5	2545	1.38	8039	1.39	280.1	1.93	178	3.3
6	10	✓	10	3285	1.07	10590	1.83	263.9	2.05	179	2.7

Table 1: Summary of the results obtained for a physical time of simulation of 0.2 s.

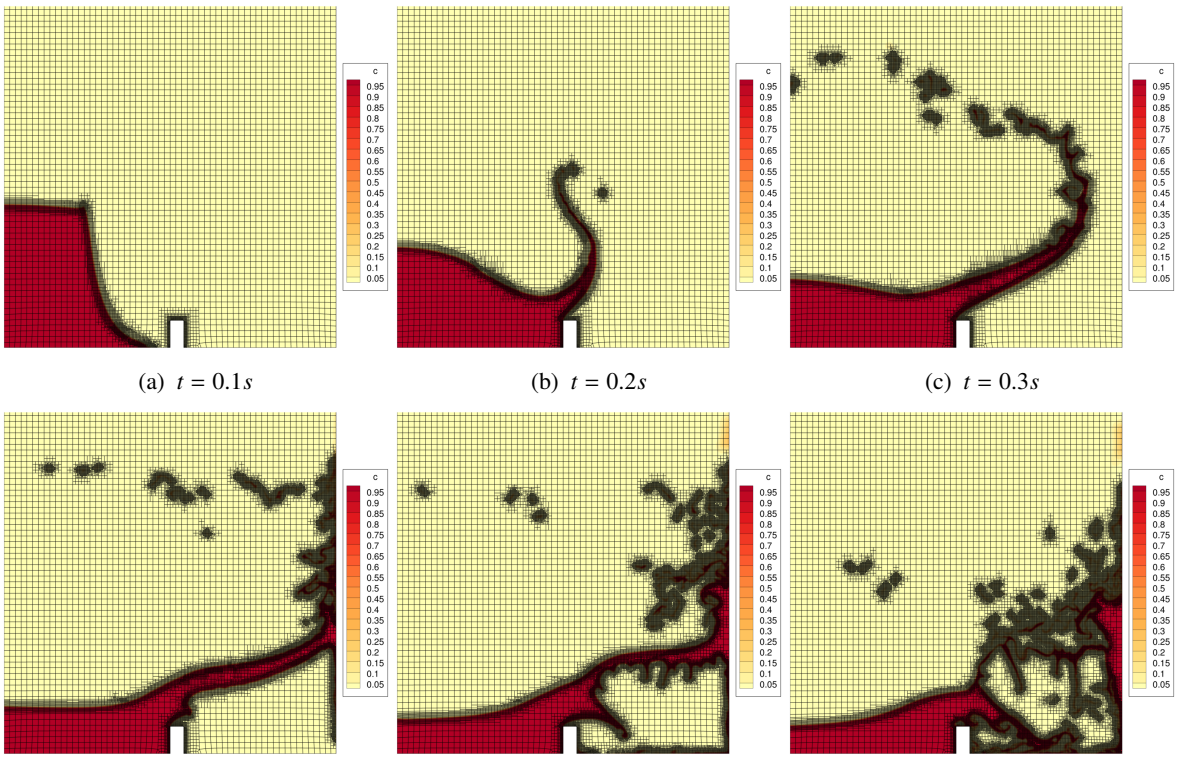

(a) $t = 0.1s$ (b) $t = 0.2s$ (c) $t = 0.3s$

(d) $t = 0.4s$ (e) $t = 0.5s$ (f) $t = 0.6s$

Figure 3: Evolution of the simulated flow for the case 5. Contours of the volume fraction on the refined grid.

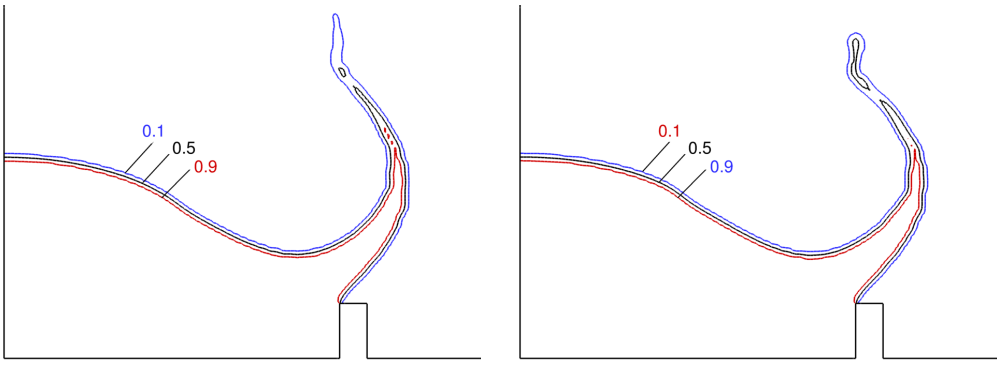

(a) $N = 1$, case 1 (b) $N = 10$, case 3

Figure 4: Contour lines of the volume fraction at $t = 0.2\,s$ with or without the time-splitting procedure.

3.3.2 Computations with adaptive grid refinement

For cases with AGR, the gains in CPU time are much weaker. This is explained by a higher $N_{c,\,mean}$ (up to 1.8 times higher for the case 6). However, for the same case, C_{tot} is 2 times smaller than the case 4, which does not use the time-splitting procedure. Given the target size specified for the AGR, which is half the size of the cells in the fixed mesh, the accuracy of Fx_{max} is increased. Even with $N_{c,\,mean}$ lower than with fixed grids, the CPU times are higher. This lack of gain is explained by the small target cell size and the law for the adaptation of the global time step to a target Courant number. The combination of these two choices causes the limitation of the usable time step to small values.

4 Conclusion and perspectives

The first results are encouraging and confirm the expectations of the time-splitting procedure. On fixed grids, the CPU time for the simulation of the dam break with obstacle test case has been reduced with a factor 3. In the case of computations using a single core and the adaptive grid refinement, the gain in CPU time is not very large. This is explained by the need to keep large safety margin of layers of cells around the free surface. However, the cost of a computation, while looking at the mean total time per cell, is halved. Thus it appears that the time-splitting procedure should be very efficient on parallel computations, even if it remains to be proved.

Acknowledgements

This study was supported by a grant from the Région Pays de la Loire (project ANOPACy). The authors gratefully acknowledge GENCI (Grand Equipement National de Calcul Intensif, Grant 2014-21308) for the HPC resources.

References

[1] J. H. Duncan. The breaking and non-breaking wave resistance of a two-dimensional hydrofoil. *Journal of Fluid Mechanics*, 126(-1):507–520, 1983.

[2] A. Hay, A. Leroyer, and M. Visonneau. H-adaptive navier–stokes simulations of free-surface flows around moving bodies. *Journal of Marine Science and Technology*, 11(1):1–18, 2006.

[3] A. Leroyer, S. Barré, J.-M. Kobus, and M. Visonneau. Influence of free surface, unsteadiness and viscous effects on oar blade hydrodynamic loads. *Journal of Sports Sciences*, 28(12):1287–1298, 2010.

[4] A. Leroyer, J. Wackers, P. Queutey, and E. Guilmineau. Numerical strategies to speed up CFD computations with free surface - application to the dynamic equilibrium of hulls. *Ocean Engineering*, 38(17–18):2070–2076, 2011.

[5] M. Manzke, J.-P. Voss, and T. Rung. Sub-cycling strategies for maritime two-phase flow simulations. In R. Ansorge, H. Bijl, A. Meister, and T. Sonar, editors, *Recent Developments in the Numerics of Nonlinear Hyperbolic Conservation Laws*, volume 120 of *Notes on Numerical Fluid Mechanics and Multidisciplinary Design*, pages 237–251. Springer Berlin Heidelberg, 2013.

[6] F. Moukalled and M. Darwish. Transient schemes for capturing interfaces of free–surface flows. *Numerical Heat Transfer, Part B: Fundamentals*, 61(3):171–203, 2012.

[7] P. Queutey and M. Visonneau. An interface capturing method for free–surface hydrodynamic flows. *Computers & fluids*, 36(9):1481–1510, 2007.

[8] Y. Robert, A. Leroyer, S. Barré, F. Rongère, P. Queutey, and M. Visonneau. Fluid mechanics in rowing : the case of the flow around the blades. In *The 2014 conference of the International Sports Engineering Association*, 2014.

[9] O. Ubbink. *Numerical prediction of two fluid systems with sharp interfaces*. PhD thesis, Imperial College, University of London, 1997.

[10] J. Wackers, G. Deng, A. Leroyer, P. Queutey, and M. Visonneau. Adaptive grid refinement for hydrodynamic flows. *Computers & Fluids*, 55:85–100, 2012.

CFD Prediction of Unsteady Cavitation Extent on Marine Propeller and its Application to Ship Radiated Noise

Nobuaki Sakamoto† and Hikaru Kamiirisa†
†National Maritime Research Institute (NMRI), Tokyo 181-0004 JAPAN
sakamoto@nmri.go.jp; kamiirisa@nmri.go.jp

1. Introduction

Ship radiated noise has been a large interest among maritime industries in terms of mariners' comfort as well as environmental protection, especially for marine mammals. On 2014, International Maritime Organization (IMO) released non-mandatory guidelines for the reduction of underwater noise from commercial shipping to address adverse impacts on marine life[1]. One of the major sources of ship radiated noise is the rotating propeller and its cavitation. They yield pressure fluctuation with blade frequency (BF) and tonal noise, in the meantime, collapse of cavitation bubble becomes source of broadband noise. Numerical estimation for these physics and resultant noise is usually challenging since they include multi-scale physics. Analytical bubble-dynamics with nonlinear Rayleigh-Plesset equation contributes to capture broadband noise with high frequency[2] yet the method requires the volumetric change of cavitation bubble in time as well as the distribution of bubble radius. The empirical formula based on full scale measurement is practical and provides rough estimation in the upper bound of sound pressure level (*SPL*) in propeller cavitation noise[3], yet the full scale measurements are usually expensive in cost and time. Viscous computational fluid dynamics (CFD) simulation is able to solve propeller cavitation based on appropriate cavitation modeling with unsteady Reynolds-averaged Navier-Stokes (URaNS) equation[4]. The solution can directly estimate the propeller cavitation noise in near field. The far field noise can also be calculated by complementary use of CFD and Ffowcs Williams Hawkings (FW-H) equation[5]. Yet the capability of viscous CFD for propeller cavitation noise is still unknown. Cavitation model is usually based on simplified Rayleigh-Plesset equation with mixtured, single-fluid model thus there may be limitations to capture growth and collapse of cavitation bubble. The pressure fluctuation may numerically be diminished due to diffusion arose from spacial and temporal discretizations. According to these backgrounds the present study aims to understand the capability of viscous CFD simulations to estimate propeller cavitation and resultant noise in near field.

2. Computational Method

2.1 Flow field

The computational results are obtained using general-purpose commercial CFD package STAR-CCM+ ver9.04.011 (double precision version). The governing equations are the continuity and URaNS equations with dimensional forms, and are solved by finite volume method. Rotational motion of a propeller is modeled either by Multiple Reference Frame (MRF) or sliding mesh technique. The k-ω Shear Stress Transport (SST) turbulence model without wall function is selected for the present simulation based on the past studies. The effect of boundary layer transition is not taken into consideration in the present study, yet the γ-Re_θ model is tested for propeller open water computation[6]. Detached Eddy Simulation (DES) is utilized especially for cavitation simulations with fine grid. As the two-phase flow modeling, Volume of Fluid (VoF) method is utilized in conjunction with the cavitation model by Schnerr and Sauer (2001). Divergence free condition is satisfied by solving pressure Poisson equation iteratively using Semi-Implicit Method for Pressure-Linked Equation (SIMPLE)-type algorithm. The order of accuracy is second in both space and time.

2.2 Sound Pressure Level

In order to estimate *SPL* originated from cavitating propeller, two methods are tested. First method is to utilize Brown's formula[3] together with the CFD simulations. It is presented in Equation (1) as

$$SPL = K + 10\log\left(BD_p^4 n^3 f^{-2}\right) + 10\log\left(A_C / A_D\right) \tag{1}$$

where SPL $[\,dB\ re 1\mu Pa/\sqrt{Hz}\ at\ 1m\,]$ is the sound pressure level, K(=163) is an empirical constant, B is the number of blades, D_p [m] is the propeller diameter, n [rps] is propeller rotation speed, f [Hz] is the

target frequency, A_c[m^2] is the area of cavitation extent on the blade, and A_D[m^2] is the area of the blade. The CFD simulation estimates A_c/A_D and the results are plugged into Eq. (1) to estimate *SPL* for certain *f*. Second method is to utilize time history of pressure sampled at certain hydrophone location directly from the CFD simulation. The data is subjected to Fast Fourier Transform (FFT) with Hann window, and then filtered by 1/3 octave band. The amplitude of the signal are integrated within the lower and upper frequency over each band width, and converted into *SPL* relative to 1μPa.

3. Simulation Design

3.1 Geometry and flow condition

The conventional propeller MP218 which used to be equipped on the training ship "Seiun 1st" is of the interest in the present study[7]. Table 1 summarizes major dimension of the propeller. In order to represent flow condition, three non-dimensional parameters are introduced as

$$Rnk = \frac{c_{0.7R}\sqrt{V_a^2 + (0.7\pi n D_p)^2}}{\nu} \tag{3}$$

$$\sigma_n = \frac{P_A + \rho g(I-h) - P_v}{0.5\rho(nD_p)^2} \tag{4}$$

$$K_T = \frac{T}{\rho n^2 D_p^4} \tag{5}$$

where *Rnk* is Kempf's Reynolds number, $c_{0.7R}$[m] is the chord length of the blade section at 70% of propeller radius *R*, V_a[m/s] is the advance velocity, ν[m^2/s] is the dynamic viscosity, σ_n is the cavitation number, P_A[Pa] is the atmospheric pressure, *g*[m/s2] is the gravitational acceleration, *I*[m] is the immersion depth of the propeller shaft, *h*[m] the reference height, P_v[Pa] is the vapor pressure, K_T is the thrust coefficient and *T*[N] is the propeller thrust. In the present study, following parameters are set in such a way that the computational flow conditions follow the experiments; *Rnk*~6.5E+05 and *n*=20.0[rps] for all the cases, K_T~0.207 and σ_n=3.06 for the cases with cavitation. Two parameters are set to quantify the property of nuclei for cavitaion, e.g. 1) density of the nuclei is set to 1.0E+14 [1/m^3], and 2) radius of the nuclei is set to 1.0[μm], which are the same as utilized by Bijlard (2014)[8].

3.2 Computational setup

The coordinate system is right-handed Cartesian, and its center is coincident with the boss center of a propeller. The flow direction is x negative to x positive, and the propeller rotates clockwise around x-axis observing from downstream. Figure 1 presents the computational grid in the blade vicinity. It consists of two cylindrical volume parts, e.g. rotator and stator, and necessary local refinements. The propeller is placed inside the rotator, and the stator shares the cylindrical sliding interface with the rotator. Total number of cells are 5.4M for propeller open water computation while it is 19M for cavitation simulations. Trimmed-cell is utilized for grid generation, and nondimensional viscous length *y+* is close to 1 in order to meet the requirement for the present turbulence model. Followed by Hasuike et al. (2009)[4]'s investigation, the distance from the coordinate center to the inflow boundary, far-field boundary and outflow boundary are $3D_p$(uniform flow)/$0.7D_p$(non-uniform flow), $5D_p$ and $5D_p$, respectively. Physical time advancement is set in such a way that the propeller rotates 1deg per time step with 20 sub iterations.

Table 1 Major dimensions of the model propeller

MPNO.	218
D_p [m]	0.221
Pitch ratio* at *r/R*=0.7	0.950
Expanded Area Ratio	0.650
Boss ratio	0.197
B [-]	5
Skew [deg.]	10.50
Rake [deg.]	6.00
Wing section	MAU

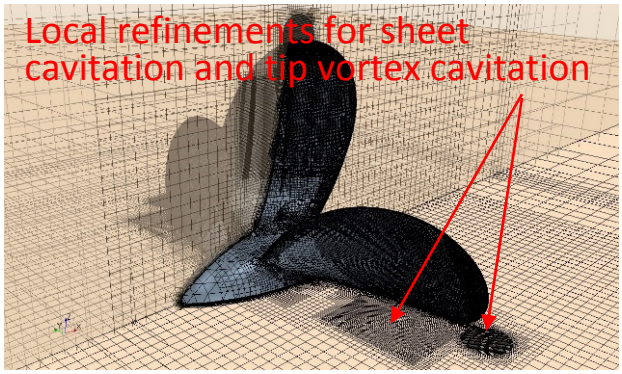

Fig.1 Computational grid in the blade vicinity

3.3 Validation data and variables

For the propeller open water characteristics (POC) of MP218, the experimental result from SR183[7] is utilized as the validation data for which the non-dimensional variables of the POC in addition to K_T are presented as

$$K_Q = \frac{Q}{\rho n^2 D_p^5}, \eta_o = \frac{J}{2\pi}\frac{K_T}{K_Q} \tag{6}$$

where K_Q is the torque coefficient, η_o is the propeller open water efficiency, ρ[kg/m^3] is the fluid density, Q[Nm] is the propeller torque, and J is the advance ratio determined by $J=V_a/nD_p$. In order to validate the distribution of the pressure coefficient C_p on the propeller blade, Ukon et al. (1989)'s measurement data[9] is adopted for which the definition of the C_p is

$$C_p = \frac{P}{0.5\rho(nD_p)^2} \tag{7}$$

where P[Pa] is the pressure on the blade.

For the cavitation extent, cavitation pattern is quantified by the time histories of the area of cavitation extent A_c[mm^2] on the key blade, and the volume of cavitation bubble V_c[mm^3] in the rotator domain. The measurement of these quantities were carried out by Kudo et al. (1989)[10] by a laser beam coupled with Charge Coupled Device (CCD). To compute A_c and V_c from the present CFD results, the following criteria are utilized;

$$\begin{aligned} A_c|_{CFD}(t) &\cong \sum_{i=1}^{N_f} s_i \beta_i(t) \text{ where } \beta_i(t) = \begin{cases} 1 \text{ if } \alpha_i(t) \geq 0.1 \\ 0 \text{ otherwise} \end{cases} \\ V_c|_{CFD}(t) &\cong \sum_{i=1}^{N_c} v_i \alpha_i(t) \text{ where } \alpha_i(t) = \begin{cases} \alpha_i(t) \text{ if } \alpha_i(t) \geq 0.1 \\ 0 \text{ otherwise} \end{cases} \end{aligned} \tag{8}$$

where N_f is the number of faces on the key blade, s_i [mm^2] is the area of discretized faces, $\beta_i(t)$ is the flag to determine the area of cavitation extent on the key blade, $\alpha_i(t)$ is the instantaneous volume fraction of gas phase, N_c is the number of cells in the rotator domain, and v_i[mm^3] is the volume of discretized cells.

For the SPL, the measurement was carried out in the small-sized cavitation tunnel with ship wake generated by wire-mesh screen[7]. As shown in Fig. 2, the receiver position was 0.29D$_p$ vertically above the propeller tip for which it was geometrically similar to the hydrophone position utilized in the full scale sea trial[7].

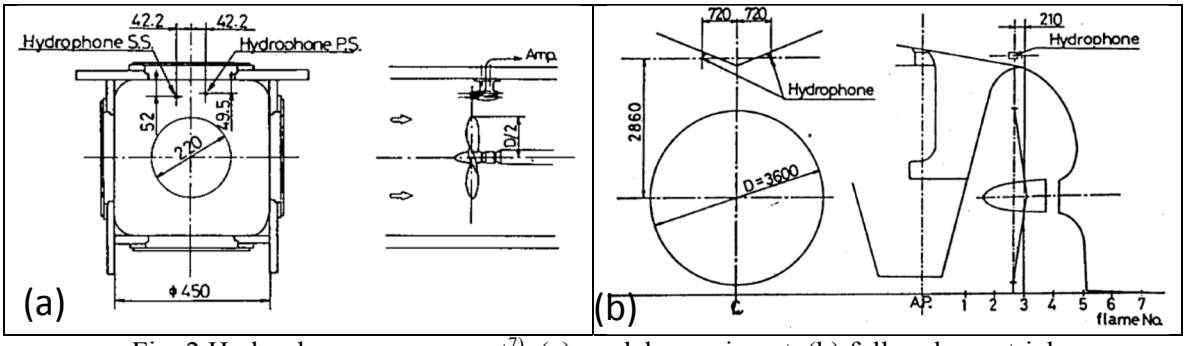

Fig. 2 Hydrophone arrangement[7]: (a) model experiment, (b) full scale sea trial

4. Results and Discussions

4.1 Preliminary results in the uniform flow (non-cavitating condition)

Figures 3(a) and 3(b) present the computational and experimental results of POC and the distribution of C_p along the chord at 0.7R, respectively. For the POC, the computational results without transition effect (termed "lowRn") show the difference δ (%Exp.) relative to the experimental data up to 3% for K_T and η_o, 0.7% for $10K_Q$ up to J=0.7. When the transition effect is considered (termed "lowRn+trans."), the δ (%Exp.) becomes up to 0.5% for K_T while it becomes 5% for $10K_Q$ and η_o. Since the circumferential velocity is smaller at the root region rather than the tip region, local Rnk at the root region is smaller and the boundary layer may be partially laminar from leading edge to a certain chord location. The transition model is likely to capture this physics which yields smaller frictional resistance

and in consequence smaller $10K_Q$ compared to the results without transition. The results in Fig. 3(a) appropriately capture this physics yet there is issue for the present transition model, i.e. it requires two input parameters: free stream turbulence intensity and free stream edge value. Both are important to trigger the onset of boundary layer transition, yet these are quite problem-dependent and are still open to question for propeller open water computation. At the target K_T (=0.207) and relevant J (=0.626), according to Fig. 3(a), the turbulence model without transition effect provides better POC than that of with transition effect. In consequence, the transition is NOT considered in the present study. The computational results of C_p distribution along the chord at $0.7R$ comprehensively agree well with the experimental data both on back and face sides at four different J.

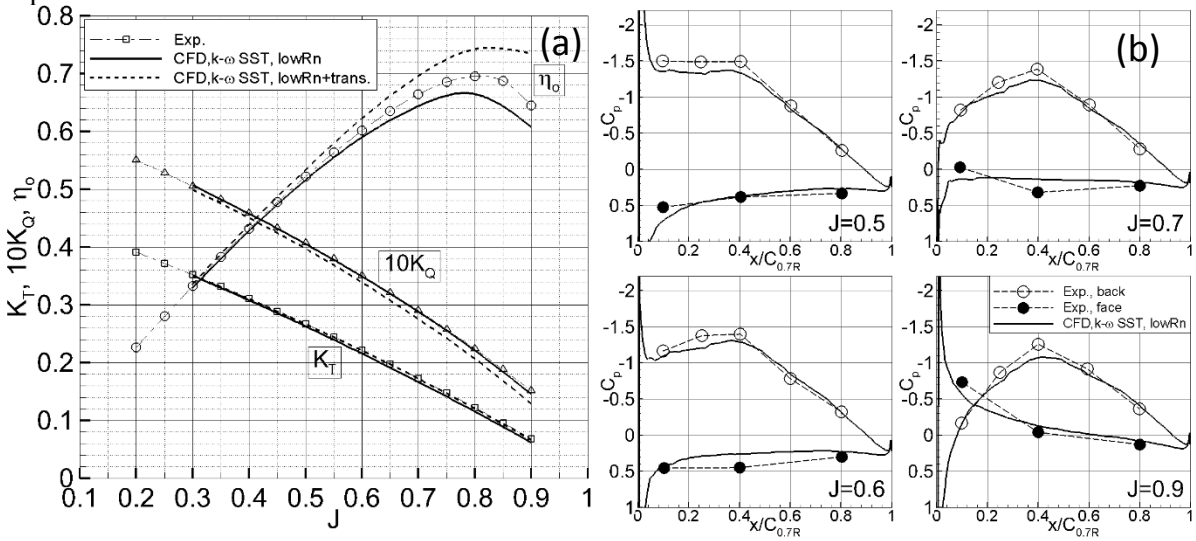

Fig.3 Preliminary validations for MP218: (a) POC, (b) distribution of C_p along the chord at $0.7R$

4.2 Cavitation extent in the ship wake

Figure 4 describes the distribution of axial velocity imposed on the inflow boundary. Radial and tangential components are set to zero. To obtain this flow pattern, wake survey was carried out at towing tank, and then the extrapolation method proposed by Sasajima&Tanaka[11] was applied in order to take scale effect into consideration. Figures 5(a) and 5(b) summarize the cavitation pattern at different blade angles θ. Overall cavitation patterns obtained by the CFD simulation show nice agreement to the experimental data. It is encouraging that the present CFD is able to resolve tip vortex cavitation very well over the whole range of blade angle.

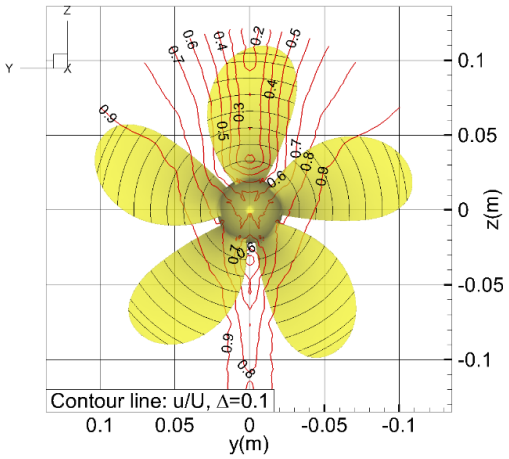

Fig. 4 Distribution of axial velocity imposed on the inflow boundary

Figures 6(a) and 6(b) present the time histories of A_c on the key blade and V_c over the rotator domain, respectively. The computational results by surface panel method (termed "SQCM")[12] are added as the reference computational results. Table 2 summarizes the computational and the experimental results of maximum variables of A_c/A_D as well as the second derivative of V_c (termed d^2V_c/dt^2) in time. The d^2V_c/dt^2 is calculated by 5-points central differencing scheme[10], and considered to be influential on pressure fluctuation and resultant noise. For the experimental data, the A_c remains almost constant at -10deg.<θ<0deg. while the V_c increases in that range which means that the thickness of cavitation bubble grows toward the blade normal direction at back side while the extent of sheet cavitation does not spread. The maximum values of the A_c and V_c are achieved at the same time when θ is 10deg. At 10deg.<θ<30deg, A_c and V_c decrease at the same time, and they finally become similar level to those of -10deg at θ=30deg. The computational results show different trends to the experimental data. The A_c and V_c grow up in parallel at -10deg.<θ<0deg. It means that the growth of the extent of

sheet cavitation on the blade yields the increase of V_c for which it is qualitatively supported by Figs. 5(a) and 5(b). At 10deg.<θ<30deg, the A_c and V_c decrease at the same time which is similar to the experimental trend, yet their rate of changes in time are much smaller than those of the experimental data. In addition, the present computational results in A_c agree well with the reference computational results[12] rather than the experimental data, yet its peak value which is to be utilized in Eq. (1) is estimated well by the present CFD in comparison to the experiment. For the V_c, the present computational result fits to the experimental result at θ=-10deg (=350deg.) to 50deg, and then it provides V_c which is 20% smaller than the experimental data at its maximum position. The computational result of d^2V_c/dt^2 is one order of magnitude smaller than that of the experimental data which indicates that the pressure fluctuation due to volumetric change of cavitation bubble could be less sensitive in the computational results than that of the experimental results.

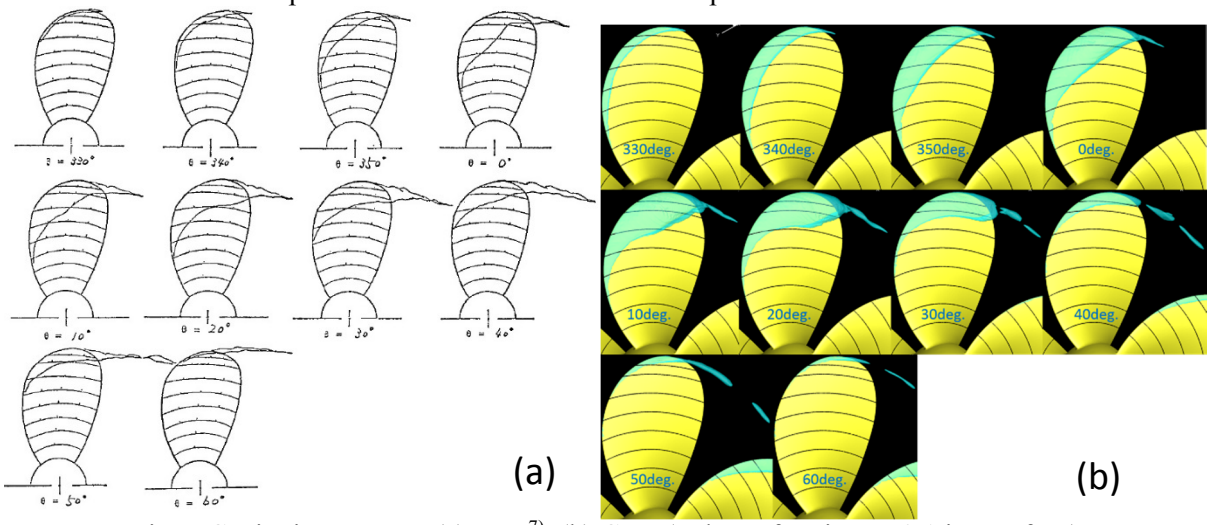

Fig. 5 Cavitation pattern: (a) Exp.[7], (b) CFD (volume fraction α=0.1 iso surface)

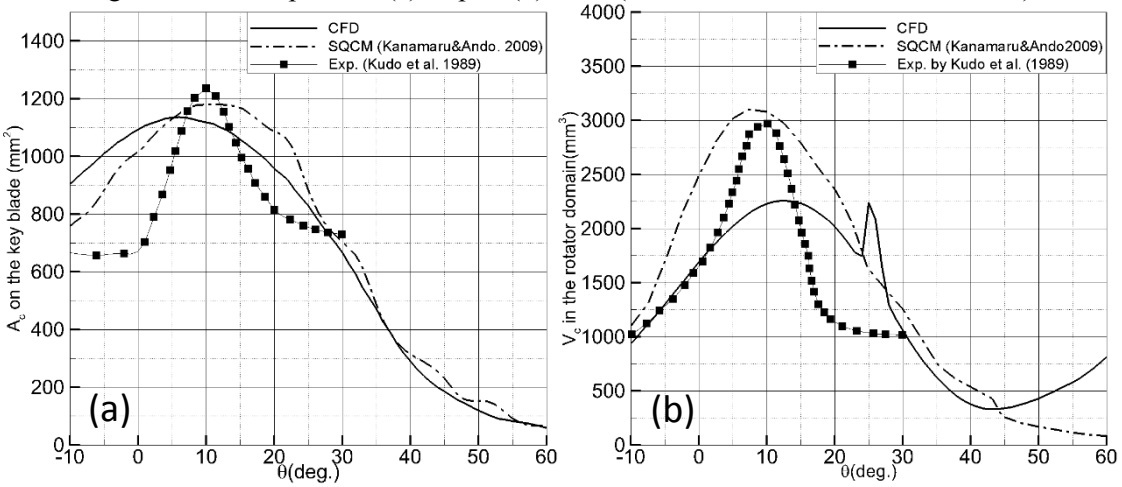

Fig. 6 Cavitation extent on the blade: (a) extent area, (b) volume of the cavitation bubble

Table 2 Maximum value of Ac/A_D and d^2V_c/dt^2

	A_c/A_D [-]		d^2V_c/dt^2 [m^3/s^2]	
	Variable	θ [deg]	Variable	θ [deg]*
Exp. (Kudo et al. 1989)	0.251	10	-2.01	10
CFD	0.231	5	-0.37	13

* θ[deg.] when the V_c becomes maximum.

4.3 Propeller cavitation noise

Figures 7(a) and 7(b) show the *SPL* evaluated at the hydrophone oriented at the port side for model and full scale, respectively. In order to scale up the *SPL* from model to full scale, Levkovskii's method[7] is utilized as

$$\left.\begin{aligned} \lambda &= D_{ps}/D_{pm} \\ \frac{f_s}{f_m} &= 1/\lambda \cdot \left(\sigma_{ns}/\sigma_{nm}\right)^{0.5} \cdot V_s/V_m \\ SPL_s - SPL_m &= 20\log_{10}\left[\lambda^{1.5} \cdot \left(\sigma_{ns}/\sigma_{nm}\right)^{0.5} \cdot V_s/V_m \cdot r_m/r_s\right] \end{aligned}\right\} \quad (9)$$

where the subscripts of "m" and "s" denote model and full scale, respectively, and $V_{s,m}=n_{s,m}D_{ps,pm}$. In the present study, σ_n is identical between model experiment and full scale measurement and thus $\sigma_{ns}/\sigma_{nm}=1$. The receiver position from the noise source is geometrically similar between model and full scale and thus $r_m/r_s=1/\lambda$. The n_s is set to 163rpm. Regardless to the difference in d^2V_c/dt^2 between the computational and experimental results, the computational result in model scale is able to capture tonal and broadband noise up to 1kHz compared to the experimental data. Unrealistic spike at 2.5kHz in the computational result is due to numerical oscillation of the pressure near the sliding interface, which is to be improved in the next release of the code. For the full scale, Levkovskii's method functions well and scaled-up results obtained from present computation agree well with the full scale measurement up to 200Hz. The Brown's formula can be practically utilized to estimate upper bound of the *SPL* due to propeller cavitation in full scale. As shown in Table 2 and Fig. 6(a), the difference in Ac/A_D is 8%Exp. which yields the difference in *SPL* less than 1dB.

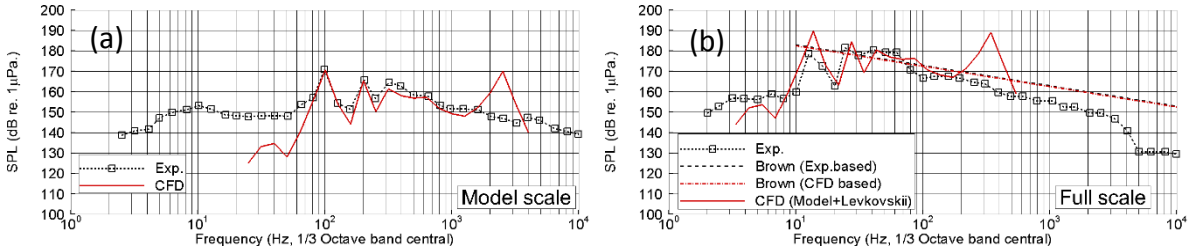

Fig. 7 *SPL* at port side receiver: (a) model scale, (b) full scale

5. Concluding remarks

Unsteady viscous CFD simulations are carried out for a non-cavitating/cavitating marine propeller under uniform/non-uniform flow. The computational results are consecutive in terms of cavitation pattern and time histories of A_c and V_c, although the latter shows remarkable difference compared to the experimental results. Detail diagnostics would be necessary in both experimental and computational results, e.g. the measurement criteria for A_c and V_c as well as the thickness of the cavitation bubble along the blade. For the propeller cavitation noise, tonal and broadband noise are very well predicted by the present computation up to certain frequencies in both model and full scale, yet the pseudo frequency due to numerical oscillation of the pressure must be removed. In consequence, the present CFD with the Brown's formula and the Levkovskii's method are likely to be encouraging methods for estimating ship radiated noise due to propeller cavitation.

References

1) International Maritime Organization, 2014, MEPC.1/Circ.833.
2) Kamiirisa and Goto, 2005, Mitsui Engineering&Shipbuilding Co., Ltd., Technical Report Vol.185.
3) Brown N.A., 1976, Proc. International Symposium on Shipboard Acoustics, pp.21-38.
4) Hasuike et al, 2009, Proc. 7th International Symposium on Cavitation, USA.
5) Hallander et al., 2012, Proc. 8th International Symposium on Cavitation, Singapore.
6) Yamada et al., 2011, Proc. JASNAOE Annual Fall Meeting, pp.31-34 (in-Japanese).
7) Japan Ship Technology Research Assoc., 1983, SR183 Final Report (in-Japanese), Report No.358.
8) Bijlard M., 2014, Proc. STAR Global Conference, Austria.
9) Ukon et al., 1989, Journal of the Society of Naval Architects of Japan, Vol. 165, pp.83-94.
10) Kudo et al., 1989, Journal of the Society of Naval Architects of Japan, Vol. 166, pp.93-103.
11) Final Report and Recommendation to the 26th ITTC, 2011, Proc. 26th ITTC, Brazil.
12) Kanemaru and Ando, 2009, J.JASNAOE, Vol.9, pp.45-53 (in-Japanese).

Drag Reduction for Ships Inspired by Dolphins

Lars-Uve Schrader, HSVA Hamburg Ship Model Basin, Hamburg/Germany, schrader@hsva.de

Dolphins possess a thick layer of lipid tissue under their skin, the "blubber". Apart from serving as a thermal insulator, the blubber is believed to alter the flow past the dolphin's body favourably, leading to diminished drag. It is hypothesised that the dolphin's flexible skin delays the transition from low-friction laminar flow to high-friction turbulent flow (flow control). Clearly, a drag-reducing mechanism of this kind would also be beneficial for ships, where it may be realised by a blubber-like compliant hull coating [1]. This paper reports the design of a water-tunnel experiment – guided by CFD simulations and theoretical calculations – for the demonstration of the potential of compliant coatings in naval engineering.

A small search and rescue (SAR) vessel serves as a demonstrator for the compliant-coating concept (Fig. 1a). Since laminar-turbulent transition occurs near the bow, it is sufficient to apply the coating in the forward section of the ship. The SAR vessel is well-suited as it features a simple bow shape (no bulb) so that the flow field around the fore ship can be approximated by a simplified boundary-layer model. In the water-tunnel experiments, a doublebody model of this vessel will be used to test the coating (Fig. 1b). Since the focus is on the bow section, all hull appendages are omitted, yielding a "clean", streamlined flow body (Fig. 1c).

Figure 1. (a) SAR vessel of the German Maritime Search and Rescue Service (DGzRS), designed by the Fassmer shipyard (picture from www.fassmer.de). (b) From the SAR vessel to the doublebody for the water-tunnel tests. (c) Close-up view of the test body

The experiments will be conducted in HSVA's Hydrodynamics and Cavitation Tunnel (HYKAT). To obtain results with relevance for field applications on real ships, the tests will be carried out at a high Reynolds number. Therefore, large values of the model size and tunnel speed are chosen (scale $\lambda = 4.5$; speed $U_0 = 10\text{m/s}$), allowing for a laboratory Reynolds number of almost one third of its field value (Tab. 1). The test model will be equipped with a load cell and mounted vertically by a strut at the ceiling of the HYKAT test section (Fig. 2a). Exchangeable

Table 1. Length, breadth, draught, speed and Reynolds number of the SAR vessel and the test body

	L_{wl} [m]	B_{wl} [m]	T [m]	U_0 [m/s]	Re_L
SAR vessel	18.20	4.61	1.285	7.7 (cruise)	117.9×10^6
Test body (scale $\lambda = 4.5$)	4.04	1.02	0.286	10.0	35.5×10^6

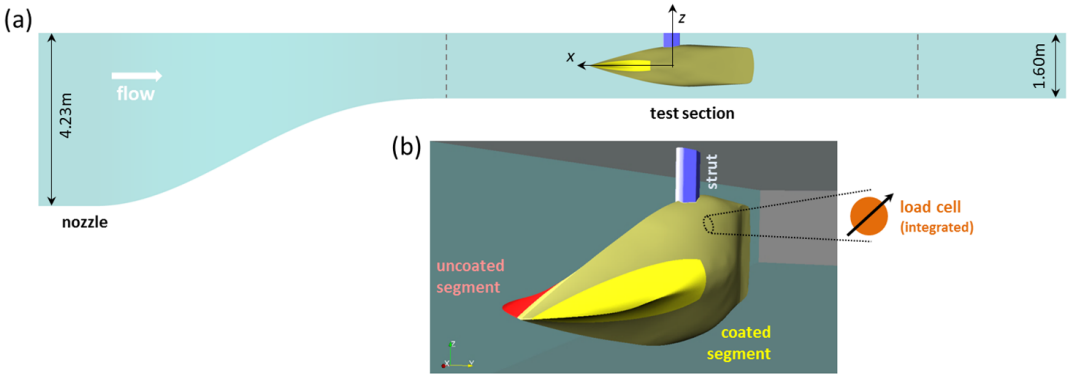

Figure 2. (a) Full-scale model of the HYKAT inflow nozzle and test section with the doublebody mounted. (b) Exchangeable bow segments for testing of different coatings

bow segments with different coatings shall be inserted into the two half-shells of the doublebody (Fig. 2b). In this way, the effect of the coating on skin friction (if any) becomes evident as a force difference between the two half-shells, generating a yaw moment around the strut axis.

CFD simulation. A full-scale CFD simulation has been conducted to support the design of the water-tunnel experiment, using HSVA's RANSE solver $FreSCo^+$. The CFD model of the experimental setup consists of the doublebody test probe, the inflow nozzle and the test section of the HYKAT facility (cf. Fig. 2a) filled with fresh water at 15°C. The inflow velocity in the nozzle is adjusted such that a speed of 10m/s is attained shortly upstream of the test body (Fig. 3a). A close-up view of the bow region reveals that the streamlines are nearly straight, parallel and roughly perpendicular to the isobars on the body surface (Fig. 3b).

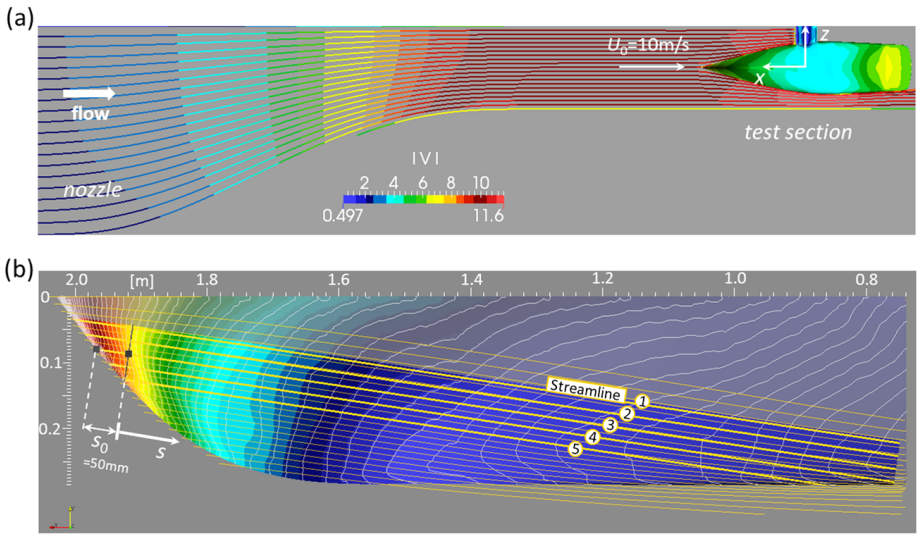

Figure 3. (a) Flow speed and streamlines in the HYKAT water tunnel and surface pressure on the test body. (b) Pressure distribution and streamlines along the bow segment of the test body. The five streamlines highlighted serve for extraction of the pressure (cf. Fig. 4a), and s is a streamline-aligned coordinate along the boundary layer (see below)

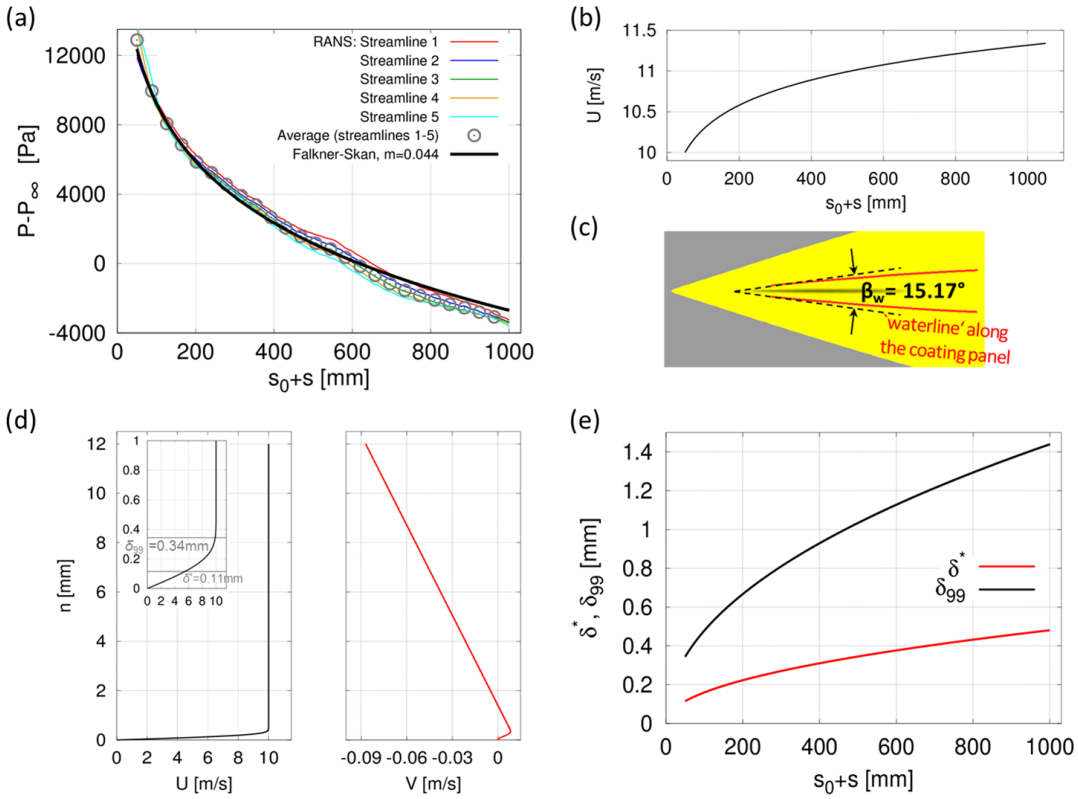

Figure 4. Accelerated Falkner-Skan boundary layer ($m = 0.044$) modelling the flow past the bow of the test body. (a) Adjustment of the Falkner-Skan pressure distribution (exponent m in Eq. 1b) to the pressure from the CFD simulation, extracted along the five streamlines marked in Fig. 3(b). (b) Streamwise distribution of the surface-tangential freestream velocity. (c) Comparison of the Falkner-Skan wedge angle to a typical opening angle at the bow. (d) Boundary-layer profiles of tangential and normal velocities. (e) Streamwise boundary-layer growth: displacement thickness and 99% thickness

Boundary-layer model. Since transition to turbulence takes place in the wall-bounded shear flow, detailed knowledge of the boundary layer is necessary. The CFD simulation does not resolve but models the boundary layer by a wall function, i.e. it cannot be directly used for a study of laminar-turbulent transition. Instead, we resort to a simplified boundary-layer model compatible with the pressure distribution on the body and the streamlines in the outer flow (cf. Fig. 3b). The class of Falkner-Skan boundary layers [2] turns out to be well-suited, defining the flow past a wedge with opening angle $\beta_w = 2\pi m/(m+1)$ (definition of m below). Falkner-Skan flow is characterised by the following distributions of freestream speed and pressure,

$$U(s) = U_0 \left(1 + \frac{s}{s_0}\right)^m \qquad \text{(1a)} \qquad \text{and} \qquad P(s) = -\frac{\rho}{2} {U_0}^2 \left[\left(1 + \frac{s}{s_0}\right)^{2m} - 1\right]. \qquad \text{(1b)}$$

U is the velocity along the streamline-aligned coordinate s (cf. Fig. 3b) and U_0 is its value at $s_0 = 50\text{mm}$ ($s = 0$), setting the distance to the "virtual origin" of the boundary layer. P is the pressure, and the exponent m determines the degree of flow acceleration (pressure drop, $m > 0$) or deceleration (pressure rise, $m < 0$). According to boundary-layer theory, Eq. (1b) is also valid along the hull surface. Hence, the Falkner-Skan model can via the exponent m in (1b) be adjusted to the surface pressure distribution obtained in the CFD simulation (cf. Fig. 3b). This exercise yields a value of $m = 0.044$ (Fig. 4a), defining a weakly accelerated freestream past a wedge with $\beta_w = 15.17°$. This value compares well with the opening angles of the bow (Fig. 4c). Once the freestream is known, the boundary-layer velocity profiles (Fig. 4d) and thickness (Fig. 4e) are obtained solving the Falkner-Skan similarity equation [2].

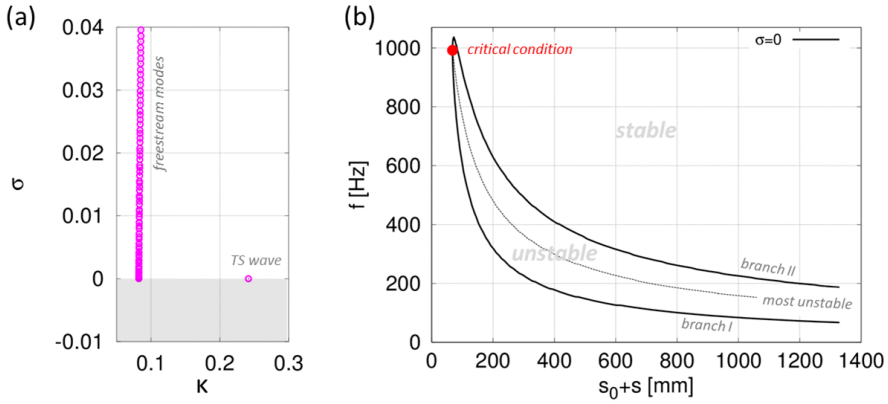

Figure 5. Instability of the Falkner-Skan boundary layer ($m = 0.044$). (a) Eigenvalue spectrum for critical condition. (b) Instability map showing frequency and location of unstable TS waves in the boundary layer. Red dot shows critical condition according to the spectrum in (a)

Boundary-layer instability. In the *natural* transition scenario, relevant in low-disturbance environments, the transition process is initiated by wave-like flow disturbances, the Tollmien-Schlichting (TS) waves [3]. These are expressed in terms of a complex wave function $\hat{u}$,

$$\hat{u} = \tilde{u}(n)\, e^{i((\kappa+i\sigma)s-\omega t)} = \tilde{u}(n)\, e^{i(\kappa s-\omega t)}\, e^{-\sigma s}. \qquad (2)$$

The quantity $\tilde{u}$ is the complex amplitude function in the wall-normal coordinate n, κ is the wavenumber and σ the growth rate in the streamwise direction s, and ω is the angular frequency in time t. From Eq. (2) follows that positive (negative) values of σ correspond to a streamwise decaying (growing) disturbance wave. Only the amplifying (unstable) TS waves with $\sigma < 0$ are of interest, being the forerunners of transition to turbulence. These are computed by Linear Stability Theory (LST) solving a simplified form of the linearised incompressible Navier-Stokes disturbance equations, the Orr-Sommerfeld/Squire equations [3]. Satisfied by (2), these constitute an eigenvalue problem, with the complex streamwise wavenumber $\kappa + i\sigma$ being the eigenvalue and the complex wave amplitude $\tilde{u}(n)$ the associated eigenfunction. Here, the LST code published in Ref. [3] has been used. The outcome is an eigenvalue spectrum containing the TS mode and a branch of freestream waves. Of particular interest is the *neutral* spectrum, characterised by a TS wave with $\sigma = 0$ (Fig. 5a). Neutral spectra have been computed for various wave frequencies and locations (Reynolds numbers) and collected in an instability map, showing TS-wave frequencies versus downstream distance from the stem of the hull model (Fig. 5b). The instability map highlights the region of unstable TS waves in the boundary layer, enclosed by a banana-shaped neutral-stability curve. The critical point (red dot in Fig. 5b) marks the shortest distance from the stem (68mm here), where the laminar flow state becomes unstable for the first time. The associated critical TS wave has a frequency of 992Hz.

Transition to turbulence. The instability map illustrates the behaviour of single disturbance waves with fixed frequency when travelling in the streamwise direction: Initially, these waves decay exponentially until branch I of the neutral-stability curve is reached (cf. Fig. 5b). Subsequently, for streamwise locations between the two branches, the TS waves undergo exponential amplification with varying growth rate, passing the contour of maximum instability. After crossing branch II at maximum amplitude, the waves start to decay again along the downstream direction. In practice, all TS waves evolve "in a competition" according to their individual growth behaviour, forming a set of growth curves (blue curves in Fig. 6a). The overall growth of the disturbance spectrum is defined by an envelope ("N-factor") encompassing the individual TS amplification curves (thick black line in Fig. 6a). According to the e^N method [4], transition to turbulence occurs when the N-factor exceeds a critical threshold N_{tr} [5],

$$N_{tr} = -8.43 - 2.4\ln(Tu), \qquad (3)$$

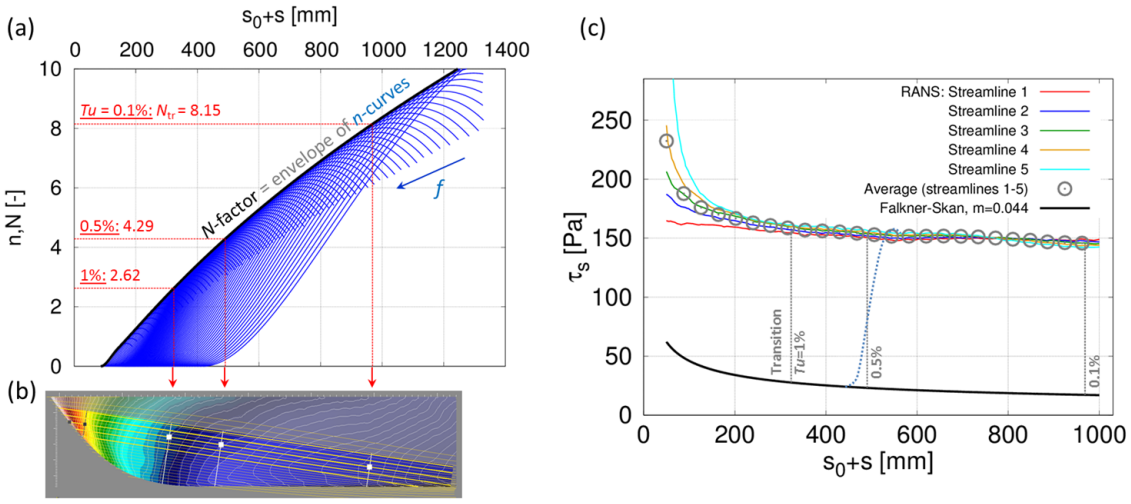

Figure 6. (a) Growth curves of TS waves with various frequencies and N-factor envelope. Evaluation of transition thresholds as per the e^N method for three different background turbulence intensities. (b) Depiction of the corresponding transition points on the bow of the test body. (c) Magnitude of shear stress in the turbulent boundary layer on the test body (from RANS computation) and in the laminar boundary layer (from Falkner-Skan model, where $\tau_{s,lam}(s) = \frac{0.4118}{\sqrt{Re_s}}\rho U(s)^2$)

Table 2. Streamwise transition location and Reynolds number and associated TS-wave frequency in the Falkner-Skan boundary layer ($m = 0.044$) for three turbulence intensities (0.1%, 0.5% and 1%)

Tu	$(s_0+s)_{tr}$ [mm]	$Re_s[\times 10^6]$	f_{tr} [Hz]
10^{-3}	968.6	9.69	211.0
5×10^{-3}	490.5	4.76	329.0
10^{-2}	323.6	3.08	426.2

where Tu is the background turbulence intensity in the water-tunnel test section. Eq. (3) has been evaluated for three different turbulence intensities (0.1%, 0.5% and 1%), and the corresponding transition points and wave frequencies have been read off from Fig. 6(a) and compiled in Tab. 2. Depending on the background noise, laminar-turbulent transition occurs between 32cm and 97cm downstream of the stem of the test body (Fig. 6b). The turbulence level in the HYKAT test section – unknown to date – will be measured when commencing the experiments. A comparison with similar water tunnels suggests a value of $Tu = 0.5\%$ as a reasonable estimate. Under this condition, the transition point would be located 49cm away from the stem, and a TS wave with 329Hz would trigger the breakdown to turbulence. It is believed that the blubber of dolphins is able to damp the turbulence-triggering TS waves. In order to transfer the dolphin's flow-control strategy to the bow of the SAR ship model, a compliant coating material with strong damping capabilities for waves in a frequency band around 329Hz is needed. If well-designed, this coating will shift the "unstable banana" (cf. Fig. 5b) towards larger distances from the vessel's stem and attenuate the growth rates of the unstable TS waves (cf. Fig. 6a). Both effects will lead to extended laminar flow, postponed turbulence and lower levels of shear stress (Fig. 6c).

Summary. This paper reports the design of a water-tunnel experiment for testing of compliant hull coatings, guided by CFD simulations and theoretical calculations. The experiment will be conducted at HSVA in a few months with the aim to clarify whether compliant coatings can be used for passive flow control at ship bows. The coating-based control is 'passive' as no input energy is necessary. This renders passive control mechanisms more efficient, more robust and cheaper than active flow-control devices (e.g. "air lubrication").

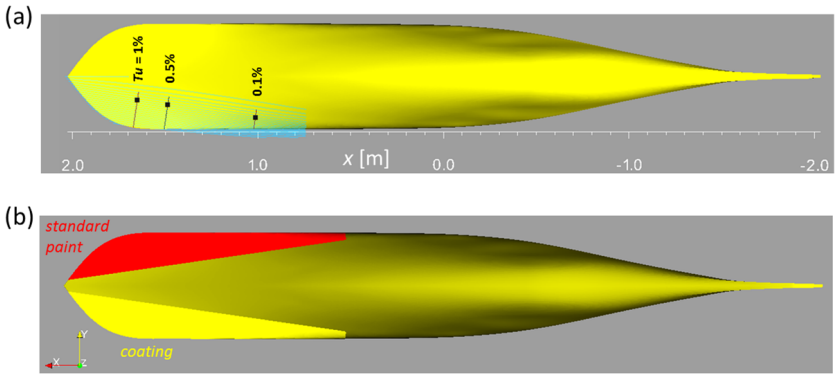

Figure 7. (a) Laminar-turbulent transition points on the water-tunnel test body for three different background turbulence levels. (b) Layout of the bow segments for testing of different compliant coatings

The underlying flow-control mechanism builds on a laminar-turbulent transition delay, leading to reduced frictional drag. In preparation of the experiment, transition points have been calculated in a boundary layer modelling the flow conditions at the bow of a small SAR vessel, considering three different turbulence intensities in the water-tunnel test section (Fig. 7a). Based on these results, exchangeable bow segments for a doublebody test model have been designed (Fig. 7b). A number of segments will be manufactured and coated with different compliant materials or standard paint for reference in order to find the best-performing coating.

Outlook. The LST code for transition prediction is currently being extended by a compliant-coating model inspired by Ref. [6]. The model parameters (e.g. stiffness and visco-elastic damping of the coating material) will be varied so as to find a parameter set suitable for transition delay. These findings will be included in the conference talk and in the final paper.

Acknowledgments. The reported work is part of the research project FLIPPER ("Flow Improvement through Compliant Hull Coating for Better Ship Performance") conducted within the ERA-Net scheme MARTEC II of the European Commission. The project is executed collaboratively by the Fraunhofer Institute for Manufacturing Technology and Advanced Materials (IFAM), Hamburg University of Technology (TUHH), the French chemicals producer ARKEMA and HSVA. Funding by the Federal Ministry for Economic Affairs and Energy of Germany (BMWi) is gratefully acknowledged. HSVA thanks the Fassmer Group and DGzRS for their permission to use the hull design of the SAR vessel in this project.

References

[1] M. Gad-el-Hak. Compliant Coatings: A Decade of Progress. *Applied Mech. Reviews* **49**, 147-157, 1996.
[2] H. Schlichting. Boundary-Layer Theory. *McGraw-Hill*, 1968.
[3] P. J. Schmid, D. S. Henningson. Stability and Transition in Shear Flows. *Springer*, 2001.
[4] A. M. O. Smith, N. Gamberoni. Transition, Pressure Gradient and Stability Theory. *Tech. Rep. ES26388, Douglas Aircraft Comp.*, 1956.
[5] L. M. Mack. A numerical method for the prediction of high speed boundary-layer transition using linear theory. *NASA SP-347*, 101-123, 1975.
[6] P. W. Carpenter, A. D. Garrad. The hydrodynamic stability of flow over Kramer-type compliant surfaces. Part 1. Tollmien-Schlichting instabilities. *J. Fluid Mech.* **155**, 465-510, 1985.

CFD Analysis of Cascade Effects in Marine Propellers with Trailing Edge Modification

Keun Woo Shin[1] and Poul Andersen[2]

[1]Propeller & Aftship R&D Department, MAN Diesel & Turbo, Frederikshavn, Denmark, keun.shin@man.eu
[2]Department of Mechanical Engineering (MEK), Technical University of Denmark (DTU), Kgs.Lyngby, Denmark, pa@mek.dtu.dk

Introduction

Propeller blades are different from a single hydrofoil in isolation due to cascade effects that blades mutually affect hydrodynamic characteristics of each other in proximity. Propeller design programs based lifting-line theory and blade element momentum theory take into account cascade effect by using cascade correction theory, which has been developed on the basis of wind tunnel tests for a row of evenly spaced airfoils. Cascade effects of marine propellers have been on research by inviscid flow solvers such as boundary element methods and vortex lattice methods, but it has not been investigated intensively by viscous flow solvers, although RANS CFD is prevalent in marine industry nowadays.

In the current work, the cascade effect of a marine propeller is analyzed by CFD simulations on a three-dimensional propeller model with varying the number of blades. The influence of trailing-edge configurations on the cascade effect is also investigated by simulating CFD with varying trailing-edge thickness and slope. The reason why the trailing edge is handled rather than other parts of blade geometry is that it can be modified without altering overall blade thrust significantly, because the loading on the aft part of a blade section near a trailing edge is relatively low, compared to the other part.

1. Test case and computational setup

A blade design is taken from a 4-blade propeller with a model-scale diameter of D=0.233 m for CFD analysis. As the propeller has a high area ratio of Ae/Ao=0.78, the distance from the trailing edge of a blade to the leading edge of the next one is relatively short. It is a controllable-pitch propeller designed for a military inspection vessel. CFD simulations have been made for the ship hull with the propeller and appendages [2].

A cylindrical domain with an inner rotating domain around a propeller model is used. The propeller model is prepared with a CP hub, blade foots and an open-water test hubcap. The hubcap is fitted in front of the propeller and an infinite downstream shaft is connected following a general open-water test setup (See Fig. 2). Propeller rotation is applied by the moving reference frame (MRF).

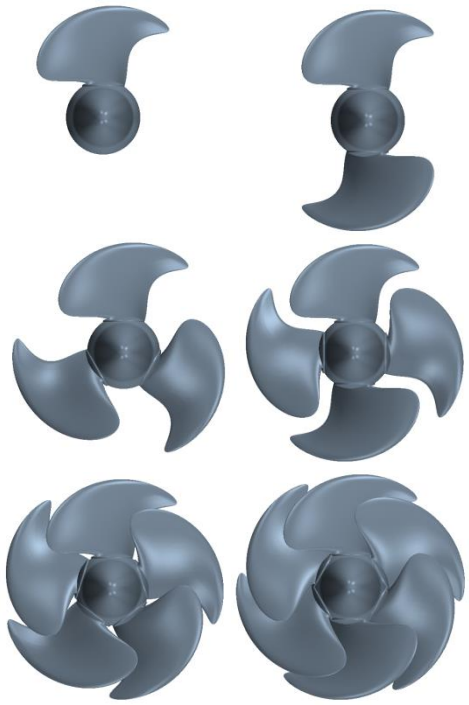

Fig. 1: *Propeller models with different numbers of blades*

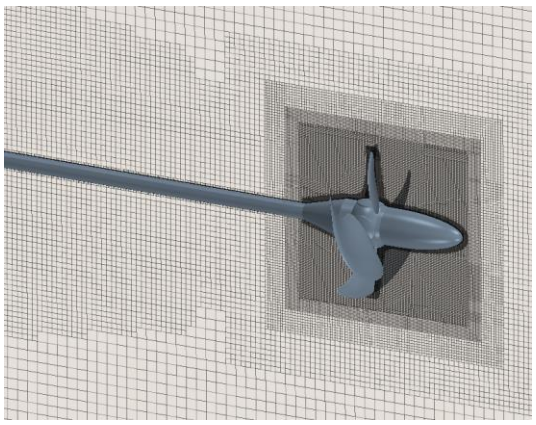

Fig. 2: *Computational grid around the propeller model with an open-water test hubcap*

A grid size of Δx=0.5-0.9 mm is applied to the surface mesh of the blade and hub. Six prism layers with a first-cell height of Δh=0.12-0.23 mm are made on wall surfaces. CFD simulations are made by StarCCM+ RANS solver with the Gamma ReTheta transition model and the k-ω SST turbulence model.

Open-water CFD computations are made for the design pitch. In Fig. 3, CFD results are compared to

those from a model test for validation of the CFD model. Deviations of CFD results are less than 3% in thrust and torque at J=0.2-0.9. The CFD computations show acceptable accuracy in a general range of propeller loading.

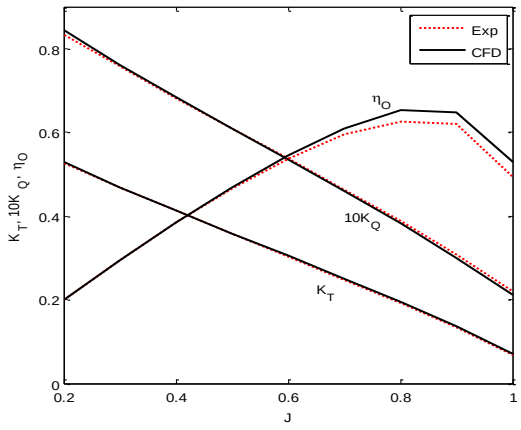

Fig. 3: *Open-water propeller characteristics from the model test and CFD*

2. CFD analysis of cascade effect

For analysis of the cascade effect, open-water CFD simulations are conducted at the design advance ratio of J=0.65 with varying the number of blades from Z=1 to 6 as shown in Fig. 1. CFD results in Fig. 4 show that K_{T1} and K_{Q1} on a single blade are reduced, as the blade spacing s gets shorter for a higher number of blades and the cascade effect is more pronounced, where s is the blade spacing on the 0.7R along the tangential direction, s=1.4$\pi R/Z$. The decreasing rates of both K_{T1} and K_{Q1} are higher at a smaller spacing. Since the decreasing rate of K_{T1} is higher than that of K_{Q1}, the single blade efficiency η_{O1} is also reduced with a higher rate at a smaller spacing (See Fig. 12), where $\eta_{O1}=J\cdot K_{T1}/(2\pi\cdot K_{Q1})$.

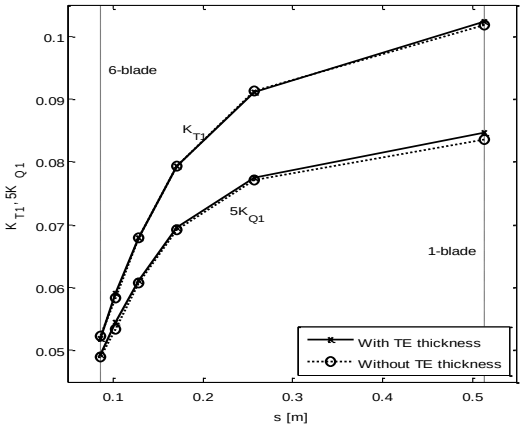

Fig. 4: K_{T1} and K_{Q1} *on a single blade as a function of blade spacing for different numbers of blades with and without a trailing-edge thickness*

C_P on the blade surface is shown in Fig. 5, where C_P is the pressure coefficient with the propeller advance speed as the reference velocity. The suction pressure is stronger on the suction side and the turbulence flow region is larger at the trailing edge of the suction side for a smaller number of the blades. The suction pressure occurs at the leading edge of the pressure side due to a negative incidence angle for a larger number of blades.

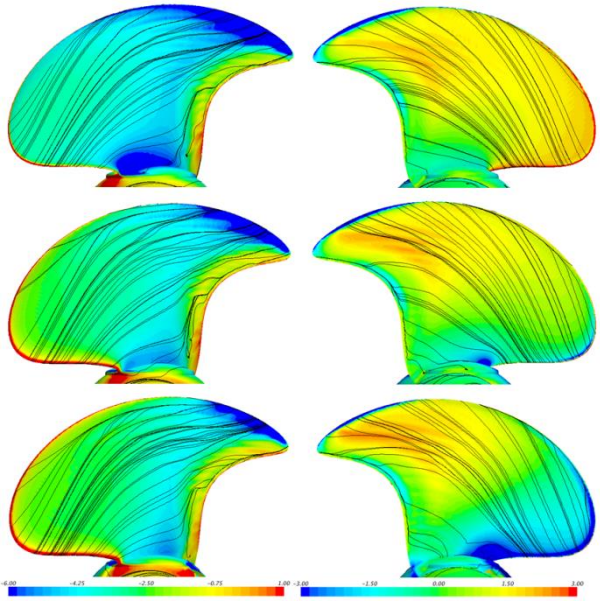

Fig. 5: *Streamlines and C_P on suction (left) and pressure (right) sides of a blade for 2- (top), 4- (middle) and 6-blade (botton) propellers: C_P contour range is -6.0 ≤C_P≤1.0 for suction side and -3.0 ≤C_P≤3.0 for pressure side*

C_P on the 0.7R section shows that the effective incidence angle is decreased for a larger number of blades. The pressure is even reversed at the leading edge for the 6-blade propeller. It is explained by the blade element theory that the reduction of the tangential velocity due to a force exerted by the blade is larger for a shorter blade spacing [1] and so the effective incidence angle is smaller for a larger number of blade.

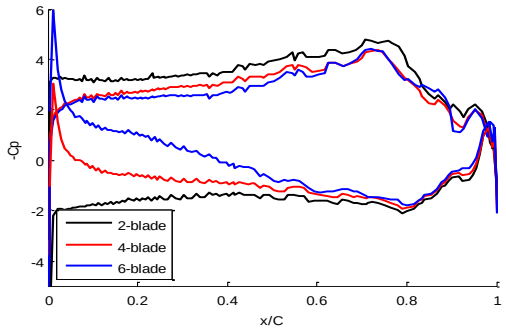

Fig. 6: C_P *on 0.7R section for 2-, 4- and 6-blade propellers*

To see what difference changes of the effective incidence angle caused by the cascade effect have from those altered simply by pitch variations,

computations are made for the 4-blade propeller with modifying the pitch angle by ±3°. The single-blade thrust T_1 for $\Delta\theta$=3° is between those for the 2-blade and the 3-blade with the design pitch. T_1 for $\Delta\theta$=-3° is about 3% lower than that for the 6-blade. When comparing the single-blade efficiency η_{O1} at the same thrust, η_{O1} for $\Delta\theta$=-3° is 10.6% higher than the extrapolated value and η_{O1} for $\Delta\theta$=3° is 10.2% lower than the interpolated value between the 2-blade and the 3-blade (See Fig. 7). It shows that η_{O1} is higher for a smaller number of blades with a lower pitch than that from a larger number of blades with a higher pitch.

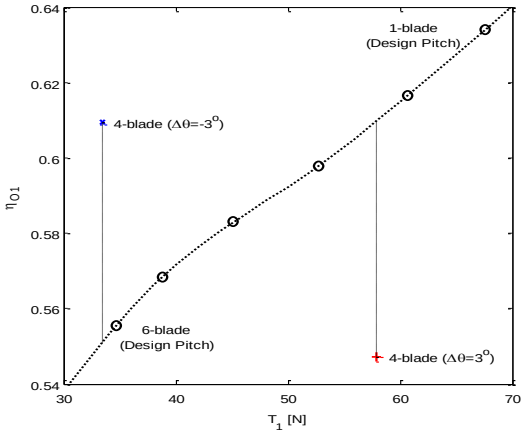

Fig. 6: *η_{O1} as a function of T_1 for different numbers of blades and for the 4-blade propeller with $\Delta\theta$=±3°*

In Fig. 7, C_P on the 0.7R is compared for the 4-blade with $\Delta\theta$=-3° and the 6-blade with the design pitch. While the negative incidence angle seems slightly larger for the 6-blade, the loading on the aft section of $x/C\geq$0.4 is quite identical. A relatively higher loading on the aft section might be part of the reason why η_{O1} at the same value of T_1 is lower for a larger number of blades. It also has an implication that leading-edge cavitation risk can be reduced by adopting a larger number of blades.

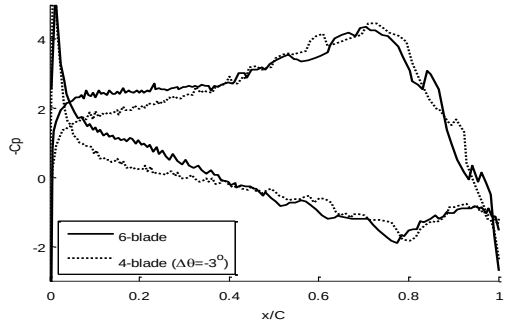

Fig. 7: *C_P on 0.7R section for 4-blade with $\Delta\theta$=-3° and 6-blade with the design pitch*

3. Trailing edge thickness

Actual marine propellers have a certain trailing-edge thickness for structural strengthening. As shown in Fig. 9, additional thickness is added to the aft section of $x/C\geq$0.7 with an elliptical rounding at the end. In the reference propeller, the maximum thickness is 68 mm and the TE thickness is 8 mm at 0.7R. CFD simulations are made for different numbers of blades with and without a TE thickness.

While T_1 is changed up and down by -1.0-0.6% for the sharp TE, Q_1 is consistently reduced by 0.6-1.9% and η_{O1} is accordingly increased by 0.6-1.4% for the sharp TE, compared to those with a TE thickness (See Fig. 4 and Table 1). The increase of η_{O1} resulted from the sharp TE is larger for a larger number of blades, because the proportion of the aft-section loading is relatively larger, as the effective incidence angle is decreased for a larger number of blades.

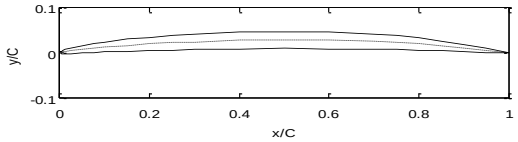

Fig. 8: *Blade section at 0.7R: meanline is shown dotted*

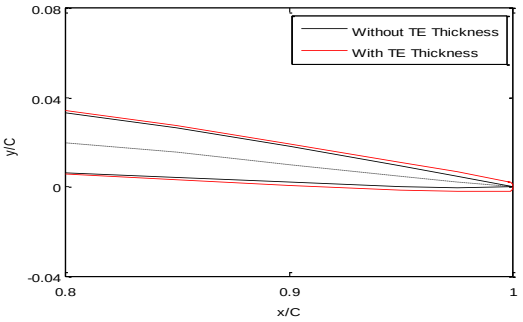

Fig. 9: *Aft section at 0.7R with and without a TE thickness*

Sharp TE	Z	1	2	3	4	5	6
	$\Delta\eta_{O1}$ [%]	0.6	0.8	0.8	0.8	0.9	1.4

Table 1: *$\Delta\eta_{O1}$ of the sharp TE compared to the case with a TE thickness*

η_{O1} lowered by a TE thickness can be related to an increase of the form drag indicated by a high gradient of C_P at $x/C\geq$0.95 (See Fig. 10). The high gradient at the TE is more noticeable for the 6-blade propeller, because the downwash at the TE is more intense for a lower or negative incidence angle.

4. Trailing edge slope

To analyze the influence of the TE slope on the cascade effect, CFD simulations are made for the TE of the blade section meanline vertically moved up and down by 25% of the maximum camber (See Fig. 11). NACA a=0.8 is used for the meanline of the reference blade section.

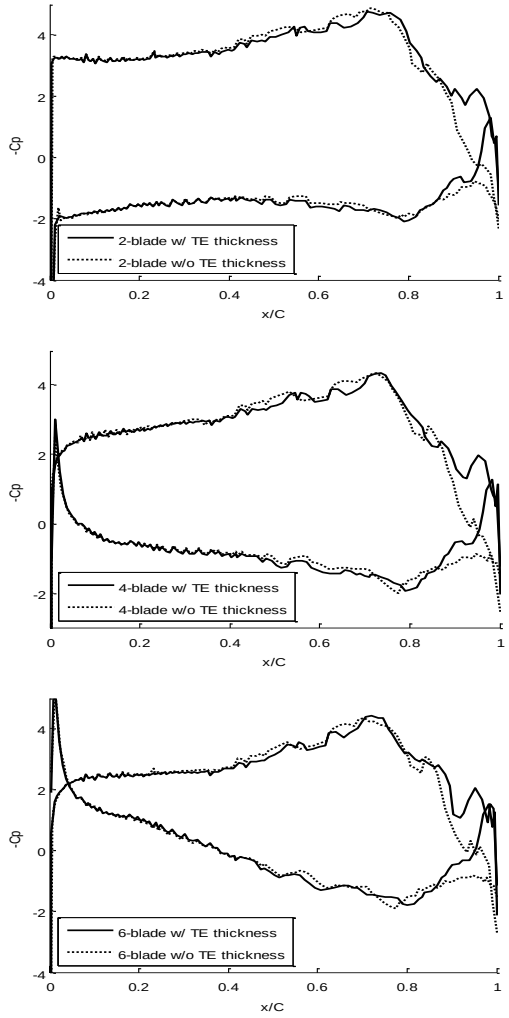

Fig. 10: *C_P on 0.7R section for 2- (top), 4- (middle) and 6-blade (bottom) propellers with and without a trailing-edge thickness*

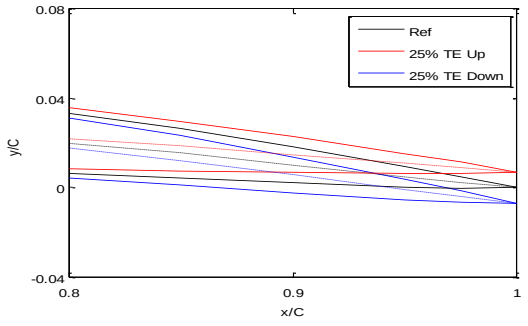

Fig. 11: *Aft part of 0.7R sections with different trailing-edge slopes*

As the resultant camber is varied by translating the TE, the sectional loading is also changed. Hence the propeller speed is increased by 0.5 rps for the TE translated 25% up and reduced by 0.5 rps for the other modified TE to have a similar level of T_1 for 4-blade cases. In CFD results, the difference of T_1 is less than 0.5% for the modified TE slopes for 4-blade cases, whereas ΔT_1 is increased for a smaller number of blades (See Fig. 12 and Table 2), because the proportion of the fore-section loading is increased, as the effective incidence angle is increased for a shorter blade spacing.

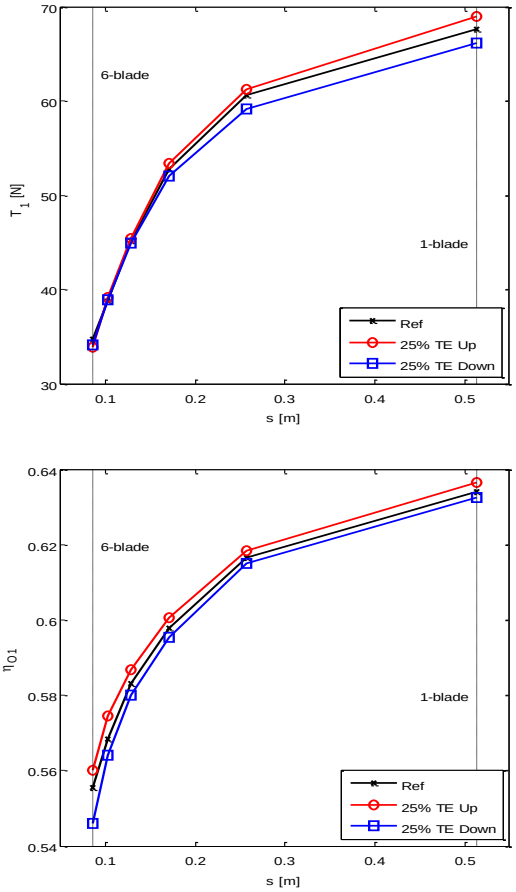

Fig. 12: *T_1 (top) and η_{O1} (bottom) as a function of blade spacing s for different numbers of blades with the trailing edge translated 25% up and down*

CFD results show that η_{O1} for the TE translated up is higher regardless of the number of blades and the efficiency gain $\Delta\eta_{O1}$ is increased for a larger number of blades. η_{O1} for the lowered TE is consistently lower and the efficiency loss is also increased for a larger number of blades. It can be related to the increase of the aft-section loading for a larger number of blades.

Z		1	2	3	4	5	6
ΔT_1 [%]	25%	2.0	1.1	1.2	0.5	0.8	-2.2
	-25%	-2.1	-2.4	-1.4	-0.4	-0.4	-1.5
$\Delta\eta_{O1}$ [%]	25%	0.4	0.3	0.5	0.7	1.0	0.8
	-25%	-0.2	-0.3	-0.4	-0.5	-0.8	-1.7

Table 2: *ΔT_1 and $\Delta\eta_{O1}$ of the cases with the trailing edge moved 25% up and down*

The comparison of C_P on the 0.7R in Fig. 13 shows that the aft-section loading at $x/C \geq 0.5$ is decreased for the TE translated up, because it is like lowering the camber in the aft section. Since the propeller speed is

increased, the fore-section loading is increased as if the pitch is increased.

The interval of two curves on both sides corresponding to the chordwise loading is smaller in the aft section for the TE translated up. The difference of the aft-section loading is increased for a larger number of blades, because the proportion of the aft-section loading is larger, as the incidence angle is smaller. It may explain why the efficiency gain for the TE translated up and the efficiency loss for the lowered TE are increased for a larger number of blades.

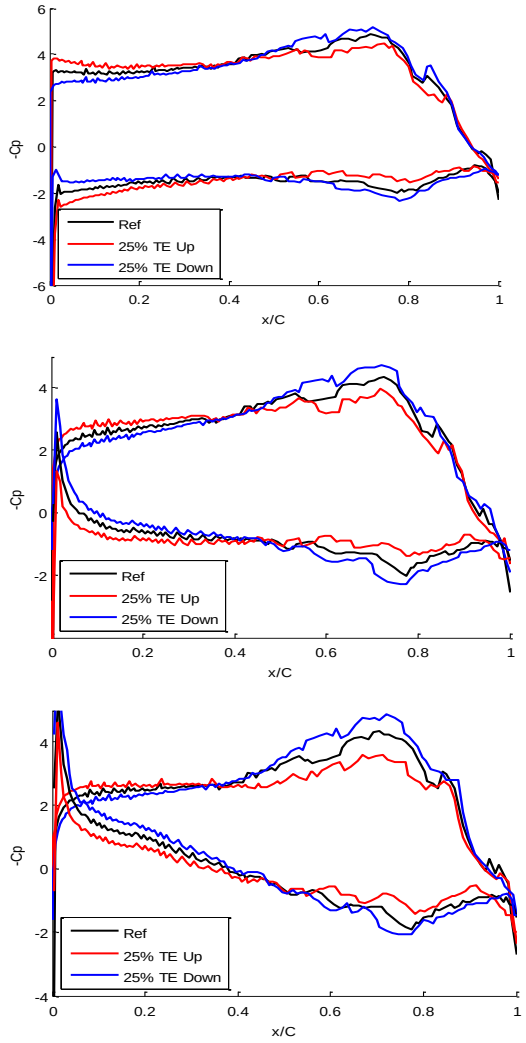

Fig. 13: *C_P on 0.7R section for 2- (top), 4- (middle) and 6-blade (bottom) propellers with the trailing edge translated 25% up and down*

5. Conclusion

CFD simulations are made with varying the number of blades. The influence of TE configurations on the cascade effect is investigated by simulating CFD with varying TE thickness and slope. CFD results are summarized as follows:

- As the blade spacing is smaller for a larger number of blades, the effective incidence angle is lower and so the single-blade thrust and efficiency are decreased
- The decreasing rates of the single-blade thrust and efficiency are higher at a smaller blade spacing
- A smaller number of blades with a lower pitch shows a higher single-blade efficiency at the same thrust than a larger number of blades with a higher pitch
- A sharp TE shows a higher efficiency than a TE with a certain thickness required for structural strengthening
- The efficiency gain for a sharp TE is larger for a larger number of blades
- A TE moved up shows a higher efficiency by lowering the aft-section loading and the efficiency gain is larger for a larger number of blades
- A lowered TE shows a lower efficiency and the efficiency loss is also larger for a larger number of blades
- The cascade effect can be alleviated by decreasing the aft-section loading and increasing the fore-section loading instead

Since the CFD simulations are made in open-water condition, the implication of the CFD analysis for propeller design in behind-hull condition with cavitation risk is limited. However, the CFD analysis implies that propeller efficiency can be improved by lowering the aft-section loading and so increasing the fore-section loading in e.g. 0.4-0.6*R* sections having low cavitation risk and little relation to hub vortex loss. On the contrary, blade sections optimized for low cavitation risk have higher aft-section loading than general NACA sections used for marine propeller blades [3]. Blade sections with higher aft-section loading can be disadvantageous in cases with a large number of blades and low cavitation risk.

References

1. Glauert, H., 1935, Aerodynamic Theory (W. F. Durand, ed.)- Airplane Propellers, Chapter V, Springer
2. Simonsen C. D. and Carstens R., 2009, Numerical flow simulation of model ship with appendages, DCMT Report
3. Zeng Z. and Kuiper G., 2009, Blade section design of marine propellers with maximum inception speed, 7th Int. Symp. on Cavitation, Ann Arbor, Michigan, USA

Recent DNS, LES and Experiments on a Cylinder with Fairings

Håkon Strandenes, Audun Yrke, Lennard Bösch, Christian Kosacki,
Bjørnar Pettersen and Helge I. Andersson
Norwegian University of Science and Technology, Trondheim, Norway
E-mail: hakon.strandenes@ntnu.no

1 Introduction

This abstract is a review of our recent work on the flow around an offshore riser design named 'short crab claw' [1]. The design is based on a circular cylinder, on which fairings have been mounted to reduce vortex-induced vibrations. The flow is considered incompressible, and the Reynolds number is $Re = 5000$.

In this abstract, we aim to make a quick summary of the work done on this configuration. We will present new LES simulations and most importantly, new experimental results obtained with particle-image velocimetry (PIV).

2 Recapitulation of previous work

Our first simulation of this case was a high-resolution DNS simulation. This simulation was done to create a high-quality reference for the later LES cases and was first presented at the NuTTS conference in 2014 [3]. The simulation was later extended and twice as long time series were included to improve the quality of the second-order correlations [2]. Both these simulations were done with the finite-volume code MGLET [4]. This code combines Cartesian grids with an immersed boundary method to capture the geometry.

At the same time, we tried to match this DNS dataset with LES (2014). Our first attempt were performed in OpenFOAM using the PISO-algorithm and a body-fitted grid. These results were not consistent with the DNS data, not even in the mean flow field [3].

We have also tried comparing the simulations with experiments [2]. Again this comparison was not very successful, as the experiments deviated significantly from both the LES and DNS simulations.

Figure 2 show the result of the DNS, the LES in OpenFOAM (2014) and the PIV dataset (2013). The differences are obvious and large.

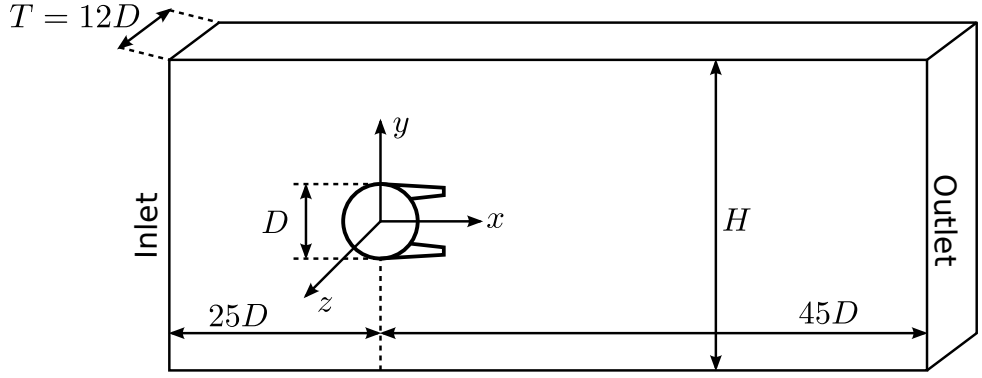

Figure 1: Simulation domain and coordinate system. The origin of the coordinate system is in the center of the circular part of the cylinder. The three directions are named streamwise (x-direction), crossflow (y-direction) and spanwise (z-direction). H is a variable height. Not to scale.

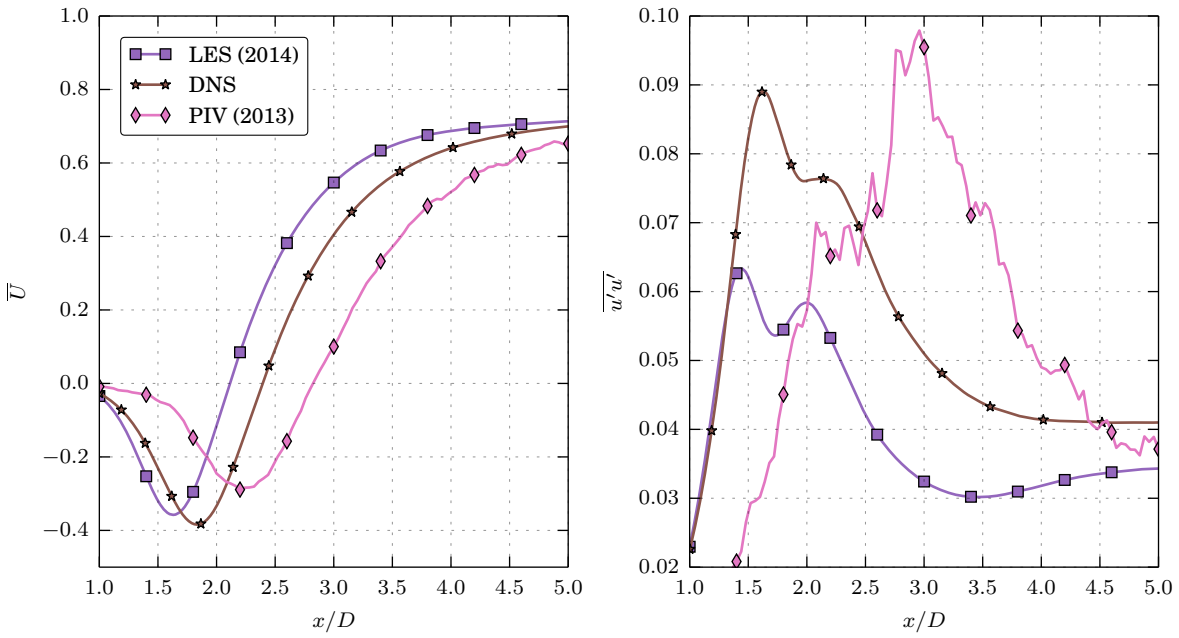

Figure 2: Data from [2] illustrating the large differences between DNS, LES and PIV. Profiles of mean velocity $\overline{U}$ and $\overline{u'u'}$ along the center line behind the cylinder. The origin of the x-axis is in the center of the cylinder.

2.1 The effect of boundary conditions

A state where neither DNS, LES nor experiments match is not a desirable state, especially unless one can explain *why* the differences occur. To close the previously mentioned differences, we decided to re-calculate all LES. At the same time, we decided to switch from OpenFOAM to MGLET for the LES as well to be able to increase the performance of our simulations.

The first 'new' LES simulation [5] were done on the same domain size as the DNS, and with a grid spacing of about twice that of the DNS. We also decided to switch from Smagorinsky to the 'WALE' subgrid scale model [6]. The resulting simulations (2015) matched very well with the DNS in all mean flow quantities.

We also decided to mimic the boundary conditions from the actual experimental facility in which the PIV experiments were conducted. The tank had a square cross-section with sides of 60 cm, and a the cylinder had a diameter of 5 cm, giving a diameter/length ratio of $D/L = 1/12$. We then narrowed down the domain to a height of $12D$ and applied no-slip boundary conditions on the four tank walls. The application of the no-slip boundary conditions changed the wake field behind the cylinder significantly, and matched our experimental data nicely, as seen in figure 3.

The result from these simulations is that we can represent the mean flow from DNS very accurately with LES. Some information regarding the fluctuations is lost, illustrated by the right plot in figure 3. However, this is as expected. We can also simulate the experimental results accurately if we apply the correct, no-slip boundary conditions.

3 New PIV experiments

The PIV data in [2] is not perfect. It contain few vortex shedding cycles, and higher order statistics are thus not converged. This is clearly seen in the right hand plot in figure 3. We therefore decided that it was necessary to make the PIV experiment over again. The new experiment was done with a similar setup as the old experiment, but with a new camera. By switching from stereo to mono-PIV, we were able to use longer measurement series. Due to image

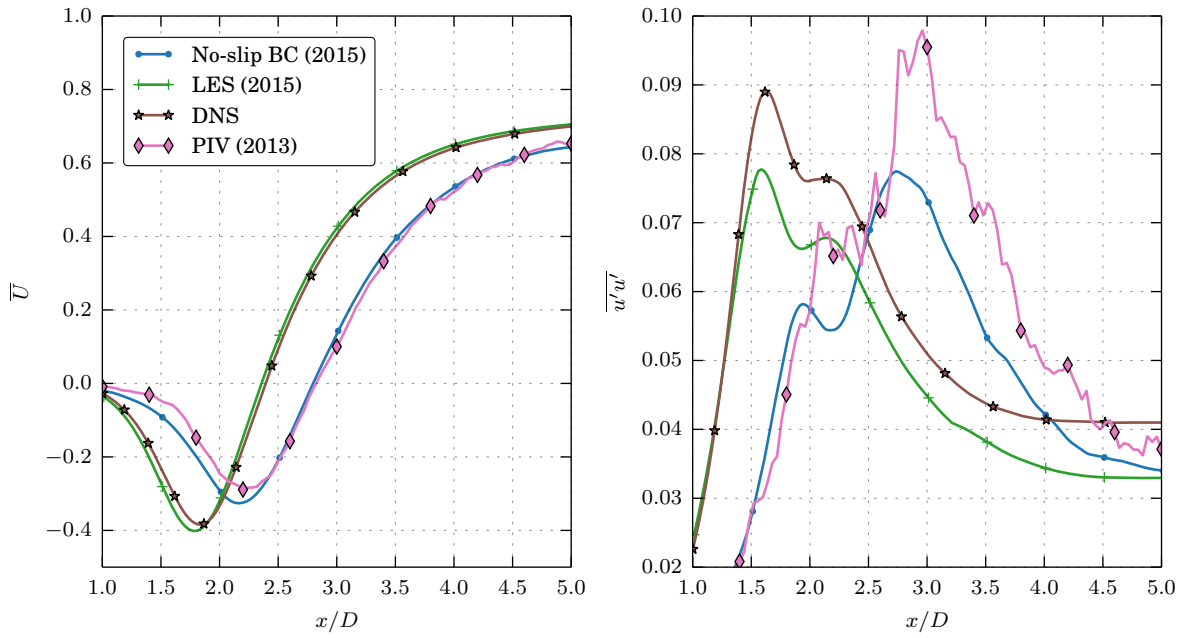

Figure 3: Data from [2] and [5]. This figure clearly show that there is a large effect of the spanwise no-slip boundary conditions encountered in a circulating water tunnel.

storage restrictions, 5 separate series containing 1600 image pairs were measured, combining mean velocities during post-processing. By assuming statistical independence between every image pair, this is acceptable.

The results show that the new experiment provide significantly better second-order statistics compared to the original experiment.

4 Additional LES simulations

The results of the first LES simulations (2014) on this case is relatively different from the most recent simulations (2015). This progress has been by trial and error and have not always been systematic in the sense that we currently cannot say which changes were important and not. We have thus decided to take a few steps back and conducted a simulation. In this we replace the WALE model with the older Smagorinsky model [7] (which was used in the original LES [3]). With this simulation we can see wether it was the subgrid scale model that changed the results or not.

Figure 5 show that the Smagorinsky SGS model is actually closer to the DNS results in the range up to $x \approx 1.8$ than the WALE model, after that they both deviate and neither can be said to be any better than the other.

5 Summary and future work

This work will never be complete. We still have a spread in the experimental data we want to explain. We believe that some of this difference might be caused by misalignment of the experimental setup. The cylinder might rotate in the tank, and it is very difficult to align it properly. We are thus currently simulating more cases where we rotate the cylinder slightly to see the effect of such a rotation. We also intend to use a laser-doppler velocimeter probe (LDV) to measure the mean velocity in specific points in the wake and compare this with the PIV data.

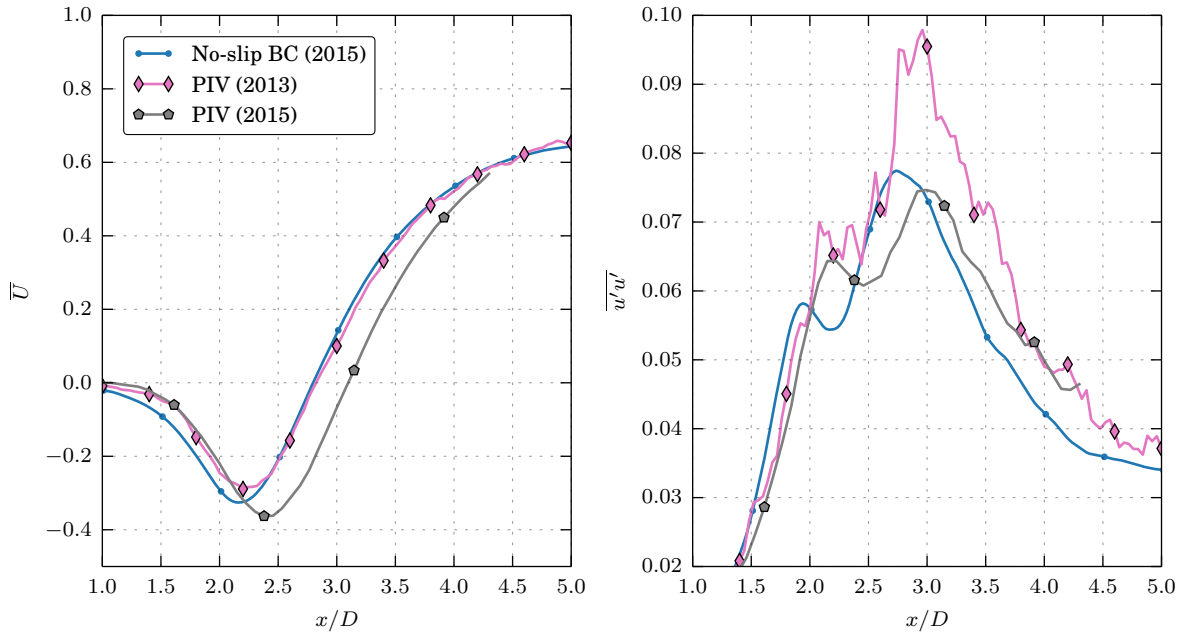

Figure 4: Data from PIV experiments together with the LES simulation with no-slip spanwise boundary conditions.

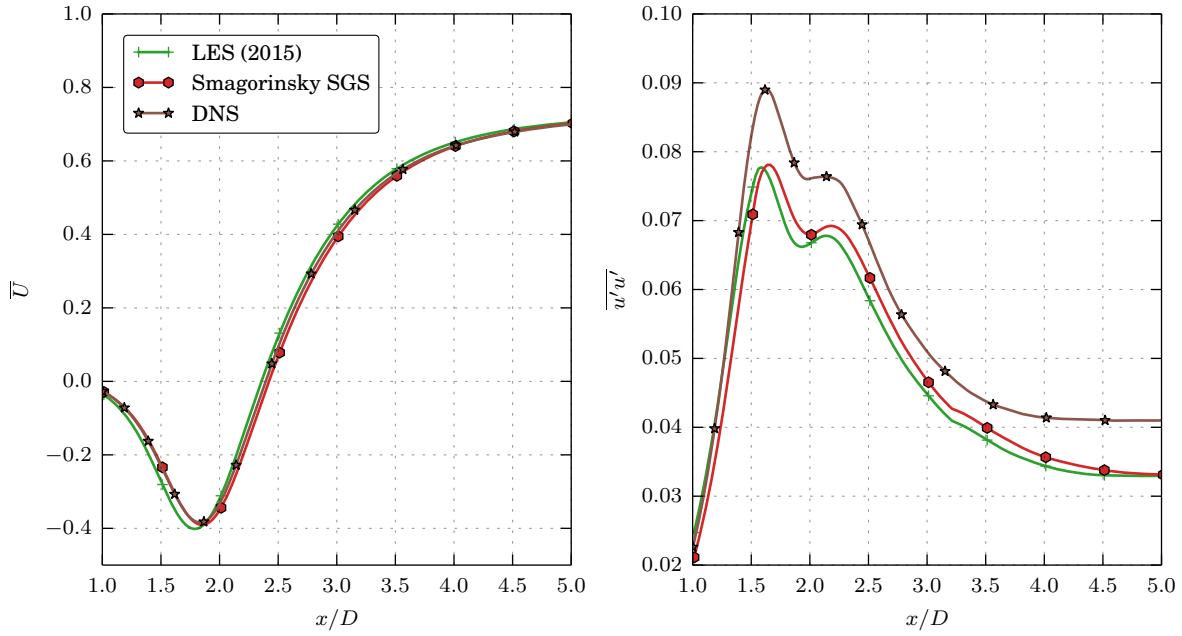

Figure 5: LES with the WALE subgrid scale model (label 'LES (2015)') compared to an identical case where the WALE model is replaced by the Smagorinsky model and our reference DNS simulation.

We also intend to increase the Reynolds number. The ultimate goal is, of course, to simulate very much higher Reynolds numbers than we present in this abstract.

References

[1] R. Baarholm, K. Skaugset, H. Lie and H. Braaten. 'Experimental studies of hydrodynamic properties and screening of riser fairing concepts for deep water applications'. In: *34th International Conference on Ocean, Offshore and Arctic Engineering*. OMAE2015-41730. St. John's, Canada, June 2015.

[2] H. Strandenes, J. P. Gallardo, J. Visscher, B. Pettersen, H. I. Andersson, H. Lie and R. Baarholm. 'A comparative study between DNS, LES and PIV for a marine riser with fairings'. In: *34th International Conference on Ocean, Offshore and Arctic Engineering*. OMAE2015-41494. St. John's, Canada, June 2015.

[3] H. Strandenes, J. P. Gallardo, B. Pettersen and H. I. Andersson. 'Comparison of LES and DNS for the flow past a cylinder with fairings'. In: *17th Numerical Towing Tank Symposium*. Marstrand, Sweeden, Sept. 2014.

[4] M. Manhart, F. Tremblay and R. Friedrich. 'MGLET: a parallel code for efficient DNS and LES of complex geometries'. In: *Parallel Computational Fluid Dynamics - Trends and Applications*. Ed. by C. B. Jenssen et al. Elsevier Science B.V., 2001, pp. 449–456.

[5] H. Strandenes, J. P. Gallardo, B. Pettersen and H. I. Andersson. 'On the effect of boundary conditions on the flow around a cylinder in a channel'. In: *8th National Conference on Computational Mechanics MekIT'15*. Ed. by B. Skallerud and H. I. Andersson. Trondheim, Norway, May 2015.

[6] F. Nicoud and F. Ducros. 'Subgrid-scale stress modelling based on the square of the velocity gradient tensor'. *Flow, Turbulence and Combustion* 62 (3) (1999), pp. 183–200.

[7] J. Smagorinsky. 'General circulation experiments with the primitive equations: I. The basic experiment'. *Monthly Weather Review* 91 (3) (1963), pp. 99–164.

Assessment of Higher–Order Forces on a Vertical Cylinder with Decomposition Model Based on SWENSE Method

Vuko Vukčević[1], Hrvoje Jasak[1] and Šime Malenica[2]

[1] *University of Zagreb, Zagreb/Croatia, {vuko.vukcevic, hrvoje.jasak@fsb.hr}*
[2] *Bureau Veritas, Paris/France, sime.malenica@bureauveritas.com*

1 Summary

Off–shore structure design often relies on accurate assessment of higher–order forces because of ringing phenomena. In this work, calculation of higher–order forces on a vertical surface piercing cylinder is carried out by a decomposition CFD model based on Spectral Wave Explicit Navier–Stokes (SWENSE) approach [1]. First, mesh and time refinement studies are carried out for a case with intermediately steep ($ka = 0.12$) incoming wave train. Second, a set of waves with different frequencies are simulated, keeping the wave steepness constant, $ka = 0.06$. Higher–order forces up to fourth order are compared with fully non–linear potential flow results [2]. A discussion on strong second order behaviour of vorticity effects in the vicinity of the cylinder is presented.

2 Introduction

CFD models based on Reynolds–Averaged Navier–Stokes (RANS) equations are progressively gaining attention in the marine industry [4] due to increase in computational resources and their ability to tackle non–linear, coupled equation sets. However, verification and validation of RANS models is still under–way [3], both for steady and transient phenomena. Transient simulations demand more CPU time compared to steady state simulations, making them more expensive to verify in terms of grid refinement and other sensitivity studies.

In this paper, we shall simulate wave diffraction problem in regular waves and assess the higher–order forces exerted on a vertical surface–piercing cylinder with a recently developed decomposition model based on SWENSE [1] method. The model is implemented in foam–extend, a fork of OpenFOAM computational continuum mechanics software. Validation of the model shall be achieved by comparing the results with fully non–linear potential flow, time–domain simulation by Ferrant et al. [2]. In order to verify the presented method, time–step and mesh refinement studies will be carried out for a representative test case.

3 Approach

The mathematical model of the incompressible, viscous, two–phase flow is modelled with momentum (Navier–Stokes) and phase continuity equations. Interface capturing is achieved with implicitly redistanced Level Set method [5] reformulated in a form suitable for Finite Volume (FV) discretisation [6]. The method does not need additional explicit redistancing. In order to efficiently model incoming waves, solution is decomposed into incident and diffracted fields following Ferrant et al. [1]. The method presented here is more general in a sense that diffracted field may contain additional phenomena not taken into account by incident wave field, such as:

viscosity, vorticity, two–phase effects, radiation effects, etc. Hence, perturbation around incident wave field is calculated via fully non–linear, viscous, two–phase equation set in the present CFD model. As a consequence, incident wave field is explicit in the CFD calculation, facilitating wave transport [7]. Governing equations are briefly presented, the reader is referred to Vukčević and Jasak [6] for detailed derivation:

- Volumetric continuity equation:

$$\nabla \bullet \mathbf{u}_D = -\nabla \bullet \mathbf{u}_I \,, \tag{1}$$

  where $\mathbf{u}_D$ is the diffracted velocity field, and $\mathbf{u}_I$ is the incident wave field. We stress that index D denotes perturbation around incident (I) field, modelling vorticity, viscosity, diffraction and possibly radiation effects.

- Momentum equation:

$$\begin{aligned} \frac{\partial(\rho \mathbf{u}_D)}{\partial t} + \nabla \bullet (\rho \mathbf{u}\mathbf{u}_D) - \nabla \bullet (\mu_{eff} \nabla \mathbf{u}_D) = -\frac{\partial(\rho \mathbf{u}_I)}{\partial t} - \nabla \bullet (\rho \mathbf{u}\mathbf{u}_I) + \nabla \bullet (\mu_{eff} \nabla \mathbf{u}_I) \\ - \nabla p_d - \mathbf{g} \bullet \mathbf{x} \nabla \rho + \nabla \mathbf{u} \bullet \nabla \mu_{eff} + \sigma \kappa \nabla \alpha \,, \end{aligned} \tag{2}$$

  where ρ is the mixture density, μ_{eff} effective viscosity of the mixture, p_d dynamic pressure, $\mathbf{g}$ gravitational acceleration, $\mathbf{x}$ position vector, σ surface tension coefficient, κ curvature of the free surface and α is the volume fraction.

- Level Set equation derived from Phase Field method [5]:

$$\begin{aligned} &\frac{\partial \psi_D}{\partial t} + \nabla \bullet (\mathbf{c}\psi_D) - \psi_D \nabla \bullet \mathbf{c} - b \nabla \bullet (\nabla \psi_D) = \\ &- \frac{\partial \psi_I}{\partial t} - \nabla \bullet (\mathbf{c}\psi_I) + \psi_I \nabla \bullet \mathbf{c} + b \nabla \bullet (\nabla \psi_I) + b \frac{\sqrt{2}}{\epsilon} \tanh\left(\frac{\psi}{\epsilon\sqrt{2}}\right) \,, \end{aligned} \tag{3}$$

  where ψ denotes Level Set field, $\mathbf{c}$ convective flux [6], b stabilisation parameter and ϵ denotes smearing distance.

Wave reflection is prevented using implicit relaxation zones [6], where the diffracted field is forced to vanish near the boundaries, leaving full potential flow solution.

Numerical discretisation of governing partial differential equations, (1), (2) and (3) is achieved with second–order accurate, polyhedral FV method in foam–extend. Terms related to incident wave field are discretised explicitly as they are known at each time–step, while diffracted fields are solved in implicit manner. Temporal discretisation is achieved via blend of Euler and Crank–Nicholson schemes. Convective terms are discretised either with second–order accurate linear upwind scheme (for momentum) or with Van Leer's TVD scheme (other convective terms). Diffusion terms are discretised using central differencing. Pressure–velocity–free surface coupling is achieved with a PIMPLE aglorithm, a combination of SIMPLE and PISO algorithms.

4 Cylinder diffraction

Diffraction of a 3–D vertical, surface piercing cylinder due to regular wave train is simulated. A deep water wave with intermediate steepness $ka = 0.12$ (Table 1 presents other geometrical and wave properties) is chosen as a benchmark test case. Block–structured mesh extends two wave lenghts in the radial direction, while the symmetry plane is used to lower the CPU time. The cells are heavily graded towards the free surface and the cylinder. There are 120 cells per wave length in the area near the cylinder and 20 cells per wave height, while the maximum aspect ratio is 166.7. The mesh consists of 552 000 cells.

Table 1: Geometry and wave parameters for the benchmark case.

Cylinder radius	r, m	1
Wave number–depth parameter	kd	8
Wave number–radius parameter	kr	0.2
Wave amplitude–depth parameter	a/d	0.015
Wave steepness parameter	ka	0.12

4.1 Time resolution study

Time resolution study has been carried out by chaning the Courant–Friedrichs–Lewy (CFL) number from 5 ($\approx$ 140 time–steps per period) to 0.125 ($\approx$ 1600 time–steps per period). 10 periods were simulated and the frequency domain analysis has been made via moving window FFT. The statistically averaged inline force harmonics are calculated as the average of the last 9 periods. The first period was excluded due to simulation start up. In–line forces are presented in dimensionless form following Ferrant et al. [2]. ρ is set to 1000 kg/m^3 and g is 9.81 m/s^2. Results of the time resolution study are presented in Figure 1. Figure 1a presents the normalized force harmonic coefficients for different CFL numbers, while Figure 1b presents relative errors compared to Ferrant et al. [2]. Relative errors for smallest CFL number are presented in Table 2. First, third and fourth order forces have a relative error less than 3%. Steady second order drift force has the largest error, 16%. Second order force has the error of approximately 12%.

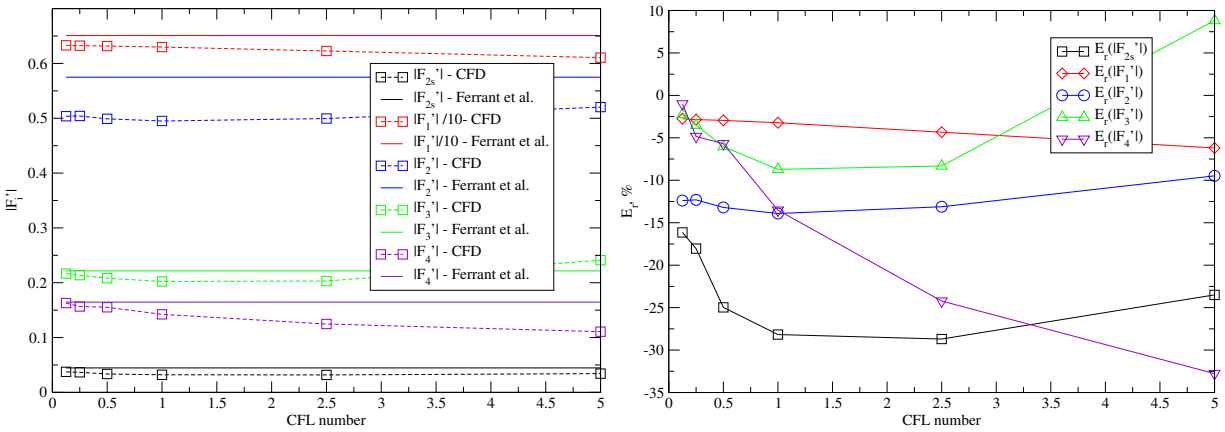

(a) Normalized force harmonics.

(b) Relative errors.

Figure 1: Vertical cylinder diffraction: time refinement study.

Table 2: Relative errors compared to Ferrant et al. (1999) [2] for $CFL = 0.125$ case.

$E_r(\lvert F_1' \rvert), \%$	$E_r(\lvert F_{2s}' \rvert), \%$	$E_r(\lvert F_2' \rvert), \%$	$E_r(\lvert F_3' \rvert), \%$	$E_r(\lvert F_4' \rvert), \%$
-2.75	-16.14	-12.39	-2.25	-1.00

4.2 Mesh refinement study

Mesh refinement study has been carried out using four meshes. Finer meshes have 25%, 50% and 75% more cells in each direction compared to the benchmark case. Same settings are used as in the previous subsection, while the CFL number was fixed at 0.25. Table 3 presents mesh refinement details. Figure 2a presents convergence of normalized force harmonics with respect to mesh refinement, while Figure 2b presents relative errors of higher order forces. It can be seen that the relative errors for higher order forces, namely third and fourth order forces exhibit oscillatory behaviour. Table 4 presents relative errors for the finest mesh.

Table 3: Mesh refinement study parameters.

Mesh refinement index	0	1	2	3
Cell count increase, %	0	25	50	75
Total cell count	552 000	1 005 700	1 854 000	2 964 500

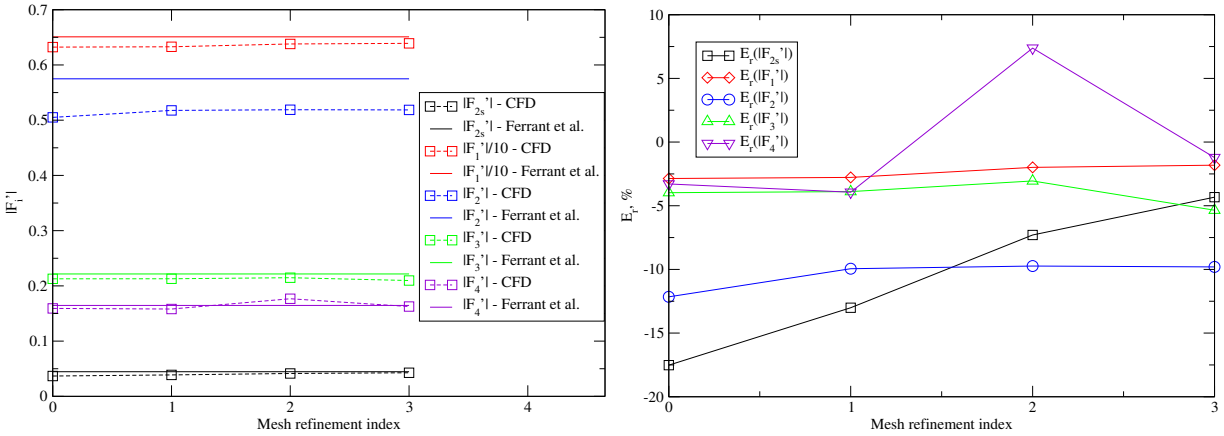

(a) Normalized force harmonics.

(b) Relative errors.

Figure 2: Vertical cylinder diffraction: mesh refinement study.

Table 4: Relative errors compared to Ferrant et al. (1999) [2] for the finest mesh.

$E_r(\lvert F_1' \rvert), \%$	$E_r(\lvert F_{2s}' \rvert), \%$	$E_r(\lvert F_2' \rvert), \%$	$E_r(\lvert F_3' \rvert), \%$	$E_r(\lvert F_4' \rvert), \%$
-1.82	-4.33	-9.80	-5.35	-1.22

4.3 Wave number study

Simulations were performed for a wave with a steepness of $ka = 0.06$, while Table 5 presents other geometrical and wave parameters. A different mesh is used for each case, such that the number of cells per wave height and length remains the same as in the base case. Figure 3 presents normalized forces for different wave number–radius parameter kr. Black, red and blue lines represent real, imaginary and absolute value of the harmonic, respectively. Observing real and imaginary parts, slight phase shift difference is revealed. The phase shift is larger for higher wave numbers, while the absolute values of the harmonics are in good agreement for all orders.

Table 5: Geometry and wave parameters for the wave number study.

Cylinder radius	r, m	1
Wave number–depth parameter	kd	8
Wave amplitude–depth parameter	a/d	0.0075
Wave steepness parameter	ka	0.06
Wave number–radius parameter	kr	0.05, 0.01, 0.15, 0.20, 0.25 and 0.30

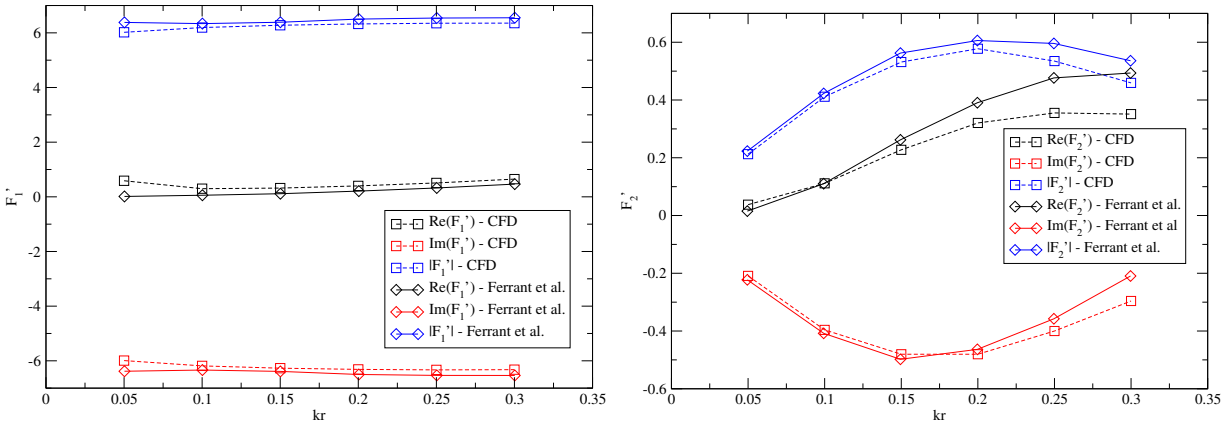

(a) Normalized first order harmonics.

(b) Normalized second order harmonics.

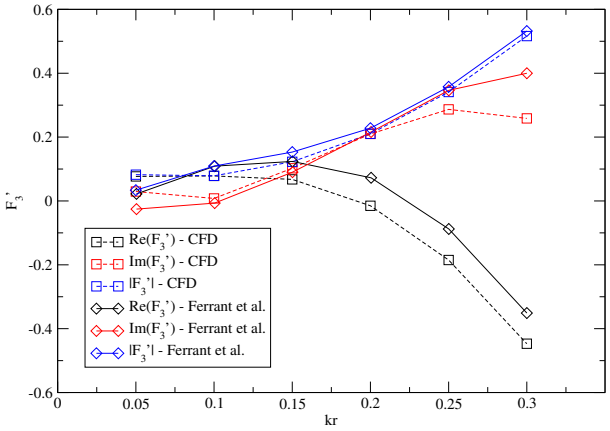

(c) Normalized third order harmonics.

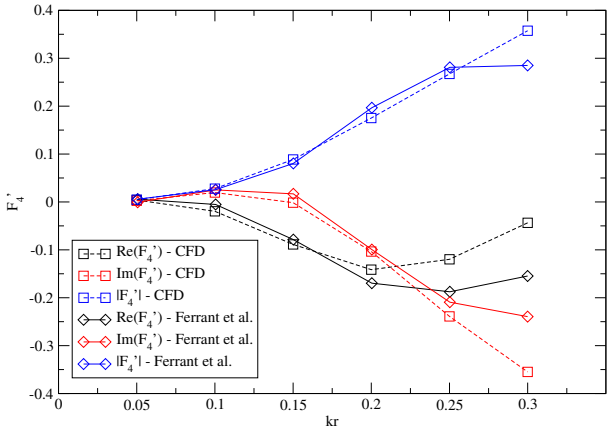

(d) Normalized fourth order harmonics.

Figure 3: Vertical cylinder diffraction: wave number study.

4.4 Vorticity effects

Vorticity effects are assessed by measuring enstrophy at three probes positioned closely in the front, at the side and in the back of the cylinder. Figure 4a presents enstrophy variation in time for three probes. The highest amount of vorticity is present at the side of the cylinder, which might be related to orthogonality of incident and diffracted waves in that region. Figure 4b presents same signals in frequency domain. Apart from the mean value, enstrophy at each probe exhibits significant second order behaviour. It was also observed that the magnitude of the enstrophy increases for higher frequencies: $kr = 0.05$ case measured enstrophy one order of magnitude smaller than the $kr = 0.3$ case. As the potential flow model does not take into account vorticity effects, authors believe that these effects are the reason for larger discrepancy for second order forces, especially for cases with higher frequency.

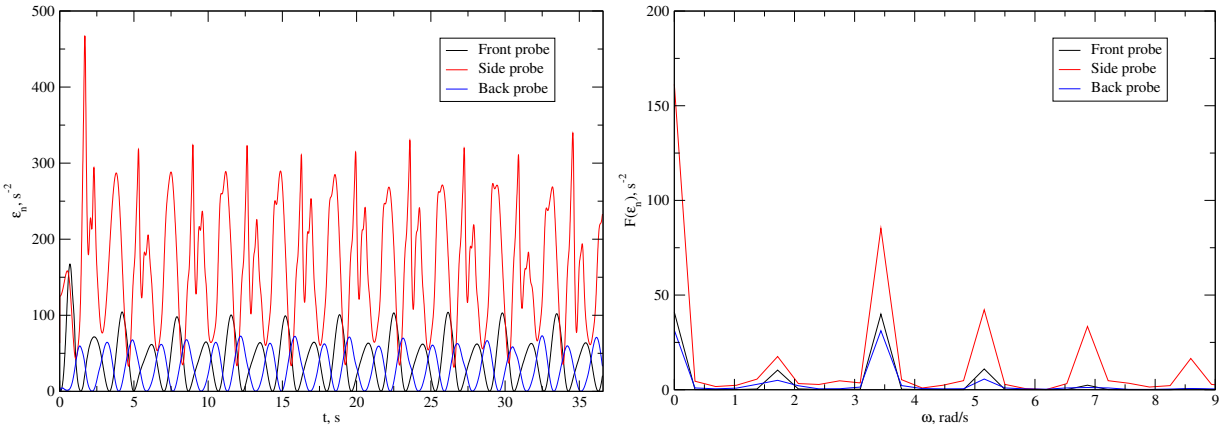

(a) Time domain.

(b) Frequency domain.

Figure 4: Enstrophy in the vicinity of the cylinder, $kr = 0.3$, $\omega = 1.718$ rad/s case.

4.5 Conclusion

Decomposition model based on SWENSE method, implicitly redistanced Level Set and implicit relaxation zones is briefly presented in this paper. Validation and verification of the model is carried out by assessing higher order forces on a circular, surface piercing cylinder. Time resolution and mesh refinement studies have been carried out for an intermediately steep wave $ka = 0.12$, showing good convergence. A set of simulations with different wave frequencies has been carried out. All results show satisfactory agreement compared to fully non–linear potential flow solution. A qualitative study of vorticity effects near the cylinder is also presented, revealing strong second order behaviour. Authors believe that vorticity effects could explain larger relative errors for second order forces, as the enstrophy is related to dissipation of the kinetic energy.

References

[1] P. Ferrant, L. Gentaz, and D. Le Touzé. A new RANSE/Potential Approach for Water Wave Diffraction. In *Proc. Numerical Towing Tank Symposium, NuTTS*, September 2002.

[2] P. Ferrant, Š. Malenica, and B. Molin. Nonlinear wave loads and runup on a vertical cylinder. In *Advances in Fluid Mechanics, Nonlinear Water Wave Interaction*. WIT Press, 1999.

[3] L. Larsson, F. Stern, and M. Vissoneau. *Numerical Ship Hydrodynamics: An assessment of the Gothenburg 2010 workshop*. Springer, 2013.

[4] F. Stern, J. Yang, Z. Wang, H. Sadat-Hosseini, M. Mousaviraad, Bhushan S., and T. Xing. Computational Ship Hydrodynamics: Nowadays and Way Forward. In *Proceedings of the 29th Symposium on Naval Hydrodynamics*, pages 1–73, August 2012.

[5] Y. Sun and C. Beckermann. Sharp interface tracking using the phase–field equation. *J. Comput. Phys.*, 220:626–653, 2007.

[6] V Vukčević and H. Jasak. Decomposition Model for Naval Hydrodynamic Applications, Part I: Computational Method. *Submitted to Ocean Engineering*, ??:???–???, 2015.

[7] V. Vukčević, H. Jasak, and Š. Malenica. Solution and Domain Decomposition Model for Naval Hydrodynamics: RANS and Potential Flow Coupling. In *VI International Conference on Computational Methods in Marine Engineering (MARINE 2015)*, pages 903–918, June 2015.

What is happening around the KVLCC2?

Jeroen Wackers, Ganbo Deng, Emmanuel Guilmineau,
Alban Leroyer, Patrick Queutey, and Michel Visonneau
LHEEA, Ecole Centrale de Nantes / CNRS-UMR 6598, 1 rue de la Noë, Nantes, France
Jeroen.Wackers@ec-nantes.fr

1 Introduction

The flow around the well-known KRISO Very Large Crude Carrier no. 2 (KVLCC2) is characterised by boundary layer thickening, flow separation, and vortex creation on the aft body of the ship, leading to a very non-homogeneous velocity field in the propeller plane (figure 1). It is known since the 1990s that the numerical simulation of such flows is highly sensitive to the treatment of the turbulence. For RANS equations, standard turbulence models perform poorly; measures like the anisotropic treatment of turbulence production are necessary in order to compute correctly the most famous aspect of the flow, the hook-shaped low-velocity zone in the main longitudinal vortex. The case is therefore justly famous as a test of turbulence models for marine flow simulation.

The focus of most studies that use the KVLCC2, such as Larsson et al. [3], is the comparison of different flow solvers or different turbulence models. To keep such studies compact and accessible, comparisons are mostly done for a few physical features only. The propeller plane with its hook shape in the axial velocity is often studied.

The objective of this paper, on the contrary, is to use a single numerical simulation of good quality to visualise the entire flow field around the aft body of the KVLCC2. We then attempt a physical analysis of this flow, searching explanations of less-studied features such as the outer boundary layer shape and the flow behind the propeller hub cap. We hope that better knowledge of the flow will allow, in the future, to understand more precisely the behaviour of different turbulence models, which may ultimately lead to better models.

The paper starts with a definition of the test case and the computation (section 2). Then section 3 presents the visualisation and analysis of the numerical solution. To assess the validity of the analysis, selected aspects of the solution are compared with experiments in section 4. The conclusion (section 5) addresses the challenges for turbulence modelling which the KVLCC2 test case still presents.

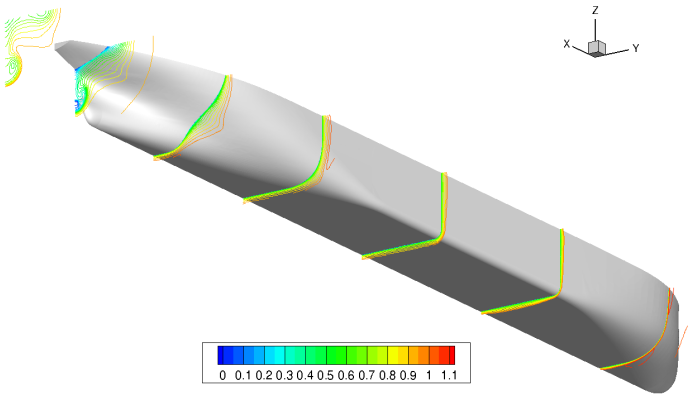

Figure 1: KVLCC2 geometry and cuts of the axial velocity.

2 Test case and numerical simulation

The case considered is the double-model flow around the KVLCC2 tanker in straight-ahead motion. The Reynolds number is $Re = 4.6 \cdot 10^6$. We compare velocities and turbulent quantities with windtunnel measurements performed at Postech [4]. The computation is performed with the ISIS-CFD flow solver [5]; it is part of a systematic grid refinement study, using automatic mesh adaptation [6]. The turbulence is modelled with the anisotropic EASM turbulence closure [1].

Half the ship is simulated. The domain runs from $4L$ in front of the bow to $9L$ behind the stern, where L is the length between perpendiculars. Sidewards and downwards, it has a size of $4L$. Boundary conditions are symmetry on the two sides of the domain which touch the hull, imposed velocity on the inflow face and the two other sides, and imposed pressure on the outflow. The hull itself has a no-slip condition, for low-Reynolds simulation of the boundary layers. The initial grids for the adaptive refinement are made with the HEXPRESS^{TM} grid generator from NUMECA Int. The target $y+$ for the first cells on the hull is 0.3, which gives 25 layers in the boundary layer grid.

Grid adaptation is performed with the flux-component Hessian criterion [7] which assures good resolution of the wake. A refinement threshold of $T_r = 1.5$ gives a refined grid of $8M$ cells. The solution on this grid is close to grid-independent, as shown in figure 2: solutions on coarser grids created with larger thresholds have a local flow which is nearly identical.

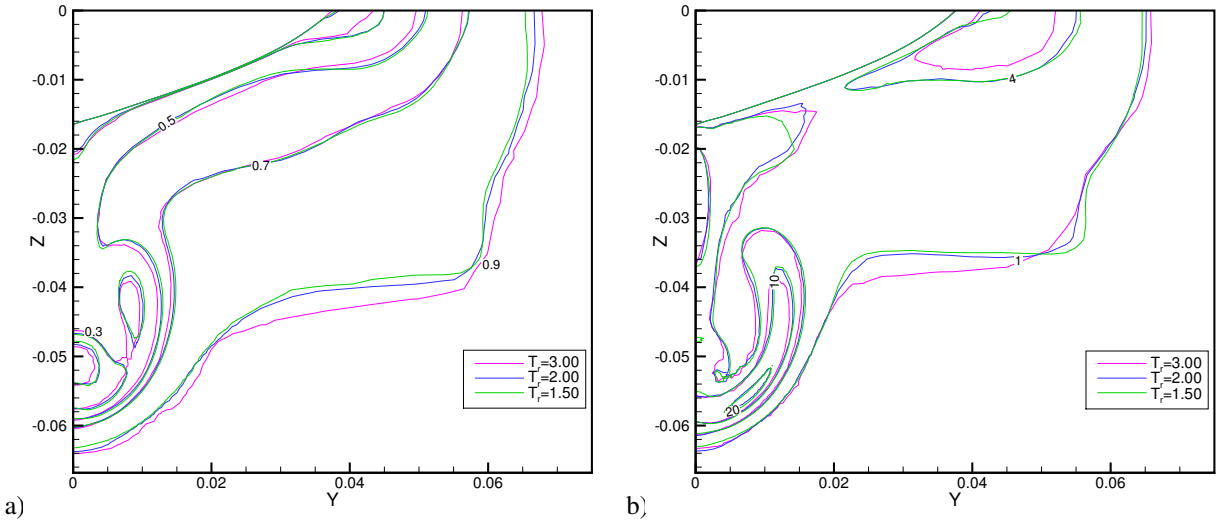

Figure 2: Grid convergence study of the axial velocity (a) and turbulence kinetic energy (b) in the propeller plane.

3 Flow analysis

Here, we identify the different phenomena in the flow simulated as in section 2, and analyse them one by one.

3.1 Visualisation

Figure 3 shows both the mean flow and the turbulence around the aft body; figure 4 gives a more detailed view of the bulb surrounding the propeller shaft and the hub cap. The mean velocity is represented by the axial velocity u and the vertical velocity w, which plays an important role in the formation of the hook shape. Vortical structures are identified with an isosurface of the second invariant Q of the velocity gradient, coloured with the helicity to show the direction of rotation. Wall and symmetry-plane streamlines complete the mean-flow visualisation.

The turbulence intensity is characterised by the turbulence kinetic energy k. To study the level of anisotropy in the turbulence, we consider that $k = \frac{1}{2}(\overline{u'u'} + \overline{v'v'} + \overline{w'w'})$, so in isotropic turbulence $\overline{u'u'} = \frac{2}{3}k$. Thus, $\overline{u'u'}/k - \frac{2}{3}$ is an indicator of anisotropy; whenever this parameter is positive, the turbulence is dominated by axial velocity fluctuations. The near-wall turbulent boundary layer is represented by the wall shear stress. Also, the amount of twist in the boundary layer is assessed by showing the wall-normal derivative of the velocity vector angle, i.e. the angle between the velocity vectors in the first and second cells next to the wall, divided by the cell-centre distance. Ideally, the twist is determined by comparing the near-wall flow direction with the angle of the flow outside the boundary layer, but the KVLCC2 aft-body boundary layer is so thick that this makes little sense: the entire aft-body flow is technically in the boundary layer!

3.2 Shoulder vorticity regions (USVR, LSVR)

The development of the KVLCC2 aft-body wake starts with the appearance of two vortical regions in the boundary layer, on the ‘shoulders’ where the flat side wall and bottom start to curve inwards; these regions are labelled USVR and LSVR, for Upper and Lower Shoulder Vorticity Region, respectively (figure 3c). The flow does not separate here, as confirmed by the non-zero wall shear stress (figure 3g, mark *A*), so the USVR and LSVR are not free vortices. However, they have a sense of rotation, shown by opposite and non-zero values of the helicity. As a result, they induce cross-flows which compress the boundary layer towards the centre of the inward-curving wall. There, the boundary layer thickens rapidly and forms a pointy shape where the converging cross-flows meet (figure 3a, *B*).

While the LSVR and USVR are pressure-driven features which do not depend much on the turbulence, they have a strong influence on the turbulent boundary layer. Figure 3b, *C* indicates that the cross-flow is zero on the wall and increases to a maximum in the centre of the boundary layer. Thus, the fluid which is displaced is mainly the high-velocity, low-turbulence fluid of the outer boundary layer. Therefore, the turbulence level in the cross-flow region (figure 3e, *D*) is lower than in the boundary layers on the horizontal and vertical walls (*E*). The anisotropy of the turbulence, seen in figure 3f, is (surprisingly!) high in the non-disturbed boundary layers on the walls (*F*). Where the cross-flows meet, the turbulence becomes isotropic (*G*). Thus, the nature of the turbulence changes; the simple convection of low-turbulence fluid to the cross-flow region may therefore not be the only explanation of the low k in this region.

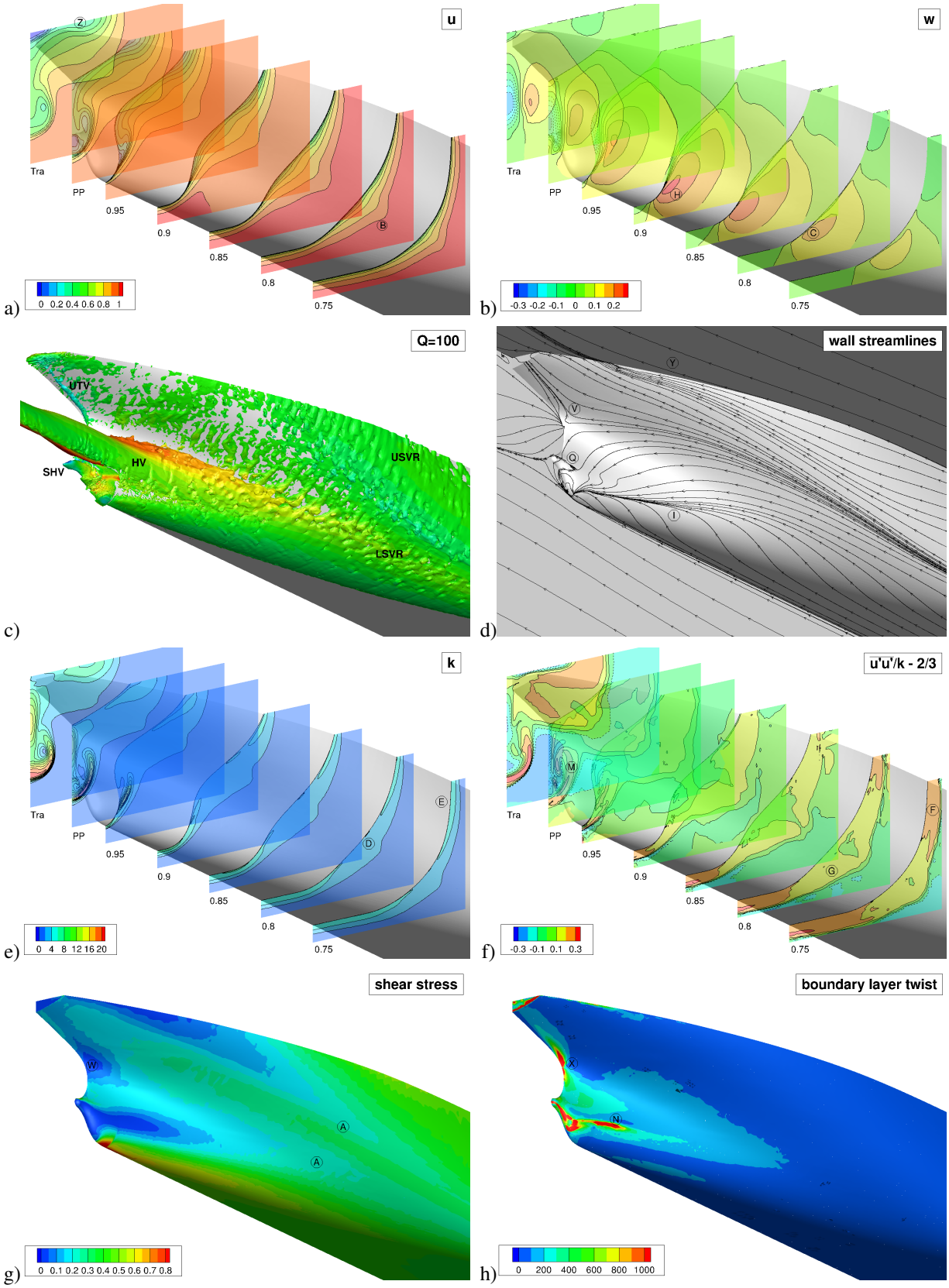

Figure 3: Visualisation of the flow on the aft part of the hull. The marks (*A*, *B*, etc.) are referenced in the text.

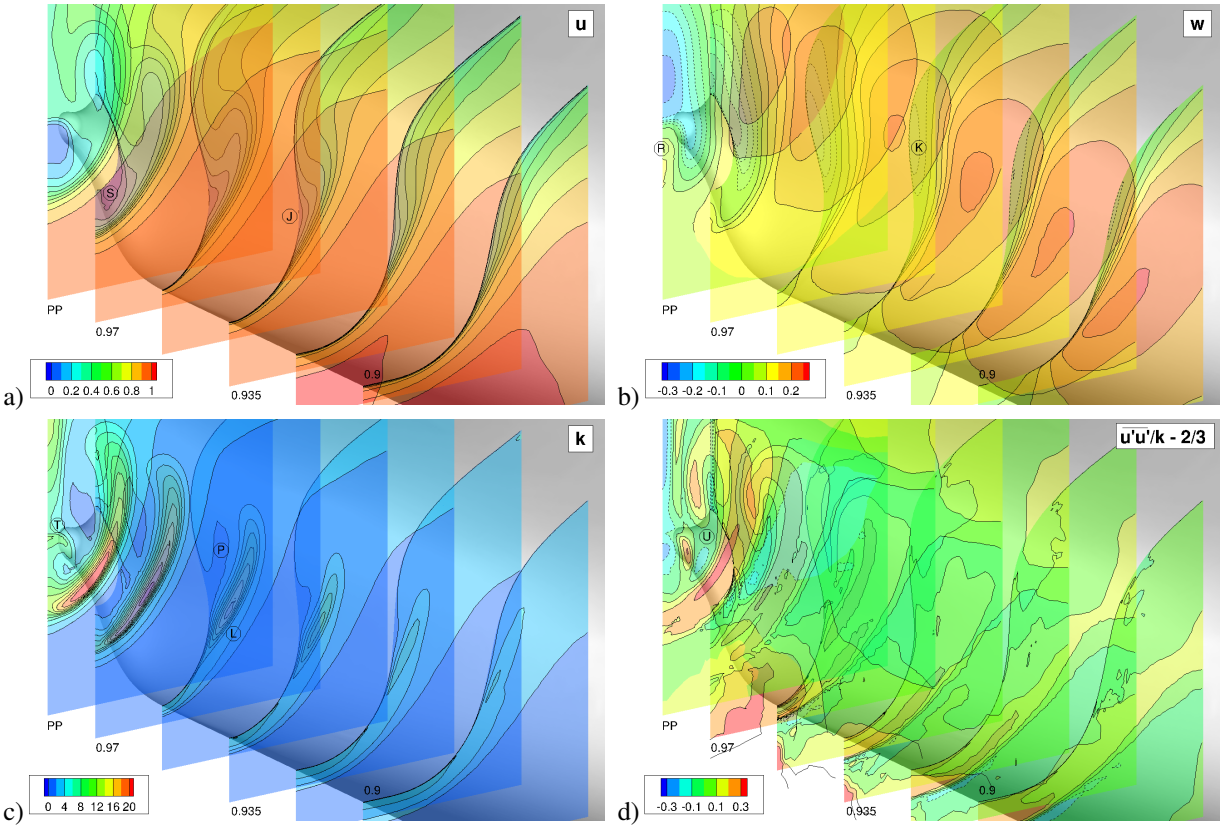

Figure 4: Visualisation of the flow on the aft part of the hull (detail of figure 3).

3.3 Hook vortex (HV)

Further back, the flow induced by the LSVR moves upwards along the hull. When this updraft flows around the bulb which surrounds the propeller axis (figure 3b, *H*), an open-type separation appears which forms the main Hook Vortex (HV), see figures 3c and d, *I*. The separation is comparable to the vortex shedding on an ogive at an angle of incidence. The core of the HV originates in the near-wall boundary layer and therefore has a low axial velocity (figure 4a, *J*). This core, and the shear layer below which connects it to the boundary layer, form the hook shape of low axial velocity which is the best-known feature of this test case. The vortex induces a downward flow on the hull (figure 4b, *K*), which gradually separates the vortex core from the hull.

Since the separation of the HV occurs on a smooth surface, it depends on the evolution of the turbulent boundary layer. And the separation line is precisely the location of the most violent turbulence production in the entire flow (figure 4c, *L*), caused by the shear in the axial velocity between the fast outer flow and the dead-water region of separated fluid. The shear in the vertical velocity is much less marked. This shear-layer turbulence, like the boundary layers, is anisotropic and dominated by axial fluctuations (figure 3f, *M*). Also, the near-wall boundary layer is strongly twisted (figure 3h, *N*).

On the contrary, the core of the HV where u is the lowest is a region of very low turbulent kinetic energy (figure 4d, *P*). A possible explanation is, that the low-velocity fluid comes from the inner part of the boundary layer which is compressed by the downward flow on the hull; this fluid close to the wall has a low k. However, the vortex core area is large compared with the very thin inner boundary layer, so an additional damping phenomenon may exist. Since the core evolves in a zone of low turbulence, it persists over a long distance.

3.4 Secondary hook vortex (SHV)

The downward velocity on the hull, induced by the HV, starts above the shaft bulb but rapidly flows around the bulb and pushes the separation point of the HV downwards (see figures 4a, *J* and 3d, *I*). Below the bulb, the downward flow separates in its turn (figure 3d, *Q*). This separated flow encounters an updraft which follows the lower part of the bulb upwards (figure 4b, *R*). Between them, these flows create the Secondary Hook Vortex (SHV), which is counter-rotating with respect to the HV. The SHV separation resembles the ones on bluff bodies with oblique aft faces; there is a significant dead-water zone with low axial velocity between the vortex and the centre plane (figure 4a, *S*). This dead-water zone, clearly visible in the propeller plane, is therefore not the direct wake of the hub cap but it is created on the hull, below and in front of the hub cap.

Just above the dead-water region, the velocity gradients are high. There is some production of turbulence in this zone (figure 4c, *T*). The vortex core appears to be a minimum of k but it is not a zone of uniform anisotropy; predominance and relative absence of axial fluctuations appear side by side (figure 4d, *U*).

3.5 Other separations and vortices

The flow on the upper part of the hull continues without major perturbations and then separates suddenly on the meeting point between the skeg and the hull below the transom, just before arriving at the end of the hull (figure 3d, *V*). The resulting, very weak under-transom vortex (UTV) follows the hull upwards. While it remains close, it is separated from the hull as seen in the shear stress (figure 3g, *W*), which is zero only at the origin of the UTV. Like the HV and SHV, the origin of the UTV is a location of strong boundary layer twist (figure 3h, *X*). Otherwise, its influence on the flow is marginal.

A much more pronounced wake is formed by the flow leaving the hull at its top edge. While the shear stress in this zone is low, the streamlines indicate that the flow remains attached throughout and leaves the hull at the upper edge (figure 3d, *Y*). In the wake, there is a significant velocity defect (figure 3a, *Z*) and some turbulence production.

4 Comparison with experiments

The preceding study is performed on numerical results, because these provide excellent resolution of details throughout the flow and allow the study of quantities which cannot be obtained from experiments. However, these results are subject to modelling errors so they could lead to false conclusions. Therefore, selected quantities in the propeller plane are compared with the windtunnel measurements, to see if these support the analysis in section 3.

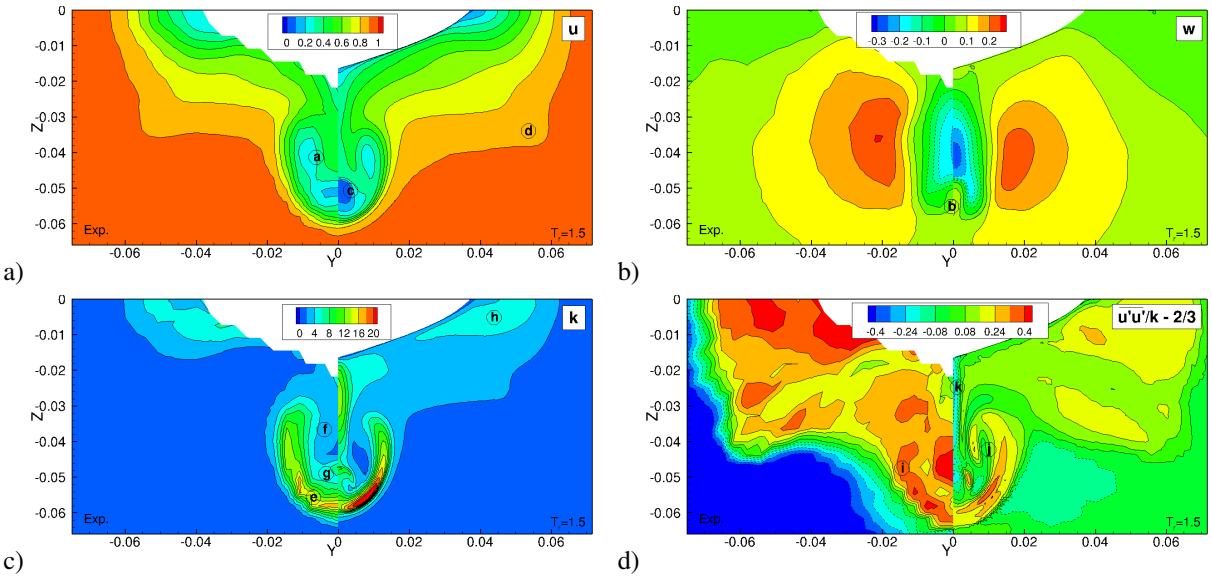

Figure 5: Comparisons of computational and experimental results in the propeller plane ($x = 0.9825L$).

The velocity measurements confirm the existence of the HV, SHV, and the USVR / LSVR. The hook shape, which is a characteristic of the HV, is very similar between computations and experiments (figure 5a, *a*). The downward jet and upward motion near the symmetry plane which form the SHV are present in the measurements (figure 5b, *b*). And while the axial velocity in the SHV core is higher in the experiments (figure 5a, *c*), this is not an error in the flow topology, since the vortex damps out so quickly: only $0.005L$ behind the propeller plane, the numerical solution has the same axial velocity as the experimental value in the propeller plane. Finally, the shape of the outer boundary layer edge (figure 5a, *d*) is due mainly to the USVR and LSVR; this shape is nearly identical between experiment and simulation, which supports the existence of these vorticity regions. The UTV is too weak and too close to the boundary to be seen in the experiments. Given the observed quality of the numerical solution, its existence is plausible, but it cannot be proved.

Figure 5c indicates that the prediction of the turbulence kinetic energy is also good. The high intensity in the HV shear layer (*e*), the low turbulence in the HV core (*f*), and the small peak of turbulence above the SHV (*g*) are confirmed, as is the slightly higher k besides the transom (*h*). The peak experimental value of k below the HV is not as high as in the simulation, but this may be due to the insufficient resolution of the measurements. Even the derived quantity of the anisotropy indicator (figure 5d) is mostly in good agreement, at least quantitatively. The predominance of longitudinal turbulence in the shear layers is confirmed (*i*); the isotropic turbulence in the HV core is not observed (*j*), but this may again be due to the insufficient resolution of the experiments.

Discrepancies are observed in the vertical symmetry plane (figure 5d, k, for example). However, the measurements are uncertain here, since the windtunnel results do not agree with towing tank measurements for the same geometry [3]. This area will be studied further in our future work.

5 Conclusion: challenges for turbulence modelling

The agreement between experiments and computations in the previous section is good, but not perfect. Due to the low numerical uncertainty (section 2) and supposing limited measurement errors, most differences can be attributed to the turbulence modelling. For these models, what can be learned from the physical analysis in section 3?

Traditionally, the challenge for simulating ships like the KVLCC2 with RANS has been the prediction of low enough turbulence in the HV core, so that this core is preserved intact. Standard turbulence models like $k-\omega$ SST produce too much turbulence viscosity near this core, so that it is damped out too quickly. Anisotropic models such as EASM produced the first simulations where the hook shape was predicted correctly.

This study shows that the driving force for the KVLCC2 aft-body flow, besides pressure effects, is boundary layer separation; thus, an additional challenge is to model these separations correctly. The separate flow regions have a very different nature:

- The flow in the USVR and LSVR remains attached, so it is within the validity region of classical RANS turbulence closures (even though the real turbulence is not at all isotropic!).
- The HV, with its axial-aligned separation line and relatively limited axial-velocity defect, is similar to the sonar dome vortex of the DTMB 5415 for which Larsson et al. [3] conclude that most RANS methods can predict the onset, given sufficiently fine grids. As noted above, the main difficulty is in preserving the low-velocity core. However, for any separation from a smooth surface, the simulated separation depends on the turbulence model, so there is a challenge here to get the separation line correct in order to predict the HV strength and position perfectly.
- The SHV separates from a surface that is not at all aligned with the main flow. Its separation, with a large low-velocity zone, resembles the one on a bluff body with an oblique aft part such as the Ahmed body (a simplified car geometry). Investigations have shown that today's RANS models are unable to predict this separation correctly; Detached-Eddy Simulation (DES) or similar techniques are required to better capture the flow, see for example [2]. By the way, this study finds that RANS overestimates the size of the recirculation zone, just like for the KVLCC2 (section 4). Thus, it remains to be seen whether RANS can ever simulate the SHV correctly.

The KVLCC2 results, confirmed by experiments, indicate that the turbulence is highly anisotropic and that the level of anisotropy depends on the position in the flow. This is not a proof that isotropic turbulence models perform badly for the KVLCC2. However, a turbulence model cannot duplicate the exact physics of the flow unless anisotropy is taken into account. Likewise, significant boundary layer twist was detected near separation zones. This could mean that wall-law boundary conditions, which use an approximated representation of the twist, may be unable to represent correctly the flow physics.

Thus, the KVLCC2 flow and especially the SHV is still a major challenge for turbulence modelling and the test case remains relevant for development work in the years to come.

Acknowledgements

This work is part of an ongoing collaboration with Alexandro Palmieri (CIRI-MAM Tecnopolo della Nautica, Università di Bologna, Italy). Computations were performed using HPC resources from GENCI (Grant2010-x2010021308), which is gratefully acknowledged.

References

[1] R. Duvigneau, M. Visonneau, and G.B. Deng. On the role played by turbulence closures in hull shape optimization at model and full scale. *J Mar Sci Techn*, **8**(1), 1–25 (2003).

[2] E. Guilmineau, G.B. Deng, and J. Wackers. Numerical simulation with a DES approach for automotive flows. *J Fluids Struct* **27**(5-6)807–816 (2011).

[3] L. Larsson, F. Stern, and M. Visonneau (eds.). *Numerical Ship Hydrodynamics. An assessment of the Gothenburg 2010 workshop.* Springer (2013).

[4] S.J. Lee, H.R. Kim, W.J. Kim, and S.H. Van. Wind tunnel tests on flow characteristics of the KRISO 3,600 TEU containership and 300K VLCC double-deck ship models. *J Ship Res*, **47**(1), 24–38 (2003).

[5] P. Queutey and M. Visonneau. An interface capturing method for free-surface hydrodynamic flows. *Comput Fluids*, **36**(9), 1481–1510 (2007).

[6] J. Wackers, G.B. Deng, E. Guilmineau, A. Leroyer, P. Queutey, and M. Visonneau. Combined refinement criteria for anisotropic grid refinement in free-surface flow simulation. *Comput Fluids*, **92**, 209–222 (2014).

[7] J. Wackers, E. Guilmineau, A. Palmieri, and P. Queutey. Hessian-based grid refinement for the simulation of surface-piercing hydrofoils. Proceedings of NuTTS 2014, Marstrand, Sweden (2014).

Numerical simulations of ship hull-propeller interaction phenomena

Michał Wawrzusiszyn, Tomasz Bugalski, Paweł Hoffmann
(Ship Design and Research Centre S.A – CTO S.A, Gdansk / Poland,
michal.wawrzusiszyn@cto.gda.pl)

Introduction

This paper presents results of current research consisting of computational analyses of 230m KRISO Container Ship (KCS) with five-bladed propeller (KP505). Investigated case is a benchmark case for forthcoming Workshop on CFD in Ship Hydrodynamics (Tokyo 2015) – Case 2.5: hull model without the rudder, free to trim and sink, rotating propeller. In this research, some earlier ideas published by Bugalski & Hoffmann 2010 and 2011, Carrica et al. 2011, Lin & Kouh 2014 and Stern et al. 2013 have been taken into consideration and further developed.

The KCS was designed to provide data for both the explication of flow around operating vessel and the CFD validation for a modern container ship with a bulbous bow. The Korea Research Institute for Ships and Ocean Engineering (now MOERI) and the Ship Research Institute (now NMRI) performed towing tank experiments to measure resistance and self-propulsion data. The results were published in the *Proceedings of the CFD Workshop Tokyo in 2005* (Hino 2005). No full scale ship exists.

Methodology

The computations were carried out at model scale using the Reynolds Averaged Navier-Stokes Equations (RANSE) method and the Realizable K-Epsilon turbulence model. Meshing and flow simulations were conducted with use of Star CCM+ 9.06 from CD-adapco. A particular solvers and settings used in computation:

- **Implicit solver:** each physical time-step involves some number of inner iterations to converge the solution for that given instant of time.
- **6-DOF (degree of freedom) Solver**: it computes fluid forces, moments, and gravitational forces on a 6-DOF body.
- **6-DOF Motion:** it moves the vertices of the grid according to motion of the body that is calculated by the 6-DOF Solver.
- **Partitioning:** it controls how the solver partitions the domain. In this case solver is partitioning each region individually.
- **Damping Boundary Distance:** a parameter of wave damping in the domain
- **Segregated Flow:** it solves the flow equations (one for each component of velocity, and one for pressure) in a segregated, or uncoupled, manner.
- **Segregated VOF (volume of fraction):** it solves the discretized volume-fraction conservation equation for each phase present in the flow.
- **K-Epsilon Turbulence:** it controls the solution of the K-Epsilon model in all the continua for which the model is activated.
- **K-Epsilon Turbulent Viscosity:** it controls the update of the turbulent viscosity.

First step was to find the optimum mesh density at which the difference of total resistance coefficient C_T reaches sufficiently low value while maintaining reasonable computational effort. Second task was to use above mesh setup for self-propulsion calculations. Motion of the hull and propeller was treated as Dynamic Fluid Body Interaction (DFBI). A body motion was divided into two dependent motions:

- hull: DFBI Rotation and Translation
- propeller: DFBI Superposed Rotation

Due to numerical convergence the self-propulsion computations were divided into three time stages (see Table 1).

The first goal of the project was to simulate numerically the flow about KCS ship hull and propeller including the free surface around the ship. The calculations were performed for the KCS ship without rudder in fixed conditions (suppressing dynamic sinkage and trim).

Main characteristics of the hull shapes, scale factors and visualizations of the hull shapes are presented below in Table 2. Model geometry is presented in Figure 1 and simulation conditions are specified in Table 3.

Stage	Parameters	Value
1	Propeller rotation	yes
	Hull trim and sinkage	fixed
	Time step	$1x10^{-2}$s
2	Propeller rotation	yes
	Hull trim and sinkage	free
	Time step	$1x10^{-2}$ s
3	Propeller rotation	yes
	Hull trim and sinkage	free
	Time step	$3x10^{-4}$ s

Tab. 1 *Parameters of the computations in each stage*

Main particulars	Unit	Value
Length b.p.	m	230.00
Length of waterline	m	232.50
Breadth	m	32.20
Draught	m	10.80
Displacement volume	m^3	52030
Surface wetted area w/o rudder	m^2	9424
Surface wetted area of rudder	m^2	115
Block coefficient	-	0.651
Midship section coefficient	-	0.985

Tab. 2 *Main hull particulars*

Computation conditions	Unit	Value
Service speed	kn	24.0
Model scale	-	31.60
Froude number F_N	-	0.260
Reynolds number R_N	-	$1.40 \cdot 10^7$
Kinematic viscosity	m^2/s	$1.138 \cdot 10^{-6}$
Water density	kg/m^3	999.1
Propeller revolutions	rps	9.5

Tab. 3 *Computation conditions*

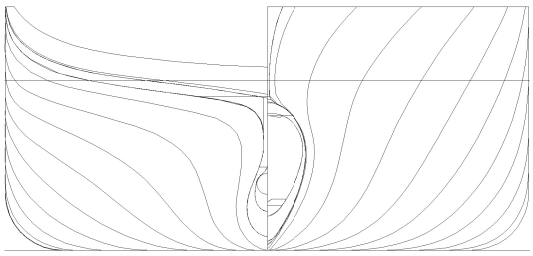

Fig. 1 Body lines of the KCS hull

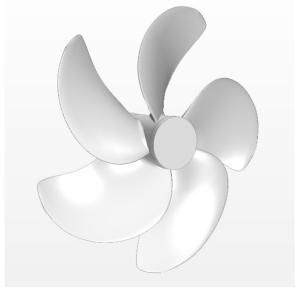

Fig. 2 *Propeller model KP505*

The propeller model No. KP505 was used (see Figure 2) for which the open water characteristics are available.

Propeller KP505	Unit	Value
Direction of rotation	-	right
Propeller diameter	m	7.90
Number of blades	-	5
Expanded area ratio	-	0.7963
Pitch ratio	-	1.1740
Blade rake / Skew back	deg	0/16.8
Profile	-	NACA66/0.8

Tab. 4 *Propeller geometry data*

Results of numerical simulations

The unstructured computational mesh of hexahedral and polyhedral cells was used for the computations. The results of study of mesh size influence on ship hull resistance (including rudder) are presented in Table 6. Finally, the total number of mesh elements used in the calculation was about 3.7 million cells. The example of mesh details are presented in Figure 3. Mesh analyses was focused mainly on comparison of resistance coefficient (C_T) value to the experimental one.

$$C_T = \frac{R_T}{0.5\rho \times v^2 \times S} \quad [-], \text{ where}$$

R_T – model resistance, ρ – water density, v – velocity, S – wetted surface area

For the meshes more dense than the *medium* one, no further considerable reduction of the computational difference was observed (see table 5). For that reason, the medium size mesh was used for further analysis. Comparison discrepancy (E%D) used in this document is defined as:

$$\text{E\%D} = \frac{(D-S)}{D} \times 100 \quad [\%], \text{ where}$$

D (EFD) – experimental value, S – CFD simulation value

Mesh type	Mesh size x10^6	Mean y+	C_T x10^3	EFD (D)	E%D [%]
Coarse	1.6	22	4.111	3.711	-10.77
Medium	3.7	16	3.801		**-2.43**
Dense	4.9	13	3.873		-4.38
Very dense	6.4	11	3.857		-3.94

Tab. 5 *Results of the mesh comparison at Fn=0.26*

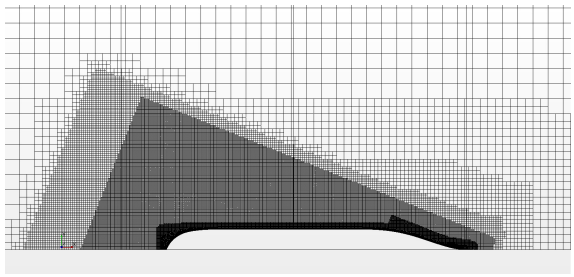

Fig. 3 *Medium mesh – top view*

Self-propulsion and open water propeller results

The self-propulsion calculations were carried out based on medium mesh size type and complete hull geometry. Total mesh elements number was 8.3x10^6 cells. Propeller rotation was modeled by DFBI Superposed Rotation option (it superimposes an additional fixed body rotation in addition to the DFBI motion).

A coefficient of pressure distribution without hydrostatic component is defined as:

$$C_P = \frac{p}{0.5 \cdot \rho \cdot v^2}, \text{ where}$$

C_P – pressure distribution coefficient,

p – hydrodynamic pressure,

ρ – water density,

v – hull speed

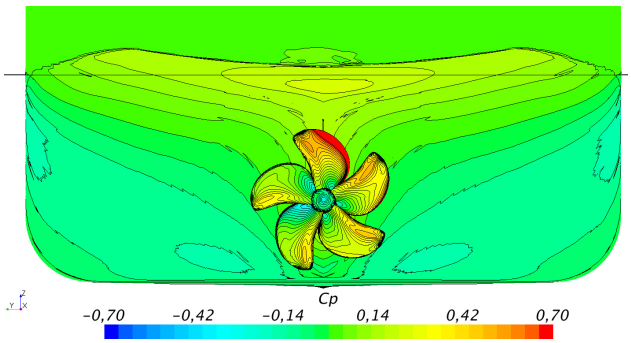

Fig. 4 *Pressure distribution on the propeller and aft*

Propeller thrust and torque coefficients are defined as:

$$K_T = \frac{T}{\rho \times D^4 \times n^2} \quad , \quad K_Q = \frac{Q}{\rho \times D^5 \times n^2} \quad [-] \text{, where}$$

ρ – water density, D – propeller diameter, n – propeller revolutions, T – propeller thrust, Q – propeller torque

The self-propulsion computations were carried out at ship service speed. A rate of revolutions of the propeller (n) was set to equal to the experimental value 9.5 rps.

The simulation with the propeller behind the ship must be run in transient mode. Applied time step is $3x10^{-4}$s. It allows to rotate the propeller around 1 degree per each time step. Comparison of experimental data (EFD) and computational results for the model hull and rotating propeller is presented in the Table 6.

Parameters		**Experiment**	**Results**
$C_{T(SP)}$ x 10^3	Value	3.966	3.902
	E%D	1.61	
K_T	Value	0.170	0.170
	E%D	0.00	
K_Q	Value	0.0288	0.0309
	E%D	-7.33	
$F_D = [R_{T(sp)}-T]$ (N)	Value	30.25	29.80
	E%D	1.50	

Tab. 6 *The self-propulsion computation results*

Obtained computation results are very close to the postprocess experimental values. Calculated C_T discrepancy is around 1.6% and calculated K_Q discrepancy is 7.3%. It was expected to obtain better convergence between measure and calculated value of K_Q. Further investigations are planned to better understand the source of differences.

As a continuation of the CFD research, the open water characteristics of the propeller were carried out for the mesh density similar to the one used in self-propulsion case. The comparison of the CFD results and experiment results are shown in Figure 5. The $K_{T(OPW-CFD)}$ difference is 8.1% and the $K_{Q(OPW-CFD)}$ difference is 1.1%.

These results show that the discrepancy between K_Q values in self-propulsion case, which occurred despite correct prediction of K_T, is originated in incorrect reproduction of open water characteristics with the use of applied mesh.

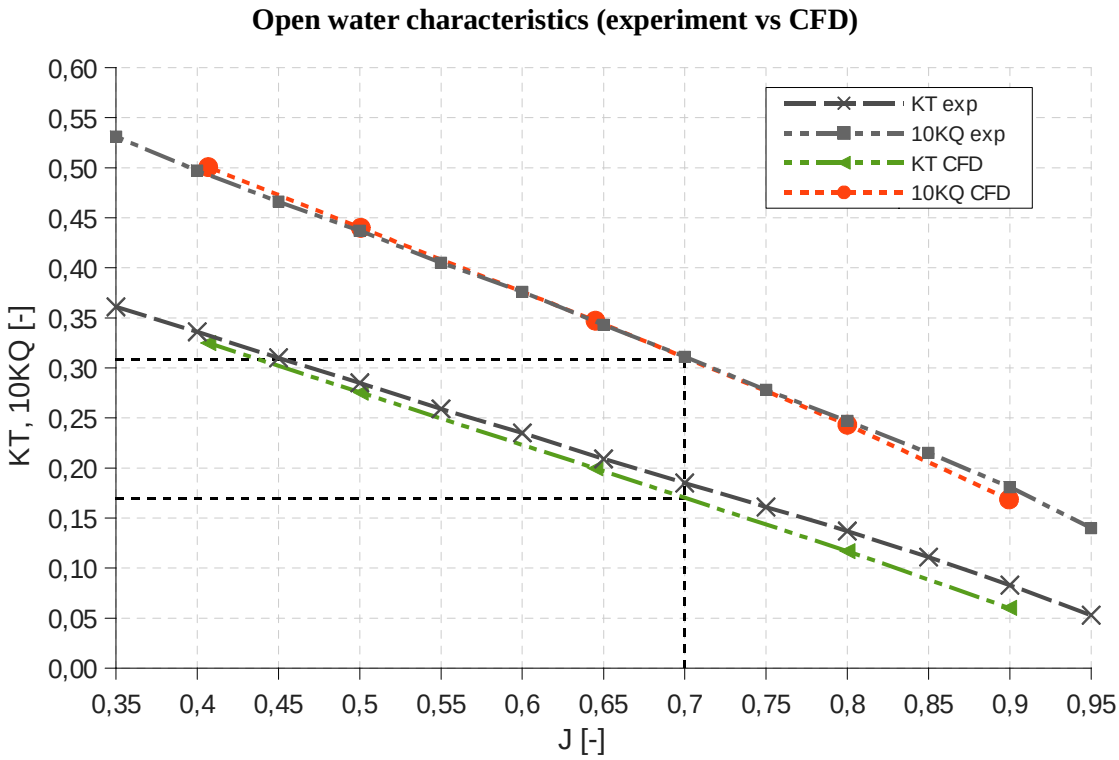

Fig. 5 *Propeller characteristics (experiment and CFD) comparison.*

Conclusions

The project goals were achieved, however computations of flow around the ship hull with rotating propeller simulating propulsion tests have an unsteady character and therefore need more time to obtain convergent result.

For the method to be practically useful, the accuracy of the calculated thrust coefficient should be close to accuracy of the resistance determination. At the present stage of development the method is sufficiently accurate in prediction of the ship hull resistance and of the propeller open water characteristics. However, the interaction phenomena are not predicted accurately enough.

Further development work is planned in this area, especially refining the propeller subdomain. The computations of open water propeller will be repeated until making sure that the mesh is sufficient for correct evaluation of open water propeller characteristics.

Acknowledgements

The research presented in this paper was created as a part of statutory work inside CTO S.A.

References

1. Bugalski, T. (1988). Computer Simulation of Self-Propulsion Test of Axisymmetric Body. Ship Propeller Department, Institute of Fluid-Flow Machinery, Polish Academy of Sciences, Gdansk, Poland. Marine and Offshore Computer Applications, 91.
2. Bugalski, T., Koronowicz, T., Szantyr, J., & Waberska, G. (1994). Computer System for Calculation of Flow, Resistance and Propulsion of Ship at the Design Stage. In CADMO'94 Southampton.
3. Bugalski, T., & Hoffmann, P. (2010). Numerical simulation of the interaction between ship hull and rotating propeller. In Proceedings of Workshop on Numerical Ship Hydrodynamics Gothenburg
   (Vol. 2).
4. Bugalski, T., & Hoffmann, P. (2011). Numerical simulation of the self-propulsion model tests. In Second International Symposium on Marine Propulsors, SMP (Vol. 11).
5. Carrica, P. M., Fu, H., & Stern, F. (2011). Computations of self-propulsion free to sink and trim and of motions in head waves of the KRISO Container Ship (KCS) model. Applied Ocean Research, 33(4), 309-320.
6. Hino, T. (ed.) (2005). Proceedings of CFD Workshop Tokyo 2005. NMRI Report 2005, Tokyo, Japan.
7. Kim, W. J., Van, D. H., Kim, D. H. (2001). ‘Measurement of flows around modern commercial ship models’. Exp. In Fluids, 31, pp. 567-578.
8. Larsson, L., & Zou, L. (2014). Evaluation of resistance, sinkage and trim, self propulsion and wave pattern predictions. In Numerical Ship Hydrodynamics (pp. 17-64). Springer Netherlands.
9. Lin, T. Y., & Kouh, J. S. (2014). On the scale effect of thrust deduction in a judicious self-propulsion procedure for a moderate-speed containership. Journal of Marine Science and Technology, 1-19.
10. Simonsen, C., Otzen, J., and Stern, F. (2008). 'EFD and CFD for KCS heaving and pitching in regular head waves'. Proceedings of 27th Symposium. Naval Hydrodynamics, Seoul, Korea.
11. STAR-CCM+ User Guide (version 9.0).
12. Stern, F., Yang, J., Wang, Z., Sadat-Hosseini, H., Mousaviraad, M., Bhushan, S., & Xing, T. (2013). Computational ship hydrodynamics: nowadays and way forward. International Shipbuilding Progress, 60(1-4).
13. Van, S. H., Kim, W. J., Yim, G. T., Kim, D. H., Lee, C. J. (1998). ‘Experimental Investigation of the Flow Characteristics Around Practical Hull Forms’. Proceedings 3rd Osaka Colloquium on Advanced CFD Applications to Ship Flow and Hull Form Design, Osaka, Japan.

Lily Pad: Towards Real-time Interactive Computational Fluid Dynamics

Gabriel D. Weymouth, University of Southampton, UK
G.D.Weymouth@soton.ac.uk

1 Introduction

Amazing advances have been made in both computing resources and computational methodologies in the last 15 years - enabling first-principle predictions of ship science flows which are fast enough to be useful in engineering. In addition, open source projects such as OpenFOAM [9] provide a free and adaptable alternative to standard engineering software. However, despite the fact that computational fluid dynamics (CFD) software is now (relatively) fast and freely available, it is still amazingly difficult to use. CFD software is complex, fussy, opaque, and poorly designed [14], even compared to other scientific software such as the free and open source R-project for statistical analysis [13].[1] Inaccessible software imposes a significant entry barrier on students and junior engineers, and even senior researchers spend less time developing insights and more time on software issues [5].

Lily Pad [1] was developed as an initial attempt to address some of these problems. The goal of Lily Pad is to lower the barrier to CFD by adopting simple high-speed methods, utilizing modern programming features and environments, and giving immediate visual feed-back to the user. The resulting software focuses on the fluid dynamics instead of the computation, making it useful for both education and research.

It would be impossible to genuinely achieve this goal unless Lily Pad was genuine CFD solver. Therefore the full two-dimensional Navier-Stokes equations are solved and the exact body boundary conditions are applied. However, most of the complications plaguing CFD are avoided by using the Boundary Data Immersion Method (BDIM [17, 7]) to immerse solid bodies into the fluid domain. Despite this simplicity (or perhaps because of it), BDIM is very accurate, it has some nice analytic properties, and has been extensively validated.

Lily Pad is written in Processing [12], a programming language initially based on Java which promotes "software literacy within the visual arts and visual literacy within technology". Lily Pad utilizes the Processing Development Environment, which integrates the writing, testing, and usage modes into a single platform. Specifically, a short script is written on the *front-page* (Fig 1a), the code is executed by pressing a button, and the flow is simultaneously simulated and visualized in a pop-up window (Fig 1b). Fig 1 is a complete working example, the default simulation of the flow around a circular cylinder. And it is interactive - the circle can be dragged around the window and the flow is updated in real-time.

While the default flow in Fig 1 is at low resolution and features fairly simple physics, the method is completely extendable, and Lily Pad simulations have already been published in the Journal of Fluid Mechanics [15, 11] and have been used to initiate and test many additional research projects, as summarized in the examples section. First, the numerical method and implementation in Lily Pad is summarized in more detail.

2 Flow Solver Methodology

Solving the incompressible Navier-Stokes equation numerically presents a few irreducible difficulties, namely time integration of the finite-scale nonlinear momentum equations and inversion of a Poisson equation for the pressure. However, the majority of the complexity in CFD software comes not from the fluid equations, but from coupling those equations to the irregular data at domain boundaries. The adoption of boundary-fitted meshes to achieve this coupling increases the memory requirements, computational effort and algorithmic complexity of the numerical method, as well as presenting conceptual and modeling difficulties to the user.

[1] To say nothing of software that people actually *enjoy* using.

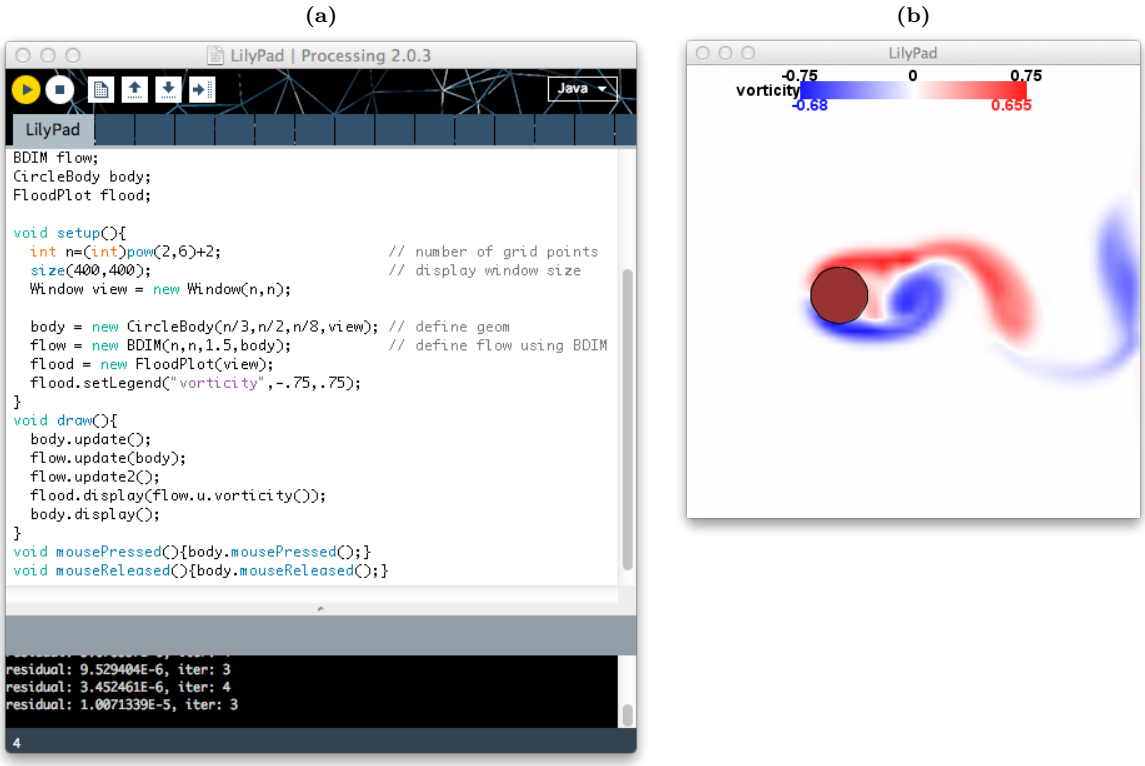

Figure 1: Lily Pad example in the Processing Development Environment: (a) complete example script, and (b) real-time interactive visualization.

Lily Pad utilizes fast and robust methods for dealing with all of these issues, starting with the adoption of the Boundary Data Immersion Method for coupling the fluid and solid equations. The basic idea of BDIM (and all Immersed Boundary methods since [10]) is to adjust the equations of motion to account for the interaction of the fluid and solid and solve those equations on a simple numerical grid. In Lily Pad this is a uniform Cartesian grid. This avoids adopting questionable physical simplifications (such as treating fluids as particles, with issues documented in [6]) or hiding the numerical complexity in a black box (such as automatic mesh refinement). Instead, the analytic governing equations themselves are adjusted, allowing the numerical method to remain as simple and efficient as possible.

The full details are in [7], but briefly, the analytic BDIM equations are obtained by the convolution of two governing equations, each valid over their own region of the total domain. In Lily Pad this is a body with prescribed velocity immersed in a 2D viscous fluid. Using a symmetric kernel with width ϵ for the convolution and keeping up to second order terms gives

$$\vec{u}_\epsilon = \mu_0 \vec{f} + (1-\mu_0)\vec{b} + \mu_1 \frac{\partial}{\partial n}\left(\vec{f}-\vec{b}\right) \quad (1)$$

$$\vec{\nabla}\cdot\vec{u}_\epsilon = (1-\mu_0)\vec{\nabla}\cdot\vec{b} - \mu_1 \frac{\partial}{\partial n}\left(\vec{\nabla}\cdot\vec{b}\right) \quad (2)$$

where $\vec{f}$ and $\vec{b}$ are the update equations for the velocity in the fluid and body domains, and where μ_0 and μ_1 are the zeroth and first moments of the kernel function with respect to the fluid domain. The convoluted velocity $\vec{u}_\epsilon$ update equation (1), takes the form of a mixing equation, with the fluid equation used in the fluid domain (where $\mu_0 = 1,\ \mu_1 = 0$) the body equation used in the body domain (where $\mu_0 = \mu_1 = 0$) and a combination of the two within ϵ of the boundary. The velocity divergence equation (2) is used to solve for the pressure required to satisfy the divergence condition in both domains, which enables volume-changing bodies found in biological flow problems to be modeled. Three important points: (a) the normal derivative term in the velocity equation (active in the boundary region) enables accurate boundary layer simulation including separation prediction [7]; (b) the presence of the kernel moments results in a variable coefficient Poisson equation for the pressure which implicitly enforces the correct

pressure boundary conditions and significantly improves force prediction [17]; and (c) the body velocity equation $\vec{b}$ can be easily coupled to the state of the fluid, enabling prescribed or predicted fluid-structure interaction simulations [15]. BDIM is therefore capable of fluid-structure interaction predictions using a uniform Cartesian grid, and this is leveraged in Lily Pad to greatly simplify the software.

Lily Pad uses implicit Large Eddy Simulation (ILES, [8]) to model the scales below the finite grid spacing in order to avoid the standard turbulence model selection and parameterization issues. Depsite its simplicity (or, again, perhaps because of it) ILES has been shown to have greater effective subgrid resolution than explicit LES models [2], but like all LES models it requires explicit time-stepping and is difficult to scale to high Reynolds number flows. Either a flux-limited QUICK or a Semi-Lagrangian convection scheme can be used. The Semi-Lagrangian scheme is universally stable, enabling larger time steps at the cost of reduced the accuracy near the body where the flow gradients are large. Additionally, because Lily Pad is two-dimensional, the results at intermediate Reynolds numbers will tend to have features of two-dimensional turbulence, which can be quite distinct from their three-dimensional counterparts [4]. Within these limitations, the choice of ILES enables a wide variety of interesting flows to be simulated in Lily Pad quickly and easily.

The variable coefficient pressure equation is solved using a Multi-Grid method with Jacobi smoothing. The unit Cartesian grid, sparse symmetric matrix, and relatively small time steps make this extremely efficient; the residual is typically driven below the tolerance level in only a single V-cycle, making determination of the pressure *less expensive* than evaluating the momentum equations.

3 Implementation and Usage

Lily Pad is written in Processing in an object-oriented programming style, using classes of objects to set up and solve the CFD system. The core classes are as follows:

- `Field` contains the data structures and method for handling scalar fields such as pressure. This includes methods for differentiation, interpolation[2] and advection of the field, as well as setting boundary conditions and displaying the scalar values on-screen.
- `VectorField` contains the methods for vector fields such as the fluid velocity, made up of two `Field` components. A projection operator (using Multi-Grid) is defined here in addition to vector differentiation and the convection/diffusion operators.
- `Body` is the parent class of all the solid geometries which are used in Lily Pad. Methods to transform (translate, rotate), query (force?, moment?, distance?) and display the body are defined.
- `BDIM` is the high-level class used on the *front-page* to set-up and solve the general solid-fluid interaction problem described by equations 1 and 2.

The default script in Fig 1 shows how these classes and methods are used in Lily Pad. The Processing front-page is broken into four parts: variable declaration, the `setup` method, the `draw` method, and additional problem specific methods. In the default script three objects are declared:

```
BDIM flow;
CircleBody body;
FloodPlot flood;
```

where `CircleBody` extends the parent `Body`; defining the geometry to be a circle and supplying some simplified methods such as the distance function. `FloodPlot` is a visualization class which makes nice flood plots to extend `Field.display`. Within `setup` we have:

```
int n = (int)pow(2,6);                    // number of grid points
size(400,400);                            // display window size
Window view = new Window(n,n);

body = new CircleBody(n/3,n/2,n/8,view); // define geom
```

[2]The unit background grid makes differentiation and interpolation operations nearly trivial.

```
flow = new BDIM(n,n,1.5,body);           // define flow using BDIM
flood = new FloodPlot(view);
flood.setLegend("vorticity",-.75,.75);
```

The first line sets the number of points in the domain. This needs to be a large power of two (Java uses the `pow` function for exponents) to allow sub-division in the multi-grid solver.[3] Next the size of the pop-up display is defined in number of pixels. The third defines a `Window` object to map the numerical grid to a portion of the display. Any number of windows may be defined and used to plot different 'views' of the simulation.

In the next block, the body is constructed. The arguments define the size of the circle, and its location in the simulation. This process is indefinitely extendable - any number of additional bodies of any size or shape can be defined to form a composite `Body` object. Note that the arguments are all given in terms of the number of grid cells, ie the diameter is $n/8 = 8$ meaning the circle is 8 grid cells wide. In Lily Pad all distances are given in terms of the unit grid spacing since it is the only predetermined length scale. This has the pedagogical value of making all dimensions into statements of "resolution". Since D is only 8, we can safely assume this simulation is under-resolved. If we increase the number of points, this will increase the resolution by the same factor, etc.

Next, the flow is constructed using the number of points, time step, and body object as arguments. The default `BDIM` object uses a unit background flow $\vec{U} = (1, 0)$, but any velocity field can be defined and used as an initial condition. Since the distance scale is the grid spacing, the time step Δt is equal to the CFL number. If Δt is set to zero, adaptive time stepping is used with $\Delta t = (\max_{\vec{x}} |u| + 3\nu)^{-1}$ to ensure explicit stability of the convective and diffusive terms. The kinematic viscosity ν is an optional argument to the `BDIM` constructor and its value needs to be set using the grid length scale. For example to match $Re_D = UD/\nu = 1000$ the grid-based Reynolds number is $Re_g = U/\nu = Re_D/D = 125$ and $\nu = 0.008$. Again, there is pedagogical value in this approach - ν is so small that the physical viscosity is likely to be drowned out by the ILES subgrid damping. Finally, the `FloodPlot` object is constructed by passing it a view, and then setting the color legend text and limits.

It is worth emphasizing that the flow solver has been set-up *in four lines of code.* In standard CFD software, setting-up the fluid domain requires tremendous time and effort and entails the explicit or implicit specification of thousands of numerical parameters (the grid!). In Lily Pad, the fluid domain set-up is a non-issue and the only effective free numerical parameter is the 'resolution'. [4]

The Processing `draw` method is looped indefinitely and is used to iterate the update and display calls:

```
body.update();
flow.update(body); flow.update2();
flood.display(flow.u.vorticity());
body.display();
```

In this code, the body is updated, taking into account any changes input by the user. Alternatively, the body can be updated using prescribed motion or fluid-structure interaction equations. The updated body is used to update the conditions for the flow, and the flow is integrated in separate predictor and corrector steps. Next the flood plot is used to display the vorticity of the flow velocity[5] and the body is displayed on top. The display commands have been optimized for speed, and the educational value of watching the flow develop in real-time can hardly be overstated.

4 Advanced Examples and Next Steps

This default example gives a basic introduction to the grammar used in a Lily Pad script, but one of the software's strengths is how easily the methods are extended to different flow types. The most basic extension is to change the body's shape and dynamics, such as in [15, 11] or a flapping foil energy extractor (Fig 2a). Increasing the number of bodies is also very simple, such as an array of 20 offshore risers (Fig 2b). Combining multiple bodies with independent dynamics extends the potential application: from blind fish swimming past obstacles (Fig 2c) and drag reducing spinning cylinders (Fig 2e) to tandem

[3] Multi-grid methods are especially well suited to object oriented programming, enabling a complete implementation in less than 90 lines of code.

[4] The kernel width ϵ is not a free parameter. Previous studies have shown that $\epsilon = 2$ is optimal.

[5] Simple chaining of commands is another advantage of the object oriented coding style.

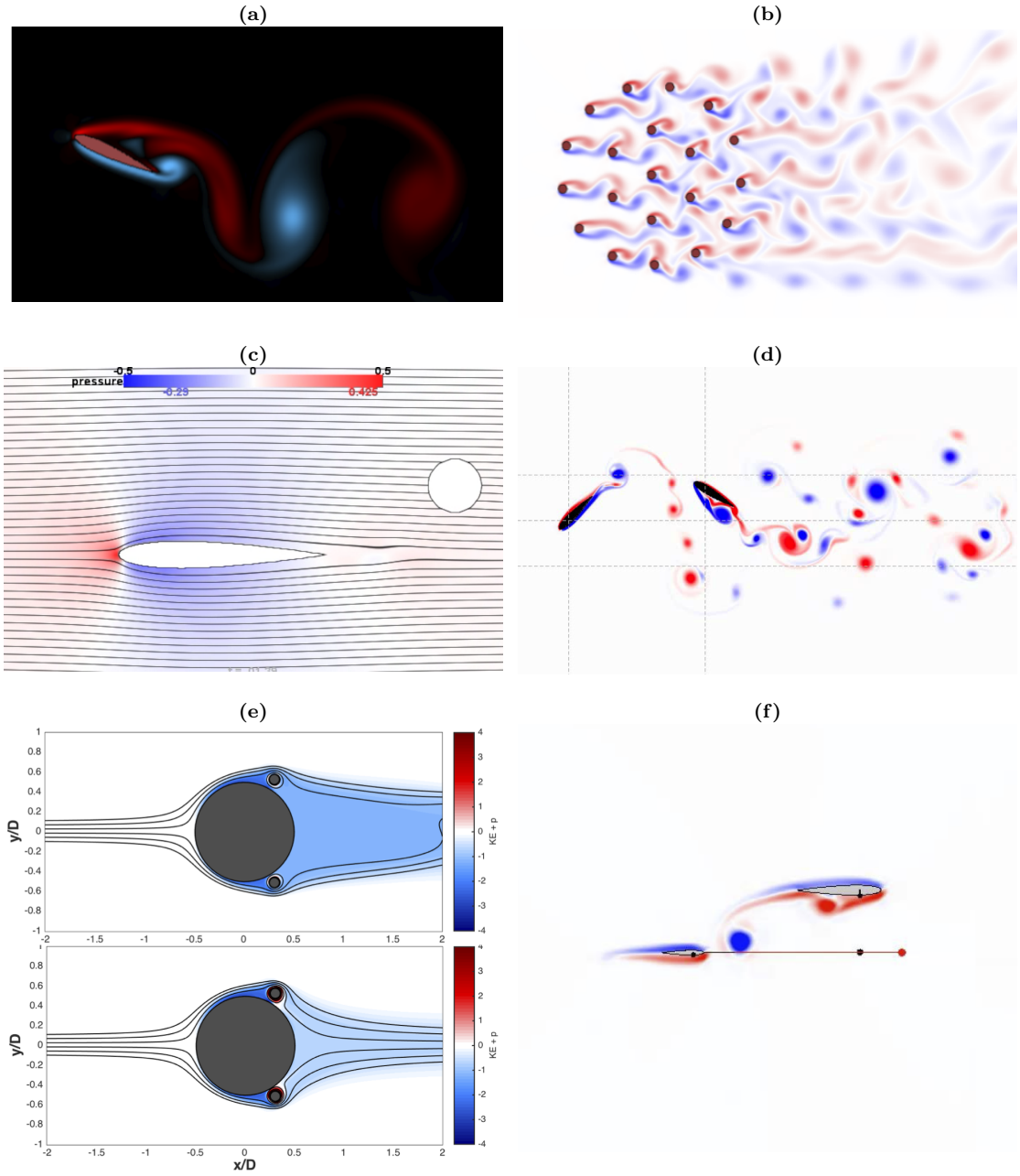

Figure 2: Lily Pad example applications courtesy of (a) Amanda Persichetti, (b) Chen Yongxin, (c) Audrey Maertens, (d) Luke Muscutt, (e) James Schulmeister, and (f) Jacob Izraelevitz.

swimming flippers of a turtle (Fig 2f) or even a Plesiosaur (Fig 2d). Extensions can also be made to the visualization and user interface, as seen on the Lily Pad website [1].

However, there are still limitations in this approach. The fundamental drawback is being restricted to two-dimensional flow. A three-dimensional version, called Lotus, is in development but 3D simulations increase the computational cost by many orders of magnitude. Lotus attempts to compensate for this by implementing multiprocessor versions (MPI and CUDA) and fast programming and visualization languages (Fortran/Paraview) but is still much slower than real-time. Advances in 2D/3D models may help bridge the gap, at least in the initial design and simulation set-up stages. High Reynolds number simulations will also require modeling advances, particularly in the development of near-wall models appropriate for Immersed Boundary methods.

Nevertheless, two-dimensional and moderate Reynolds number simulations still have great value,

especially in education. All the results in Fig 2 are student projects, and most were developed by students without formal training in CFD. Lily Pad's ability to quickly and easily go from concept to simulation has helped all of these students add depth to their studies. In addition, Lily Pad has been used to develop stand-alone demo applications which are excellent for education and outreach [3, 16]. As such, Lily Pad has at least partially achieved its goal of lowering the barrier to CFD, and is a first step towards more general real-time interactive solvers.

References

[1] Lily pad: Real-time two-dimensional fluid dynamics simulations in processing. `http://github.com/weymouth/lily-pad`. Accessed: 2015-09-29.

[2] Stuart Dalziel Andrew Aspden, Nikos Nikiforakis and John B. Bell. Analysis of implicit les methods. *Communications in Applied Mathematics and Computational Science*, 3(1):103–126, 2008.

[3] CNN MainSail. How has foiling made boats much faster? `http://edition.cnn.com/videos/tv/2015/03/11/spc-mainsail-design-special-b.cnn/video/playlists/intl-mainsail`. Accessed: 2015-09-29.

[4] Y Couder and C Basdevant. Experimental and numerical study of vortex couples in two-dimensional flows. *Journal of Fluid Mechanics*, 173:225–251, 1986.

[5] Derek Groen, Xiaohu Guo, James A Grogan, Ulf D Schiller, and James M Osborne. Software development practices in academia: a case study comparison. *arXiv preprint arXiv:1506.05272*, 2015.

[6] Areti Kiara, Kelli Hendrickson, and Dick KP Yue. Sph for incompressible free-surface flows. part i: Error analysis of the basic assumptions. *Computers & Fluids*, 86:611–624, 2013.

[7] Audrey P Maertens and Gabriel D Weymouth. Accurate cartesian-grid simulations of near-body flows at intermediate reynolds numbers. *Computer Methods in Applied Mechanics and Engineering*, 283:106–129, 2015.

[8] LG Margolin. Finite scale theory: The role of the observer in classical fluid flow. *Mechanics Research Communications*, 2013.

[9] OpenFOAM Foundation. Openfoam. `http://www.openfoam.org`. Accessed: 2015-09-29.

[10] Charles S. Peskin. Flow patterns around heart valves: A numerical method. *Journal of Computational Physics*, 10(2):252 – 271, 1972.

[11] Delyle T. Polet, David E. Rival, and Gabriel D. Weymouth. Unteady dynamics of rapid perching manoeuvres. *Journal of Fluid Mechanics*, 767(323–341), 2015.

[12] Processing Foundation. Processing. `http://www.processing.org`. Accessed: 2015-09-29.

[13] R Core Team. R: A language and environment for statistical computing. `http://www.R-project.org`. Accessed: 2015-09-29.

[14] Damian Rouson, Jim Xia, and Xiaofeng Xu. *Scientific software design: the object-oriented way*. Cambridge University Press, 2011.

[15] G. D. Weymouth. Chaotic rotation of a towed elliptical cylinder. *Journal of Fluid Mechanics*, 743:385–398, 3 2014.

[16] Gabriel D Weymouth. Interactive research examples. `http://web.mit.edu/weymouth/www`. Accessed: 2015-09-29.

[17] Gabriel D. Weymouth and Dick K.-P. Yue. Boundary data immersion method for cartesian-grid simulations of fluid-body interaction problems. *Journal of Computational Physics*, 230(16):6233–6247, July 2011.

RANS Hydrodynamic Characterization of a USV SWATH Configuration Including Design Optimization

Stefano Zaghi, Cecilia Leotardi, Roberto Muscari, Giulio Dubbioso,
Matteo Diez, Riccardo Broglia

CNR-INSEAN, Natl. Research Council-Marine Technology Research Inst., Rome, Italy
(stefano.zaghi@cnr.it; c.leotardi@insean.it; roberto.muscari@cnr.it; giulioantonino.dubbioso@cnr.it;
riccardo.broglia@cnr.it; matteo.diez@cnr.it)

1 Introduction

Unmanned Surface Vehicles (USVs) are widely employed for both military and civil applications (*e.g.* costal raids, mine search and rescue, research activities related to sea and littoral investigations, etc.). A number of prototypes and actual operating USV designs has been developed in the last decades, providing increasing energy and stability performances. Effectiveness and efficiency (*e.g.* environmentally-friendly performances, maximum operative range and endurance as well as detection performances) of such vehicles have been largely improved by the enhancement, in terms of reliability and compactness, of hybrid and/or fully electric propulsion systems, of real-time and remote accessible on-board monitoring systems and high range/bandwidth transmission data devices.

Within the USV PERMARE research project,[1] CNR-INSEAN is responsible for the development of a USV system able to launch and recover autonomous vehicles of different nature (*e.g.* gliders, autonomous underwater vehicles, motor-gliders, wire-guided remote underwater vehicles) The cutting-edge aspects of the project are the non-conventional hull design and the propulsion system with propellers in mantle. The former consists in a SWATH (Small Waterplane Area Twin Hulls) configuration, optimized to ensure high-level resistance and seakeeping performances (higher autonomy and operation capability). The latter combines propulsive efficiency and low noise (reduced installed power and higher efficiency in measurements). The SWATH is designed as a two torpedoes connected to the upper platform by a couple of struts. Enhanced stability performances are achieved including an active stabilization system, effective at all operational speeds.

The objective of the present work is the hydrodynamic characterization of the baseline design and the subsequent design optimization for the total resistance reduction at the design speed. The hydrodynamic characterization of the baseline SWATH is performed using the in-house RANS solver χnavis [7, 8, 9, 12, 5, 16]) The RANS computations are compared to results evaluated by a steady potential flow solver [1] used in earlier research for deterministic [6] and stochastic [10] optimization applications. A systematic parametric analysis of the total resistance coefficient, varying the main geometric particulars (*i.e.* struts clearance and interaxis distance) is presented, as well as a preliminary design optimization.

2 SWATH design

The USV PERMARE SWATH is designed as a two torpedoes connected to the upper platform by a couple of NACA 0012 profiled twin narrow struts for each hull (for a total of four struts). The SWATH configuration has been chosen in fulfilment of the USV PERMARE design specifications: reduced resistance and increased sea keeping performances. Figure 1 shows an overview of the baseline design, whereas Tab. 1 summarizes the SWATH main particulars.

Table 1: Main geometric particulars

REFERENCE LENGTH	L_{REF}	$5.000\,[m]$
TORPEDOES DIAMETER	D	$0.450\,[m]$
INTERAXIS DISTANCE	I_0	$2.500\,[m]$
STRUTS CLEARANCE	C_0	$0.686\,[m]$

3 RANS hydrodynamic characterization

3.1 Mathematical and Numerical Models

Within the assumption of an incompressible fluid, the set of equations in non-dimensional integral form with respect to a moving control volume $\mathscr{V}$ read as

$$\oint_{S(\mathscr{V})} U\cdot\nu\,\mathrm{d}S = 0 \quad \text{and} \quad \rho\,\frac{\partial}{\partial t}\int_{\mathscr{V}} U\,\mathrm{d}V + \oint_{S(\mathscr{V})}(\mathscr{F}_c-\mathscr{F}_d)\cdot\nu\,\mathrm{d}S = 0 \tag{1}$$

[1] USV PERMARE research project is funded by Ministry of Education and Research (MIUR, grant DM62573).

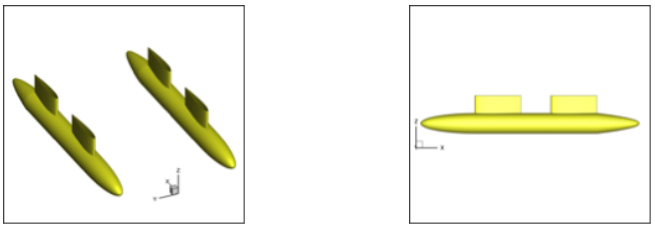

Figure 1: SWATH prospective and lateral orthographic views

where $S(\mathscr{V})$ is the control volume boundary, ν the outward unit normal, $U=(u_1,u_2,u_3)$ is the fluid velocity and $\mathscr{F}_c$ and $\mathscr{F}_d$ represent Eulerian (advection and pressure) and diffusive fluxes, respectively defined as

$$\mathscr{F}_c = p\mathbf{I} + \rho\,(U-V)\,U \quad \text{and} \quad \mathscr{F}_d = \frac{\rho}{Re}\left[\text{grad}U + (\text{grad}U)^{\text{T}}\right] \tag{2}$$

where V is the local velocity of the boundary of the control volume, ρ is the fluid density, $p = P + \rho z/Fr^2$ is the hydrodynamic pressure (*i.e.* the difference between the total pressure P and the hydrostatic pressure $-z/Fr^2$), g is the acceleration of gravity, parallel to the vertical axis z (positive upward), Fr is the Froude number and Re the Reynolds number.

The numerical solution of the governing equations 1 is computed by means of a simulation code χnavis; the code yields the numerical solution of the Unsteady Reynolds averaged Navier Stokes equations with proper boundary and initial conditions. The algorithm is formulated as a finite volume scheme, with variable co-located at cell centers. Turbulent stresses are taken into account by the Boussinesq hypothesis, with several turbulence models (both algebraic and differential) implemented. Free surface effects are taken into account by a single phase level-set algorithm. Complex geometries and multiple bodies in relative motion are handled by a dynamical overlapping grid approach. High performance computing is achieved by an efficient shared and distributed memory parallelization ([2] and [5]). For more details on the numerical code used the interested reader is referred to [7, 8, 9, 12] and [16]

3.2 Numerical Setup

The SWATH is fixed at even keel conditions, the sinkage is $0.425m$. Uniform inflow conditions have been considered, with free stream velocity $1kn \leq U \leq 6kn$. The reference length is the length of the vehicle ($L_{REF} = 5m$). The corresponding Reynolds, Froude and Weber numbers for the selected operative conditions are summarized in Tab. 2. Simulations have been performed at model scale, assuming fresh water conditions[2]: 1) $\rho[kg/m^3] = 999.103$; 2) $g[m/s^2] = 9.80665$; 3) $\nu[m^2/s] = 1.139\cdot 10^{-6}$; 4) $\sigma[N/m] = 7.280\cdot 10^{-2}$.

Table 2: Operative conditions

Inflow velocity $U[knot]$	Inflow velocity $U[m/s]$	Froude Number Fr	Reynolds Number Re	Weber Number We
1.0	0.514	0.073	$2.259\cdot 10^6$	$1.347\cdot 10^2$
2.0	1.029	0.147	$4.518\cdot 10^6$	$2.695\cdot 10^2$
3.0	1.543	0.220	$6.777\cdot 10^6$	$4.042\cdot 10^2$
4.0	2.058	0.294	$9.036\cdot 10^6$	$5.390\cdot 10^2$
4.5	2.315	0.331	$1.016\cdot 10^7$	$6.064\cdot 10^2$
5.0	2.572	0.367	$1.129\cdot 10^7$	$6.738\cdot 10^2$
5.5	2.829	0.404	$1.242\cdot 10^7$	$7.411\cdot 10^2$
6.0	3.087	0.441	$1.355\cdot 10^7$	$8.085\cdot 10^2$

Exploiting the flexibility of the chimera overlapping grids a high-quality body-fitted mesh has been realized. Figure 2 shows an overview of the main topologies realized. The grids is composed by 92 partially overlapping blocks, for a total of about 5.6 millions volumes. Grid resolution is clustered to the wall with normal spacing ensuring $y^+ \leq 1$ for the Reynolds numbers considered. The boundary conditions are set considering the symmetry on the $y = 2.5m$ plane (this allows to simulate the presence of the twin hull), the uniform inflow condition on the $x = 0$ plane and the outflow (non reflecting) boundary condition for the other boundaries.

3.3 RANS results

The estimation of the resistance for the speed range considered is summarized in Tab. 3. In the table, verification assessment for the total resistance is also repoted; uncertainty has been estimated following the Roache's method (*i.e.* $Uncertainty = \left|\frac{R_{fine}-R_{coarse}}{4R_{fine}-R_{coarse}}\right|$).

[2]It has been considered water at 15 degrees accordingly to ITTC recommendations.

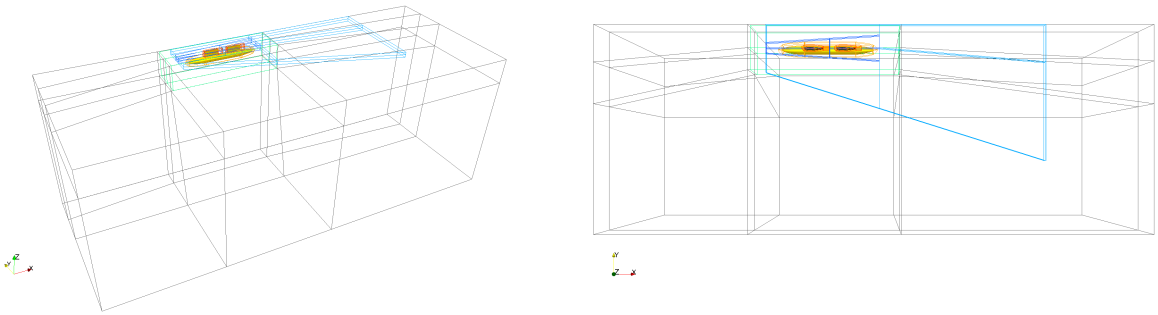

Figure 2: Topology overview: black far background, light green near background, light blue free surface, blue near free surface, orange hull, red struts

Table 3: Non-dimensional resistance results and verification analysis

INFLOW VELOCITY $U[knot]$	FROUDE NUMBER Fr	COARSE GRID	MEDIUM GRID	FINE GRID	Grid uncertainty [%]
1.0	0.073	$4.583 \cdot 10^{-4}$	$5.869 \cdot 10^{-4}$	$4.869 \cdot 10^{-4}$	7.35
2.0	0.147	$1.124 \cdot 10^{-3}$	$7.848 \cdot 10^{-4}$	$6.767 \cdot 10^{-4}$	5.62
3.0	0.220	$1.291 \cdot 10^{-3}$	$9.273 \cdot 10^{-4}$	$8.188 \cdot 10^{-4}$	4.62
4.0	0.294	$1.505 \cdot 10^{-3}$	$1.324 \cdot 10^{-3}$	$1.298 \cdot 10^{-3}$	0.65
4.5	0.331	$1.359 \cdot 10^{-3}$	$1.024 \cdot 10^{-3}$	$9.095 \cdot 10^{-4}$	4.40
5.0	0.367	$1.347 \cdot 10^{-3}$	$9.705 \cdot 10^{-4}$	$8.480 \cdot 10^{-4}$	5.06
5.5	0.404	$1.523 \cdot 10^{-3}$	$1.145 \cdot 10^{-3}$	$1.027 \cdot 10^{-3}$	3.97
6.0	0.441	$1.687 \cdot 10^{-3}$	$1.303 \cdot 10^{-3}$	$1.210 \cdot 10^{-3}$	2.65

Grid convergence results are rather satisfactory in the whole speed range, though a high uncertainty value (*i.e.* 7.35%) is observed at low Froude numbers. This is due to lack in the grid resolution around the free surface, yelding to inaccuracies in the computation of the short and small waves at the lower Froude numbers.

In order to evaluate the interaction effects of the twin hulls, the pressure, the viscous and the total resistance are evaluated for both the complete and the demi SWATH. Figure 3 shows the resistance trends for both configurations. The total resistance curves show the presence of two humps, which are typical of multihull vessels as it has been already shown in previous studies (*e.g.* [15, 3]). The local maximum and minimum are related to the position of the wave trough. Both complete and demi SWATH configurations show the local minimum close to $U = 4.5kn$, $Fr = 0.35$.

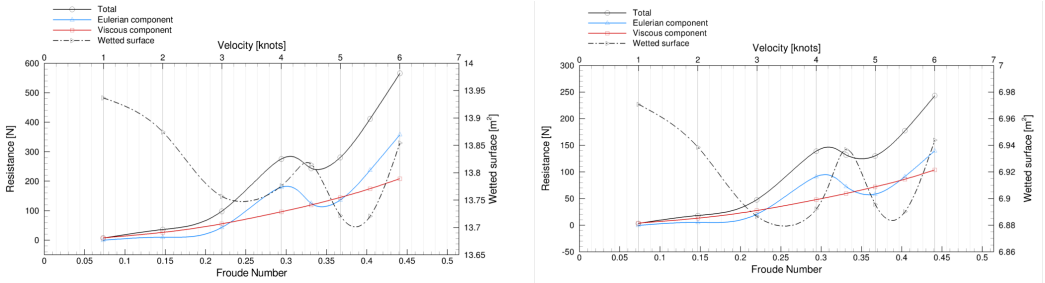

Figure 3: Resistance analysis: complete and demi SWATH

The estimation of the augmented resistance due to the interference between the twin hulls is evaluated using the interference factor, defined as $IF = \frac{R^C - 2R^d}{2R^d}$ (where C and D indicates quantities corresponding to the complete and the demi SWATH, respectively).

Figure 4 shows the interference factor versus the Froude number; where IF is negative there is a *constructive* interference [4, 15]. Both the Eulerian and the viscous contributions to IF are reported. Maximum constructive interference is attained around $U = 4.5kn$.

Figure 5 shows the wave patterns for all the conditions under analysis for the complete SWATH configuration. It is worth noting that for $U = 5kn$ the transversal wave almost vanishes, causing a reduction of the non viscous (mainly the wave) resistance component.

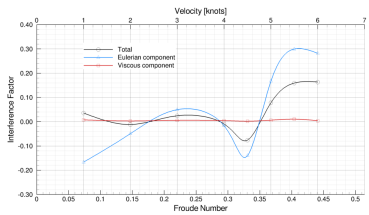

Figure 4: Interference Factor analysis

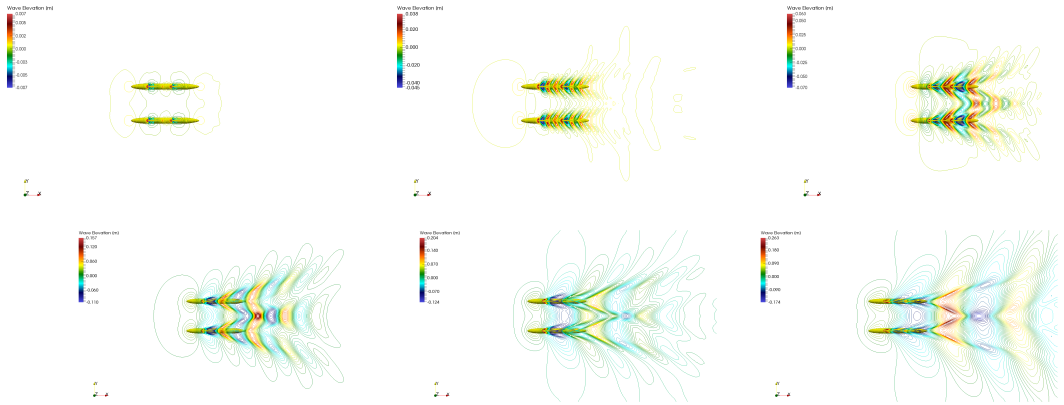

Figure 5: Wave elevation patterns respectively at $U = 1kn$, $U = 2kn$, $U = 3kn$, $U = 4kn$, $U = 5kn$ and $U = 6kn$

4 Preliminary simulation-based design optimization

The objective function is the total resistance (R_T) in calm water at $U = 5kn$ (*i.e.* cruise condition). Design modifications are defined using orthogonal functions, ψ_j ($j = 1,...,N$), defined over surface-body patches as

$$\psi_j(\xi,\eta) := \alpha_j \left\{ \left[1 - \cos\left(\frac{p\pi\xi}{L_\xi} + \phi_p \right) \right] \left[1 - \cos\left(\frac{q\pi\eta}{L_\eta} + \phi_q \right) \right] \right\} \mathbf{e}_{k(j)}; \quad (\xi,\eta) \in [0;L_\xi] \times [0;L_\eta] \tag{3}$$

where the coefficient α_j is the corresponding design variable; p and q define the order of the function in ξ and η direction respectively; ϕ_p and ϕ_q are the corresponding spatial phases; L_ξ and L_η define the patch dimension and $\mathbf{e}_{k(j)}$ is a unit vector. Modifications may be applied in x, y or z direction ($k(j) = 1,2$, or 3 respectively). Herein a two dimensional design space is considered. The corresponding orthogonal patches, used to modify fore (ψ_1) and aft (ψ_2) fairings, are defined using $(p,q)_{1,2} = (2,2)$, $(\phi_p,\phi_q)_{1,2} = (0,0)$, $(\alpha_{min},\alpha_{max})_{1,2} = (-10,10)$, $(x_{min},x_{max})_{1,2} = (-1,1)$ and $k_{1,2} = 2$. Geometric constraints include fixed length and displacement.

Within the optimization task, the resistance is evaluated using the steady potential flow solver (WARP, WAve Resistance Program, [1]). The flow is computed using the Neumann-Kelvin linearization. The frictional resistance is estimated using a flat-plate approximation based on the local Reynolds number [13].

The computational domain for the free surface is defined within 1 hull length upstream, 3 lengths downstream and 1.5 lengths aside. A panel grid with 15k elements is used [11].

Figure 6 shows the comparison between potential flow results and grid convergent RANS solutions. The agreement is reasonable in the whole speed range. Specifically, the wave resistance coefficient trend is well captured, although a difference between the peak values ($Fr = 0.294$, $U = 4kn$) is significant. The friction resistance coefficients evaluated with the two solvers, are considerably close and the total resistance coefficient behaves accordingly. The dimensional total resistance shows a remarkable agreement in the entire speed range, especially for low and high speed values.

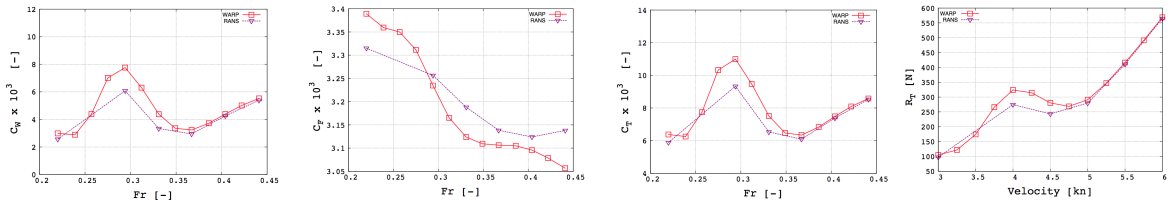

Figure 6: Potential flow *vs* RANS computations (wave, frictional, total resistance coefficient and total resistance)

A preliminary parametric analysis is performed considering a variable struts clearance, namely C (equal to 0.5, 0.75 and 1 the original struts clearance C_0) and a variable interaxis distance (I) between torpedoes (equal to 0.75, 1, 1.5 and 2 the original interaxis distance I_0). This is performed by linear superposition of strut and torpedo effects [11]. Figure 7 shows the contour plots of the total resistance coefficients C_T versus C and I, obtained using a thin plate spline (TPS) interpolation of the simulation results (represented by circles). It may be noted that the struts clearance has significant effects on the resistance at low speeds. Furthermore, an increase of the interaxis distance induces a reduction of the total resistance coefficient.

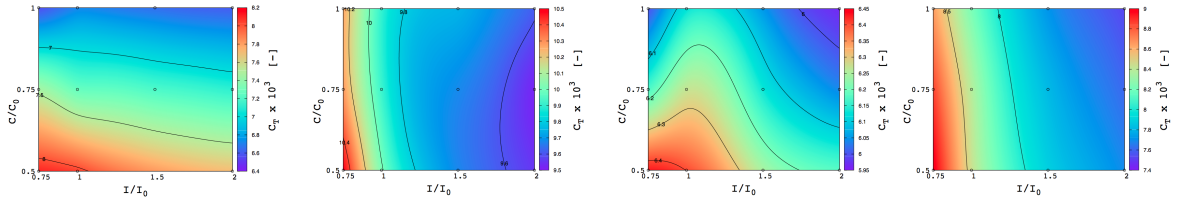

Figure 7: Effects of variable interaxis distance and variable struts clearance on total resistance coefficient ($U = 3,4,5$ and $6kn$) using TPS interpolation

Therefore, the design optimization is performed on a modified SWATH configuration with interaxis distance $I = 1.5I_0$. A deterministic version of the particle swarm optimization algorithm (DPSO) is used for design optimization (see for details [14]), using 128 iterations per design variable. The optimal configuration, corresponding to design variables values x_1=0 and $x_2 = -1$, is presented in Fig. 8. The total resistance reduction obtained for $U = 5kn$ is about 3.5%.

Figure 8 shows a comparison between the optimized and the original total resistance versus the speed. The optimized configuration performs slightly better than the original for $U = 3 \div 4kn$ and for $U = 5 \div 6kn$.

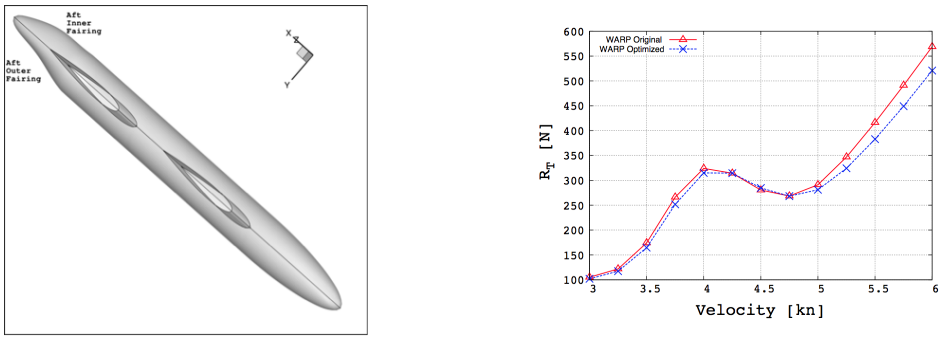

Figure 8: Optimal configuration and resistance parametric analysis

5 Conclusions

The hydrodynamic characterization of the USV PERMARE SWATH has been performed using a RANS-based solver, considering operating speed ranging from 1 to 6 kn (Fr ranges from 0.073 to 0.441). Results show that performances, in terms of resistance, are strongly related to the wave resistance component. The estimation of the twin hull interaction reveals that the maximum constructive interference is achieved for $U = 4.5kn$.

The RANS-based computations have been compared to results computed by a steady potential flow solver. Wave, friction and total resistance coefficients and dimensional total resistance are in reasonable agreement in the whole speed range examined ($3kn \leq U \leq 6kn$). A systematic parametric analysis of the total resistance coefficient, varying the struts clearance and interaxis distance has been performed. For low speeds, the struts clearance shows significant effects on the resistance. Increasing the interaxis distance allows for total resistance reductions in the whole range of speeds. On the basis of these outcomes, the shape design optimization has been performed using a DPSO algorithm, and orthogonal base functions to modify fore and aft fairings. The interaxis distance has been set equal to 1.5 of the original one and fixed reference length and displacement have been considered. The total resistance reduction obtained for $U = 5kn$ is about 3.5%. Also, the optimized configuration presents overall better performances than the original, in the whole speed range. Future work includes a verification of the optimized configuration performances by RANS.

Acknowledgements

This work was supported by Distretto Ligure delle Tecnologie Marine (DTLM) under the research project USV PERMARE, funding of Ministry of Education and Research (MIUR, grant DM62573).

References

[1] P. Bassanini, U. Bulgarelli, E.F. Campana, and F. Lalli. The wave resistance problem in a boundary integral formulation. *Surveys on Mathematics for Industry*, 4:151–194, 1994.

[2] R. Broglia, A. Di Mascio, and G. Amati. A Parallel Unsteady RANS Code for the Numerical Simulations of Free Surface Flows. In 2^{nd} *International Conference on Marine Research and Trasportation, Ischia, Naples, Italy*, June 2007.

[3] R. Broglia, B. Jacob, S. Zaghi, F. Stern, and A. Olivieri. Experimental investigation of interference effects for high-speed catamarans. *Ocean Engineering*, 76(0):75–85, 2014.

[4] R. Broglia, S. Zaghi, and A. Di Mascio. Numerical simulation of interference effects for a high-speed catamaran. *Journal of Marine Science and Technology*, 16:254–269, 2011.

[5] R. Broglia, S. Zaghi, R. Muscari, and F. Salvadore. Enabling hydrodynamics solver for efficient parallel simulations. In *Proceedings International Conference on High Performance Computing & Simulation (HPCS)*, pages 803–810, Bologna, Italy, July 2014.

[6] Emilio F Campana, Daniele Peri, Yusuke Tahara, and Frederick Stern. Shape optimization in ship hydrodynamics using computational fluid dynamics. *Computer methods in applied mechanics and engineering*, 196(1):634–651, 2006.

[7] A. Di Mascio, R. Broglia, and B. Favini. A second order Godunov-type scheme for naval hydrodynamics In *Godunov Methods: Theory and Applications*, volume 26, pages 253–261. Kluwer Academic/Plenum Publishers, 2001.

[8] A. Di Mascio, R. Broglia, and R. Muscari. On the application of the single-phase level set method to naval hydrodynamic flows *Computers & Fluids*, 36(5):868–886, 2007.

[9] A. Di Mascio, R. Broglia, and R. Muscari. Prediction of hydrodynamic coefficients of ship hulls by high-order Godunov-type methods *Journal of Marine Science and Technology*, 14(1):19–29, 2009.

[10] M. Diez, E.F. Campana, and F. Stern. Design-space dimensionality reduction in shape optimization by Karhunen-Loève expansion. *Computer Methods in Applied Mechanics and Engineering*, 283:1525 – 1544, 2015.

[11] C. Leotardi and M. Diez. Design optimization of an Unmanned Surface Vehicle for research activities using potential flow computations. Technical report, CNR-INSEAN, 2015.

[12] R. Muscari, R. Broglia, and A. Di Mascio. An overlapping grids approach for moving bodies problems. In 16^{th} *International Offshore and Offshore and Polar Engineering Conference Proceedings*, pages 243–248, San Francisco, California, USA, May 28-June 2 2006. ISOPE The International Society of Offshore and Polar Engineers, Cupertino, CA, 95015-0189, USA.

[13] H. Schlichting and K. Gersten. *Boundary-Layer Theory*. Springer-Verlag, Berlin, 2000.

[14] A. Serani, M. Diez, C. Leotardi, D. Peri, G. Fasano, U. Iemma, and E.F. Campana. On the use of synchronous and asynchronous single-objective deterministic particle swarm optimization in ship design problems. In *Proceedings of the 1st International Conference in Engeneering and Applied Sciences Optimization*, Kos, Greece, June 4-6, 2014.

[15] S. Zaghi, R. Broglia, and A. Di Mascio. Analysis of the interference effects for high-speed catamarans by model tests and numerical simulations. *Ocean Engineering*, 38(17-18):2110–2122, 2011.

[16] S. Zaghi, A. Di Mascio, R. Broglia, and R. Muscari. Application of dynamic overlapping grids to the simulation of the flow around a fully-appended submarine. *Mathematics and Computers in Simulation*, 116(0):75–88, 2015.

Numerical Study on Air Cavity Flows

Oleksandr Zverkhovskyi * [a,d], Maarten Kerkvliet[b], Arjan Lampe[b], Guilherme Vaz[b] and Tom van Terwisga[b,c]

[a]MARIN Academy, Wageningen, NL ; [b]MARIN, Wageningen, NL ; [c]Delft University of Technology, NL ; [d]DAMEN Shipyards Gorinchem, NL

1 Introduction

One of the most promising viscous drag reduction techniques for ships is so-called air lubrication. Particularly, a stable air layer created on the bottom reduces the wetted area and therefore reduces the resistance of a ship due to the negligibly small viscous drag of air compared to water. The air cavity and air chamber concepts are considered as the most effective and practical ways to form a stable air layer on the bottom capable to reduce the total drag by 10-20% for cargo ships ([1], [2]). These concepts are shown in Figure 1. The air cavity concept is based on injecting air behind a small obstruction that separates the flow which is called a cavitator. The cavitator is extended in the span-wise direction and typically has a rectangular or triangular cross section with a sharp edge. In the developed stage the length of an air cavity is limited to the length of a half the gravity-wave length and it should be restricted by skegs/keels on the sides. The air chamber is created by injecting air into a recess formed in the bottom. Provided the recess has sufficient depth, the free surface is not limited by the wave length and can have a multi-wave profile. The shape of the free-surface at different flow conditions and air injection rates is of interest.

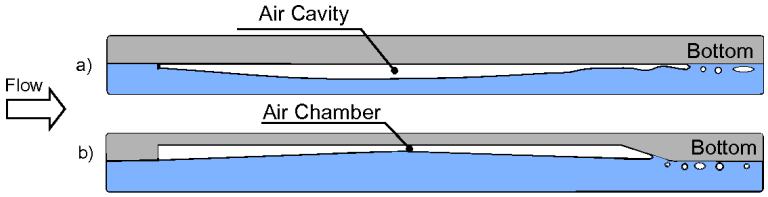

Figure 1: Air cavity and air chamber concepts.

For cargo ships, a series of air chambers or cavities behind each other have to be created on the bottom separated from each other in longitudinal direction. The effectiveness of such a system with periodically changing condition from no-slip (on wetted part) to slip (along the air cavity/chamber) is difficult to be modelled numerically. This work is focused on the numerical study of two problems: the drag reduction prediction by air cavities with known size and the free-surface simulation of air chambers and cavities. All the results presented here are obtained by using ReFRESCO [3]. ReFRESCO is a viscous-flow CFD code that solves multiphase (unsteady) incompressible flows with the RANS equations, complemented with turbulence models, cavitation models and volume-fraction transport equations for different phases. More information about ReFRESCO can be found in [4].

2 Flat plate with a cavity – drag reduction

2.1 Numerical set-up

In this part of the study the following simplifications have been made. The simulations are performed in 2D. For a certain velocity the cavity length and thickness are known (from experiments [2]). The cavity is represented in the computational domain by a half elliptical body that has a fixed geometry. The surface along the cavity has a slip wall boundary condition. In this way the free surface shape does not have to be solved. This simplification allows to perform one-phase flow computation of the flow over a flat plate with a cavity of a certain predefined shape. The outflow of air from the cavity is neglected. An example of the domain for the case of the flat plate with one cavity is shown in Figure 2. The shape of the cavity is symmetrical. It starts with a vertical obstruction, which represents the cavitator, and has a height of 1.5mm. The boundary condition of the cavitator is a no-slip wall. From the top point of the cavitator the surface of the cavity is approximated by a half-ellipse with its middle point at the height of 10mm from the plate level. The surface of the half-ellipse as well as the

*Corresponding author's e-mail: sasha.zverkhovskyi@damen.com

closing surface of the cavity have a slip wall boundary condition. The other boundary conditions are shown in Figure 2.

The $k-\omega$ SST-2003 turbulence model was used for the computations. Since this turbulence model requires small y^+ values [5], grid clustering was applied towards the wall to ensure that $y^+ << 1$. In addition, the clustering was applied on the cavitator and along the cavity surface. However, the size of the first cell on the cavity surface is much larger (by factor of 100) than the one at the wall. Applying a small height of the first cell on a free slip wall results in poor iterative convergence of the solution and appears to be not necessary to resolve the flow features along the cavity surface.

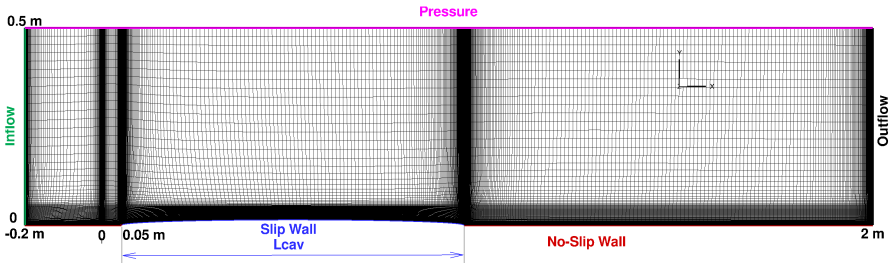

Grid	$cells$	y^+, max	y^+, avg	rel. step
G1	72778	0.023	0.015	1
G2	46200	0.03	0.019	1.26
G3	29440	0.039	0.026	1.57
G4	18509	0.047	0.033	1.98
G5	11924	0.065	0.042	2.47
G7	7236	0.092	0.057	3.17

Figure 2: Schematic overview of geometrical set-up and boundary conditions of the flat plate with a cavity.

2.2 Drag reduction

The drag force on the wall and cavitator was monitored in order to define the total resistance of the flat plate. To ensure a negligible contribution to the numerical error an iterative convergence criterion (L_{inf}) was set, at least, to $1 \cdot 10^{-7}$ for all quantities. The wall shear stress is integrated on the wall from the coordinate X=0 to X=2m. An example of the velocity distribution in the domain normalized by the free stream velocity is shown in Figure 3. The flow is from left to right. For better visualization of the velocity gradient in the boundary layer the plot is stretched in vertical direction by factor of 5. As can be seen from Figure 3(a), there is a deceleration of the flow before the cavity. The boundary layer that is formed at first decays along the cavity surface. After the cavity the formation of a new boundary layer can be observed.

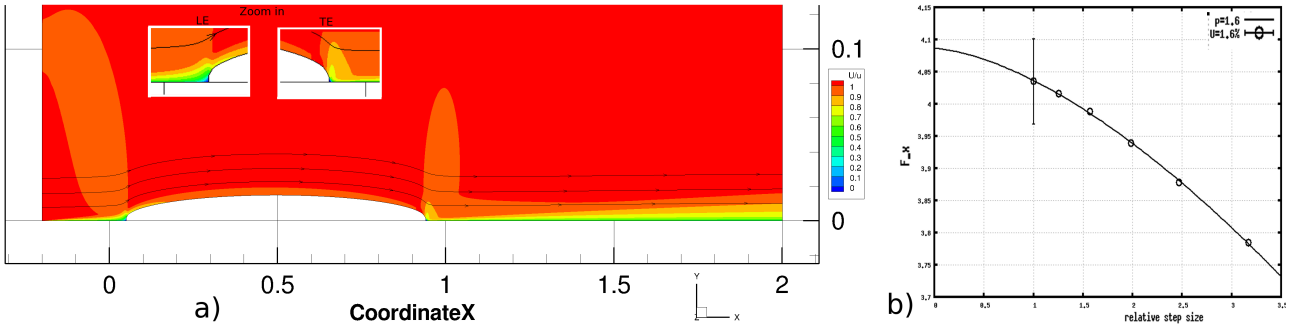

Figure 3: a) - Velocity field (V_x) normalized by the free stream velocity and streamlines along a flat plate with a single cavity of $L = 0.89m$ at $V = 1.41m/s$. The flow is from left to right. The figure is stretched in the vertical direction by a factor 5. b) - numerical uncertainty of the total force on the plate

The local friction coefficient distribution along the plate at V=1.41m/s (Lcav=0.89m), $Re = 3.1 \cdot 10^7$, is shown in Figure 4. Due to the deceleration of the flow before the cavity the local friction coefficient reduces to zero when approaching the cavitator. It is followed by the shear free zone along the cavity surface. A region with a high friction coefficient can be observed directly after the cavity which indicates the formation of a new boundary layer. The local friction coefficient for the case with cavity can be compared with the conventional (numerical) friction line along a flat plate of the same length (including the 0.2m long part at the front which is not shown on the plot). For the given case the wetted area is reduced by 44.5% but the friction drag on the plate is reduced by only 39.4%. If we take into account the drag of the cavitator (pressure drag) the drag reduction on the plate with cavity equals to 31.3% (2D).

The numerical uncertainty of the simulations for the total force was estimated based on the grid density variation by the procedure described in [6] and the results are shown in Figure 3(b). The maximum uncertainty value the total force on the plate with the cavity is 1.6%. For the other test cases the uncertainty was even smaller.

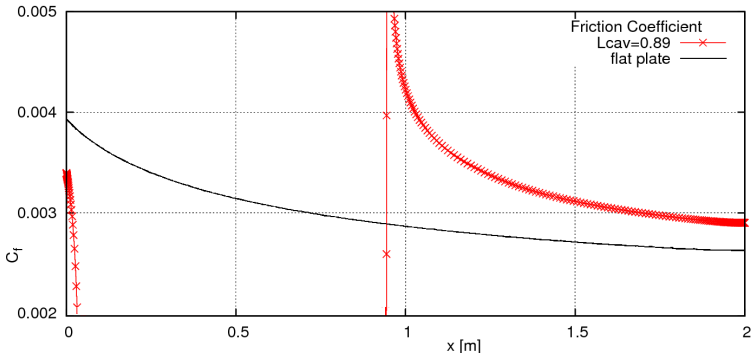

Figure 4: Local friction coefficient distribution on the flat plate with a single cavity. $C_f = 0$ along the cavity surface. The reference flat plate line was computed with the same numerical settings but without the cavity.

2.3 Velocity profile analysis

The next part consists of the comparison of the simulated boundary layer profile at certain locations of a cavity with experiments presented in [2]. In the experiments the velocity profiles were measured by a 2D PIV system before, in the middle, and behind a cavity with the length of 0.5m at V=1.25m/s. The geometry of the cavity, normalized velocity distribution in the computational domain and position of the measurements can be seen in Figure 5.

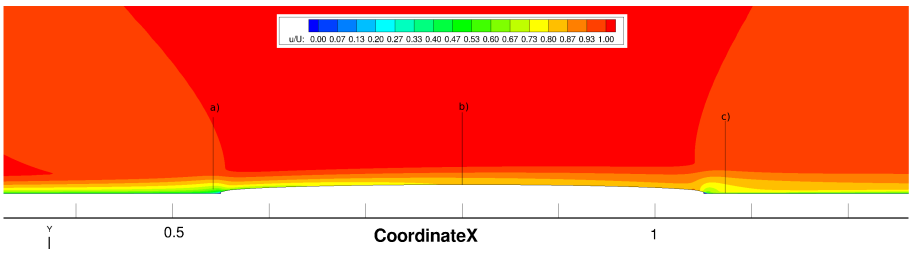

Figure 5: Computed velocity field (normalized with the free-stream velocity) along the flat plate with cavity of $L = 0.5m$ at $V = 1.25m/s$. The flow is from left to right. a), b), and c) are location of measurements.

The length of the flat plate before the cavity was chosen in such a way that the calculated velocity profile before the cavity matches as close as possible the measured one. This is shown in Figure 6(a). The shape of the calculated profile seems more turbulent. The comparison of the calculated and measured velocity profiles in the middle and behind the cavity are shown in Figure 6 ((b) and (c) respectively).

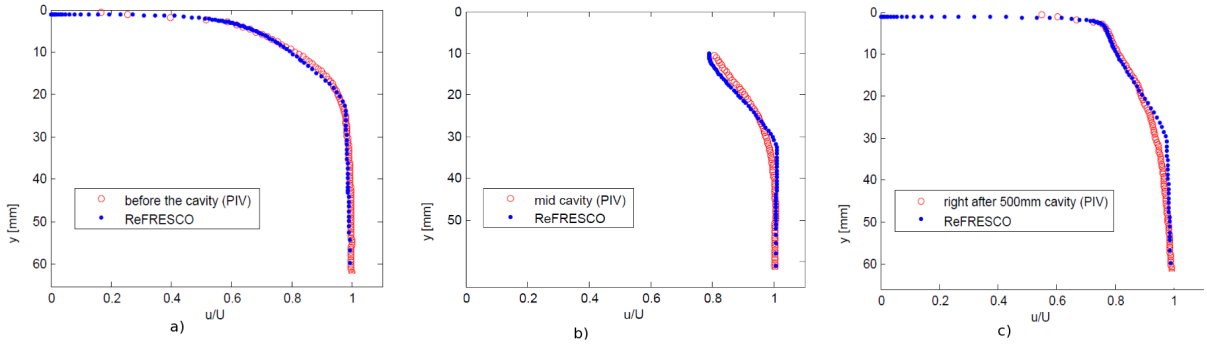

Figure 6: Comparison of the calculated and measured velocity profiles: 30mm before the cavity (a), at the middle (b) and 30mm behind the cavity (c).

From Figure 6(b) we can see that the water flow is displaced by the cavity 10mm away from the wall. Although there is a small differences between the measured and calculated velocity profiles the general trend is similar. The boundary layer is displaced further from the wall and tends to restore to the uniform profile. The difference between the measured and calculated velocity at the cavity surface is about 2%. The results of the calculations for the case behind the cavity are also in a reasonably good agreement with the measurements. Unfortunately, insufficient resolution of the measurements close the wall does not allow to compare the viscous sublayer of the boundary layer which determines the shear stress at the wall.

3 Backward facing step (BFS) and air chamber cases – free-surface flow simulations

A simple 2D case of a free-surface flow behind a backward-facing step is investigated first Figure 7(a). The goals of the test are to find out a satisfying setup for the grid topology and efficient numerical settings for the air chamber and air cavity flows. The flow regime behind a backward-facing step (also know as a transom-stern flow) depends on the transom Froude number $Fn_{tr} = U/\sqrt{gT}$, based on the initial submergence depth of a step T [7]. In this study the attention was given to the dry-transom regime which is representative for the air chambers. For a 2-D inviscid flow this regime occurs at $Fn_{tr} \geq 2.26$ and generates a wave system behind the step [7]. With increasing Froude number the waves become less steep and from $Fn > 3$ the wave length and amplitude match well with the linear theory. From the linear theory it is know that the wave length $\lambda = 2\pi U^2/g$ and the wave amplitude $A = \sqrt{2}T$. After the sensitivity study of the solution for the grid refinement, domains size, time step the results of the simulations were compared with the literature and linear theory. A set of simulations was performed for different Froude numbers by varying the inlet velocity. The relation between the wave steepness ($2A/\lambda$) and the Froude number obtained in this work is in a good agreement with the ones obtained by PARNASSOS and the nonlinear potential solution of Vanden-Broek presented in [7] and for $Fn > 3$ matches well with the linear theory.

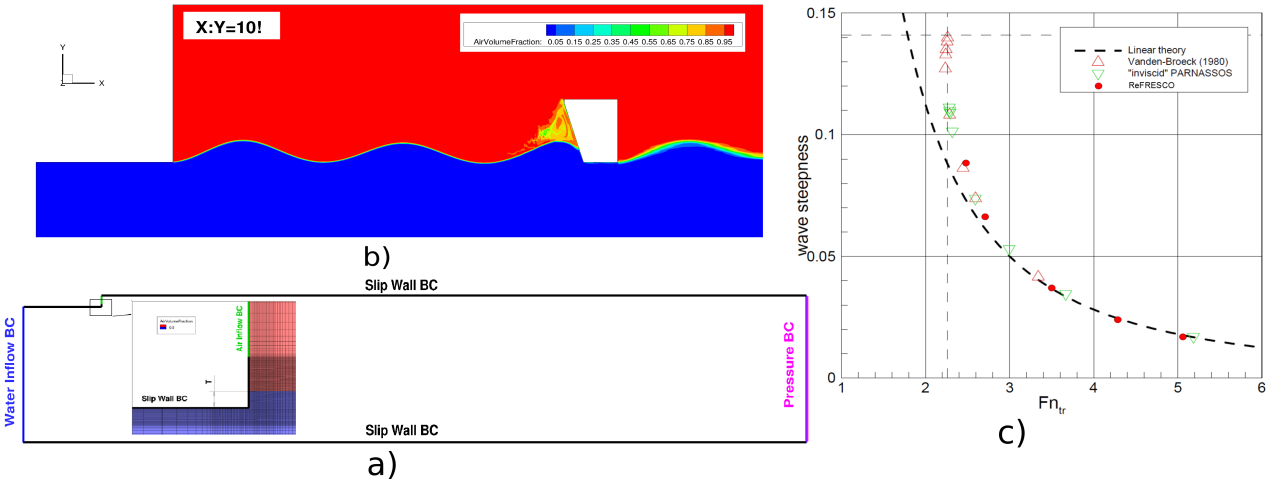

Figure 7: a) - The computational domain and boundary conditions for the backward-facing step. b) - The wave pattern in air chamber.

An air chamber is different from the backward-facing step by having a limited length of the free surface which at a certain location re-attaches to the ship's hull Figure 7(b). A fixed pressure in the chamber was set by the initial submergence depth T. Additional simulations with air chamber showed that the free-surface profile is similar to the one as in the BFS for the same velocity and submergence depth. However, in the air chamber at some velocity fluctuation of the wave amplitude was observed due to the instabilities in the closure part at certain re-attachment patterns. Also, the wave length can be influenced by the boundary layer build-up on the surface upstream of the chamber. But, in general, a good estimation of the wave length and amplitude in the air chamber can be done based on the linear theory for a certain velocity and pressure (submergence depth) in the chamber ($\lambda = 2\pi U^2/g$ and $A = \sqrt{2}T$).

4 Air cavity case

The air cavity is created on the flat plate by injecting air behind a cavitator that separates the flow. By injecting sufficient amount of air the cavity grows to its stable length that equals a half gravity wave length. The goal of this test case is to find out if the shape of a cavity can be computed correctly at given flow speed and injected air flow rate (not with a fixed air pressure as in the air chamber case).

4.1 Numerical set-up

A 2-D domain for the air cavity case and the used boundary conditions are shown in Figure 8 (G1). It has a rectangular shape 6x1.6m with the wall boundary condition on the top side, pressure boundary condition on the bottom, inflow and outflow boundary conditions on the left and right sides respectively. The cavitator of 1.5 by 0.5mm is located on the top side 2m away from the beginning of the domain. Additional appendage to

the domain behind the cavitator is used to introduce air into the flow (see Figure 8). The size of the air supply channel is 5 by 25mm. Air-water mixture leaves the domain on the right-hand side with the outflow BC. The domain is initialized with water/air content as shown in Figure 8.

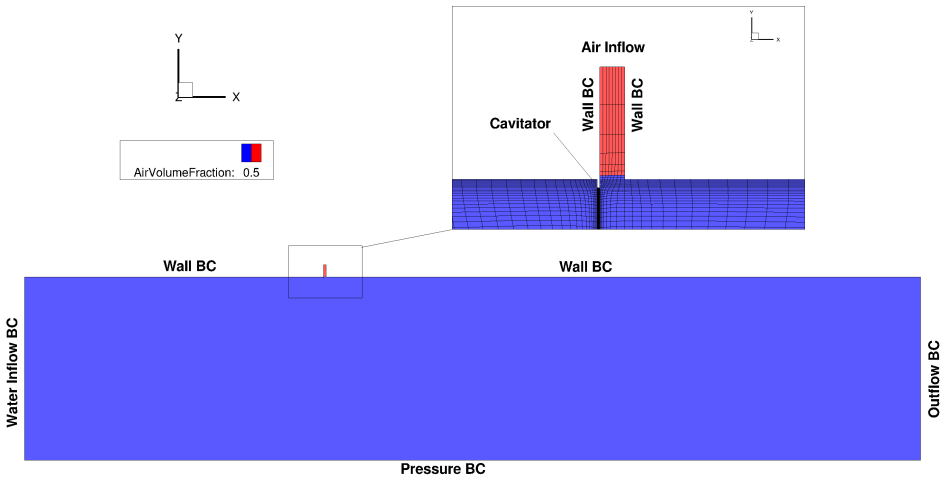

Grid	$cells$	y^+, avg
G1(2D)	90k	0.26
G2(3D)	0.32M	5.6
G3(3D)	1.8M	2.5
G4(3D)	3.6M	2.5
G5(3D)	5M	2.5

Figure 8: The computational domain and boundary conditions for air cavity case.

A set of four 3-D grids was created to study the 3-D effects and grid size dependency. The number of cells in each grid is G2=324k G3=1832k, G4=3664k, and G5=5039k. The boundary conditions were the same as in 2-D case, with the two additional faces of the 3-D domain having symmetry and wall boundary conditions.

4.2 Results

2-D unsteady simulations have been performed first. After initialization of the domain, water starts to flow from left to right and air is being injected behind the cavitator with the same inlet velocity as water and the cavity starts to grow. In this case the injection air flow rate exceeds the one that is escaping the cavity at the closure. As a result, the pressure in the cavity increases and the volume of the cavity grows as the simulation time goes on. The volume of the cavity increases by increasing the length and the thickness of the cavity. At some moment in time the cavity reaches the size of a stable cavity (Figure 9) when it should stop growing as air outflow should go to infinity after this point. But, it does not happen in our simulation at the given air injection flow rate. The balance of air flow occurs at much larger pressure and size of the cavity. Additional simulations show that the size of the cavity depends on the air flow rate, which should not be the case (as long as the flow rate is high enough to initiate the cavity, then the cavity should grow to its stable length according to the measurements).

It was found that the pressure and, as a result, the size of the cavity can not be simulated correctly at given air injection rate due to the fact that the air leakage from the end cavity is not modeled correctly with the used numerical approach. When applying the slip wall boundary condition to the wall the cavity grows even further.

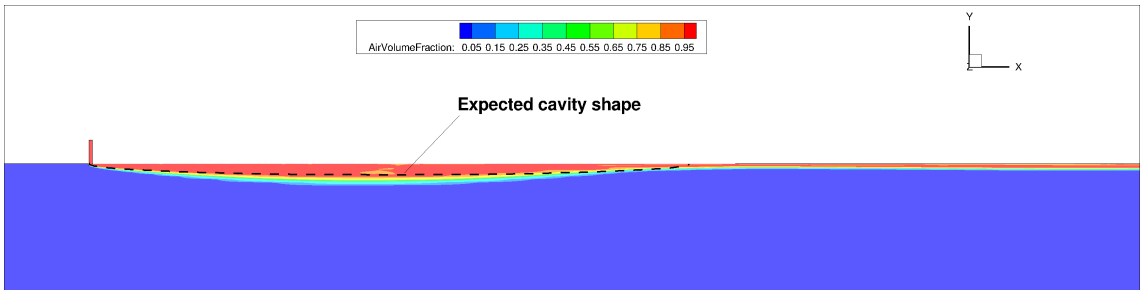

Figure 9: Developing air cavity that matches the expected length. Cavity size not at stable length. 2D.

Furthermore, it was checked if the 3-D simulation would improve the air leakage at the cavity closure. A developing cavity after 40 time steps (dt=0.005s) is shown in Figure 10 on different grids (view from the bottom). The cavity has a clear 3-D shape with some influence of the surface with the wall BC. On the finest grid the shape of the cavity looks realistic compared to the experiment.

Although the 3-D simulations slightly improve the air convection, it is still does not represent the air outflow from the cavity as it occurs in the experiments. The grid density variation did not show any significant effect

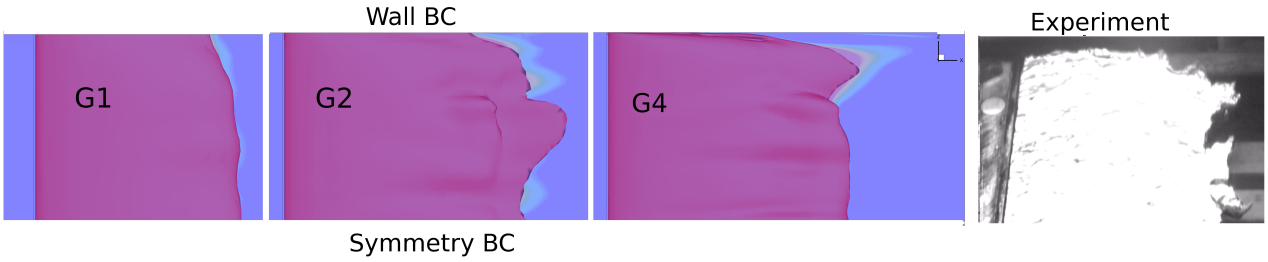

Figure 10: Developing air cavity (in red) on different grids: G1, G2 and G4 (bottom view). The flow from left to right.

on the air leakage within the varied grid density. Additional simulations were performed with a smaller air inflow velocity ($V_{air} = 0.1 \text{x} V_{water}$). In this case, for the given air flux, the length of the cavity was smaller than expected. As a result, the length of a cavity depends on the injected air flow rate and does not become stable at the length equal to half a gravity wave length. Because the air leakage is not modeled in the right way, the pressure does not establish correctly for a certain air injection rate. However, if we prescribe a correct air pressure as a boundary condition, then the shape of the free-surface is correct as same it was seen for the BFS and air chamber cases.

5 Conclusions and recommendations

In this paper it was investigated the application of the CFD for the drag reduction study on air lubrication. It was shown that the efficiency of the drag reduction by air cavities with a known geometry can be computed using the suggested simplifications. The results of the computations give detailed information on the local flow, confirming the presence of a region with high shear stress after the cavity.

The simulation results of the wave generated behind a backward facing step in the dry-transom regime is in a good agreement with the literature. For the air chambers the wave profile is similar to the one generated behind a backward facing step. A good estimation of the wave length and amplitude can be done based on the linear theory for a known velocity and air pressure.

The free-surface simulations of the air cavity with a prescribed air pressure in it, as same as for the BFS and air chamber flows, gives the right shape of the free surface. But, the air leakage from the closure of the cavity could not be correctly computed with the multi-phase homogeneous mixture VoF approach used in this work. As a result, the pressure in the cavity is difficult to establish correctly for a fixed air injection rate. Improving the volume fraction transport equation by adding a diffusion term could help to model the closure region more accurately. This deserves further investigation.

References

[1] Yu. Gorbachev and E. Amromin. Ship Drag Reduction by Hull Ventilation from Laval to Near Future: Challenges and Successes. *ATMA 2012*, 2012.

[2] O. Zverkhovskyi. Ship Drag Reduction by Air Cavities. *PhD thesis*, 2014.

[3] http://www.refresco.org.

[4] G. Vaz, F. Jaouen, and M. Hoekstra. Free-surface Viscous Flow Computations: Validation of URANS Code REFRESCO. 28th International Conference on Ocean, Offshore and Arctic Engineering (OMAE), Honolulu, Hawaii, May-June 2009.

[5] M. Kerkvliet. Influence of the Numerical Uncertainty of a Generic Submarine Model by Changing the Wall-Normal Distribution of the Wall-Bounded Grid Cells. *em 16th Numerical Towing Tank Symposium (NuTTS)*, Mulheim, Germany, September 2013.

[6] L. Eça and M. Hoekstra. A Procedure for the Eestimation of the Numerical Uncertainty of cfd Calculations Based on Grid Refinement Studies. *Journal of Computational Physics*, 104âĂŞ130, 2014.

[7] B. Starke and Raven H. Computation of Transom-Stern Flows Using a Steady Free-Surface Fitting RANS Method. 9th International Conference on Numerical Ship Hydrodynamics, Ann Arbor, Michigan, 2007.

CALL FOR PAPERS

19th Numerical Towing Tank Symposium (NuTTS'16)

St Pierre d'Oléron, France, 3-4 October 2016

Topics:

- Nonlinear flows around marine structures (LES, RANSE, Euler with or w/o free surface)
- Free-surface flows around marine structures (3-d ship seakeeping, free-surface viscous flows)
- Related topics (validation experiments, numerical techniques, grid generation, etc)

Deadlines:

Early feedback (optional):	30 March 2016
Extended Abstracts received:	1 July 2016
Payment received:	1 July 2016 (to be confirmed)

You are invited to participate in the above event. The objective of the event is to provide a forum for informal discussions among experts in the field and to disseminate latest results. Younger workers and Ph.D. students are especially encouraged to participate. The event will be held at the holiday village La Vieille Perrotine on the island of Oléron. All participants stay and have meals together to maximize interaction and discussion.

The extended abstracts of the proposed talk will be directly reproduced in pdf proceedings. Work in progress, encountered problems, etc. should be discussed in an open, informal atmosphere (no ties!) among colleagues. The first page of the extended abstract should be headed with the title and authors' names, affiliation and email address in a compact form to economize on space. Academic titles and page numbers shall be omitted. The extended abstract shall neither contain an abstract of the abstract, nor keywords, nor further headers. Font size shall be 11pt Times New Roman, except for title (14 pt). Extended abstracts should be limited to 6 pages in A4 format with 2.5 cm margin. An early reply will help us in organizing the event better. For the early feedback, a tentative title or topic will suffice.

The conference location can be easily reached by train from the major airports in France (bus transport from the nearest train station will be provided) but the number of trains per day is limited. To facilitate travel, the conference schedule has been altered with respect to previous NuTTS conferences: the arrival is on Sunday evening, with two full days of presentations on Monday and Tuesday, dinner on Tuesday night, and departure Wednesday morning.

Following the tradition of previous NuTTS events, the fees will be kept low to allow a maximum number of scientists to attend. The registration fees including accommodation (3 nights) and all meals during the symposium will be:

350 Euro PhD candidates and students
400 Euro authors
450 Euro other participants

Contact: Jeroen Wackers
jeroen.wackers@ec-nantes.fr

Sponsors: To be announced